RECENT ADVANCES in MECHANICS, MECHATRONICS and CIVIL, CHEMICAL and INDUSTRIAL ENGINEERING

Proceedings of the 2015 International Conference on Civil Engineering (CIVILENG 2015)
Proceedings of the 2015 International Conference on Continuum Mechanics (COME 2015)
Proceedings of the 2015 International Conference on Industrial Engineering (INDE 2015)
Proceedings of the 2015 International Conference on Materials (MATERIALS 2015)
Proceedings of the 2015 International Conference on Mechatronics and Robotics, Structural Analysis (MEROSTA 2015)
Proceedings of the 2015 International Conference on Chemistry and Chemical Engineering (CCE 2015)

Zakynthos Island, Greece
July 16-20, 2015

RECENT ADVANCES in MECHANICS, MECHATRONICS and CIVIL, CHEMICAL and INDUSTRIAL ENGINEERING

Proceedings of the 2015 International Conference on Civil Engineering (CIVILENG 2015)
Proceedings of the 2015 International Conference on Continuum Mechanics (COME 2015)
Proceedings of the 2015 International Conference on Industrial Engineering (INDE 2015)
Proceedings of the 2015 International Conference on Materials (MATERIALS 2015)
Proceedings of the 2015 International Conference on Mechatronics and Robotics, Structural Analysis (MEROSTA 2015)
Proceedings of the 2015 International Conference on Chemistry and Chemical Engineering (CCE 2015)

Zakynthos Island, Greece
July 16-20, 2015

All papers of the present volume were peer reviewed by no less than two independent reviewers. Acceptance was granted when both reviewers' recommendations were positive.

Series: Mathematics and Computers in Science and Engineering Series | 49

ISSN: 2227-4588
ISBN: 978-1-61804-325-2

RECENT ADVANCES in MECHANICS, MECHATRONICS and CIVIL, CHEMICAL and INDUSTRIAL ENGINEERING

Proceedings of the 2015 International Conference on Civil Engineering (CIVILENG 2015)
Proceedings of the 2015 International Conference on Continuum Mechanics (COME 2015)
Proceedings of the 2015 International Conference on Industrial Engineering (INDE 2015)
Proceedings of the 2015 International Conference on Materials (MATERIALS 2015)
Proceedings of the 2015 International Conference on Mechatronics and Robotics, Structural Analysis (MEROSTA 2015)
Proceedings of the 2015 International Conference on Chemistry and Chemical Engineering (CCE 2015)

Zakynthos Island, Greece
July 16-20, 2015

Organizing Committee

Editor:
Prof. Imre J. Rudas, Obuda University, Hungary

Associate Editor:
Prof. Dora Foti

Program Committee:
Prof. Bharat Doshi, John Hopkins University, Mayrland, USA
Prof. Gang Yao, University of Illinois at Urbana - Champaign, USA
Prof. Lu Peng, Luisian State University, Baton Rouge, LA, USA
Prof. Y. Baudoin, Royal Military Academy, Brussels, Belgium
Prof. Fotios Rigas, School of Chemical Engineering, National Technical University of Athens, Greece.
Prof. S. Sohrab, Northwestern University, IL, USA
Prof. A. Stamou, National Technical University of Athens, Greece
Prof. A. I. Zouboulis, Dept. of Chemistry, Aristotle University of Thessaloniki, Greece
Prof. Z. A. Vale, ISEP - Instituto Superior de Engenharia do Porto Rua Antonio Bernardino de Almeida, Portugal
Prof. M. Heiermann, Dr., Department of Technology Assessment and Substance Flow, Potsdam, Germany
Prof. I. Kazachkov, National Technical University of Ukraine (NTUU KPI), Kyiv, Ukraine
Prof. A. M.A. Kazim, UAE University, United Arab Emirates
Prof. A. Kurbatskiy, Novosibirsk State University, Department of Physics, Russia
Prof. S. Linderoth, Head of Research on Fuel Cells and Materials Chemistry at Riso National Laboratory. Denmark
Prof. P. Lunghi, Dipartimento di Ingegneria Industriale, University degli Studi di Perugia, Italy
Prof. J. Van Mierlo, Department of Electrotechnical Engineering and Energy Technology (ETEC) Vrije Universiteit Brussel, Belgium
Prof. Pavel Loskot, Swansea University, UK
Prof. N. Afgan, UNESCO Chair Holder, Instituto Superior Tecnico, Lisbon, Portugal
Prof. F. Akgun, Gebze Kocaeli, Turkey
Prof. Fernando Alvarez, Prof. of Economics, University of Chicago, USA
Prof. Mark J. Perry, Prof. of Finance and Business Economics, University of Michigan-Flit, USA
Prof. Biswa Nath Datta, IEEE Fellow, Distinguished Research Prof., Northern Illinois University, USA
Prof. Panos Pardalos, Distinguished Prof. Director, Center for Applied Optimization, University of Florida, USA
Prof. Gamal Elnagar, University of South Carolina Upstate,Spartanburg, SC, USA
Prof. Luis Tavares Rua, Cmte Guyubricht, 119. Conj. Jardim Costa do Sol. Atalaia, Brazil
Prof. Igor Kuzle, Faculty of electrical engineering and computing, Zagreb, Croatia
Prof. Maria do Rosario Alves Calado, University of Beira Interior, Portugal
Prof. Gheorghe-Daniel Andreescu, "Politehnica" University of Timisoara, Romania
Prof. Jiri Strouhal, University of Economics Prague, Czech Republic
Prof. Morris Adelman, Prof. of Economics, Emeritus, MIT, USA
Prof. Germano Lambert-Torres, Itajuba,MG, Brazil
Prof. Jiri Klima, Technical faculty of CZU in Prague, Czech Republic
Prof. Goricanec Darko, University of Maribor, Maribor, Slovenia
Prof. Ze Santos, Rua A, 119. Conj. Jardim Costa do Sol, Brazil
Prof. Ehab Bayoumi, Chalmers University of Technology,Goteborg, Sweden
Prof. Robert L. Bishop, Prof. of Economics, Emeritus, MIT, USA
Prof. Glenn Loury, Prof. of Economics, Brown University, USA
Prof. Patricia Jota, Av. Amazonas 7675, BH, MG, Brazil
Prof. S. Ozdogan, Marmara University, Goztepe Campus, Kuyubasi, Kadikoy, Istanbul, Turkey
Prof. Zhuo Li, Beijing University Of Technology, Beijing, China
Prof. Pradip Majumdar, Northern Illinois University, Dekalb, Illinois, USA

Additional Reviewers

Bazil Taha Ahmed	Universidad Autonoma de Madrid, Spain
James Vance	The University of Virginia's College at Wise, VA, USA
Sorinel Oprisan	College of Charleston, CA, USA
M. Javed Khan	Tuskegee University, AL, USA
Jon Burley	Michigan State University, MI, USA
Xiang Bai	Huazhong University of Science and Technology, China
Hessam Ghasemnejad	Kingston University London, UK
Angel F. Tenorio	Universidad Pablo de Olavide, Spain
Yamagishi Hiromitsu	Ehime University, Japan
Imre Rudas	Obuda University, Budapest, Hungary
Takuya Yamano	Kanagawa University, Japan
Abelha Antonio	Universidade do Minho, Portugal
Andrey Dmitriev	Russian Academy of Sciences, Russia
Valeri Mladenov	Technical University of Sofia, Bulgaria
Francesco Zirilli	Sapienza Universita di Roma, Italy
Ole Christian Boe	Norwegian Military Academy, Norway
Masaji Tanaka	Okayama University of Science, Japan
Jose Flores	The University of South Dakota, SD, USA
Kazuhiko Natori	Toho University, Japan
Matthias Buyle	Artesis Hogeschool Antwerpen, Belgium
Frederic Kuznik	National Institute of Applied Sciences, Lyon, France
Minhui Yan	Shanghai Maritime University, China
Eleazar Jimenez Serrano	Kyushu University, Japan
Konstantin Volkov	Kingston University London, UK
Miguel Carriegos	Universidad de Leon, Spain
Zhong-Jie Han	Tianjin University, China
Francesco Rotondo	Polytechnic of Bari University, Italy
George Barreto	Pontificia Universidad Javeriana, Colombia
Moran Wang	Tsinghua University, China
Alejandro Fuentes-Penna	Universidad Autónoma del Estado de Hidalgo, Mexico
Shinji Osada	Gifu University School of Medicine, Japan
Kei Eguchi	Fukuoka Institute of Technology, Japan
Philippe Dondon	Institut polytechnique de Bordeaux, France
Dmitrijs Serdjuks	Riga Technical University, Latvia
Deolinda Rasteiro	Coimbra Institute of Engineering, Portugal
Stavros Ponis	National Technical University of Athens, Greece
Tetsuya Shimamura	Saitama University, Japan
João Bastos	Instituto Superior de Engenharia do Porto, Portugal
Genqi Xu	Tianjin University, China
Santoso Wibowo	CQ University, Australia
Tetsuya Yoshida	Hokkaido University, Japan
José Carlos Metrôlho	Instituto Politecnico de Castelo Branco, Portugal

Table of Contents

Plenary Lecture 1

Efficient Jet Noise Simulations

Professor Anastasios Lyrintzis
Distinguished Professor and Chair
Aerospace Engineering
Embry-Riddle Aeronautical University
Daytona Beach, FL
E-mail: lyrintzi@erau.edu

Abstract: Jet noise is an important issue concerns for people living or working in the vicinity of airports, stringent noise regulations, and military operational requirements. Processing speeds and memory limitations of existing supercomputers limit the faithfulness of these simulations. Thus the simulations are not accurate enough to allow design and testing of noise reduction strategies. In order to simulate realistic situations very fine grids (e.g. on the order of tens of billions of points) are sometimes needed, requiring significant computational resources. Thus very efficient algorithms are needed. An efficient, petascalable code has been developed based on the large eddy simulation (LES) technique. The code is a high-order multi-block structured solver capable of simulating both subsonic jets and supersonic jets with shock waves. Recent advancements have targeted improved prediction accuracy by enabling inclusion of nozzle geometries in simulations. A digital filter-based approximate turbulent inflow boundary condition is used. A wall model is employed in the nozzle walls to save computational time. Finally, a ghost-point-based immersed boundary method is implemented to allow simulation of complex nozzle shapes that show promise of noise reduction, e. g. chevrons, lobed mixers, beveling, and corrugations. We will show validation efforts and summarize future research directions.

Brief Biography of the Speaker: Dr. Lyrintzis' primary research interests are in the area numerical methods with applications in aerodynamics and aeroacoustics. His research endeavors have been supported by NSF, NASA, ARO, the US Navy and other agencies and industries. He has co-authored more than 180 refereed articles and he has advised 18 Ph.D. students. It should be noted that 7 of Dr. Lyrintzis' advisees are Professors at Universities and one has received the NSF CAREER award. Dr. Lyrintzis is an AIAA Associate Fellow, an ASME Fellow, and a Boeing Welliver Fellow. He has been a member of the AIAA Aeroacoustics Technical Committee (vice-chair 05-07, chair 07-09), the AHS Acoustics Committee, and the ASME Coordinating Group for CFD. He has co-organized the 10th AIAA/CEAS Aeroacoustics Conference, Manchester, UK, as well as many Sessions and Forums in AIAA, ASME and AHS Conferences and he is currently an Associate editor for the AIAA Journal and the International Journal of Aeroacoustics. Finally, Dr. Lyrintzis has participated in the development of award-winning (American Helicopter Society, Howard Hughes Award, NASA Group Achievement Award) TRAC (TiltRotor Aeroacoustic Codes) system of codes from NASA Langley.

ISBN: 978-1-61804-325-2

Curved-Crease Origami-Inspired Footbridge:

The Structural and Aesthetic Influence of Aperture Patterns

Luca Nagy, Landolf Rhode-Barbarigos, and Sigrid Adriaenssens

Abstract**—**Origami, the craft of folding paper, has been a source of inspiration for developable systems in various engineering disciplines, as it results in lightweight and stiff structures. In this design study, a single-crease arc is employed as driver for the design of a 56m carbonfiber-foam composite footbridge system. The design concept of the origami-inspired footbridge is enhanced with aperture patterns in the walls of the cross-section. Apertures provide ventilation, natural lighting and views, while achieving an aesthetic design intent. Aperture patterns are created parametrically by varying the number of cutouts, their shape, orientation and size, whether aperture rows are stacked or staggered, and in case of polygonal cutouts, the number of vertices and the corner-fillet radius. Six patterns, selected to align with conventional truss typologies (Pratt, Town lattice, Vierendeel), are investigated using Finite Element analysis. This selection ensures structural soundness, and helps follow recommendations regarding aesthetics in bridge design discussed by bridge designers Christian Menn and Fritz Leonhardt. The structural impact of the aperture patterns is evaluated according to AASHTO footbridge design-code. The curved-crease origami footbridge with the Pratt truss-like aperture pattern is found to meet the controlling AASHTO deflection limit with the lowest volume of material, suggesting higher structural efficiency.

Keywords**—** origami, curved crease, footbridge, design, aperture patterns.

I. Introduction

ORIGAMI can be used to design developable three dimensional shapes and stiffened structures due to folding planes. Curved-crease origami was first explored for artistic purposes during the Bauhaus (1919-1933, Germany) by Josef Albers [1]. In his preliminary course on Paper Study in 1927-28, he and his students created sculptures by folding paper along curves instead. Since then several artists used curved crease origami to create sculptures from paper and other sheet materials. Similar to traditional straight-crease origami, curved-crease origami creates three dimensional shapes made of developable surfaces. However, curved-crease folding reflects a hybrid of both folding and bending of its surfaces [2-4].

The goal of this paper is to investigate a curved-crease origami-inspired footbridge concept from a structural and aesthetic perspective, using cutout patterns in the walls of the closed cross-section. To achieve this goal, Section 2 presents the design of the curved-crease origami-inspired footbridge. Section 3 describes the method of aperture pattern generation, and the aesthetic and structural impact of selected patterns. Finally, Section 4 presents the conclusions of this study.

Luca Nagy was with Princeton University, Princeton NJ, USA and is now with the University of Toronto, Toronto ON, Canada (email: luca.nagy@mail.utoronto.ca). Landolf Rhode-Barbarigos, was with Princeton University, Princeton NJ, USA and is now with the University of Miami, Coral Gables FL, USA (email: landolfrb@miami.edu). Sigrid Adriaenssens is with Princeton University, Princeton NJ, USA (phone: 609-258-4661; e-mail: sadriaen@princeton.edu).

II. Design of a Curved-Crease Origami-Inspired Footbridge Structure

A. Description of the Footbridge Structure

The proposed footbridge system is composed of two single curved 40 m radius arcs, approximated with a segmented design. The two arcs connect in plane forming an S-shaped 56 m span beam. The S-shape geometry of the beam enhances its structural behavior by increasing the horizontal stiffness against wind and other lateral loads. Moreover, a change in length due to temperature results in a slight change of the S-shape curvature instead of longitudinal stresses in the entire beam. Fig. 1 shows a schematic drawing, while Fig. 2 shows technical drawings of the footbridge. The S-shaped beam is assumed fixed at each end and a deck width of 4 m complying with footbridge design codes [5] is assumed.

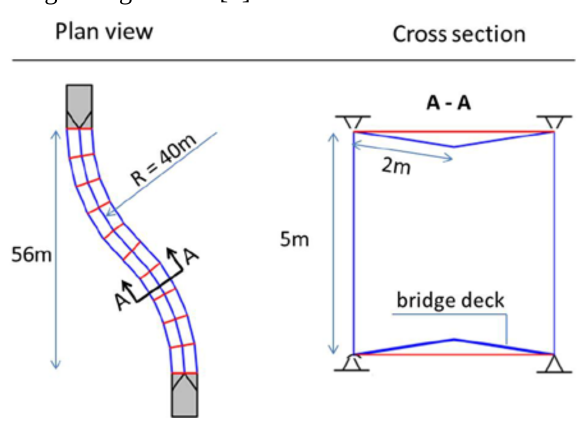

Fig. 1: Schematic drawing of the curved-crease origami-inspired movable footbridge design.

In cross-sectional view, the curved-crease origami-inspired footbridge has an innovative tubular profile with creases implemented on its top and bottom flanges. Two single-crease plates, inclined at a 15° angle, form the flanges of the girder section (see Fig. 1). Avoiding a flat geometry increases in-plane flexural stiffness of the flange supporting the deck structure. Flanges are connected with 5 m tall planar vertical webs. Webs and flanges are divided into the same number of quadrilateral segments. This cross-section with a single curved-crease in its flanges has substantial flexural and torsional stiffness.

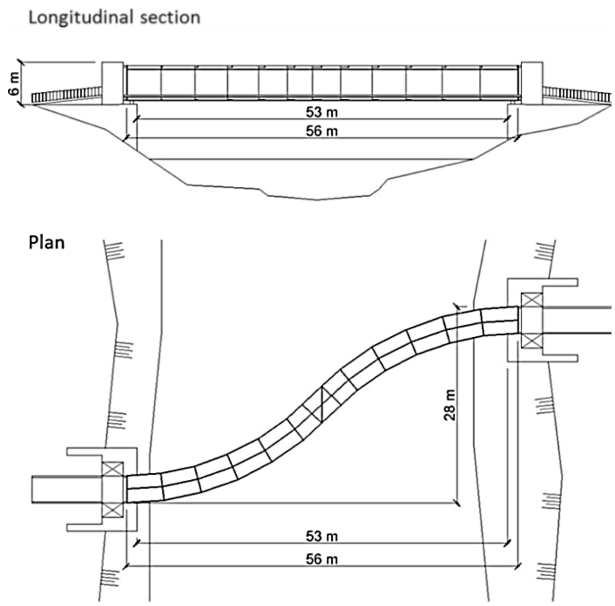

Fig. 2: Longitudinal cross-section and plan of the footbridge design.

B. Finite Element Analysis of the Curved-Crease Origami-Inspired Movable Footbridge

In the finite element (FE) analysis, the panels composing the curved-crease origami-inspired footbridge are assumed to be made of a carbon fiber-foam composite material. Carbon fiber-foam has been successfully used before in civil engineering applications [6-7] offering high strength and low weight compared to traditional engineering materials [8-12]. The selected composite is a 65 mm thick sandwich material, with two layers of carbon-fiber on the outside and a layer of foam in the middle. Carbon-fiber layers carry the bending forces, while the foam layer is inserted in between to increase the second moment of inertia for the material. A linear elastic behavior is assumed in this study. Material properties are based on information provided by commercially available products from DragonPlate [13] and are presented in Table 1. Internal stiffeners (created by changing the ratio of materials in the carbonfiber-foam composite) are assumed so that local plate buckling does not occur. Static analyses and sizing are performed according to AASHTO codes [5, 14-15]. Linear static analysis is performed in the FE software AXIS [16]. The dynamic behavior of the structure is outside the scope of this research.

Table 1: Material properties for the carbon-fiber and foam composite

Material property	Value
Volumetric weight	$\rho = 200$ kg/m³
Modulus of elasticity	$E = 2250$ N/mm²
Design strength (Tensile, compressive, shear)	$f_y = 250$ N/mm²
Poisson ratio	$\nu = 0.3$
Coefficient of thermal expansion	$\alpha_T = 4.5$ 10-5 1/°C

The analysis of the structure is conducted with a pedestrian load of 4.3 kN/m² (90 psf) in addition to the self-weight of 1.15 kN/ m2 (24 psf, calculated per plan area), and the weight of the carbon-fiber sandwich material deck of 0.5 kN/m2 (10.5 psf). Loads and load combinations are assembled according to AASHTO guidelines [15]. Wind loads and temperature are also considered, however, combinations involving these loads do not control design. Snow and other loads are not considered in this preliminary design.

The design of the curved-crease origami-inspired footbridge is deflection controlled as maximum stresses in the carbon-fiber sandwich panels do not exceed 150 N/mm2 or 60% of the design yield stress of the carbon-fiber sandwich material in any load combination. For the evaluation of deflection, the L / 360 = 155 mm limit [5] is employed. A camber equal to the deflection from dead load is assumed. Therefore, the deflection limit applies to the deflection resulting from service loads. The 5 m overall height of the cross-section and the 65 mm wall thickness are both determined by this deflection limit.

III. Aesthetic Considerations and Their Influence on the Design

The design of the curved-crease origami-inspired footbridge is enhanced by aesthetic considerations, staying true to its origins in art. The closed cross sectional profile requires the implementation of openings to allow air and light inside in the structure, and to improve the experience of pedestrians walking across the bridge. Cutouts in the walls provide thus an opportunity for the implementation of aesthetic considerations in the design process.

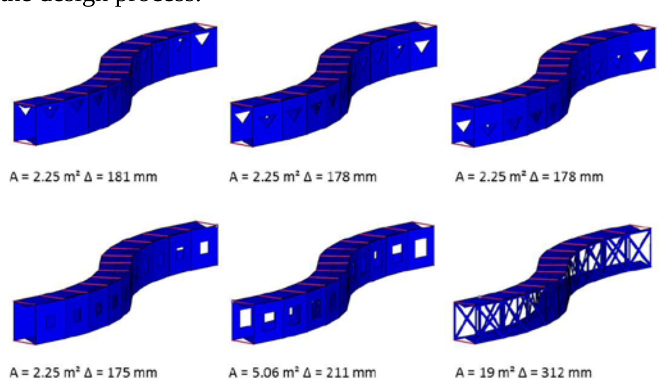

Fig. 3: Preliminary Finite Element study of cutout shapes.

Preliminary FE analyses on selected cutouts, such as triangles and squares, revealed that the location and shape of the cutouts have little effect on the maximum midspan deflection (Δ) under self-weight and uniform pedestrian load (see Fig. 3). The determining factor of the maximum deflection is the cumulative aperture area (A) for each segment. Therefore, apertures can be designed freely regarding shape, following aesthetic considerations.

In this study, apertures have multiple functions. First, they serve for ventilation and natural lighting. This goal is the easiest one to meet, as the number of cutouts employed is assumed to be sufficient. Second, the selected pattern should express some aspect of how the bridge functions. Third, apertures should have an overall aesthetically pleasing effect. The second and third goals are discussed in further detail.

To meet the second goal, aperture patterns are designed to reflect the way the curved-crease origami-inspired footbridge functions. Since material is removed from the walls only, the relevant internal forces are the shear forces (see Fig. 4). Shear forces resulting from a bending moment have a value of zero at midspan, and increase towards the two fixed supports of the structure. Therefore, to express the main forces the walls of the structure carry, the aperture pattern progresses similarly, with more removed area towards midspan, and less at the supports.

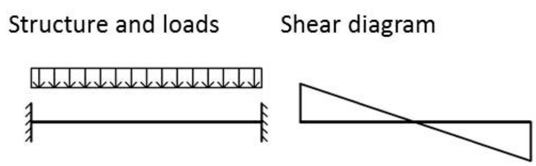

Fig. 4: Shear force diagrams.

The third goal of creating an aesthetically pleasing structure is defined with the help of Fritz Leonhardt, a German engineer who wrote on aesthetics in design. He claimed that the truism that ‘there is no accounting for taste’ is only valid if aesthetics are not studied [17]. Once they are, several guidelines emerge that can guide an engineer to fulfil the sometimes ignored functions of structures to be “comfortable”, “beautiful”, or “cozy”, in addition to safe and economical. In addition to Leonhardt, Christian Menn [18] also outlined aesthetic guidelines for bridge design. The main points that both agree on are slenderness, lightness or transparency, order or regularity (including symmetry, and aesthetic homogeneity), and integration into the environment.

Footbridge design tends to have more leeway on aesthetic rules due to its smaller scale, which allows more “play” with design without becoming too uneconomical. Therefore, the footbridge design looks to incorporate some, but not all, of the aesthetic guidelines by these structural designers. The aperture pattern is designed to have an ordered feel with symmetry and proportionality, but occasionally might violate rules such as limiting the direction of lines to no more than three [17], or simplicity [18]. The pattern generation method detailed below allows for the creation of a nearly unlimited number of designs, even with the guidelines described above. The number of possible patterns is reduced by focusing on designs that resemble to traditional structural designs and thus reflect Leonhardt’s and Menn’s guidelines. These traditional structure types are the Pratt truss, the Town lattice truss, and the Vierendeel truss (Fig. 5).

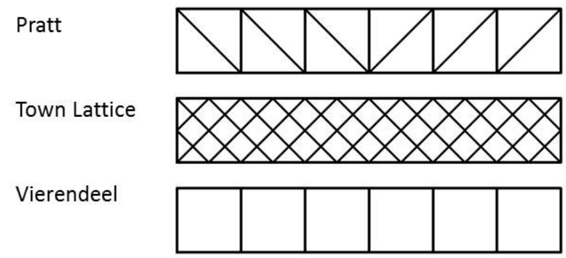

Fig. 5: Traditional truss types used for the aperture design.

A. Aperture Pattern Generation

Patterns are generated using parametric geometry definition in Grasshopper, and extension of Rhinoceros 5.0 [19-20]. Pattern generation is implemented so that cutout parameters could be varied separately for each panel. The parameters to be varied are the number of cutouts (length of array in the horizontal and vertical direction), the shape and size of cutouts, in case of polygonal cutouts, the number of vertices, the corner fillet radius (used to avoid sharp corners that would create stress concentrations), the orientation of the cutout shapes, and whether the rows are stacked or staggered. For examples of how each parameter can be varied, see Fig. 6-10.

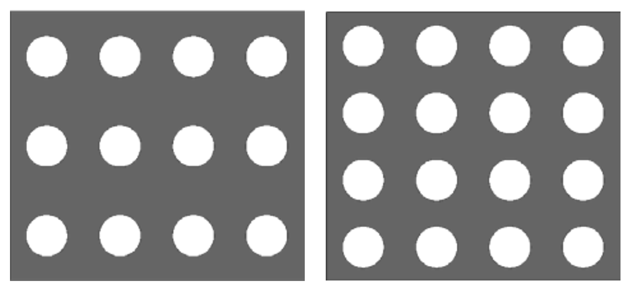

Fig. 6: Panels with different (4x3 versus 4x4) cutout arrays.

Fig. 7: Panels with different cutout sizes.

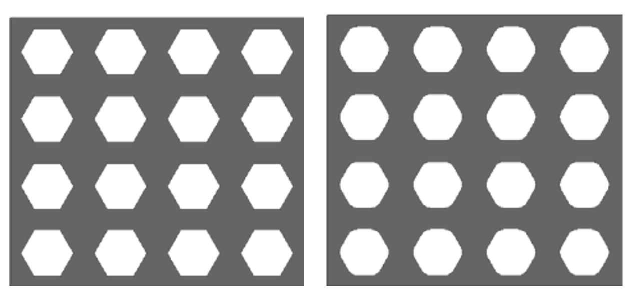

Fig. 8: Panels without (left) and with (right) filleted corners.

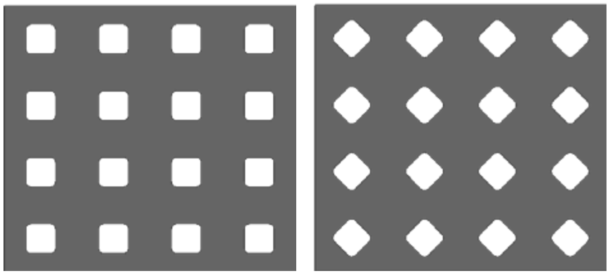

Fig. 9: Patterns with different rotation angles.

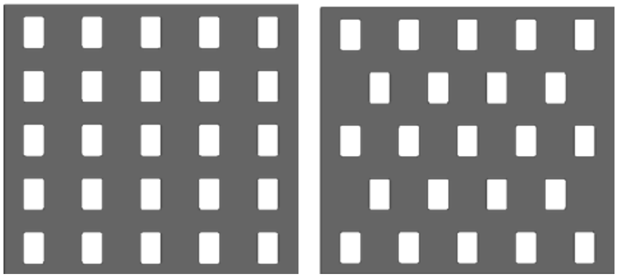

Fig. 10: Patterns with stacked (left) or staggered (right) cutouts.

The six patterns selected in this study are aligned with a traditional type of truss structure - a Pratt truss, a Town lattice truss, or the Vierendeel truss - or their combinations. These patterns also meet the three main design goals detailed earlier. They offer sufficient ventilation and natural light, they express the shear forces in the cross section walls, and they follow the crucial aesthetic guidelines that both Menn and Leonhardt agree on for bridge design. Fig. 11-16 show the side view of one half of the bridge (due to the curved shape of the bridge, panels in a side view appear to slightly shorter towards the middle, even though their dimensions are constant). The cutout pattern is then mirrored.

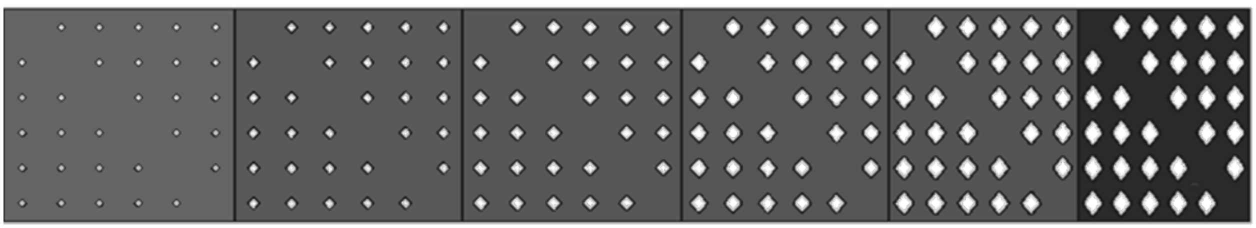

Fig. 11: Pratt truss-like cutout pattern.

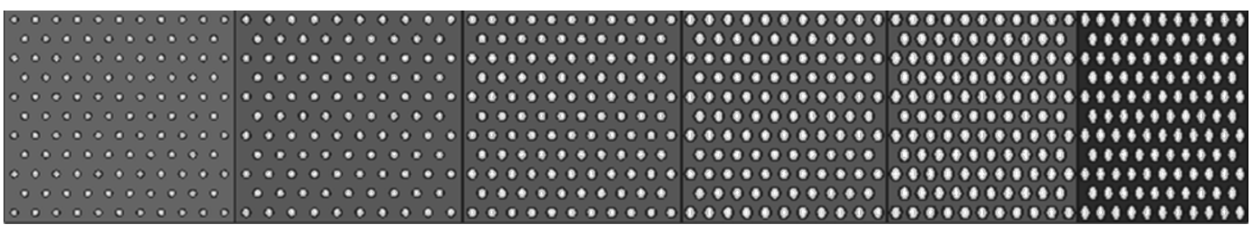

Fig. 12: Lattice truss-like pattern.

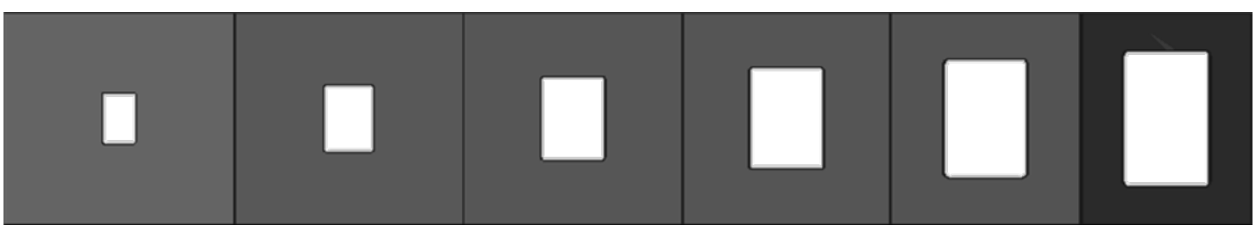

Fig. 13: Vierendeel truss-like pattern.

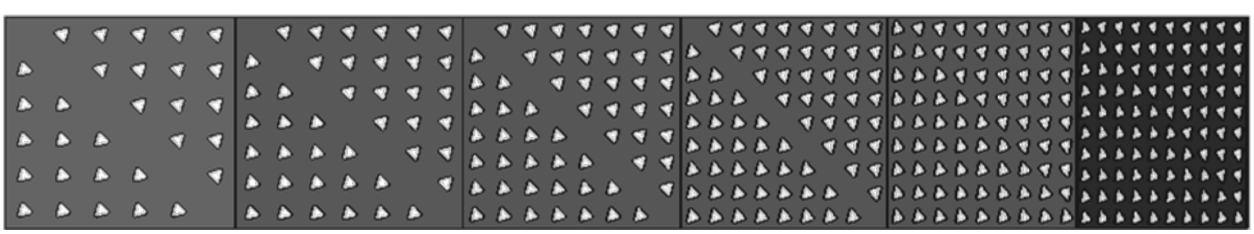

Fig. 14: Pratt to lattice truss pattern.

ISBN: 978-1-61804-325-2

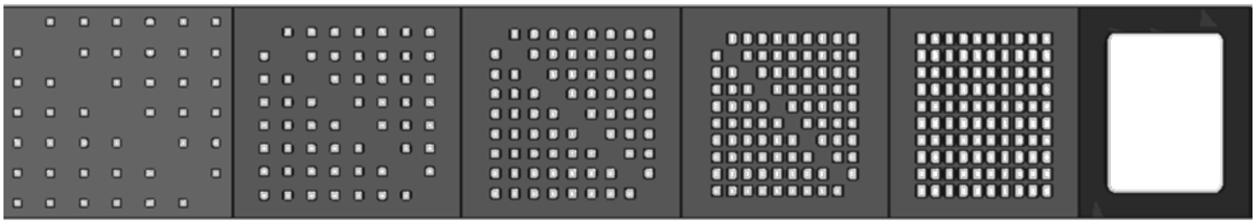

Fig. 15: Pratt to Vierendeel truss pattern.

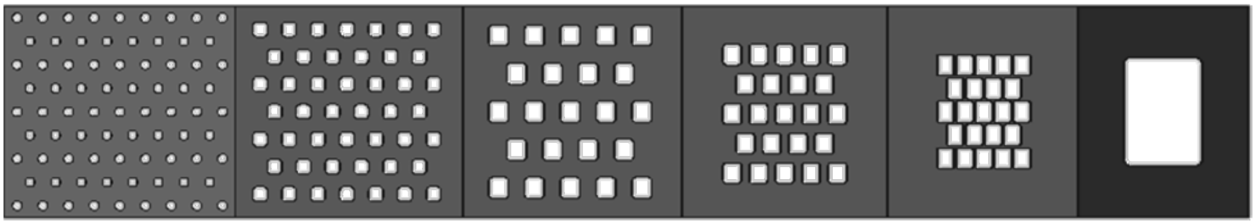

Fig. 16: Lattice to Vierendeel truss pattern.

B. Analysis of Selected Patterns

The selected six aperture designs are analyzed using AXIS Finite Element software [9]. Designs are compared to each other and to the original configuration of the structure without cutouts, using the total volume of carbonfiber-foam composite material required to meet the deflection requirement. These designs are controlled by deflection, as the stresses do not exceed 150 kN/mm2, staying well below the allowed design strength. The design of the structure remains deflection controlled even with added cutouts. The analysis is performed by keeping a fixed thickness (90mm) for the flanges, and modifying wall thickness between the different designs until the deflection limit (L/360) is met (see Table 2). Wall thicknesses are adjusted at 5 mm steps, since a design more exact than that may not be reliably met by the available construction methods. Therefore, net deflection values vary within a range of 6 mm (from 148 mm to 154 mm), but still remain within the deflection limit.

Table 2: Total required carbonfiber volume to meet the 155 mm deflection limit, assuming different flange (deck support and roof) and web (wall) thickness. Net deflection is defined after camber equal to the deflection under dead load.

	Thickness [mm]	Max. Deflection [mm]			CF-foam vol. [m³]
		Dead Load	Live+Dead Load	Net	
Original configuration (no cutouts)	40	55	203	148	70.24
Pratt (Fig. 11)	50	58	212	154	69.51
Lattice (Fig. 12)	60	58	210	152	73.76
Vierendeel (Fig. 13)	60	57	208	151	76.47
Pratt to Lattice (Fig. 14)	60	58	208	150	74.06
Pratt to Vierendeel (Fig. 15)	80	59	211	152	82.55
Lattice to Vierendeel (Fig. 16)	65	59	213	154	76.28

It is also shown that only the Pratt aperture design (see Fig. 17) performs better than the other patterns, as well as the original design (without apertures). However, using variable wall thicknesses across the segments, or using more advanced optimization techniques, other aperture patterns could lead to a more efficient aperture pattern.

IV. Conclusion

In this paper, the design of a curved-crease origami-inspired footbridge is enhanced by adding aperture patterns. Apertures are employed to provide ventilation and natural lighting, while expressing structural function and highlighting the artistic origins of the origami-inspired system. Aperture patterns are inspired by the traditional truss types of the Pratt (diagonal) truss, the Town lattice truss, and the Vierendeel truss, as well as their combinations. Analyses reveal that the Pratt aperture pattern performs better than the original design (without cutouts) and other patterns, minimizing the total volume of carbonfiber-foam composite material volume required to meet the deflection limit. The structural impact of aperture patterns in the walls of the curved, closed cross-section footbridge can be attributed to the total removed area remaining thus largely independent of cutout shape and location. Therefore, the aperture designs can be used for the expression of how the structure functions, or to meet purely aesthetic goals.

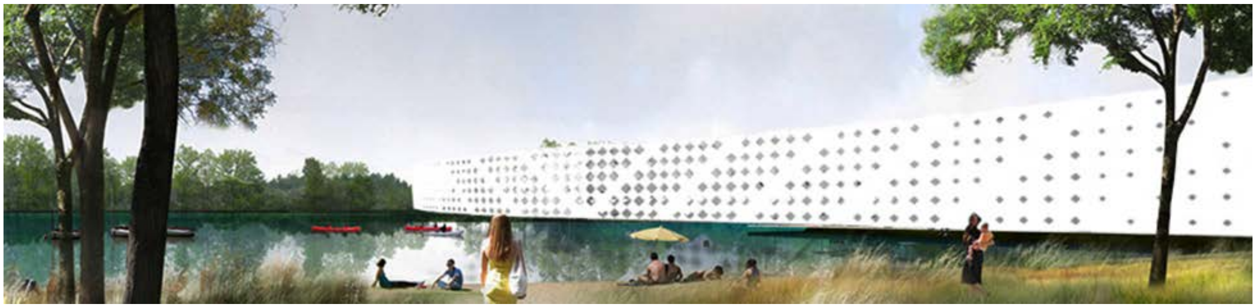

REFERENCES

[1] Wingler, Hans. Bauhaus: Weimar, Dessau, Berlin, Chicago. Boston: MIT Press, 1969.

[2] Tachi, Tomohiro, and Gregory Ebbs. "Designing One-Dof Mechanisms for Architecture by Rationalizing Curved Folding " In International Symposium on Algorithmic Design for architecture and Urban Design. Tokyo, Japan, 2011.B. Smith, "An approach to graphs of linear forms (Unpublished work style)," unpublished.

[3] Tachi, Tomohiro, Matrin L. Demaine, Erik L. Demaine, Duks Koschitz. "Curved Crease Folding: A Review of Art, Design and Mathematics." IABSE-IASS Symposium: Taller, Longer, Lighter, London, England, Sep 20-23, 2011.

[4] BARNES M., ADRIAENSSENS S., KRUPKA M., "A novel torsion/bending element for dynamic relaxation modeling", Computers and Structures, 19 (1), 2013, pp 60–67.

[5] AASHTO. "LRFD Guide Specifications for Design of Pedestrian Bridges, 2nd Edition." Washington, DC., 2009.C. J. Kaufman, Rocky Mountain Research Lab., Boulder, CO, private communication, May 1995.

[6] Anon. 2011. "Carbon Composite Pedestrian Bridge Installed in Madrid." Reinforced Plastics 55, no. 3 (2011): 43-44.M. Young, *The Techincal Writers Handbook.* Mill Valley, CA: University Science, 1989.

[7] Kendall, David. "Opportunities in Composites: Fiber Reinforced Polymer (FRP) Composite Bridges." edited by National Composites Network, 2004.

[8] TYSMANS T., ADRIAENSSENS S., CUYPERS H., WASTIELS J., "Structural Analysis of small span Textile Reinforced Concrete Shells with Double Curvature", Composites Science and Technology, Vol. 69, No. 11-12, 2009, pp. 1790 – 1796

[9] CAUBERD N., TYSMANS T., ADRIAENSSENS S., WASTIELS J., MOALLERT M., BELKASSEN B., "Shells elements of textile reinforced concrete using fabric formwork: a case study", Advances in Structural Engineering, Vol. 15, No. 4, 2012, pp. 677 – 689.

[10] RICHARDSON J.N., ADRIAENSSENS S., COELHO R.F., BOUILLARD P., "Coupled form finding and grid optimization approach for single layer gridshells", Engineering Structures, Vol. 52, 2013, pp. 230–239.

[11] ADRIAENSSENS S., NEY L., BODARWE E., WILLIAMS C., "Finding the form of an irregular meshed steel and glass shell based on construction constraints" Journal of Architectural Engineering. Vol. 18, No. 3, 2012, pp.206-213.

[12] ADRIAENSSENS S., "Feasibility study of medium span spliced spline stressed membranes", International Journal of Space Structures, Vol. 23, No. 4, 2008, p. 243-251.

[13] Allred, and Associates Inc. 2014 "Dragonplate Carbon Fiber Structural Components." Accessed: February 10. http://dragonplate.com/default.asp

[14] AASHTO. "Movable Highway Bridge Design Specifications." Washington, DC., 2007.

[15] AASHTO. "LRFD Bridge Design Specifications." Washington, DC., 2010.

[16] Galea (2013) Axis Vm 11. Inter-CAD Kft.

[17] Leonhardt, F., The Significance of Aesthetics in Structures. Journal of the International Association for Bridge and Structural Engineering, 1985. 96(2): 74-76.

[18] Menn, C., Aesthetics in Bridge Design. Bulletin of the International Association for Shell and Spatial Structures, 1983. 26(88): 53-62.J. G. Kreifeldt, "An analysis of surface-detected EMG as an amplitude-modulated noise," presented at the 1989 Int. Conf. Medicine and Biological Engineering, Chicago, IL.

[19] McNeel, Robert & Associates (1993-2012). Grasshopper Build 0.9.0014.

[20] McNeel, Robert & Associates (2012). Rhinoceros Version 5.0.

Influence of Strengthening of Ceilings in Historic Buildings on Perception of Communication Vibrations

Kozioł Krzysztof *

Abstract— Development of transport infrastructure leads to an increase in the activities of the dynamic nature of the surrounding buildings. This may contribute to deterioration of comfort staying in their people. There is therefore a need to solve this problem. The belief that increasing the rigidity of items will improve the comfort of the people in it is not always right. Each solution requires the analysis of dynamic nature especially if the interference will change the nature of its response.

Keywords— traffic induced vibrations, vibration propagation, dynamic response of the building, paraseismic vibrations

I. INTRODUCTION

Long-term operation of buildings and changing environmental influences impose repair or modernization requirement. In 'old' buildings, where ceilings were mainly made of wood, the heat-moisture conditions are not always satisfied, which caused moisture condensation in the compartments and finally turned to the corrosion of supports, thereby is a requirement of the main beams renovation.

Development of road infrastructure, construction of the metro or tram rails causes additional loadings affecting the building, which are not taken into account during its design. These actions may negatively affect the object itself, but as a rule are the cause of deterioration in the residents comfort.

Criteria for assessing the impact of vibration on the structure and people staying in it are contained in the Polish standard PN-85/B-02170 - Hazard evaluation of vibration transmitted by the ground on buildings and PN-88/B-02171 - Assessment of the impact of vibrations on people in buildings. These standards are not design guidelines, but define the limits at which the dynamic loads act negatively on humans and selected objects. In terms of vibration reception by the people PN-88/B-02171 refers to any type of structure. But if one talks about buildings the PN-88/B-02171 standard narrows down the type of structure. It refers to masonry buildings (for manual raising) and structures constructed with large blocks. For this group of objects, mentioned standard defines so called Dynamic Influence Scales (DIS - SWD in polish). Wherein imposes additional criteria that divide structures being subjected to the SWD-I or SWD-II scale.

- SWD-I scale (PN-85/B-02170 – Fig. 1) refers to the buildings with compact shape with small external dimensions of the horizontal projection (up to 15m), one or two-storey and satisfying the condition that the building height cannot exceed any of the building plan dimensions - Fig. 1.
- SWD-II scale (PN-85/B-02170 – Fig. 2) refers to buildings with height up to five floors above ground level and height, which satisfies the condition that it cannot be greater than twice the maximum width of the building in plan. Additionally, it can be used for low buildings (up to maximum two storey's) that do not satisfy the conditions for applying SWD-I scale.

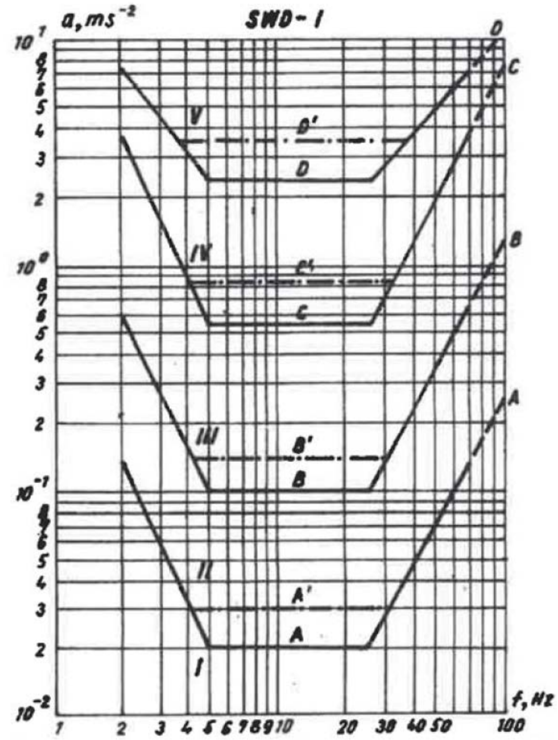

Fig. 1. SWD-I scale expressed in accelerations

*) Assistant Professor – Cracow University of Technology e-mail: kkoziol@pk.edu.pl

Vertical components presented in the graphs refer to the maximum horizontal acceleration of structure excitations in 1/3 octave bands.

- In each of these scales (Fig.1 and Fig.2) they are specified zones of dynamic harmfulness. For example Zone II characterized vibrations perceptible for building but not dangerous for its construction; followed only by accelerated wear of the building and the first cracks in expeditions, plasters etc. Zone V determines the vibrations causing the failure of the building, collapse of the walls, falling ceilings, etc. If such vibrations occur, the building cannot be used due to lose of human life.

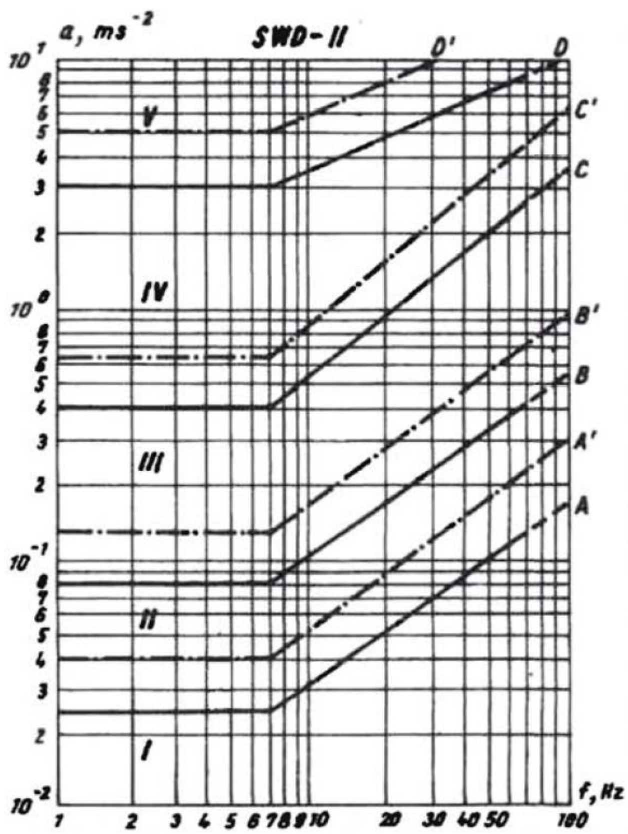

Fig.2. SWD-II scale expressed in accelerations

However, It should be noted that the standard functions unchanged since 1985, and over its term construction materials have much more evolved. For example, deformability of the plaster increased, especially external ones (from almost zero to several hundred percent). So a natural consequence for this kind of wall finishing would be to move or even eliminate limit A (lower zone of appreciability vibrations by the building and the lower limit of the dynamic impact), below which one cannot take into account the dynamic influences.

The obvious conclusion is, that in the case of using PN-85/B-02170 it should be impose on criteria for the materials used in the structure (with very low ductility), which generally is satisfied for historic buildings.

PN-88/B-02171 specifies the level of vibration perceptibility by human in horizontal and vertical directions and defines the multiplier of threshold in order to obtain comfort threshold (Table 1).The value of multiplication factor depends on:

- destination of the room,
- occurrence time,
- nature of the vibrations,
- repeatability of vibration.

Tabl.1.Multiplier PN-88 / B-02171 with respect to the threshold of perceptibility of vibrations depending on the room destination

Purpose room	**time of the vibrations**	**the value of the dither factor**	
		determined at more than 10 times per day	**occasional**
hospital (operating rooms), laboratory	all day	1	1
hospital (people hall)	day	2	8
	night	1	4
apartments	day	4	32
	night	1,4	4
office rooms	all day	4	64
workshop	all day	8	128

Fig.3 shows the perceptibility thresholds and vibration comfort by man for horizontal and vertical directions in a residential area.

In order to determine the effect of vibrations on people inside the buildings, the horizontal and vertical movement of the point of the ceiling in the most unfavorable position for each terce vibrations should be analyzed. This means, that at various points in the ceiling different vibration frequencies may decide about the comfort. During measurements of the impact of vibrations on the people inside the buildings, choosing a proper location of the gauge is the key factor. Analyzing the effect of vibrations on people we base on the average values of vibration receiving. To obtain unambiguous results of the impact of vibrations on people, it should be imposed proper restrictions on the time of signal measurement. According to the standard, the initial point of analyzed vibration means the time, at which the amplitude of the chosen parameter reaches 0.2 of the maximum value of this parameter and the end time when drops below 0.2 this value.

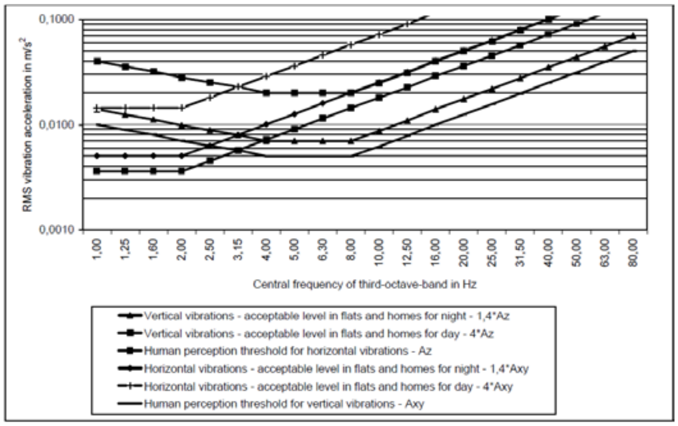

Fig.3 Curves of perceptibility and comfort of vibrations in the living room

Knowing the criteria of vibrations impact on people and buildings it can be concluded that for buildings subject to the SWD scales with constant ambient conditions (in terms of communication vibrations) renovation of floors in the building should not have greater importance on the impact of vibrations on the structure. This happens because, as it does not change the nature of extortion and very little static scheme and load

However, it may affect the comfort of vibrations perceptibility by humans.

During the impact analysis of vibrations II underground line in Warsaw on buildings located in the dynamic influence zone one of the historic buildings was investigated in order to find the relationship between the change in the stiffness of the ceiling and the impact of vibrations on people in this building.

II. Assumptions

Examined building is located in the Warsaw in Praga North district above main track of the underground line (Fig. 4).

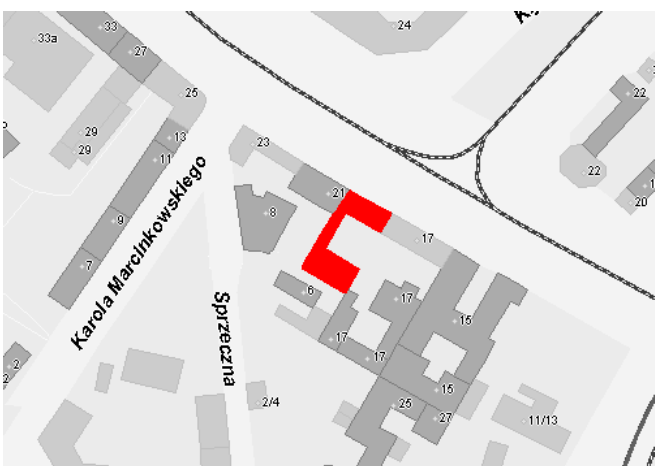

Fig. 4. Structure location

Object in the plan is quite similar to the C-shaped with subsequent dimensions: outer segments adjacent to Market Street and located on the property 21,4x12,9[m], inner segment 20,5x7,0[m] located inside the property. The building has a height of 15,3[m]. It is a four-storey structure with a basement and functional attic. The depth of foundation of the building is 3.2[m]. The building was built in 1920. Object is built on (Table 2) sand and gravel, 12m below ground level there are stiff clays. The level of ground water table is below the foundation level.

Tabl.2. Underground structure

Scheme of the subsoil		
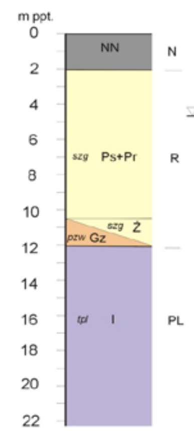	**Soil types in the substrate**	On the surface embankments with thickness up to 2[m] **(N)**, below fluvial deposits **(R):** medium dense medium and coarse sands and gravels at the sill level discontinuous layer of clay, below 12[m] below the surface there are Pliocene sediments (**EN**): stiff silt to a depth of 22[m] below ground level.
	Stratification	Layer arrangement irregular, discontinuous layer of clay.
	Ground water	Groundwater is unconfined at a depth of 4.5[m] below ground level.

The building has been built in wall system, in outer segments (parallel to Market Street) is designed as a two-section in the middle segment - one-section. Structure is made without dilatation. Foundations, basement walls and over ground storeys are built of solid brick on cement and lime mortar. Floors above basements are constructed as a segmental, and between the above-ground storeys as beam ceilings made with wooden beams. Staircases made as wood with steel cheeks and ceramic-steel staircase landings. The building is in bad technical condition with a lot of cracks. It is entered in the register of monuments. View of the facade of the building is shown on Fig. 5. Figure 6 shows the spatial model of the structure including ground floor

Fig.5. View of the east facade of the building from the Targowa street.

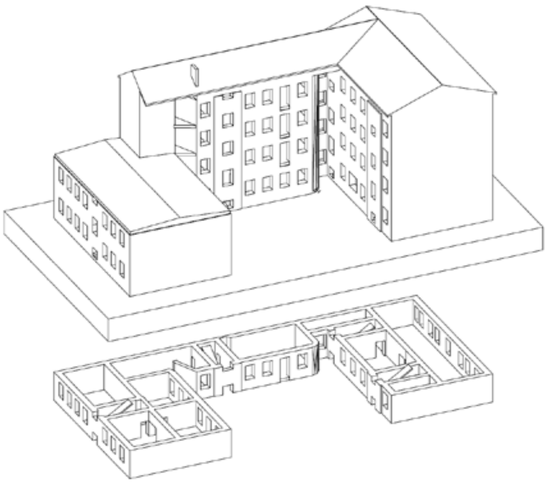

Fig.6.Visualization of the computational model.

Characteristics parameters of the structural elements, plasters, load values, the geometry used in the FEM model were taken from the archive design documentation. This numerical model has been carefully checked with regard to its response to a dynamic excitations. Vibration measurements were carried out by Laboratory of Strains and Vibrations of Buildings located in Cracow University of Technology. Response of the structure on its foundation from the side of excitation (from Market Street) and two selected points on the ceilings and IV were measured. The waveforms measured on the foundation were used as kinematic excitation for computational model and the responses recorded on floors were used for comparison with computed ones as shown in Fig. 7 and Fig. 8 in octave form of vibration impacts on people in the building.

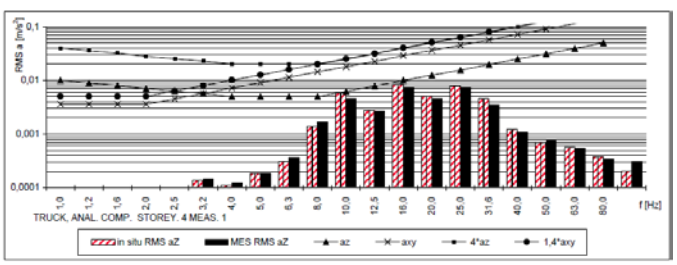

Fig.7.Comparative analysis of the impact on the people of the vertical vibration on the 4th floor of the building in case of passing truck (measurement 1) - according to in situ investigations and numerical simulation

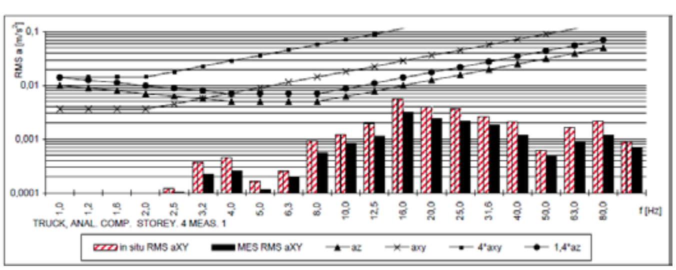

Fig.8.Comparative analysis of the impact on the people of the horizontal vibration on the 4th floor of the building in case of passing truck (measurement 1) - according to in situ investigations and numerical simulation

In case of vibration in the vertical direction, author was able to get a very good convergence - a difference of 18% for the dominant response frequency. In the case of vibrations in the horizontal direction - 34%. FEM model convergence was considered sufficient. FEM model was subjected to expected excitations (taken from the survey database of the Cracow University of Technology) for similar facilities situated on similar ground conditions and the same distance from dynamic excitations.

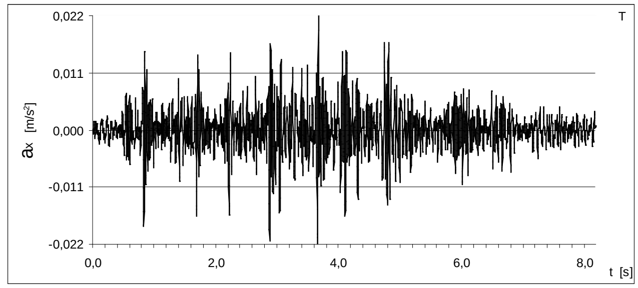

Fig.9. Predicted load in a vertical direction resulting from a passing tram.

Excitations came from car, tram and subway passages. Exemplary building loadings in the vertical direction coming from a passing tram was shown in Fig. 9.

It appeared that for each of the analyzed load we are dealing with exceeding the vibration comfort as shown in Fig. 10

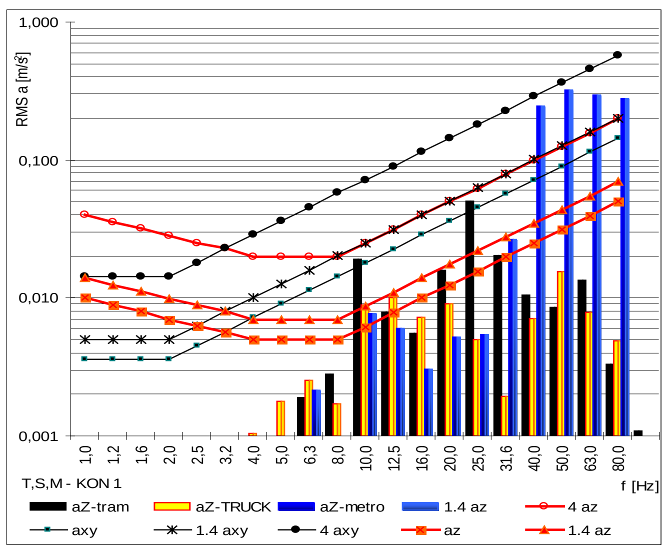

Fig.10. Effects on humans in case of initial variant of the ceiling

It was decided to carry out the analysis of two different variants of the modernized ceiling (dimension 9600x6000mm). Following cases were considered:

- The ceiling in the primary system (results shown in figure 11) - Figure 11a, where the load-bearing beams are beams of size 180x240[mm] distributed at 1200[mm].
- The ceiling, where the main beams height has been increased by 100 mm (rys.11b) - full cooperation of the original beams and additional ones has been provided.

ISBN: 978-1-61804-325-2

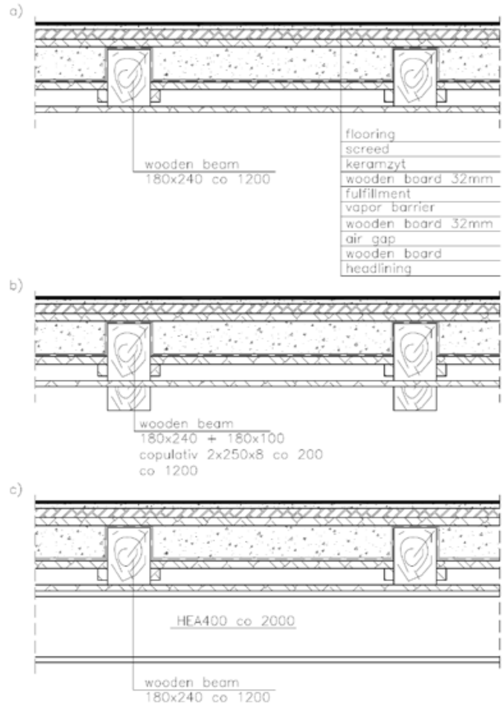

Fig.11.Analyzed ceiling models

- The ceiling, where in the direction of the long side at 2000[mm] the steel girder HEA300 was introduced - Fig. 11c.

Natural vibration frequency analysis - Table 3 shows that the ceiling "c" is the stiffest structure (it has the highest value of the first natural frequency).

Tabl.3. Natural frequencies of the ceiling

ON.	Ceiling frequencies [Hz]		
	a	b	c
1	2,21	3,69	4,09
2	3,21	4,39	9,07
3	8,06	6,3	11,51
4	17,02	23,07	17,18
5	28,96	30,44	18,34

The building with discussed variants of the ceiling, was subjected to the movement of trams, cars and the subway. The results are summarized in the form of the vibration perceptibility factor (WOD), which is the ratio of the resulting vibrations to the vibration threshold of perceptibility, and is shown in Fig. 12. Analysis revealed that the stiffening of the floor does not always go together with the reduction of vibration perception by the people. For excitations with dominant higher frequencies of vibration additional stiffness of the floor increases WOD. Therefore, the strengthening of type “c” for excitations frequency above 30[Hz] could be worse than the system in its original form (ceiling type “a”). It should be noted, however, that the solution "c" causes another character of construction response than the other two types. Steel beams used to strengthen the ceiling in type "C", give it rigidity in the direction perpendicular to the primary beams, which causes that sooner than for the case of "a" and "b" character there appear "half-waves" in a direction perpendicular to the original beams.

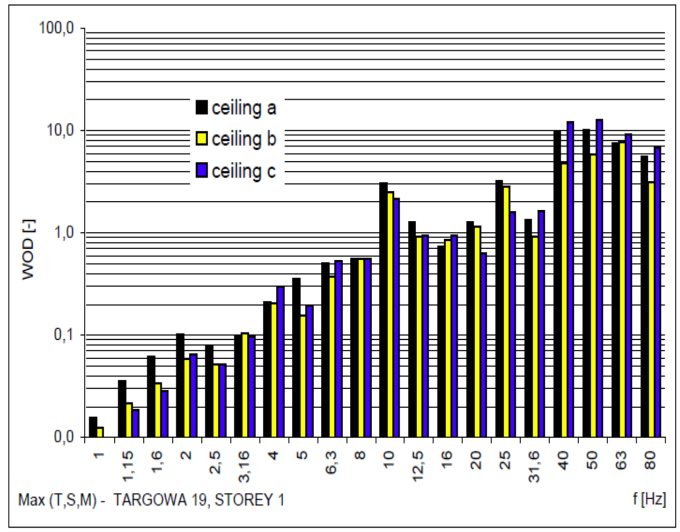

Fig.12. Effects on humans for different variants of the ceiling

III. Conclusion

In case of dynamic loadings increasing the stiffness of the elements do not always leads to reduced response of the object, especially if the interference with the structure will change the nature of its response. In the analyzed case, increasing the stiffness of the ceiling using additional steel beams in a direction perpendicular to the original grid (wooden balls) causes the appearance of a "half-waves" in mode shapes in a direction perpendicular to the initial beams arrangement. The main response parameter of the structure is the amplitude-frequency characteristics of the excitation. Increasing the stiffness of the ceiling (which manifests itself by increasing the value of the first natural frequency) decreases the vibration perceptibility in pre-resonant frequencies (in this case up to frequency to 1.6Hz - Fig.12).

It is quite important to detuning the ceiling in order to "move" the dominant excitation frequencies from resonant frequency of the ceiling after its strengthening - fig.12 ceiling "c" although is the stiffest one has a major influence to the frequency of 4 Hz because it was his first natural frequency.

References

[1] Kozioł K., Stypuła K.: Pomiary drgań i symulacje komputerowe w projektowaniu wibroizolacji nawierzchni szynowych. Mat. VIII konf. Nowoczesne technologie i systemy zarządzania w kolejnictwie. Zeszyty Naukowo-Techniczne Stowarzyszenia Inżynierów i Techników Komunikacji RP, Oddział w Krakowie, Zakopane, 2-4.12.2009 r.

[2] Stypula K., Koziol K.: Effects of changes to the track superstructure on human perception of rail-induced vibrations in a selected building near the rail tunnel in Warsaw – predictions and measurements. Proceedings of the 7th European Conference on Structural Dynamics, EURODYN 2008, 7-9 July 2008 Southampton, s. 58.

[3] Kawecki J., Kozioł K. & Stypuła K.: Application of measurement database in dynamic diagnostics and design. Proc. of the International Conference on Experimental Vibration Analysis for Civil Engineering

Structures EVACES'09, 14-16 October 2009, Wrocław, Poland. Edited by Jan Bień. Wrocław University of Technology, s. 181-182.

[4] Kozioł K., Stypuła K.: Wybrane przykłady zastosowań obliczeń symulacyjnych w projektowaniu wibroizolacji nawierzchni szynowych w Polsce. Materiały V Seminarium „Wpływ hałasu i drgań wywołanych eksploatacją transportu szynowego na budynki i ludzi w budynkach – diagnostyka i zapobieganie" WIBROSZYN-2010. Kraków, 9-10 września 2010, s. 33-59.

Ambient vibration testing and operational modal analysis of a historic tower

M. Diaferio, D. Foti, and N. I. Giannoccaro

***Abstract*—**An accurate knowledge of the dynamical parameters of structures is definitely useful for seismic assessment and for the design of risk mitigation interventions. In this paper, the opportunities provided by dynamic identification techniques for the non-destructive evaluation of heritage structures are discussed with focus on the bell tower of Announziata (Corfù, Greece), a masonry tower, which shows a high damaged scenario and, consequently, a high vulnerability to dynamic and seismic forces. The paper presents the experimental investigations and operational modal analysis results, useful for defining the finite element model of the tower. The monitoring system consists of several elements properly connected: in total twenty-four accelerometers have been positioned, eight for each of the three floors and oriented according to the orthogonal directions x and y. This configuration has been also conditioned by many operative problems about the position of the instrumentation due to the limited accessibility of the structure, not only to the main access but also to reach the top. It is important to emphasize that the data obtained are not connected to external events detected during the acquisitions, so it is possible to identify with a certain confidence the first six frequencies of the tower and their corresponding mode shapes.

***Keywords*—** Non-destructive tests, operational modal analysis, model updating, dynamic analysis.

I. INTRODUCTION

IN the preservation of architectural heritages it is important a careful study of the structure and of its dynamic characteristics in order to describe its actual behavior [1-3]. The necessity of identifying unknown geometrical data and material properties is due to the usual impossibility of conducting classical tests for their evaluation; so the numerical models may be validated only by means of non-destructive techniques. In literature various methods have been proposed for estimating the mechanical properties of the structural materials also in the presence of retrofitting interventions by means of innovative materials [4-9], however these procedures allow to evaluate only local properties and the extension to the global structure is too much burdensome for practical applications. Other approaches makes use of the experimental evaluation of the modal parameters of the structure. The modal parameters may be compared with those of the model and the unknown materials and geometrical parameters may be estimated for obtaining an accurate FE model. These techniques have the advantage of providing information on the overall structure with a reasonable experimental effort [10-32]. In this paper, the case of study is the bell tower of Announziata, a masonry tower (Fig. 1), which shows a high damaged scenario. The bell tower of the church is located in the town of Corfù, Greece. The church was built in 1394 and it was one part of a Roman monastery, nowadays the only existing one. The interior of the church [1] contained the tombs of generals who died in the sea battle of Naupactus (1571). The church of Announziata was bombed during the second world war and it suffered from cracking; then it collapsed in March 1952 when long term phenomena and earthquakes contributed to increase the damage. So, from 1952 only the campanile of the medieval monastery has survived to the present day with heavy cracking. It is possible to observe deep vertical and diagonal cracking, deterioration of mortar on the stone walls and development of creepers in the masonry. The bell tower is a stone tower with an almost square plan section. A double arch (Fig. 1) supported by a stone column in the center is present at each of the four façades.

Fig. 1. Announziata bell tower.

M. Diaferio is with the Technical University of Bari, Department Sciences in Civil Engineering and Architecture, Bari, 70125 ITALY (e-mail: mariella.diaferio@poliba.it).

D. Foti is with the Technical University of Bari, Department Sciences in Civil Engineering and Architecture, Bari, 70125 ITALY (e-mail: dora.foti@poliba.it).

N. I. Giannoccaro is with the University of Salento, Department of Innovation Engineering, Lecce, 73100 ITALY (e-mail: ivan.giannoccaro@unisalento.it).

ISBN: 978-1-61804-325-2

The structure of the tower is made with masonry walls and the three floor systems made by solid bricks are supported by vaults. At the top of the tower there is the bell cell with four bells. The current state of the tower may be defined critical, with many damages and cracking.

The possibility of defining a detailed Finite Element (FE) model of the tower taking into account the experimental modal identification data may be considered very important for getting information about the structural health of the tower. To this aim, the present paper shows all the details and results of the experimental modal identification procedure able to complete the preliminary analysis presented in [31-32].

II. Experimental setup and identification procedure

The Announziata tower was instrumented with 24 high sensitivity seismic accelerometers ICP PCB 393B31 placed on 12 positions (labelled with numbers 1-12 on the plans in Fig. 2) on 3 different levels; 8 accelerometers were placed on the four corners of the first floor (position 1-4 in Fig. 2b), 8 were placed on the four corners of the second floor (number 5-8 in Fig. 2b), and 8 were placed on the basis of the four columns (numbers 9-12 in Fig. 2b). Appropriate rectangular blocks were designed and realized in order to ensure the orthogonality of the couple of accelerometers placed on the same position. The accelerometers were inserted with screws on the threads realized on the perpendicular faces of the block).

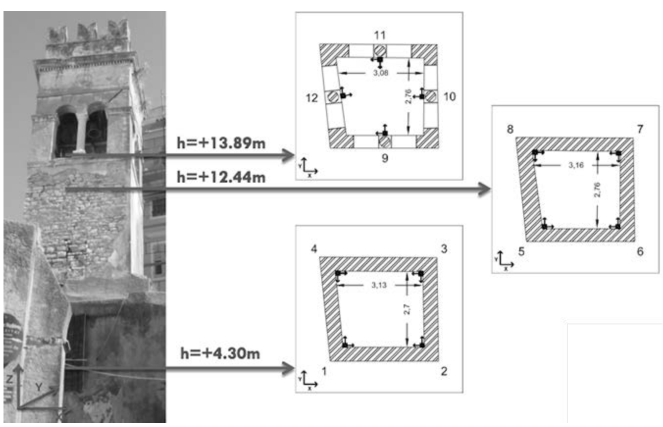

Fig. 2. Annunziata bell tower and layout of the experimental setup.

It was not possible to achieve the belfry of the campanile to place accelerometers on the top of the tower; also it must be considered the very compromised situation of the building, let fall into decay in the last years. It was very difficult, also, to reach the first floor.

The bell tower is positioned in the city center, in a crowded area especially during the day time. There is a main entrance road open to the car passage and a rotatory (Fig. 3) very close to the tower where cars and trucks can select the preferential way. The continuous passage of bikes, cars, motorcars and pedestrians has characterized all the environmental tests.

Preliminary tests were carried out on 12th October 2012; in the day after several consecutive tests were conducted. The data acquisition was carried out by recordings of 10 minutes with a frequency of 1024 Hz, which has been subsequently decimated by a factor equal to 4 to have a frequency of 256 Hz. About 10 consecutive acquisitions were carried out and, in each acquisition, all the relevant events (passage of cars, motorbike, other possible disturbs), were noted. An heavy rain, unfortunately, occurred in the night between 12th and 13th October, and infiltration of water was verified on the instrumentation that was placed on the second floor and on the basis of the columns.


Fig. 3. Position of the Announziata bell tower.

III. Identification results

The analysis of the experimental results was subsequently performed. A specific software [33] was used for the extraction of the modal parameters from ambient vibration data. The model defined by means of this software is shown in Figure 4 with the corresponding reference system *xyz*.

A preliminary analysis was conducted on the time series recorded by the accelerometers for evaluating the effects of the urban traffic and the functionality of the accelerometers considering the difficult environmental conditions.

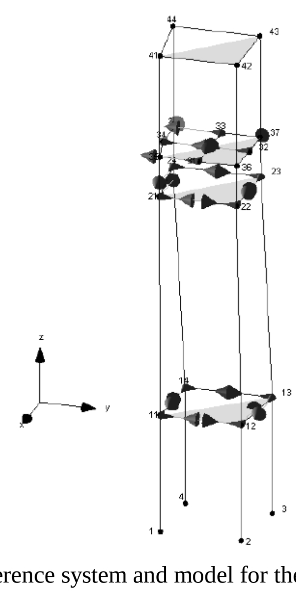
Fig. 4 Reference system and model for the identification

The preliminary analysis allowed to individuate that some accelerometers were not performing properly: the ones placed in positions 23 (both directions *x* and *y*), 24 (direction *x*) and 32 (direction *y*) (see the model in Fig. 4). In addition, the preliminary analysis permitted to clearly highlight the effects of external disturbances. In Figs 5-7 the time histories of three opportunely selected tests (named a, b, c) are shown in relation to the accelerometers placed in positions 21 and 22 of Fig. 4 (both the directions *x* and *y*). It is evident from Figs. 5-7 the extreme sensibility of the experimental setup to external events: for test a (Fig. 5), there was heavy and continuous traffic after 260-280 seconds and some spurious events after about 440, 540 and 560 seconds from the starting time. For test b (Fig. 6) there are not evident effects on the time histories, while on test c (Fig. 7) heavy traffic effects are evident at the beginning of the registration (80-120 sec) and at the end of the registration (400-480 sec) for the accelerometers along *x* axis (left column of Fig. 7), while some spurious events are evident after around 510 sec. The time histories of the selected tests seem to be very different each other for the external disturbances that influence the accelerometers data.

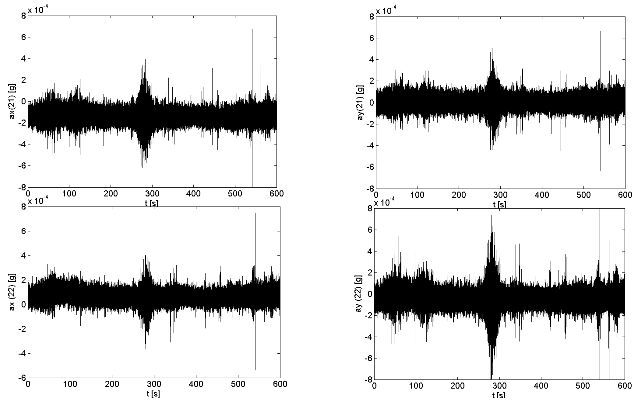

Fig.5 acquisition signals for points 21 and 22 for test a.

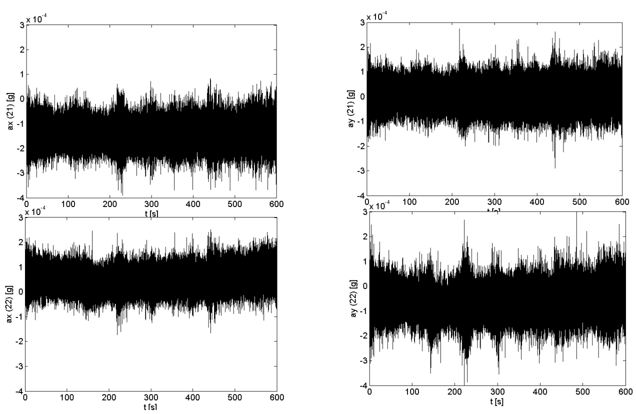

Fig.6 acquisition signals for points 21 and 22 for test b.

It is important to emphasize [32] that the data results are closely connected to external events detected during the acquisitions, so the preliminary analysis was conducted on the time signals of the accelerometers. For this reason, a wide experimental analysis was carried out repeating the acquisition for 14 times in two consecutive days.

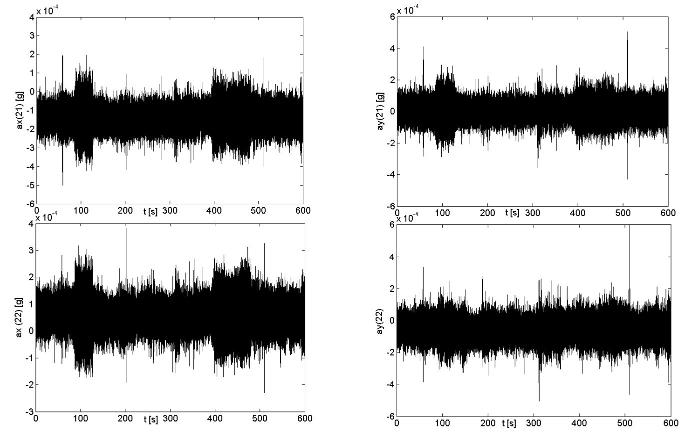

Fig.7 acquisition signals for points 21 and 22 for test c.

The frequencies of the building and the modal shapes time histories were identified for all the tests with a simple operational modal analysis (OMA). In particular, for each analysis [33] two different OMA methods were used: the Enhanced Frequency Domain Decomposition (EFDD) in the frequency domain and the Stochastic Subspace Identification (SSI) using Unweigthed Principal Components (UPC) in the time domain [34-35]. The estimated frequencies for all the tests are named using the number of the date (first number 1 or 2 considering the first or second day) and the number of acquisition (second number 1, 2…5 for the first day, 1, 2…9 for the second day). Table 1 shows the frequencies evaluated by means of the SSI method. The identified frequencies are consistent for all the tests and for both methods; the SSI method permits to evaluate in each case all the frequencies, while the EFDD method in some cases is not able to identify the frequencies of higher order.

Table 1. Identified frequencies [Hz] with SSI method for all the tests

Fr.	1-1	1-2	1-3	1-4	1-5	2-1	2-2	2-3	2-4	2-5	2-6	2-7	2-8	2-9
1	2.61	2.61	2.61	2.60	2.61	2.63	2.62	2.62	2.63	2.62	2.62	2.63	2.65	2.63
2	2.83	2.83	2.82	2.81	2.82	2.82	2.82	2.84	2.83	2.82	2.82	2.84	2.84	2.83
3	5.50	5.47	5.48	-	5.46	5.52	5.44	5.51	5.51	5.50	5.51	5.52	5.55	5.55
4	7.04	7.05	7.05	7.05	7.05	7.05	7.04	7.02	7.03	7.07	7.03	7.05	7.07	7.06
5	8.04	8.01	8.03	7.99	8.021	8.01	8.01	8.01	8.04	8.05	8.03	8.05	8.0	8.03
6	11.28	11.3	11.27	11.14	11.19	11.32	11.25	11.28	11.3	11.37	11.31	11.29	11.32	11.29

In Table 2 a statistical analysis of the identification results is shown: it can be observed that the mean values are almost the same for both methods and that the standard deviation is very low ensuring a good repeatability and consistence of the identified frequencies nevertheless the different casual events. The frequencies identified by means of the mean value may be considered a stable experimental benchmark that characterizes the dynamical behavior of the tower.

Figs. 8 and 9 show the identification diagrams using SSI and EFDD methods, respectively, for test 2-4.

The identified frequencies were analyzed for detecting the mode shapes. It was observed that in all the tests of Table 1, the six identified mode shapes perfectly correspond to the ones expected for the tower. In detail, the first and second frequency were identified as the first couple of flexional modes on the *y* and *x* axes, respectively, the third frequency was the torsional mode, the fourth and fifth were the second couple of flexional modes on the *y* and *x* axes, respectively, and the sixth is the second torsional mode. Fig. 10 shows graphically the experimental identified mode shapes for test 2-4 by mean of the SSI method.

Table 2. Statistical analysis about the identified frequencies considering all the 14 performed tests

Frequency number	Mean value [Hz] (SSI)	Standard deviation (SSI)	Mean value [Hz] (EFDD)	Standard deviation (EFDD)
1	2.625	0.0125	2.616	0.0157
2	2.832	0.0078	2.828	0.0071
3	5.505	0.0325	5.526	0.0220
4	7.052	0.0152	7.067	0.0526
5	8.027	0.0191	8.051	0.0497
6	11.280	0.0571	11.323	0.1137

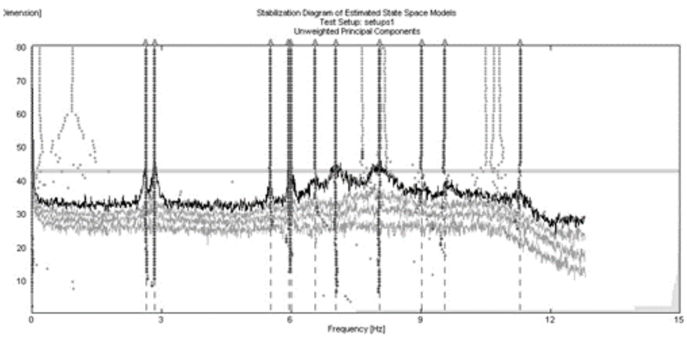

Fig.8 Identification by using SSI for test 2-4.

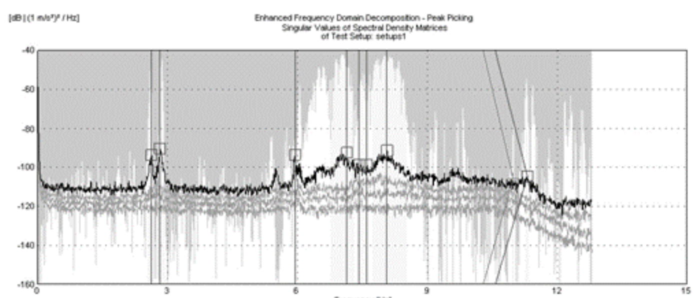

Fig.9 Identification by using EFDD for test 2-4.

IV. Finite element model

A preliminary finite element (FE) model of the Announziata tower has been realized considering the plan section as perfectly squared. The structure is realized with brickwork walls and the three floor systems are made by full bricks supported by vaults that in turn are supported by the walls parallel to the N-S axis of the building.

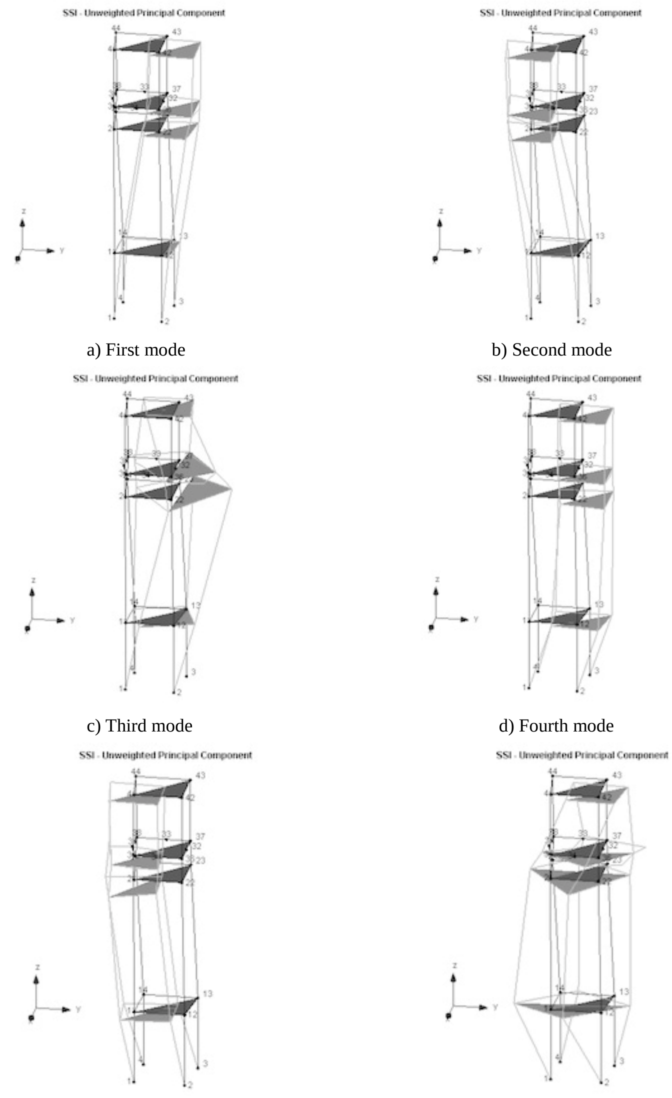

a) First mode b) Second mode

c) Third mode d) Fourth mode

e) Fifth mode f) Sixth mode

Fig.10 Identification of mode shapes of test 2-4 using the SSI method.

The materials characteristics (characteristic strength in compression f_{wd}, elastic modulus E, weight per unit volume γ_s and mass per unit of volume m_s) have been deduced by [1] where the properties have been defined on the basis of Eurocode-6. In [1] the pattern of vertical cracking has been taken into account considering a reduction of the elastic modulus of the masonry; in detail, it has been adopted the following elastic modulus for the cracked masonry:

$$E = \frac{2}{3} \cdot E_{initial} \tag{1}$$

where $E_{initial}$ is the elastic modulus of the undamaged masonry. The considered material properties for the vertical walls of the tower (material 1), for the three solid brick floors of the campanile (material 2), and for the stone column (material 3) are reported in Table 3. Finally for the vaults filling material γ_s has been assumed equal to 10 kN/m^3.

The three dimensional FE model of the tower has been defined by means of the SAP2000 [36]. The model has two typologies of elements, the 'frame' and the 'shell'. The frame ones are prismatic linear elements used to model structural components such as the stone columns supporting the bell tower openings and the bells' supporting framework (Fig. 11a). The shell elements have been used for modeling the masonry walls, such as the vertical walls; for the vaults caps (Fig. 11b) specific shell elements with 4 nodes have been used for combining the membrane behavior with that of a flexible plate.

Table 3: Materials' properties by Eurocode-6

Material	f_{wd} [MPa]	E [Mpa]	γ_s [kN/m^3]	m_s [kg/m^3]
1	0.87	1740	22	2243
2	0.66	1318	18	1835
3	n.a.	2600	18	1835

An adequate mesh was created in such a way to model the real behavior of the structural elements. The preliminary mesh was composed by 362 shell elements and 10 frames for a total of 404 nodes. In order to increase the reliability of the numerical model, the mesh was refined (Fig.11c) dividing opportunely the starting elements (the thickened model has 10541 elements and 10668 nodes).

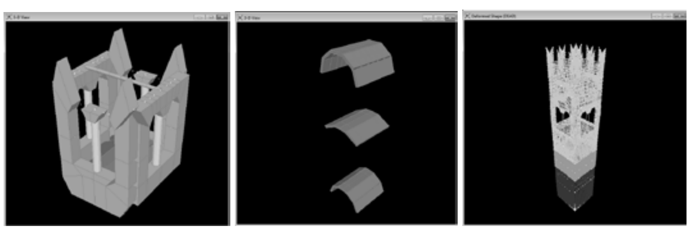

Fig.11 a) detail of the columns b) details of the vaults c) FE model.

The vaults filling material, that does not have a structural function, has been considered in the model as a load acting on the caps, while the bells have been modeled as added masses.

The weight P of the three bells, having different diameter D, has been estimated by Eq.(2) [37].

$$P = 580.8 \cdot D^{2.7839} \qquad (2)$$

Considering no inclination signs on the tower, the tower has been modelled as fixed at the base. The adjacent buildings effects have also been considered in the model, introducing some joint constraints on the lateral walls connected to the adjacent units.

The starting dynamical analysis of the FE model gives the results shown in Table 4, referred to the first 7 frequencies of the model.

For each identified mode, Table 4 reported also the excited percentage mass in the two principal direction *x* (U_x) and *y* (U_y) and the rotations around *z* axis (R_z) in such a way as to identify the typology of each mode.

Table 4: Modal frequencies and participating mass ratios of the FE model

Mode number	Frequency [Hz]	U_x	U_y	R_z
1	2.215	0.0003	0.37	0.13
2	2.393	0.33	0.0003	0.09
3	5.367	6·10(-8)	0.0012	0.15
4	8.901	10(-6)	0.24	0.1
5	11.07	0.13	1.1·10(-9)	0.04
6	12.46	4.8·10(-7)	6.5·10(-5)	1.7·10(-5)
7	14.48	1.9·10(-6)	0.011	0.011

The participating mass ratios in Table 4 and the animation of the mode shapes clearly indicate that the first and the fourth modes of the model are flexional on *y* direction, the second and the fifth are flexional on *x* direction, the third and the seventh are mainly torsional, while the sixth is a mode referred to a local movement on the *z* axis.

The model frequencies calculated in this work are closer to the identified ones with respect to the ones reported in [1], even if the same material properties have been used. This is due to the major complexity and accuracy of the FE model (Fig. 11c) and the careful observation of the architectural details. Anyway an updating procedure will also be considered for improving the quality of the model and its adherence to the identified frequencies.

In the forthcoming part of the research the model will be updated in order to match the identification results [38], the main objective of this study will be the characterization of the behavior of the cracked masonry and the interaction between the tower and the surrounding buildings.

V. Conclusions

The dynamic identification of Annunziata bell tower presented in this study is characterized by many difficulties especially for the high damaged state of the tower, the impossibility to achieve the higher floors of the structure and the presence of heavy external disturbances in environmental conditions. The tower is a historical heritage of Corfu; so it was very important and interesting to apply a non-destructive strategy to identify its dynamic behavior.

For the modal identification two different statistical approaches in different domains were used in order to evaluate the frequencies of the structure. The statistical analysis performed on the identified frequencies shows the extreme repeatability and consistency of the first six estimated frequencies with respect to all the tests and the two adopted methods. This demonstrates that, nevertheless the different casual events, the identified frequencies were persistent in all the cases.

The analysis carried out in this paper shows also that the influence of material data assumed for the calculation is relevant especially in presence of an important damage state of the building. Therefore, a considerable effort is required in defining a reliable model that could efficiently describe the identified experimental dynamical properties.

ISBN: 978-1-61804-325-2

ACKNOWLEDGMENT

The authors gratefully acknowledge the funding by European Union and by National Funds of Greece and Italy, European Territorial Cooperation Programme "Greece-Italy 2007-2013", under grants of the project Structural Monitoring of ARTistic and historical BUIlding Testimonies (S.M.ART. BUIL.T.).

REFERENCES

[1]S.S. Kouris, M. Karaveziroglou-Weber "Dynamic investigation and strengthening on mansonry bell tower". *Protection of Historical Buildings, PROHITECH 2009*, pp. 941-947, 2009.

[2]P.B. Lourenço. "Computations of historical masonry constructions", *Pro Struct Eng*, vol. 4,no. 3, pp. 301-319, 2002.

[3]M. Diaferio, "Dynamic analysis of a historical fortified tower", *Key Engineering Materials*, vol. 628, pp. 178-184, 2015, doi: 10.4028/www.scientific.net/KEM.628.178.

[4] L. Binda, G. Lenzi, A. Saisi. "NDE of masonry structures: use of radar tests for the characterization of stone masonries". *NDT & E International* vol.31 (6), pp. 411–419, 1998.

[5]R. Fosdick, P. Foti, A. Fraddosio, s. Marzano. "Shear driven planar Couette and Taylor-like instabilities for a class of compressible isotropic elastic solids". *Zeitschrift fur Angewandte Mathematik und Physik (ZAMP*), vol. 61, no. 3, pp. 537-554, June 2010.

[6]L. Pagnotta "Recent progress in identification methods for the elastic characterization of materials", *Int J of Mech, Is. 4,* vol. 2, pp. 129-140, 2008.

[7]P. Foti, "Stress-induced phase transformations of an isotropic incompressible elastic body subject to a triaxial stress state", *Journal of Elasticity*, vol. 84, no.3 pp. 197-221, 2006.

[8] L. Binda, L. Zanzi, M. Lualdi, P. Condoleo, "The use of georadar to assess damage to a masonry Bell Tower in Cremona, Italy". *NDT & E International* vol. 38, pp. 171–179, 2005.

[9]P. D'Ambrosio, d. De Tommasi, P. Foti, M. D. Piccioni, "Pairwise deformations of an incompressible elastic body under dead-load tractions", *Journal of Elasticity*, vol. 73, pp. 237-249, 2003.

[10] S. Ivorra and F.J. Pallares, "Dynamic investigations on a masonry bell tower", *Eng Struct.* vol 28, no.5, pp. 660-667, 2006.

[11] C. Gentile, A. Saisi, "Ambient vibration testing of historic masonry towers for structural identification and damage assessment". *Constr Build Mater*, vol. 21, no.6, pp. 1311-21, 2007.

[12] M. Diaferio, D. Foti and V. Sepe, "Dynamic Identification of the Tower of the Provincial Administration of Bari, Italy", In: *Eleventh Int Conf on Civil, Structural and Environmental Eng Computing*, Malta, paper n. 2, 18-21 Sept. 2007.

[13] M. Diaferio, D. Foti, M. Mongelli, N.I. Giannoccaro and P. Andersen, "Operational Modal Analysis of a Historical Tower in Bari". In: *Con Proc of the Society for Experimental Mechanics Series, "IMAC XXIX".* vol. 7, pp. 335-342, doi: 10.1007/978-1-4419-9316-8_31, 2011.

[14] D. Foti, S. Ivorra and M.F. Sabbà, "Dynamic investigation of an ancient masonry bell tower with operational modal analysis: A non-destructive experimental technique to obtain the dynamic characteristics of a structure", *Open Constr and Build Tech J*, vol. 6, pp. 384-391, 2012.

[15] G. Russo, O. Bergamo, L. Damiani, D. Lugato. "Experimental analysis of the ``Saint Andrea" Masonry Bell Tower in Venice. A new method for the determination of ``Tower Global Young's Modulus E'," *Engineering Structures*, Vol. 32, pp. 353- 360, 2010.

[16] D. Foti. M. Diaferio, N.I. Giannoccaro and M. Mongelli, "Ambient vibration testing, dynamic identification and model updating of a historic tower", *NDT & E Int*, vol. 47, pp. 88-95, 2012.

[17] L. Ramos, L. Marques, P. Lourenco, G. De Roeck, A. Campos-Costa, J. Roque. "Monitoring historical masonry structures with operational modal analysis: two case studies", *Mechanical Systems and Signal Processing*, Vol. 24 No. 5, pp.1291-1305, 2010.

[18] A. D'Ambrisi, V. Mariani, M. Mezzi. "Seismic assessment of a historical masonry tower with nonlinear static and dynamic analyses tuned on ambient vibration tests", *Engineering Structures*, Vol. 36, pp. 210-219, 2012.

[19] M. Diaferio, D. Foti and N.I. Giannoccaro, "Identification of the modal properties of a building of the Greek heritage", *Key Eng Mat*, Trans Tech Publications, Switzerland, Vol. 628, pp 150-159, 2015, doi: 10.4028/www.scientific.net/KEM.628.150..

[20] C. Gentile, A.Saisi,"Operational modal testing of historic structures at different levels of excitation",*Constr. Build. Mater.*,Vol.48,pp.1273-85, 2013.

[21] D. Foti, "Non-destructive techniques and monitoring for the evolutive damage detection of an ancient masonry structure", *Key Eng Mat*, vol. 628, pp. 168-177, 2015.

[22] M. Diaferio, D. Foti, N.I Giannoccaro, "Non-destructive monitoring of an old masonry clock tower with forced and environmental actions", in *Proc. XXII International Forum Le Vie dei Mercanti*, Editor La Scuola di Pitagora, in "Fabbrica della Conoscenza", pp. 815-824, 2014.

[23] A. Tomaszewska, C. Szymczak, "Identification of the Vistula Mounting tower model using measured modal data", *Engineering Structures*, vol. 42, pp. 342-348, 2012.

[24] D. Foti, "Identification of the modal properties of a Medieval tower next to a landslide" *Proc International Forum "Le Vie dei Mercanti"*, Editor La Scuola di Pitagora, in "Fabbrica della Conoscenza, pp. 1302-1311, 2014.

[25] M.Diaferio, D. Foti, N.I.Giannoccaro, "Optimal model of a masonry building structure with wooden floors". In *Advances in Engineering Mechanics and Materials- Proc. CIVILENG 2014 the 2014 International Conference on Civil Engineering*, Santorini Island, Greece, pp.105-109, 18-20 July 2014.

[26] M. Diaferio, D. Foti, N.I. Giannoccaro, "Non-destructive characterization and identification of the modal parameters of an old masonry tower". In *Proc. 2014 IEEE Workshop on Environmental, Energy, and Structural Monitoring Systems,* Naples, Italy, September

[27] G. Osmancikli, S. Uçak, F. Nur Turan, T. Türker, A. Bayraktar "Investigation of restoration effects on the dynamic characteristics of the Hagia Sophia bell-tower by ambient vibration test", *Construction and Building Material*s, Vol. 29, pp. 564-572, 2012.

[28] M. Diaferio, D. Foti, N.I. Giannoccaro, S. Ivorra. "Optimal model through identified frequencies of a masonry building structure with wooden floors". *International Journal of Mechanics*, vol.8, pp. 282-288, ISSN: 1998-4448, 2014,

[29] M. Diaferio, D. Foti, N.I. Giannoccaro "Identification of the modal properties of an instrumented building". In. *Proc. IOMAC 2009 -3rd International Operational Modal Analysis Conferenc*e, , pp. 357-364, Portonovo; Italy; 4-6 May 2009

[30] A.A. Rizzo, N.I. Giannoccaro and A. Messina, "Analysis of operational modal identification techniques performances and their applicability for damage detection", *Key Eng Mat*, Trans Tech Publications, Switzerland, Vol. 628, pp 143-149, 2015.

[31] D. Foti, N.I. Giannoccaro, R. Nobile, M. Diaferio, M.F. Sabbà "Dynamic Identification and Non-Destructive Characterization of a Greek Heritage Building". In: *EVACES 2013*. Ouro Petro, Brasil, 20-30 October 2013

[32] A.S. Carone, D. Foti, N.I. Giannoccaro, R. Nobile. "Non- destructive characterization and dynamic identification of an historical bell tower". In. *Proc. of. 4th International Conference on Integrity, Reliability and Failure, IRF 2013*, Funchal (Portugal) 23-27 June ISBN 978-972-8826-28-4, Paper Ref. 3988, pp. 1-14, 2013

[33] ARTeMIS Extractor Pro software. Issued by Structural Vibration Solutions ApS. NOVI Science Park, Niels Jernes Vej 10, DK 9220 Aalborg East, Denmark, 2013.

[34] B. Peeters and G. De Roeck, "Stochastic system identification for operational modal analysis: A review", *ASME J of Dyn Sys, Measurement, and Control*, Vol.123, No.4, pp. 659-667, 2001,

[35] P. Van Overschee, B. De Moor, "*Subspace identification for linear systems: theory-implementation-applications*", Kluwer Academic Publishers, 1996.

[36] SAP2000TM CSI Analysis Reference Manual ver. 14.1. Computers and Structures, Inc. Berkeley, California, USA, 2009.

[37] S.Ivorra, S. Llop y Bayo. "Determinacion de algunas magnitudes fisicas caracteristicas de una campana". *XIV Congreso de Conservación y Restauración de bienes culturales.* pp. 1-12, Valladolid-2002.

[38] Dynamic Design Solution NV (DDS). 'Fem Tools Model Updating Theoretical Manual, vers.3.6'. Dynamic Design Solution NV (DDS) Interleuvenlaan 64 – 3001 – Leuven – Belgium; 2012

Development of brushless MEMS micromotor with multilayer ceramic magnetic circuit

M. Takato, Y. Yokozeki, K. Saito, and F. Uchikoba

***Abstract*—**This paper proposed an electromagnetic induction type brushless MEMS micromotor with a multilayer ceramic magnetic circuit. The developed micromotor was combined with the silicon structural parts by a micro electro mechanical systems (MEMS) fabrication process and a ceramic circuit by a multilayer ceramic technology. The MEMS process realized miniature structural parts. The multilayer ceramic technology could form a miniature three-dimensional structure coil. The dimensions of sideways, endways and height of the fabricated MEMS micromotor were 11 mm, 11 mm and 5.5 mm, respectively. The developed MEMS micromotor was controlled by the motor driving circuit. The maximum rotational speed was 4200 rpm at the input frequency of 69.9 Hz. The developed MEMS micromotor with the load weight of 53.7 mg showed the rotational motion, and the rotational speed was 2254 rpm.

***Keywords*—**Electromagnetic induction type, MEMS, Micromotor, Multilayer ceramic technology

I. Introduction

MICROMOTORS are used for various fields such as portable electronic devices or a micro stage [1-11]. To achieve the micromotor, miniature components are requires. Conventionally, the structural components are fabricated by a mechanical machining process. However, it is faced to the limitation of the miniaturization. Therefore, micro electro mechanical systems (MEMS) process has been focused for the micromotors. The MEMS process can fabricate the miniature component that has both a high-aspect-ratio and a high-accuracy. Moreover, this process is suitable to combine with the control integrated circuit (IC) because it is based on the IC production process.

Many researches of the MEMS micromotor have been reported such as an electrostatic type. In the MEMS process, the fabricated structures are formed in a planar structure. Therefore, the electrostatic type is suitable to MEMS micromotor because this type is based on the planar structure [5-9]. Previously, the MEMS electrostatic micromotor that showed the rotor diameter of 120 μm and the rotational speed of 50 rpm was reported [9]. However, the electrostatic type motor requires high voltage and it shows low torque. On the other hand, the commercial size motor is usually uses an electromagnetic induction type because it shows a high torque by low voltage. The conventional electromagnetic induction type motor has a magnetic circuit that is formed by a winding wire as a three-dimensional structure. However, the winding wire is a problem for the miniaturization because it is difficult to combine with the MEMS structure. Therefore, the MEMS electromagnetic induction type motor adopts a spiral structure coil [10-11]. The spiral coil pattern can be fabricated by sputtering or deposition coating of the MEMS process. However, the spiral coil has some problem for the miniaturization. The spiral pattern is characterized by extending to a planar direction. Therefore, the magnetic circuit requires the large area for catching the divergence magnetic flux and increasing the turn number. Large area of the coil pattern requires a long length coil, and it shows high internal resistance. Many researchers solve these problems by forming the complex three-phase pattern of the coil structure.

In this paper, we focused a multilayer ceramic technology. The multilayer ceramic technology is used for the miniature electro components such as a ceramic conductor and a ceramic inductor. This technology can realize the miniature three-dimensional pattern without the winding wire. In this technology, ceramic sheets that are made from mixture of ceramic powder and organic materials are used. The fabricated ceramic sheets are formed an electrode on the surface of the ceramic sheet. The electrode pattern is made from a conductor paste and it is patterned by the screen printing technology. The through-via pattern is shaped by the drilling machining and filling the conductive paste by the screen printing technology to connect between an upper layer and a lower layer. The patterned ceramic sheets are stacked for forming the three-dimensional pattern inside the ceramic material. The laminated specimens are firing, and then, the miniature electro components are achieved.

In this paper, we propose the electromagnetic induction type MEMS micromotor that has millimeter scale structural body. To realize the miniaturization, the developed motor is combined with the MEMS structural parts and the multilayer ceramic magnetic circuit. Moreover, the developed MEMS micromotor is a brushless motor and it is controlled by a developed motor driving circuit. The brushless motor is not a mechanical contact. Therefore, it is suitable to the miniaturization because a

M. Takato is with Department of Precision Machinery and Engineering, Collage of Science and Technology, Nihon University, 7-24-1 Narashinodai Funabashi, Chiba Japan (phone: +81-47-469-5343; fax: +81-47-467-9504; e-mail: takato@eme.cst.nihon-u.ac.jp).

Y. Yokozeki is with Precision Machinery and Engineering, Graduate school of Science and Technology, Nihon University, 7-24-1 Narashinodai Funabashi, Chiba Japan.

K. Saito and F. Uchikoba are with Department of Precision Machinery and Engineering, Collage of Science and Technology, Nihon University, 7-24-1 Narashinodai Funabashi, Chiba Japan (e-mail: kensaito@eme.cst.nihon-u.ac.jp, uchikoba@eme.cst.nihon-u.ac.jp).

ISBN: 978-1-61804-325-2

frictional force is a profound effect to the micromotor. In the driving circuit, hall IC is used for detecting the rotational motion of the motor. The developed MEMS micromotor is discussed the rotational motion and the ceramic material of the magnetic circuit. In addition, the comparison the results between the driving circuit and the waveform generator is discussed.

II. Design of Electromagnetic Induction Type MEMS Micromotor

A. Electromagnetic Induction Type MEMS Micromotor

Fig. 1 shows the design of the developed electromagnetic induction type MEMS micromotor. An axial gap type three-phase alternating current synchronous motor is employed for designed MEMS motor because it shows the stable rotational motion. Schematic illustration of the cross-sectional image of the developed MEM micromotor is shown in Fig. 2. This motor is combined with the silicon structure and the ceramic magnetic circuit. The sideways, endways and height of the developed motor are 11mm, 11 mm and 6 mm, respectively. A 2-pole ring-shaped neodymium magnet is attached to the rotor inside the silicon structural parts. The outside diameter, inside diameter, and height of the magnet are 8 mm, 2 mm, and 0.5 mm, respectively. The diameter of the rotary shaft is 600 μm. The magnet and flux-capturing magnetic circuit are arranged beneath the rotor. The multilayer ceramic coils for the magnetic circuits are setting and holding in the silicon case. The hall IC that detects the rotational motion of the rotor is attached to the top frame of the silicon structure.

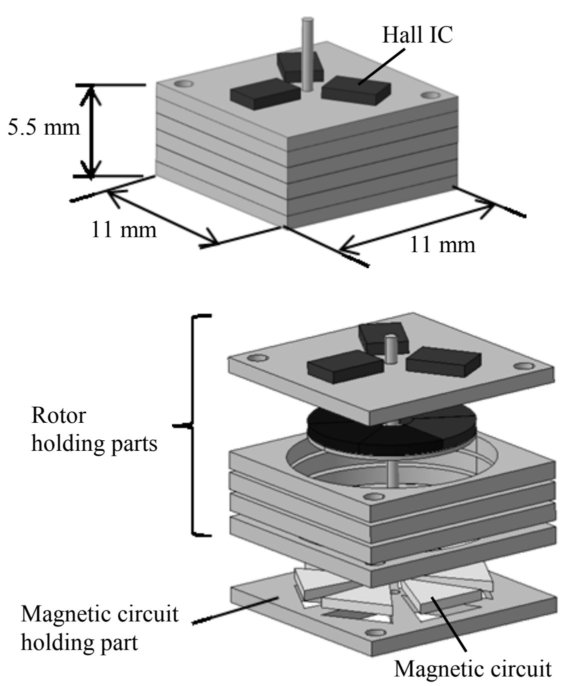

Fig. 1 design of developed electromagnetic induction type MEMS micromotor (a) overall view (b) development view

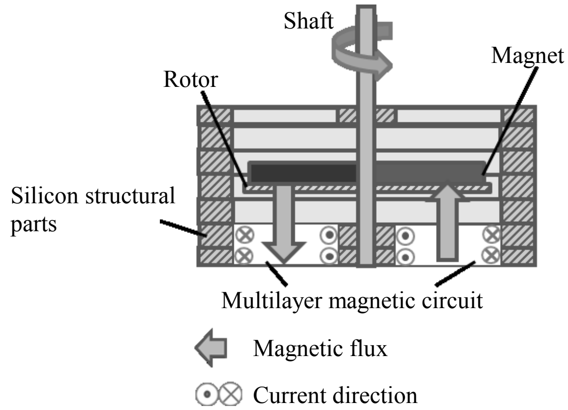

Fig. 2 schematic illustration of cross-sectional image of MEMS micromotor

B. MEMS Structural Parts

The structural parts of the MEMS micromotor are fabricated by the MEMS process. The MEMS parts are a top frame, holding parts for the rotor and the magnetic circuit. The top frame has the cavity structure for setting the hall IC. The upper layers that are holding the rotor are formed the circle pattern of the diameter is 10.0 mm. The lower layers for holding the multilayer ceramic magnetic circuit are formed the six square patterns. The dimensions of the base and the height of all square patterns are 3.64 mm and 3.90 mm, respectively. The fabricated multilayer ceramic magnetic circuit is set to the through-square pattern. The rotor is made from the silicon, and the diameter is 8.01 mm. Fig. 3 shows the design of the structural silicon parts of the developed MEMS micromotor.

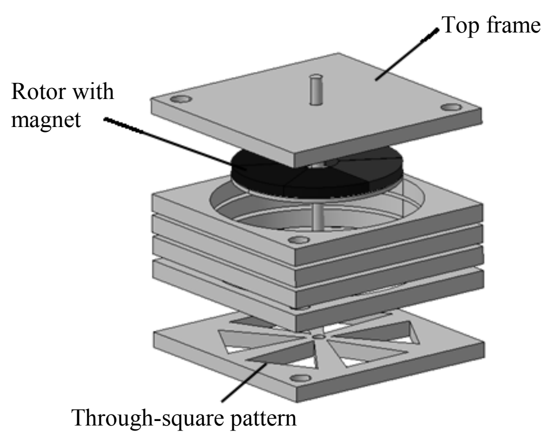

Fig. 3 design of silicon structural parts of developed MEMS micromotor

C. Multilayer Ceramic Magnetic Circuit

The magnetic circuit is made from low-temperature co-fired ceramic (LTCC) that is mixture with the alumina powder and glass powder. LTCC is usually used for insulation material of the ceramic multilayer substrate. The conductive pattern such as the electrode and the coil pattern is silver paste. The printed pattern of the silver paste shows 15/16 turn coil pattern. And then, the multilayer ceramic magnetic circuit has 30-turn helical coil by laminating the 36 patterned ceramic sheets. The multilayer ceramic coil that is used for the magnetic circuit is square shape. The dimensions of the base and the height of square multilayer ceramic coil are 3.5 mm and 3.9 mm, respectively. An electrode formed on the reverse face of the circuit applies a driving voltage to the magnetic circuit via a connected wire. Fig. 4 shows the design of the multilayer ceramic coil for the magnetic circuit.

The magnetic circuit for the micromotor requires connection into the three-phase coil. Therefore, the fabricated six ceramic coils are connected to the opposite coils in series each other. The ceramic coils that are divided into three pairs are connected in a star arrangement. Fig. 5 shows the schematic illustration of the arrangement of the multilayer ceramic coil for the magnetic circuit.

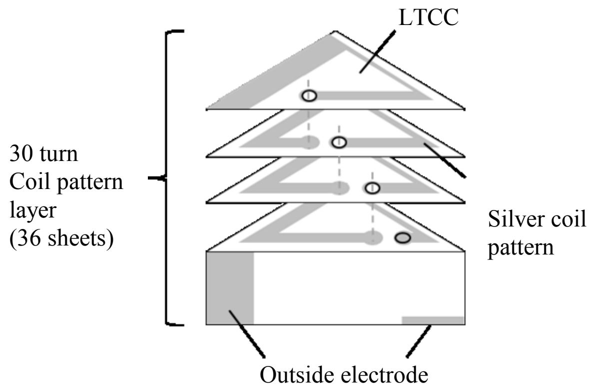

Fig. 4 design of multilayer ceramic coil for magnetic circuit

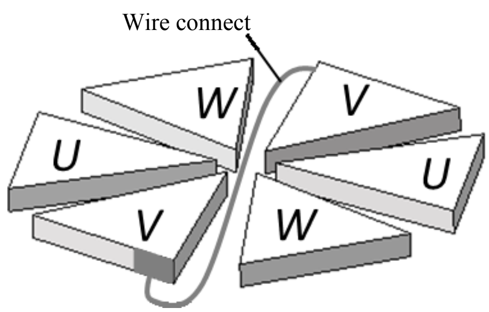

Fig. 5 schematic illustration of the arrangement of multilayer ceramic coil for the magnetic circuit

D. Motor Driving Circuit

The fabricated driving circuit is employed a three-phase output DC/AC converter. Driving pulse is a rectangular waveform. To detect the rotational motion of the developed MEMS micromotor, the hall IC is used. The output of the hall IC is amplified, and it is inputted into the driving circuit. Fig. 6 shows the schematic illustration of the connection of the driving circuit and the developed three-phase synchronous MEMS micromotor. Fig. 7 shows the circuit diagram of the single phase driving circuit.

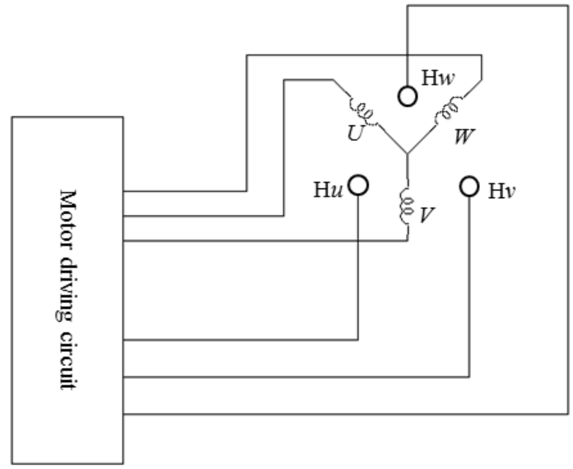

Fig. 6 schematic illustration of connection of driving circuit and developed MEMS micromotor

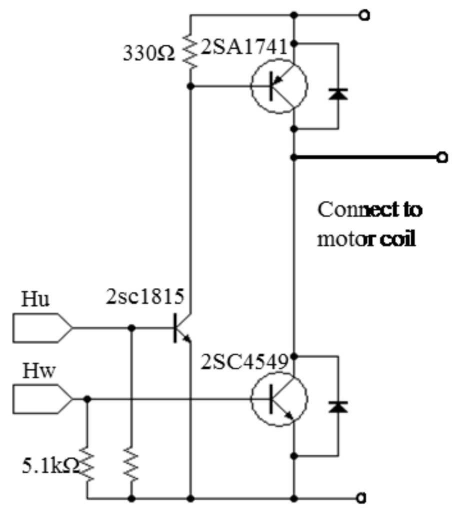

Fig. 7 circuit diagram of single phase driving circuit

III. Fabrication Procedure and Rotational Experiment

A. MEMS Process

In the MEMS process, the structural parts and the rotor were fabricated from single crystal silicon wafer. The photolithographic process was used for the pattering. Each silicon wafer was washed, deposited with an aluminum layer by physical vapor deposition, and coated with a photoresist. The designed pattern was exposed to the resist layer and developed by soaking in the developer. The aluminum layer on the specimen was then chemically etched, leaving an imprint of the designed pattern. The patterned wafer was dry etched by high-aspect-ratio inductively coupled plasma etching combined with a Bosch process [12]. The parts were achieved after removing the aluminum and washing. Through these processes, the silicon parts were fabricated. The obtained parts were

ISBN: 978-1-61804-325-2

assembled by hand. Fig. 8 shows the schematic illustration of the MEMS process.

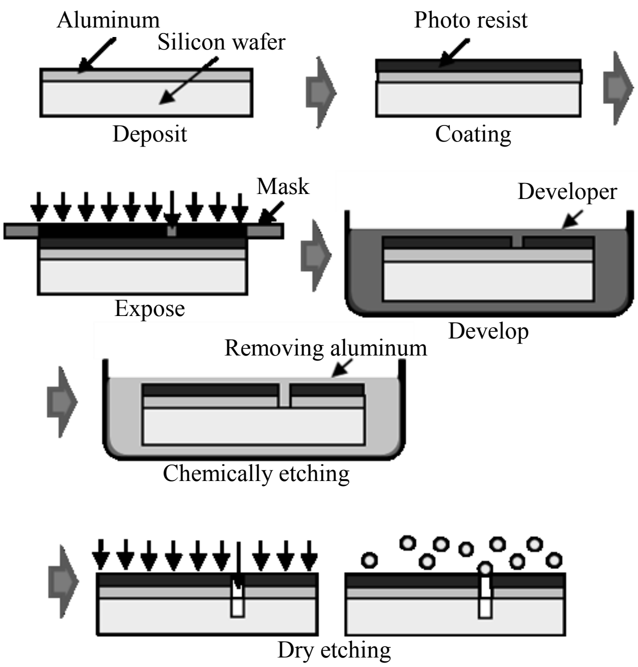

Fig. 8 schematic illustration of MEMS process

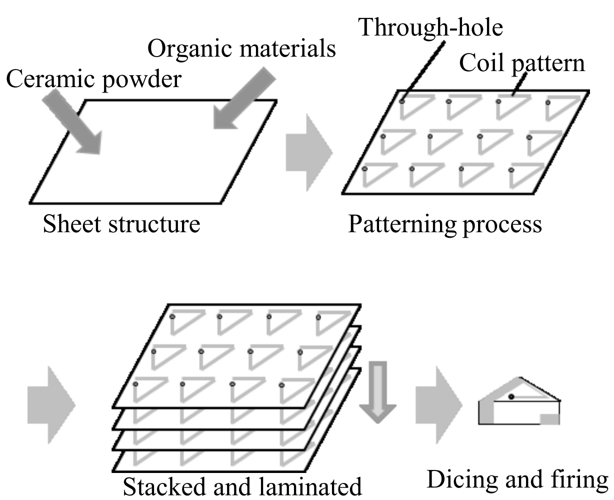

Fig. 9 schematic illustration of the multilayer ceramic technology

B. *Multilayer Ceramic Technology*

The conventional multilayer ceramic process is called green sheet process in which slurry is formed in the sheet structure. In the fabrication process, the slurry was a mixture of the LTCC powder, binder, dispersing agent, plasticizer, and organic materials. The sheet structure was formed by the doctor blade method. The through-hole for connecting the upper and lower layers was formed on the ceramic sheet. The coil pattern and via pattern were printed to the LTCC green sheet by screen printing technology. Multiple sheets were stacked, and the multilayered specimen was diced into the designed part. Finally, the specimen was fired and the outside electrode was formed. Fig. 9 shows the schematic illustration of the multilayer ceramic technology.

C. *Rotational Experiment*

In the rotational experiment by the fabricated driving circuit, DC power sources were used for the driving circuit and hall IC, each other. The driving waveform of the interphase voltage was measured by an oscilloscope. The rotational motion was observed by the motion of the flag that attached to the motor shaft.

Moreover, the rotating by the waveform generator was experimented to compare with the rotational motion by the driving circuit. Fig. 10 shows the arrangement of the rotation experiment. The coil was subjected to a driving voltage generated by a waveform generator. Three input voltages, phase-shifted by 120°, were applied to the three single-phase coils. The input voltage was measured by the oscilloscope.

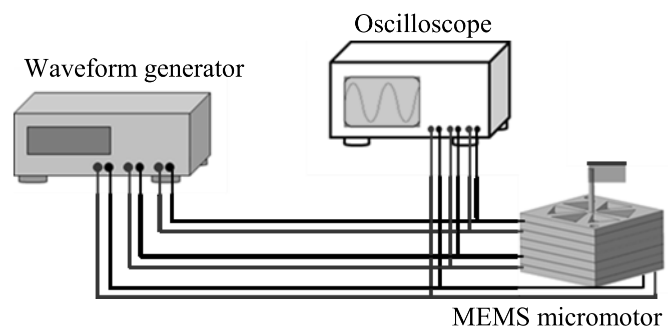

Fig. 10 arrangement of rotational experiment by waveform generator

IV. Results and Discusses

Fig. 11 shows the fabricated MEMS structural parts. The diameters of the through-circle pattern for holding the rotor and the rotor were 10.0 mm and 8.01 mm, respectively. In the lower layer for holding the multilayer ceramic coil formed six square patterns that were arranged to be shifted by $\pi/3$ radian. The dimensions of the base and height of the through-square patterns were 3.64 mm and 3.90 mm, respectively. The size of the hole for the shaft was measured by the by an optical confocal microscope. The diameter of the holes fell within 619 μm to 622 μm. Designed diameter of the hole was 620 μm, and the size error was found less than ± 3 μm.

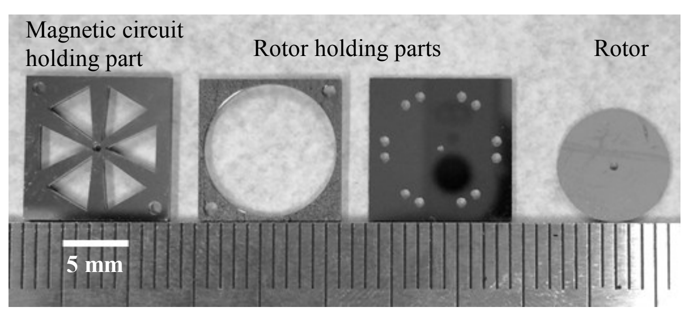

Fig. 11 fabricated MEMS structural parts

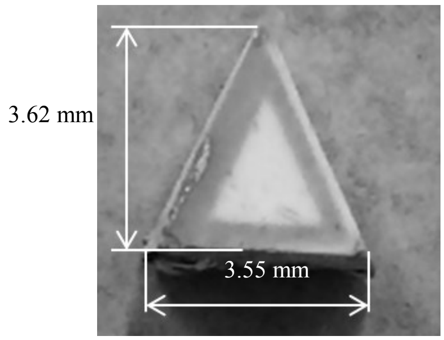

Fig. 12 fabricated multilayer ceramic coil for magnetic circuit

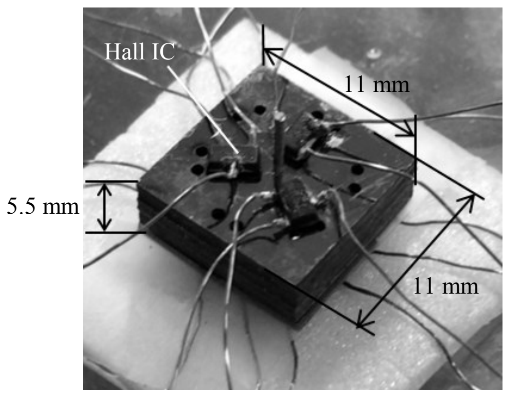

Fig. 13 assembled MEMS micromotor with MEMS parts and magnetic circuit

Fig. 12 shows the fabricated multilayer ceramic coil for the magnetic circuit. The average dimensions between the six ceramic coils of the base, height and thickness were 3.55 mm, 3.62 mm and 1.46 mm, respectively. As a result, the miniature three-dimensional structure coil was realized by the multilayer ceramic technology. The maximum and minimum clearance between the multilayer ceramic coil and the through-square pattern on lower silicon layer for holding the magnetic circuit were 473 μm and 54.6 μm, respectively. Therefore, it was possible to combine with the fabricated multilayer ceramic coils and the MEMS structural parts. However, the achieved output values of inductance showed the dispersion.

Fig. 13 shows the fabricated MEMS micromotor that was combined with the MEMS structural parts and the multilayer ceramic magnetic circuit. The sideways, endways and height were 11 mm, 11 mm and 5.5 mm, respectively. In this figure, the three IC for detection the rotational motion of the rotor was attached to the top frame. The dimension between the rotor and the IC was 800 μm.

In the rotational experiment, the rotational motion was observed by a high-speed camera. Fig. 14 shows the rotational motion of the fabricated MEMS micromotor at the stable rotational motion of 4200 rpm. The line in this figure shows the position of the flag that attached to the shaft. In the rotational experiment, after driving the motor drive circuit, the rotational speed increased from the stopped state. And then, the rotor showed the stable motion at 4200 rpm after about 5 seconds. Fig. 15 shows the waveform of the input voltage at the stable motion. By this result, the frequency was 69.9 Hz, and the input voltage of the *U* phase, *V* phase and *W* phase were 3.2 $V_{p\text{-}p}$, 2.1 $V_{p\text{-}p}$ and 2.1 $V_{p\text{-}p}$, respectively. The output waveform shows the deformation. The reason of the deformation of the output waveform is the difference of the property of the multilayer ceramic coil. The proposed MEMS micromotor required six separated coil structures, and these coils were paired by wire connecting. This problem will be solved by fabricating the paired coil pattern in the single ceramic coil structure and forming the connecting pattern on the bottom layer.

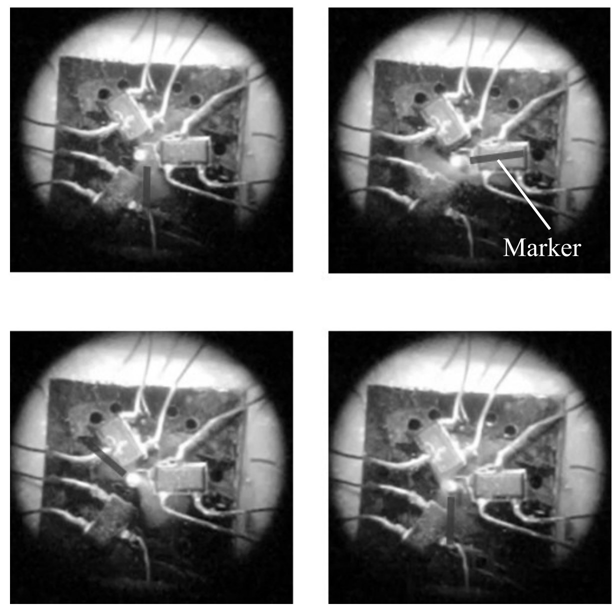

Fig. 14 rotational motion by driving circuit

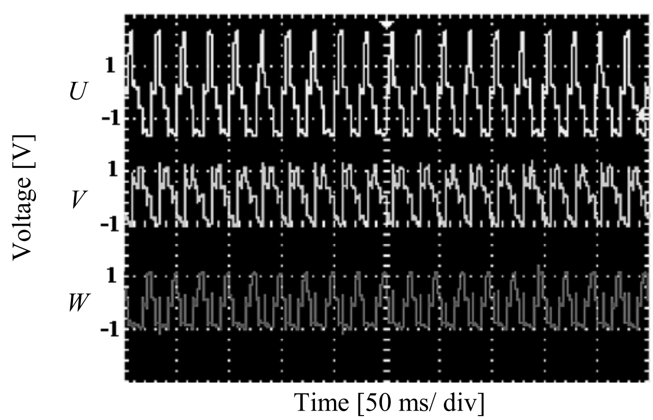

Fig. 15 output waveform of driving circuit

Table 1 results of rotational speed with load weight.

Weight [mg]	Rotational speed [rpm]	Initial torque
0	4200	Not require
53.7	2254	Not require
107.4	1440	Require
161.1	660	Require

The rotational motion of the fabricated MEMS micromotor that had a weight as a load was shown in table 1. In these results, the fabricated MEMS micromotor showed the rotational speed of 2254 rpm with 53.7 mg weight. However, the rotational motion with the weight of 107.4 mg and 161.1 mg required an initial torque. In this paper, the fabricated ceramic coil was not introduced the magnetic material and a deflection yoke. Therefore, the magnetic flux from the magnet that attached to the rotor was diverging. For achieve more large torque, it is required to introduce the ferrite ceramic material as the magnetic material.

The results were compared at the driving methods. The result of the rotational speed that was generated by the waveform generator was 480 rpm at 8Hz. The reason of the difference was the time of the synchronization. By the waveform generator, the input frequency was changed discretely. However, the driving circuit changes the input voltage continuously. In the future work, the driving circuit and hall IC will be constructed into the MEMS structural parts. It will realize the miniaturization of the MEMS micromotor that including the driving circuit.

V. Conclusion

This paper proposed the electromagnetic induction type brushless MEMS micromotor. The developed MEMS micromotor was combined with the MEMS structural parts and the multilayer ceramic coil for the magnetic circuit. The dimensions of sideways, endways and height of the MEMS micromotor were 11 mm, 11 mm and 5.5 mm, respectively. The MEMS structural parts constructed the upper layer for holding the rotor, the lower layer for holding the magnetic circuit, and the rotor that was attached to the 2-pole magnet. The six multilayer ceramic coils were arranged in the through-square pattern that was formed on the silicon lower layer. The dimensions of the base, height and thickness of the multilayer ceramic coil were 3.55 mm, 3.62 mm and 1.46 mm, respectively. By using the multilayer ceramic technology, the miniature three-dimensional structure coils were achieved without the winding wire.

The fabricated electromagnetic induction type MEMS micromotor was controlled by the motor driving circuit. The maximum rotational speed was 4200 rpm at the input frequency of 69.9 Hz. Moreover, the fabricated micromotor with the load weight of 53.7 mg showed the rotational motion, and the rotational speed was 2254 rpm.

The maximum rotational speed was compared between the driving circuit and the waveform generator. The rotational speed when the micromotor was controlled by the waveform generator was 480 rpm. The reason of the difference was the time of the synchronization. In the driving circuit, the hall IC was used for detecting the rotational motion. As a result, the driving circuit could change the input frequency continuously. In the future work, the driving circuit and hall IC will be constructed into the MEMS structural parts.

Acknowledgment

The sample of this study was fabricated by the facility at the Research Center for Micro Functional Devices, Nihon University. This study was supported by the CST research project of Nihon University. Furthermore, this study was partial supported by the Hosokawa Powder Technology Foundation.

References

[1] M. Mehregany, K. J. Gabriel, and W. S. N. Trimmer, "Micro gears and turbines etched from silicon," Sensors and Actuators, vol. 12, Nov/Dec. 1987, pp. 341–348.

[2] L.-S. Fan, Y.-C. Tai, and R. S. Muller, "Integrated movable micromechanical structures for sensors and actuators," *IEEE Trans. Electron Devices*, vol. 35, Jun. 1988, pp. 724–730.

[3] T. Morita, R. Yoshida, Y. Okamoto, M. Kuribayashi Kurosawa, and T. Higuchi, "A smooth impact rotation motor using a multi-layered torsional piezoelectric actuator," *IEEE Trans. Ultrasonics, Ferroelectrics, and Frequency Control*, vol. 46, Nov. 1999, pp. 1439–1445.

[4] Y. Suzuki, K. Tani, and T. Sakuhara, "Development of a new type piezoelectric micromotor," Sensors and Actuators A: Physical, vol. 83, May 2000, pp. 244–248.

[5] E. Sarajlic, C. Yamahata, M. Cordero and H. Fujita, "Three-phase electrostatic rotary stepper micromotor with a flexural pivot bearing," *J.of Microelectromechanical Systems*, vol. 19, Apr. 2010, pp. 338-349.

[6] L.-S. Fan, Y.-C. Tai, and R. S. Muller, "IC-processed electrostatic micro-motors," presented at Int. Electron Devices Meeting. Technical Digest, San Francisco, CA, December 11-14, 1988, pp. 666–669.

[7] K. Suzuki and H. Tanigawa, "Single crystal silicon rotational micromotors," presented at IEEE Micro Electro Mechanical Systems. An Investigation of Micro Structures, Sensors, Actuators, Machines and Robots, Nara, January 30- February 2, 1991, pp. 15–20.

[8] T. C. Neugebauer, D. J. Perreault, J. H. Lang, and C. Livermore, "A six-phase multilevel inverter for MEMS electrostatic induction micromotors," *IEEE Trans. Circuits and Systems II: Express Briefs*, vol. 51, Feb. 2004, pp. 49–56.

[9] Y-C. Tai, L-S. Fan, and R. S. Muller, "IC-processed micro-motors: design, technology, and testing," presented at IEEE Micro Electro Mechanical Systems. An Investigation of Micro Structures, Sensors, Actuators, Machines and Robots, Salt Lake City, February 20-22, 1989, pp. 1–6.

[10] S. Merzaghi, C. Koechli, and Y. Perriard, "Development of a hybrid MEMS BLDC micromotor," *IEEE Trans. Industry Applications*, vol. 47, Jan/Feb. 2011, pp. 3–11.

[11] B. Liu, "Research on the torque characteristic of disc micromotor on axial magnetic field," presented at 2012 2nd Int. Conf. on Consumer Electronics, Communications and Networks, Yichang, April 21-23, 2012, pp. 3480-3484.

[12] J. K. Bhardwaj and H. Ashraf, "Advanced silicon etching using high-density plasmas," in *Proc. SPIE Micromachining and Microfabrication Process Technology*, Austin, 1995, pp.224–233.

Pedestrian Excitation of a Polyester-Rope Footbridge

Edward M. Segal, Landolf Rhode-Barbarigos, Sigrid Adriaenssens, and Theodore P. Zoli

***Abstract*—**Dynamic testing of an experimental 64 m span polyester-rope footbridge (Ait Bayoud, Morocco, 2013) was conducted to inform the design of future bridges. The objective of this paper is to compare accelerations from single and group pedestrian excitation tests to minimum pedestrian comfort (serviceability) limits. In each test, the pedestrians walked in-sync with a metronome set to a frequency within the range that may be susceptible to pedestrian vibrations. For single pedestrian tests conducted near the bridge's natural frequencies, the comfort limits in the vertical and lateral directions at a given bridge location are typically exceeded for short time periods. For group pedestrian tests performed at the same frequencies, accelerations approached or exceeded the limits for longer durations. These results indicate that future polyester-rope footbridges that must meet comfort criteria should adapt the Ait Bayoud design.

***Keywords*—**dynamic performance, full-scale test, pedestrian excitation, polyester-rope suspended footbridge, vibration.

I. Introduction

An experimental 64 m span polyester-rope suspended footbridge, the first of its kind, was completed in Ait Bayoud, Morocco in 2013 (Fig. 1). The suspended footbridge is a form-found structure. It can thus be analyzed using closed form formulations [1] as well as numerical techniques such as dynamic relaxation [2]. Form-finding techniques have been employed for the design and optimization of structures of different nature [3-5] and design criteria [6-7]. The community in this rural area is tolerant of steep walking slopes and pedestrian vibrations, so no static or dynamic serviceability criteria were considered during design. The bridge was only required to meet a static strength criterion. Selecting to not meet any pedestrian vibration comfort (serviceability) limits is often acceptable in rural areas. For example, according to the footbridge classification system in the Service d'Études Techniques des Routes et Autoroutes (Sétra) technical guide, the Ait Bayoud bridge is a Class IV or "seldom used footbridge, built to link sparsely populated areas or to ensure continuity of the pedestrian footpath in motorway or express lane areas" [8] that has no comfort requirements. As this bridge is intended to serve not only as an important component in the local community's transport network, but also as a prototype, dynamic testing can provide insight to inform the design of future bridges so that more stringent comfort limits can be met where applicable.

The American Association of State Highway and Transportation Officials (AASHTO) pedestrian bridge guidelines [9] indicate that bridges with natural frequencies less than 1.3 Hz and 3Hz in the lateral and vertical directions, respectively, may be susceptible to pedestrian vibrations. A bridge with lower frequencies may still meet pedestrian comfort criteria if its accelerations are within acceptable limits. The Sétra technical guide [8] is referenced directly by AASHTO [9] as providing a potential method for evaluating dynamic performance. Sétra's recommendations are one of the many available approaches to the problem. The International Federation for Structural Concrete [10] summarizes both acceleration and natural frequency limits for a range of international standards.

For the Ait Bayoud bridge, a numerical eigenanalysis predicts the fundamental lateral and vertical natural frequencies are 0.51 Hz and 0.53 Hz, respectively. Additionally, higher natural frequencies are approximate harmonics of the fundamental natural frequencies. Consequently, not only the fundamental natural frequencies, but also a few of the subsequent natural frequencies fall below the stated AASHTO limits. These low natural frequencies are expected based on the bridge's low stiffness. Suspended footbridges have low stiffness compared to other bridge types like trusses and arches and polyester rope's inherent stiffness is low relative to that of steel cable. Prestressing the suspended ropes increases the system's stiffness, but the bridge is still quite flexible. The Ait Bayoud bridge is also very light; it has a self-weight of approximately 0.55 kN/m2. This combination of low weight and stiffness suggests that the structure will be lively, i.e. move noticeably under dynamic pedestrian loads. The complete details and results of the numerical analysis performed on the bridge are subjects of future work.

Full-scale testing of footbridges using pedestrian excitation can be used to examine a structure's accelerations. Typologies where such tests have been performed include suspension bridges [11] and stress ribbons [12], [13], and [14], which are both structural types that are similar in form to suspended footbridges. The objective of this paper is to compare accelerations from dynamic, single and group pedestrian excitation tests performed on the Ait Bayoud bridge to minimum pedestrian comfort limits.

Figure 1: Polyester-rope suspended footbridge in Ait Bayoud, Morocco during a group walking test.

II. SERVICEABILITY CRITERIA: PEDESTRIAL COMFORT LIMITS

Acceleration test results are compared to minimum comfort limits presented in Sétra's technical guide for footbridge Classes I to III. These limits are 0.8 m/s2 (0.082 g) and 2.5 m/s2 (0.255 g) in the lateral and vertical directions, respectively [15]. Lateral limits related to "lock-in" provided by Sétra [15] are not included in this study.

III. TEST SETUP

Six tri-axial micro-electro mechanical system (MEMS) accelerometers [15] were anchored to the top of the bridge deck at the locations shown in Fig. 2. Lateral and vertical acceleration time series at each of the accelerometers during all of the tests were recorded. The sampling rate was 100 Hz. Initial accelerometer deviations from zero were corrected by shifting the acceleration times based on average acceleration data found over 10 to 30 second intervals recorded before testing.

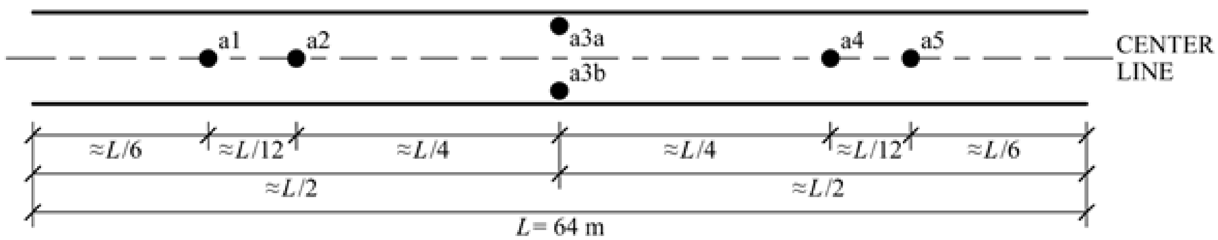

Figure 2: Plan view of the accelerometer locations on the bridge deck

Figure 3: Single pedestrian walking from the west end to the east end of the bridge.

IV. SINGLE PEDESTRIAN WALKING TESTS

A. *Experimental Procedure*

A set of eleven single pedestrian walking tests was performed. In each test, the pedestrian walked approximately in-sync with a metronome set to the desired frequency. One test was performed for each frequency that is a multiple of 0.25 Hz in the range, 0.5 Hz to 3Hz. This range extends to AASHTO's upper limit of 3 Hz for potential vibration problems in the vertical direction and includes frequencies close to the numerically determined bridge natural frequencies. A set of ambient vibration and free vibration tests performed to validate the vertical natural frequencies uncovered values that differ from the numerical predictions. The results of the ambient vibration and free vibration tests were not post-processed until after returning from Morocco, so the walking tests were not performed at the vertical natural frequencies found experimentally (approximately 0.68 Hz, 1.32 Hz, and 2.12 Hz) and therefore, did capture the bridge behaviour during resonance. The experimental natural frequencies are identified in Figure 4. Figure 4 shows the power spectral density (PSD) versus frequency plot from the free vibration test providing the overall (from all tests and accelerometers) maximum peak amplitudes.

ISBN: 978-1-61804-325-2

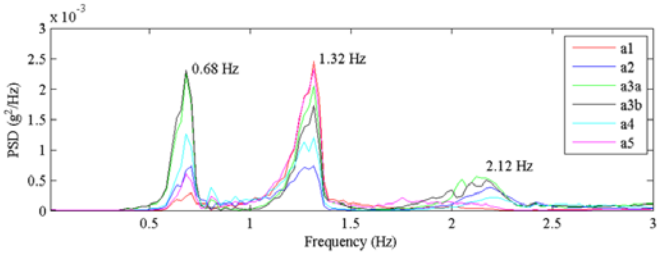

Figure 4: Power spectral density versus frequency for the six accelerometers in a free vibration test

In the tests, the pedestrian typically began at the west end of the bridge, walked to the east end of the bridge, turned around, and walked back to midspan where he stopped abruptly. For the 0.5 Hz and 0.75 Hz tests, the pedestrian stopped after walking to the east end of the bridge. Figure 3 shows the pedestrian mid-stride while walking across the bridge.

B. Results and Discussion

Table 1 presents the maximum (absolute values) for lateral (H) and vertical (V) accelerations among all of the accelerometers for each test. In all cases the maximum accelerations exceed Sétra's [8] 0.082 g and 0.255 g comfort limits in the lateral and vertical directions, respectively. Figures 5 and 6 present the acceleration time series for the accelerometers with the maximum accelerations in tests in which the walking frequency is closest to the experimentally found vertical natural frequencies: test s2 (walking frequency of 0.75 Hz is closest to 0.68 Hz), test s4 (walking frequency of 1.25 is closest to 1.32 Hz), and tests s7 and s8 (walking frequencies of 2.00 Hz and 2.25 Hz bracket 2.12 Hz). During this set of tests the comfort limits (represented with dashed lines in the plots) are typically exceeded at a particular accelerometer for only short durations of time.

Table 1: Results for single pedestrian walking tests

Test	Walking frequency (Hz)	Maximum |acceleration| (g) *H*	Maximum |acceleration| (g) *V*
s1	0.50	0.386, a2	1.017, a2
s2	0.75	0.392, a2	0.812, a2
s3	1.00	0.340, a2	0.865, a4
s4	1.25	0.533, a2	0.958, a4
s5	1.50	0.274, a4	1.124, a4
s6	1.75	0.338, a5	0.919, a5
s7	2.00	0.423, a5	1.221, a2
s8	2.25	0.637, a2	1.567, a5
s9	2.50	0.648, a2	1.289, a4
s10	2.75	1.410, a2	2.275, a5
s11	3.00	0.855, a2	2.549, a1

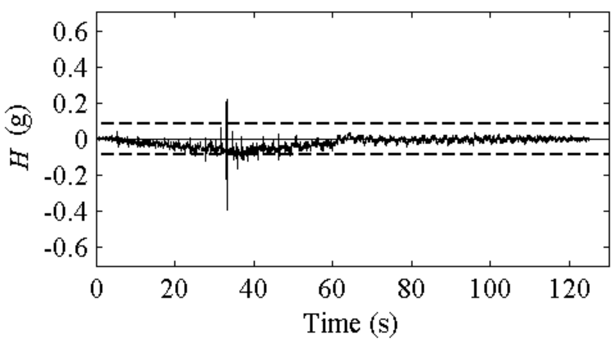

a. Test s2, accelerometer a2

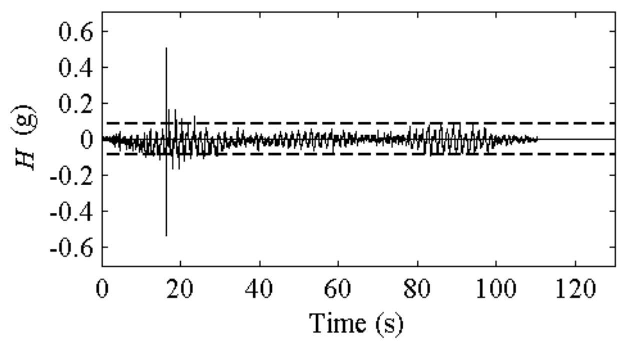

b. Test s4, accelerometer a2

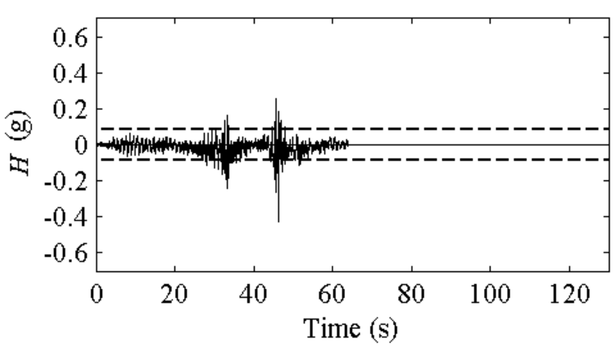

c. Test s7, accelerometer a5

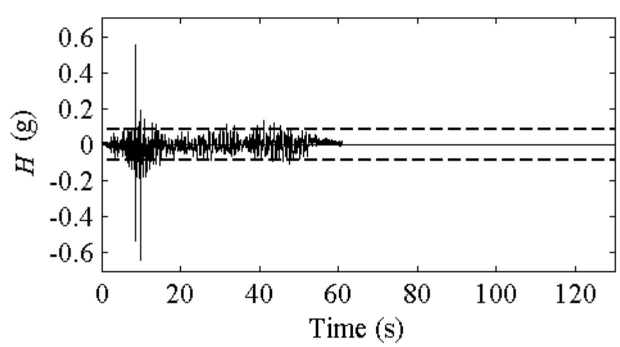

d. Test s8, accelerometer a2

ISBN: 978-1-61804-325-2

Figure 5: Acceleration time series for the lateral (a-d) accelerations for a set of the single pedestrian walking tests

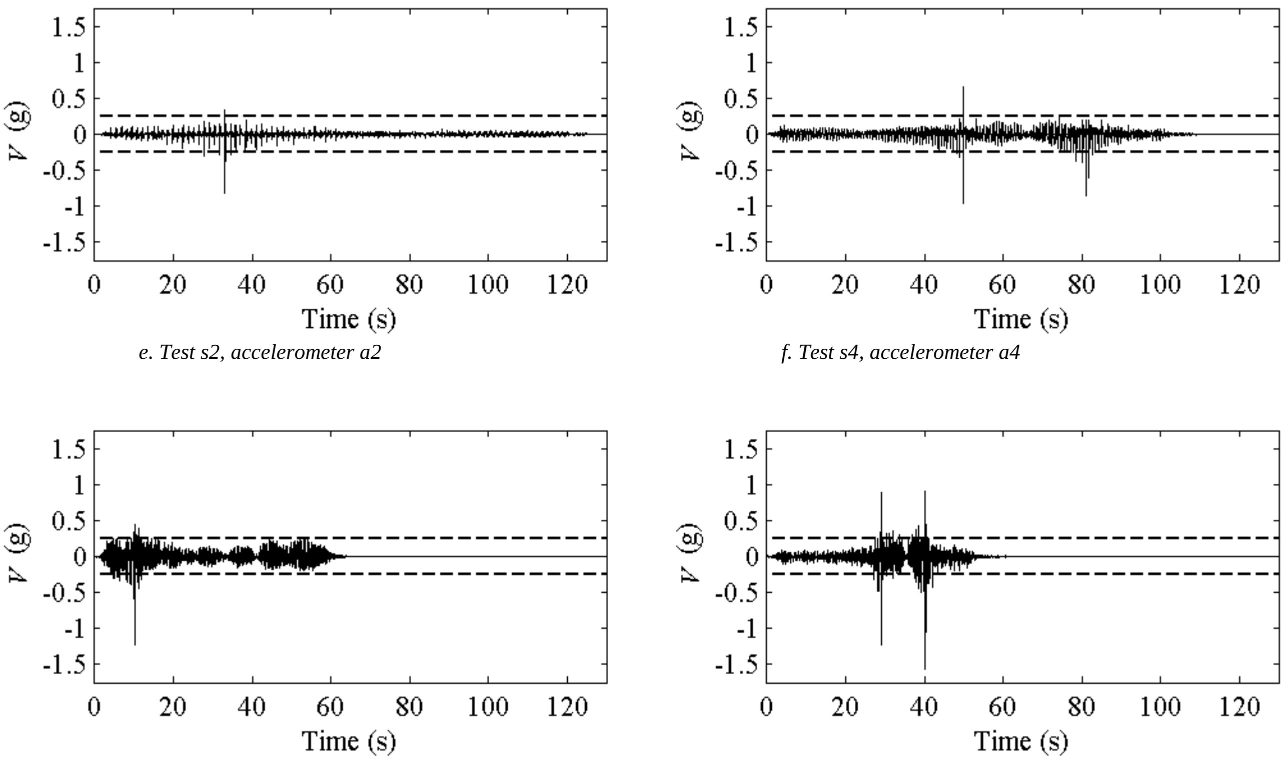

e. Test s2, accelerometer a2 *f. Test s4, accelerometer a4*

g. Test s7, accelerometer a2 *h. Test s8, accelerometer a5*

Figure 6: Acceleration time series for the vertical (e-h) accelerations for a set of the single pedestrian walking tests

V. Group Walking Tests

A. Experimental Procedure

A set of eight group walking tests was performed. In each test, four pedestrians walked approximately in-sync with a metronome set to the desired frequency. One test was performed for each frequency that is a multiple of 0.25 Hz in the range, 0.75 Hz to 2.5 Hz. These tests include the approximate numerical (second and higher modes), but not the experimentally found natural frequencies. The range here differs from the single pedestrian test. The lower end of the range was increased above that of the numerically predicted fundamental frequency because walking at 0.5 Hz was determined to be an unrealistic walking pace; it is very slow. Testing stopped after 2.5 Hz, because higher frequencies required walking at paces that were too fast to allow the pedestrians to synchronize.

In all tests, the group began at the west end of the bridge, walked to the east end of the bridge, turned around, and walked back to midspan where the pedestrians stopped abruptly. Fig. 5 shows the group of pedestrians in two different tests walking across the bridge.

B. Results and Discussion

Table 2 presents the maximum (absolute values) for lateral (H) and vertical (V) accelerations among all of the accelerometers for each test. As was the case in the single pedestrian tests, the maximum accelerations for the crowd tests exceed Sétra's [8] 0.082 g and 0.255 g limits in the lateral and vertical directions, respectively. Figure 7 presents a set of acceleration time series. Again, the acceleration time series shown are for accelerometers with the maximum accelerations in tests in which the walking frequency is closest to the experimentally found vertical natural frequencies. The plots show that during this set of tests, accelerations frequently are close to or exceed the comfort limits (shown in dashed lines). Had the tests been performed at walking frequencies closer to the actual natural frequencies of the bridge, it is expected that the resulting resonance would lead to even higher accelerations.

Table 2: Results for group walking tests

Test	Walking frequency (Hz)	Maximum |acceleration| (g)	
		H	*V*
g1	0.75	0.566, a5	1.678, a1
g2	1.00	0.663, a2	3.411, a2
g3	1.25	0.463, a5	1.940, a1
g4	1.50	0.526, a5	2.411, a3b
g5	1.75	0.718, a2	2.519, a5
g6	2.00	0.684, a2	2.690, a2
g7	2.25	0.959, a5	2.271, a3a
g8	2.50	0.904, a5	1.847, a5

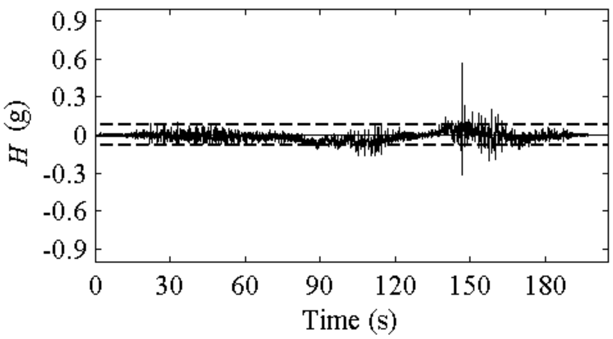

a. Test g1, accelerometer a5

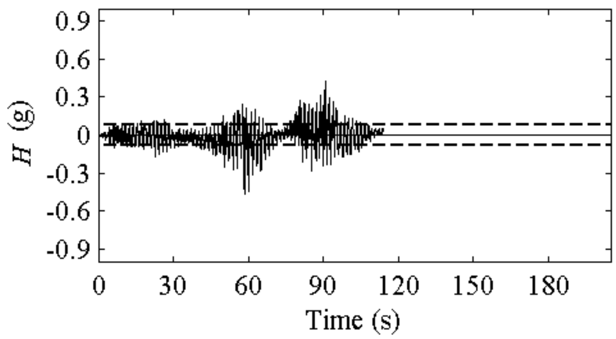

b. Test g3, accelerometer a5

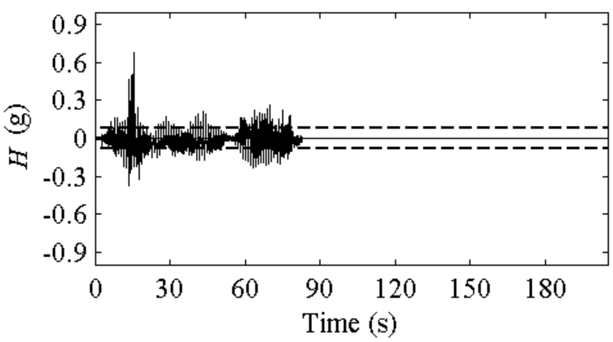

c. Test g6, accelerometer a2

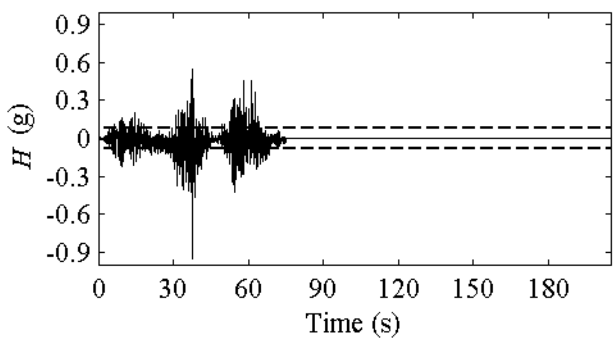

d. Test g7, accelerometer a5

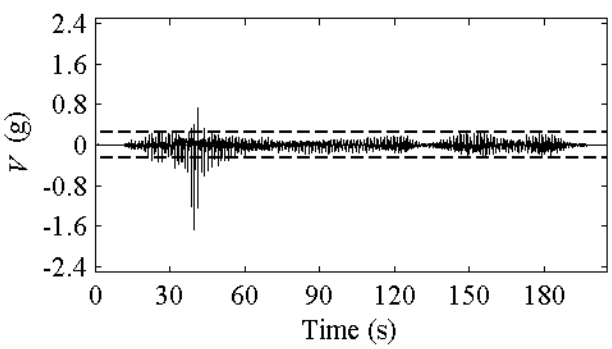

e. Test g1, accelerometer al

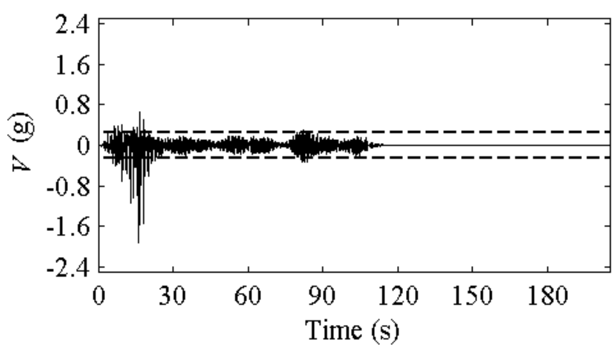

f. Test g3, accelerometer a1

ISBN: 978-1-61804-325-2

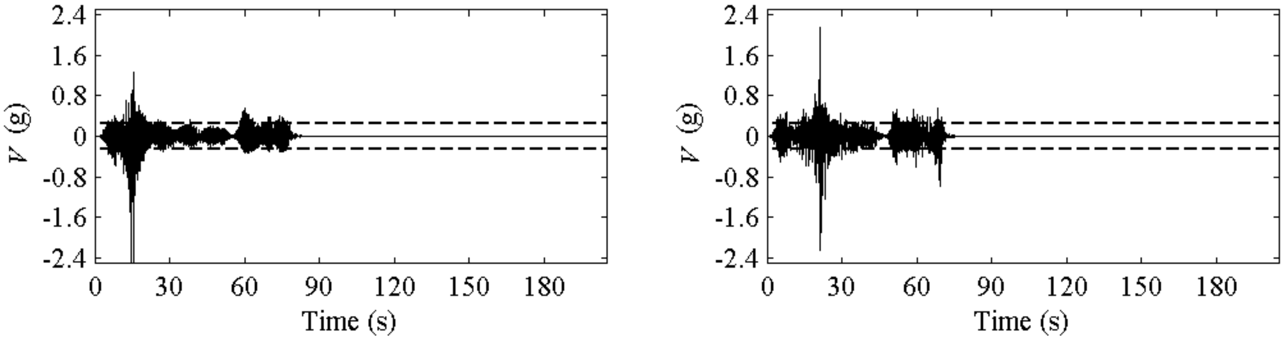

g. Test g6, accelerometer a2

h. Test g7, accelerometer a3a

Figure 7: Acceleration time series for the lateral (a – d) and vertical (e – h) accelerations for a set of the group walking tests

VI. Conclusions

This paper presented a set of dynamic, single and group pedestrian excitation tests performed on the first polyester-rope suspended footbridge built at a significant scale. Due to the bridge's low stiffness and weight it was anticipated that the bridge would be lively. Test results confirm this expected behaviour. The bridge has maximum accelerations that do not meet Sétra's minimum pedestrian comfort limits for footbridge Classes I to III. As the number of people on the bridge increases, the duration of time at which the limits are exceeded at a particular bridge location also increases. Synchronization of pedestrians with the bridge's natural frequencies was not done in this study; pedestrians walked at frequencies near, but not exactly at the experimentally found bridge natural frequencies. Walking at the natural frequencies is expected to lead to greater accelerations and durations of time in which comfort limits are not met.

The authors emphasize that the design of the Ait Bayoud bridge is not flawed and that modifications to the bridge to meet Sétra's minimum comfort limits for a Class I, II, or III footbridge are not necessary. The community is accepting of pedestrian vibrations and this rural bridge can be classified according to Sétra as a Class IV footbridge that has no comfort requirements.

Future owners of suspended polyester-rope footbridges may wish for their structure to meet minimum comfort limits such as those suggested for footbridge Classes I to III. To meet these limits, the design used for the Ait Bayoud bridge should be adapted. If a design's natural frequencies cannot be shifted outside the range of potential vulnerability by stiffening the structure through the use of additional prestress or elements (e.g., stays, underslung ropes, etc.) then the design's accelerations under pedestrian excitation should be reduced. Accelerations could be reduced through supplemental dampers or additional mass. In rural areas, utilizing locally sourced additional mass may be more feasible than using supplemental dampers.

Acknowledgment

Columbia University Engineers Without Borders students and U.S. Peace Corps volunteers assisted with setting up and performing the pedestrian vibration tests. Additionally, the authors would like to thank Maria Gibbs (University of Notre Dame, USA), Professor Branko Glisic (Princeton University, USA), Amin Karbassi (Basler and Hofmann AG, Switzerland), Justin Steinhouse (HNTB, USA), and Ryan Woodward (HNTB, USA) for discussions related to this work.

References

[1] IRVINE M. Cable structures. Mineola: Dover Publications, Inc.; 1981.

[2] BARNES M., ADRIAENSSENS S., KRUPKA M., "A novel torsion/bending element for dynamic relaxation modeling", Computers and Structures, 19 (1), 2013, pp 60–67.

[3] TYSMANS T., ADRIAENSSENS S., CUYPERS H., WASTIELS J., "Structural Analysis of small span Textile Reinforced Concrete Shells with Double Curvature", Composites Science and Technology, Vol. 69, No. 11-12, 2009, pp. 1790 – 1796

[4] ADRIAENSSENS S., "Feasibility study of medium span spliced spline stressed membranes", International Journal of Space Structures, Vol. 23, No. 4, 2008, p. 243-251.

[5] CAUBERD N., TYSMANS T., ADRIAENSSENS S., WASTIELS J., MOALLERT M., BELKASSEN B., "Shells elements of textile reinforced concrete using fabric formwork: a case study", Advances in Structural Engineering, Vol. 15, No. 4, 2012, pp. 677 – 689.

[6] RICHARDSON J.N., ADRIAENSSENS S., COELHO R.F., BOUILLARD P., "Coupled form finding and grid optimization approach for single layer gridshells", Engineering Structures, Vol. 52, 2013, pp. 230–239.

[7] ADRIAENSSENS S., NEY L., BODARWE E., WILLIAMS C., "Finding the form of an irregular meshed steel and glass shell based on construction constraints" Journal of Architectural Engineering. Vol. 18, No. 3, 2012, pp.206-213.

[8] SERVICE D'ÉTUDES TECHNIQUES DES ROUTES ET AUTOROUTES, Technical Guide -- Footbridges: Assessment of Vibrational Behaviour of Footbridges Under Pedestrian Loading, Paris, 2006.

[9] AMERICAN ASSOCIATION OF STATE HIGHWAY AND TRANSPORTATION OFFICIALS (AASHTO), LRFD Guide Specifications for the Design of Pedestrian Bridges, 2nd Ed., Washington, D.C., 2009.

[10] WORKING PARTY 1.1.2. OF THE INTERNATIONAL FEDERATION FOR STRUCTURAL CONCRETE (FIB), TASK GROUP 1.2., fib Bulletin No. 32: Guidelines for the Design of Footbridges, Lausanne, 2005.

[11] DALLARD P., FITZPATRICK T., FLINT A., LOW A.,SMITH R.R., WILLFORD, M., and ROCHE, M., "London Millennium Bridge: Pedestrian-Induced Lateral Vibration," ASCE Journal of Bridge Engineering, Vol. 6, No. 6, 2001, pp. 412-417.

[12] CAETANO E. and CUNHA Á., "Experimental and Numerical Assessment of the Dynamic Behaviour of a Stress-Ribbon Footbridge," Structural Concrete, Vol. 5, No. 1, 2004, pp. 29-38.
[13] CAETANO E, CUNHA Á., and MOUTINHO C., "Vandal Loads and Induced Vibrations on a Footbridge," ASCE Journal of Bridge Engineering, Vol. 16, No. 3, 2011, pp. 375-382.
[14] MAGALHÃES F., CUNHA Á., and CAETANO, E., "Dynamic Testing of the New Coimbra Footbridge Before Implementation of Control Devices," IMAC-XXV: Conference & Exposition on Structural Dynamics - Celebrating 25 Years of IMAC, Orlando, 2007.
[15] SENSR, http://www.sensr.com, 2014.

Cohesive crack growth modelling in heterogeneous materials

Jiří Vala and Vladislav Kozák

Abstract—**Prediction of the crack growth of the brittle and quasi-brittle fracture of structural materials is studied. Crack extension is simulated by means of element extinction algorithms (cohesive elements respectively). The principal effort is concentrated on the application of the cohesive zone model with the various traction separation laws. Determination of micromechanical parameters is based on the combination of static tests, microscopic observation and numerical calibration procedures. The attention is paid on the influence of initial value of *J*-integral and the slope of *R*-curve which is modelled by the 3-dimensional finite element method. The practical applications refer to the modelling of the fracture behaviour of structural steels, intermetalic alloys and fibre composites.**

Index Terms—**Brittle fracture, cohesive crack growth, traction separation law, computational modelling.**

I. Introduction

DEVELOPMENT and design of advanced equipments and components introduces the question how to ensure the operational security. Safety factors are connected with and dependent on the presence of the defects originated during production or service of the given part or components. An effort is concentrated on the description, eventually prediction of the fracture behaviour of bodies with a priori cracks or defects created during service loading.

Cohesive crack models are nowadays widely used to predict cracking processes in the materials. The importance of the cohesive zone approach is emphasized to analyze the localization and failure in engineering materials. The micromechanical modeling encounters a new problem that is different from assumption of continuum mechanics. The material is not uniform on the microscale, but a material element has its own complex microstructure and the concept of a representative volume element (RVE) has been introduced. The material separation and damage of the structure is described by the interface element. Using this technique, the behavior of the material is split into two parts: i) the damage of the free continuum with arbitrary material law and ii) the cohesive interface between the continuum elements.

From a variety of damage models, the cohesive models, derived in [1] and [2], seem to be especially perspective for practical applications. Thanks to their phenomenological character, they can be adapted for various kinds of materials and damages. Cohesive models or (more often) cohesive zone models (CZM) by [3] are used to simulate fracture and fragmentation processes in metallic, polymeric, ceramic materials and composites. Instead of an infinitely sharp crack envisaged in linear elastic fracture, the energy from the process zone is transferred from external work both in the forward and wake regions of the expanding crack. Base principle of CZM is using cohesive elements for crack and damage modelling, while the classical continuum elements are undamaged. In terms of modelling, the separation of materials is realized using cohesive elements in the boundary line between classical elements of continuum. Using cohesive models, the behaviour of materials is considered using two types of elements: i) the former element for classical continuum, ii) the latter connecting cohesive element. The separation of such connecting cohesive elements is computed from the displacement of neighbouring continuum elements. Generally the separation is dependent on the normal and shear stresses.

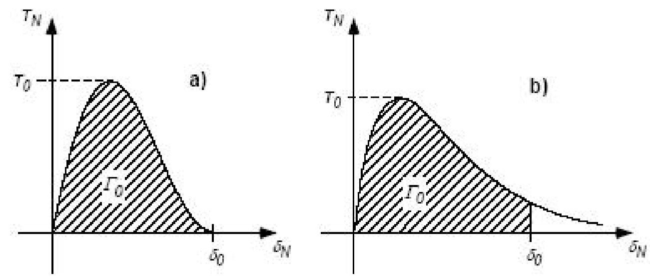

Fig. 1. Examples of the traction - separation law.

In case of the cohesive models we need to identify the hypothetical crack tip to determine the crack driving force by using traction-separation models that are expressed in the shape of the T-δ curve. The maximum value of T has usually the character of cohesive strength; there is the physical crack tip where the separation has the maximum value at this distance, i. e. the crack is fully separated and the energy absorption for decohesion is total, as analyzed in [4]; for the illustration see two versions of the traction - separation law on Figure 1. The concept of the cohesive zone model has been widely employed to investigate various material failure phenomena; here we shall mention only some results important for our further considerations, whereas much more historical conjunctions including application scopes can be found in [5] and [6].

Since the analytic computational approaches give significant result only in very special cases, typically for the simulation of well-organized experiments, which is often valid also for semianalytic considerations, relying on classical infinite functions series and numerical quadrature, the majority of recent computational algorithms works with finite elements or similar techniques, namely with various implementations of the extended finite element method (XFEM) by [7] or [8], or with the cohesive segments method by [9], handling the

ISBN: 978-1-61804-325-2

nucleation, growth and coalescence of multiple cracks. Some advantages of meshfree cohesive modelling of failure, namely of the reproducing kernel particle method (RKPM) within the framework of wavelet theory, are noticed in [10], together with the comparison of the cohesive zone approach and the atomistic view. The analysis of quasistatic brittle fracture in inhomogeneous media by [11] relies on the method of iterated conformal maps, distinguishing between fracture patterns in three basic modes. Really, there are three ways of applying a force to enable a crack to propagate: i) opening mode (tensile stress is normal to the plane of the crack), ii) sliding mode (shear stress acts parallel to the plane of the crack and perpendicular to the crack front) and iii) tearing mode (shear stress acts parallel to the plane of the crack and parallel to the crack front). The brittle-to-ductile transition (BDT), as well as the fracture toughness of semi-brittle materials, is studied the competition between the bond breaking at the crack tip and the mechanisms that govern crack tip plasticity at the atomic scale in [12]. The element-free Galerkin method (EFG), introduced in [13], substitutes the standard Galerkin finite element technique by the implementation of interface elements for the representation of displacement discontinuities due to cracks.

Limited accuracy of all crack growth predictions, depending on the creation of geometric singularities due to certain nonlocal constitutive relations, motivates the development of still alternative approaches, utilizing i) statistical considerations, ii) fractal theory, iii) advanced geometrical description of macro- and microfractured zones or iv) both physical and mathematical homogenization and scale-bridging. In the following remarks we shall try to preserve this classification, although some recent approaches cannot be assigned to just one of the classes i) – iv). Starting with i), whereas the Weibull function in [14] is introduced as simple mathematical relation that is capable of describing the variability in strength, [15] presents the complete Weibull fracture statistics of ceramics and [16] understands the brittle crack growth as the forced separation of chemically bonded surfaces, working with the survival probability within the separation zone. In ii) the generalization of [11] to fractal cracks, derived in [1], opens the way to the fractal-based mesoscopic analysis of damage and fracture in heterogeneous materials by [20], as well as to such discrete cohesive crack modelling by [21]; [22] then works with the fractal statistics of fragmentation (breaking a solid into separate fragments caused by multiple fractures) of brittle materials, supported by original experiments and signal processing techniques. From the point of view of iii) the most difficult problem is to complete the general nonlinear geometrical concept of [23] by the adequate physical considerations, including material characteristics identifiable in engineering practice, as documented by [24]. In iv) the RVE-based average approaches for a cohesive zone by [25] and [26] are still the most frequent; however, the exploitation of more advanced bridging between macro- and microscale models of cohesive fracture, as in [27], as well as of the formal mathematical homogenization like the Γ-convergence for rapidly oscillating functions in [28], should be noticed.

Regardless of quite different material structures, other size of specimens, particles in a matrix, etc., similar approaches are applied also to the composites utilized in civil engineering, as for the a masonry composite made of brick units and mortar arranged forming layers by [29] and in most applications for concrete. Some additional physical processes should not be neglected in this case: namely the cohesive damage friction interface model, suggested in [30], accounts for water pressure on crack propagation, whereas the semianalytic approach of [31] to reinforced cementitious composites is able to study the effects of fracture toughness, of crack bridging and of initial unbridged flaw size, thanks to the very special physical and geometric setting, due to the need of easy comparison with standard experimental results. The multi-scale approaches like [32] and fractal ones like [33] have been developped for concrete, too.

II. Physical and mathematical background

Let us introduce the basic physical and mathematical assumptions and notations of the cohesive zone approach, needed in this paper to understand (at certain minimal generality level) the crack behaviour of some material classes, important in engineering practice. A lot of potential improvements could be inspired by *Introduction*; however, the implementation of a general geometrical description of finite structured deformation, as well as of results from classical or fuzzy statistics, fractal theory or two-scale and similar types of convergences on homogenization structures would make this text very reader-unfriendly.

As a model problem, let us consider a domain Ω in the 3-dimensional Euclidean space R^3, occupied by a deformable body, supplied with the Cartesian coordinate system $x = (x_1, x_2, x_3)$; some (local, formally outward) unit normals $n = (n_1, n_2, n_3)$ are assumed to exist (almost) everywhere on the boundary $\partial\Omega$ of Ω in R^3. We shall study the behaviour of a deformable body on certain time interval I, starting from the zero time.

Let $u = (u_1, u_2, u_3)$ denote the displacement related to the above mentioned reference geometrical configuration; their zero-time initial values (compatible with Eq. 1), as formulated below) are prescribed. In the following considerations, i, j, k and l will be Einstein summation indices from the set $\{1, 2, 3\}$; if no comments are added, all relation will be valid for all values of free indices from this set. For simplicity, an index i preceded by a comma means a partial derivative with respect to x_i: e. g. $\psi_{j,i}$ can be used instead of the full notation $\partial\psi_j/\partial x_i$. Unlike such derivatives, an upper dot means a partial derivative with respect to any time t taken from I. the following equations should be then valid on I (without additional explanations).

Let us suppose that $\partial\Omega$ can be decomposed to its disjoint parts Γ, Θ and Ξ. We shall consider the Dirichlet boundary conditions

$$u_i = 0 \qquad \text{on } \Theta \tag{1}$$

and the following loads: the volume ones $f = (f_1, f_2, f_3)$ on Ω and the surface ones $g = (g_1, g_2, g_3)$ on Γ. The knowledge of the material density ρ on Ω will be needed, too. The notation Ξ is reserved for the crack; its time development is possible.

For the stresses σ_{ij} the well-known Cauchy equilibrium condition reads

$$\sigma_{ij,j} + f_i = \rho \ddot{u}_i \qquad \text{on } \Omega \,, \tag{2}$$

together with the Neumann boundary conditions

$$\sigma_{ij} n_j = g_i \qquad \text{on } \Gamma \,. \tag{3}$$

Moreover, introducing the strains $\varepsilon_{kl}(u)$, for the small strain approximation identifiable with $(u_{k,l} + u_{l,k})/2$, we need some constitutive relations to obtain σ_{ij}, typically

$$\dot{\sigma}_{ij} = G_{ij}(\dot{\varepsilon}(u)) \qquad \text{on } \Omega \tag{4}$$

with some prescribed mapping G_{ij} where ε can be considered as a symmetrical matrix of all $\varepsilon_{kl}(u)$, following [9], p. 72. In the simplest case the choice $G_{ij}(\varepsilon(u)) = C_{ijkl}\varepsilon_{kl}(u)$ leads to the Hooke law with constant characteristics C_{ijkl} (thus time derivatives can be removed) generating a symmetrical positive definite matrix (which still admits nonhomogeneous and anisotropic materials).

Up to now, at least with empty Ξ (which may be the initial case), we have only the standard problem of deformation of linear (or similar) elastic body. Let us moreover suppose that Ξ, representing a crack, consists of two identical parts Ξ^+ and Ξ^-, distinguished by the opposite orientation of n only. The value of u on the crack tip, because of the irregularity of such point, must be evaluated separately, using some J- or K-nonlocal stress integrals; this can lead to the irreversible enlargement of Ξ in time. Nevertheless, the 2-dimensional simplifications are utilized in most computational tools – cf. [7], p. 831.

The Neumann boundary condition analogous to Eq. 3 with 0 instead of g_i could be considered on Ξ outside the cohesive zone; To force the material nonpenetrability, for the notation $\delta u_i = u_i^+ - u_i^-$ where u_i^+ and u_i^- have to be understood in the sense of traces of u from Ω then we should check also $\delta u_i n_i \geq 0$ (which is rarely done in practical algorithms).

Inside the cohesive zone the physical considerations are more delicate: a new constitutive relation has to be introduced on Ξ (active on its part), e. g. in the form presented in [9], pp. 73 and 77,

$$\dot{\tau}_i = \gamma_i(\delta \dot{u}) \qquad \text{on } \Xi \tag{5}$$

with some prescribed mapping γ_i where $\delta \dot{u}$ can be introduced in the similar way as δu and the discontinuity tractions τ_i replace g_i from Eq. 3. The most simple form of such relation seems to be $\dot{\tau}_i = \kappa \delta \dot{u}$ with certain tangent stiffness of the traction separation law. One can observe very special forms, as rectangular, (piecewise) linear, etc., of cohesive laws in engineering practice (cf. [7], p. 816); for more details see the following section and all relevant references.

Introducing the set of admissible displacements $\mathcal{V}$ as those displacement from appropriate function spaces satisfying Eq. 1 (Lebesgue, Sobolev, Bochner, etc. spaces are exploited in most cases to guarantee the formal correctness of all formulations and the existence and uniqueness of variational or weak solutions, at least for linear and selected semilinear problems), applying the Green - Ostrogradskiĭ theorem (on the integration by parts), we are able to convert (2) and (3) to

$$\begin{aligned} &(\varepsilon_{ij}(v), \sigma_{ij}) - (v_i, \rho \ddot{u}_i) + \langle \delta v_i, \tau_i \rangle \\ &= (v_i, f_i) + \langle v_i, g_i \rangle \quad \forall \; v \in \mathcal{V} \,; \end{aligned} \tag{6}$$

here (ψ, ϕ) mean the integrals of $\psi(x)\phi(x)$ over Ω (with hidden Einstein sums), $\langle \psi, \phi \rangle$ and $\langle \psi, \phi \rangle_*$ then the similar integrals over Γ and Ξ_+, respectively. Both constititive relations Eq. 4 and Eq. 5 are supposed to be hidden in Eq. 6. Consequently some integral equation of the type Eq. 6, representing the Galerkin formulation of our model problem, is applied in most numerical algorithms based on (classical or extended) finite element techniques and occurs also in derivation of numerous meshless algorithms, both dynamic and quasistatic ones.

III. Crack behaviour of selected materials

A. *Structural steels*

The standard tensile experiments have been used to determine material curve for characterization of the elastoplastic behaviour of tested material. The relation σ_e - ϵ_e was found, but key problem is the validity of this relation after necking. According to many experimental observations in [5] the new approximate curve was received. For forged 42CrMo4 steel the ductile fracture was predicted and $J - \Delta a$ curve is calculated by cohesive elements using Warp3D and Abaqus codes.

For the determination of the cohesive stress, T_0 in the case of normal fracture (mode I) a set of twelve experiments for tensile notched bars was done. The mean value of the cohesive stress T0 was determined from the above mentioned set and from the computations for the material curve received from the waisted tensile specimens; T_0 is then 2000 MPa. For determination of the stress-strain distribution the standard FEM Abaqus package with CAX4 elements was used. The standard CT specimens were used for J-integral determination according the ASTM 1820-99a procedure (based on measurement of the $J - \Delta a$ curve). The experimentally determined value of J_i was found to be 115 MPa.mm. This value was calibrated using numerical procedure using WarpD.

The numerical modelling was realized with all material curves. The standard FEM package Abaqus has been utilized. Set of computations were applied to the calibration of the cohesive parameters used for $J - \Delta a$ curve prediction. Various combinations for T_0 and J_i were tested. In Figure 2 the values J_i are marked as Cohe_1, Cohe_2 and Cohe_3 (J_i with values 110, 120, 130) and received data were compared with the experimental values. The best correlation was found for first value of J_i=110 MPa.mm. From the above analyses follows the prime combination of the cohesive parameters (T_0=2000 MPa, J_i=110 MPa.mm).

Single three point bend specimen SE(B) has been used for experimental prediction of the $J - R$ curve. Using the cohesive parameters received on the notched specimens T_0 and J_i on the CT specimens the numerical simulation of the stable crack growth was done and $J - R$ curve was predicted – see Figure 3. The FE mesh consists from 8560 nodes and 7155 element C3D8 (Abaqus). Owing to numerical instability more than 1000 loading steps were applied.

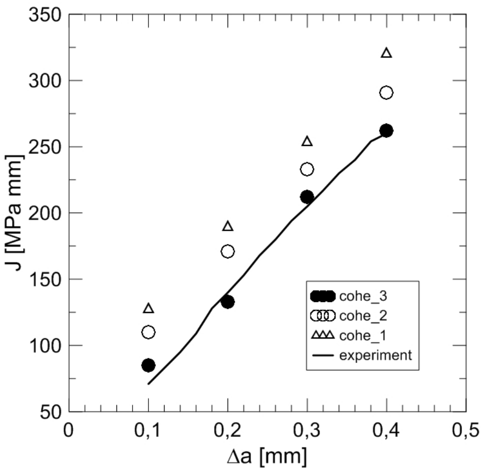

Fig. 2. J_i calibration on CT specimen.

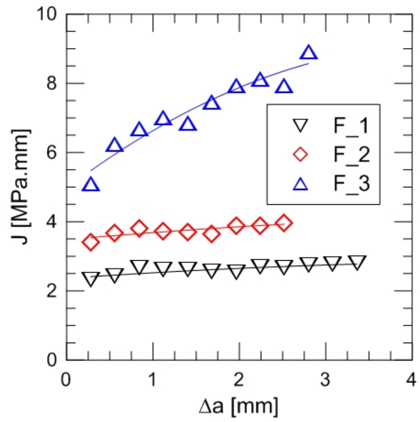

Fig. 5. $J - R$ curve: $K = 14$ MPa.m$^{1/2}$, $K = 16.3$ MPa.m$^{1/2}$, $K = 20$ MPa.m$^{1/2}$ (sharp notch, $\sigma_y = 200$ MPa).

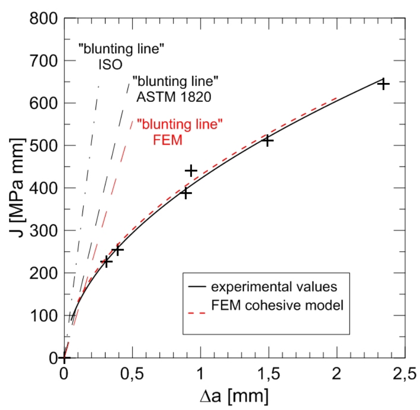

Fig. 3. $J - R$ curve for SE(B) specimen.

B. Intermetallic alloy TiAl

Main goal of the experimental work was the evaluation of the flexural strength tests in the temperature range from room temperature up to 800 C for the intermetallic alloy TiAl (see [36]). The materials used in this investigation had the composition Ti-48Al-2Cr-2Nb-1B and Ti-46Al-0,7Cr-0,1Si-7Nb-0,2Ni (marked I and F).

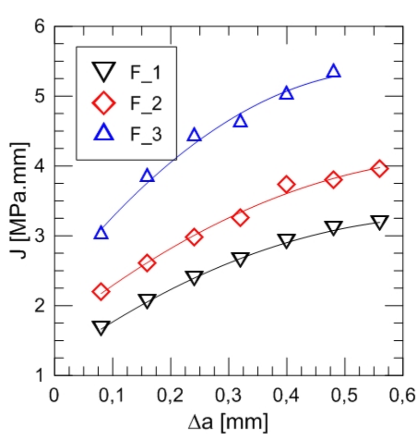

Fig. 4. $J - R$ curve: $K = 14$ MPa.m$^{1/2}$, $K = 16.3$ MPa.m$^{1/2}$, $K = 20$ MPa.m$^{1/2}$ (Chevron notch, $\sigma_y = 200$ MPa).

The FEM mesh with two modifications was created for the stress analysis. The first one had 10000 C3D8 elements and second one 90000 elements. After some numerical test was found that there is a very small discrepancy between them and a mesh with smaller density of elements was used for next computations. The cohesive 3D elements COH3D8 with zero thickness were used for cohesive zone modelling using FEM packages Abaqus and Warp3D.

The input parameters of the cohesive model with linear damage development for alloy I were determined following experiments for fracture toughness. In this way the fracture energy was assigned expressing the area below the TSL. Parameter T_0 was evaluated from the values of fracture stresses. The value δ_0 was found using the area below the TSL. Procedure for the exponential traction separation law implemented in Warp3D was very similar. Obtained cohesive parameters were used in FEM computation for 3PB test. F-alloy modelling can be seen in Figure 4. J-integral in Warp3D is continually computed ahead the crack tip and his positions are changing during the element killing. Thereafter the construction of the $J - R$ curve can by constructed very precisely.

According the experimental observation the $J - R$ curve reflects various types of microstructures. The flat curves represents the duplex microstructure, rapidly increasing curves the lamelar microstructure and the curve between the nearly lamelar microstructure. In the following Figure 5 and Figure 6 one can see the influence of the notch shape on the microstructure damage processes.

C. Long fibre composites

The failure of composites has been investigated extensively from the micromechanical point of view. When a crack propagates in a composite material in a direction perpendicular to that of reinforced fibres, the failure process typically involves four basic mechanisms: matrix cracking, fibre/matrix debonding, fibre breakage and fibre pull-out. Critical problems in application of these materials are the interfaces between matrix and reinforcing fibres. The interface is very strip area with primary key property including the fracture toughness,

ISBN: 978-1-61804-325-2

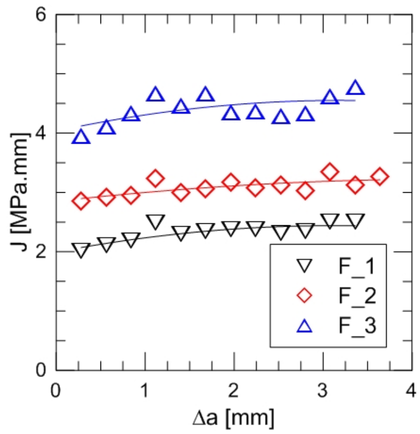

Fig. 6. $J-R$ curve: $K = 14$ MPa.m$^{1/2}$, $K = 16,3$ MPa.m$^{1/2}$, $K = 20$ MPa.m$^{1/2}$ (sharp notch, $\sigma_y = 300$ MPa).

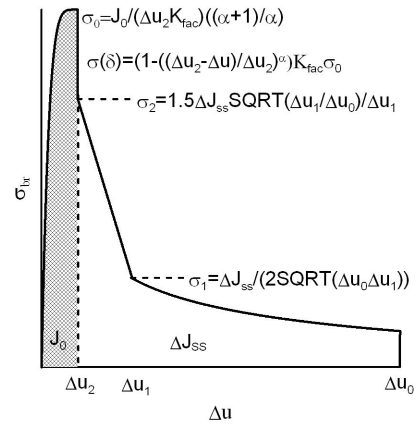

Fig. 7. Traction separation (bridging) law modification.

strength and fracture behaviour. This interface plays the crucial role in stress transferring between reinforcement and matrix and so it determines the mechanical and fracture behaviour. The separation is given by the common influence between normal and tangential directions at the interface. Compound materials consist of two or more constituents with different properties complementing other. The degrading properties of one constituent are leveled off by better properties of the others. Damage evolution is sensitive to morphological parameters of the microstructure such as volume fraction, size and spatial distribution of reinforcements, interfacial strength and size defect.

For glass fibre composites, the interfacial properties are controlled by the sizing, which is applied to the glass fibres during manufacture. The change of sizing results in changes of these properties. This leads to the influence to the mechanical properties such as strength and fracture toughness. The concept of strength is used for characterizing crack initiation in composite design, while fracture toughness determines crack growth and damage development. Bridging occurs during cracking in mode I crack growth along the fibre direction. This failure mode plays an important role during delamination of fibre composites and cracks splitting around holes and notches. The fibre bridging zone must be modelled as a discrete mechanism on its own; failure is not just controlled by the cracking at the crack tip. The failure process can be described by a bridging law, which describes the relationship between the crack opening displacement and the local bridging tractions resulting from the bridging ligaments. This paper derives the necessary basics and equations to implement these laws into the commercial finite element code Abaqus with a cohesive user element. Different numerical adjustments of the bridging law will be discussed in detail in oral presentation. Crack aspects, such as crack opening shape and the influence of bridging law parameters, are studied based on the numerical results.

Now consider the specimen having a crack with bridging fibres across the crack faces near the tip. The bridging law is then taken to be identical at each point along the bridging zone. Since fibres will fail when loaded sufficiently, we assume the existence of a characteristic crack opening δ_0, beyond which the closure traction vanishes. Shrinking the path of the J-integral to the crack faces and around the crack tip gives

$$J = \int_0^{\delta^*} \sigma(\delta)\,\mathrm{d}\delta + J_{TIP} \tag{7}$$

where J_{TIP} is the J-integral evaluated around the crack tip (during cracking is equal to the fracture energy of the tip, J_0). The integral is the energy dissipation in the bridging zone and δ^* is the end-opening of the bridging zone at the notch root. The bridging law can be determined by differentiating Eq. 7:

$$\sigma(\delta^*) = \frac{\partial J_R}{\partial \delta^*} \tag{8}$$

where J_R is the value of J during crack growth. Initially, the crack is unbridged. Thus in Eq. 8 crack growth initiates when $J_R = J_{TIP} = J_0$. As the crack grows, J_R increases in accordance with Eq. 7. When the end opening of the bridging zone δ^* reaches δ_0, the overall R-curve attains its steady state value J_{ss}.

There are a variety of possible methods for implementing cohesive laws within commercial finite element programs. The most versatile is the development and programming of cohesive elements. These elements are in most cases defined with zero thickness and prescribe stresses based on the relative displacement of the nodes of the element. Similar work has also been undertaken with spring elements (force-opening relation), although in this case there might be simplifications required when calculating the equivalent nodal spring forces from the surrounding elements. The procedure is not straight forward when springs are connected to elements with non-linear shape functions, such as 8-node elements.

The constitutive expression can be expressed either with a linear displacement term for Δu, or with a coupled form, where Δu is included with non-linear dependence. The preferred option depends on the form of the constitutive equation Eq. 7 and its numerical implementation:

$$J_R(\delta^*) = J_0 + \Delta J_{SS}\left(\frac{\delta^*}{\delta_0}\right)^{1/2}. \tag{9}$$

Two points need to be addressed during the numerical adjustment: removal of the stress singularity at $\Delta u = 0$ and

ISBN: 978-1-61804-325-2

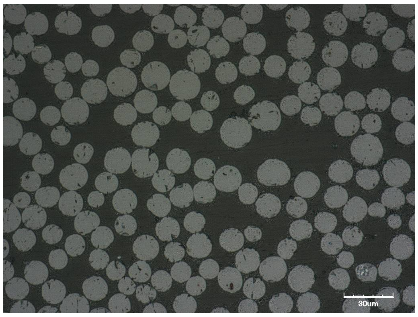

Fig. 8. Image of the microstructure.

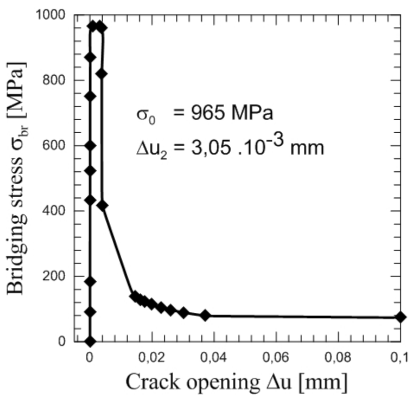

Fig. 9. Traction separation law after calibration procedure.

incorporation of the initial fracture strength J_0 improved traction separation law as can be seen in Figure 7. The material used for the bridging stresses modelling was a commercially available SiC Nicalon fibre reinforced borosilicate glass matrix composite (see Figure 8). Properties of the glass matrix, SiC fibres and composite were: Young modulus 63, 198, 118 GPa, Poisson ratio 0.22, 0.20, 0.21, tensile strength 60, 2750, 600-700 MPa.

For the crack growth modelling the following data determined experimentally were used: J_0 = 6200 J/m^2, J_{ss} = 18500 J/m^2, Δu_c = 0.1 mm, Δu_1 = 0.013 mm. Calibrated data and the final shape of the bridging law can be seen on the following Figure 9.

D. Ceramics

Ceramics such as silicon nitride (Si3N4) are acknowledged as the first choice for modern bearing applications. However, in addition to severe working conditions such as high temperatures and corrosive environments, rolling where elements are subjected to high cyclic contact stresses during service [1]. It is well recognized that the properties of ceramics can be profoundly enhanced by suitably tailoring the microstructure based on realistic application and working conditions. Namely, the effects of tailoring the grain structure on the fracture toughness of silicon nitride were demonstrated in [2]. Similarly, the influence of boundary phase manipulation and the effect of grain bridging on the strength and toughness were illustrated in [3]. In order to improve the lifetime of ceramic components and realize cost and energy efficient manufacturing processes, two main issues have to be addressed: i) materials with increased functionality and optimum properties should be fabricated and tailored for a wide diversity of requirements (materials design and optimisation); ii) the progress of degradation processes should be predicted and evaluated (damage analysis), focusing in particular on damage mechanisms occurring under realistic working and loading conditions. his knowledge leads to the design of materials with superior performance in machine components.

Two directions were investigated (in the pressing direction and perpendicular to this direction). The level of anisotropy in elastic modulus values is relatively low: around 1 GPa, i. e. E_A = 293.07 GPa and E_B = 293.83 GPa; Poisson ratio has been determined to be 0.283.

The extended finite element method (XFEM) was first introduced by [34]. It is an extension of the conventional finite element method based on the conception of partition of unity by [35]. The presence of discontinuities is ensured by special enriched function. For purpose of fracture analysis, the enrichment function typically consist of the near tip asymptotic functions that captures singularity around the crack tip and the discontinuous function that represents the jump in displacements across the crack tip surfaces. The approximation for displacement vector function u with the partition of unity enrichment is

$$u_{XFEM} = \sum_{i \in I} N_i(x) u_i + \sum_{i \in J} N_i(x) H(x) a_i + \sum_{i \in K} \left[N_i(x) \sum_{\alpha=1}^{4} F_\alpha(x) b_{i\alpha} \right] \tag{10}$$

where $N_i(x)$ are the usual nodal shape functions; u_i is nodal displacement vector associated with the continuous part of the finite element solution, the second term is product of the nodal enriched degree of freedom vector a_i, and associated with discontinuous jump function $H(x)$ across the crack surfaces, the third term is the product of the nodal enriched degree of the freedom vector $b_{i\alpha}$ and associated elastic asymptotic crack tip function, F_α (x).

The formulae and laws that govern the behaviour of the XFEM cohesive segments for crack propagation are very similar to those used for cohesive elements with traction separation law. The similarities extend to the linear elastic traction separation model, damage initiation criteria and similar damage evaluation law. Input parameters used for modelling using Abaqus are: the maximum principal stress criterion 1000 MPa, damage evolution $K = 5.3$ MPa.m$^{1/2}$, Young modulus 293 000 MPa, Poisson ratio 0.283.

Saturation in the $J - R$ curve has been reached for XFEM modelling substantially later than for the cohesive zone approach. Usually the crack length was greater than 20 μm. This observation is predicable because the XFEM model is not incorporating the bridging mechanism into the cohesive law. The expected behaviour of the $J - R$ curve based on the literature data should be different and the saturation is expected for the crack lengths in the interval of 10-15 μm. The discrepancy comparing literature with our results can be seen in the different microstructure and / or due to numerical

ISBN: 978-1-61804-325-2

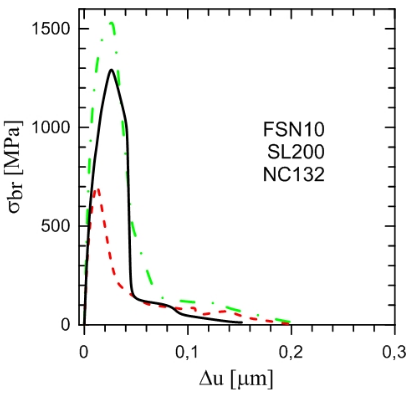

Fig. 10. Bridging law after calibration procedure.

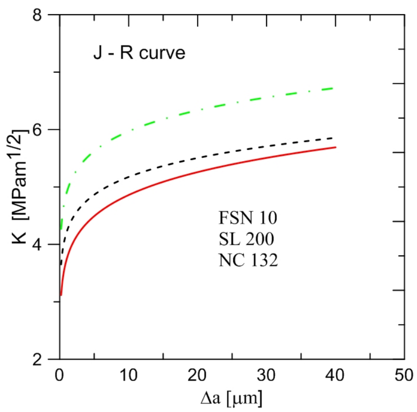

Fig. 11. J-R curve prediction.

oscillation which can lead to the underestimation of K-values.

IV. Conclusion

The cohesive zone modelling has the capacity to investigate the interplay between the local microstructure and the various material properties (mainly fracture toughness). The shape of the $J-R$ curve is more determined by the material curve than by the shape of the traction separation law and reflects the material microstructure. Knowledge and practice experiences

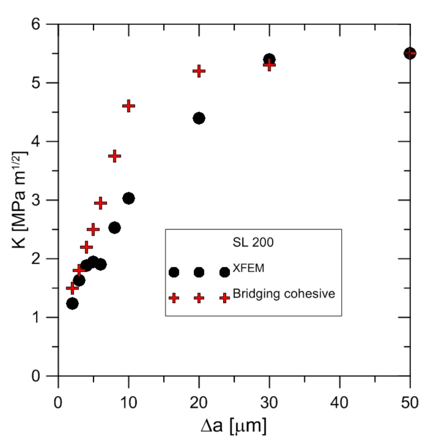

Fig. 12. J-R curve prediction for XFEM and cohesive modelling.

how to use cohesive elements for the ductile and brittle fracture has been obtained and the crack growth modelling for heterogeneous materials has been tested too. Modelling has been confronted with the classical fracture mechanics concepts. Increased attention has been applied to intermetallics and to the influence of the microstructure on the fracture process. To determine the basic material characteristics of intermetallic alloys is not the standard thing. Therefore for the numerical modelling the parametric approach has been applied to find the connection between fracture micromechanisms and input data. Obtained results and running analysis of the microstructure will enable to concentrate our future work for crack prediction in dimension close to grain size.

For fibre composites in mode I crack growth in unidirectional fibre composites is modelled; fibre cross-over bridging occurs during cracking along the fibre direction. Crack-bridging mechanisms can provide substantial increases in the toughness coupled with the strength in ceramics and saturation in the $J-R$ curve has been reached for XFEM modelling substantially later than for the cohesive zone approach.

Acknowledgment

The authors would like to thank to the financial support of the project of specific university research at Brno University of Technology, No. FAST-S-15-2824.

References

[1] G. I. Barenblatt, The formation of equilibrium cracks during brittle fracture. *PMM (Prikladnaya Matematika i Mekhanika)* 3 (1959), 434–444.
[2] D. S. Dugdale, Yielding of steel sheets containing slits. *Journal of the Mechanics and Physics of Solids* 8 (1960), 100–104.
[3] C. Shet and N. Chandra, Analysis of energy balance when using cohesive zone models to simulate fracture process. *ASME Journal of Engineering Materials and Technology* 124 (2002), 440–450.
[4] H. Li and N. Chandra, Analysis of crack growth and crack-tip plasticity in ductile materials using cohesive zone models. *International Journal of Plasticity* 19 (2003), 849–882.
[5] J. Planas, M. Elices, G. V. Guinea, F. J. Gómez, D. A. Cendón and I. Arbilla, Generalizations and specializations of cohesive crack models. *Engineering Fracture Mechanics* 70 (2003), 1759-1776.
[6] K. Park and G. H. Paulino, Cohesive zone models: A critical review of traction-separation relationships across fracture surfaces. *Applied Mechanics Reviews* 64 (2011), 060802: 1–20.
[7] N. Moës and T. Belytschko, Extended finite element method for cohesive crack growth, *Engineering Fracture Mechanics* 69 (2002), 813-833.
[8] S. Li and S. Ghosh, Multiple cohesive crack growth in brittle materials by the extended Voronoi cell finite element model, *International Journal of Fracture* 141 (2006), 373-393.
[9] J. J. C. Remmers, R. de Borst and A. Needleman, The simulation of dynamic crack propagation using the cohesive segments method. *Journal of the Mechanics and Physics of Solids* 56 (2008), 70-92.
[10] P. A. Klein, J. W. Foulk, E. P. Chen, S. A. Wimmer and H. J. Gao, Physics-based modelling of brittle fracture: cohesive formulations and the application of meshfree methods. *Theoretical and Applied Fracture Mechanics* 37 (2001), 99–166.
[11] F. Barra, A. Levermann and I. Procaccia, Quasistatic brittle fracture in inhomogeneous media and iterated conformal maps: modes I, II, and III. *Physical review E* 66 (2002), 066122: 1–16.
[12] P. Gumbsch, Modelling brittle and semi-brittle fracture processes. *Materials Science and Engineering A* 319-321 (2001), 1-7.
[13] B. Chong, Simulation of crack growth using cohesive crack method. KSCE Journal of Civil Engineering 14 (2010), 765–772.
[14] P. B. Warren, Fracture of brittle materials: effects of test method and threshold stress on the Weibull modulus. *Journal of the European Ceramic Society* 21 (2001), 335–342.

[15] R. Danzer, P. Supancic, J. Pascual and T. Lube, Fracture statistics of ceramics Weibull statistics and deviations from Weibull statistics. *Engineering Fracture Mechanics* 74 (2007), 2919-2932.

[16] L. B. Freund, Brittle crack growth modeled as the forced separation of chemical bonds within a K-field. *Journal of the Mechanics and Physics of Solids* 64 (2014), 212-222.

[17] Z. Shabir, E. Van der Giessen, C. A. Duarte and A. Simone, The role of cohesive properties on intergranular crack propagation in brittle polycrystals. *Modelling and Simulation in Materials Science and Engineering* 19 (2011), 035006: 1–21.

[18] G. Hütter, T. Linse, S. Roth, U. Mülich and M. Kuna, A modeling approach for the complete ductile-brittle transition region: cohesive zone in combination with a non-local Gurson-model, *International Journal of Fracture* 185 (2014), 129–153.

[19] A. Yavari, Generalization of Barenblatt's cohesive fracture theory for fractal cracks. *Fractals-Complex Geometry Patterns and Scaling in Nature and Society* 10 (2002), 189–198.

[20] A. Carpinteri, B. Chiaia and P. Cornetti, A mesoscopic theory of damage and fracture in heterogeneous materials. *Theoretical and Applied Fracture Mechanics* 41 (2004), 43-50.

[21] M. P. Wnuk and A. Yavari, A discrete cohesive model for fractal cracks. *Engineering Fracture Mechanics* 76 (2009), 548-559.

[22] M. Davydova and S. Uvarov, Fractal statistics of brittle fragmentation. *Frattura ed Integrità Strutturale* 24 (2013), 60–68.

[23] G. Del Piero and D. R. Owen, Structured deformations of continua. *Archive for Rational Mechanics and Analysis* 124 (1993), 99–155.

[24] M. arc Frančis and G. Royer-Carfagni, Structured deformation of damaged continua with cohesive-frictional sliding rough fractures. *European Journal of Mechanics / A Solids* 24 (2005), 644-660.

[25] D. H. Allen and Ch. R. Searcy, A micromechanical model for a viscoelastic cohesive zone. *International Journal of Fracture* 107 (2001), 159-176.

[26] S. Li and G. Wang, On damage theory of a cohesive medium, *International Journal of Engineering Science* 42 (2004) 861885

[27] C. V. Verhoosel1, J. J. C. Remmers, M. A. Gutiérrez and R. de Borst, Computational homogenisation for adhesive and cohesive failure in quasi-brittle solids. *International Journal for Numerical Methods in Engineering* 83 (2010), 1155-1179.

[28] S. May, J. Vignollet, and R. de Borst, A numerical assessment of phase-field models for brittle and cohesive fracture: Γ-convergence and stress oscillations. *European Journal of Mechanics / A Solids*, to appear (2015), 27 pp. (doi: 10.1016/j.euromechsol.2015.02.002).

[29] E. Reyes, M. J. Casati and J. C. Gálvez, Cohesive crack model for mixed mode fracture of brick masonry. *International Journal of Fracture* 151 (2008), 29–55.

[30] G. Alfano, S. Marfia and E. Sacco, A cohesive damagefriction interface model accounting for water pressure on crack propagation. Computer Methods in Applied Mechanics and Engineering 196 (2006), 192-209.

[31] J. Zhang, Ch. K. Y. Leung and Y. Gao, Simulation of crack propagation of fiber reinforced cementitious composite under direct tension. *Engineering Fracture Mechanics* 78 (2011), 2439-2454.

[32] A. Karamnejad, V. P. Nguyen and L. J. Sluys, A rate-dependent multi-scale crack model for concrete. VIII International Conference on Fracture Mechanics of Concrete and Concrete Structures *Proceedings of FraMCoS-8 (8th International Conference on Fracture Mechanics of Concrete and Concrete Structures)* in Toledo (2013), 48: 1–11.

[33] H. Zhang and D. Wei, Fracture and damage behaviors of concrete in the fractal space. *Journal of Modern Physics* 1 (2010), 48–58.

[34] T. Belytschko and T. Black, Elastic crack growth in finite element with minimal remeshing. *International Journal of Numerical Methods in Engineering* 46 (1999), 601–620.

[35] I. Babuška and U. Banerjee, Stable generalized finite element method (SGFEM). *Computer Methods in Applied Mechanics and Engineering* 201 (2012), 91–111.

[36] M. Lengauer and R. Danzer, Silicon nitride tools for the hot rolling of high-alloyed steel and superalloy wires - crack growth and lifetime prediction. *Journal of the European Ceramic Society* 28 (2008), 2289-2298.

Jiří Vala (*1956) is professor at the Brno University of Technology, Faculty of Civil Engineering, Czech Republic, 602 00 Brno, Veveří 95, e-mail *vala.j@fce.vutbr.cz*.

Vladislav Kozák (*1954) is researcher at the Institute of Physics of Materials in Brno, Academy of Sciences of the Czech Republic, 616 62 Brno, Žižkova 22, e-mail *kozak@ipm.cz*.

The Effect of Filler Size, Rheology Control Agent Content and Temperature Variation on Viscosity of Epoxy Resin System

F.Nihal TÜZÜN

Engineering Faculty of Hitit University , Department of Chemical Engineering, , 19030, Çorum, TURKEY

Abstract— In this study, viscosity variation for three different epoxy resin adhesives including three different fillers was determined with increasing the CABOSIL TS 720 content from 1% to 5% and reducing the filler content from 19.9 to 15.9% at the temperatures of 25, 40 60, 70 and 80^{0}C. Variation of viscosity was also determined for SHELL resin system consisting of EPIKOTE® 828 epoxy resin and EPIKURE® 3090 polyamidoamine curing agent. Calcite with having three different particle diameters of 0.7, 0.9 and 10 µm was used as filler. CABOSIL® TS 720 used as rheology control agent was an other filler. Viscosity models were developed with measuring the viscosity by using HA model Brookfield type DV-II+Pro Viscometer with SC4-27 spindle at constant shear rate. It was found that viscosity increased as CABOSIL® TS 720 content increased and viscosity decreased with increasing the temperature. Generally, the adhesive prepared by the calcite with the particle diameter of 0.7 µm gave the lowest viscosity value.

Keywords— Adhesives, epoxy resin, viscosity, fillers, particle size distribution

I. INTRODUCTION

Fluids are generaly separated into two categories known as Newtonian and non-Newtonian. In Newtonian fluids, viscosity does not vary with changing shear rates, whereas, viscosities of non-Newtonian fluids vary at different shear rates. Non-Newtonian fluids are also divided into two groups as time independent non-Newtonian and time dependent non-Newtonian. Time independent non-Newtonian fluids show pseudoplastic, dilatant behaviour when time dependent non-Newtonian fluids represent thixotropic, rheopectic behaviour [1].

Epoxy resins extensively used in coating and adhesive industry demonstrate both thixotropic and rheopectic behaviour together. Viscosity measurement of a thermoset material during processing is very complicated due to kinetic rate of conversion from a liquid to a solid material [2].

Fumed silicas are commonly used in coating and adhesive industry as rheological control agents [3]. CABOSIL® TS 720 treated fumed silica is a very efficient thixotrope for epoxy resin adhesives., giving a stable sag resistance at vertical surfaces without changing other properties such as cure rate or lap shear tensile strengths of adhesives [4].

Temperature, shear rate and loading level of filler are factors influencing the rheology of the epoxy resins and effect of those factors was also studied (5-12). Investigations including epoxy resin and fumed silica were met(14-19).

The rheological properties of composites and the variations during hardening process were explored on literature data (20-21)..Kinetics of the chemical reactions during hardening were also investigated(22-27).

The aim of the study is to investigate rhe variations in the rheological properties of the epoxy resin depending on rheology control agent content, filler size and temperature,

2. EXPERIMENTAL

Fifteen different types of adhesives were prepared with the addition of EPIKOTE® 828 epoxy resin and EPIKURE® 3090 polyamidoamine curing agent with a ratio of 1:1 by weight. CABOSIL® TS 720 rheology control agent was increased from 1 to, 2, 3, 4 and 5% , while one of three fillers (calcite with the mean particle diameter of 0.7 µm, calcite with the average particle diameter of 0.9 µm, calcite with the mean particle diameter of 10 µm) was decreasing from 19.9 to 15.9%. Those adhesives were also mixed by a mechanical stirrer for five minutes approximately to insure the complete mixing. Then, viscosity of the samples was measured by using HA model Brookfield type DV-II + Proviscometer with the usage of complete computer control in terms of ‘’Rheocalc’’ software collecting data automatically. Variation of viscosity was also measured with changing the temperature from 25 to 40, 60, 70 and 80^{0}C by providing temperature control between water jacket of small sample adapter and water bath.

3. RESULTS AND DISCUSSION

Viscosity variation and thixotropy are very important in the application of epoxy resin adhesives before hardening in spite

This work was supported by the GAZİ UNIVERSITY with the project number of 28/2004-06.

of the fact that the observation of rheopexy during the curing reaction. Application time can be adjusted with respect to the amount of fumed silica known as CABOSIL® TS 720. For this reason, viscosity variation and thixotropic, rheopectic behaviour of epoxy resin adhesives including five different CABOSIL® TS 720 content and calcite with three different particle diameters at the temperatures of 25, 40, 60, 70 and 80^{0}C were investigated in this study. Thixotropic, rheopectic behaviour and viscosity variation of three compositions were determined by increasing the CABOSIL® TS 720 content from 1% to 2, 3, 4 and 5% and decreasing the filler content from 19.9 % to 18.9, 17.9, 16.9 and 15.9% at equal amount for each temperature in terms of constant shear rate. However, thixotropy was not observed for all compositions, while rheopexy was attained for all compositions because of the curing reaction between epoxy resin and curing agent. Viscosity models depending on time for each adhesive were developed as well and results are given in Tables 1, 2, 3, 4 and 5.

Viscosity variation of three adhesives including calcite with three different particle diameters of 0.7 µm, 0.9 µm and 10 µm at 25^{0}C was observed for the CABOSIL® TS 720 content of 1, 2, 3, 4 and 5% . Only the composition containing calcite with the particle diameter of 0.9 µm gave thixotropy, while other compositions were demonstrating no thixotropy for the CABOSIL® TS 720 content of 1%. When the CABOSIL® TS 720 content was increased to 2%, lower thixotropy was observed for the compositions having calcite with the particle diameters of 0.7 and 0.9 µm, whereas, thixotropy was not attained for the composition containing calcite with the particle diameter of 10 µm. Thixotropy and rheopexy were obtained for three compositions definitely at the CABOSIL® TS 720 content of 3 and 4%. No thixotropy was followed for two compositions including calcite with the particle diameters of 0.7 µm and 0.9 µm, while other composition including calcite with the particle diameter of 10 µm was representing thixotropy and rheopexy at the CABOSIL® TS 720 content of 5%. This effect is also easily observed from Table 1, therefore, the adhesives containing calcite with the particle diameter of 0.7 and 0.9 µm gave only line equations in viscosity model for CABOSIL® TS 720 content of 1, 2 and 5%, while these adhesives were indicating polynomial equations in viscosity model for CABOSIL® TS 720 content of 3 and 4%. It was generally determined that viscosity and thixotropy increased as CABOSIL® TS 720 content increased. The reason why thixotropy increases with increasing the CABOSIL® TS 720 content is that the process of epoxy hardening is retarded by the presence of filler based on silica with low particle size distribution (5). It acts as curing retardation agent for a while as a consequence of the aggregates between the solid particles and the polymer chain by van der Waals forces(4). In general, higher viscosity values were observed for the adhesives including calcite with the particle diameters of 0.7 µm and 0.9 µm at the temperature of 25^{0}C for all CABOSIL® TS 720 content except for 4%. The reason for this can be explained in terms of reducing the particle size of the filler. This effect leads to an increase in the number of particles and higher number of smaller particles results in more particle-particle interactions and an increased viscosity (28-33). For this reason, the composition including calcite with the highest particle diameter of 10 µm gave the lowest viscosity for the CABOSIL® TS 720 content of 2, 3 and 5% at the temperature of 25^{0}C. Since, low filler contents and large particle sizes resulted in low viscosity resin (16-19). Lower particle size effect on viscosity is observed from Figures 1, 2, 3 and Table 1.

Table 1. Viscosity models of SHELL adhesives with respect to CABOSIL TS 720 content and particle diameter at the temperature of 25^{0}C

CABOSIL TS 720 content (%)	Viscosity variation	Particle diameter (µm)	Viscosity models at the temperature of 25^{0}C
1	High	0.9	V=8.719t+37085
	Medium	10	V=5.528t+29782
	Low	0.7	V=7.299t+22187
2	High	0.9	V=11.3t+76851
	Medium	0.7	V=8.923t+66873
	Low	10	V=10.17t+48233
3	High	0.7	V=0.003t^2-1.443t+21390
	Medium	0.9	V=0.005t^2-21.14t+16429
	Low	10	V=0.013t^2-62.38t+15070
4	High	10	V=0.049t^2-251.3t+2E+06
	Medium	0.9	V=0.052t^2-394.9t+2E+06
	Low	0.7	V=0.027t^2-267.3t+1E+06
5	High	0.9	V=17194t+3E+07
	Medium	0.7	V=13068t+3E+07
	Low	10	V=1.477t2-10087t+4E+07

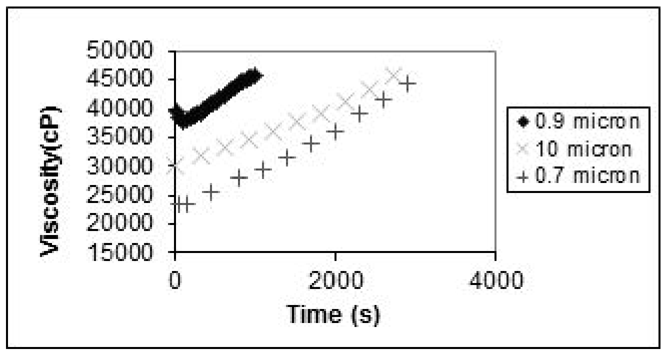

Figure 1 Viscosity variation of SHELL adhesive according to three different fillers for CABOSIL TS 720 content of 1% at the temperature of 25^{0}C

Viscosity variation of three compositions including SHELL resin system, calcite with three different particle diameters of 0.7 µm, 0.9 µm and 10 µm at 40^{0}C was detected for the CABOSIL® TS 720 content of 1, 2, 3, 4 and 5%. Even though, a little bit effect of thixotropy was observed for three compositions at the CABOSIL® TS 720 content of 1%, a rise in thixotropy was attained with an increase in CABOSIL® TS 720 content until 4 %. When the CABOSIL® TS 720 content was increased to 5%, viscosity increased and higher

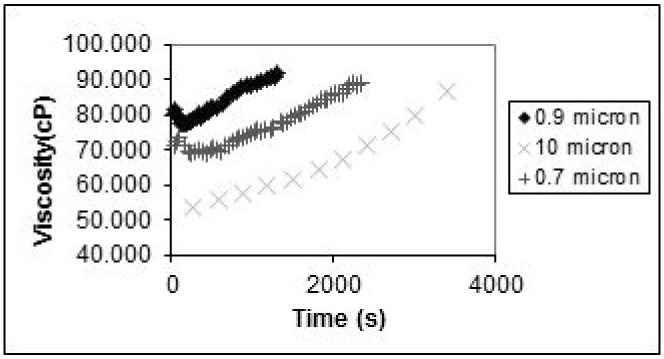

Figure 2 Viscosity alteration of SHELL adhesive including three different fillers for CABOSIL TS 720 content of 2 % at the temperature of 25^0C

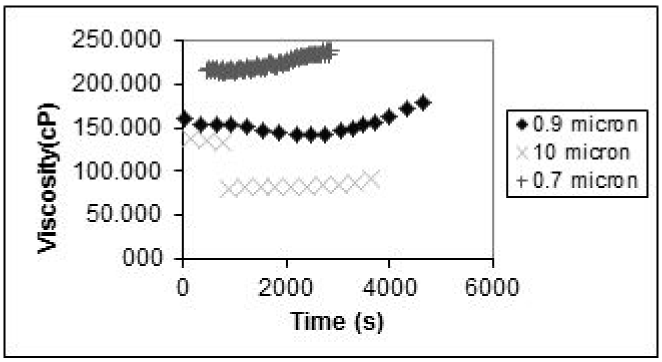

Figure 3 Viscosity variation of SHELL adhesive with respect to three different fillers for CABOSIL TS 720 content of 3 % at the temperature of 25^0C

thixotropy was obtained than at the CABOSIL® TS 720 content of 4% for two compositions including calcite with the particle diameters of 0.9 µm and 10 µm. However, other composition containing calcite with the particle diameter of 0.7 µm indicated lower thixotropy than at the CABOSIL® TS 720 content of 4%. Results showed that viscosity and thixotropy generally increased with increasing the CABOSIL® TS 720 content. Although, the adhesive with having the particle diameter of 0.9 µm gave the highest viscosity at the temperature of 40^0C for the CABOSIL® TS 720 content of 1, 2 and 3% , the lowest viscosity values were observed for the CABOSIL® TS 720 content of 4 and 5% at the same temperature. This effect may be expressed owing to the influence of particle size distribution between silica and calcite with reducing the calcite amount and increasing the CABOSIL® TS 720 content(28-32). Effect of CABOSIL® TS 720 content on viscosity and thixotropy is given in Figures 4, 5, 6, 7, 8 and Table 2.

Table 2. Viscosity models of SHELL adhesives with respect to CABOSIL TS 720 content and particle diameter at the temperature of 40^0C

Cabosil TS 720 content(%)	Viscosity variation	Particle diameter(µm)	Viscosity models at the temperature of 40^0C
1	High	0.9	$V=0.004t^2-0.199t+7723$
	Medium	10	$V=0.003t^2-3.822t+7029$
	Low	0.7	$V=0.003t^2-2.17t+5733$
2	High	0.9	$V=0.004t^2-1.645t+15358$
	Medium	10	$V=0.005t^2-5.078t+13203$
	Low	0.7	$V=0.006t^2-6.124t+11064$
3	High	0.9	$V=0.009t^2-13.85t+35083$
	Medium	10	$V=0.008t^2-14.46t+31403$
	Low	0.7	$V=0.01t^2-17.87t+26091$
4	High	10	$V=0.042t^2-126.7t+19752$
	Medium	0.7	$V=0.049t^2-154t+20406$
	Low	0.9	$V=0.028t^2-79.3t+12364$
5	High	10	$V=5.786t^2-28214t+6E+07$
	Medium	0.7	$V=5.64t^2-11989t+3E+07$
	Low	0.9	$V=7.336t^2-25520t+3E+07$

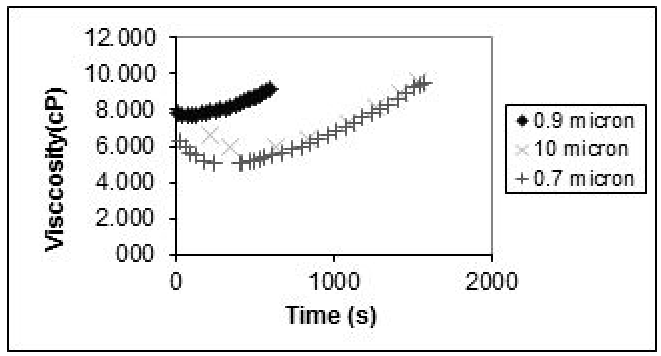

Figure 4 Viscosity alteration of SHELL adhesive according to three different fillers for CABOSIL TS 720 content of 1 % at the temperature of 40^0C

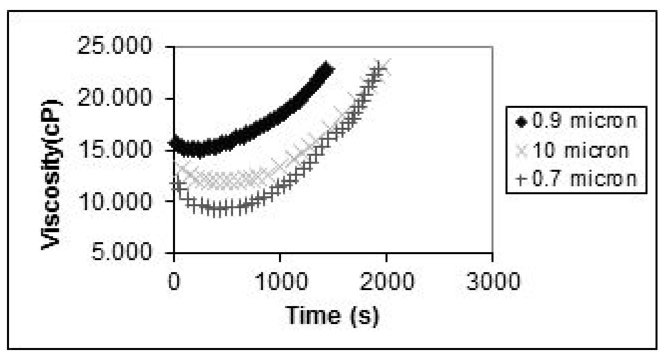

Figure 5 Viscosity variation of SHELL adhesive having three different fillers for CABOSIL TS 720 content of 2 % at the temperature of 40^0C

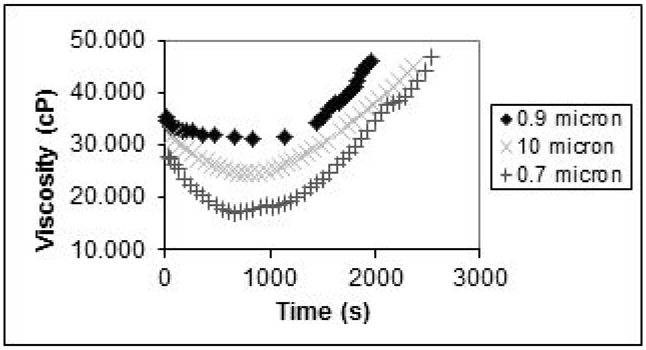

Figure 6 Variation of viscosity for SHELL adhesive including three different fillers with CABOSIL TS 720 content of 3% at the temperature of 40^0C

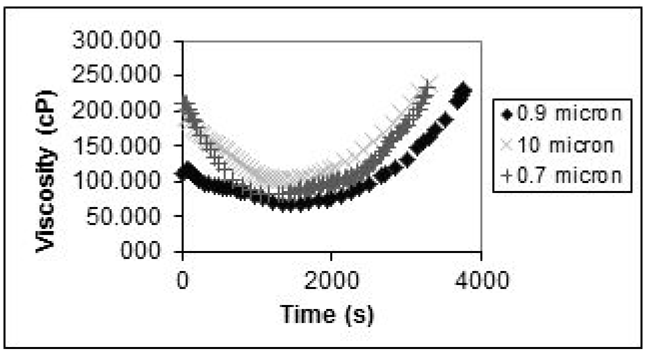

Figure 7 Alteration of viscosity for SHELL adhesive containing three different fillers for CABOSIL TS 720 content of 4 % at the temperature of 40^0C

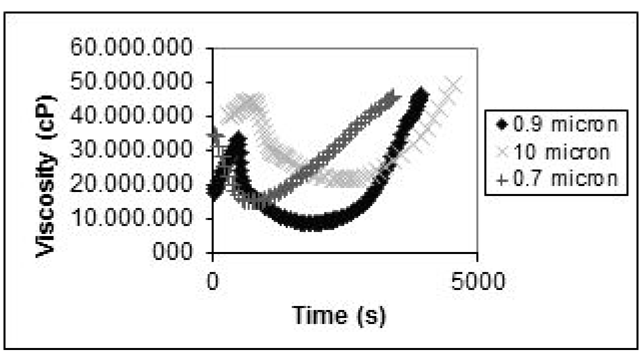

Figure 8 Viscosity variation of SHELL adhesive with respect to three different fillers for CABOSIL TS 720 content of 5 % at the temperature of 40^0C

Viscosity variation of three compositions including calcite with three different particle diameters of 0.7 µm, 0.9 µm and 10 µm at 60^0C was determined for the CABOSIL® TS 720 content of 1, 2, 3, 4 and 5% and results are represented in Table 3.

Table 3. Viscosity models of SHELL adhesives with respect to CABOSIL TS 720 content and particle diameter at the temperature of 60^0C

CabosilTS 720 content(%)	Viscosity variation	Particle diameter(µm)	Viscosity models at the temperature of 60^0C
1	High	10	$V=0.01t^2-3.142t+2698$
	Medium	0.9	$V=0.012t^2-7.619t+3775$
	Low	0.7	$V=0.009t^2-7.245t+3019$
2	High	10	$V=0.072t^2-41.06t+14474$
	Medium	0.7	$V=0.029t^2-22.98t+7753$
	Low	0.9	$V=0.027t^2-19.63t+5260$
3	High	0.9	$V=0.039t^2-21.49t+10693$
	Medium	10	$V=0.037t^2-28.43t+14179$
	Low	0.7	$V=0.034t^2-36.9t+16012$
4	High	10	$V=0.087t^2-85.98t+41568$
	Medium	0.9	$V=0.066t^2-51.91t+25708$
	Low	0.7	$V=0.066t^2-66.9t+31144$
5	High	10	$V=0.934t^2-1150t+48303$
	Medium	0.9	$V=0.628t^2-720.4t+34171$
	Low	0.7	$V=0.528t^2-816.6t+41246$

Thixotropy also increased with increasing the CABOSIL® TS 720 content from 1 to 2, 3, 4 and 5% for three compositions. However, viscosity decreases as temperature increases (15) and viscosity increases with increasing the CABOSIL® TS 720 content (4), whereas, particle size distribution of fillers is an important parameter on viscosity as well. This effect is apparently determined from the viscosity results obtained. Even though, lower viscosity values were attained than the temperatures of 25 and 40^0C, the highest viscosity values varied between the adhesives containing calcite having the particle diameter of 0.9 and 10 µm owing to the particle size distribution of silica and calcite depending on the content(28-32). The effect of temperature on viscosity is indicated in Figures 3, 6 and 9.

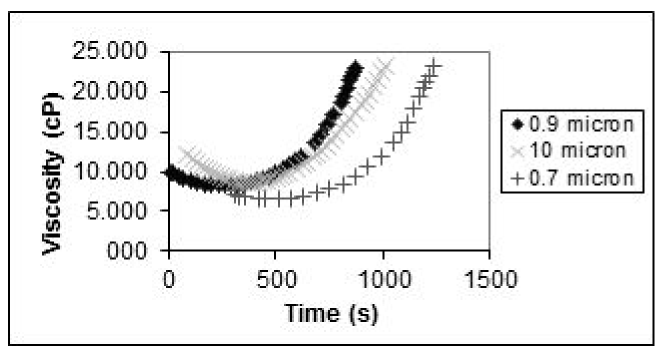

Figure 9 Variation of viscosity for SHELL adhesive including three different fillers with CABOSIL TS 720 content of 3 % at the temperature of 60^0C

Viscosity variation of three compositions including calcite with three different particle diameters of 0.7 µm, 0.9 µm and 10 µm at 70^0C was observed for the CABOSIL® TS 720 content of 1, 2, 3, 4 and 5% and the viscosity models developed are shown in Table 4.

ISBN: 978-1-61804-325-2

Table 4. Viscosity models of SHELL adhesives with respect to CABOSIL TS 720 content and particle diameter at the temperature of 70^0C

Cabosil TS 720 content(%)	Viscosity variation	Particle diameter (µm)	Viscosity models at the temperature of 70^0C
1	High	0.9	$V=0.02t^2-7.581t+2518$
	Medium	10	$V=0.019t^2-8.597t+2531$
	Low	0.7	$V=0.022t^2-10t+2246$
2	High	0.9	$V=0.044t^2-15.84t+4399$
	Medium	10	$V=0.043t^2-24.19t+6332$
	Low	0.7	$V=0.016t^2-8.041t+2451$
3	High	0.9	$V=0.139t^2-54.3t+11962$
	Medium	10	$V=0.122t^2-73.41t+18818$
	Low	0.7	$V=0.081t^2-46.2t+11570$
4	High	0.9	$V=0.763t^2-367.76t+44308$
	Medium	10	$V=0.785t^2-640.8t+19118$
	Low	0.7	$V=0.795t^2-721.2t+20705$
5	High	0.9	$V=1.516t^2-1074t+30990$
	Medium	10	$V=1.090t^2-1147t+53046$
	Low	0.7	$V=2.437t^2-2530t+84978$

Thixotropy was attained in three compositions for the CABOSIL® TS 720 content of 1%.When the CABOSIL® TS 720 content was varied to 2%, thixotropy was followed for two compositions having calcite with the particle diameters of 0.7 µm and 10 µm and other composition containing calcite with the particle diameter of 0.9 µm demonstrated no thixotropy nearly. Thixotropy increased for the compositions including calcite with the particle diameters of 0.9 µm and 10 µm at the CABOSIL® TS 720 content of 3%, almost no variation was observed for the composition having calcite with the particle diameter of 0.7 µm. When the CABOSIL® TS 720 content was increased to 4%, thixotropy increased for the compositions containing calcite with the particle diameters of 0.7 µm and 10 µm, whereas, nearly constant and lower viscosity was obtained in the composition including calcite with the particle diameter of 0.9 µm with respect to other compositions. Thixotropy also increased for three compositions, while CABOSIL® TS 720 content was varied to 5%. It was observed that viscosity and thixotropy generally increased with an increase in CABOSIL® TS 720 content. However, the lowest and the highest viscosity having adhesives were found as calcite with the particle diameter of 0.7 µm and calcite with the particle diameter of 0.9 µm respectively. This order was not affected by particle size distribution of silica and calcite with increasing the CABOSIL® TS 720 and decreasing the calcite content at the temperature of 70^0C.
Viscosity variation of three compositions including SHELL resin system, calcite with three different particle diameters of 0.7 µm, 0.9 µm and 10 µm at 80^0C was detected for the CABOSIL® TS 720 content of 1, 2, 3, 4 and 5% and viscosity variation is explained with models given in Table 5.

Three compositions showed thixotropy for the CABOSIL® TS 720 content of 1%. When the CABOSIL® TS 720 content was increased to 2%, thixotropy rise was followed with respect to the CABOSIL® TS 720 content of 1% for two compositions containing calcite with the particle diameters of 0.7 µm and 0.9 µm, whereas, no thixotropy was observed for the the composition having with the particle diameter of 10 µm.

Table 5. Viscosity models of SHELL adhesives with respect to CABOSIL TS 720 content and particle diameter at the temperature of 80^0C

Cabosil TS 720 content (%)	Viscosity variation	Particle diameter (µm)	Viscosity models at the temperature of 80^0C
1	High	0.9	$V=0.043t^2-14.36t+3122$
	Medium	10	$V=0.035t^2-14.4t+2699$
	Low	0.7	$V=0.031t^2-11.44t+2080$
2	High	10	$V=0.164t^2-24.44t+3219$
	Medium	0.9	$V=0.049t^2-16.12t+3133$
	Low	0.7	$V=0.038t^2-16.89t+3315$
3	High	10	$V=5.37t^2-66.61t+4814$
	Medium	0.9	$V=0.106t^2-31.28t+6583$
	Low	0.7	$V=0.08t^2-41.13t+8173$
4	High	10	$V=1.727t^2-1002t+22118$
	Medium	0.9	$V=0.833t^2-539.1t+16440$
	Low	0.7	$V=1.884t^2-1427t+30929$
5	High	10	$V=43.13t^2-29158t+3E+07$
	Medium	0.9	$V=21.97t^2-1262t+9E+06$
	Low	0.7	$V=36.34t^2-32200t+2E+07$

An increase in thixotropy was detected with the CABOSIL® TS 720 content of 3% according to the CABOSIL® TS 720 content of 2% for the composition containing calcite with the particle diameter of 0.7 µm, while thixotropy was decreasing for the composition having calcite with the particle diameter of 0.9 µm and no thixotropy was attained for the composition including calcite with the particle diameter of 10 µm. Thixotropy increased for three compositions, when the CABOSIL® TS 720 content was varied to 4%. Lower thixotropy, then, an increase in viscosity was obtained for three compositions with the CABOSIL® TS 720 content of 5%. Results demonstrated that viscosity and thixotropy generally increased with an increase in CABOSIL® TS 720 content, effect of temperature was also sensible.
It was found that the adhesive containing calcite with the particle diameter of 0.7 µm had the lowest viscosity for CABOSIL® TS 720 content of 1, 2, 3, 4 and 5% at the temperatures of 60, 70 and 80^0C. The reason of this can be explained by means of higher particle packing effect of a polydisperse composition with a broad size distribution than a monodisperse composition besides having the effect of decreasing the viscosity because of the temperature rise(28-32). However, the adhesive including calcite with having the particle diameter of 0.9 µm had generally lower viscosity values than the adhesive with the particle diameter of 10 µm for the CABOSIL® TS 720 content of 1, 2, 3, 4 and 5% at the temperatures of 60 and 80^0C. The calcite with the particle diameter of 0.9 µm is known as coated calcite and surface of calcite is treated with fatty acids. For this reason, particle-particle interactions reduced and viscosity decreased in addition to the high temperature effect(33).
In general, results attained from experimental calculations showed that viscosity and thixotropy increased as CABOSIL® TS 720 content increased(4) and thixotropy decreased with increasing the temperature (14). Even though, a decrease in thixotropy was obtained with an increase in temperature for epoxy resin adhesives, rheopexy also decreased at the temperature of 80^0C due to high reaction rate.
In spite of very complex viscosity variation was observed due to curing reaction, the best results both in viscosity and thixotropy were obtained at the temperatures of 40^0C, 60^0C and 70^0C with the CABOSIL® TS 720 content of 4 and 5% for calcite with the particle diameter of 0.7 µm.

4. CONCLUSION

Viscosity decreased as temperature increased and viscosity increased with increasing the CABOSIL® TS 720 content.

Rheopexy and thixotropy also decreased as temperature increased.

The best results both in viscosity and thixotropy were attained at the temperatures of 40^0C, 60^0C and 70^0C with the CABOSIL® TS 720 content of 4 and 5% for calcite with the particle diameter of 0.7 µm.

It was deducted that particle size, particle size distribution and temperature data were significant with developing adhesives having specific rheological properties.

5. ACKNOWLEDGMENT

The author expresses her sincere appreciation to GAZİ UNIVERSITY for financial supports in providing the Brookfield viscometer utilized.

The author also would like to thank to HITIT UNIVERSITY for financial support in the preparation of this work

6. REFERENCES

[1] Brookfield Engineering Labs, Inc., ''Manual of Brookfield DV-II+ Pro Programmable Viscometer'', USA, 2004.
[2] R.P. Theriault, T.A Osswald, J.M.Castro, ''Numerical model of viscosity of an epoxy prepreg resin system'', Polymer Composites, 20(5), pp.628-633, 1999.
[3] A.Torro-Palau, J.C. Fernandez-Garcia, A.C. Orgiles-Barcelo, M.M. Pastor-Blas, J.M. Martin-Martinez, ''Comparison of the properties of polyurethane adhesives containing fumed silica or sepiolite as filler'', Journal of Adhesion, Vol.61, n.1-4, pp.195-211, 1997.
[4] CABOT CORPORATION, ''CABOSIL® TS 720 Treated Fumed Silica'', USA, 2001.
[5] Kogan, E.G., Kutseba, S.A., Kulichikhin, V.G., ''Effect of the nature of the filler on rheological and rheokinetic properties of composites based on epoxy resins'', Fibre Chemistry, 20(3), p.206-209, 1989.
[6] Martin, J.E., Adolf, D., Wilcoxon, J.P., '' Rheology of the incipient gel : Theory and data for epoxies'', Polymer Preprints, 30(1), p.83-84, 1989.
[7] Laza, J.M., Julian, C.A., Larrauri, E., Rodriguez, M., ''Thermal scanning rheometer analysis of curing kinetic of an epoxy resin'', Polymer, .40(1), p.35-45, 1999.
[8] Saeki, J., Kaneda, A., ''Flow analysis of an epoxy compound for low pressure transfer molding in a circular cross-sectional channel'', JSME International Journal, Section 2, 33(3), p.486-493, 1990.
[9] Kim, H., Char, K., ''Effect of phase separation on rheological properties during the isothermal curing of epoxy thoughened with thermoplastic polymer'', Industrial and Engineering Chemistry Research, 39(4), p.955-959, 2000.
[10] Simpson, J.O., Bidstrup, S.A., ''Rheological and dielectric changes during isothermal epoxy-amine cure'', Journal of Polymer Science, Polymer Physics Edition, 33(1), p.55-62, 1995.
[11] Imaz, J.J., Valea, A., Cortazar, M., Mondragon, I., '' Correlations between rheological and thermal behaviour of TGDDM/m-PDA epoxy systems'', European Polymer Journal'', 30(5), p. 561-565, 1994.
[12] Galgoci, E.C., Pigneri, A.M., Young, G.C., Tait, R.A., ''International SAMPE Symposium and Exhibition'', 3, p.1224-1235, 1989.
[13] ERCIYES MIKRON CORPORATION, ''The analysis certificates of calcite with the particle diameters of 0.7 µm, 0.9 µm and 10 µ'', TURKEY, 2004.
[14] Mustata, F., Bicu, I., ''Plastified epoxy resins modified by hydrophilic and hydrophobic silica'', Polymer Plastics Technology and Engineering, 37(2), p.127-140, 1998.
[15] McCabe, W.L., Smith, J.C., Harriott, P., ''Unit Operations of Chemical Engineering'', McGraw Hill Book Company, Fourth Edition, NewYork, 1985.
[16] Chang, R-Y., Lin, Y., Lin, F-S., ''Study of the chemorheology of a highly filled epoxy molding compound'', Annual Technical Conference-ANTEC, Conference Proceedings, 2, p.1397-1401, 1998.
[17] Kaindl, A.F., Schoen, L., Borsi, H., ''Influence of epoxy system formulation on partial discharge behaviour of resin impregnated coils'', Conference on Electrical Insulation and Dielectric Phenomena'', 1, p.218-221, 1999.
[18] Petti, M.A., ''New fused silica fillers for epoxy moulding compounds: An evaluation of the rheological and moisture absorption properties''International SAMPE Electronics Conference, 7, p.526-540, 1994.
[19] Sawan, S.P., Muni, K.P., Svelnis, S.M., ''Viscometric properties of phenoxy solutions containing hydrophilic or hydrophobic fumed silica'', Polymer Preprints, 27(2), p.278-279, 1986.
[20] Riccardi, C.C., Adabo, H.E., Williams, J.J., ''Curing reaction of epoxy resins with diamines'', J.Appl. Polym.Sci., 29(8), p.2481, 1984.
[21] Kulichikhin, S.G., "Kinetics of change of the physical and mechanical properties of binders during curing''Mech. of Composite Mater., 22(6), pp.761-765, 1986.
[22] Theriault, R.P., Osswald, T.A., Castro, J.M., ''Numerical model of viscosity of an epoxy prepreg resin system'', Polymer Composites, 20(5), p.628-633, 1999.
[23] Laza, J.M., Julian, C.A., Larrauri, E., Rodriguez, M., ''Thermal scanning rheometer analysis of curing kinetic of an epoxy resin'', Polymer, 40(1), p.35-45, 1999.
[24] Han, C.D., Lem, K-W., ''Chemorheology of thermosetting resins. I. The chemorheology and curing kinetics of unsaturated polyester resin'', J.Appl. Polym.Sci., 28, p.3155-3183, 1983.
[25] Roller, M.B.,''Characterization of the time-temperature-viscosity behaviour of curing B-staged epoxy resin'', Polymer Engineering and Science, 15(6), p.406, 1975.
[26] Roller, M.B.,''Rheology of curing thermosets: A review'', Polymer Engineering and Science, 26(6), p.432, 1986.
[27] White, R.P., ''Time-temperature superpositioning of viscosity-time profiles of three high temperature epoxy resins'', Polymer Engineering and Science, 14(1), p.50, 1974.
[28] Behzadfar, E., Abdolrasouli, M.H., Sharif, F., Nazockdast, H.,'''Effect of solid loading and aggregate size on the rheological behavior of PMOS/Calcium carbonate suspensions'', Brazilian Journal of Chemical Enginering, 26(4), 2009.
[29] Barnes, H.A., ''Review of the rheology of filled viscoelastic systems'', The British Society of Rheology, pp.1-49. 2003.
[30] Litchfield,, D.W., Baird, D.G.,''The rhelogy of high aspect ratio nano-particle filled liquids'', Rheology Reviews, pp.1-60, 2006.
[31] Mueller, S., ''The rheology of suspensions of solid particles'', Proceedings of Royal Society, 2009.
[32] Krieger, K., ''Renewable Energy : Biofuels heat up'', Nature, 508(7497), pp.448, 2014.
[33] Osman, M.A., Atallah, A., Schweizer, T., Ottinger,H.C., ''Particle-particle and particle-matrix interactions in calcite filled high-density polyethylene-steady shear'', J.Rheol., 48(5):1167-84, 2004.

The influence of passive safety systems on head injuries suffered by the vehicle's driver

Oana V. Oţăt, Nicolae Dumitru, and Victor Oţăt

***Abstract* -** The present research paper underpins a thorough comparative study aiming to determine the influence of the active security systems upon the injuries suffered at the collision moment. Hence, a series of statistical data on road accidents casuistry have been analysed in order to establish the type of impact to be investigated and the particular human body region mostly exposed to severe injuries. By means of Virtual Crash software we simulated a frontal-type collision of a vehicle against a rigid wall, at a speed of 50 km/h. The kinematic parameters obtained following this simulation have been further applied in a numerical modelling of four distinct situations, using this time the LS-DYNA software package. Throughout the undertaken study, we have considered those situations in which the vehicle's driver is restrained with a seat belt while the vehicle has been provided with an airbag system. Aiming to underpin a comparative analysis, we have also investigated those situations in which the driver is not secured with the retaining system and the vehicle is not equipped with an airbag.

Keywords— passive safety, frontal impact, dummy kinematics, head injury criteria.

I. INTRODUCTION

The ever increasing necessity for road transportation development, both for freight and for passenger transport, in the context of a road infrastructure that has not undergone much change in the last decades, has led to an increased density of flow traffic. Admittedly, the main negative effect of road congestion is the steady growth of the number of accidents, particularly those with serious consequences.

In order to reduce both the number of traffic overcrowdings as well as the injuries' severity, in case of an accident, among the most actual solutions adopted by vehicle manufacturers was a large-scale implementation of active and passive safety systems in order to increase their effectiveness. Thus, the airbag system is a well-known example of passive safety systems, already integrated in the mass production, and closely related to the seat belt, the widely acknowledged safety system element, which has been the subject matter of a series of recent research studies within this field of investigation.

Oţăt V. Oana, PhD Candidate, Eng., Faculty of Mechanical Engineering, University of Craiova, Automotive, Transportation and Industrial Engineering Department, Romania (corresponding author, phone: +40 0735157400; e-mail: otatoana@yahoo.com).

Dumitru Nicolae, Prof. PhD Eng., Faculty of Mechanical Engineering, University of Craiova, Applied Mechanics and Civil Engineering Department, Romania (e-mail: nicolae_dtru@yahoo.com).

Oţăt Victor, Prof. PhD Eng., Faculty of Mechanical Engineering, University of Craiova, Automotive, Transportation and Industrial Engineering Department, Romania (e-mail: otatvictor@yahoo.com).

A close and critical reading of mainstream literature indicates that a series of scientific research studies analyses the casuistry occurrence of traffic accidents, as well as the type and the severity of the injuries suffered by of the occupants of the vehicle.

An essential research study on the analysis of the driver's kinematic behavior is indicated in [1], aiming at quantifying the whole-body kinematic response of the post mortem human surrogates (PMHS) tested in the same frontal impact condition. Within this research study the three-dimensional displacement corridors development has been introduced in order to quantify the whole-body kinematic response of restrained PMHS for a frontal impact conducted in a controlled laboratory environment.

In terms of development and optimization of the active safety systems, K. Preston White et al. describe in [2] recent enhancements of a software which enables the use of vehicle and occupant simulation models in order to determine the design and the restraint systems meant to increase the occupant impact protection, being also applied to establish the optimal design of a passenger vehicle involved in frontal collisions.

A method to develop injury prediction algorithms by statistical analysis of numerical crash reconstructions using dummy models is presented in [3]. The normal or out of position of the occupants correlated with the operating mode of the airbag system leads to a further research topic.

In [4] Louden indicates, how the air bags are affecting the occupants (Hybrid III 3-year-old, 6-year-old and SID-IIs - 5th percentile adult female side impact dummy) in different OOP test modes for all rows in the vehicle. In [5] some recommended procedures are envisaged in order to evaluate the occupant injury risk due to side airbags deploying. An overview of the actual status with regard to the simulation methods for the deployment process of an airbag is provided in [6], a research paper entitled *On the simulation of out-of-position load cases with the ale-method*. By means of the case-control study of real-world crashed vehicles conducted in [8], the reduction in number of head, face, chest and neck injuries in airbag-equipped vehicles is being highlighted, although the numbers of upper extremity injuries increased.

According to [7], frontal impacts have been defined as follows: non-rollover and principal direction of force (DOF1)

= 11, 12, or 1 o'clock positions or DOF1 = 10 or 2 o'clock positions with the crash damage forward of the A-pillar.

The salient regulations in force, which establish the prerequisites of vehicle testing in frontal impact simulations, are the Federal Motor Vehicle Safety Standards (FMVSS208) and the ECE (UN Economic Commission for Europe).

According to the USA FMVSS 208 and the CMVSS 208 Canada, frontal impact testing shall be conducted at a vehicle velocity of 48 km / h, with a rigid barrier and a 100% overlapping. However, according to the European regulations ECE / 96/79, [8] the front velocity on frontal impact shall be between 48.3 km / h and 53.1 km / h.

II. ROAD ACCIDENTS STATISTICS

In order to establish the type of collision that generates serious injury and even the death of a vehicle occupant, a statistical assessment of road traffic accidents has been carried out. Thus, for this study the following criteria have been taken into consideration: the type of collision, the human body parts exposed to the most severe injuries as well as the type of the driver.

Prior to this case study, in order to determine the most vulnerable road user, statistical data on road accidents have been thoroughly analysed. This study was divided into four main categories, as follows:

2.1. The identification of the type of transport with the highest rate of fatalities caused by road accidents:

Figure 1 [9] indicates a comparison of the male and female fatality distribution by road user type for four age groups. Accordingly, it can be observed that regardless age and sex classification, most of the victims are the occupants of vehicles, at the rate of over 40% in all cases.

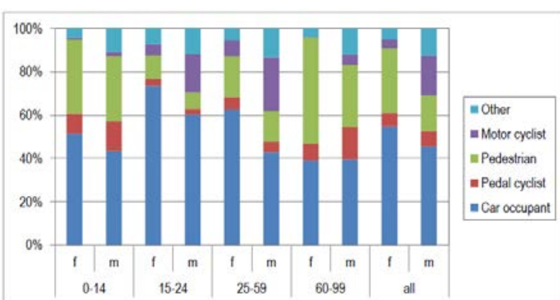

Fig.1. Distribution of fatalities by road user type [9]

2.2. Type of vehicle occupant: Male vs. female

In order to select the most appropriate type of dummy that will be used within this case study, we have first analysed the statistical data in Figure 2. As shown in Figure 2, the highest death rate is registered among male vehicle drivers, i.e. 35% of all fatalities recorded.

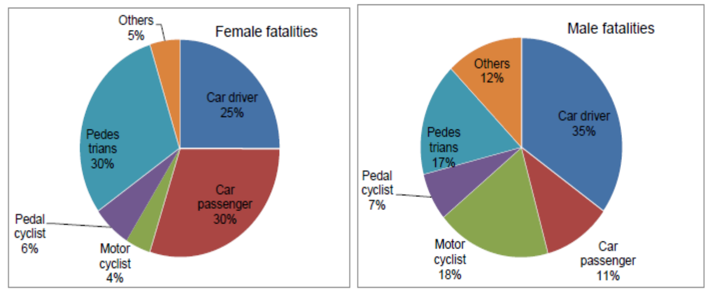

Fig.2. Distribution of male and female fatalities by means of transport [9]

2.3. Type of car occupant: passenger *vs*. driver

Figure 3 [9] indicated the proportion of fatalities by road user type on three types of road. Thus, regardless of the road type, vehicles' rivers have been reported as the most frequently encountered road traffic victims.

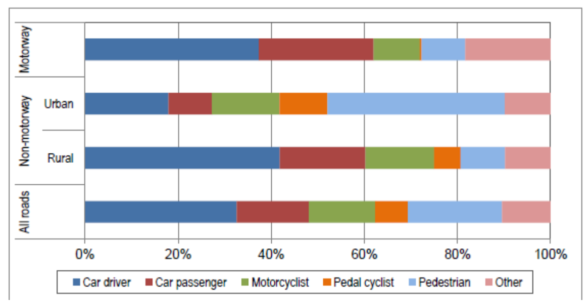

Fig.3. Distribution of fatalities by road user type [9]

2.4. Injured body part

Figure 4 [9] illustrates the distribution of the injured body parts with various road user types. As indicated below, the ratio of head injuries as well as the ratio of neck and throat injuries is most frequently recorded among car occupants, presumably linked to the incidence of whip-lash.

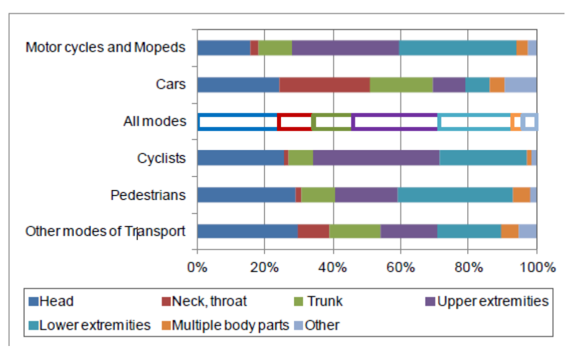

Fig.4. Body part injured by mode of transport [9]

Based on the above-indicated statistical analysis, it has been established that the highest amount of injuries and fatalities caused by road accidents was recorded among male car drivers. The most commonly affected body part due to road accidents is the upper part of the human body, i.e. the head, neck and thorax regions.

ISBN: 978-1-61804-325-2

III. DUMMY POSITIONING

3.1 The dummy-type used

In line with the above illustrated statistics, the study of the influence of passive safety systems in a frontal crash test shall be performed on a Hybrid III dummy-type - 50th percentile male, which was placed on the driver's seat.

Figure 5 indicates the geometry of the Hybrid III-type dummy to be used throughout the proposed study.

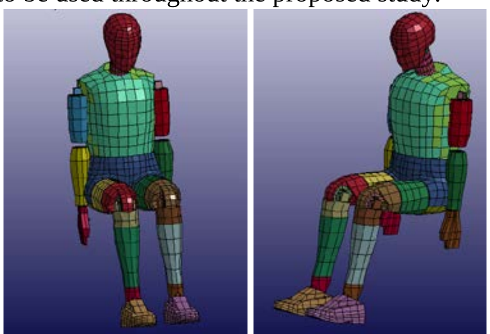

Fig.5. Hybrid III – 50th percentile male

3.2 Dummy positioning

The following step in implementing the numerical simulations of the driver's kinematic and dynamic behavior during frontal impacts consisted in the design of the seat-steering wheel-dashboard assembly. Once this assembly was designed, the dummy was also positioned.

The normal position of the dummy was considered and the percentile male Hybrid III dummy - WAS Placed 50th in the centered position in relation to thorax- 50th was placed in a thorax- centered position in relation to the steering wheel, at a distance of 350 mm.

The joints of the upper and lower limb(s) of the dummy were positioned as indicated below, in relation to the global coordinating system:

- the full arm up down joint was set at an angle of -40˚
- the elbow joint at an angle of -70˚
- the hands were placed on the wheel at an angle of -10˚
- the knee joint was set at an angle of -40˚
- the foot joint was set at an angle of -3˚
-

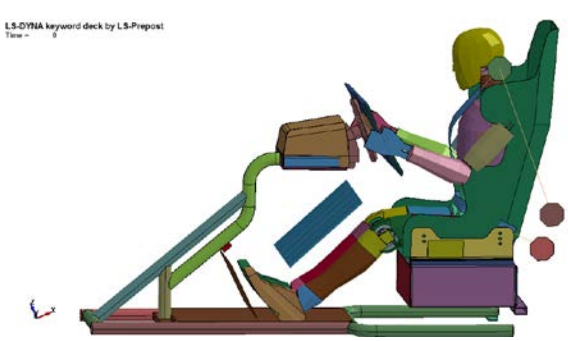

Fig.6. Normal position belted dummy

IV. PASSIVE SAFETY SYSTEMS

The present research study aims therefore to provide a comparative analysis with regard to the influence of the passive safety systems upon the behavior and the injuries caused to the vehicle driver in the head region during a frontal collision.

In addition, it is necessary to define and to fix the seat belt at the level of the dummy's body components. The contact between the seat belt and the dummy is of a node – area type, and it has been defined in the dummy's torso and pelvis region, as shown in Figure 7.

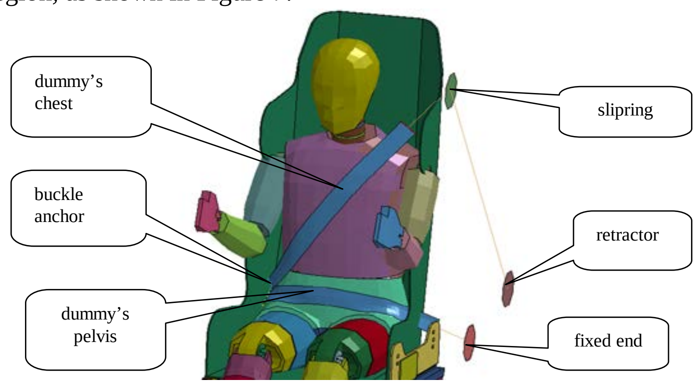

Fig.7. Seatbelt fitting

The second passive safety system that has been defined during the simulation was the airbag, positioned on the steering wheel assembly.

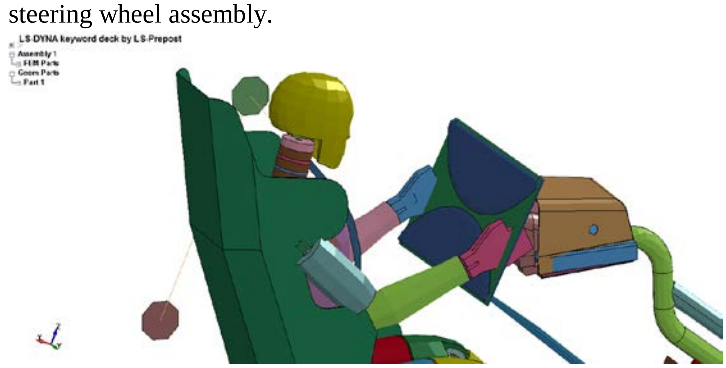

Fig.8. Airbag positioning

The airbag inflator follows the curve for mass flow rate, indicated in Figure 9.

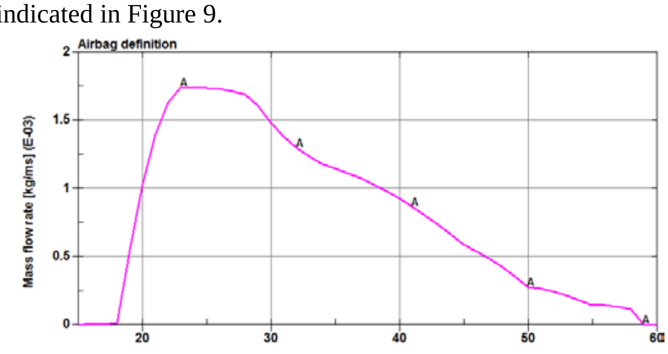

Fig.9. Airbag inflator

V. COLLISION TYPE AND PRESCRIBED MOTION

In order to determine the motion curve of the vehicle during the pre-crash, crash and post-crash phase and to determine the kinematic parameters required for the dynamic impact analysis, a frontal-type collision simulation was obtained by means of the software Virtual Crash.

Thus, a frontal impact between a mid-size sedan vehicle and a rigid wall has been considered, where the main force direction (PDoF) has been oriented in a 12 o'clock position and a 100% overlapping degree.

The initial vehicle velocity during the pre-crash phase has been set at 50 km / h.

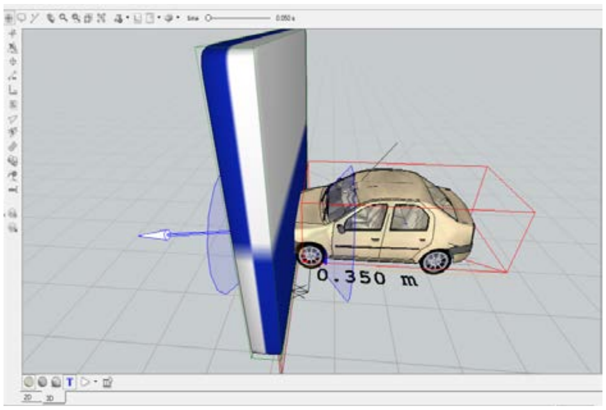

Fig.10. Frontal collision between a vehicle and a rigid wall in Virtual Crash

According to the velocity diagram in relation to time, the highest velocity variation was obtained within a time interval of 110 ms, during which the velocity rate ranged from the 0 [mm/ms] baseline and reached the maximum value vmax = 13,686 [mm/ms] at the final moment of tf=110 ms.

Based on the simulation performed by means of Virtual Crash we have established the velocity time variation diagram, as a prerequisite for the simulation used by the LS-DYNA software package as indicated in Figure 11.

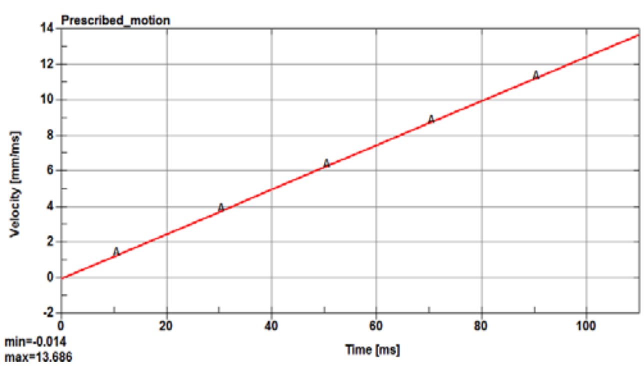

Fig.11. The velocity variation curve for vehicle's movement

VI. THE ANALYSED SITUATIONS

In order to establish the major influence on the driver's behavior as well as the most severe injury degree, four different situations concerning the position of the dummy have been analysed during the impact moment, as follows:

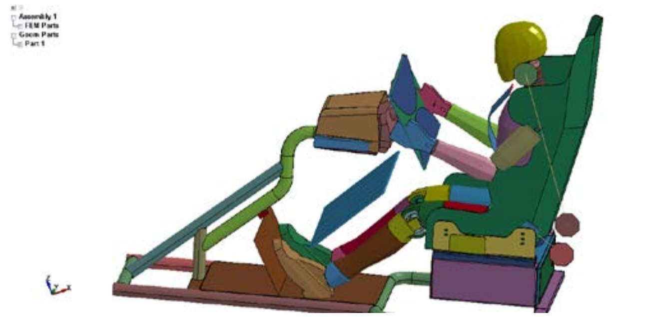

Fig.12. Test A - normal position with seat belt and airbag systems

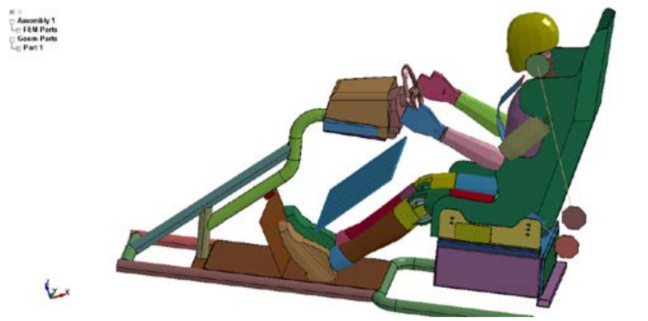

Fig.13. Test B - normal position with seat belt, without an airbag system

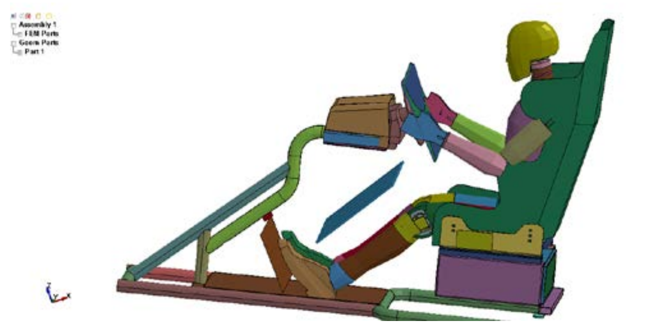

Fig.14. Test C - normal position without seat belt and airbag system

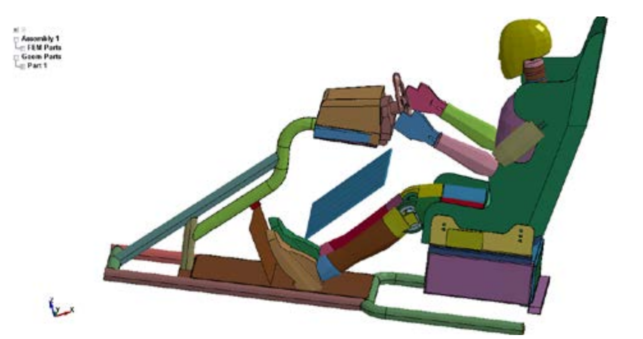

Fig.15. Test D - normal position without seat belt and airbag system

The analysis carried out in all the above mentioned situations focused on the kinematic and the dynamic behavior of the mechanism.

VII. RESULTS AND DISCUSSION

The assessment of the driver's injury degree in the head region at the moment of the frontal impact can be completed by means of two parameters:

- the head acceleration

According to the FMVSS 208 Regulation, the maximum acceleration in the head region is 80 [g].

- HIC (head injury criteria)

To determine the brain lesions in the head region according to the complex curve of acceleration, we have established as a factor the Head Injury Criteria.

Where t1 and t2 indicate the initial and the time (in seconds) and a (t) is the acceleration resulted (in g), measured in the center of gravity of the head region.

$$HIC = \left\{ (t_2 - t_1) \left[\frac{1}{t_2 - t_1} \int_{t_1}^{t_2} a(t)dt \right]^{2.5} \right\} max \quad (1)$$

According to FMVSS 208 and CMVSS 208 Regulations in case of frontal, the maximal values of HIC, compatible with the driver's survival are as follows:

HIC 15 (throughout a 15 ms interval) < 700

HIC 36 (throughout a 36 interval ms) < 1000

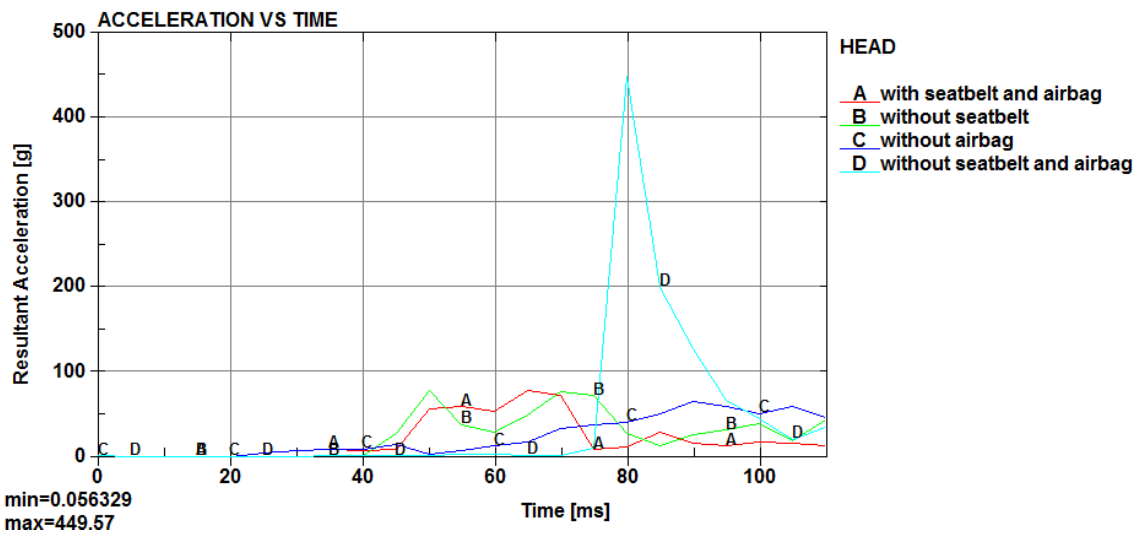

Fig.16. Head acceleration

According to the variation of acceleration over time, as in Figure 16, we have registered that the acceleration highest value in the head region is recorded in situation D, i.e. the driver's normal position without restraint and airbag system.

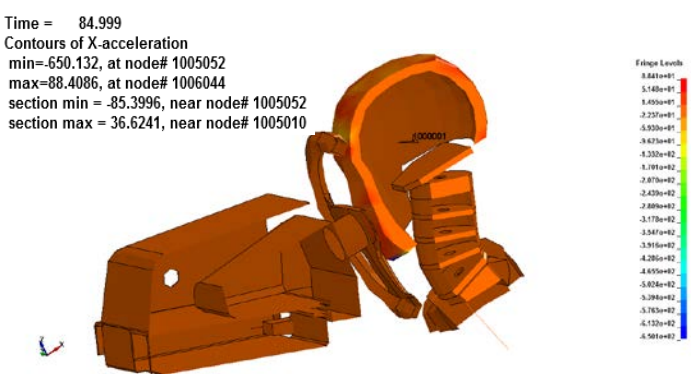

Fig.17. Contours of head acceleration – test D

As indicated in Table 1, the lowest acceleration value in the head region was registered in that situation when the driver is restrained by a seatbelt while a frontal airbag system is missing, i.e. test C. In this situation the maximum value of the acceleration recorded does not exceed the limit of 80 g, which is compatible with the driver's survival. During the simulation, we could notice that due to the restraint system, the dummy's head moves longitudinally, according to the X axis direction, though it does not get in contact with the steering wheel, while the missing airbag prevents any impact in the head region of the dummy. Also in this situation, the maximum recorded acceleration value does not exceed the acceleration limit, thus the injuries suffered are compatible with the driver's as well.

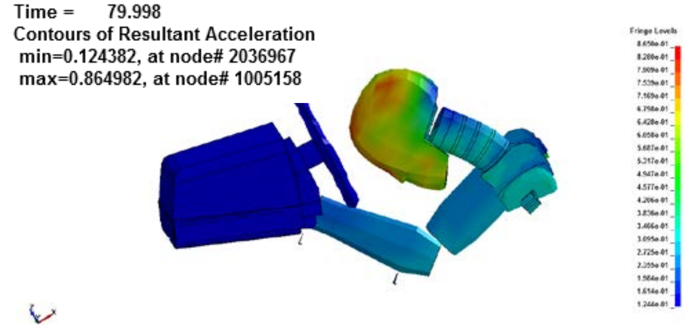

Fig.18. Contours of head acceleration – test C

ISBN: 978-1-61804-325-2

The close values of the acceleration in the dummy's head region obtained in A (with restraint and airbag system) and in B (without restraint system, but with an airbag system), indicate that the degree of injury is primarily influenced by the existence of the frontal airbag system. Thus, in B, that at the impact moment, the entire body, having not been retained by the seat belt, moves freely not only in the head region, subsequently indicating lower acceleration values in the head region.

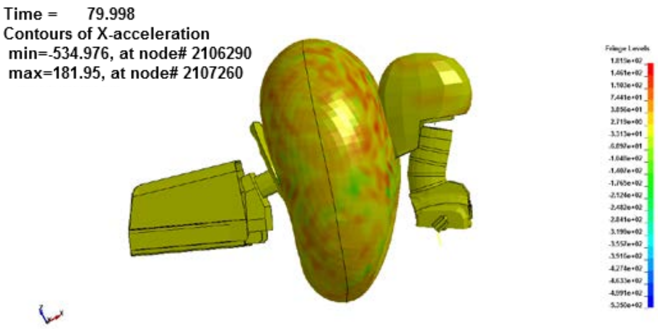

Fig.19. Contours of head acceleration – test B

The results obtained following the analysis of the above-illustrated situations are indicated in Table 1.

Table 1 – Resultant acceleration and HIC

Nr. test \ Parameter	Max resultant acceleration [g]	HIC 36
Test A	79	714
Test B	70	600
Test C	64	626
Test D	449	1566

Comparing the values obtained in the situation where the driver has not been restrained with a seat belt and the vehicle has not been equipped with an airbag system, we have drown the conclusion that the maximum values as established by the CMVSS 208 and FMVSS 208 regulations are outdated . Thus, in situation D, the driver's injuries degree in the head region is not compatible with the driver's survival.

Figure 20 indicates the acceleration variation and the head injury criteria for the situations when the driver is secured by a restraint system and the vehicle is equipped with an airbag system.

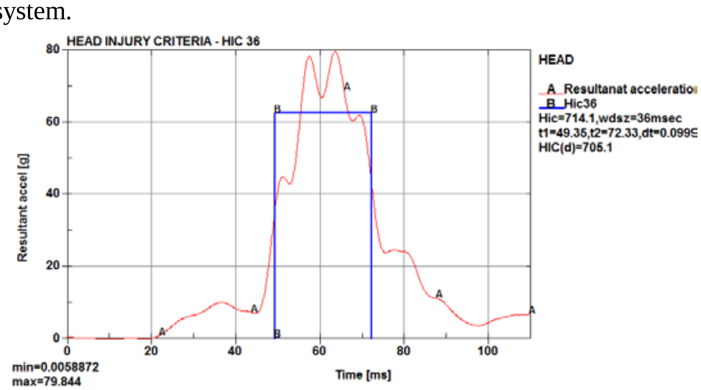

Fig.20. Head injury criteria – test A

VII. Conclusion

To put in a nutshell, according to the results obtained following the analysis of the above-mentioned situations, during a frontal collision against a rigid wall at a speed of 50 km/h, the passive safety systems point out a considerable influence upon the driver's degree of injury.

The most severe injuries are to be registered in such situations when the driver is not secured by a retention system and the vehicle is not provided with an airbag system.

The influence of at least one passive safety system (be it a retention seat belt system or an airbag system) triggers acceleration values and head injury criteria which are situated below the maximum limit established according to crash tests regulations.

Acknowledgment

This work was supported by the strategic grant POSDRU/159/1.5/S/133255, Project ID 133255 (2014), co-financed by the European Social Fund within the Sectorial Operational Program Human Resources Development 2007-2013.

References

[1] Joseph H. Ash, David J. Lessley, Jason L. Forman, Qi Zhang, C. Greg Shaw, Jeff R. Crandall, "Whole-Body Kinematics: Response Corridors for Restrained PMHS in Frontal Impacts", IRC-12-21 IRCOBI Conference 2012.

[2] K. Preston White, Jr., W. Thomas HollowelI, H. Clay Gabler, Ill, Walter D. Pilkey, "Simulation Optimization of the Crashworthiness of a Passenger Vehicle in Frontal Collisions using Response Surface Methodology", SAE paper 850512.

[3] Maika Katagiri , Yusuke Miyazaki , Jonas Pramudita, Sadayuki Ujihashi, "Development of occupant injury prediction algorithms for advanced automatic collision notification by numerical crash reconstructions", SAE Paper Number 13-0149.

[4] Louden, A., "Side air bag out-of-position testing of recent model year vehicles", National Highway Traffic Safety Administration United States, Paper Number: 07-213.

[5] Lund, A., "Recommended procedures for evaluating occupant injury risk from deploying side airbags", Side Airbag Out-of-Position Injury Technical Working Group B-2 (Alliance, AIAM, AORC, IIHS), First revision 2003.

[6] Haufe, A., Franz, U., "On the simulation of out-of-position load cases with the ale-method", Airbag 2004 - 7th International Symposium and Exhibition on Sophisticated Safety Systems.

[7] William T. Hollowell, Hampton C. Gabler, Sheldon L. Stucki, Stephen Summers, James R. Hackney, "Updated review of potential test procedures for FMVSS No. 208", Office of Vehicle Safety Research, October 1999.

[8] E/ECE/324, Regulation N0.33, page 26, Annex 4 – Frontal Impact Test Against a Barrier

[9] Brandstaetter, C., et al. (2012) Annual Statistical Report, Deliverable D3.9 of the EC FP7 project DaCoTA.

Design and Analysis of Large Amplitude Ultrasonic Atomizer

Yun-Jui Yang, Yung Ting, Jia-Ci Chen, Yen-Lung Lee, Amelia Sugondo

Abstract—Different from the general ultrasonic atomizer operating at high frequency, the proposed one is driven at much lower frequency but with larger amplitude. For this application purpose, a simple structure constructed with a hollow tube encircled with piezoelectric actuators is considered to use. Instead of using a ring type of ceramics, three pieces of same size sectional-type of d_{33} ceramic actuators are employed around the hollow tube with equal distance to generate higher radial vibration. While the tube fixed at both ends is vibrated with assigned vibration mode shape, a suitable wave is formed to produce larger amplitude in need. The fluid inside the tube will flow out smoothly from a very small hole implemented on the largest amplitude of the waveform. Thereafter, atomization occurs on the tube surface around the hole immediately while enough oscillation frequency and amplitude is provided. With such design structure, several cases with different tube length, resonance frequency, vibration amplitude are investigated for comparison. Particle size of 5~30μm and uniform spray distribution is the target for an example of industry-used spray fluid with viscosity of about 8~12cp. A measurement system is set up including high speed camera, laser as a light source, and software Image J for estimation of particle size and particle distribution. Water is used for experimental testing in this study. While drives the hollow tube with operating frequency of 45.3 kHz and the maximum amplitude is great than 6.8μm, atomization occurs with average particle diameter of 28.3μm and good uniformity and distribution. However, increasing vibration amplitude, on the contrary, the diameter of the particle becomes larger. For example, while increases amplitude up to 9μm, atomization occurs with average particle diameter of 34μm, and the uniformity and distribution becomes worse. This interesting phenomenon may result from large amplitude at enough vibration frequency easily makes atomization occur but large amplitude engenders with large particle diameter.

Keywords—piezoelectric actuator, radial vibration, ultrasonic atomization

I. Introduction

Ultrasonic coating techniques can be applied include textile, artificial leather or synthetic leather, paper or cardboard, fiberboard, plastic film, cellophane, composite materials, a variety of irregular shapes, and in recent years has greatly used in solar Coating and also battery Coating[1]. In Photoelectric industry, for example, the use of adhesives can improve the performance and durability in LCD or plasma displays, organic light-emitting diode (OLED). Adhesives can produce a barrier effect to increase the resistance to against yellow light, and thus increase the transmittance better contrast, and improved brightness and clarity, the reliability of products and reduce maintenance costs. Using a coating technique is feasible and appropriate processing methods. According to the industry-average particle diameter of the coating is 5 ~ 30μm, spray rate about 10in / s or less. But generally more difficult to produce ultrasonic nebulizer must be used for this particle size MHz frequency vibration levels. However, in such case the operation produce a high frequency that easily produces heat for the ultrasonic atomizer, and even detracts from the effectiveness of the piezoelectric material life, and disadvantages such as low efficiency of conversion. Therefore, we design a new type of hollow cylindrical atomizer, they have a greater use of the amplitude and the frequency is low, you can still get good atomized droplets of particle diameter size and the distribution, and also better atomization speed [2-3].

II. Design and Analysis

A sectional shape of piezoelectric ceramics which is radially polarized for an actuator[4], shown in figure 2.1 .The inner and outer surface are coated by silver electrode, through a high-voltage polarization, it becoming d33 Type of acuator.

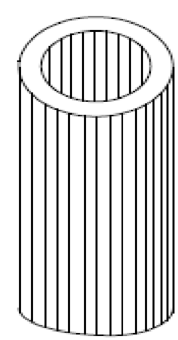

Figure2.1

In our previous study, three pieces of piezoelectric actuator is mounted around the hollow steel tube with equal distance will obtain larger performance [5]. In figure 2.2, it is seen that a three-phase vibration is generated to expand the vibration effect. ANSYS is used for structural analysis. According to the pre sent study, the frequency range of 40~70kHzand the amplitude demand for 75μm is demanding. Figure 2.3 shows several case studies of modal simulation in the above assigned frequency range. Amplitude of the selected mode is investigated using

[1] Corresponding author: Yung Ting, E-mail: yung@cycu.edu.tw
Dept. of Mech. Eng., Chung Yuan Christian University, 200 Chung Pei Rd., Chung Li 32023, Taiwan
Tel: +886-3-265-4319 Fax: +886-3-2654399

harmonic analysis shown in Figure2.4. Resonance frequency is used to measure the system by suing impedance analyzer shown . As seen, experimental and analytical results resonance frequency and vibration amplitude are in a close approximation.

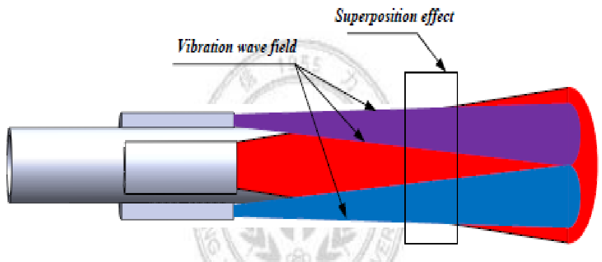

Figure2.2

In modal analysis use of finite element analysis software to analyze the hollow tube atomizer [6]. When the resonance frequency is applied to the atomization to obtain the desired design is expected within the deformed shape, the main analysis Has a natural resonance frequency of the modal design structure, amplitude harmonic analysis.

According to the present study is expecting the frequency range 40 kHz~70 kHz and the amplitude demand for 75 μ m. Because the hollow tube atomizer at 40 kHz~70 kHz modal several types, as shown in figure 2.3

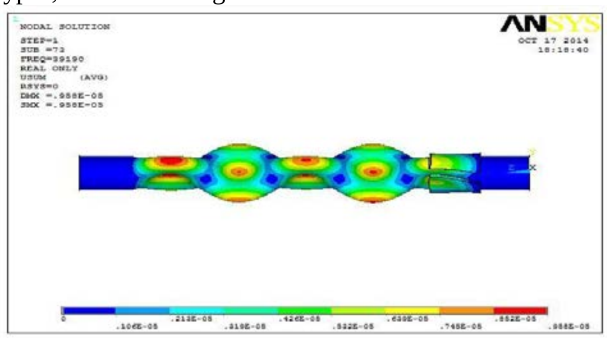

Figure2.3 (39 kHz)

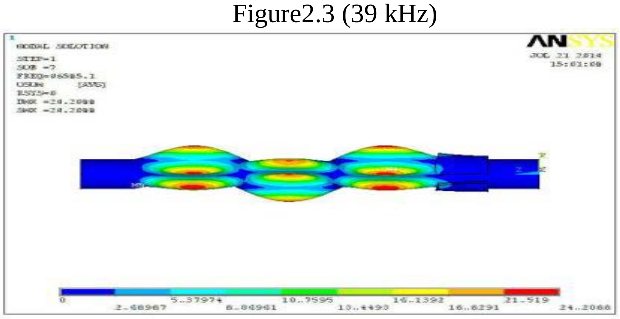

Figure2.3 (46 kHz)

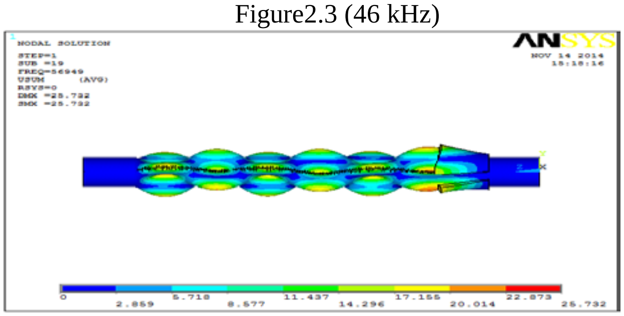

Figure2.3 (52 kHz)

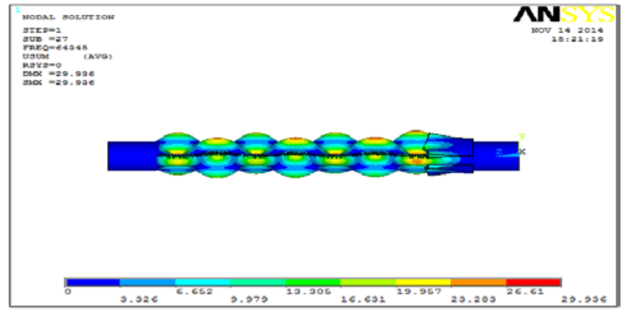

Figure2.3 (64 kHz)

The design of the vibration modes, depending on the amplitude of 7.5μm. Upon learning of harmonic analysis to the amplitude of the selected mode is available. Finally, the results of the modal analysis of resonance and resistance. The amount of anti-analyzer test results comparing the actual driving frequency can be used as a reference.

Resonance modal analysis results basically only obtained the structure of the natural resonant frequency corresponding to the deformation mode, cannot simulate the actual amplitude; therefore, require harmonic analysis to obtain the actual structure under external harmonic vibration amplitude, as shown in figure 2.4

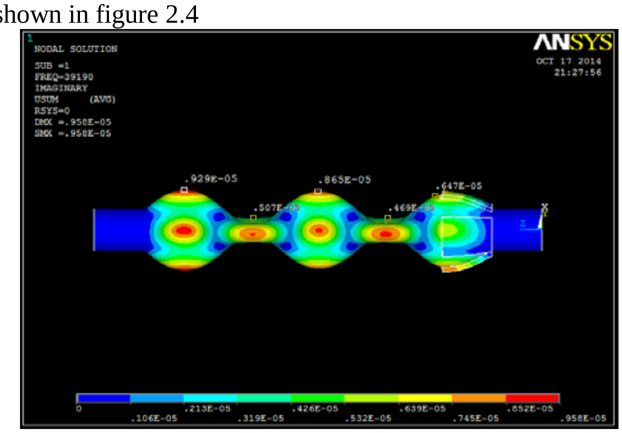

Figure2.4(9.5 μ m)

III. EXPERIMENT

Hollow tube atomizer amplitude measurements, the reference point is the point of maximum amplitude point , by over the actual driving test to obtain a hollow tube atomizer actual driving frequency of about 46kHz, while applying an AC signal power± 200V, use laser vibration measurement system (Polytec OFV-5000) with the laser signal decoding controller (Polytec OFV-511), the measurement of the amplitude of the reference point, the feedback signal to the digital oscilloscope (Tektronix TDS2004B)show the relative value of its output voltage, the entity indicated on Figure 3.1, and then through the converter voltage and displacement relationship, that produced the amplitude value of the piezoelectric vibrator

ISBN: 978-1-61804-325-2

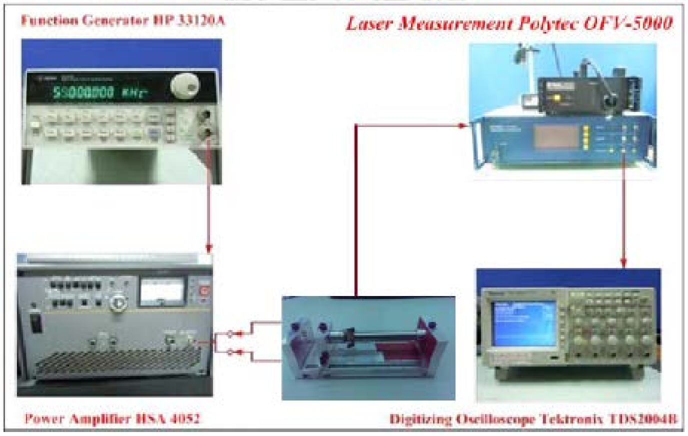

Figure3.1

Particle size measurement of the hollow tube atomizer [7], after the measured maximum amplitude point, by using the point as atomization point. Common methods such as the use of speed cameras, laser diffraction particle size analyzer Etc. For measuring the particle size experiment, a system formed in this laboratory experiment was carried out, the system comprises a micro-droplets image observation principle, hollow tube atomizer, clamping platform, image processing four parts, shown as figure 3.2

Figure3.2

IV. RESULT

By using Laser vibration measurement system (Polytec OFV-5000) measuring the maximum amplitude with laser signal decoding controller(Polytec OFV-511) the feedback signal shown as figure 4.1 the result maximum voltage is 9.2V and the scale of the laser signal decoding controller is $1\mu m/V$, so the maximum amplitude is $9.2V \times 1\mu m/V = 9.2\mu m$

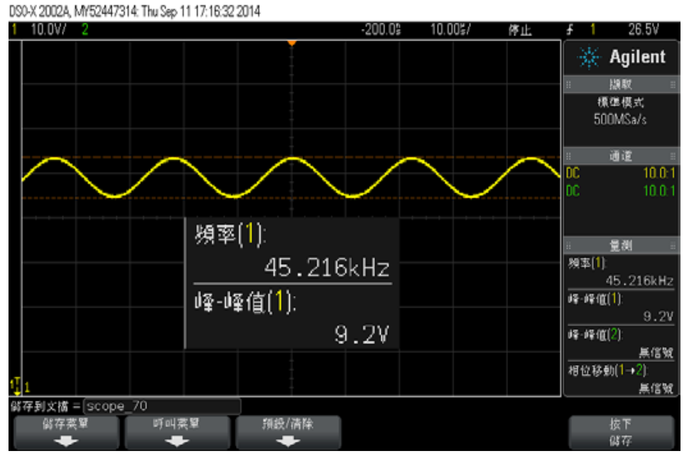

Figure4.1

This is the use of high-speed cameras (basler acA1300-30gm) to shoot atomization phenomenon. The film of atomization is that shooting in frequency 46 kHz and amplitude $9.2\mu m$ shown by the computer system after capture photos shown as figure 4.2 By using software Image J to measure the particle size of droplet[8].

Figure 4.2

V. CONCLUSION

This development of hollow tube atomizer, with high amplitude and low frequency can achieve the effect of atomization, can effectively reduce the issue of heating problem, and has the advantage of better electromechanical energy-conversion efficiency and low failure rate, etc. if that atomization particle size and distribution are satisfied. The use of piezoelectric ceramic material and the metal tube in two different physical properties, amplified piezoelectric vibration amplitude, the design of the piezoelectric actuator and the setup, the use of piezoelectric actuator element as a driving source, and atomizer clamped at both ends. But also for finding the maximum deformation point and amplitude values of a hollow cylinder, using ANSYS finite element analysis software, to explore modal movement of the actuating element with its suit of the excitation frequency, the simulation results in line with the frequency of the compare the result from analysis and experiment can see that the amplitude is $9.5\mu m$ and $92\mu m$, and the modal frequency is that 39kHzand 46kHz.

REFERENCES

[1] A. B. D. Nandiyanto and K. Okuyama, "Progress in Developing Spray-drying Methods for the Production of Controlled Morphology Particles: From the Nanometer to Submicrometer Size Ranges," Advanced Powder Technology, Vol. 22, Issue 1, pp. 1-19, 2011.

[2] M. Dobre, L. Bolle, "Practical Design of Ultrasonic Spray Devices: Experimental Testing of Several Atomizer Geometries," Experimental Thermal and Fluid Science, Vol.26, Issue 2-4, pp. 205-211, 2002.

[3] J. O. Kim, K. H. Kyo, G. J. Hyung, "Radial Vibration Characteristics of Piezoelectric Cylindrical Transducers", Journal of Sound and Vibration, Vol. 276, pp.1135-1144, 2004.

[4] S. C. Tsai, Y. L. Song, T. K. Tseng, Y.F. Chou, W. J. Chen, "High Frequency Silicon Based Ultrasonic Nozzle Using Multiple Fourier Horns", IEEE Transactions on Ultrasonic, Ferroelectrics, and Frequency Control, Vol. 51, pp.277-285, 2004.

[5] S. C. Tsai, Y. L. Song, T. K. Tseng, Y.F. Chou, W. J. Chen, "High Frequency Silicon Based Ultrasonic Nozzle Using Multiple Fourier Horns", IEEE Transactions on Ultrasonic, Ferroelectrics, and Frequency Control, Vol. 51, pp.277-285, 2004.

[6] R. W. C. Lewis, et al., "Finite Element and Experimental Analysis of the Vibration Response of Radially Poled Piezoceramic Cylinders," J. of Ferroelectrics, pp.95-106, 2009.

[7] L. M. Lourenco, A. Krothapalli, J. M. Buchlin and M. L. Riethmuller, "A Non-Invasive Experimental Technique for the Measurement of Unsteady Velocity and Vorticity Fields", AIAA Journal, Vol. 24, pp. 1715-1717, 1986.

[8] R. Lind, "Open Source Software for Image Processing and Analysis: Picture This with ImageJ," Open Source Software in Life Science Research, pp. 131-149, 2012

Determination to a plan model of the automotives moving used for the stability analysis

Loreta Simniceanu, Victor Otat, Mario Trotea

Abstract— This paper presents some researches regarding the stability of automotives, a plan model of automotive is taking into account. For this automotives plan model a mathematical model is found under nonlinear differential equations system form, which can be used in analyses stability of the automotive.

Keywords—automotive, mathematical model, nonlinear differential equations, plan model, stability.

I. Introduction

IN this paper we are proposing a mathematical model for automotives moving, a model who includes some of the position parameters and moving parameters.

This mathematical model can be used into a preliminary stability analyzes by dynamic systems theory or classical mechanic theory appling.

II. The mathematical model of automotives moving

2.1. The mechanical plan model of automotive

The next references systems are taking into account:

- a reference system is attaching to the suspended mass of the vehicle; this system has the origin in center mass point of this, and Ox, Oy axle making the plan of principal direction of displacement; the Oz axle is perpendicular to Ox, Oy axles;
- a fixed $O_1x_1y_1z_1$ coordinate system presented in Fig. 1.

Notations:

- C1, C2, C3, C4 - the center of contact area between tire and road;
- F_{x1}, F_{x2}, F_{x3}, F_{x4} - the longitudinal forces of contact area between tires and road;
- F_{y1}, F_{y2}, F_{y3}, F_{y4} - the lateral forces of contact area between tire and road;
- δ_1, δ_2 - the cornering angle for front axle;

The next degree of freedom is taking into account:

- x, define the displacement along longitudinal axle;
- y, define the displacement along transversal axle;
- u, define the displacement along vertical axle;
- θ_1, define the circular displacement of suspended mass around Ox axle;
- θ_2, define the circular displacement of suspended mass around Oy axle;
- φ, define the circular displacement of suspended mass around Oz axle.

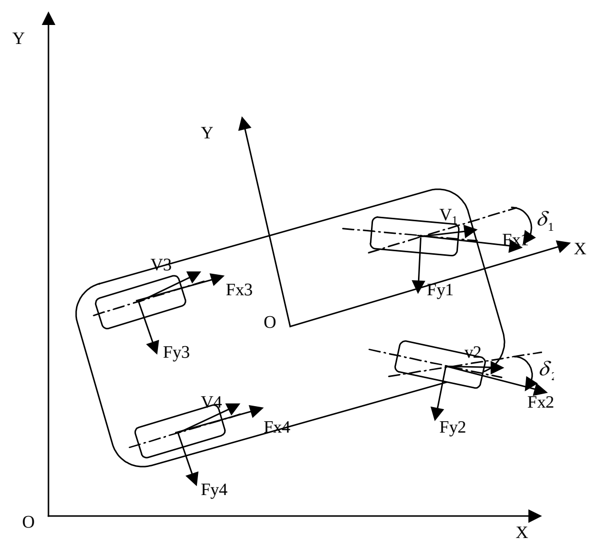

Fig. 1. The plan model of vehicle

2.2. The mathematical model of vehicles moving

The connection between the two basis vectors of those systems $\{i\} = \left\{ \vec{i}, \vec{j}, \vec{k} \right\}^T$ and $\{i_1\} = \left\{ \vec{i_1}, \vec{j_1}, \vec{k_1} \right\}$ may be written under the next form:

$$\{i\} = [S]\{i_1\}^T, \tag{1}$$

where $[S]$ is the matrix used for base changes and it has the form:

$$S = \begin{bmatrix} \cos\varphi & \sin\varphi & 1 \\ -\sin\varphi & \cos\varphi & 1 \\ 0 & 0 & 1 \end{bmatrix} \tag{2}$$

A first moving equation gang is obtained by applying the derivative impulse axiom:

$$m \cdot \overrightarrow{a_0} = \vec{R} \tag{3}$$

Where:

- $\vec{R}$ is the resultant of all external forces who acting over the vehicle;
- $\vec{a_0}$ is the mass point acceleration;

The forces who are acting on vehicle tires, included in road plan, and who are projected on axes of referential system attach to vehicle, are:

$$\vec{F}_{e1} = \left(F_{x1} \cdot \cos\delta_1 - F_{y1} \cdot \sin\delta_1\right) \cdot \vec{i} - \left(F_{x1} \cdot \sin\delta_1 + F_{y1} \cdot \cos\delta_1\right) \cdot \vec{j}$$

$$\vec{F}_{e2} = \left(F_{x2} \cdot \cos\delta_2 - F_{y2} \cdot \sin\delta_2\right) \cdot \vec{i} - \left(F_{x2} \cdot \sin\delta_2 + F_{y2} \cdot \cos\delta_2\right) \cdot \vec{j} \quad (4)$$

$$\vec{F}_{e3} = F_{x3} \cdot \vec{i} - F_{y3} \cdot \vec{j}$$

$$\vec{F}_{e4} = F_{x4} \cdot \vec{i} - F_{y4} \cdot \vec{j}$$

Where: - F_x, F_y are the longitudinal force, relative the lateral force included in road plan;

- δ_1, δ_2 are the cornering angle for front axle wheels;

The next forces are acting on suspended mass of the vehicle:

$\vec{F} = F_x \cdot \vec{i} + F_y \cdot \vec{j} + F_z \cdot \vec{k}$ - the external resultant force (rolling resistance, windage, pitch resistance, weight force etc).

The acceleration and the forces are replacement in (3) relation and a projection on the proper axle system are doing, the first moving equations are obtained:

$$m \cdot a_x = F_{x1} \cdot \cos\delta_1 - F_{y1} \cdot \sin\delta_1 + F_{x2} \cdot \cos\delta_2 - F_{y2} \cdot \sin\delta_2 + F_{x3} + F_{x4} + F_x$$

$$m \cdot a_y = -F_{x1} \cdot \sin\delta_1 - F_{y1} \cdot \cos\delta_1 - F_{x2} \cdot \sin\delta_2 - F_{y2} \cdot \cos\delta_2 - F_{y3} - F_{y4} + F_y \quad (5)$$

The second equations gang is obtained by using the derivative kinetic moment axiom:

$$m\vec{r_c} X \vec{a_0} + \vec{\vec{J}}_0 \cdot \vec{\varepsilon} + \vec{\omega} X \left(\vec{\vec{J}}_0 \cdot \vec{\omega}\right) = \vec{M_0} \quad (6)$$

Where:

- $\vec{r_c}$ is the position vector of mass centre towards proper axle system ($\vec{r_c}$ =0)
- $\vec{\omega} = \omega_x \vec{i} + \omega_y \vec{j} + \omega_z \vec{k}$ (7)
- $\vec{\varepsilon} = \varepsilon_x \vec{i} + \varepsilon_y \vec{j} + \varepsilon_z \vec{k}$
- $\vec{\vec{J}}_0$ is inertial tensor of vehicle towards proper system and it has attached the next matrix:

$$\vec{\vec{J}}_0 \to \begin{pmatrix} J_{11} & J_{12} & J_{13} \\ J_{21} & J_{22} & J_{23} \\ J_{31} & J_{32} & J_{33} \end{pmatrix}$$

For to written the lateral forces we will use a nonlinear dependence:

$$Y_k = c_{k1} \cdot \alpha_k - c_{k3} \cdot \alpha_k^{\ 3}, \ k=1,2,3,4$$

c_{k1}, c_{k3} -$[N/rad]$ stiffness coefficients for each wheel;

α - The stiffness angle of tire.

The determination of stiffness angles is doing taking into consideration the kinematics conditions. The next cinematic relations may be written:

$$\vec{v}_C = v_x \cdot \vec{i} + v_y \cdot \vec{j}$$

$$\vec{v}_{C1} = \vec{v}_C + \vec{\omega} \times \vec{CC}_1 = v_x \cdot \vec{i} + v_y \cdot \vec{j} + \begin{vmatrix} \vec{i} & \vec{j} & \vec{k} \\ 0 & 0 & \omega \\ a & \frac{e}{2} & 0 \end{vmatrix}$$

$$= (v_x - \frac{e}{2} \cdot \omega) \cdot \vec{i} + (v_y + a \cdot \omega) \cdot \vec{j}$$

$$tg(-\delta_1 + \alpha_1) = \frac{-(v_y + a \cdot \omega)}{v_x - \frac{e}{2} \cdot \omega}$$

$$\alpha_1 = \delta_1 - arctg \frac{v_y + a \cdot \omega}{v_x - \frac{e}{2} \cdot \omega} \quad (8)$$

$$\vec{v}_{C2} = \vec{v}_C + \vec{\omega} \times \vec{CC}_2 = v_x \cdot \vec{i} + v_y \cdot \vec{j} + \begin{vmatrix} \vec{i} & \vec{j} & \vec{k} \\ 0 & 0 & \omega \\ a & -\frac{e}{2} & 0 \end{vmatrix}$$

$$= (v_x + \frac{e}{2} \cdot \omega) \cdot \vec{i} + (v_y + a \cdot \omega) \cdot \vec{j}$$

$$tg(-\delta_2 + \alpha_2) = \frac{-(v_y + a \cdot \omega)}{v_x + \frac{e}{2} \cdot \omega}$$

$$\alpha_2 = \delta_2 - arctg \frac{v_y + a \cdot \omega}{v_x + \frac{e}{2} \cdot \omega} \quad (9)$$

$$\vec{v}_{C3} = \vec{v}_C + \vec{\omega} \times \vec{CC}_3 = v_x \cdot \vec{i} + v_y \cdot \vec{j} + \begin{vmatrix} \vec{i} & \vec{j} & \vec{k} \\ 0 & 0 & \omega \\ -b & \frac{e}{2} & 0 \end{vmatrix}$$

$$= (v_x - \frac{e}{2} \cdot \omega) \cdot \vec{i} + (v_y - b \cdot \omega) \cdot \vec{j}$$

$$tg(\alpha_3) = \frac{v_y - b \cdot \omega}{v_x - \frac{e}{2} \cdot \omega} \quad \alpha_3 = arctg \frac{v_y - b \cdot \omega}{v_x - \frac{e}{2} \cdot \omega} \tag{10}$$

$$\vec{v}_{C4} = \vec{v}_C + \vec{\omega} \times \vec{CC}_4 = v_x \cdot \vec{i} + v_y \cdot \vec{j} + \begin{vmatrix} \vec{i} & \vec{j} & \vec{k} \\ 0 & 0 & \omega \\ -b & -\frac{e}{2} & 0 \end{vmatrix}$$

$$= (v_x + \frac{e}{2} \cdot \omega) \cdot \vec{i} + (v_y - b \cdot \omega) \cdot \vec{j}$$

$$tg(\alpha_4) = \frac{v_y - b \cdot \omega}{v_x + \frac{e}{2} \cdot \omega}$$

$$\alpha_4 = arctg \frac{v_y - b \cdot \omega}{v_x + \frac{e}{2} \cdot \omega} \tag{11}$$

Taking into account this relations, and we replacing the expressions for lateral forces and stiffness ((8), (9), (10), (11)), the next system of equations are obtained:

$$\dot{\omega} = \frac{1}{J_x} \cdot \left\{ -\frac{e}{2} \cdot \left(F_{x1} \cdot \cos \delta_1 - \left(c_{11} \cdot \alpha_1 - c_{13} \cdot \alpha_1^3 \right) \cdot \sin \delta_1 \right) \right.$$

$$- a \left(F_{x1} \cdot \sin \delta_1 + \left(c_{11} \cdot \alpha_1 - c_{13} \cdot \alpha_1^3 \right) \cdot \cos \delta_1 \right)$$

$$+ \frac{e}{2} \cdot \left(F_{x2} \cdot \cos \delta_2 - \left(c_{21} \cdot \alpha_2 - c_{23} \cdot \alpha_2^3 \right) \cdot \sin \delta_2 \right)$$

$$- a \cdot \left(F_{x2} \cdot \sin \delta_2 + \left(c_{21} \cdot \alpha_2 - c_{23} \cdot \alpha_2^3 \right) \cdot \cos \delta_2 \right)$$

$$+ \frac{e}{2} \cdot \left(-F_{x3} + F_{x4} \right) + b \cdot (c_{31} \cdot \left(arctg \frac{v_y - b \cdot \omega}{v_x - \frac{e}{2} \cdot \omega} \right) -$$

$$c_{33} \cdot \left(arctg \frac{v_y - b \cdot \omega}{v_x - \frac{e}{2} \cdot \omega} \right)^3 + c_{41} \cdot \left(arctg \frac{v_y - b \cdot \omega}{v_x + \frac{e}{2} \cdot \omega} \right)$$

$$\left. - c_{43} \cdot \left(arctg \frac{v_y - b \cdot \omega}{v_x + \frac{e}{2} \cdot \omega} \right)^3) \right\}$$

$$\dot{v}_y = \frac{1}{m} \cdot \{ F_{x1} \cdot \sin \delta_1 + F_{x2} \cdot \sin \delta_2$$

$$+ (c_{11} \cdot \left(\delta_1 - arctg \frac{v_y + a \cdot \omega}{v_x - \frac{e}{2} \cdot \omega} \right) -$$

$$c_{13} \cdot \left(\delta_1 - arctg \frac{v_y + a \cdot \omega}{v_x - \frac{e}{2} \cdot \omega} \right)^3) \cdot \cos \delta_1$$

$$+ (c_{21} \cdot \left(\delta_2 - arctg \frac{v_y + a \cdot \omega}{v_x + \frac{e}{2} \cdot \omega} \right) -$$

$$c_{23} \cdot \left(\delta_2 - arctg \frac{v_y + a \cdot \omega}{v_x + \frac{e}{2} \cdot \omega} \right)^3) \cdot \cos \delta_2$$

$$+\left(c_{31}\cdot\left(arctg\frac{v_y-b\cdot\omega}{v_x-\frac{e}{2}\cdot\omega}\right)-c_{33}\cdot\left(arctg\frac{v_y-b\cdot\omega}{v_x-\frac{e}{2}\cdot\omega}\right)^3\right)$$

$$+\left(c_{41}\cdot\left(arctg\frac{v_y-b\cdot\omega}{v_x+\frac{e}{2}\cdot\omega}\right)-c_{43}\cdot\left(arctg\frac{v_y-b\cdot\omega}{v_x+\frac{e}{2}\cdot\omega}\right)^3\right)\}$$

$$-\omega\cdot v_x$$

$$\dot{y}=v_y\cdot\cos\varphi+v_x\cdot\sin\varphi$$

$$\dot{\varphi}=\omega \qquad (12)$$

A system that modeling the vehicle plan moving are obtained, and this system has y, v_y, φ, ω variables and the velocity v_x is considerate constant.
This system are presented under nonlinear differential equations system form, so that it will be resolved using a computer support and it can provide some preliminary informations about automotives stability.

REFERENCES

[1] Baker L.G., Gollub P.J., Chaotic dynamics an introduction, Cambridge University Press, 1990.

[2] Ceaikovski, I.P., Issledovanie protessa stabilizatii upravleaemîh koles primeneniem analogovoi E.V.M.,în Avtomobilnaia promîslennost, XXXIII, nr.6, 1967.

[3] Ciudakov, E.A., Teoria automobilului. Traducere din limba rusã. Institutul de documentare Bucuresti 1958.

[4] Guckenheimer, J., Holmes, Ph., Nonlinear oscillations, dynamical systems and bifurcations of vector fields, Springer-Verlag, New York Berlin Heidelberg Tokyo, 1983.

[5] Legouis, D.T., Modelisation et analyse de la dynamique du systeme vehicule pilot, Ingenieurs de l'Automobile oct. 1987, p.101-106.

[6] Voinea, P. R., Stroe, I., Sisteme dinamice, Institutul Politehnic Bucuresti,1994.

[7] Simniceanu, L., Aplicatii ale teoriei sistemelor dinamice în dinamica automobilelor, Institutul Politehnic Bucuresti, 2005.

[8] V. Oţăt, D-tru Bolcu, Walter Thierheimer, L. Simniceanu; Dinamica autovehiculelor, Universitaria Publishing, Craiova, 2005;

[9] D-tru Neagoe, D-tru Bolcu, Studiul stabilitatii si maniabilitatii autovehiculelor. Cercetari experimentale si teoretice, Universitaria Publishing, Craiova, 2008.

[10] Bogdan Constantin; Bogdan Mihaela-Liana, Simniceanu Loreta; Dincă Liviu, *Experimental Equipment For Study Of Landing Gear Mechanisms,* Annals of DAAAM for 2007, ISSN 1726-9679, pp.51, editor B.Katalinic, Published by DAAAM International, Vienna, Austria, 2007, site: http: www.scientific.thomson.com/products/proceedings.

[11] Bogdan Constantin; Bogdan Mihaela-Liana, Popa Dragos, Experimental Research about dynamics behavior of landing gear, Proccedings of the 19-th International DAAAM Vienna, 2008, http: www.scientific.thomson.com/products/proceedings.

Filtration Magnetophoresis Process: an Approach to Choosing a Speed Regime

D.A. Sandulyak, V.V. Sleptsov, A.A. Sandulyak, A.V. Sandulyak, V.A. Ershova, A.V. Doroshenko

Abstract - The paper considers a non-trivial approach to defining the necessary working speed of filtration (in a granular magnetized matrix) of a liquid when performing a magnetophoresis of the ferroparticles present. The approach makes provisions for testing experimental speed dependence of the filtration magnetophoresis efficiency so it can comply with analytical expression of efficiency, the latter including speed parameter. Herewith, their target adjusted transformation and mutual juxtaposition of the obtained results yields direct data on a limiting (critical) value of speed differentiating pre-crisis and crisis regimes of magnetophoresis. To elaborate such an approach we assume employing as an argument not the speed, but Reynolds number. The defined limiting (critical) value of this number ([Re] $\cong$ 600) turned out to be consistent for magnetophoresis of ferroparticles in aqueous slurry of a magnetite, thermal power plant condensate, liquid ammonia, which allows determining (and forecasting) a limiting speed of filtration for any medium being conducted through the zone of filtrational magnetophoresis.

Keywords - filtration magnetophoresis, pre-crisis regime, discontinuity of speed dependence, a limiting speed, Reynolds limiting number.

I. Introduction

Industries widely use the process of magnetic separation of ferroparticles (particles having ferro- and ferromagnetic properties) from various media flows containing these ferroparticles, the process being carried out at different speeds of the flow in the operating zone of magnetophoresis (magnetic separation working zone) [1-11].

One of the key issues of magnetophoresis is how to choose a substantiated value of this speed, in particular, the filtration speed υ when performing the filtration magnetophoresis using magnetized porous, e.g. granular, matrices. Thus, a quite understandable wish to increase υ (in order to raise the productivity of magnetophoretic equipment) must still be limited by value $\upsilon = [\upsilon]$, starting from which any further increase of υ will have a destructive effect on magnetophoresis process.

At first sight, value $\upsilon = [\upsilon]$ must be set so as not to allow a significant drop in magnetophoresis efficiency ψ (ψ is a relative decrease of ferroparticles concentration due to magnetophoresis, it is usually shown in %); for this we should undoubtedly have a relevant speed dependence of ψ efficiency.

Alongside with that, we have all prerequisites to formulate a more objective principle to substantiate the value of limiting speed $\upsilon=[\upsilon]$ if we employ a reputable expression for ψ efficiency as a resulting parameter which functionally binds individual parameters of magnetophoresis:

$$\psi = \lambda\left[1 - \exp\left(-\frac{ABL}{\eta \upsilon d^2}\right)\right], \qquad (1)$$

or, if we use a more preferable (in terms of analysis and illustration of the functional role of individual parameters) expression for one more resulting parameter (ξ-parameter):

$$\xi = -\ln\left(1 - \frac{\psi}{\lambda}\right) = \frac{ABL}{\eta \upsilon d^2}, \qquad (2)$$

which is essentially a functional connection of individual parameters of magnetophoresis in the expression exponent (1) for ψ. Here, λ is a share of magneto-active fraction of ferroparticles (it is defined by one of the magneto-control methods, in particular [12]), B is field average induction in the matrix, L and d are the length (thickness of the layer) and diameter of matrix granules respectively, η is a dynamic viscosity of the flow, A is a parameter characterizing ferroparticles predisposition to magnetophoresis (the parameter first and foremost takes into consideration their magnetic susceptibility and dimensions).

II. Main results and their discussion

Guided by exponential expression (2) for ξ-parameter, the principle of substantiating the limit-

This work was supported by Russian Federation Ministry of Education and Science.

D.A. Sandulyak, PhD-student, is with the Moscow State University of Instrument Engineering and Computer Science (MGUPI), Russian Federation (e-mail: d.sandulyak@mail.ru).

V.V. Sleptsov, professor, is with the MGUPI, Russian Federation (e-mail: Sleptsov_VV@mgupi.ru).

A. A. Sandulyak, Doctor in Technical Sciences, is with MGUPI, Russian Federation (corresponding author to provide phone: 007-903-723-52-44; e-mail: anna.sandulyak@mail.ru).

A. V. Sandulyak, professor, is with MGUPI, Russian Federation (e-mail: a.sandulyak@mail.ru).

V. A. Ershova, PhD in Technical Sciences, is with Moscow State University of Civil Engineering (MGSU), Russian Federation, (e-mail: v.ershova@mail.ru).

A.V. Doroshenko, PhD in Technical Sciences, is with Moscow State University of Civil Engineering (MGSU), Russian Federation, (e-mail: pochta.avd@gmail.com).

ing speed $\upsilon=[\upsilon]$ must be stated unequivocally, viz. it is a limit value of filtration speed υ, when connection $\xi\sim1/\upsilon$ supervening from it is observed.

However, it is in this nonlinear view, after the recalculation of ψ data (from the obtained experimental dependence of ψ efficiency on υ speed) into data ξ according to the definition for ξ in expression (2), that is difficult to determine a specific value of $\upsilon=[\upsilon]$ which initiates the break of the connection.

Yet, this information becomes available (and the approach itself acquires practical appeal) if factual experimental dependences of ψ onυ can be represented in coordinates $1/\xi$ on υ and by this dependence adjusted to the task at hand we can trace the point of transition of dependence $1/\xi$ on υ from linear to a nonlinear one. The abscissa of this point signifying the change of character of this speed dependence itself will correlate to the value $\upsilon=[\upsilon]$ we are much interested in.

To support the validity of this approach we further provide and analyze the corresponding experimental data.

Figures 1*a*, 2*a*, 3*a* show the results of experiments to obtain speed dependences of magnetophoresis (ψ on υ) in granular matrices consisting of loadings of balls of various diameter; the parameters of conducted magnetophoresis are given in Table 1. During the experiments we employed artificially prepared aqueous slurry of a magnetite (the size of particles amounted to 10-15μm), condensate of thermal electric power plant, and liquid ammonia which all featured some ferro-impurities.

Table 1. Parameters of magnetophoresis performed (Fig. 1 – 3)

Medium analyzed	Dynamic and kinematic viscosity $\eta,\times10^{-3}Pa\cdot s$ $\nu,\times10^{-6}m^2/s$	Filter-matrix length *L, cm*	Average induction *B,T*	Ball diameter *d, mm*
Magnetite aqueous slurry (Fig.1), λ=1	1 1	4.2	0.3	5.7
Thermoelectric power plant condensate(Fig.2), $\lambda\cong0{,}8$	0.65 0.65	100	0.62	5
Liquid ammonia (Fig.3), $\lambda\cong0{,}75$	0.23 0.38	20	0.62	2.4

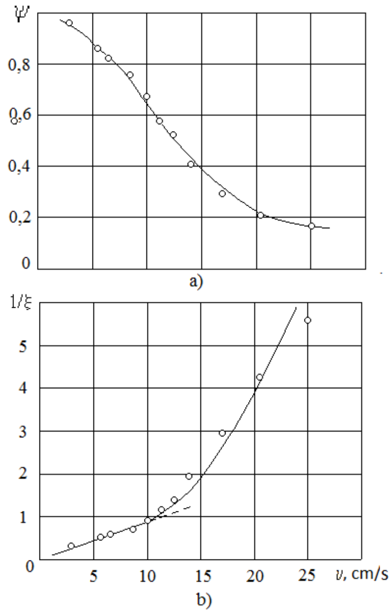

Figure 1. Dependences of ferroparticles magnetophoresis efficiency ψ for magnetite aqueous slurry (*a*) and an inverse ξ-parameter of magnetophoresis (*b*) on the filtration speed υ; the abscissa of the linear and non-linear sections junction of dependence$1/\xi$ on υ corresponds to the limiting (pre-crisis) value $\upsilon=[\upsilon]$; the data is given in Table 1.

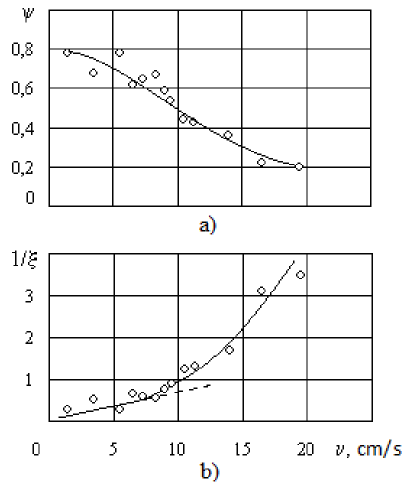

Figure 2. The same dependences as in Fig. 1, but for ferro-impurities in thermoelectric power plant condensate.

As discussed above, providing we change these ‘primary’ speed dependences (Fig. 1*a*, 2*a*, 3*a*) into recommended ones $1/\xi$ on υ (Fig.1*b*, 2*b*, 3*b*), we can really quite graphically witness the presence of two clearly marked sections, linear and non-linear one. These sections are demarcated by individual values of limiting speed $\upsilon=[\upsilon]$. Thus, $[\upsilon]$=(10-11) *cm/s* for magnetite slurry, $[\upsilon]$=(7-8) *cm/s* for condensate, $[\upsilon]$=(9-10) *cm/s* for liquid ammonia (Fig.1*b*, 2*b*, 3*b*).

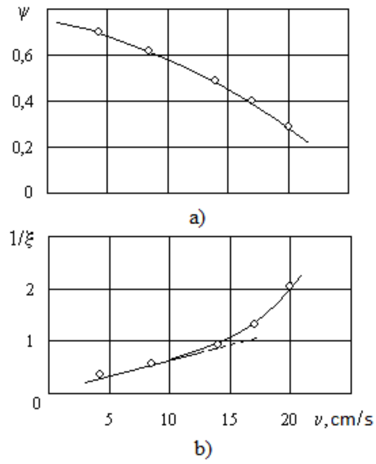

Figure 3. The same dependences as in Fig. 1, but for ferro-impurities in liquid ammonia.

In this case, the operative range of speed υ is the one lying within a linear section ($\upsilon \leq [\upsilon]$) for each of the dependences $1/\xi$ on υ (Fig.1*b*, 2*b*, 3*b*), i.e. the section of the dependence consistent with expression (2) and therefore correlating to basic expression (1).

Any further (with $\upsilon > [\upsilon]$) steeper nonlinear climb of these dependences (Fig.1*b*, 2*b*, 3*b*) resulting from breaking (towards increase) the discussed functional role of the filtration speed indicates the beginning and following development of the crisis in the process of ferroparticles magnetophoresis in the matrix. It is conditioned by arising turbulence and its penetration into more active (for magnetic capture of ferroparticles) near-contact zones of the granules.

It should be noted that with $\upsilon > [\upsilon]$ (but not with $\upsilon >> [\upsilon]$) magnetophoresis is performed with positive (and maybe even a satisfactory) efficiency ψ. However, in contrast to a pre-crisis speed regime, the influence of υ on ξ and consequently on ψ becomes strongly depressive (judging by the data in Fig. 1 – 3 it happens almost by a quadratic law). In this case, the compensation of such influence by means of increasing the filter-matrix length L or field average induction B (by raising the magnetizing field intensity) is considerably complicated owing to an unfavorable break of functional connections featured in (1) and (2).

Having at our disposal dependences $1/\xi$ on υ (Fig.1*b*, 2*b*, 3*b*) and with a view towards obtaining a more general outcome, we are definitely interested in depicting the data $1/\xi$ on υ in more universal coordinates, viz. in those $1/\xi$ on *Re*.

As to calculating Reynolds number for the considered case of (filtration) magnetophoresis, with known kinematic viscosity of the flow v it is usual to express this number in terms of the filtration speed υ and it is common practice to do it in terms of matrix granule average diameter d, i.e. $Re = \upsilon d/v$.

Hence, in addition to the values of filtration limiting speed $[\upsilon]$ defined by the aforementioned experimental and illustrational way, it is possible to assess the value of limiting (critical) Reynolds number [*Re*], moreover, it can be done by a similar experimental-and-illustrational approach.

Alongside with that, we should specially emphasize the following. To solve the task of obtaining dependence $1/\xi$ on *Re* and defining [*Re*] value basing on it, the corresponding experiments must be conducted only with matrices which fit such tasks to the greatest possible extent. Naturally, we speak here about matrices consisting of ideal granules, i.e. balls (precisely these matrices were employed to carry out the experiments described above).

It relation to this, we should warn that the data obtained using other matrices, in particular, those loaded by broken chips, can hardly be used to solve the task as the evaluation of characteristic dimensions of 'granules or chunks' of chip matrices is rather conditional. Therefore, there may occur possible inevitable inaccuracies in defining limiting number [*Re*], including to be sure the cases when the corresponding data for poly-ball and chip matrices are analyzed together.

Ergo, using the received data $1/\xi$ on υ (Fig.1*b*, 2*b*, 3*b*) and the corresponding values of balls diameter d together with kinematic flow viscosity v (Table 1), we can go over, as is shown before, from abscissa υ to abscissa *Re* (Fig.1*c*, 2*c*, 3*c*). Then by the juncture of linear (pre-crisis, operating) and non-linear (crisis) sections of dependences $1/\xi$ on *Re* it is easy to establish that the value of limiting (critical in terms of conducting filtration magnetophoresis) Reynolds number amounts to $[Re] \approx 600$; the number is common for all media studied here.

Let us draw your attention to the fact that this number is an order higher than hydrodynamic critical number $Re = \{Re\} = 60...70$ at which the condition of moving liquid in a poly-ball matrix transgresses from laminar to turbulent one. A seeming contradiction (at first sight, the beginning of magnetophoresis crisis should coincide with the beginning of the flow eddy formation) is explained by the following. Firstly, the development of ferroparticles magnetophoresis crisis in a poly-ball matrix is connected with development of turbulent flow of the flux not in the overall volume of the pore (pores) of filter-matrix, but in the so-called capture zones which being localized in the vicinity of granule contact points are located somewhat at the periphery of the pore channels. In these zones there persists a

ISBN: 978-1-61804-325-2

laminar condition of the flow favorable for magnetic capture and retaining of ferroparticles (here local *Re* numbers reach *Re*<6...8) even with an overall developed turbulent condition in the nucleus of the 'micro-flow' (in any of pore channels). Secondly, in

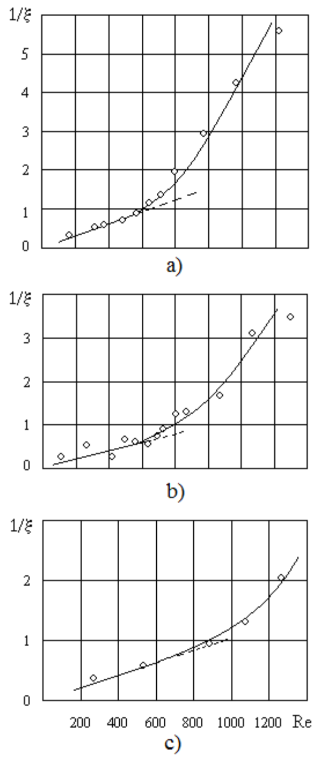

Figure 4. The impact of Reynolds number on the inverse ξ-parameter of ferroparticles (ferro-impurities) magnetophoresis: for magnetite aqueous slurry (*a*), condensate (*b*), liquid ammonia (*c*) by data in Fig. 1 – 3; the abscissas of linear and non-linear sections junctions of dependences $1/\xi$ on *Re* correlate to the limiting (critical) value of $Re = [Re]$.

the near-contact zone of granules magnetic power factor [13-16] responsible for capturing and retaining ferroparticles is the highest (extreme).

Having the value of critical (let us repeat, in terms of magnetophoresis technology) Reynolds number $[Re] \cong 600$, we can get a calculating formula to determine the limiting (pre-crisis) speed of filtration, i.e. the extreme speed for magnetophoresis (magnetic separation). Thus, basing on connection $[Re]=[\upsilon]d/\nu$, this speed even at the conceptual stage of filtration magnetophoresis of ferro-impurities in some media can be calculated, using expression:

$$[\upsilon] = \frac{[\mathrm{Re}]\cdot \nu}{d} \cong 600\frac{\nu}{d}, \qquad (3)$$

according to which (and to the results given above), the limiting speed $[\upsilon]$, in contrast to limiting Reynolds number $[Re]$, is not a constant value, but it varies with kinematic viscosity ν of the medium and granule diameter in the filter-matrix used.

III. Conclusion

During magnetophoresis of ferroparticles present in technological and other flows, in particular with magnetophoresis using granular magnetized matrices, it is principally important to observe a required operating speed of the flow υ. This speed should ensure the required productivity of the magnetophoretic equipment and at the same time should not adversely influence the magnetophoresis itself (magnetic separation).

Instead of seemingly obvious commonly practiced approach which states the inadmissibility of significant reduction of magnetophoresis efficiency ψ, we consider and analyze a quite different, nontrivial solution. Its essence reduces to testing the speed dependence ψ as to its correlation to the analytical expression for ψ, including the speed parameter υ. Transforming this expression in order to get another (alternative to parameter ψ) resulting parameter $\xi=-\ln(1-\psi/\lambda)$ and using experimentally obtained dependence of ψ on υ allows identifying linear and non-linear sections on a specially pictured dependence $1/\xi$ on υ. These sections depict pre-crisis and crisis regimes of magnetophoresis and the abscissa of their junction corresponds to the limiting (extreme) value of the operating speed $\upsilon=[\upsilon]$.

Developing such an approach, we use Reynolds number, not the flow (filtration) speed as an argument. In this case, the abscissa of the junction of linear and non-linear additionally obtained dependence $1/\xi$ on *Re* serves as a more universal value. According to the data received when processing magnetite aqueous slurry, thermoelectric power plant condensate, and liquid ammonia in ferroparticles magnetophoresis, the given abscissa correlates to value $Re=[Re] \cong 600$. It allows even at the stage of preparing for filtration magnetophoresis to make forecasting calculations of filtration speed limiting values as $[\upsilon]= [Re]\cdot\nu/d$ for any media with known values of its kinematic viscosity ν and diameter *d* of the granules used in the filter-matrix.

References:

[1] Newns A., Pascoe R.D. 2002. Influence of path length and slurry velocity on the removal of iron from kaolin using a high gradient magnetic separator. *Minerals Engineering* 15: 465-467.

[2] Ying T.-Y., Yiacoumi S., Tsouris C. 2000. High-gradient magnetically seeded filtration. Chemical Engineering Science 55: 1101-1113.

[3] Svoboda J. 2001. A realistic description of the process of high-gradient magnetic separation. Minerals Engineering 14(11): 1493-1503.

[4] Arajs S., Moyer C.A., Aidun R., Matijevic E. 1985. Magnetic filtration of submicroscopic particles through a packed bed of spheres. Journal of Applied Physics 57: 4286.

[5] Ritter J.A., Ebner A.D., Karen D.D., Krystle L.S. 2004. Application of high gradient magnetic separation principles to magnetic drug targeting. Journal of Magnetism and Magnetic Materials 280: 184-201.
[6] Chen H., Bockenfeld D., Rempfer D., Kaminski M.D., Liu X., Rosengart A. J. 2008. Preliminary 3-D analysis of a high gradient magnetic separator for biomedical applications. Journal of Magnetism and Magnetic Materials 320: 279-284.
[7] Chen H., Ebner A.D., Kaminski M.D., Rosengart A. J., Ritter J.A. 2005. Analysis of magnetic drug carrier particle capture by a magnetizable intravascular stent – 2: Parametric study with multi-wire two-dimensional model. Journal of Magnetism and Magnetic Materials. 293: 616-632.
[8] Nandy K., Chaudhuri S., Ganguly R., Puri I.K. Analytical model for the magnetophoretic capture of magnetic microspheres in microfluidic devices. 2008. Journal of Magnetism and Magnetic Materials 320: 1398-1405.
[9] Pamme N., Manz A. O-chip free-flow magnetophoresis: Continuous flow separation of magnetic particles and agglomerates // Analytical Chemistry. 2004. 76 (24), pp.7250-7256.
[10] Ravnik J., Hriberšek M. High gradient magnetic particle separation in viscous flows by 3D BEM. 2013. Computational Mechanics 51 (4): 465-474.
[11] Xinyu Wu, Huiying Wu, Yandong Hu. 2011. Enhancement of separation efficiency on continuous magnetophoresis by utilizing L/T-shaped microchannels. Microfluidics and Nanofluidics 11 (1): 11-24.
[12] Sandulyak A.V., Garaschenko V.I., Korkhov O.Y. 1985. Method of Determining the Quantity of Solid Fraction of Ferromagnetic Matter in a Fluid. Patent 4492921 US.
[13]Sandulyak A.V., Sandulyak A.A., Ershova V.A. 2007. Magnetization Curve of a Granulated Medium in Terms of the Channel-by-Channel Magnetization Model (New Approach). *Doklady Physics* 52 (4): 179–181.
[14] Sandulyak A.V., Sandulyak A.A., Ershova V.A. 2009. On the model of channel-by-channel magnetization of a granular medium (with a radial permeability profile of a quasi-continuous channel). *Technical Physics* 54(5): 743 – 745.
[15]Sandulyak A.A. Ershova V.A., Ershov D.V., Sandulyak A.V. 2010. On the properties of short granular magnets with unordered granule chains: a field between the granules. *Solid State Physics* 52(10): 1967-1974.
[16] Sandulyak A.A., Sandulyak A.V., Oreshkin D., Popova M. 2014. Applied Model of Magnetization of a Granulated Material *Applied Mechanics and Materials* 467: 76-80.

Low cost minerals as oxygen carriers for Chemical Looping Combustion (CLC)

Antigoni Evdou, Vassilis Zaspalis, and Lori Nalbandian

Abstract— Chemical Looping Combustion (CLC) is an in-situ CO_2 capture technology that offers a solution for CO_2 separation without energy penalty via the use of a solid oxygen carrier which delivers oxygen to the fuel, instead of air. The oxygen carrier materials are a cornerstone in the CLC technique. In place of costly manufactured materials, cheap, naturally occurring mineral resources with comparable compositions are needed. In the present work two minerals with high content of Fe and Mn oxides are studied as candidate "oxygen carriers" for the CLC process. Both materials exhibit satisfactory performance in terms of Oxygen Transfer Capacity (OTC), activity towards CH_4 oxidation, low selectivity to CO and H_2, and stability in multiple redox cycles. The materials are physicochemically characterized before and after their use, in order to investigate changes in their physicochemical properties as a result of multiple redox cycles.

***Keywords* —** chemical looping combustion, minerals, oxygen carrier.

I. Introduction

The combustion of fossil fuels is one of the major sources of carbon dioxide (CO_2) which is a greenhouse gas. Concern about the global climate change prompted research on lowering CO_2 emissions during fossil fuel combustion. Commercial CO_2 capture technologies that exist today are expensive and energy intensive. The main disadvantage of these techniques is the large amount of energy that is required for the separation, reducing the overall efficiency of a power plant.

Chemical looping combustion (CLC) has been suggested as an energy-efficient method for producing high purity CO_2 from combustion of fuel. It is a novel combustion technology [1] that involves the use of an oxygen carrier, such as metal oxides, that transports oxygen from the air to the fuel, thereby avoiding direct contact between fuel and air.

The CLC system comprises two reactors, an air reactor and a fuel reactor. In the fuel reactor, the fuel reacts with the metal oxide. The reduced metal oxide is oxidized in the air reactor to form metal oxide. The regenerated metal oxide is ready to initiate a second cycle. The exit stream from the fuel reactor contains only CO_2 and H_2O, thus after condensation of the H_2O, produces a pure CO_2 stream that can be directly sequestrated. The significant advantage of CLC compared to normal combustion is that a concentrated CO_2 stream, which is not diluted by N_2, can be obtained spending minimal energy for separation.

The main challenge in the technology of Chemical Looping Combustion is to find suitable materials for use as "oxygen carriers". In order to be a viable candidate for the CLC process, the oxygen carrier material (OCM) must meet the following criteria [2]:

- sufficient oxygen transfer capacity
- satisfactory reactivity over the multiple cycles
- high mechanical integrity
- low tendency to agglomeration, fragmentation and attrition
- good resistance to sintering
- low possibility of deactivation by carbon deposition or sulphur compounds
- low cost
- environmental friendly

Experiments carried out using methane and syngas as fuel, show that Fe, Mn, Cu and Ni oxides are the most suitable, presenting the following relative reactivity NiO > CuO > Mn_3O_4 > Fe_2O_3 [4], [5]. However, nickel and copper oxides have a considerably higher cost. Conversely, materials containing Fe and Mn are attracting considerable interest, mainly because of their high availability and low cost [1]-[6].

It has been proven that pure iron oxide sources have to some extent difficulties to fully combust the fuel unless a high load of material is circulated. Another issue with these materials is related to the swelling of the material after several cycles, which is detrimental if long life-time is required [1]. On the other hand, manganese oxides are very promising oxygen carrier materials, given the fact that they can convert the fuel and give full combustion. However, attrition issues with such materials have often been observed.

This study was co-financed by European Union- European Regional Development Fund and the General Secretariat for Research and Technology Hellas, project No. 13FENCO–13–478A ‘Minerals for Sustainable COst and energy efficient Chemical Looping Combustion Technology’– MINERAL SCOUT.

A. Evdou is with the Laboratory of Inorganic Materials, Chemical Process and Energy Resources Institute, Centre for Research and Technology-Hellas, 6th km, Harilaou-Thermi Rd, 57001 Thermi-Thessaloniki, Greece and the Laboratory of Materials Technology, Department of Chemical Engineering, Aristotle University of Thessaloniki, 54124 Thessaloniki, Greece (e-mail: antigoni@cperi.certh.gr).

V. Zaspalis is with the Laboratory of Inorganic Materials, Chemical Process and Energy Resources Institute, Centre for Research and Technology-Hellas, 6th km, Harilaou-Thermi Rd, 57001 Thermi-Thessaloniki, Greece and the Laboratory of Materials Technology, Department of Chemical Engineering, Aristotle University of Thessaloniki, 54124 Thessaloniki, Greece (e-mail: zaspalis@cperi.certh.gr).

L. Nalbandian is with the Laboratory of Inorganic Materials, Chemical Process and Energy Resources Institute, Centre for Research and Technology-Hellas, 6th km, Harilaou-Thermi Rd, 57001 Thermi-Thessaloniki, Greece (corresponding author to provide phone: +302310498142; fax: +302310498131; e-mail: nalbanti@cperi.certh.gr).

As a means to enhance the mechanical strength of the particles, to be used in a circulating bed, a binder can be added to the redox active phase, however this would decrease the OTC and the activity of the Oxygen Carrier. Alternatively, one of the redox active phases could also act as an inherent support. It has been previously demonstrated that iron oxide can stabilize the performance of manganese oxides, thus mixed Fe-Mn oxides show great potentials as oxygen carrier materials for CLC [6]-[8].

Since CLC technology requires a significant amount of oxide carrier, the use of natural minerals would be advantageous. Raw minerals from different mining ores are natural choices for OCM since sufficient amounts are available within reasonable cost, even though such minerals might have high composition and quality variations [3]. In the present work the use of two minerals with high content of Fe and Mn oxides as oxygen carriers in Chemical Looping Combustion is explored. The performance of the candidate materials is ranked by taking into account their Oxygen Transfer Capacity (OTC), the methane conversion during the fuel oxidation step as well as the H_2 and CO selectivities, and their stability after repeated redox cycles.

II. EXPERIMENTAL PART

The minerals were selected based on their content in iron and manganese oxides, as well as trace elements content, their non-toxicity, low cost and availability.

The following natural materials are tested in this study:

1. a Fe-Mn based mineral, from El-Waleed - Egypt named “Sinai-A, low grade”, with code name S12
2. a Fe-Mn based mineral, from El-Waleed - Egypt named “Sinai-A, medium grade”, with code name S22

Samples of both fresh materials and materials used in several redox cycles are physicochemically characterized by using the following methods:

- Elemental analysis by Inductively Coupled Plasma Optical Emission Spectroscopy (ICP-OES), using a Perkin Elmer, Optima 4300DV instrument,
- N_2 adsorption – desorption isotherms at the boiling point of liquid nitrogen (77 K) using a Micromeritics, Tristar instrument, to determine specific surface area, pore volume and pore size distribution,
- X-ray diffraction (XRD) for the identification of the crystalline phases formed in the prepared samples Powder XRD patterns are recorded with a Siemens D500 X-ray diffractometer,
- Morphological observation and elemental Microanalysis of the samples at a Scanning Electron Microscope (JEOL 6300) equipped with an X-ray EDS analyzer (Oxford Isis 2000).

The capability of the materials to deliver oxygen at high temperatures and convert CH_4 to synthesis gas during the fuel oxidation step, as well as their ability to reversibly pick up oxygen during the solid oxidation step is evaluated by pulse reaction experiments in a fixed bed pulse reactor. Reaction experiments with the materials in powder form are performed at 1273K, in a reaction unit (Altamira AMI-1) using a U-type quartz reactor into which 200±3 mg solid material is inserted. A detailed description of the experimental unit is provided elsewhere [9], [10]. During the fuel oxidation step, methane is fed to the reactor at constant volume pulses, through a special closed loop valve. Each pulse has of volume of 100μL. During the solid oxidation step, oxygen is injected to the reactor, also at constant volume pulses, at its entrance before the solid OC. The products at the output of the reactor are continuously monitored by mass spectrometer (Balzers, Omnistar) and analyzed quantitatively, based on calibration curves for all reactants and products of the process.

III. RESULTS – DISCUSSION

The specific surface area of the materials, as received, without any pretreatment, as measured by N_2 sorption, is presented in Table I.

Table I: Surface area of materials

	S12	***S22***
Surface area (m^2/g)	27.61	20.83

In Table II the elemental composition, , of the 2 materials is presented, as measured by ICP-OES in the form of oxides. Both materials have high concentrations of Fe and Mn oxides. Si, Ca, Al and Ba oxides appear also at significant levels. S12 has the highest Fe content, while S22 has higher concentrations of Mn and Si oxides.

Table II. Elemental composition of materials

	S12 (% wt)	***S22 (% wt)***
Fe_2O_3	60.05	32.71
MnO_2	23.26	39.06
SiO_2	10.94	21.40
CaO	1.31	2.47
Al_2O_3	1.92	1.28
BaO	0.92	1.44
MgO	0.61	0.61
Na_2O	0.32	0.28
ZnO	0.19	0.28
K_2O	0.22	0.18
TiO_2	0.10	0.10
Co_2O_3	0.01	0.01
NiO	0.02	0.02
V_2O_5	0.03	0.01
Cr_2O_3	0.000	0.01
CuO	0.03	0.08
PbO_2	0.03	0.03
AsO_2	0.01	0.01
Total	**100**	**100**

The XRD patterns of the two mineral samples, as received, without any pretreatment are presented in Fig. 6 and 7, where also the crystalline phase identification for both materials is included. It is observed that for both materials the main phases are hematite (Fe_2O_3), tetravalent manganese oxide (MnO_2) and silica (SiO_2). The relative intensities of the peaks are in agreement with the concentration of each oxide, as measured by elemental analysis (Table II).

In Fig. 1 the amount of oxygen exchanged by the mineral, “Sinai-A, low grade” (S12) is presented during an experiment which includes 8 multiple reduction – oxidation cycles. It can be observed that in the 1^{rst} cycle an oxygen transfer capacity (OTC) of 1% wt is observed, the OTC is gradually decreasing during the first 4 cycles, however, it appears that the material is activated after cycle No 5, reaching an OTC of 1.6% in cycle No 8.

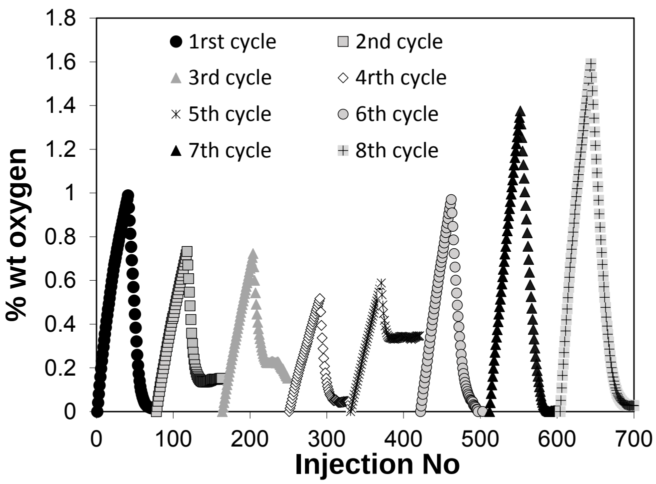

Fig. 1 Oxygen loss and uptake of sample “Sinai-A, low grade” (S12), during 8 subsequent reduction – oxidation cycles

In Fig. 2 the amount of oxygen exchanged by the mineral, “Sinai-A, medium grade” (S22) is presented during an experiment which includes 9 multiple reduction – oxidation cycles. It can be observed that the oxygen transfer capacity (OTC) of the sample in the 1^{rst} cycle is 1.1% wt, higher than the corresponding OTC of S12 material. However it is gradually decreasing during subsequent cycles and is stabilized, during cycles 3-9, at 0.5±0.1% wt.

In Fig. 3a the reactivity of the natural material S12 is presented, expressed as % wt conversion of methane during the fuel oxidation step vs. oxygen deficiency during 8 subsequent reduction – oxidation cycles. The mineral has a moderate initial reactivity converting only ~40% at the 1^{rst} cycle, when the material id fully oxidized.

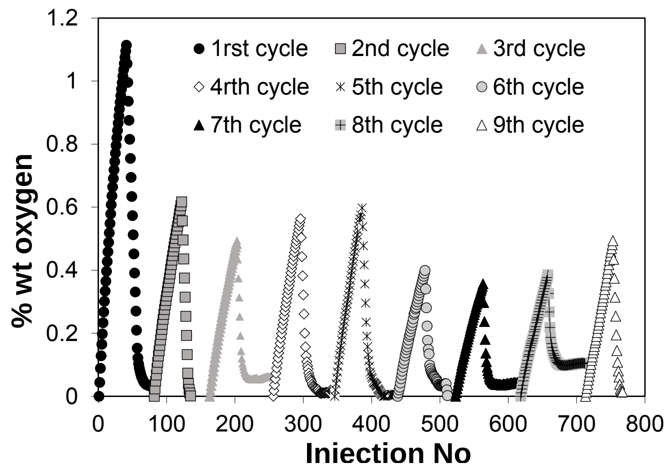

Fig. 2 Oxygen loss and uptake of sample “Sinai-A, medium grade” (S22), during 9 subsequent reduction – oxidation cycles

However, after the activation of the material beyond the 5^{th} cycle, shown also in Fig. 2, its initial reactivity increases reaching initial methane conversion of ~55% at the 8^{th} cycle. During all cycles, the initial reactivity of the fully oxidized material decreases with increasing oxygen deficiency, reaching a methane conversion of ~30% at the end of 8^{th} cycle.

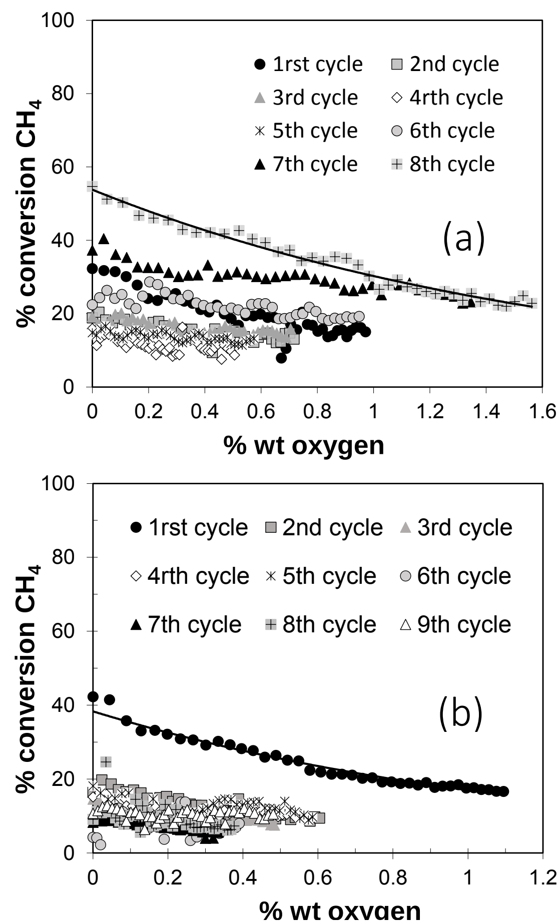

Fig. 3 Methane conversion by the (a) S12 sample, and (b) S22 sample, vs. oxygen deficiency during multiple reduction – oxidation cycles

In Fig. 3b the reactivity of the natural material S22 is presented, expressed as % wt conversion of methane during the fuel oxidation step vs. oxygen deficiency during 9 multiple reduction – oxidation cycles. The initial conversion at the beginning of the 1st cycle, 40%, is not recovered from the material in the subsequent cycles.

Since the materials are candidate Oxygen Carriers for Chemical Looping Combustion, they must have very low selectivity towards CO and H_2 during fuel oxidation. In Fig. 4a and 5a the CO and H_2 selectivities are presented for the S12 material, during 8 subsequent redox cycles as a function of its oxygen deficiency. It can be observed that both selectivities increase with increasing oxygen deficiency of the solid and change with increasing cycle number. In all cases, selectivity towards CO does not exceed 20% while the corresponding selectivity towards H_2 is always lower than 10%. It can be also observed that both CO and H_2 selectivities increase with decreasing reactivity of the material, which can be readily attributed to the decreased availability of lattice oxygen from the solid. In Fig. 4b and 5b the CO and H_2 selectivities are presented for the S22 material, during 9 subsequent redox cycles as a function of its oxygen deficiency. It can be observed that both selectivities are lower than 10% even at the maximum oxygen deficiency, in all subsequent cycles.

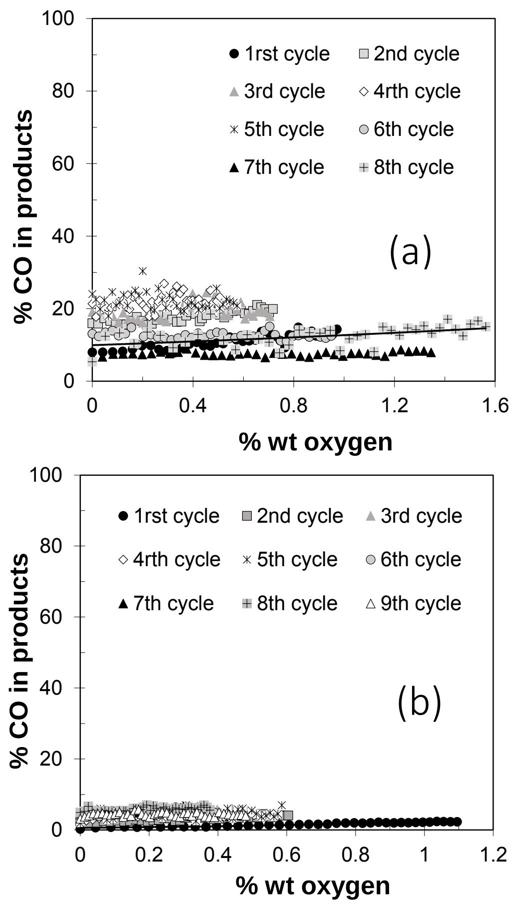

Fig. 4 Selectivity towards CO by the (a) S12 sample, and (b) S22 sample, during multiple reduction – oxidation cycles

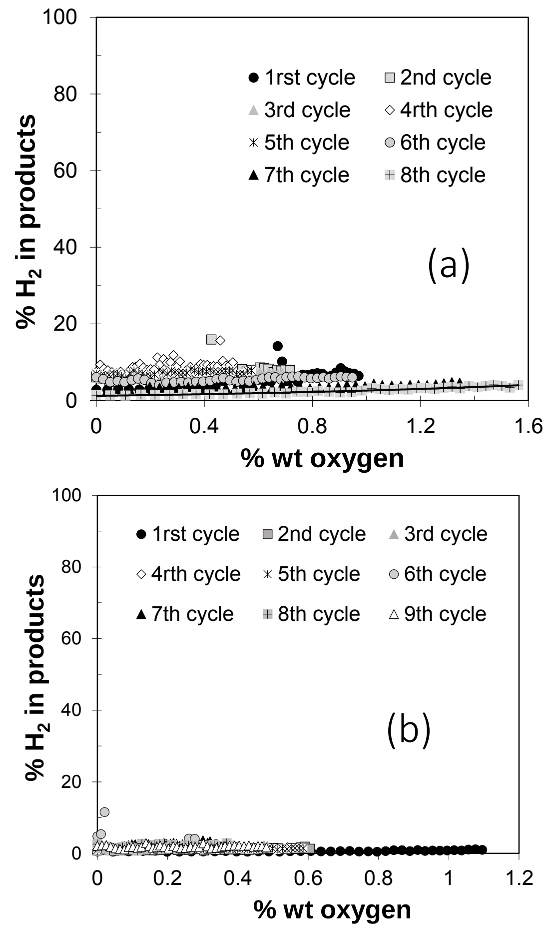

Fig. 5 Selectivity towards H_2 by the (a) S12 sample, and (b) S22 sample, during multiple reduction – oxidation cycles

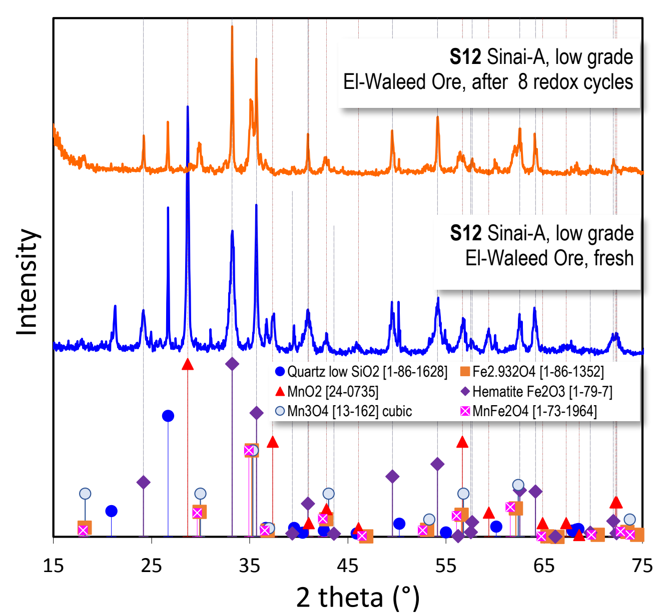

Fig. 6 X-ray diffraction (XRD) patterns of the S12 mineral sample, fresh and after 8 redox cycles

The XRD patterns of the S12 mineral sample, fresh and after 8 redox cycles are compared in Fig. 6. Identification of crystalline phases is also included in the Figure. In the fresh sample iron is trivalent, in the hematite (Fe_2O_3) phase and manganese is tetravalent, in the MnO_2 phase. It can be observed in the XRD pattern of the “reacted” sample that all peaks attributed to MnO_2 completely disappear, indicating that MnO_2 has decomposed. Also the peaks attributed to Fe_2O_3 are much less intense. New peaks arise in the XRD of the “used” sample which are attributed to spinel type oxides, either simple Fe_3O_4, Mn_3O_4, or mixed $MnFe_2O_4$. In Fig.7 the XRD patterns of the S22 mineral sample, fresh and after 9 redox cycles are compared. Despite the differences in the elemental composition of two minerals, the changes observed in the samples that have undergone multiple redox cycles are identical. Also in the S22 sample, the 4-valent manganese oxide disappears with simultaneous formation of a spinel phase, while part of hematite is also converted to magnetite.

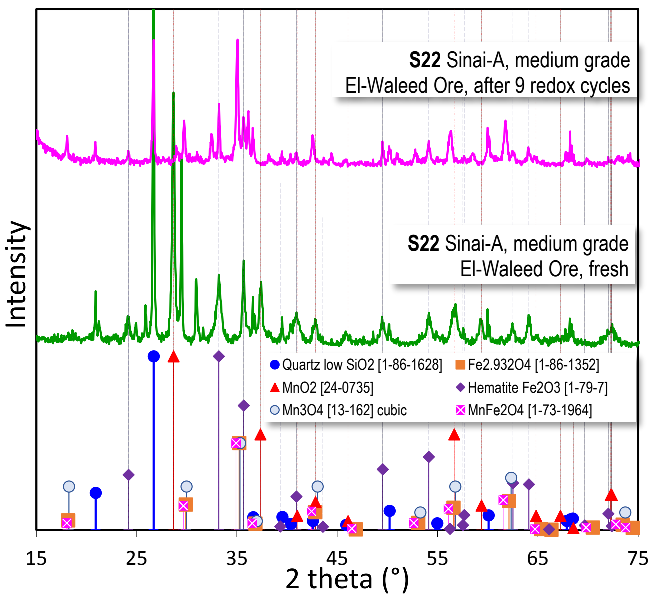

Fig. 7 X-ray diffraction (XRD) patterns of the S22 mineral sample, fresh and after 9 redox cycles

Both materials studied are natural minerals and show, as expected, great composition heterogeneity. Fig. 8 shows the elemental mapping of the "fresh" material S12, at relatively low magnification (X200), to include a sufficient number of grains. It is observed that there are grains composed almost entirely of iron oxides, and other grains contain almost only Mn oxides. There are of course granules containing both elements. The maps of the lower concentrations elements, e.g. Si, Al, Ca, K, Mg show that they, also, are not evenly distributed. In the images of Fig. 8 either whole grains or large grain parts can be observed, with concentrations of these elements much higher than average.

In Table III, Scanning Electron Microscopy (SEM) images are compared, of the S12 mineral, fresh and after 8 redox cycles, at the same magnification level in each row.

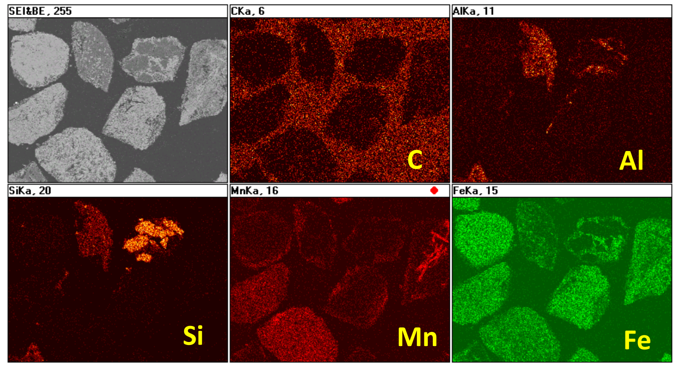

Fig. 8 Elemental mapping of the "fresh" material S12, at low magnification (X200)

The particles in the first raw are rich in Mn while those in the second raw are composed almost 100% by Fe-oxides. A completely different effect in the morphology of the particles can be observed, of subjecting the material to multiple redox cycles, depending on their chemical composition. While the Mn-rich particles undergo extensive erosion, the Fe-rich particles remain almost unaffected. It is observed that the extent of disintegration is a function of the duration, the intensity and the number of redox cycles that the material suffered.

Table III. Scanning Electron Microscopy (SEM) images of the S12 mineral, fresh and after 8 redox cycles at 1223K.

	S12 sample fresh	***S12 sample after 8 cycles***
X 500 Mn-rich particle	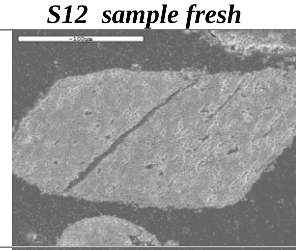	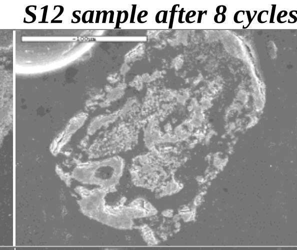
X 500 Fe-rich particle	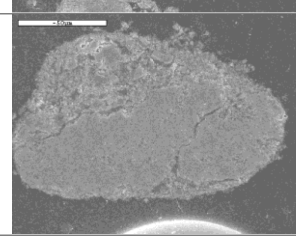	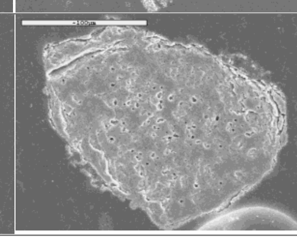

IV. CONCLUSIONS

The two examined natural materials have the ability to deliver lattice oxygen to a fuel and to regain it in the presence of air. The S12 material, with a high content of Fe oxides (60%) and ratio Fe/Mn≈2.5 shows higher values than the S22 material, with lower level of Fe oxide (33%) and ratio Fe/Mn≈1, as regards both the Oxygen Transfer Capacity (OTC) and the activity towards CH_4 conversion

The S12 material is further activated after 4 oxidation - reduction cycles. Both materials lead to complete combustion of methane, with selectivities towards CO and H_2 lower than 10%. Therefore both minerals are promising candidate materials for use as "oxygen carriers" in the chemical looping combustion process (CLC) with the best performance shown by the S12, which is considered a low grade mineral.

Physicochemical characterization of samples of the natural materials, fresh – unreacted and "reacted" at subsequent redox cycles, revealed that repetitive reduction–oxidation reactions affect seriously both the crystalline structure of the materials and their particle morphology. Most of the Mn and Fe oxides are converted into magnetic cubic spinels in the "reacted" samples. Furthermore multiple redox cycles at high temperature, cause erosion to the Mn particles, which leads to extensive breaking of the large particles and the formation of smaller particles, while the particles which are rich in Fe do not undergo any change in their morphology.

REFERENCES

[1] J. Adanez, A. Abad, F. Garcia-Labiano, P. Gayan, L.F. de Diego, "Progress in chemical-looping combustion and reforming technologies," *Progress in Energy and Combustion Science*, vol. 38, pp. 215-282, Apr. 2012.

[2] M. Johansson, T. Mattisson, A. Lyngfelt, "Comparison of oxygen carriers for chemical-looping combustion," *Thermal Science*, vol. 10, pp. 93-107, 2006.

[3] A. Fossdal, E. Bakken, B.A. Øye, C. Schøning, I. Kaus, T. Mokkelbost, Y. Larring, "Study of inexpensive oxygen carriers for chemical looping combustion," *International Journal of Greenhouse Gas Control*, vol. 5, pp. 483-488, May 2011.

[4] M. Johansson, PhD Thesis, Chalmers University of Technology, Göteborg, Sweden, 2007.

[5] A. Abad, J. Adánez, F. García-Labiano, L. F. de Diego, P. Gayán, J. Celaya, "Mapping of the range of operational conditions for Cu-, Fe-, and Ni-based oxygen carriers in chemical-looping combustion," *Chemical Engineering Science*, vol. 62, pp. 533-549, 2007.

[6] A. Lambert, C. Delquié, I. Clémeneçon, E. Comte, V. Lefebvre, J. Rousseau, B. Durand, "Synthesis and characterization of bimetallic Fe/Mn oxides for chemical looping combustion," *Energy Procedia*, vol. 1, pp. 375-381, 2009.

[7] G. Azimi, H. Leion, T. Mattisson, M. Ryden, F. Snijkers, A. Lyngfelt, "Mn-Fe oxides with support of $MgAl_2O_4$, CeO_2, ZrO_2 and Y_2O_3-ZrO_2 for chemical-looping combustion and chemical-looping with oxygen uncoupling" *Industrial & Engineering Chemistry Research*, vol. 53, pp. 10358-10365, 2014.

[8] E. Ksepko, R. V. Siriwardane, H. Tian, T. Simonyi, M. Sciazko, "Effect of H_2S on chemical looping combustion of coal-derived synthesis gas over Fe-Mn oxides supported on sepiolite, ZrO_2, and Al_2O_3," *Energy & Fuels*, vol. 26, pp. 2461-2472, 2012.

[9] A. Evdou, V. Zaspalis, L. Nalbandian, "$La_{1-x}Sr_xFeO_{3-\delta}$ perovskites as redox materials for application in a membrane reactor for simultaneous production of pure hydrogen and synthesis gas," *Fuel*, vol. 89, pp. 1265-1273, June 2010.

[10] L. Nalbandian, A. Evdou, V. Zaspalis, "$La_{1-x}Sr_xM_yFe_{1-y}O_{3-\delta}$ perovskites as oxygen-carrier materials for chemical-looping reforming," *Journal of Hydrogen Energy*, vol. 36, pp. 6657-6670, June 2011.

The methodology of automated cost estimating in civil engineering in Slovakia

Peter Mesároš, Juraj Talian, Tomáš Mandičák, Daniela Káposztásová

***Abstract*—** The aim of the paper is to present the methodology of automated creation of construction cost estimations and budgets in Slovakia. Paper discuss methods of data transfer from CAD applications to cost estimating software in the IFCxml data format. For proper identification of single items of construction budget shall be suitably processed data 3D model. Processing data model ensures proper use of the proposed Assistent with the identification data. The own methodology of automated creation of construction budgets consists of several steps: creating a 3D model data, export data from CAD application to cost estimating application, import and processing in the cost estimating application. Also, benefits and disadvantages of the proposed methodology are identified.

***Keywords*—**automated cost estimating and budgeting in civil engineering, data exchange, IFCxml.

I. Introduction

Accurate processing of the budget is dependent on obtaining as much information in the initial phase of the project. Lack of information in the early stages of the project has resulted in higher costs during implementation [1].

To reduce the difference of planned and actual costs will help the automated system of budgeting. Such a system is a prerequisite for effective planning costs already during the design phase. The basic condition of the automated system of budgeting is to use a software environment that directly communicates between the CAD software and software for creating construction budgets. Direct communication is dependent on the use of data format, ensuring complete data transfer with proper identification. From the foregoing examination of the most suitable transmission format was evaluated IFCxml general data format, which is generated from international exchange format IFC. Article discusses the methodology of the construction budget automated formation in Slovakia.

*The paper presents the results of the project “Identification of key competencies of university students for the needs of knowledge society development in Slovakia”, which is supported by the Ministry of Education, Science, Research and Sport of the Slovak Republic in supplying incentives for research and development from the state budget in accordance with Act no. 185/2009 Z. z. on incentives for research and development and on supplementing Act. 595/2003 Z. z. Income Tax, as amended, by Act no. 40/2011 Z. z.

Peter Mesároš, Juraj Talian, Tomáš Mandičák are now with the Institute of Technology and Management in Construction, Faculty of Civil Engineering, Technical university of Košice, Slovakia (peter.mesaros@tuke.sk, juraj.talian@tuke.sk, tomas.mandicak@tuke.sk)
Daniela Káposztásová are now with the Institute of Architectural Engineering, Faculty of Civil Engineering, Technical university of Košice, Slovakia (daniela.kaposztasova@tuke.sk)

II. Project Creation In the CAD System

Basis of automated budgeting is adequate processing of complex 3D models in CAD applications with the appropriate structure of the project as precise identification of all structures.

A. *Structure of the project*

Please suitable data 3D model for the transmission of data must be processed in accordance with the structure of the transmission IFC [2]. Each BIM application allows creating building projects in a virtual environment with the appropriate project structure for data transfer via IFC. Virtual 3D model is created by films that represent the different assemblies such as outer walls, horizontal support structure, masonry infill 2D data as well as part drawings (eg. Text, dimensions and labels). Each of the sheets are defined by a pair of standard planes that bound the overall height of the floor [3]. Each construction is defined by ground shape and height, which is parametrically based on the standard plane. If the distances from the standard design planes zero height of the structure is the same as the distance of standard planes. In case the designer requires that the construction was lower (eg. Lower wall construction) to set parameters for distance upper edge structures from top standard plane as required.

The object foils are defined as a space for each floor, and it is therefore necessary to assign individual foil to the floor of the structure. Floors are the smallest part of the structure of the object. Several floors can be broken down into building sections that make up the whole building.

Any design data model is proposed parametric. In addition to basic geometric parameters of construction it includes parametric data defining not only merchandising base structure itself, but also other parameters such price may be of the construction or identification features. Identification data associated with CAD applications each structure does not comply with precise identification of the computerized system, therefore, to precede to the identification of new structures.

B. *Identification of structures*

CAD application assigns each object two identification codes during design. It is software code and code IFC. Software code defines each object in the project and each CAD application has a different identification codes. In order to use international data exchange format IFC must have been created unique identification code GUID (Global Unique Identifier). GUID code is actually identification number similar to those of a unique identification number for the civic authorities. Even in the event of changes in certain parameters of structural member identification number does not change. An example of identification parameters can be door assembly which includes a GUID code 22 digit code 6 [4]:

3vHRQ8oT0Hsm00051Mm008

GUID is a unique 128-bit number compressed up to 22 character string. The unique GUID of code is suitable for a graphics system to avoid confusion of the object, but not suitable for the budget of matching parameters of the same construction.

In order to IFC format in the secondary format used IFCxml was necessary to create a new identification parameter which would be the same for each of the same structure (e.g., two partitions of the same material). For this reason, it joined the two structures associated with all codes and code TSKP proposed new code labeled CodeText. TSKP code based on class of TSKP (class of structures and works), which has a five-character codes and is the most common basis for grading structures and work [5]. Where there is no TSKP code was necessary to proceed to create the new text of the code to a given construction can be identified. The new text code designated as Codetext follows the structure class of TSKP and ZOCM and is of matching each parallel structure. Codetextu structure is made up of five levels where the first level describes the building structure, the other producer; the product itself is the third and fifth level of the individual characteristics of the building structure. As in the case TSKP code and the new code is written in the structure of IFCxml to ifcPropertySingleValue assigned the identification number (ID) [6]. Export all the data from the CAD application in a single file IFCxml in the XML structure.

AEC CAD application database contains general design elements that contain new identification elements, but allows create your own database. An example is Allplan 2015, which allows you to create custom database design elements referred to as an assistant. Designer to simplify their work can assign frequently used to design assistant. The designer was forced to assign an identification parameter of each construction proceeded to the establishment of assistants fundamental structures, including the identification elements. Such an approach 3D modeling with the help of assistants to ensure proper identification structures for automated budgeting.

C. 3D modeling

The process of creating a model must be based on an appropriate project structure using the structures of identification parameters. Designer in the project's structure must be defined according to the structure of the project IFC to the division of the individual floors, sub-objects and objects. Each floor will be assigned foil structures and auxiliary 2D data. Film structures are assigned default planes that define the overall height of the floor. To simplify the filtering structures or other data designer can assign each transparency level structures. Levels can assign an automatically according to the type of construction or designer can assign manually. Once the project structure defined (system films and levels) can a designer approach to modeling construction. Selecting individual structures from Assistant structures does 3D object modeling.

In the event that during the design of the data model required an assistant construction does not, you need to create a data structure of the general structure provided from 3D CAD applications. The general structure must be accompanied by the identification data (ID). If the designer does not complete construction of the identification data, the structure will not be automatically generated in the construction budget.

The principle of the formation of the 3D model data is shown in the flowchart (see FIG. 1).

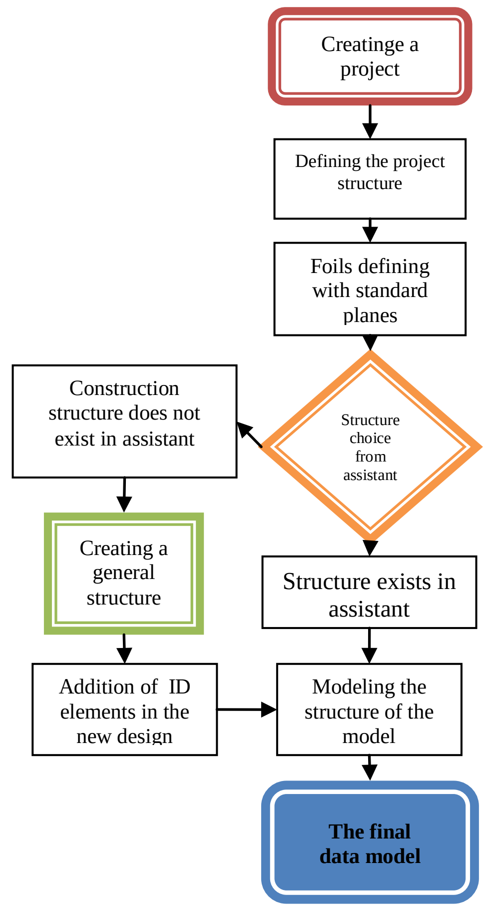

Fig. 1 Flowchart of creation 3D model data Source: own processing

III. DATA TRANSFER FROM CAD TO BUDGET SOFTWARE

Data transfer from CAD to budgetary application is provided by IFC data in the appropriate data structure based on the principle of labeling IFCxml XML structure. Choosing this format was based on previous research and studies elaborated by Zhang [6], where it was evaluated as the most appropriate format. Data transfer process is based on a simple data export in the AEC CAD applications and subsequent import in the budget application.

IFCxml data file includes all the structure, in which are associated with geometric, identification, parameter, etc. material. Based on the identification of each construction budget assigns to the price of retail database automatically. In case the construction is not a complete code application allows semi-automatic assignment. If the construction does not contain the code in this case must assign budgeter budget item manually. After assigning each list price of the items all structures Budgeter can process the entire budget.

The general process of data transfer is shown in the flow chart in FIG. 2.

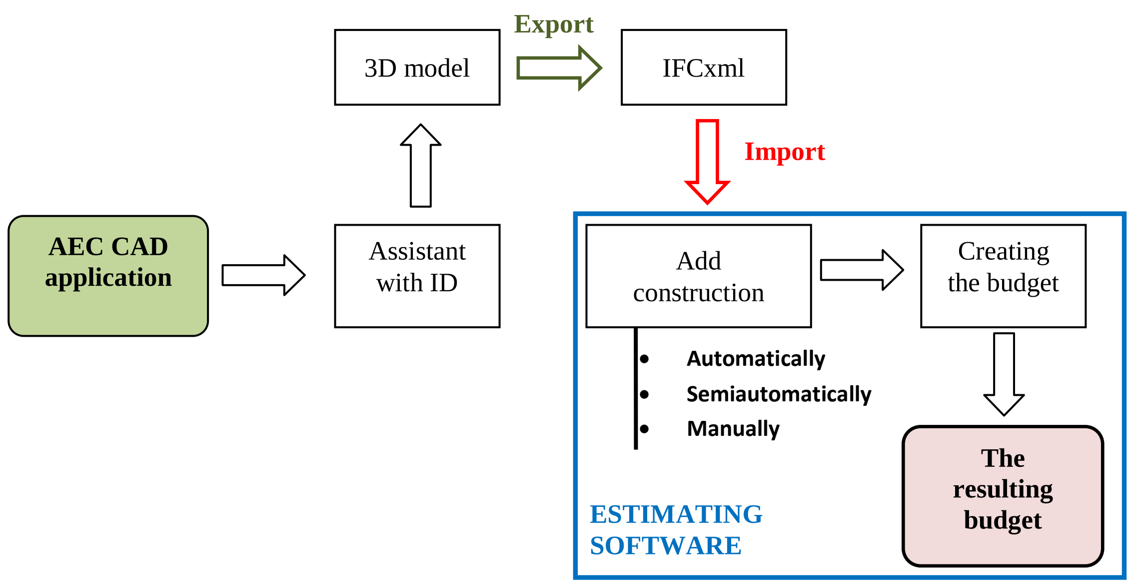

Fig. 2 The process of data transferring from AEC CAD program into the budget. Source: own processing

IV. Data Processing For The Financial Software

The final phase of construction budgets automated creation of AEC CAD application is processing imported data in the budget application and development of the final indicative budget. Processing Importing data from CAD applications to budgetary application is directly dependent on the identification of model elements and correct assignments pertaining to items from a database program. Assigning items retail financial database program or individual model elements (structure) is done automatically, semi-automatic or manual.

A. Automatic assignment

Automatic assignment of items at list database based on full identification of transmitted elements. If the transmitted construction contains a full TSKP code that also contains a budget price of list database application you can then be automated assignment of list items.

Budget application compares TSKP code imported element to the existing price list items, and if a consensus budget then the application automatically assigns the item. The individual items are automatically joining to individual sections of building structures TSKP items by code.

Model can contain more of the same items that application then assigns the same database items. In this case, the generated budget will contain several of the same items that need to be coupled. Links of the same items can be automatically into one item with tantalization amount or manually into a single item or more. Such a merger of individual items but must allow the budget application. Calculus program budget allows it. Another case is when Budgeter wants to create a separate entry for each floor.

While budget software cannot recognize which items are first storey and the second floor. Looking ahead, this problem can be solved on the basis of information on the location of model elements in the space. All CAD application contains information on the geometric distribution building on different floors with altitude data of the coordinates. Based on these interfaces it is possible to create conditions that assign a model element incumbent's floor. That budget application could assign each item floors will need software program. If the program will be able to divide each item by floor, it is possible given Assign the exact costs of moving materials at the site. In addition to the height position of the various elements it is also possible to use location data, which can simplify the proposal in the context of deployment of landfill site to reduce the distance landfills. These data allow builders to clarify and streamline the process while reducing the total cost of constructing the building.

B. Semi-automatic assignment

Semiautomatic assignment of list price of the items imported elements is the case when elements TSKP not a complete code, but only partial. In this case the engine is able

ISBN: 978-1-61804-325-2

to assign a specific building element section, but is unable to assign a particular item. Assigning a specific item from the price-list database remains up to the user, but the program can simplify the selection of individual items only construction section. Before the assignment of individual elements of the items can be individual items combined to reduce the number of matching items.

partial budget is necessary to check and replenish the missing items (for example, bonuses, transfers). Consequently, it is necessary to supplement the budget side of budget costs.

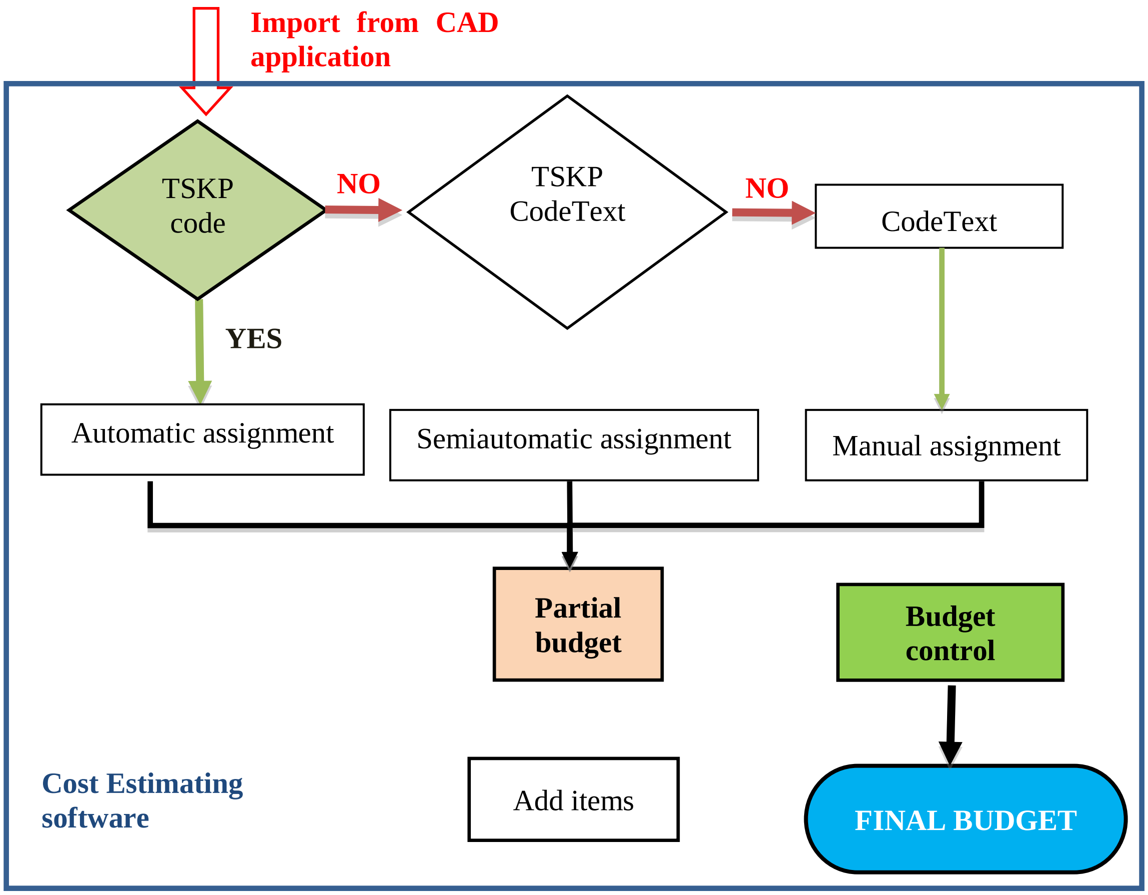

Fig. 3 Data processing in the financial software

C. *Manual assignment*

The latter method of matching elements to imported items is the most time consuming. It is a manual of matching the items and it may be the case if the element contains no TSKP code, or where the code is incorrect. In this case the user is forced to manually search item list prices, and if the database is not must create a new item. The simplification of matching the element to the proper construction of section contains every element except the new code TSKP Codetext, which facilitates the identification of the construction. The main reason for the lack of TSKP code is case of new materials or new technologies that the price-list database are not. But even in this case the advantage of generating budget of direct export significant due to the automated report creation and assessment of the structural model.

After assigning the list prices of all imported constructions items in the financial processing software partial budget. The

V. CONCLUSION

Automated budgeting in Slovakia IFCxml of data generated automatically from the AEC CAD applications is a possibility of automated budgeting. The basic condition for making the budget is accurate identification of individual components and subsequent assignment list price of items from that element. The article describes all the conditions for automated processing of construction budgets, creating a suitable 3D model in CAD applications, data transmission and subsequent processing of the application budget. the possibilities of matching of list items in the budget application (automatic, semi-automatic and manual) are presented in our methodology. The most preferred method is automatic assignment, but that is dependent on complete identification of the individual elements in CAD applications but also the completeness of the budget at list database applications.

REFERENCES

[1] BuildingSmart. IFC4 Release Summary, http://www.buildingsmart-ech.org/specifications/ifc-releases/ifc4-release

[2] Harrison, F. and Lock, D. (2001). Advanced Procect Management, A Structured Approach, 4th Rvised edition, In: Gower Publishing Ltd., 2001

[3] http://www.zelenarchitektura.sk/2012/10/integrovane-planovanie-zmena-pristupu-k-navrhovaniu-budov/

[4] http://www.allplan.net/home/download0/downloadifcviewer

[5] Venkataraman, R., Pinto, J. (2008) Cost and Value management in projects: In: John Wiley & Sons, Inc., New Jersey USA , 2008.

[6] ZHANG, Jiemin et al. (2010). Improving the usability of standard schemas In: Information Systems. Elsevier, 2010.

ISBN: 978-1-61804-325-2

Progressive Collapse Evaluation of an Industrial Building

Marin Lupoae, Cătălin Baciu, Patricia Murzea, Dan-Ilie Buliga

***Abstract*—**The paper presents the evaluation of the potential of occurrence and propagation of the progressive collapse for an industrial building made of precast and cast in place elements. The performed experimental tests aimed to initiate the collapse by destroying, through explosion, a column situated at the ground level, on the contour of the building, at half the distance of the long side of the construction, using charges placed in boreholes. A model was developed for the numerical evaluation using the method of applied elements and a demolition scenario was used through which the column was instantaneously removed. The analysis of the numerical and experimental results showed that there is a good concordance between the displacements on the vertical direction of the node located above the removed column. Using these results the potential of occurrence and development of collapse was studied, using scenarios of column removal in according to GSA 2003 as well as scenarios in which two or three columns were removed. The evaluation was based on the determination of the rotations of the beam ends. The obtained results highlighted the importance of the manner in which the structure is designed and built, of the height regime and structural conformity, on the collapse.

***Keywords*—** applied element method, explosive demolition, progressive collapse, precast concrete elements.

I. Introduction

PROGRESSIVE collapse became a subject of interest for researchers especially after the partial collapse of the 22-storey tower in Ronan Point and its importance increased significantly after the worldwide escalation of terrorist activities, reaching its climax after the events of 11/2001.

The term **progressive collapse** [2] is used to describe the propagation, as a chain reaction, of a local failure thus leading to the total or partial crash of the building, the resulted damage being disproportional with respect to the initial cause.

The issue of the progressive collapse for the reinforced concrete structures is well addressed in the specialized literature considering the existing regulations and design codes [1-7] as well as the numerous published papers [8-22]. Under the existing regulations [2] two alternative design methods are provided to ensure the necessary strength of the buildings to this kind of phenomenon: the **direct and indirect** methods.

The evaluation of the potential of occurrence and propagation of the progressive collapse, using the direct method [4-5], involves the removal of some of the vertical support elements in order to test the capacity of the structure to redistribute the additional resulting efforts. The experimental studies performed by various authors on this subject consisted in the removal through explosion of an exterior column situated on the middle of the longest side of the construction [8], of an interior column [9], or of two exterior adjoining columns [10] and for the static tests mechanical jacks [11-12] or mechanical damages were employed [13]. Numerical analyses were performed according to the specifications of the existing norms [4-5] taking into account nonlinear dynamic analyses [16-19], dynamic linear and nonlinear analyses [15] and also static and dynamic, linear and nonlinear analyses [20]. The instantaneous removal of the support element according to GSA 2003 does not depend on the type of event which led to its destruction. This approach, although justified from the point of view of the simplification of the analysis has the disadvantage that in the case of an explosion the effects on the structure can be significant and the structural response can be considerably different in comparison to the case of the instantaneous removal. Thus, Shi [21] showed, after an analysis in three steps, that the obtained results based on the predictions regarding the progressive collapse are better if *non-zero initial conditions and initial damage of the structural members caused by the blast loads* are taken into account. Also, in paper [22] the differences between the behavior of a G+5S (ground floor + 5 storey) building in the case of the damage of a column as a result of a local blast (when the action is manifested on a small number of elements) and that of an explosion from the distance (when the effect is a global one, at the level of the entire structure) were highlighted through numerical analyses.

The issue of progressive collapse for structures with precast elements is less approached and discussed in the specialized literature. According to the specifications of GSA 2003 [4] the evaluation of the potential of occurrence and propagation of the progressive collapse in irregular structures or in those made of precast elements has to be treated with increased attention. Although progressive collapse may appear in almost all types of structures, failure in the precast structures may occur more often due to the lack of structural continuity in the nodes (in the connection zone of the elements). There are numerous papers which analyze the behavior of the precast elements [23-24] and their connections [25-26] at cyclic loads,

Marin Lupoae is with Military Technical Academy, Bucharest, Romania, 39-49 Geeorge Cosbuc Blv., 050141, phone +40213354660; fax: +40213355763; e-mail: mlupoae@mta.ro.

Cătălin Baciu is with Military Technical Academy, Bucharest, Romania; e-mail: baciucatalin2001@yahoo.com.

Patricia Murzea is with Military Technical Academy, Bucharest, Romania; e-mail: murzea_patricia@yahoo.com.

Dan-Ilie Buliga is with Military Technical Academy, Bucharest, Romania; e-mail: dan.ilie.buliga@gmail.com.

fewer papers which investigate the seismic capacity of structures made of precast elements in order to determine their vulnerability [27] and even less which approach the aspects concerning the collapse of such structures [28]. Thus, Pekau [28] performs an analysis of the behavior of the precast panel shear walls using the method of distinct elements (DEM). Integrity analyses of a twelve-storey, three-bay precast panel shear wall in different conditions with respect to earthquakes and progressive collapse are performed focusing on the shear ductility demands of the mechanical connectors in the vertical joints. The whole progressive collapse processes of the panel wall in various conditions are also simulated.

The current paper approaches, in the first part, the response of a precast industrial structure made of reinforced concrete frames, in the case of the removal through blast of an exterior column situated at ground level on the middle of the longest side of the building. In the second part of the paper, the structural response when two or three columns were removed, considering different configurations, was determined using the method of applied elements. The aim was to asses the manner in which the efforts are redistributed mainly through the evaluation of the rotation of the beams.

II. EXPERIMENTAL TEST

A. *Building Characteristics*

The building used for the present study was part of a group of structures situated on the platform of an old chemical plant, built in 1980 but never put into service. When the tests were performed the entire industrial platform was decommissioned thus facilitating the possibility of conducting all the required experimental activities.

The building was made of four sections, designed as reinforced concrete structures. The main elements (columns, transversal beams, roof elements) were precast and the longitudinal and secondary beams, the intermediate floors and the access stairs were cast in place.

The further description of the building will concentrate on the first section, Fig. 1, the one subjected to the experimental study.

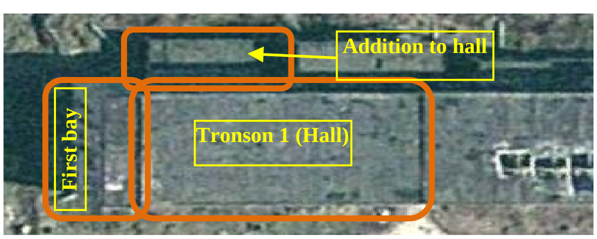

Fig. 1 Aerial view of the building

The structure of the section was regular in plan, with 9 bays and 4 spans, each having 6m, Fig. 3. The first bay had the height regime G+5S, whereas for the other bays the height regime was G+2S (the last floor was built on the height of the 2nd, 3rd and 4th floors and on the first bay), Fig. 2. The last level of the structure, between axes 2 – 10, was designed as a production hall with a high clear height (11.30m), with two spans each of 12m, with running beams placed on the cantilevers of the columns at the elevation of +17.75m, where gantries necessary for carrying out the production processes were installed.

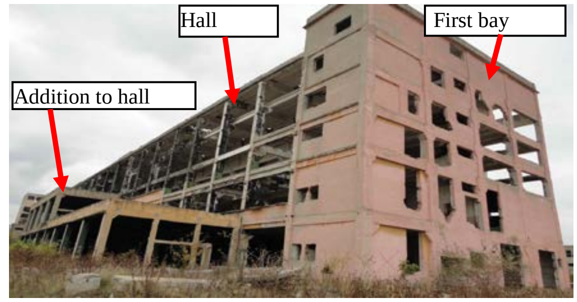

Fig. 2 The section on which experimental tests were performed

The intermediate floors were made of cast in place reinforced concrete elements having the thickness of the concrete slab of 20 cm for the first level and 15 cm for the second level. In order to efficiently withstand and redistribute the live loads, the floors had intermediate secondary beams (GS-25x50cm), arranged at a distance of 2m between the axes, on the longitudinal direction of the building.

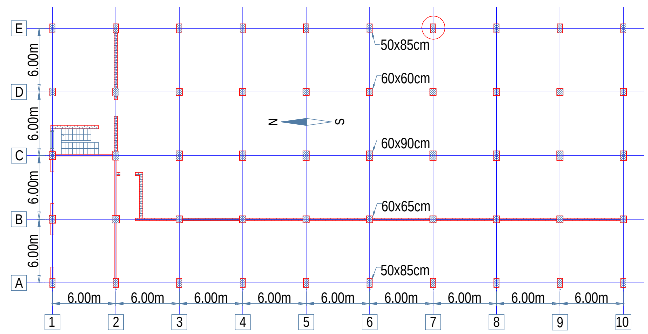

Fig. 3 Axes plan of the investigated section of the building

The precast reinforced concrete columns were designed with cantilevers on which the transversal beams were supported. The geometrical dimensions and the reinforcing details of the columns are presented in Table I.

Table I Geometry and reinforcing details of the columns

Columns for the ground, first and second level

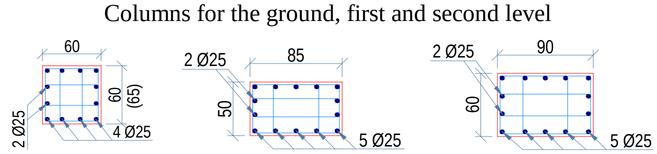

Columns for the third level

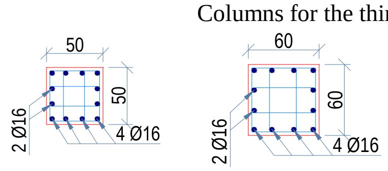

All the stirrups for the columns are Φ10/10cm

The transversal beams (A-E direction) were precast and supplementary concrete was cast in place over them, on the cantilevers of the columns, to ensure the appropriate structural behavior (all elements working together as a whole), Fig. 4. Two of the types of the longitudinal reinforcing bars of the beams (marks 3 and 4) stopped at the column and the rebars mark 5 along with the rebars mark 6 ensured the connection between the beam and the column at the upper part. Also, in order to withstand the shearing forces with high values at the beam ends, in the area of the supplementary cast in place concrete, the longitudinal rebars exiting the beam and the column were enclosed with stirrups Φ 10/10cm, fixed on the cantilevers of the columns and locked in place after the assembly of the longitudinal rebars. At the lower part of the beam the connection with the column was made through metallic plates fixed both on the haunch of the column as well as on the lower part of the beam. The monolithic floors were cast in place after the fixing of these transversal beams which were designed to have at the upper part, on their entire length, elements ensuring their working together with the reinforced concrete slab.

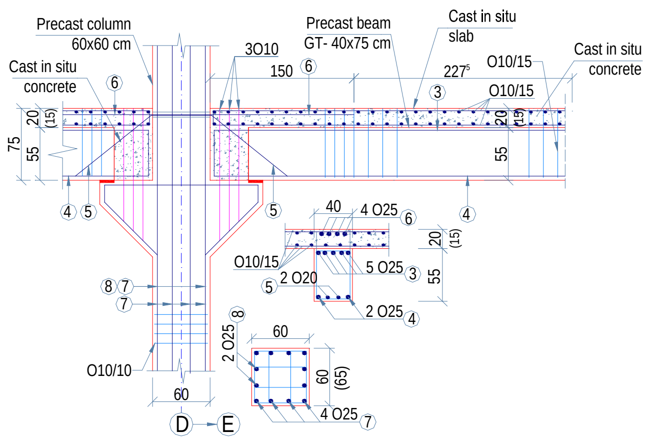

Fig. 4 Transversal precast beam - precast columns joint details

The longitudinal beams (3-10 direction) were cast in place together with the reinforced concrete slab and their working together with the column was ensured by the passage of some of the rebars of the beam through holes especially left in the column. Thus, at the bottom side, the reinforcing bars stopped at the contact with the column and the connection with it was made through other rebars, which passed through the column.

The slabs were cast in place together with the longitudinal principal and secondary beams. Reinforcing bars Φ10/15 cm were used on both directions, top and bottom. In the slab above floor 1, multiple holes having a technological purpose were made, with the dimensions 4.00x4.00m, which were bordered by secondary beams having the cross-sectional dimensions 25x50cm.

B. *Carrying Out the Experiment*

The aim of the experimental tests was the measurement of the vertical displacement of the node located directly above column E7, Fig. 3. According to the GSA analysis scenarios for the occurrence and propagation of the collapse, a column situated at the ground level, in the middle of the longest side of the building, was removed. The removal was done instantaneously, through explosion. This kind of removal was possible because the construction was going to be demolished. For the instantaneous removal, explosive charges placed inside several boreholes made directly into the column were used, Fig. 5. The employed method is the closest to the recommendations of GSA, namely the instantaneous removal of a support element, regardless of the type of threat. The energy produced after the detonation of the explosive charges was mostly consumed in the fragmentation and throwing of the concrete pieces, Fig. 5b, and thus the aerial shock wave resulted from the blast had very little values and did not influence the behavior of the structure after the column removal.

a) The layout of the explosive charges network

b) Concrete damage and rebars bending after the detonation of the charges

Fig. 5 The column before and after the detonation of the explosive charges

Measuring the absolute displacement of the structure on the vertical direction was facilitated by the existence of an auxiliary structure. The gap between the two buildings was 5cm. For the displacement measurements an inductive displacement transducer was used. The body of the transducer was fixed on the column of the adjacent structure (the fixed column) by means of a steel plate whereas the plunger of the transducer was fixed using a hot rolled steel profile at 15cm above the slab of the first floor on the E7 column. The head of the plunger was fixed with a bolt nut on the hot rolled steel profile. Thus, the head of the plunger could move together with the structure of the hall after the destruction of the ground floor column.

III. NUMERICAL SIMULATION

A. *Applied Element Method*

For the structural model the applied element method (AEM) was used, which combines features of both the finite element method as well as the discrete element method. The main advantage of this method is that it can describe the behavior of the structural system from the application of the forces, the crack propagation and the separation of the structural elements to the total collapse [29], [30].

The structure is modeled as an ensemble of small elements, with special shape and determined dimensions. These types of elements do not deform, the change in their position being considered as for a rigid medium. AEM elements are connected using the entire surface of the elements, through a series of connecting springs that adopt all the material types and properties. Each group of springs completely represents the stresses and deformations of a certain volume and each element has six degrees of freedom. This modeling method allowed the study of the initiation and propagation of cracks and of the failure of the structure using only one initial model. The location of the failure is determined during the cyclic process.

For modeling the concrete under compression, the Maekawa compression model is used [31]. For the reinforcing springs the model presented by Ristic *et al.* [32] is used. The tangent stiffness of the reinforcement is calculated based on the strain of the reinforcing spring, loading status (either loading or unloading) and the previous history of the steel spring which controls the Bauschinger effect.

B. Geometrical Model

The geometrical model of the hall is shown in the following figure (Fig. 6). The first bay of the building was not modeled in order to reduce the number of elements and the computation time. Instead, the holes in the slab above floor 1, the running beams and the enclosure elements along the E axis were accurately modeled. The considered loadings are only those from the self weight of the building and a load of 100 kg/m^2 from the existing finishes.

In order to model the longitudinal reinforcing of the beams as well as the rebars which make the connection between the longitudinal and transversal beams and columns, new reinforcing manners (styles) were defined for the longitudinal reinforcing within the program.

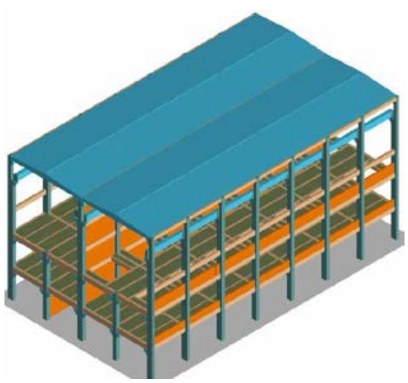

Fig. 6 Geometrical model of the hall

For the longitudinal beams a reinforcing style was defined in which two rebars are lifted at the upper side (rebars 4) and are then passing through the column, in the vicinity of the node, Fig. 7. Also, the connection between the rebars at the upper side of the beams which are joined in the same node is done through the rebars 3, at the upper part and the rebars 5, at the lower part, Fig. 7.

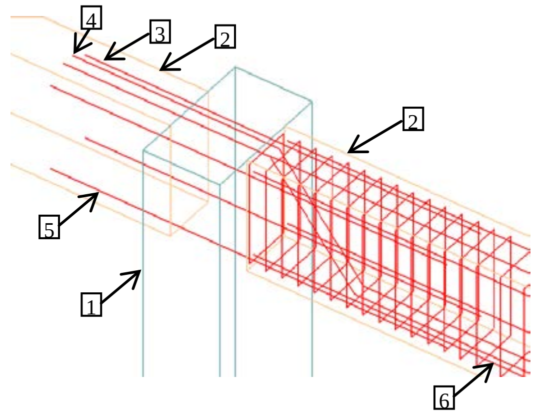

Fig. 7 Defining a new reinforcing style for the longitudinal beams: 1-column, 2- longitudinal beams; 3-longitudinal connection reinforcing, top; 4- rebars stretching from bottom to top; 5- longitudinal connection reinforcing, bottom; 6-beam rebars

For the transversal beams, the lifted rebars are mark 6 and the rebars mark 4 ensure the connection with the reinforcing bars mark 5 from each beam, stopping at the column, Fig. 8. For the cast in place concrete model a beam without reinforcing bars was defined and the connection with the column was made through the mark 7 stirrups of the haunch. The inclination of the stirrups occurred as a result of the transformation of a beam into an element with 8 nodes in order to obtain the shape of the haunch. Also, the connection between the transversal beam and the haunch was made using metallic plates (8) arranged both on the beam as well as on the haunch.

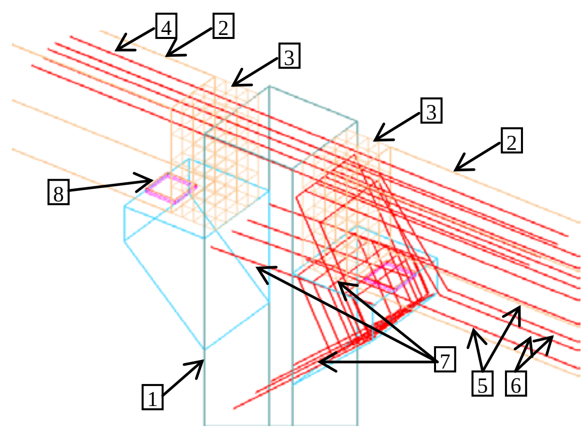

Fig. 8 Defining a new reinforcing style for the transversal beams: 1-column, 2- transversal beams; 3-cast in place concrete; 4- longitudinal connection reinforcing, top; 5,6-beam rebars; 7-haunch rebars; 8-metallic plates.

C. Column Removal Scenarios

The demolition scenario was used as a column removal scenario, being predefined within the program. This scenario is frequently used for the demolition with explosives and for the progressive collapse cases when the user knows the elements which are to be destroyed.

Table II Column removal scenarios

Scenario	No. of removed columns	Layout	Positioning
1.	1	Exterior - long side	E-7
2.	1	Exterior - short side	C-10
3.	1	Exterior - corner	E-10
4.	1	Interior	C-7
5.	2	Exterior - long side Exterior - corner	E-9 E-10
6.	2	Exterior - short side Exterior - corner	D-10 E-10
7.	2	Exterior - long side Exterior - long side	E-7 E-6
8.	2	Interior Interior	C-7 D-7
9.	3	Exterior - corner Exterior - long side Exterior - short side	E-10 E-9 D-10
10.	3	Exterior - corner Exterior - long side Exterior - long side	E-10 E-9 E-8
11.	3	Exterior - long side Exterior - long side Exterior - long side	E-8 E-7 E-6

During this demolition scenario both the elements which are to be destroyed as well as the time when they will be instantaneously removed are specified. The column removal was instantaneously done at the time t=0.00s. The advantage of using this method consists in the reduction of the computation time compared to the explosion solution.

Because the studied construction has a reduced height regime and was designed to withstand high loads, other scenarios of removal of the vertical supports were used besides those specified in GSA 2003, Table II. The column removal according to scenarios 1-4 was performed according to GSA 2003 (exterior column on the long side, short side and corner of interior column) and the other scenarios were based on 1-4 but were improved by removing other support elements as well. The notations from the column "Positioning" are considered according to Fig. 3.

IV. RESULTS AND DISCUSSIONS

A. *E-7 Column Removal*

Following the detonation of the explosive charges placed in the boreholes made in the column E7 the concrete was thrown almost entirely, except in the zone of the column of the neighboring construction, Fig. 5b. The stirrups were straightened and some were thrown out of the column and the longitudinal reinforcing bars were bent. The bending of the longitudinal rebars occurred mainly due to the action of the shock wave and due to the propulsion of the concrete fragments and not as a result of the vertical displacement of the structure after the column destruction.

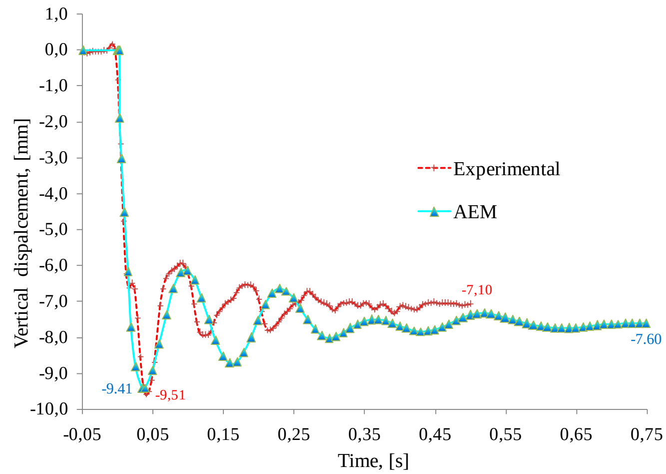

Fig. 9 Experimental and analytical vertical displacements of joint E7 for the second floor

The vertical displacement of the node located above the blast damaged column is shown in Fig. 9. Immediately after the detonation of the explosive charges the sensor measured a displacement along the positive direction of the axis Z of approximately 1 mm as a result of the action of the shock wave on the metallic support on which the transducer was installed. After the damage of the column the structure did not directly displace until the maximum value was reached. It had a first displacement until the value of -6.5 mm at t = 0.02s, followed by a light displacement along the positive direction of the axis Z and then a downward displacement occurred until the maxim value of -9.51 mm at time t = 0.044s. As a consequence of the redistribution of the efforts between the structural elements, the structure then oscillated around the permanent value of the vertical displacement, respectively -7.1 mm. It is thus observed that the permanent final displacement represents 66% of the maximum recorded displacement. The maximum vertical displacement of the node located directly above the one destroyed by the blast is comparable in terms of size with the ones obtained by Sasani *et al.* [8] and and Sasani and Sagiroglu [33], for constructions with different height regimes and structural layouts.

The graphical representation of the vertical displacement of node E7, situated above the damaged column, obtained from the numerical simulation, Fig. 9, indicates a maxim value of 9.41 mm, different than the value of - 9.61 mm resulted from the experimental measurements (a difference between them of 2%). There also appears a difference between the times at which the maximum values are recorded, namely 0.035s for the numerical solution and 0.041s for the experimental one. Also, the numerical results show a final displacement of 7.60 mm which is higher by 7% in comparison to the final experimental displacement of 7.10mm. It can be seen that the oscillations of the structure in the experimental case are damped faster than the ones from the numerical simulation.

After the removal of the column E7 a change in the shape of the bending moment occurs for the transversal or longitudinal beams connected to the axis of the removed column, Fig. 10 and Fig. 11.

ISBN: 978-1-61804-325-2

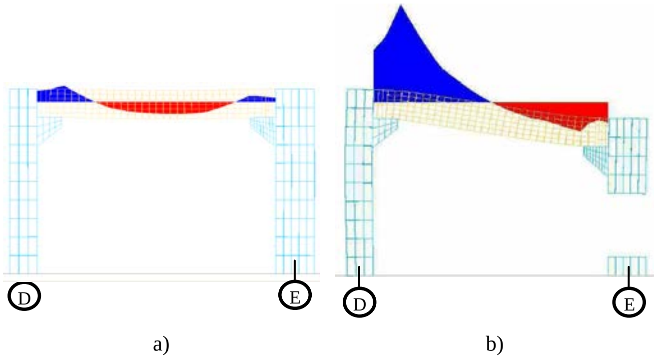

Fig. 10 Bending moment distribution in the transversal beam D7-E7 on the second floor before and after the column removal (not to scale)

This change in the shape of the bending moment corresponds to the behavior of the structure which develops mechanisms capable of redistributing the additional efforts occurring as a result of the removal of a vertical support element.

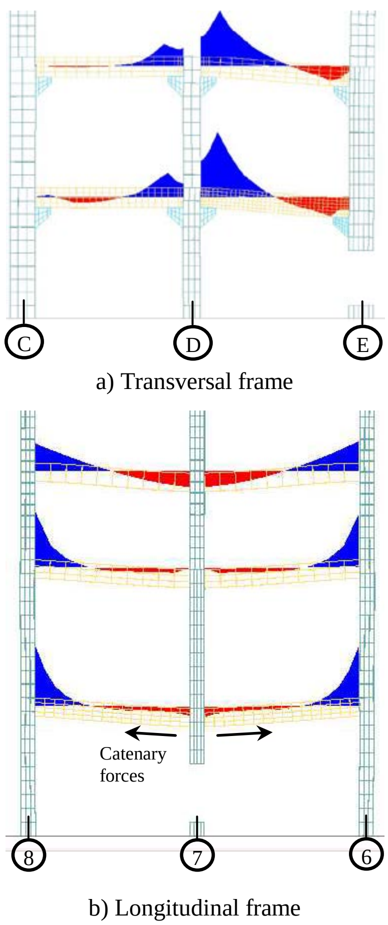

Fig. 11 Bending moment distribution in transversal and longitudinal beams after the column removal (not to scale)

Such mechanisms which can increase the capacity of the structure to resist failure (collapse) include: catenary action of slab and beams allowing the gravity load to span to adjacent elements; b) Vierendeel action from the moment frame above a damaged column and c) gravity load support provided by the nonstructural elements such as partitions and infills. The catenary action in beams involves large deformations and utilizes tensile forces to balance the amplified gravity loads due to the doubling of the span (associated with the loss of a middle column) and the dynamic effect (associated with the sudden loss of the supporting force), Fig. 11b.

The Vierendeel action can be characterized by the relative vertical displacement between beam ends and the double curvature deformations of beams and columns. Such a deformed shape (Fig. 10, after the column removal) provides shear forces in beams in order to redistribute the vertical loads following the column removal.

An important observation is related to the shape of the moment around the support (the haunch) of the transversal beams, Fig. 10 and Fig. 11a. It can be seen that the maximum moment is outside the support area and thus also outside the zone where the elements are working together. An immediate effect is represented by the cracking mechanism of the concrete for the beam D7-E7, Fig. 12. Thus, the cracking of the beam is more pronounced outside the support zone of the beam (on the haunch) and continues on the connection zone of the beam to the column but at a reduced level.

According to UFC [5] the beam and column rotations after the removal of a vertical supporting element must be checked. The rotation of the beams and columns is computed by dividing the maximum deformation Δ to the length L of the element (the length of the beam on the longitudinal direction or the distance between the support elements of the transversal beams), Fig. 12.

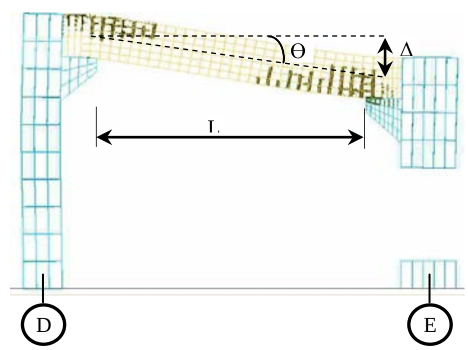

Fig. 12 Cracking state of the beam D7-E7 corresponding to the maximum bending moment (not to scale)

The limit value of the rotation angle for the beams according to table 4-1 from UFC [5] is 3.61 degrees. Similar values are presented in [34] as well: the average yield rotation is 0.34° and the average ultimate rotation of a plastic hinge is 3.4°, respectively.

The graphical representation of the variation of the rotations of the longitudinal and transversal beams which connect in joint E7, above the damaged column, is shown in Fig. 13.

ISBN: 978-1-61804-325-2

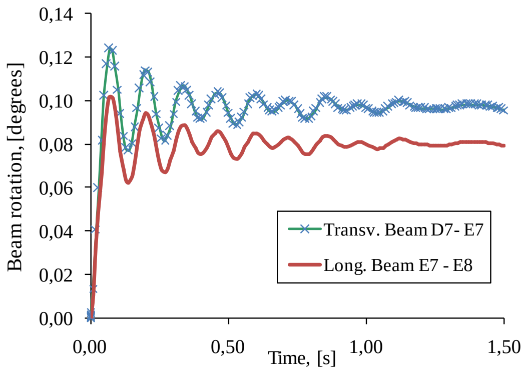

Fig. 13 The time variation of the rotation of the longitudinal and transversal beams after the removal of the column E7

The difference between the maximum rotations of the two beams occurs due to the free length of the beams. If for the longitudinal beam this value is of 5.225 m (the distance between the columns E7 and E8) for the transversal one it is 4.175 m (the distance between the haunches of the columns E7 and D7). The maximum values of these rotations (0.10 degrees for the longitudinal beam and 0.12 degrees for the transversal beam) are under the limit values established in UFC.

B. Column Removal According to Scenarios 2-11

After the column removal according to the scenarios from Table I, the rotations shown in Table III were obtained.

Table III Rotation values for the beam ends considering the analyzed scenarios

Scenario	Transversal Beams		Longitudinal Beams	
	Notation[1]	Rotation[2] [degrees]	Notation [1]	Rotation [2] [degrees]
1.	D7-E7	0.12	E7-E8	0.10
2.	B10-C10	0.0276	C9-C10	0.0127
3.	D10-E10	0.203	E9-E10	0.138
4.	D7-C7	0.0085	C8-C7	0.0056
5.	D10-E10 D9-E9	0.79 0.51	E8-E9 E9-E10	0.14 0.35
6.	C10-D10 D10-E10	0.30 0.07	D9-D10 E9-E10	0.17 0.30
7.	D7-E7 D6-E6	0.30 0.27	E8-E7 E5-E6	0.17 0.19
8.	B7-C7 E7-D7	0.03 0.10	C8-C7 D8-D7	0.012 0.038
9.	C10-D10 D10-E10 D9-E9	0.75 0.64 0.97	E9-E10 D9-D10	0.29 0.50
10.	D10-E10 D9-E9 D8-E8	57 57 57	-	-
11.	D8-E8 D7-E7 D6-E6	0.51 0.82 0.52	E9-E8 E5-E6	0.38 0.37

[1]) The value of the rotation was determined for the end of the beam indicated in the second term of the notation (e.g.: D7-E7 – the rotation is determined for the end of the E7 beam).

[2]) The limit value of the rotation angle for the beams, according to UFC [5], is 3.61 degrees.

By comparing the values of the beam rotations from Table III with the limit value indicated in UFC it is found that only in scenario no. 10 the beam rotations exceed the failure limit of these elements. Thus, the collapse of the frame whose columns were destroyed occurs, Fig. 14.

The collapse does not propagate outside the frame on the one hand due to the transversal dimensions of the beams and columns adjoining the removed elements and on the other hand due to the structural conformity at the upper part, namely the lack of connection elements (slabs and beams).

For the scenarios performed according to GSA 2003 (scenarios 1-4) it is found that the highest rotations are those corresponding to the corner column removal E10 (0.203 degrees for the transversal beam and 0.138 degrees for the longitudinal beam), followed by those corresponding to the removal of the exterior column located in the middle of the longest side E7 (0.12 degrees for the transversal beam and 0.1 degrees for the longitudinal beam). For scenarios 1 to 4 the values of the rotations are smaller than the yielding limit of the reinforcing steel bars, 0.34 degrees according to [34].

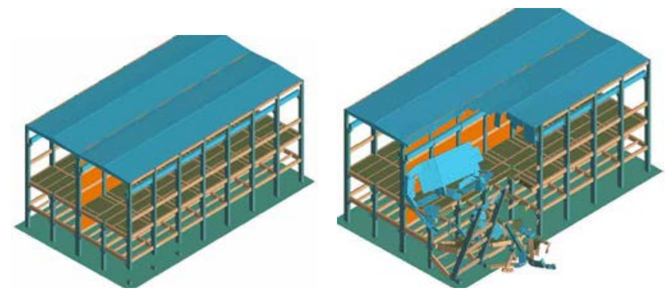

Fig. 14 Collapse of the frame E-D-10-9-8

For scenarios 5 to 11, the highest rotations of the beams are found is the 5th scenario, corresponding to the removal of the corner column E10 and of the adjacent one on the longest side E9. In this case the rotations of the transversal beams (0.79 for beam D10-E10 and 0.51 for beam D9-E9) are larger than the plastic hinge development limit. The rotations of the longitudinal beams (0.14 for beam E8-E9 and 0.35 for beam E9-E10) are however lower than the corresponding yielding limit of the reinforcing steel bars. The final effect is: failure to initiate the collapse of the frame which had its columns removed.

V. Conclusion

The evaluation of the potential of occurrence and propagation of the progressive collapse for an industrial hall made of precast elements was performed by using both experimental tests as well as numerical simulations. The developed numerical model, using the applied elements method, was validated by the experimental study. The numerical analyses performed by increasing the number of removed columns, starting from one column according to the GSA 2003 recommendations, and ending with three columns, led in just a single case to the initiation of the collapse. Even in this case, however, the collapse was limited to the frame whose columns were initially removed. No deterioration of the joints beam-column was observed in any of the analyzed cases due to the manner in which the connection of the precast elements was made (using cast in place concrete).

It was found that in most of the cases the displacements of the nodes located above the removed columns produced only the cracking of the reinforced concrete elements without leading to the yielding of the rebars.

One of the possible applications of this paper could be the assessment of the level of deterioration of the structural elements after the failure of a vertical support element. Based on the traced capacity curves the behavior of the elements adjacent to the area of the failure initiation, considering any removal scenario for one or more vertical support elements, can be estimated.

ACKNOWLEDGMENT

This paper has been financially supported within the project entitled "Horizon 2020 - Doctoral and Postdoctoral Studies: Promoting the National Interest through Excellence, Competitiveness and Responsibility in the Field of Romanian Fundamental and Applied Scientific Research", contract number POSDRU/159/1.5/S/140106. This project is co-financed by the European Social Fund through Sectorial Operational Programme for Human Resources Development 2007-2013. Investing in people!

REFERENCES

[1] EuroCode 1. Actions on structures. Part 1.7: General Actions - Accidental actions, European Committee for Standardization, 2005
[2] ASCE/SEI 7, Minimum design loads for buildings and other structures, Reston (VA): Structural Engineering Institute, American Society of Civil Engineers, 2005
[3] Office of the Deputy Prime Minister, "The building regulations 2000, Part A, Schedule 1: A3, Disproportionate collapse", London (UK), 2004
[4] GSA. Progressive collapse analysis and design guidelines for new federal office buildings and major modernization projects. Washington (DC): US General Service Administration; 2003.
[5] DOD. Design of building to resist progressive collapse. Unified Facility Criteria, UFC 4-023-03. Washington (DC): US Department of Defense; 2009.
[6] ISC. ISC Security Design Criteria for New Federal Office Buildings and Major Modernization Projects, Interagency Security Committee, Washington, DC, 2004
[7] NIST. Best practices for reducing the potential for progressive collapse in buildings. US National Institute of Standards and Technology (NIST), Washington, DC, 2007.
[8] M. Sasani, M. Bazan, S. Sagiroglu, "Experimental and Analytical Progressive Collapse Evaluation of Actual Reinforced Concrete Structure", *ACI Structural Journal*, V. 104, No. 6, November-December 2007
[9] M. Sasani, M. Bazan, S. Sagiroglu," Gravity Load Redistribution and Progressive Collapse Resistance of 20-Story Reinforced Concrete Structure following Loss of Interior Column", *ACI Structural Journal*, V. 107, No. 6, November-December 2010
[10] M. Sasani, "Response of a reinforced concrete infilled-frame structure to removal of two adjacent columns", *Engineering Structures 30* (2008), 2478–2491
[11] W.-J. Yi, Q.-F. He, Y. Xiao, K. Sashi, X. Kunnath, " Experimental Study on Progressive Collapse-Resistant Behavior of Reinforced Concrete Frame Structures", *ACI Structural Journal*, V. 105, No. 4, July-August 2008
[12] Qian K., Li B., "Slab Effects on Response of Reinforced Concrete Substructures after Loss of Corner Column", *ACI Structural Journal*, V. 109, No. 6, November-December 2012.
[13] J. Yu, K.-T. Tan, "Experimental and numerical investigation on progressive collapse resistance of reinforced concrete beam column sub-assemblages", *Engineering Structures,Volume 55*, October 2013, 90-106
[14] S. Kokot, A. Anthoine, P. Negro, G. Solomos, "Static and dynamic analysis of a reinforced concrete flat slab frame building for progressive collapse", *Engineering Structures 40* (2012) 205–217
[15] M.-H. Tsai, B.-H. Lin, " Investigation of progressive collapse resistance and inelastic response for an earthquake-resistant RC building subjected to column failure", *Engineering Structures 30* (2008) 3619_3628
[16] S. Pujol, J.P. Smith-Pardo, "A new perspective on the effects of abrupt column removal", *Engineering Structures 31* (2009) 869_874
[17] R. Jayasooriya, D. Thambiratnam, N. Perera, V. Kosse, " Blast and residual capacity analysis of reinforced concrete framed build", *Engineering Structures 33* (2011) 3483–3495
[18] H. Salem, A.K. El-Fouly, H.S. Tagel-Din, "Toward an economic design of reinforced concrete structures against progressive collapse", *Engineering Structures 33* (2011) pp. 3341–3350
[19] H. Helmy, H. Salem, S. Mourad, "Progressive collapse assessment of framed reinforced concrete structures according to UFC guidelines for alternative path method", *Engineering Structures 42* (2012) pp. 127–141
[20] O. Mohamed, "Assessment of progressive collapse potential in corner floor panels of reinforced concrete buildings", *Engineering Structures 31* (2009) 749_757
[21] Y. Shi, Z. Li, X. Li, H. Hao, "A new method for progressive collapse analysis of RC frames under blast loading", *Engineering Structures 32* (2010) 1691_1703
[22] M. Lupoae, C. Baciu, D. Constantin, H. Puscau, "Aspects concerning progressive collapse of a reinforced concrete frame structure with infill walls", *Lecture Notes in Engineering and Computer Science, World Congress on Engineering*, Vol. III, No. 2, pag. 2198 – 2204, 2011
[23] Y.H. Chai, J.D. Anderson, "Seismic response of perforated lightweight aggregate concrete wall panels for low-rise modular classrooms", *Engineering Structures 27* (2005) 593–604
[24] C.C Chou, H.-J. Chang, J. T. Hewes, "Two-plastic-hinge and two dimensional finite element models for post-tensioned precast concrete segmental bridge columns", *Engineering Structures 46* (2013) 205–217
[25] R.A. Hawileh, A. Rahman, H. Tabatabai, "Nonlinear finite element analysis and modeling of a precast hybrid beam–column connection subjected to cyclic loads", *Applied Mathematical Modelling 34* (2010) 2562–2583
[26] H.H. Korkmaz, T. Tankut, "Performance of a precast concrete beam-to-beam connection subject to reversed cyclic loading", *Engineering Structures 27 (2005) 1392–1407*
[27] G. Magliulo, G. Fabbrocino, G. , Manfredi, "Seismic assessment of existing precast industrial buildings using static and dynamic nonlinear analyses", *Engineering Structures 30* (2008) 2580–2588
[28] O.A. Pekau, Y. Cui, "Progressive collapse simulation of precast panel shear walls during earthquakes", *Computers and Structures 84* (2006) 400–412
[29] K. Meguro, H.S. Tagel-Din, "Applied Element Method Used for Large Displacement Structural Analysis", *Journal of Natural Disaster Science*, vol. 24, No 1, 2002, pp 25-34
[30] H. Tagel-Din, N.A. Rahman, "The Applied Element Method: The Ultimate Analysis of Progressive Collapse", *Structure Magazine*, No 4, April 2006, pp 30-33.
[31] K. Maekawa, H. Okamura, "The deformational behavior and constitutive equation of concrete using the elasto-plastic and fracture model", J Faculty Eng Univ Tokyo (B) 1983;37(2):253–328.
[32] D. Ristic, Y. Yamada, H. Iemura, "Stress–strain based modeling of hysteretic structures under earthquake induced bending and varying axial loads", *Research report No. 86-ST-01*, School of Civil Engineering, Kyoto University, Kyoto, Japan; 1986.
[33] M. Sasani, S. Sagiroglu, "Progressive Collapse Resistance of Hotel San Diego", *Journal of Structural Engineering*, Vol. 134, No. 3, March 2008, pp. 478-488.
[34] Y. Li, X. Lu, H. Guan, L. Ye, "An improved tie force method for progressive collapse resistance design of reinforced concrete frame structures", *Engineering Structures 33* (2011) 2931–2942.

Investigation of mineral oxygen carriers for Chemical Looping Combustion process

Antonios C. Psarras, Eleni F. Iliopoulou

Abstract—In the present study two natural minerals rich in iron and manganese oxides are investigated as potential "oxygen carriers" for the Chemical Looping Combustion (CLC) process. A fluidized bed reactor is utilized for the evaluation of the ores. Both materials showed moderate performance in CH_4 combustion, whereas the selectivity towards CO_2 was more satisfactory. As far as the Oxygen Transfer Capacity (OTC) is concerned, the materials provided quite lower oxygen to the fuel gas than expected from their composition.

Keywords—Mineral oxygen carriers, chemical looping combustion.

I. Introduction

GLOBAL warming is undoubtedly real, and there is a scientific consensus about it [1]. The anthropogenic climate change is caused by emission of so called greenhouse gases. Among greenhouse gases emitted by human activities Carbon dioxide (CO_2) is considered to have the largest effect on climate change. Continued extraction and combustion of fossil fuels have increased the atmospheric CO_2 concentration from a preindustrial level of 280 to 430 ppm [2]. Fossil fuel-based power plants contributes about one third of global CO_2 emissions [3,4]. The use of alternate energy resources like solar energy, wind energy and biomass provides an option to reduce CO_2 emissions, but the current huge demand for fossil fuels suggests that such fuels still will be the predominant energy source in coming decades [5].

One possible way to reduce emissions of CO_2 from fossil fuel combustion is so called Carbon Capture and Storage. Basically, CO_2 could be captured at point sources such as power plants and transported to certain storage sites, where it could be stored and prevented from reaching the atmosphere. This way, it would be possible to continue to generate heat and power by combustion of fossil fuels, without contributing to climate change. Examples of potential storage sites are deep saline aquifers and depleted natural gas fields. Most technologies for capturing CO_2 include large scale gas separation and thus involve considerable costs and also a distinct energy penalty. Chemical looping combustion (CLC) with inherent separation of CO_2 could possibly provide cheaper and more efficient CO_2 capture compared to the alternatives [5]. The concept of chemical looping was originally proposed by Richter and Knoche [6]. Later, Ishida et al. [7] significantly contributed on this novel concept. The main idea of the CLC is to split the combustion of fossil fuels into separate oxidation and reduction reactions by introducing a suitable metal oxide as an oxygen carrier.

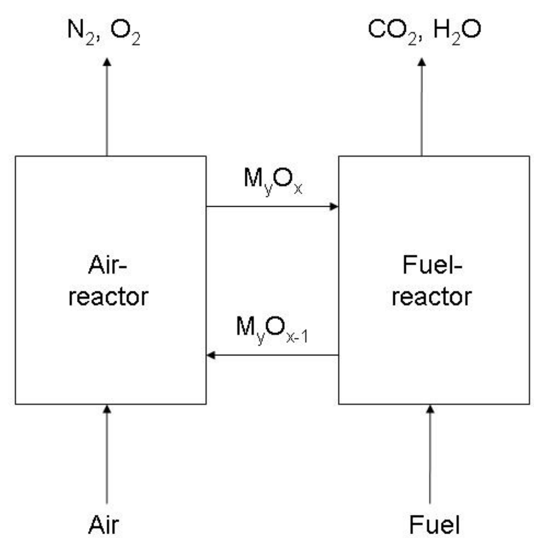

Fig. 1 Basic concept of CLC-process and oxygen carrier circulation [8]

Basic concept of CLC is illustrated at Fig. 1. Oxygen carrier circulates between an air and a fuel reactor. In the air reactor, the oxygen carrier is oxidized, which is always an exothermic reaction. The air reactor has inlet from air and outlet of depleted air. The outlet contains nitrogen and a decreased amount of oxygen. The outlet is also hotter than the inlet because of the exothermic reaction. These gases can be released without harm to nature. The oxygen carrier flow is taken to fuel reactor where a reduction reaction takes place. The reduction reaction can be either exothermic or endothermic depending on the oxygen carrier. Fuel is the inlet for fuel reaction and the outlet contains mainly CO_2 and small amounts of H_2O. This way, almost pure CO_2 is obtained after steam has been removed by condensation [9]. The reduction and the oxidation reactions are presented at Eq. 1 and 2.

This study was co-financed by European Union- European Regional Development Fund and the General Secretariat for Research and Technology Hellas, project No. 13FENCO–13–478A 'Minerals for Sustainable COst and energy efficient Chemical Looping Combustion Technology'– MINERAL SCOUT.

A.C. Psarras is with the Laboratory of Environmental Fuels and Hydrocarbons, Chemical Process and Energy Resources Institute, Centre for Research and Technology-Hellas, 6th km, Harilaou-Thermi Rd, 57001 Thermi-Thessaloniki, Greece (corresponding author to provide phone: +302310498351; fax: +302310498380; e-mail: psarras@cperi.certh.gr).

E.F. Iliopoulou is with the Laboratory of Environmental Fuels and Hydrocarbons, Chemical Process and Energy Resources Institute, Centre for Research and Technology-Hellas, 6th km, Harilaou-Thermi Rd, 57001 Thermi-Thessaloniki, Greece (e-mail: eh@cperi.certh.gr).

$$(2n+m)M_yO_x + C_nH_{2m} \Rightarrow (2n+m)M_yO_{x-1} + mH_2O + nCO_2 \quad (1)$$

$$O_2 + 2M_xO_{y-1} \Rightarrow 2M_xO_y \quad (2)$$

A main challenge in chemical looping combustion (CLC) technology is to find a cheap oxygen carrier, available in large quantities, with sufficient oxygen capacity, high reactivity in reduction by fuel gas and ability to withstand a high number of reduction / oxidation cycles, without significant physical degradation or loss in performance [10]. Since CLC technology requires significant amounts of environmentally friendly oxide carrier, the development of efficient oxygen transfer materials based on natural minerals would be advantageous.

Many oxygen carrier materials for CLC are referred in the literature, focusing on primary oxides, either as industrial waste or as synthetic materials, such as NiO, Fe_2O_3 and Mn_3O_4. Moreover, some studies of mixed oxides have appeared. In example, Fe–Mn oxides [11] and mixed metal oxides of NiO, Fe_2O_3 and Mn_3O_4 [12] attracted the research interest.

The objective of the current study is to find a mineral as oxygen carrier, available in large quantities, with sufficient oxygen capacity and ability to withstand a high number of reduction/oxidation cycles without significant loss in performance. The focus has mainly been on materials that can replace Ni/NiO which is the best performing material for natural gas, but is problematic due to cost and toxicity. For the same reasons some other elements are also considered as unwanted for CLC like As, Sb, V, Cl and Cr. On the other hand, minerals possessing high, <25%, Fe and Mn contents in their composition and a Fe/Mn ratio equal from 1 to 1/10 are fulfilling the composition criteria for an oxygen carrier candidate.

II. Experimental

A. Materials

Two Egyptian ores were selected as oxygen carrier candidates. It should be mentioned that the ores are of the same origin, but with distinct compositions. The main criteria used for selection of the candidates were; theoretical oxygen capacity, availability and non-toxicity. The significant Fe and Mn contents of these minerals are responsible for their Redox properties. The mineral materials will be referred as EGA and EGB for the high and low Mn content respectively. The materials were characterized using ICP for their composition and N_2 physisorption (BET method) for the surface area quantification. The results of the materials characterization are presented in Table I. The mineral materials were evaluated without any pretreatment, besides sieving. The particles size range was 125 – 180 μm.

Table I. Surface areas and composition of the Egyptian ores of the study

	EGA (% wt)	EGB (% wt)
Surface Area (m^2/g)	27.61	20.83
Fe_2O_3	60.05	32.71
MnO_2	23.26	39.06
SiO_2	10.94	21.40
CaO	1.31	2.47
Al_2O_3	1.92	1.28
BaO	0.92	1.44
MgO	0.61	0.61
Na_2O	0.32	0.28
ZnO	0.19	0.28
K_2O	0.22	0.18
TiO_2	0.10	0.10
Co_2O_3	0.01	0.01
NiO	0.02	0.02
V_2O_5	0.03	0.01
Cr_2O_3	0.000	0.01
CuO	0.03	0.08
PbO_2	0.03	0.03
AsO_2	0.01	0.01

B. Experimental Unit

The minerals were evaluated in an experimental set up that utilizes a single fluidized bed reactor. The reactor was designed and manufactured by high purity quartz material due to its higher thermal resistance compared to the conventional quartz. A fritted disc placed in the middle of the reactor is equally distributing the inlet gas in the cross section making the fluidization feasible. Moreover, a small quartz cyclone is adjusted to the reactor outlet in order to avoid any fine particles escape. The reactor design and the overall schematic diagram of the unit are presented in Fig. 2 and 3 respectively. A furnace is installed capable for the high temperatures necessary for the CLC process. A Mass Spectrometer (MS) is used for the analysis of the reactor outlet gas stream. The cycles are realized by switching between reductive and oxidative gas flows via separate mass flow controllers.

ISBN: 978-1-61804-325-2

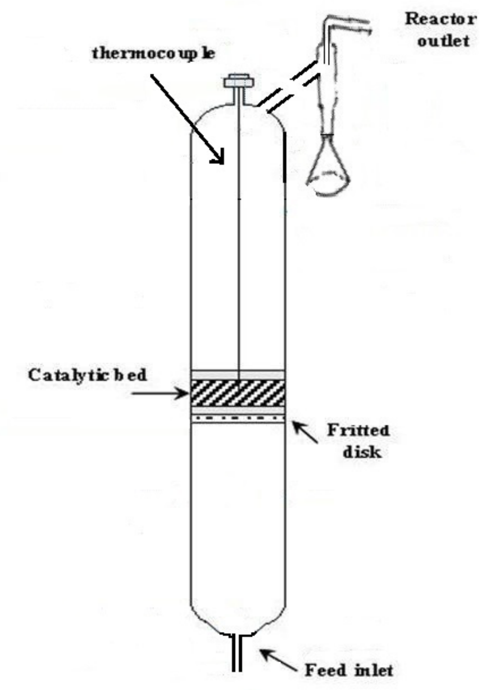

Fig. 2 Fluidized bed reactor design for CLC process

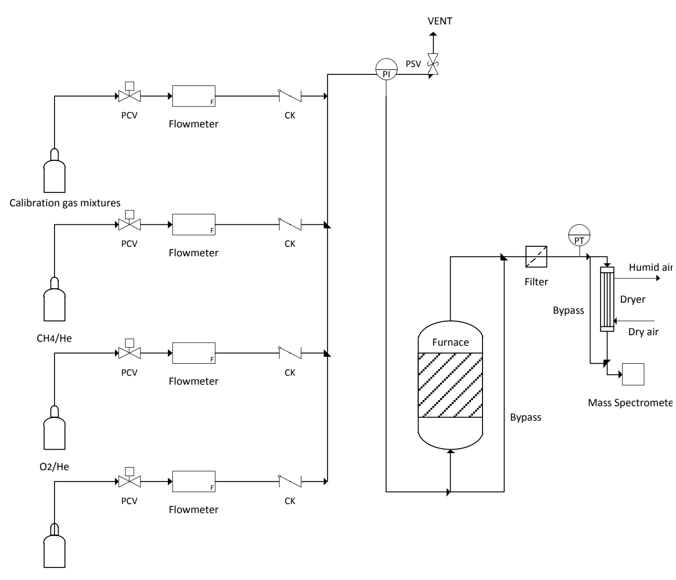

Fig. 3 Schematic diagram of the experimental unit for CLC process

C. *Evaluation protocol*

The mineral materials were evaluated as CLC candidates through a series of consecutive Redox cycles at 1000°C. Each cycle consists of a reductive and an oxidative step with a purging step in the middle and at the end of the cycle. This flushing step is used in order to avoid mixing of the reducing and the oxidizing gases. The sequence of the steps in detail is:

- Reducing step: 10% CH_4, 90% He
- Purging step: 100% He
- Oxidizing step: 20% O_2, 80% He
- Purging step: 100% He

The duration of each step is set to 30 sec for the reductive and 3 min. for the oxidative step, whereas the flushing step lasts for 5 min. to ensure that no mixing is realized. The gas flows were calculated in accordance to the minimum and the terminal fluidization velocity

III. RESULTS AND DISCUSSION

The results of the chemical looping combustion performance of the two minerals are presented in the Fig. 4 -8. The EGA mineral (Fig. 4-5) showed high activity during the first cycle, but the selectivity towards CO_2, which is the desired product, was poor. After the second cycle the selectivity was improved significantly, while the activity decayed drastically. In the following cycles the conversion of CH_4 remained low and the selectivity stabilized at 60 – 70% CO_2.

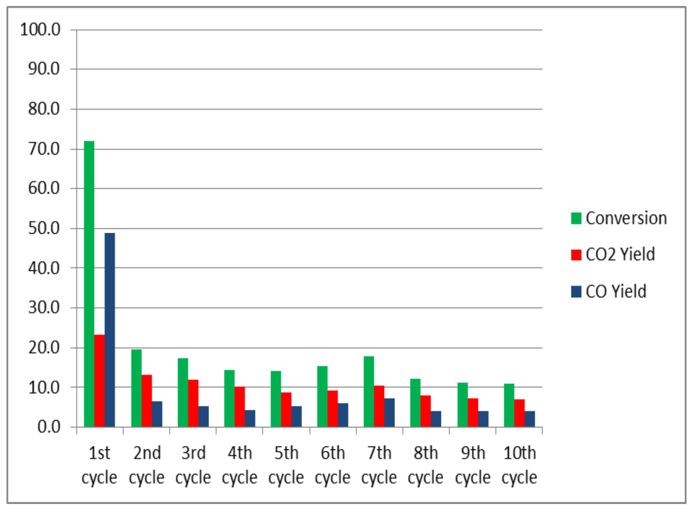

Fig. 4 Conversion (%), CO_2 and CO yields (%) over EGA mineral

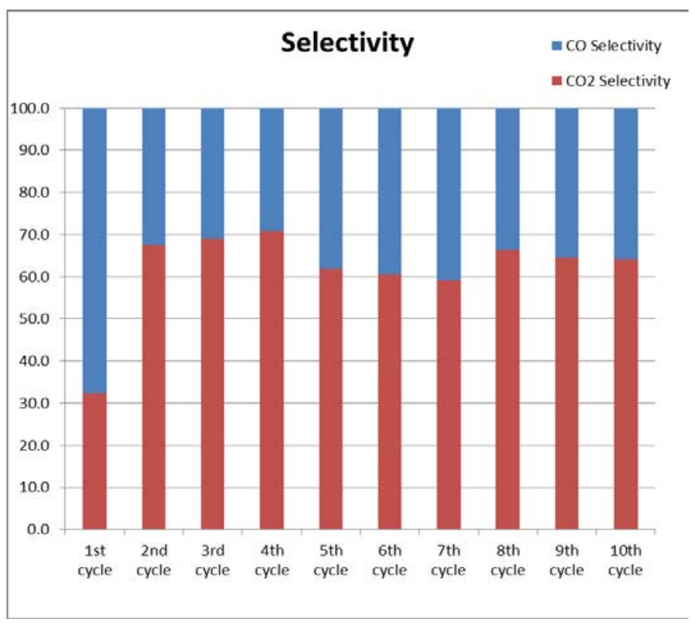

Fig. 5 CO_2 and CO selectivity over EGA mineral

The performance of EGB mineral is depicted in Fig. 6 and Fig. 7. It can be seen that the CH_4 conversion was relatively low even at the first cycle, but the selectivity towards CO_2 was very encouraging (>80%). Unfortunately, the conversion decreased throughout the consecutive experimental cycles, while the selectivity also decayed. The selectivity seems to decrease with a steady trend and the projection is far from encouraging.

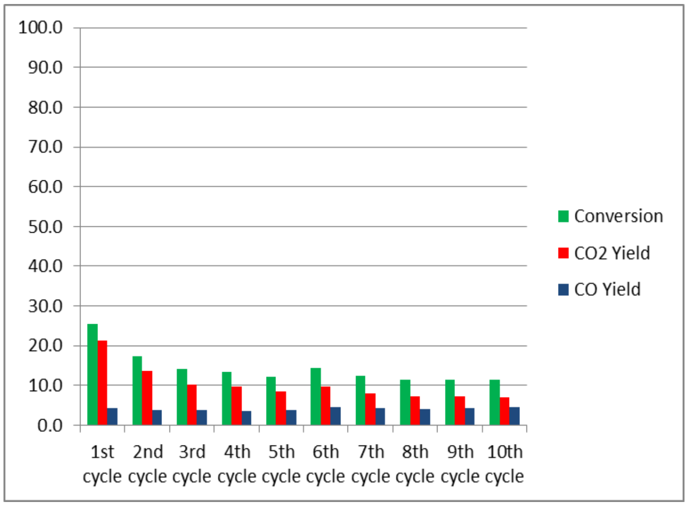

Fig. 6 Conversion (%), CO_2 and CO yields (%) over EGB mineral

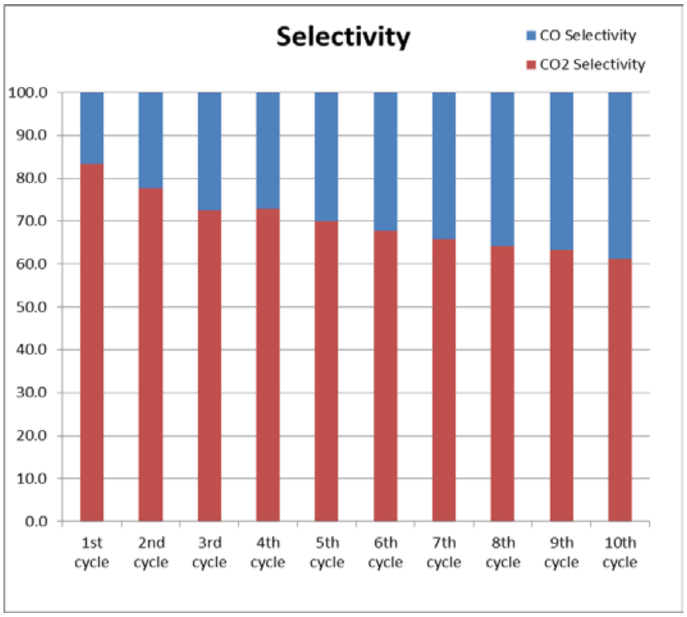

Fig. 7 CO_2 and CO selectivity over EGB mineral

The weight percentage of the solid oxygen carrier that is supplied as oxygen to the fuel gas for both minerals can be seen in Fig. 8. After the first cycle the oxygen capacity was reduced for both ores, but the decay on the EGA sample was more significant. The oxygen capacity during the subsequent cycles was very similar for both ores, but quite low compared to the theoretically calculated oxygen capacity.

The overall performance of the Egyptian ores for the chemical looping combustion process in a fluidized bed reactor showed moderate activity in methane combustion and a moderate selectivity towards CO_2. Although the potential oxygen capacity is significant, the observed oxygen release by the solid was quite low. This is probably attributed to the fluidization inside the reactor that stresses a lot the solid particles. As a result, the solids are poorly fluidized after the first Redox cycle causing problems to the mass and heat transfer inside the reaction zone.

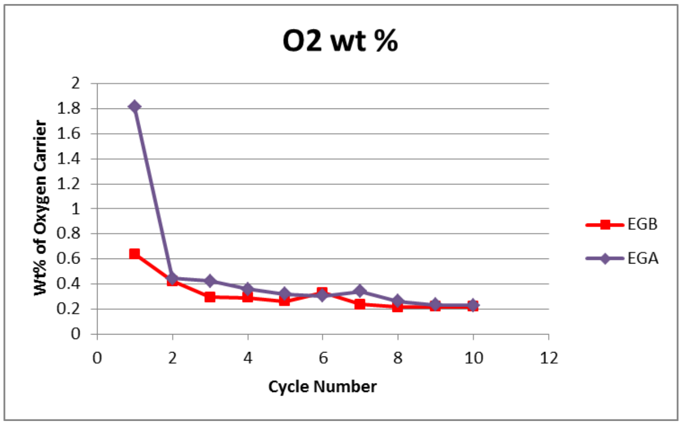

Fig. 8 Comparison of the oxygen capacity of both ores

IV. Conclusions

The two mineral materials of the present study exhibited some activity during chemical looping combustion of methane in a fluidized bed reactor. Thus, the materials are able to provide oxygen for the combustion of methane and regain the lost oxygen up to some extent in the presence of air. Their performance was moderate and their weight percentage that was provided as oxygen to the fuel gas was significantly lower than the theoretically available. This moderate performance is attributed to the gradual loss of fluidization inside the reaction zone, probably due to minerals moderate mechanical strength.

References

[1] B. Metz, O. Davidson, H. de Coninck, M. Loos, L. Meyer, *Carbon dioxide capture and storage*, Cambridge University Press: New York, 2005.

[2] B. Nordell, "Thermal pollution causes global warming", *Global and planetary change*, vol. 38, pp. 305–312, 2003

[3] A. Abad, J. Adánez, F. Garćia-Labiano, L.F. de Diego, P. Gayán, J. Celaya, "Mapping of the range of operational conditions for Cu-, Fe-, and Ni-based oxygen carriers in chemical-looping combustion", *Chemical Engineering Science*, vol. 62, pp. 533–549, 2007a

[4] W.P. Nel, C.J. Copper, "Implications of fossil fuel constraints on economic growth and global warming", *Energy Policy*, vol. 37, pp.166–180, 2009

[5] P. Hallberg, D. Jing, M. Rydén, T. Mattisson, A. Lyngfelt, "Chemical-Looping Combustion and Chemical-Looping with Oxygen Uncoupling experiments in a batch reactor using spray dried CaMn(1-x)MxO3-δ (M=Ti, Fe, Mg) particles as Oxygen Carrier", *Energy & Fuels*, vol. 27(3), pp. 1473-1481, 2013

[6] H. Richter, K. Knocke, "Reversibility of combustion processes", *American Chemical Society Symposium Series*, vol. 235, pp. 71–86, 1983

[7] M. Ishida, D. Zheng, T. Akehata, "Evaluation of a chemicallooping-combustion power-generation system by graphic exergy analysis", *Energy*, vol. 12(2), pp. 147–154, 1987

[8] M. Johansson, PhD Thesis, Chalmers University of Technology, Göteborg, Sweden, 2007
[9] M. M. Hossain & H. I. de Lasa, "Chemical-looping combustion (clc) for inherent co2 separations–a review", *Chemical Engineering Science*, vol 63(18), pp. 4433– 4451, 2008
[10] A. Fossdal, E. Bakken, B.A. Øye, C. Schøning, I. Kaus, T. Mokkelbost, Y. Larring, "Study of inexpensive oxygen carriers for chemical looping combustion," *International Journal of Greenhouse Gas Control*, vol. 5, pp. 483-488, 2011
[11] A. Lambert, C. Delquié, I. Clémeneçon, E. Comte, V. Lefebvre, J. Rousseau, B. Durand,. "Synthesis and characterization of bimetallic Fe/Mn oxides for chemical looping combustion", *Energy Procedia*, vol. 1(1), pp. 375–381, 2009
[12] M. Rydén, A. Lyngfelt, T. Mattisson, D. Chen, A. Holmen, E. Bjørgum, "Novel oxygen-carrier materials for chemical-looping combustion and chemicallooping reforming, $La_xSr_{1-x}Fe_yCo_{1-y}O_{3-\delta}$ perovskites and mixed-metal oxides of NiO, Fe_2O_3 and Mn_3O_4", *Int. J. Greenhouse Gas Control*, vol. 2, pp. 21–36, 2008

Phenomena Occurring in Achieving Integrated Circuit Boards Using Ultraviolet Light

Ion BARBU
"Transilvania" University Brasov, ibarbu@unitbv.ro

Abstract— To make a mechatronic prototype is essential to make firs a printed circuit board. Making a single board (prototype) in a factory would cost a lot, for this reason, it's needed to be found a method by which this can be done at home without any problems.

A highly precise method is presented in this project. With this method by applying a layer of photoresist on the board and by exposing it to ultraviolet radiation with a mask, printed circuit boards can be made at home easily. The same method is used in the production of printed circuit boards.

To make it possible to achieve printed circuit boards using this process, it is needed a source of ultraviolet radiation controlled by a countdown timer, named UV exposure box.

The project contains the exact description of the method and the manner of building an exposure system.

Keywords— mechatronic**,** PCB, ultraviolet, lights, photoresist, programing.

I. Introduction

A printed circuit board (PCB) is a plate that is designed to support mechanical and electronic components to make electrical connections between these components. A circuit board is made of an insulating layer with variable thickness, which is a layer of copper on one side, both sides, or multiple layers. The insulating layer is a material generally known as FR4 (Flame Retardant stands for 4) and has a thickness of 1.6 mm, but it is not the standard value. FR4 is a glass fiber material of printed wiring boards are manufactured with a thickness of 0.8 mm and 1.6 mm. Also, in general, use FR408 materials and FR5. Flexibles circuit uses a plastic called polyamide with a high temperature melting. To start making a PSB, firs of all begins with design the operational circuit (schematic design) using a specialized software to design PCB, which will be transferred on the plate using more technologies. This can be chemically or mechanically. There are many methods to make a transfer a design on plate, a good example is the transfer chemical route which are using a photoresist material, irradiated with ultraviolet beams of a specific frequency.

II. Existing Ultraviolet Sources

Ultraviolet radiation is electromagnetic radiation outside the visible light spectrum with wavelength of between 100 and 400 nanometers (nm). Ultraviolet radiation is divided into three categories:

- UV-A
    - UV-A BLB
    - UV-A BL
- UV-B
- UV-C
    - UV-V

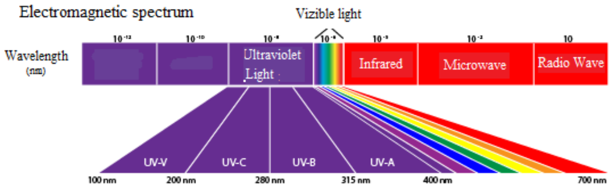

Fig.2.1. Electromagnetic spectrum that defines where are the sources of radiation and ultraviolet radiation[5]

UV-A has a wavelength range between 315-400 nanometers. There are two types of UV - A ultraviolet sources:

- UV-A BLB (black light blue) is a light source such as a fluorescent lamp having a color filter on the wall of the tube closed to prevent the passage of radiation of a certain wavelength. These types of radiation sources used most often at parties because certain materials shine like phosphorus from exposure to these types of radiation and visual effects occur.
- UV -A light source BL (Black Light) not of said filter comprises, therefore emits a radiation with a wave length comprised in a range much higher than the BLB UV -A, visible light and transmitting right . BL UV –A radiation is used for the application of photosensitizing applications photochemical reaction and traps for catching insects. For tan skin are using fluorescent radiation of wavelength between 315 and 345 nm.

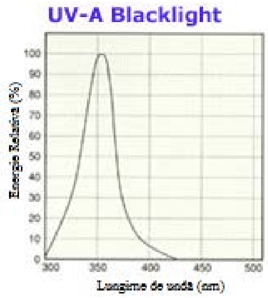

Fig. 2.2. Wavelength for UV-A BL [6]

UV-B radiation has wavelengths between 280-315 nanometers. These wavelengths are much more dangerous than the wavelengths present in the case of UV-A sources. This radiation does not penetrate deep into the skin as UV-A, but that can cause burns, cancer or other skin diseases. Ozone partial switching off of this radiation, UV-B radiation has a good side, helps the body to produce vitamin D. Sources of UV-B phototherapy are used in dermatological tests or inspections material resistance to UV radiation.

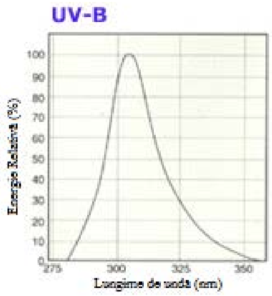

Fig. 2.3. Wavelength for UV-B BL [6]

UV-C radiation source of wavelength are typically between 200-280 nanometers. These sources are used for any infection, purify air, water, surfaces. There are sources of ultraviolet radiation in the wavelength range between 10 and 200 nm and are referred to as "Vacuum Ultraviolet" because this radiation is absorbed by air

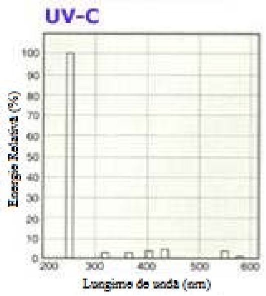

Fig. 2.4. Wavelength for UV-C [6]

III. METHOD FOR MAKING PCB'S AT HOME

There are two methods commonly used, which can be achieved using PCB's relatively simple:

- The first method is the transfer of toner to the plate with raw wiring (thermal transfer);
- The second method consists in depositing a photoresist layer wiring board raw and exposure to ultraviolet radiation plate.

In this project the focus is on the second method therefore still will briefly present the first method then describes in detail the second method. Regardless of which method is used for the first step is realizing plate printed circuit operating in specialized software for design the electronic circuits necessary to realization printed boards, in this case using EAGLE software.

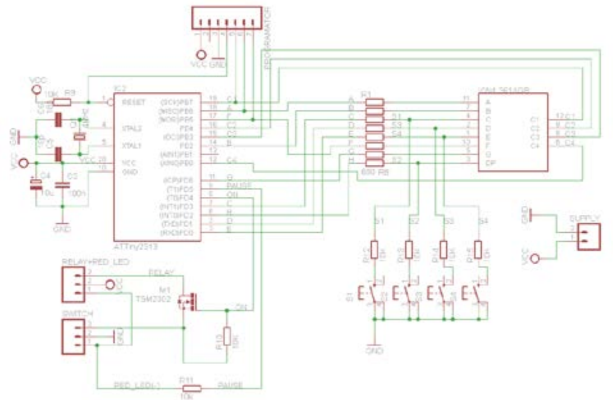
Fig.3.1. Timer circuit diagram for count the exposure time on ultraviolet for making PCB's

Circuit diagram will be transformed into an electronic circuit to be transferred to PCB.

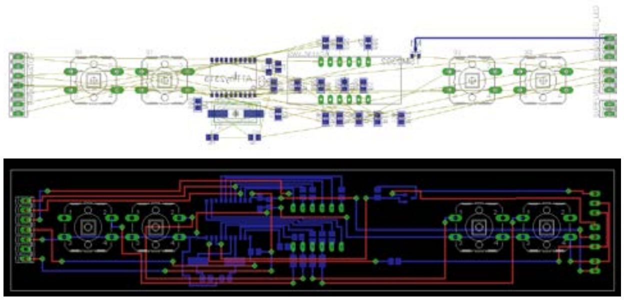
Fig.3.2. Timer circuit diagram design with EAGLE software

Once completed the design of this electronic circuit will be printed using a laser printer and a semi-transparent sheet. It is important to use a laser printer for this kind of print and semi-transparent sheet because the ultraviolet lights works better. If the sheet is perfectly transparent and glossy the lights are reflected and the process will be degraded.

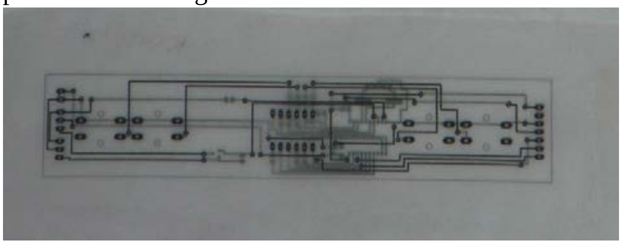
Fig.3.3. Timer circuit diagram printed on a Semitransparent sheet

The circuits were printed on a sheet temperature resistant.

It is very important that the film used to be resistant to temperature, not laser printer drum stick. There were problems transparencies, laser printer prints circuit faults (breaks) and therefore the plate is allowed more time exposed to ultraviolet light circuit lines that remain are broken plate broken sign that ultraviolet light penetrated through the imperfections printed circuit printer left, and if leave less time exposure is underexposed photoresist sign that it does not dissolve caustic soda solution later.

First cut the wiring to the desired size, rinse thoroughly with detergent. After washing, the plate does not catch your fingers copper layer. If oxidation copper layer is not going to wash the plate, it can polish with very fine sandpaper. It is not recommended to use a rough sandpaper that scratches visible copper surface for the application of photoresist lake is not distributed evenly on the plate. Positive photoresist spray 100 ml 20 covering an area of 2 m2 and 200 ml tube 4 m2 , and the range of sensitivity of the photoresist varnish is between 360-410 nm , is applied to the surface of the copper plate. Application is made in a room with very little light, the photoresist is sensitive to red light because of this is used for illumination, a red light source. After the photoresist is applied in a layer as thin as possible and as evenly distributed, the thickness of the photoresist layer greatly influences the time necessary for exposure to ultraviolet light. If the lake is not evenly distributed, it may happen that in some areas like to be under exposed. After applying photoresist lake must dry as dust quickly to block adhesion. For quick-drying plate can be inserted into an electric furnace where it is dried for 20 minutes by gradually increasing the temperature up to a maximum of 70 ° C. Above this temperature deteriorates the lake and not to be photoresist. Insert plate photoresist applied and dried between two sheets printed circuit semitransparent , stick the paper in several places so that the wiring does not move to paper.

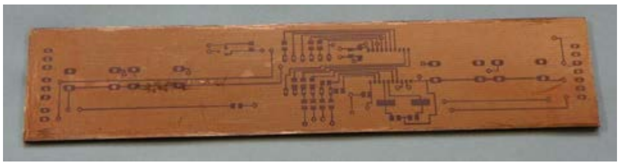

Fig.3.4. Circuit diagram transferred on the plate - side one

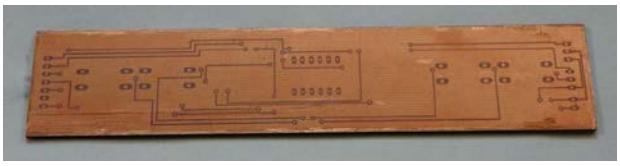

Fig.3.5. Circuit diagram transferred on the plate - side two

The whole set is introduced into the system with ultraviolet lights presented and exposed to a time - dependent radiation source , the radiation source distance from the plate , the thickness of the photoresist . After exposure the plates were placed in a solution containing 7 grams of sodium hydroxide (NaOH) dissolved in one liter of water, where the exposed photoresist material to be dissolved within 2 minutes. If dissolved means that plate was underexposed, if exposure time was too short. After this operation, the plate is placed in a solution of chloride where corrosion occurs (removal of copper which is useless)

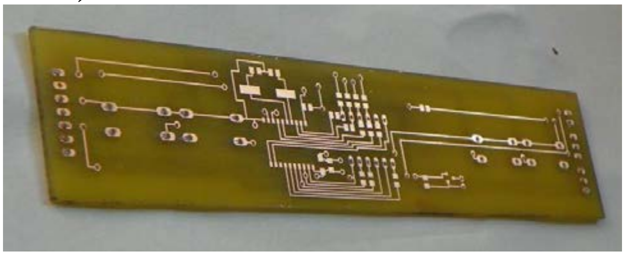

Fig.3.6. Final circuit diagram result after corrosion(removal of copper which is useless) - side one

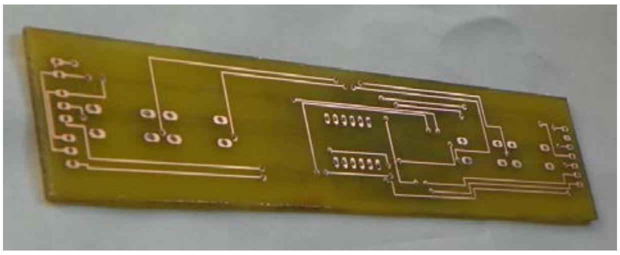

Fig.3.7. al circuit diagram result after corrosion (removal of copper which is useless) - side one

Fig.3.8. Final timer board with electronic components
- front view -

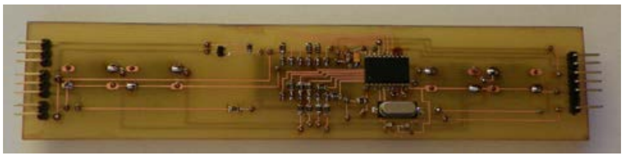

Fig.3.9. Final timer board with electronic components
- back view -

IV. HOME-MADE SYSTEM FOR EXPOSURE TO ULTRAVIOLET LIGHT

For tests was use a home-made system for exposure to ultraviolet light. The system begins with the dismantling of the old scanner inoperative. Manual exposure can be made of many things, for example in a bag or a box of

ISBN: 978-1-61804-325-2

pale, there are many possibilities. The scanner has the dimensions 450 x 260 x 48, and the glass surface is 300 x 220 mm.

Fig.4.1. Scanner housing converted to ultraviolet light exposure system use for PCB-s technology

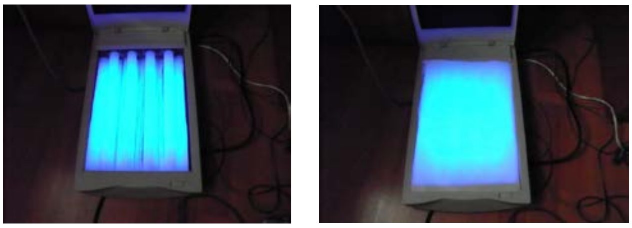

Fig.4.2. Ultraviolet light exposure system
- without semitransparent sheet put on scanner glass – left;
- with semitransparent sheet put on scanner glass – right.

To see better the areas where UV radiation is lower compared to other areas, place a thin, transparent over the scanner glass. It is seen that at the edges, especially at the ends of the fluorescent tubes radiation is much lower than the middle area. Between the tubes are observed less enlightened areas to areas above the tubes. To minimize this undesirable effect is joined a matte film that disperses light to the inside of the bottle. Sticking foil as evenly and without bubbles is such a plastic card with a little detergent dissolved in water. It put some soapy water on the glass, because glass slide film, after which the card using air bubbles to disappear all pull out.

V. Conclusion

If the lake photoresist was not applied uniformly and therefore remained a spot of photoresist that leads to the deposition of dust particles in the lake causing those spots binding line circuit , which compromise the plate.

After etching plate in ferric chloride, places remaining photoresist copper spots on the plate does not corrode.

In places where they are glued to dust (dirt) the copper remaining points, in some cases the compact circuit is a critical operation problem. If the plate was polished with an abrasive belt hard enough to apply photoresist layer applied tapers where the plate was polished, it made after exposure, the photoresist area wiped, caustic soda bath so route electronic circuit has been compromised. Due to imperfections of printing on foil after etching slight interruption occurred route points.

After exposure it is difficult to see small defects on the trail, and after etching these defects increases exponentially.

To solve the problem with printing, on transparencies mistakes instead of foil to shall to use tracing paper, if on tracing paper appear not interrupt routing problem.

The plate was exposed to UV radiation for 45 seconds on one side, and on the other side for 1 minute and 15 seconds. The part that was exposed 45 seconds track was full with lacquer discontinued route. If a face exposed 1 minute and 15 seconds the coating layer was very thin in some places even disappear altogether.

If the photoresist plate applied manually by industrial and not sprayed, the plate requires more exposure for 5-10 seconds to Positive photoresist plates 20 hand applied, but has the advantage that the photoresist is applied uniformly and in a layer very thin.

After exposure and developing the photoresist remaining on the wiring is yellow and has a very similar color to the color of copper, then before corrosion can decide if the circuit is good or not. If the photoresist is applied to a clean plate without oxidations in a very thin layer , evenly and in a clean environment can be achieved pleasing compact and thin routes close to optimal results will not hide imperfections hard to see with the eye freely and so harmful in electronic circuits.

References

[1] C. Alexandru, I.Barbu, „Modeling the Windshield Wiper Mechanisms as Multi-Body Systems" - Proceedings of the IX IFToMM International …, 2004, pp 29-34.

[2] D.M.Barbu, I.Barbu, „Dynamical model for an original mechatronical rehabilitation system" - The 8th WSEAS International Conference on System Science and Simulation in Engineering, Genova, Italy, pp. 626-273.

[3] C. Alexandru, I. Barbu „Functional Design of the Windshield Wiper Mechanisms using Virtual Models" - Proceedings of the 9th IFToMM Conference, Liberec, 2004, pp 23-28

[4] C. Alexandru, „The mechatronic model of a photovoltaic tracking system" - International Review on Modelling and Simulations, 2008, pp 64-74.

[5] http://chem-is-easy.blogspot.ro/2012/11/the-chemistry-of-skin-protection.html.

[6] http://www.topbulb.com/find/uv.asp

Strength Deterioration of Reinforced Concrete Columns Exposed to Chloride Attack

R. Greco, G.C. Marano

***Abstract*—**This paper focuses on reinforced concrete columns load carrying capacity degradation over time due to chloride induced steel pitting corrosion. The structural element is exposed to marine environment and the effects of corrosion are described by the time degradation of the axial-bending interaction diagram. Because chlorides ingress and consequent pitting corrosion propagation are both time-dependent mechanisms, the study adopts a time-variant predictive approach to evaluate residual strength of corroded reinforced concrete columns at different lifetimes. Corrosion initiation and propagation process is modelled by taking into account all the parameters, such as external environmental conditions, concrete mix proportion, concrete cover and so on, which influence the time evolution of the corrosion phenomenon and its effects on the residual strength of RC columns.

***Keywords*—** concrete structures, diffusion coefficient, marine environment, pitting corrosion, surface chloride concentration, strength deterioration.

I. Introduction

Corrosion of reinforcing steel is widely accepted as the main reason of Reinforced Concrete (RC) structures premature deterioration. One of the main sources of corrosion phenomenon is exposition to chloride attack in marine environments and de-icing salts. In these circumstances, RC members may undergo structural strength degradation due to loss of steel rebar cross sectional area and loss of bond between steel and concrete. While the strength reduction of concrete members suffering corrosion can be directly related to the reduction of the rebar area, the effects on stiffness and ductility of the overall structure are associated with complex mechanisms. These include lack of confinement due to corrosion of transversal reinforcements and bond deterioration between reinforcement and surrounding concrete. These combined mechanisms can significantly reduce in long-term local strength and global ductility and modify sensibly the structural performance during lifetime.

Moreover at present, for design of RC elements in view of special serviceability limit states, modern Codes and Standards [1] define all possible sources of RC elements deterioration and group them in environmental classes. Moreover, for each class different sub-classes are defined in relation to the aggressive level of the degradation source. Then, for each class some rules and limitations are imposed for structural design. These regard mix proportion, materials mechanical properties, working and curing conditions, minimal structural dimensions and so on. In other words, once the sources of the chemical and/or physical attacks have been identified, Technical Codes [1] impose to designers specific requirements in projects, typically concerning the minimum concrete cover, the maximum water/cement ratio, the minimum cement content, the crack width limitation, the air content, the cement type, the coating of concrete surface and others. However, no procedure is provided to assess the time decreasing of structural load carrying capacity with corrosion process evolution.

The present study focuses on the evaluation of residual strength of RC columns subject to pitting corrosion in chloride aggressive environments. Because chlorides ingress and consequent pitting corrosion propagation are both time-dependent mechanisms, the study adopts a time-variant predictive approach to evaluate residual strength of corroded columns at different lifetimes. Even if the approach here presented can be developed for all chloride induced corrosion scenarios, the study focuses on marine environments and their corresponding classes, as currently defined by European Standards [1]. In more details, the residual strength of RC columns designed according to prescriptions for XS exposure classes is evaluated in terms of axial-bending interaction diagrams at selected lifetimes. Therefore, for each XS exposure class, a consistent corrosion initiation and propagation model is developed, taking into account all the relevant factors affecting the corrosion phenomenon. These are the minimum water/cement ratio, minimum cover and minimum cement content prescribed for the specific class, critical chloride concentration, surface chloride concentration characterizing the exposure class and others.

Based on this model, time-variant axial-bending interaction diagrams for columns subject to pitting attack in marine environments are obtained, showing structural load carrying capacity reduction over time.

II. Modelling of pitting corrosion

A typical cause of RC elements degradation in aggressive chloride environments is pitting (or localized) steel corrosion. Pitting generates an iron oxide that is different from rust resulting from uniform corrosion; it presents a lower volume for unit mass, therefore it is not able to cause the disruption of the concrete cover. In particular, salts pray in marine environments and the use of deicing salts may generate

ISBN: 978-1-61804-325-2

chlorides penetrating the concrete cover and initiating corrosion. Chlorides from the environment penetrate the concrete, producing a concentration profile characterized by high chloride content at the exterior surface and decreasing content at a growing depth. The chloride content needs to arrive at a critical value to begin on the steel surface the corrosion process. After this starting event, pitting corrosion propagates and induces loss of steel rebar cross-sectional area. Different experimental investigations show that the maximum pit depth due to pitting corrosion, P_{max}, is greater than the one due to a general corrosion, P_{av}. The pitting factor R [2] is defined as:

$$R = \frac{P_{\max}}{P_{av}} > 1 \tag{1}$$

The maximum pit depth in a reinforcing bar is given by:

$$p(\mathrm{t}) = 0.0116 i_{corr} R t \tag{2}$$

In equation (1) p is in *mm*, i_{corr} is the corrosion rate, expressed as current density in $\mu A / cm^2$ (for steel, 1 $\mu A / cm^2 \approx 11.60 \mu A / yr$) t is the time (in year) since corrosion initiation time. Vu and Stewart [3] give the corrosion rate:

$$i^{(1)}{}_{corr} = \frac{3.78\left(1 - w_c\right)^{-1.54}}{c} \tag{3}$$

where wc is the water/cement ratio and c is the depth of the reinforcement (cm). However, the corrosion rate is not a fixed parameter as its value decreases with time. Duprat [4] used a decreasing factor of $t^{-0.3}$. In this study, the following law is adopted:

$$i_{corr}(t) = 0.85 i^{(1)}_{corr} t^{-0.29} \tag{4}$$

In order to define the residual area of a steel bar subject to pitting corrosion, the hemispherical- form model represented in Fig.1 is assumed [5]. Through geometrical considerations, it is possible to obtain residual steel bar area for a maximum pit depth $p(t)$ for a bar with diameter D_0.

$$a(t) = 2 p(t) \sqrt{1 - \left(\frac{p(t)}{D_0}\right)} \tag{5}$$

$$A_{pit}(t) = \begin{cases} A_1 + A_2 & if\ p(t) \leq \dfrac{D_0}{\sqrt{2}} \\ \dfrac{\pi D^2{}_0}{4} - A_1 + A_2 & if\ \dfrac{D_0}{\sqrt{2}} \leq p(t) \leq D_0 \\ \dfrac{\pi D^2{}_0}{4} & if\ p(t) \geq D_0 \end{cases} \tag{6}$$

$$\vartheta_1(t) = 2 \arcsin\left(\frac{a(t)}{D_0}\right); \vartheta_2(t) = 2 \arcsin\left(\frac{a(t)}{2 p(t)}\right) \tag{7}$$

$$\begin{aligned} A_1(t) &= 0.5\left[\vartheta_1(t)\left(\frac{D_0}{2}\right)^2 - a(t)\left|\frac{D_0}{2} - \frac{p(t)^2}{D_0}\right|\right] \\ A_2(t) &= 0.5\left[\vartheta_2(t) p(t)^2 - a(t)\frac{p(t)^2}{D_0}\right] \end{aligned} \tag{8}$$

$$A_{st}(t) = \frac{\pi D_0^2}{4} - A_{pit}(t) \tag{9}$$

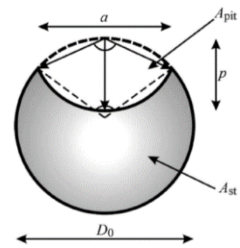

Fig. 1 Pitting corrosion model

Different models for chloride penetration have been proposed. A simplified procedure is based on the hypothesis that the ingress of chlorides is a diffusion process modeled by means of Fick's second law, as first realized by Collepardi et al. [6]:

$$C(\mathrm{x}, \mathrm{t}) = C_s\left[1 - erf\left(\frac{x}{2\sqrt{D_a t}}\right)\right] \tag{10}$$

(where $C(x,t)$ is the chloride content (kg/m3) at distance x (m) from the surface at a generic time instant t (s); Cs is the surface chloride concentration (kg/m3) and Da is the apparent diffusion coefficient (m2/years). Although equation (5) adequately describes the behavior of the concentration of chlorides in the RC structures, the assumption of a constant diffusion coefficient restricts the use of this equation. The chloride diffusion coefficient decreases with time due to several issues such as continued hydration and chloride binding. Therefore, the diffusion coefficient could be written as a power function [7]:

$$D_c(t) = D_{ref}\left(\frac{t_{ref}}{t}\right)^m = K_0 t^{-m} \tag{11}$$

where Dc (t) is the diffusion coefficient at time t; D_{ref} is the diffusion coefficient at the reference time t_{ref} and m is a constant that depends on the mix proportions. K_0 incorporates all the constants and is defined as the effective diffusion coefficient at time t_{ref}. Generally, is evaluated considering the effective diffusion coefficient at 28 days: 0 K

$$D_{ref\,(28)} = 10^{(-12.06 + 2.4 w_c)} \tag{12}$$

The ageing coefficient m in equation (11) is:

$$m = 2.5 w_c - 0.6 \tag{13}$$

For a more realistic prediction of chloride diffusion in concrete, therefore the time dependence of the diffusion coefficient needs to be incorporated into the analysis procedure, thus properly deriving Fick's second law. This model was developed by Mangat and Molloy [8], leading to the following equation:

ISBN: 978-1-61804-325-2

$$C(\mathrm{x},\mathrm{t}) = C_s \left[1 - erf \left(\frac{x}{2\sqrt{\frac{K_0}{1-m} t^{1-m}}} \right) \right] \tag{14}$$

III. CRITICAL ION CONCENTRATION

The critical chloride ion concentration (or chloride concentration threshold level) C_{crit} is one of the main parameters affecting the service life of RC structures. In fact, when a certain amount of chlorides, commonly referred "critical chloride content" C_{crit}, penetrates into the concrete cover at the level of the reinforcement deep, there is a high probability of depassivation. Schiessl and Raupach [9] stated that the critical chloride ion concentration could be defined as the chloride content that was necessary to sustain local passive film breakdown at the steel depth before the process of corrosion initiation. JSCE [10] defined the critical value of 1.2 kg/m^3 to initiate reinforcement corrosion. In effect, critical chloride value depends on the roughness of steel surface, concrete properties, and the aggressiveness of the environment.

Even if the methodology proposed in this study can be applied for all environments the study will be carried out considering chloride attack in marine environments and their corresponding classes, according to definitions currently given by the European Standards EN 1992-1 [1] (Table I).

TABLE I
EXPOSURE CLASSES RELATED CORROSION INDUCED BY CHLORIDES FROM SEA WATER

Class	Description	Informative examples
XS1	Exposed to airborne salt but not in direct contact with sea water	Structures near to or on the cost
XS2	Permanently submerged	Parts of marine structures
XS3	Tidal, splash and spray zones	Parts of marine structures

In the following, the environmental exposure class XS (corrosion induced by chlorides from sea water) will be considered. Three subclasses are distinguished: XS1, areas exposed to airborne salt but not in direct contact with sea water; XS2, permanently submerged areas; and XS3, tidal, splash and spray zones. With regard to C_{crit}, the following values are adopted in this study according to each exposure class and w_c ratio [11].

TABLE II
CRITICAL CHLORIDE CONTENT C_{CRIT} FOR XS EXPOSURE CLASSES

Water/cement ratio	XS1; XS2	XS3
$w_c \le 0.3$	0.6%	0.5%
$0.3 \le w_c \le 0.4$	0.5%	0.4%
$w_c \ge 0.4$	0.4%	0.3%

The surface chloride ion concentration depends on many factors, for example, the distance of the structure from the sea, the region of structure (i.e., atmospheric, tidal, splash, or submerged zones), and concrete properties. Several researchers have proposed close-formed solutions for both time independent and dependent surface chloride ion concentration. Costa and Appleton [12] presented an experimental study where the parameters used in the penetration model were calibrated to allow the prediction of long term chloride content in concrete. In the study, the surface chloride models were considered depending on concrete mix proportion and exposure conditions. The results showed however that the concrete mix does not affect significantly the surface chloride content.

In this study the values listed in table 3 are adopted for surface chloride concentration in marine exposure classes XS [11].

In table III, nominal values and covariance coefficients of surface chloride ion concentration for each environmental class are furnished. These data are used to define a nominal and a worst environment scenario, respectively: nominal scenario is obtained considering nominal value of chloride surface concentration, while in worst scenario, chloride surface concentration is defined as $\mu + \mathrm{cov}\,\mu$.

TABLE III
SURFACE CHLORIDE ION CONCENTRATION IN XS EXPOSURE CLASSES

Exposure class	*Nominal value*	*Cov*
XS1	2,31% (weight of binder)	0.10
XS2	6,93% (weight of binder)	0.10
XS3	4,05% (weight of binder)	0.10

IV. AXIAL –BENDING INTERACTION DIAGRAM FOR DETERIORATED RC COLUMNS IN XS EXPOSURE CLASS

For design of RC elements in view of special serviceability limit states such as corrosion due to chloride penetration, current Technical Codes impose some rules and limitations. These prescriptions regard materials compositions and their mechanical properties, working and curing conditions, minimal structural dimensions and so on. In other words, once the sources of the chemical and/or physical attacks have been identified, Technical Codes impose to designers specific requirements in projects, typically concerning the minimum concrete cover, the maximum water/cement ratio, the minimum cement content, the crack width limitation, the air content, the cement type, the coating of concrete surface and others.

Therefore, once the aggressive environment has been fixed, designers can define the maximum water/cement ratio, the strength class, the minimum cement content and the minimum concrete cover, as in Table IV. Prescription in table 4 are applicable for an "assigned expected" lifetime for common structures (50 years), and for Portland cement. For structures whose expected service life is 100 years, a larger minimum concrete cover is specified..

TABLE IV
INDICATIVE REQUIREMENTS FOR XS CLASSES

Class	Max w/c ratio	Strength class (MPa)	Minimum cement content (kg/m^3)	Minimum concrete cover (mm)
XS1	0.50	C30/37	300	35 (45 mm—100 years)
XS2	0.45	C35/45	320	40(50 mm—100 years)
XS3	0.45	C35/45	340	45(55 mm—100 years)

In this study a predictive model to evaluate deterioration of load carrying capacity of columns designed in XS exposure classes is developed. The initiation and propagation model is elaborated for XS1 exposure class assigning the admissible minimum values of concrete cover and cement content, and the maximum value of wc ratio (Table IV). Moreover, critical chloride concentration and chloride surface concentration are assumed according to literature data for the selected class. It is obvious that the quality of the evaluation depends strongly on input data. In case of chloride ingress models, a wide variation in some of involved parameters exists. Particularly, the surface chloride concentration is one of the less certain parameter ([14], [15]).

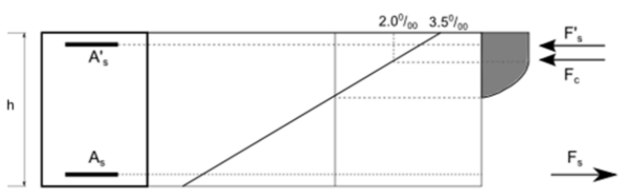

Fig. 2 Rectangular RC section whit symmetric reinforcing steel area: ultimate strain distribution diagrams and correspondent resultant forces

Interaction diagrams for RC section are generally computed by assuming a series of strain distributions, each corresponding to a particular point of the interaction diagram, and then computing the corresponding values P_{rd} and M_{rd}. Once enough such points have been computed, the results are summarized in an interaction diagram. A rectangular cross section whit symmetric reinforcing steel area is considered in this study (figure 2). For concrete, the parabola rectangle stress – strain diagram is adopted with calculus compression strength fcd. The maximum compressive strain is set at 0.0035 for neutral axis internal to the section and varying between 0.0035 and 0.002 for neutral axis external to the section (valid for fck lower than 50MPa, where fck is the concrete characteristic cube strength). For steel, the stress – strain diagram is described by an elastic perfectly plastic model in both tension and compression, with the following calculus parameters: yielding strength fyd =391,3 MPa; elastic modulus Es=200.000MPa (figure 3). The location of the neutral axis and the strain in each level of reinforcement are computed from the strain distribution. This information is then used to compute the size of the compression region and the stress in each layer of reinforcement. The forces in the concrete and steel layers are computed by multiplying the stresses by the corresponding areas on which they act. Finally, the calculus resistant axial force Prd is computed by adding forces in concrete and steel, and the calculus resistant bending moment Mrd is calculated by adding moments of these forces around section plastic centroid. The cross section of reinforcing bars varies with the time according to equations (9).

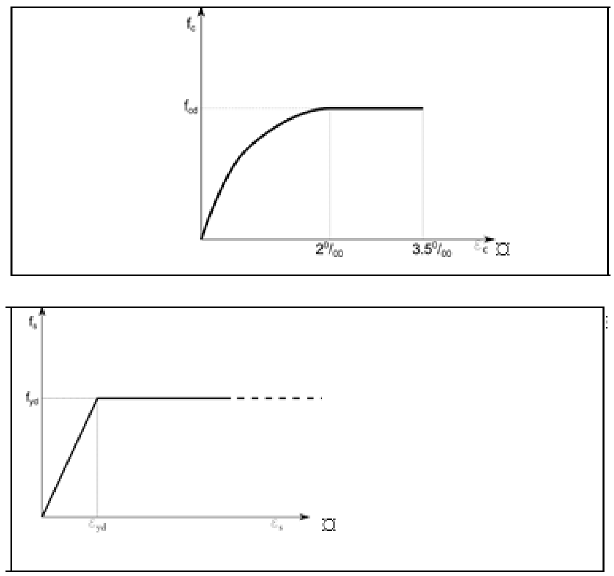

Fig. 3 Concrete and steel calculus stress-strain diagrams

A RC column with a rectangular section with dimensions b=30cm and h=50cm and symmetric reinforcing steel area is examined. The aim is to investigate the evolution of the axial-bending interaction diagram as consequence of the pitting phenomenon induced by chlorides. Calculus compression strength of the concrete is fcd=14,167 MPa. It is assumed that the structural element has been designed according to the requirements on minimum concrete cover, maximum water/cement ratio and minimum cement content for XS1 class (Table 1) for 50 years expected lifetime. Axial-bending interaction diagram is evaluated at t=0 years, t=50 years, t=100 years and t=150 years. Figure 2 shows time-variant interaction diagrams for the RC column in the XS1 exposure class assuming a nominal aggressive scenario. A low pitting factor (R=4) is considered. Results show that the strength of the column designed for a service life of 50 years decreases over the target lifetime and obvious over increasing lifetimes (100 years and 150 years). This result points out that prescriptive limits concerning the minimum concrete cover, the maximum water/cement ratio and the minimum cement content for the XS1 class don't guarantee that initial load carrying capacity of the column is the same over 50 years. If the ultimate strength corresponding to balanced rupture is considered, the reduction over the time is reported in Table 5 with reference to Mrd. The ultimate bending Mrd after 50 years is reduced of 3.65%.

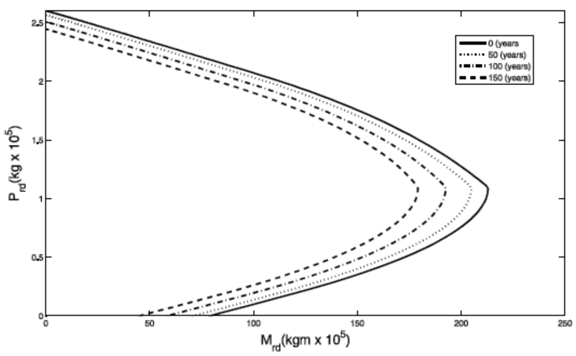

Fig. 2 Time -variant interaction diagrams for XS1 class

Corrosion of steel rebar is the most common cause of deterioration of RC members. It is the primary state that limits the service life of concrete structures, particularly, in severe environments such as marine ones. This paper presents a strength deterioration evaluation method for RC columns exposed to chloride pitting attack in marine environments, obtaining time-variant axial-bending interaction diagrams. The initiation and propagation model is elaborated for XS exposure classes, assigning the admissible minimum values of concrete cover and cement content, and the maximum value of wc ratio prescribed for each class. Moreover, critical chloride concentration and chloride surface concentration are assumed according to literature data for the selected classes.

The results obtained show that prescriptive limits for 50 years are unable to guarantee structural performances over these target lifetimes. More in detail, the minimum concrete cover prescribed for 50 years lifetime is insufficient and therefore it should be increased to guarantee unchanged performance over this target lifetime. Moreover, also the maximum water/cement ratio seems to be inadequate. The proposed model furnishes a good quantitative estimate of the remaining strength of corroded concrete columns members, which helps in establishing design details.

REFERENCES

[1] EN 1992-1-1—Eurocode 2 Design of concrete structures. Part 1-1: general rules and rules for buildings. CEN, Brussels (2004)

[2] Gonzalez, J.A., Andrade C., Alonso C., Feliu S.: Comparison of rates of general corrosion and maximum pitting penetration on concrete embedded steel reinforcement. *Cement Concrete Research* 25 (2), 257–264 (1995)

[3] Vu, K.A., Stewart, M.G.: Structural reliability of concrete bridges including improved chloride induced corrosion models. *Structural Safety* 22, 313–333 (2004)

[4] Duprat, F.: Reliability of RC beams under chloride ingress. *Construction and Building Materials* 21 (8), 1605–1616 (2007)

[5] Val, D.V., Melchers, R.E.: Reliability of deteriorating RC slab bridges. *Journal of Structural Engineering* 123 (12), 313–333 (2000)

[6] Collepardi, C.M., Marcialis, A., Turriziani, R.: Penetration of chloride ions into cement pastes and concrete. *Journal American Ceramic Society* 55 (10), 534–535 (1972)

[7] Tapan, M., Aboutaha, R.S.: Load carrying capacity of deteriorated reinforced concrete columns. *Computers and Concrete* 6(6), 473-490 (2009)

[8] Mangat, P.S., Molloy, B.T.: Prediction of longterm chloride concentration in concrete. *Material Structures* 27 (6), 338–346 (1994)

[9] Schiessl P, Raupach M.. Influence of concrete composition and microclimate on the critical chloride content in concrete. In Proc. 3rd Int. Symp. "*Corrosion of Reinforcement in Concrete*". Wishaw, UK. Elsevier Applied Science, 49-58 (1990)

[10] Japan Society of Civil Engineering: Standard specifications for concrete structures-2002, *Materials and construction* (2002)

[11] Marques PF, Costa A, Lanata F: Service life of RC structures: chloride induced corrosion: prescriptive versus performance-based methodologies. *Materials and Structure* 45, 277-296 (2012).

[12] Costa A, Appleton J: Chloride penetration into concrete in marine environment - Part I1: Prediction of long term chloride penetration. *Materials and Structures* 32, 354-359 (1999)

[13] Marano GC, Quaranta G, Sgobba S, Greco R, Mezzina M. Fuzzy reliability analysis of RC structures by using an improved time-dependent model of chloride ingress. *Structure and Infrastructure Engineering* 6(1-2): 205-223,(2010).

[14] Marano GC, Quaranta G, Mezzina M: Fuzzy Time-Dependent Reliability Analysis of RC Beams Subject to Pitting Corrosion. *Journal of Materials in Civil Engineering*, 20(9): 578-587, (2008).

Study of Dielectric Behavior of PEN (Polyethylene-Naphtalate) by Dielectric Spectroscopy

F. Benabed, T. Seghier
Laboratoire d'étude et de développement des matériaux semi conducteur et diélectriques (LED MASD),
Université Amar Telidji
Laghouat, Algérie

S.Boudrâa, M.Belkheiri
Laboratoire d'étude et de développement des matériaux semi conducteur et diélectriques (LED MASD),
Université Amar Telidji
Laghouat, Algérie

***Abstract*—The method of dielectric spectroscopy is an instrument of choice for the diagnosis of insulation used in high voltage and also to assess the quality of the insulation of HV equipment such as transformers, cables, capacitors, etc..**

This method allows to estimating the state and the quality of the insulation using the dielectric response of the frequency range. In this article, we have presented results of dielectric studies in polyethylene naphtalate by means of dielectric relaxation spectroscopy (DRS) in frequency range 10^{-2} - 10^{6} Hz and temperature between -60 and 140 °C, we will invest this method on solid insulation PEN "Polyethylene Naphtalate" to measure the dielectric properties and evaluate the performance of this insulator.

Keywords—dielectric relaxation;* polyethylene naphtalate*; dielectric spectroscopy.

I. INTRODUCTION

Solid dielectrics, namely polymers are widely used in insulation of HV systems, they are present in almost all units of production or transmission of electrical energy, which results in a steady development in the design of these dielectrics, therefore we must follow this development and improve the methods of diagnosing the condition of insulation systems for both understanding how they react vis-à-vis the implementation of a electric field in the long term and also find the parameters that come into play in the failure of these systems[1].

In this paper, we present the dielectric proprieties of : poly (ethylene naphthalate) PEN, which is widely employed in electrical Engineering, polyethylene naphthalate is a thermoplastic polyester, it is a semi-crystalline material used mainly in the electrical and electronic fields[2] .The chemical structure of PEN is shown in Fig.1.

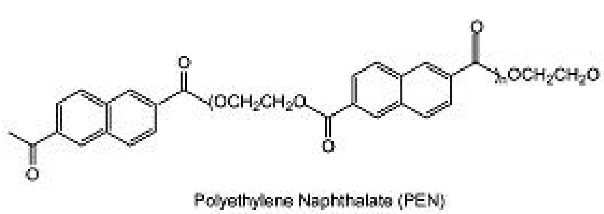

Fig.1. Chemical structure of PEN

The study of dielectric properties such as permittivity ε', conductivity σ and loss factor Tanδ for this solid material is made by dielectric spectroscopy.

II. DIELECTRIC SPECTROSCOPY

Dielectric spectroscopy, which is based on the measurement of current and voltage (amplitude and phase AC system) is a method widely used to study the dielectric properties of polymers such as (ε ', tanδ …)[3,4].

Its scope is very high frequencies (~ THz) are used to characterize all phenomena type atomic and electronic polarization, down to very low frequencies (~ MHz) to characterize the different interfaces which may exist between constituents of the material [5].

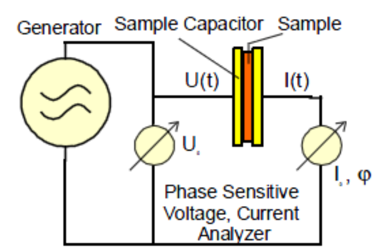

Fig.2. Principle of dielectric spectroscopy measurement

Under an alternative (ac) sinusoidal supplied voltage, the real part of permittivity and ε' and loss factor Tanδ is computed using the following equations:

$$\varepsilon^{'} = \frac{C_p\, d}{\varepsilon_0 A} \qquad (1)$$

$$tan\delta = \frac{\epsilon''}{\epsilon'} = \frac{1}{R_p C_p \omega} \qquad (2)$$

Where ε_0 is the vacuum permittivity, d the thickness of the sample polymer, A the electrode area and ω the angular frequency.

The static (dc) conductivity has been derived from the (ac) conductivity measurements at low frequency:

$$\sigma_{ac}(\omega) = \omega\varepsilon_0\varepsilon^{''}(\omega) = \sigma_{dc} + K\omega^n \qquad (3)$$

Where K is an empiric parameter and n represents the high frequency slope of the (ac)conductivity (from 0 to 1) [6].

III. EXPERIMENTAL METHOD

Measurements of the real part of the permittivity ε', the loss factor Tanδ and the conductivity for polymer samples were performed under AC voltage 1V in the frequency range 10^{-2} Hz to 1 MHz using a Broad Band Dielectric Controller (Novocontrol), Alpha, Beta Analyzer with temperature range was varied between -60 °C to 140°C.

The experimental setup is shown in Fig. 3.

Fig.3. Scheme of the experimental setup :
1 – PC, 2 – Control System (temperature and frequency),
3 – System, 4 – Measurement Cell.

The sample of the solid insulation used in this study is shown in Fig.3; circular gold electrodes were sputtered onto the free surface of the samples for this operation we used Scancoat 6 Sputter Coater for sputtering thin, high quality gold films.

The electrodes have a circular shape with a diameter of 16mm. The thickness of the samples is 0.027mm.

Fig.4. Picture of PEN the solid insulation sample.

IV. RESULTS AND DISCUSSION

The experimental results of the study of frequency and temperature dependencies of the overall loss factor Tanδ , real part of the permittivity **ε′** for the samples of PEN are illustrated in Fig.5 and 6.

From Fig.5and 6, we can see an important increasing in value of **ε′** and Tanδ at low frequencies and high temperature which can be explained by the presence of a relaxation mechanism in this domain of frequency called **α**-relaxation associated with the glass-rubber transition in the amorphous regions[7]. Also, the contribution of the conductivity effects due the bulk interfacial polarization between the amorphous and crystalline regions possibly causes this increase [8, 9].

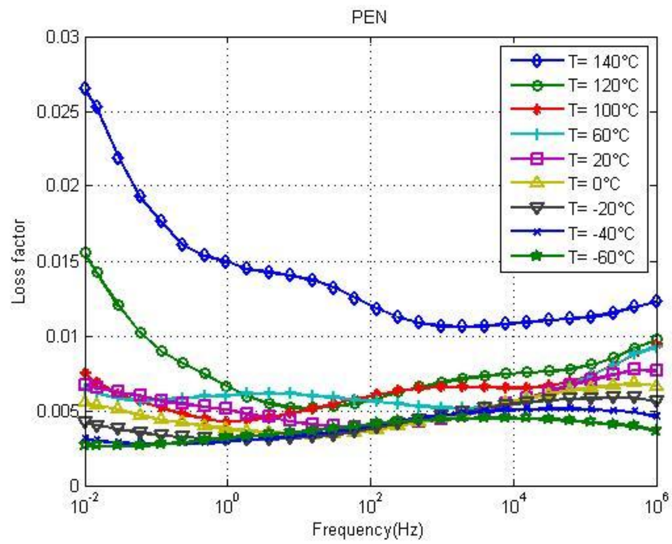

Fig.5. Loss factor Tan(δ) of PEN as function of frequency for different temperature

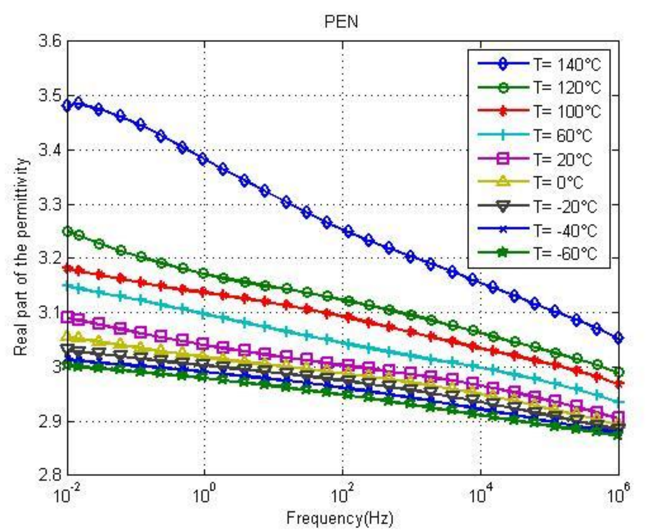

Fig.6. The real part of the permittivity **ε**’of PEN as function of frequency for different temperature

Fig.7, show the variation of the real part of conductivity σ' versus frequency for different temperatures, it is clear that σ' increases with frequency with small effect of temperature.

For more details, we presented the variations of the real part of the permittivity **ε**’, the Loss factor Tan(δ) and the real part Conductivity σ' as a function of frequency and temperature in 3D curves, on figures 8, 9 and 10 respectively.

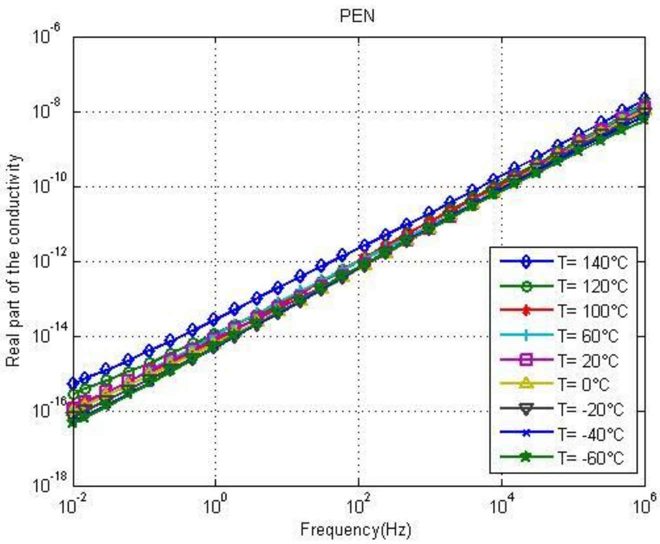

Fig.7. The real part Conductivity $\sigma'(\Omega^{-1}cm^{-1})$ of PEN as function of frequency for different temperature

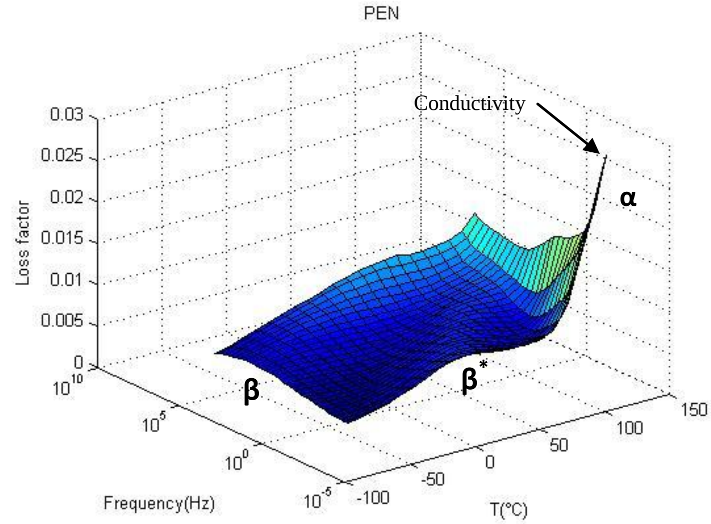

Fig.9. Loss factor $Tan(\delta)$of PEN as function of frequency and temperature

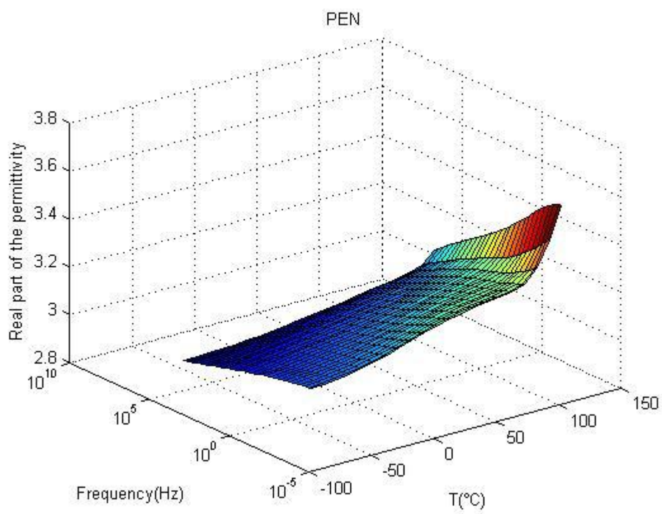

Fig.8. The real part of the permittivity ε'of PEN as function of frequency and temperature

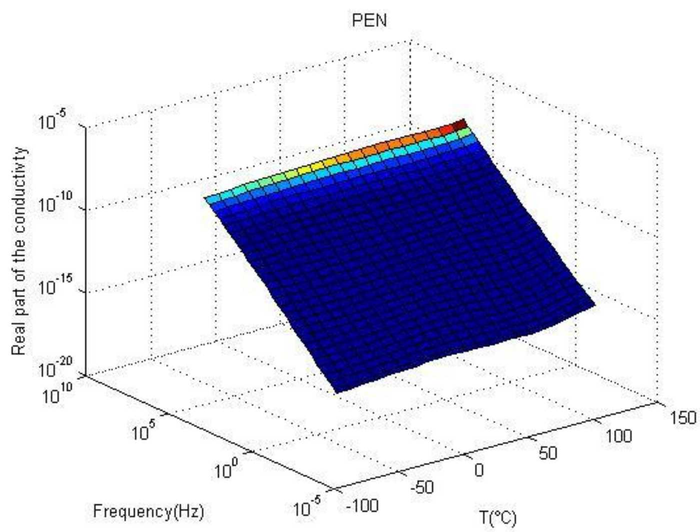

Fig.10. The real part Conductivity $\sigma'(\Omega^{-1}cm^{-1})$ of PEN as function of frequency and temperature

In Fig.8 and 10, the values of the real part of the permittivity ε' rises with temperature and decreases with frequency, in contrast to the actual values of the conductivity σ', which increases with the frequency with a slight increase when the temperature goes up to the glass transition temperature $T_g \approx 122°C$,that can be explained by the role of T_g on the motion of charge carriers[8].

In addition to the **α**-relaxation described above, from Fig.9, we note the presence of **β*** and **β** processes (in order of decreasing temperature) : The two sub-T_g, relaxations **β** and **β*** are associated to local motions of ester groups (like for PET) and to partially cooperative movements of naphthalene aggregates respectively[10]. The **β***-relaxation appears at temperatures at ≈ 80°C to 100°C and **β**-relaxation of PEN shows up at low temperatures similar to those in the case of PET [11].

Since the naphthalene group present in the repeat unit of PEN is not symmetric with respect to the main chain axis, the motions of this group about the main chain would imply changes in the dipolar moment giving rise to the **β***-process[11].

ISBN: 978-1-61804-325-2

V. Conclusion

In this work we have presented results of electrical and dielectric studies in Polyethylene Naphtalate PEN, by using of dielectric relaxation spectroscopy (DRS in frequency range 10^{-2}- 10^{6} Hz and temperature between -60 °C and 140 °C.

The obtained results show three relaxations **α, β*** and **β,** which contribute to the increasing values of the loss factor Tanδ, the real part of permittivity **ε**' and the real part of conductivity σ', when temperature goes up to the glass transition temperature T_g ,that can be explained by the role of T_g on the motion of charge carriers.

We find that the dielectric permittivity takes higher value at low frequency this fact is attributed to the contribution of the conductivity effects due the bulk interfacial polarization between the amorphous and crystalline regions

ACKNOWLEDGEMENTS

This work was performed in the laboratory OF LAPLACE at the Paul Sabatier University of Toulouse, The authors would like to thank the personal for their support in materials as well as all the collaborators of this work.

References

[1] J. P. van Bolhuis, E. Gulski, and J. J. Smit, "Monitoring and Diagnostic of Transformer Solid Insulation", IEEE Transactions on Power delivery, Vol. 17, N. 2, April 2002
[2] N. Doulache-Khemici, M.W. Khemici, A. Gourari and M. Bendaoud ,"Contribution to the Study of the Structural Relaxation of Amorphous Polyethylene Naphtalate (PEN) by DSC Experiment",IEEE, 2011, pp.135-136.
[3] E. Dantras, E. Dudognon, A. Bernès, C. Lacabanne, " Study of Polymers with Various Chemical structures and Chain architectures by thermally Stimulated Currents and Broadband Dielectric Spectroscopy", IEEE Transactions on Dielectrics and electrical Insulation, Vol. 11, pp.312-319, April 2004.
[4] O.S., Gene, S.M,. Lebedev, Y.P., Pokholkov, S.N., Tkachenko, V.A.,Volokhin, E.I,. Cherkashina, "Study of Dielectric Relaxation Spectra of Composite Materials by the Dielectric Spectroscopy Method", Proceedings of *2005* International Symposium on Electrical Insulating Materials, June *5-9.* 2005, Kitakyushu, Japan
[5] J., Ross Macdonald, "Impedance spectroscopy", Annals of Biomedical Engineering, Vol. 20, pp. 289-305, 1992.
[6] R. Khazaka, M-L Locatelli, S. Diaham , "Conductivity Spectroscopy and Conduction Current Measurements of Poly imide Thin Films during High Temperature Aging", IEEE, pp.107-108,2011.
[7] J.P.Bellomo, T.Lebey, J.M.Oraison, F.Peltier, "Comparative Study of the influence of Thermal Ageing on PET and PEN Polymers", IEEE 5th International Conference on Conduction and Breakdown in Solid Dielectrics, 1995, pp.442-46.
[8] G. G. Raju , Dielectrics in Electric Fields, New York: Marcel Dekker Inc., 2003, pp. 97–280.
[9] K. K. Chi, Dielectric phenomena in solids: with emphasis on physical concepts of electronic processes, Elsevier Academic Press, USA, 2004, pp .94-97.
[10] C. Hakme, I. Stevenson, L. David, B. Sixou, A. Voice, G. Seytre, G.Boiteux, " Molecular mobility in poly(ethy1ene naphthalene 2,6 dicarhoxylate)(PEN) dielectric films", Inrevnarionol Conference OH Solid Dielecrrics, Tortlouse. France, July 5-9, 2004.
[11] S.Farikov, Handbook of Thermoplastic Polyesters: Homopolymers, Copolymers, Blends and Composites, Wiley-VCH, Germany, 2002.

Visualisation study of an occluded artery with an "end to side" anastomosis

A. Romeos, A. Giannadakis, I. Kalogirou, K. Perrakis, T. Panidis

***Abstract*—** The hemodynamic field of an occluded artery with an 'end to side' anastomosis is studied experimentally. The influence of a distal end to side anastomosis to the formation of vortical structures and flow field evolution are discussed, via a visualisation approach, as a function of Reynolds number. In this manuscript both the steady and pulsatile flow cases are considered. Qualitative results show the influence of the inlet flow conditions (Reynolds and Womersley number) on the formation of vortical structures and the rearrangement of the hemodynamic field downstream the anastomosis.

***Keywords*—** Biofluids, Anastomosis, Stenosis, Hemodynamics

I. Introduction

THE cardiovascular system primary function is the transport of nutrient and waste throughout the body. The heart pumps blood through a sophisticated network of branching tubes. The arteries, far from inert tubes, adapt to varying flow and pressure conditions by enlarging or shrinking to meet changing hemodynamic demands. The typical Reynolds number range of blood flow in the body varies from 1 in small arterioles to approximately 4000 in the largest artery, the aorta. Thus the flow spans a range in which viscous forces are dominant on one end and inertial forces are more important on the other [1].

Atherosclerosis is a critical cardiovascular disease, characterized by the deposition of atheromatous plaques containing cholesterol and lipids on a layer on the inner walls of the large and medium-sized arteries, resulting in a reduction in the cross-sectional area of the vessel lumen and an impeded or blocked blood flow [2]. The phenomenon of atherosclerosis has been recognised as one of the most severe arterial diseases as it can lead to stenosis of arteries and consequently to heart or brain stroke.

The bypassing of critically stenosed arteries (>75%), using either an autologous vein or prosthetic graft, is a common surgical procedure. Various schemes of artery bypassing methods have been adopted by the Surgeons' community such as "end to side" or "side to side" anastomosis, sequential anastomosis, Π or Y graft anastomosis etc [3], [4].

Unfortunately, the effectiveness of the bypass is compromised in the medium and long term by the development of anastomotic Intimal Hyperplasia (IH) (accelerated growth of smooth muscle cells and surrounding matrix) [5]. This abnormal, progressive thickening of the layer of the artery inner wall is prominent at the heel, toe and along the suture line where the graft is fixed to the recipient vessel, and on the artery floor opposite the junction. Intimal hyperplasia causes the gradual narrowing of the vessel lumen, and is a major factor responsible for bypass graft failure.

Various hypotheses on the influence of local hemodynamics have been presented in the literature. In particular, the theories that are based on the influence of low or oscillating wall shear stresses at or near the anastomoses have gained attention. Several researchers [6]-[10] have shown that low shear stress and oscillating shear forces at the arterial floor and the heel, plus a high Wall Shear Stress (WSS) gradient at the toe probably promote IH development. These phenomena have been also correlated with the presence of flow separation causing vortex formation, flow recirculation, and flow stagnation at the region of anastomosis and especially where pathologic studies have reported discrete development of IH, denoting that the configuration of an anastomosis may be a factor in the localization of Intimal Hyperplasia.

The work presented below is focusing to the case of "end to side anastomosis", where there are still open issues regarding the understanding of the interaction of the vortical structure, formed due to arterial stenosis with a bypass graft and it is part of an ongoing research held in Laboratory of Applied Thermodynamics, University of Patras and the Laboratory of Fluid Mechanics, TEI of Western Greece [11]-[13].

II. Experimental Procedure

A. Experimental Configuration

The details of the experimental configuration are depicted in

May 30, 2015. This work was supported by the TEI of Western Greece's "EPEAEK-ARXIMIDIS III" Research Program., financed by The European Union & the Ministry of Education, Lifelong Learning and Religious Affairs of Greece.

A. Romeos is with the Laboratory of Fluid Mechanics, Department of Mechanical Engineering, TEI of Western Greece, (e-mail: alekosromeos@gmail.com)

A. Giannadakis is with the Laboratory of Fluid Mechanics, Department of Mechanical Engineering, TEI of Western Greece, (e-mail: ngiannad@gmail.com)

I. Kalogirou is with the Laboratory of Fluid Mechanics, Department of Mechanical Engineering, TEI of Western Greece, (e-mail: kalogirou@teiwest.gr)

K. Perrakis is with the Laboratory of Applied Thermodynamics, Department of Mechanical Engineering and Aeronautics, University of Patras (e-mail: perrakis@mech.upatras.gr)

T. Panidis is with the Laboratory of Applied Thermodynamics, Department of Mechanical Engineering and Aeronautics, University of Patras (e-mail: panidis@mech.upatras.gr).

Fig. 1. Two major flow lines co-exist, so that the experimental model of the stenosis and the anastomosis can be studied under steady (straight line) or pulsatile (dash & dash dot lines) flow conditions. Pressure and flow stabilisation are achieved through a combination of reservoirs and tanks, shown in Fig.1. Flow distribution and regulation are imposed through ball valves, while flow rate measurement is implemented through a Rotameter (steady flow) or Electromagnetic Flow Meters attached to the stenosis and anastomosis flow line (pulsatile flow). For the case of the steady flow, mass flow distribution between the stenosis and anastomosis flow line is accounted for via the continuity equation.

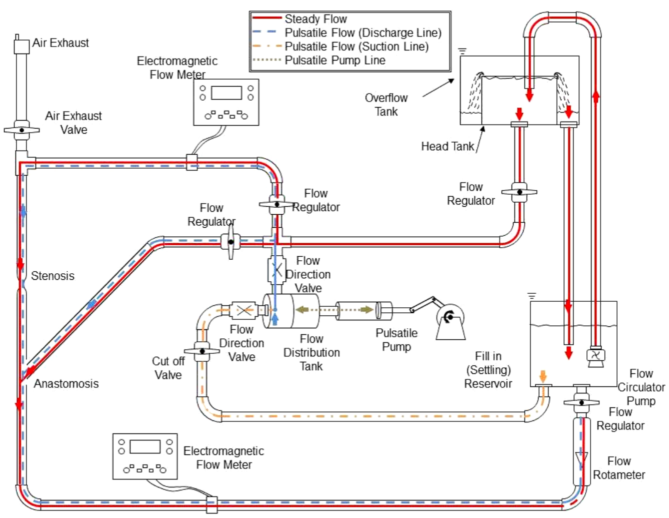

Fig.1 Experimental Apparatus Schematic

As shown in Fig. 2 the artery model under consideration is constructed by Plexiglas material that is internally machined so that index matching is achieved (the working fluid consisting of a water-glycerin mixture has a refractive index close to that of the Plexiglas), and that light difraction is decreased. Both the artery and the anastomosis models' inner diameters (tube, D) are 24 mm, while the stenosis' inner diameter (contraction, d) is 12 mm. The occlusion of the "artery model" is 75%, while the angle of insertion for the anastomotic "graft model" is 45^o.

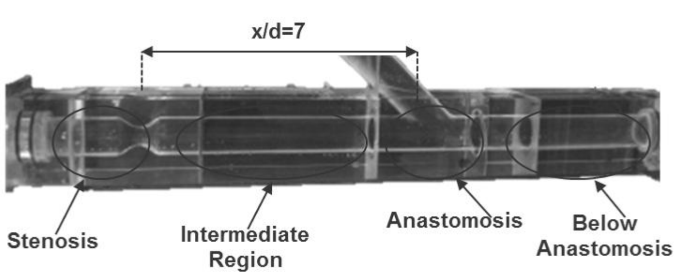

Fig.2 Experimental Configuration Design

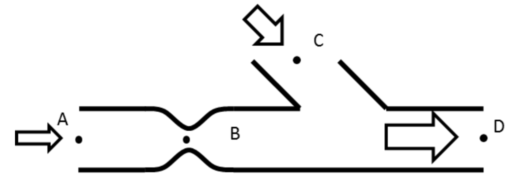

Fig. 3 Flow Configuration Schematic

B. Experimental Approach of Blood Flow

A water-glycerine mixture (55%-45%) with a dynamic viscosity similar to that of blood (μ=3.5cP) is used as the flow medium attaining similar Reynolds numbers with the modelled flow.

As the cyclic nature of the heart pump creates pulsatile conditions in all arteries, a piston driven diaphragmatic pump (Fig.4) is used to simulate heart's systolic and diastolic cycle as shown in Fig. 5. The piston's movement is controlled via a peripheral, software based, automation system simulating the heart flow cycle characteristics.

Fig.4 Pulsatile Pump

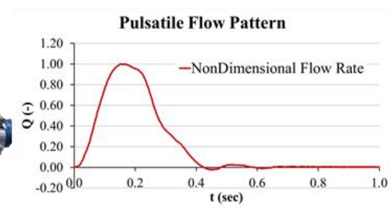

Fig. 5 Heart Cycle Simulation

C. Visualisation Technique

The visualisation of the model artery flow field was carried out by making screenshots at various successive positions along the model, as indicated in Fig. 2. The visualisation technique used was the laser sheet illumination method. A thin sheet of laser light illuminated the symmetry plane of the observation region which extended from the tube just upstream of the stenosis, to the tube immediately downstream anastomosis. Hollow glass spherical particles with mean diameter <150 μm were used as seeding material for capturing characteristic coherent structure and flow trajectory patterns. A variety of digital cameras operating at appropriate to the investigated flow attributes shutter speeds and apertures were used, to elucidate local structure. The flow rate ratio of the stenosis/anastomosis balance was specified as 35% to 65% of the total flow rate, respectively.

D. Inlet Flow Conditions

The "hemodynamic" field of the occluded "artery" model (no anastomosis present) is investigated for eight different Reynolds numbers varying from Re_A=373-933 for the case under steady flow conditions.

With the presence of the anastomosis, two Reynolds numbers Re_D= 1007 and Re_D=3183, respectively, are considered for steady flow conditions. Reynolds number is

ISBN: 978-1-61804-325-2

calculated with respect to the total mass flow rate by applying the continuity equation at point D as shown in Fig.3.

Visualisation study of the pulsatile flow case is performed by setting the total duration of the cycle to approximately 1 sec, corresponding to 60 heartbeats per minute or a supply rate of 60 cm^3/cycle. The above inflow conditions correspond to the higher supply flow rate (Re_D=3183) of the steady flow case. The corresponding Womersley number is 30.

III. Results and Discussion

A. "Hemodynamic" Field of the Occluded "Artery" Model as a Function of Reynolds Number

The main objective here is the discussion of the complex interaction field occurring in the mixing region of the flow evolving downstream of the stenosis and the bypass stream ejected in the anastomosis region.

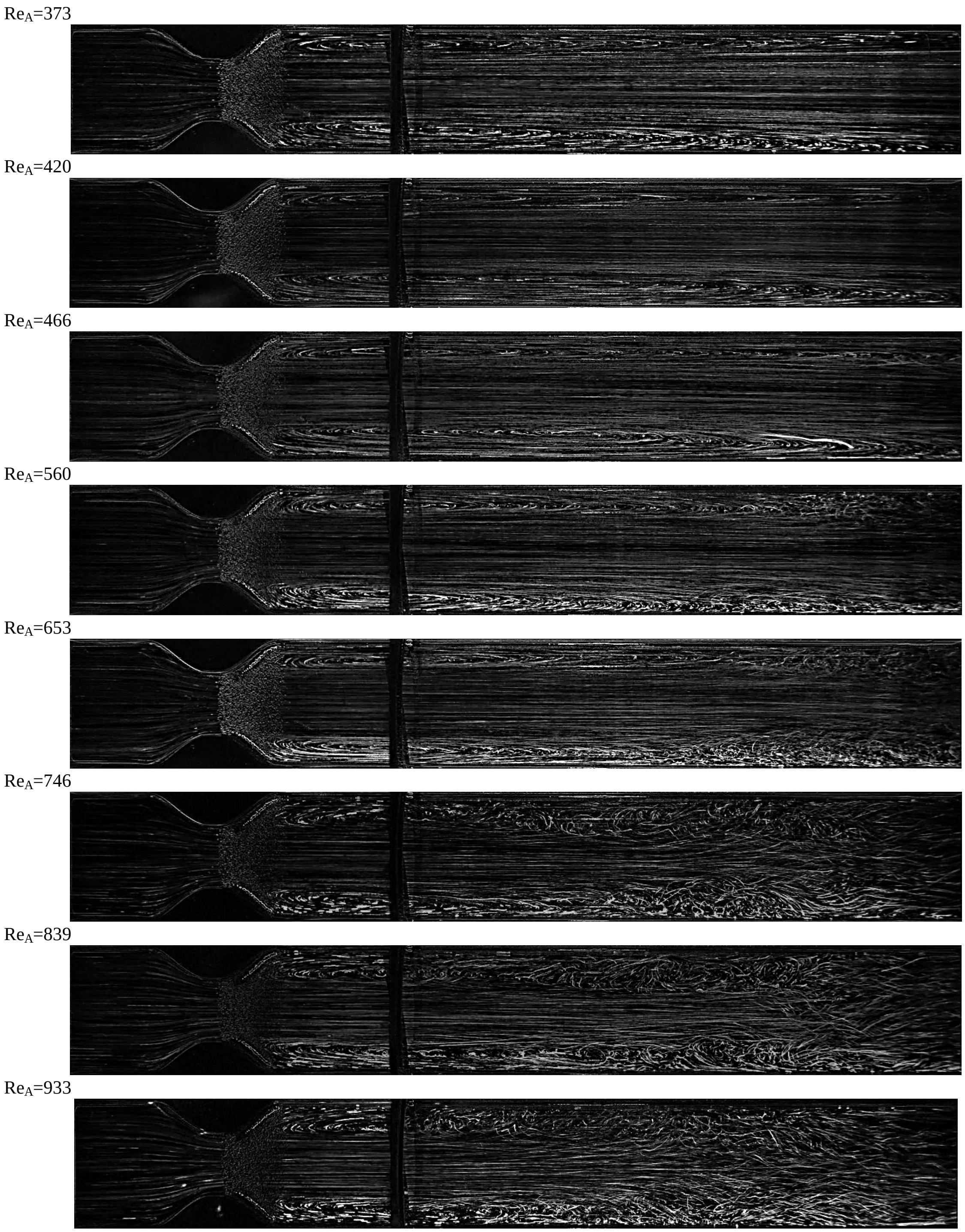

Fig. 6 "Hemodynamic" field visualisation of an "occluded" artery model

However, a better appreciation of the complicated nature of the flow regime established in the merging section of the above streams can be gained by examining the stenosis configuration in the absence of anastomosis first.

Fig.6 presents the flow patterns attained in the region immediately after the contraction of the stenosis, extending up to approximately 12 contraction diameters, d, (6 tube diameters, D) downstream as a function of Reynolds number. The Reynolds numbers indicated in the figure are based on the tube diameter (upstream or downstream of the contraction) and cover the range 373 – 933. Clearly, a jet like flow issuing from the contraction is seen to interact with swirling motions located along the tube walls in all images presented. The near wall (upper and lower) recirculating regions originate in the diverging section of the stenosis due to boundary layer separation caused by an adverse pressure gradient prevailing in this section.

The vorticity of each recirculating bubble has the same sign as that of the corresponding boundary layer over which it develops, i.e. counter clockwise and clockwise rotation in the upper and bottom duct wall respectively. However, the streamwise extent of the near wall recirculating areas decreases with increasing Reynolds number. It ranges from approximately 6D at Re=373, to approximately 2D at Re=933, suggesting an inverse proportionality between recirculation length and Reynolds number attained. Beyond those distances, recirculating bubble fluid is shed in the flow direction, the near wall swirling motion becomes diffused and mixes with the core jet flow. The mixing of the near wall recirculation zone with the initially irrotational core flow becomes more intense and is apparent in the presented images, as the Reynolds number increases. The lateral extent of the mixing patterns due to entrainment of near wall fluid into the core zone increases with increasing Reynolds number. At the same time, the central “irrotational” region diminishes in length. Within the 6D region of observation in the presented photographs (just 1D ahead the anastomosis, located at 7D in the subsequent experiments), a qualitatively different in character flow approaches the merging region with varying Reynolds number. From the relatively “unmixed” strongly inhomogeneous situation at Re=373, to an intensely mixed far more homogeneous, (compared to the low Re case), flow configuration at Re=933.

B. “Hemodynamic” Field of a Bypassed “Occluded” Artery with an “End to Side” Anastomosis: The “Steady Flow” Case

In this section a discussion is carried out regarding the development of the flow field for the case that the occluded “artery model” is by-passed with an “end to side” anastomotic “graft”. Qualitative results of the “hemodynamic” field are presented for two Reynolds numbers based on the merging flow characteristics after the anastomosis and the duct diameter, D, under steady inlet flow conditions. The low Reynolds number case (Re_D=1007 presented in Fig.7) corresponds to Re_A=353 for the inlet flow conditions prevailing upstream of the stenosis..

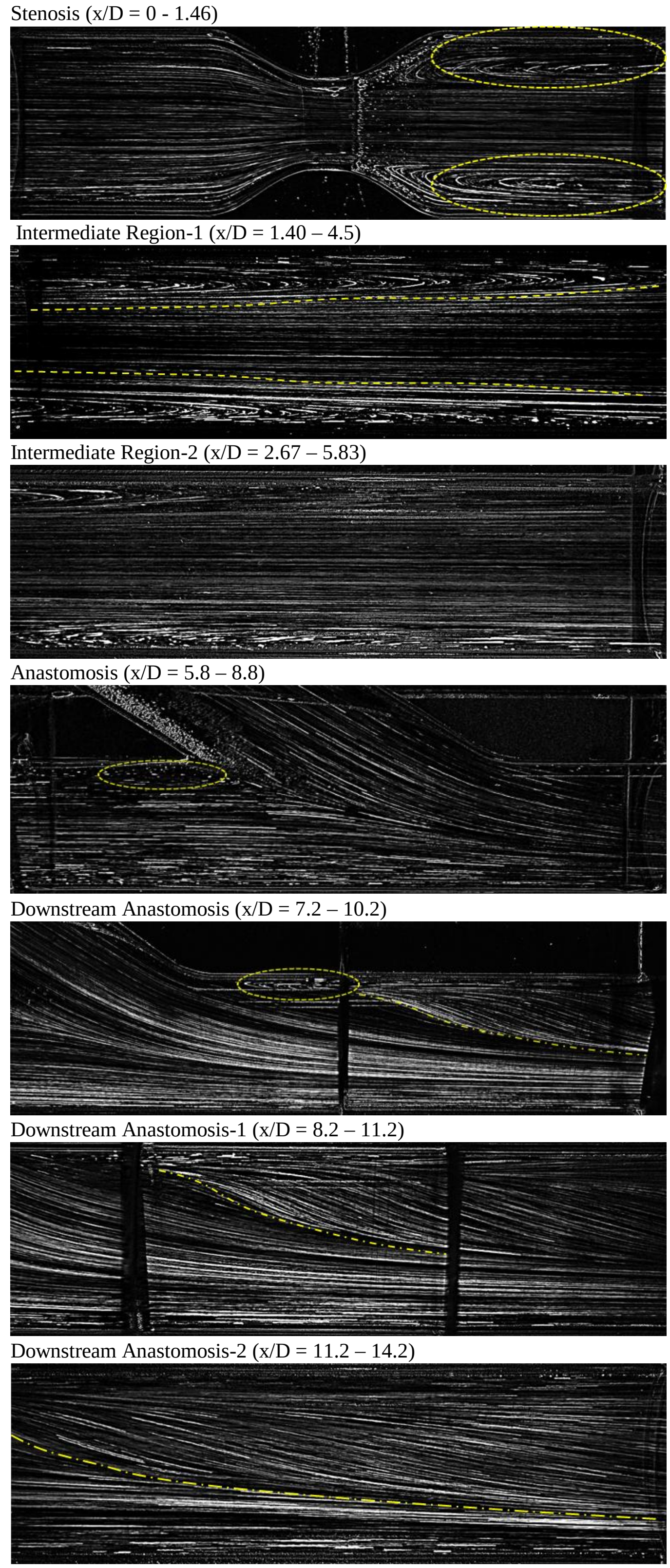

Fig. 7 Visualisation of a bypassed “occluded” artery for Re_D=1007

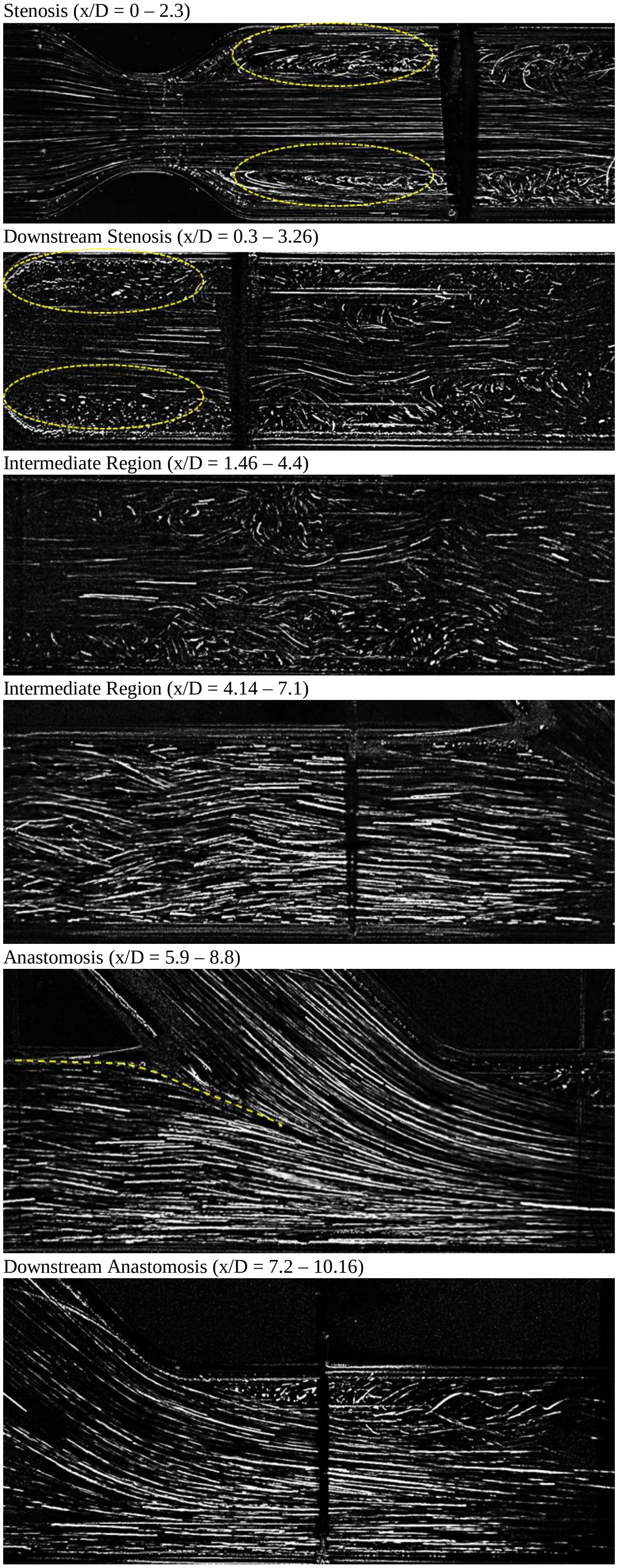

Fig. 8 Visualisation of a bypassed “occluded” artery for Re_D=3183

This configuration is quite close to the Re_A=373 case discussed in the previous section. Similarly, the high Re case (Re_D=3183 in Fig.8) corresponds to Re_A=1114 inlet condition, close to the high Re case (Re_A=933) of the occluded artery of the previous section.

The low Re case depicted in Fig. 7 exhibits identical overall signature regarding the flow approaching to the anastomosis region with the low Re occluded situation of the previous case in the absence of anastomosis. This indicates that the emerging graft flow seems to have no upstream effects. A small recirculation area with streamwise extent ~0.8D is observed at the anastomosis heel, as a result of the duct upper boundary layer blockage produced by the incoming graft fluid. Flow separation and reversal occurs on the opposite side of the anastomosis graft, at the toe region. The axial velocities are higher in the lower half of the main tube, as seen in the last four photos of Fig. 7, in a manner similar to that found when a developed flow enters a curved bend.

A far more homogeneous flow approaches the graft mixing region for the high Re case (Re_D=3183), presented in Fig. 8. In this case, it is hard to distinguish and unambiguously, clarify (as far as the visualization technique allows), the existence of a recirculation zone at the heel region. Flow separation is more intense at the toe than in the low Re case and the origin of the separation area has moved further upstream at the tip of the toe region. The high momentum inlet graft flow penetrates deeper the weak mainstream flow in this configuration as the axial velocity streakline lengths indicate.

C. “Hemodynamic” Field of a Bypassed “Occluded” Artery with an “End to Side” Anastomosis: The “Pulsatile Flow” Case

The “hemodynamic” field’s visualisation study of a bypassed “occluded” artery with an “end to side” anastomosis is discussed below for two characteristic instants of blood flow cycle: (a) maximum discharge flow rate (systolic) phase and (b) reversal (diastolic) phase. As shown in Fig. 5, these two instants correspond to the maximum flow rate (0.1 - 0.2 sec) and the reversal of flow (0.4 - 0.6 sec).

During phase (a) presented in Fig.9, strong axial motion is observed throughout the “artery” model, while secondary radial motions are observed near the walls. These secondary motions extend for about 3.0D downstream the stenosis, while strong mixing with the central jet – like motion occurs at about 3.5D downstream the stenosis in the streamwise direction. From this point downstream, flow in the artery model becomes turbulent reaching the anastomosis “heel” by having acquired fully developed flow characteristics. Flow coming from the artery model is being forced to follow the trajectory of the one entering from the “anastomotic graft” due to the significantly higher momentum. Small corner effects are observed at the “heel” of the anastomosis, where a backflow motion appears. Secondary motions reappear at the “toe” of the anastomosis and extend for about 3.5D in the streamwise direction (near the wall of the artery model), where backflow movements are

ISBN: 978-1-61804-325-2

apparent.

Backflow motion and flow recirculation trends are the main characteristics of the presented instant of the diastolic phase (b) as it is depicted in Fig. 9. Wide and spreading recirculation zones appear at the upstream side of the stenosis, while the whole of the artery model's volume is occupied by secondary vortical structures.

A characteristic feature of the diastolic phase is the fact that the recirculating structures formed downstream the anastomosis, during the systolic phase, have moved upstream, forming a wide vortex that covers almost the whole of the anastomosis's cross section area, an observation similar to that made by Hughes and How [14].

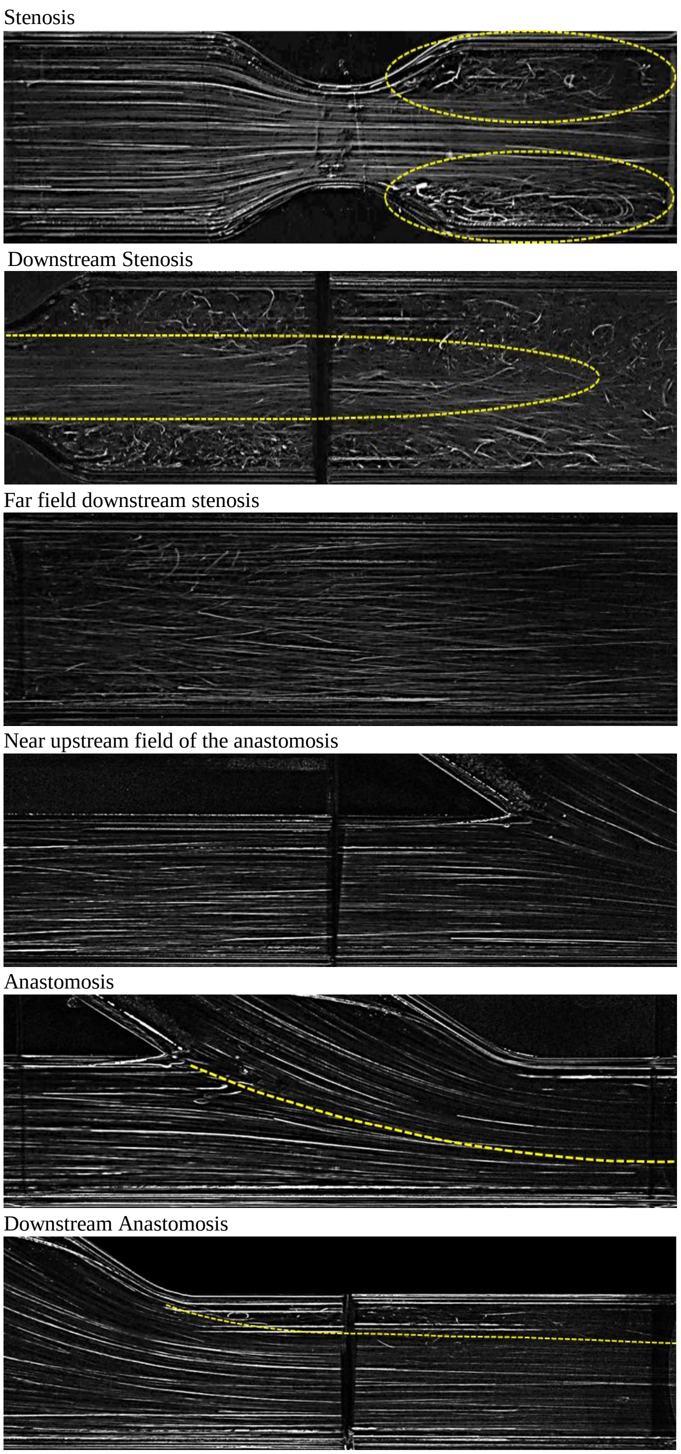

Fig. 9 Visualisation of a bypassed "occluded" artery W=30 (Systolic Phase)

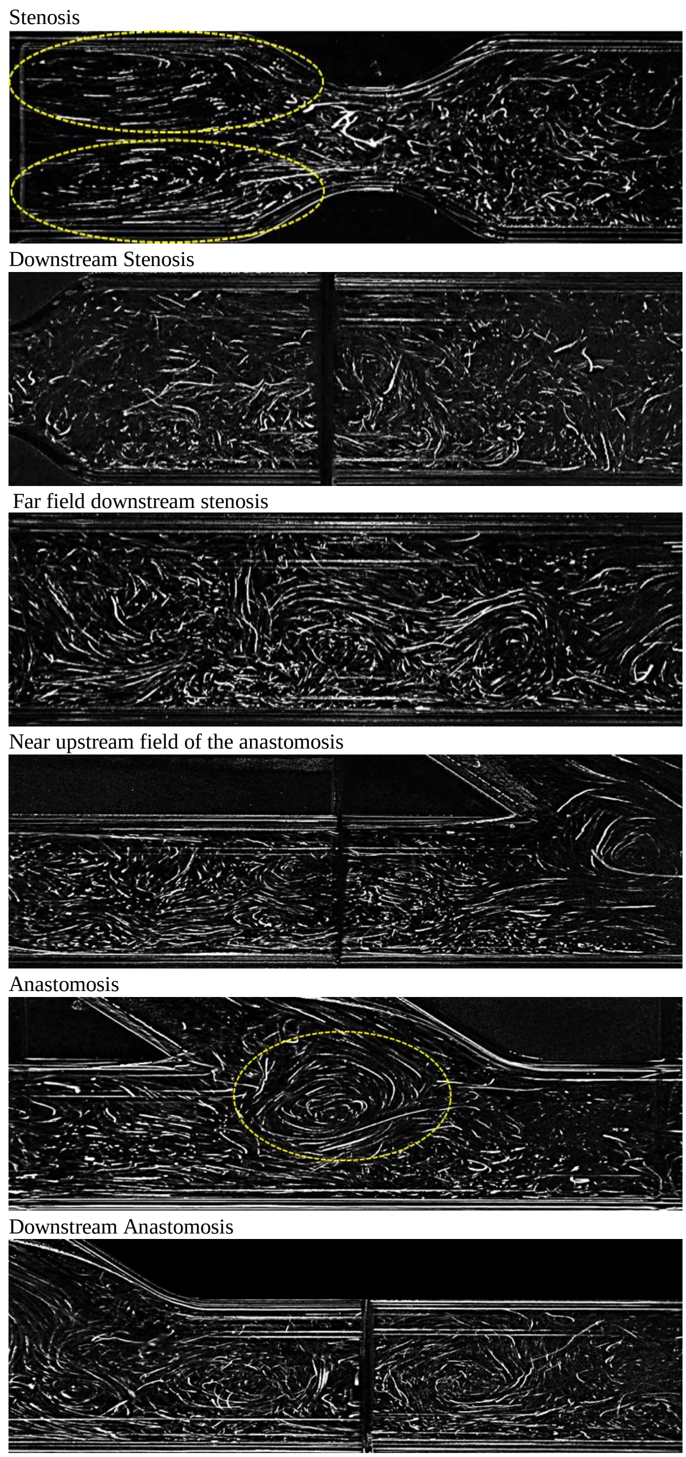

Fig. 10 Visualisation of a bypassed "occluded" artery W=30 (Diastolic Phase)

REFERENCES

[1] N. David Ku, Blood Flow in Arteries, Annu. Rev. Fluid Mech., 1997, Vol.29 , pp. 399–434,

[2] Q. Aike., L. Youjun, L. Siyang, Z. Hu, Numerical Simulation of Physiological Blood Flow in 2-way Coronary Artery Bypass Grafts, J. Biological Physics, 2005, Vol. 31: 161-182H. Poor, *An Introduction to Signal Detection and Estimation*. New York: Springer-Verlag, 1985, ch. 4.

[3] Loth F., Fischer P.F., Bassiouny H.S., 2008, Blood Flow in End to Side Anastomosis, Annu. Rev. Fluid Mech., Vol.40: 367-393

[4] Bassiouny H.S., White S., Glagov S., Choi E., Giddens D.P., Zarins C.K., 1992, Anastomotic intimal hyperplasia: mechanical injury or flow induced, J. Vasc. Surg. Vol. 15:708–16

[5] Giordana S, Sherwin SJ, Peiro J, Doorly DJ, Crane JS, et al. 2005. Local and global geometric influence on steady flow in distal anastomoses of peripheral bypass grafts. J. Biomech. Eng., Vol. 127:1087–9

[6] Keynton RS, Evancho MM, Sims RL, Rodway NV, Gobin A, Rittgers SE., 2001, Intimal hyperplasia and wall shear in arterial bypass graft distal anastomoses: an in vivo model study. J. Biomech. Eng., Vol. 123:464–7

[7] Kohler TR, Kirkman TR, Kraiss LW, Zierler BK, Clowes AW, 1991, Increased blood flow inhibits neointimal hyperplasia in endothelialized vascular grafts, Circ. Res., Vol. 69:1557–65

[8] Loth, F., Jones, S.A., Zarins, C.K., Giddens, D.P., Nassar, R.F., Glagov, S. and Bassiouny, H.S., 2002, Relative Contribution of Wall Shear Stress and Injury in Experimental Intimal Thickening at PTFE End-to-Side Arterial Anastomoses, J. Biomech. Eng., Vol.124: 44–51

[9] Politis A.K., Stavropoulos G.P., Christolis M.N., Panagopoulos P.G., Vlachos N.S., Markatos N.C., 2008, Numerical modelling of simulated blood flow in idealized composite arterial coronary grafts: Transient flow Journal of Biomechanics, Vol.41(1): 25-39

[10] Politis A.K., Stavropoulos G.P., Christolis M.N., Panagopoulos P.G., Vlachos N.S., Markatos N.C, 2007, Numerical modeling of simulated blood flow in idealized composite arterial coronary grafts: Steady state simulations Journal of Biomechanics, Vol. 40(5):1125-1136

[11] A. Giannadakis, K. Perrakis, E. Apostolakis, D. Mavrilas, Experimental and numerical investigation of the flow field in a model of human arteries (the double stenosis case), AERC 2006, 3rd Annual European Rheology Conference, April 27-29, Hersonisos – Crete, 2006

[12] A. Giannadakis, D. Mavrilas, E. Apostolakis, K. Perrakis, An approach to study the flow field in a model of sequential stenosed human arteries, Fifth World Congress of Biomechanics - Munich 2006

[13] A. Giannadakis, K. Perrakis, T. Panidis, A. Romeos, Experimental Investigation of the Hemodynamic Field of Occluded Arteries with Double Stenosis, 10th International Workshop on Biomedical Engineering, October 5-7, Kos- Greece, 2011

[14] Hughes, P.E., How, T.V, 1996, Effects of Geometry and Flow Division on Flow Structures in Models of the Distal End-to-Side Anastomosis, Journal of Biomechanics, Vol.29 (7): 855-872

Shear connection of composite steel and concrete structures using pcb-W technology

V. Přivřelová

Abstract— The paper presents one of the possibilities of shear connection of steel and concrete parts of a composite beam. Using this innovative system, called pcb-W (precast composite beam – coupled in Web) technology, the longitudinal shear forces between steel and concrete are transmitted by composite dowels instead of headed studs. The paper deals with the verification of the behavior of these composite dowels in particular with the failure modes and bearing capacity of the composite dowels and with the stress distribution in the steel dowels. At the end the paper gives some suggestions for the further development of the pcb-W technology.

Keywords—composite beams, fiber reinforced concrete, high performance concrete, high strength steel, pcb-W technology.

I. Introduction

COMPOSITE constructions are gaining more and more importance across Europe. This increase in demand leads to very innovative and more economical solutions for such composite structures. During my recent studies I focused on the topic of material strength classes, material properties and added values of materials for composite steel and concrete single supported beams designed according to [1].

The purpose of such research, mentioned also in [2]-[4], was to evaluate the most suitable cross section of steel and concrete beam with high strength materials. A further step of my research is to specify the shear connection of the steel and concrete part of the composite beam. The choice of the shear connection was highly influenced by previous parametric study and by the possibility to cooperate with the Vladimír Fišer Company. Thus, the final choice of shear connection is pcb-W technology, as was described in greater detail in [5].

The aim of this paper is to introduce this innovative system as well as the pcb technology which is the base for pcb-W technology. The paper is going to focus on the failure modes of shear connectors when using pcb-W technology; it mentions a few words about the intentions of my research and about the forthcoming laboratory test.

A. pcb construction technology

The development of pcb technology, which is the abbreviation of “precast composite beam”, was initiated by Munich engineering office Schmitt Stumpf Frühauf und Partner (today known as SSF Ingenieure GmbH) especially for composite bridges. The pcb technology can be applied to road bridges, railway bridges as well as pedestrian bridges. So far, about 300 bridges have been realized in Germany using this technology, of which approximately 150 have been designed by SSF Company [6].

In Czech Republic two road bridges, one railway bridge and a pedestrian bridge have been realized so far. The Vladimír Fišer Company bought know-how and rights to this protected solution in 2010 and continues with the development.

Pcb girders are composite elements that consist of an open or closed welded steel-section and a thin prefabricated concrete flange, see Fig. 1. Such elements are completed with additional concrete on the construction site which is especially economic and time-efficient since no formwork is required. The shear transmission between steel and concrete is accomplished by headed studs using short studs for the prefabricated concrete and longer ones for in-situ concrete [7]. The prefabricated concrete flange is engaged as structural concrete and as formwork for covering in-situ concrete plate. After setting the prefabricated girders on sub-structure the concrete deck is cast in-situ without any further formwork. This is a big advantage especially for bridges crossing existing railways or highways, because the closure of traffic ways underneath can be minimized to only a few minutes for the assembling of each girder.

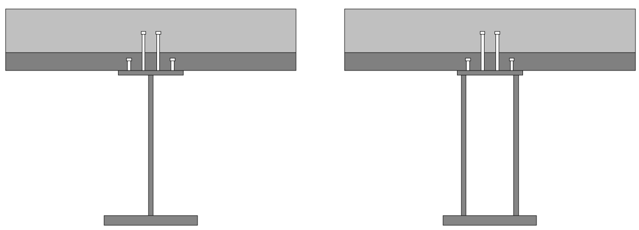

Fig. 1: Open and closed pcb girder

B. pcb-W technology

For the bridge spans up to 30 m and high slenderness of the bridge fields it is worth to leave out the upper steel flange and use the pcb-W technology. It is the combination of pcb technology and a method of rolled girders in concrete (W), which is a traditional method used frequently for railway bridges since the 1st half of 20th century. The rolled girders are with this method cast-in in a concrete slab. However, the rate of bridges using this method has been degreasing for the last decades due to high consumption of steel, high costs and

The presented results were obtained with the support of the project FAST-J-15-2695.

bad dynamic properties [8].

Since 2003 SSF Ingenieure GmbH has been developing the pcb-W construction method, which combines the advantages of pcb and W construction technologies. Pcb-W (precast composite beam coupled in web) uses rolled sections cut into two halves along the web using a specific cutting geometry that two T-sections arise. These T-sections are embedded into lower part of concrete deck or into a concrete beam which generates the composite dowels, see Fig. 2.

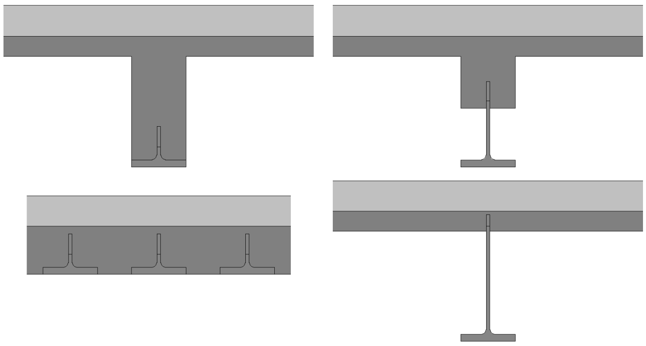

Fig. 2: Cross-sections pf pcb-W girders

The longitudinal shear force is then transformed by these composite dowels instead of headed studs. This system leads to great economic advantages compared to welded sections because material-consumptions for the upper flange, headed studs and effort for welding can be saved. Major advantage of external reinforcement elements compared to conventional concrete or pre-stressed solutions is an increased internal lever arm (Fig. 3). Compared to pre-stressed cross-sections an increase up to 20% can be realized for the internal lever arm which leads to more efficient cross-sections with considerably increased stiffness and more economical use of materials [7].

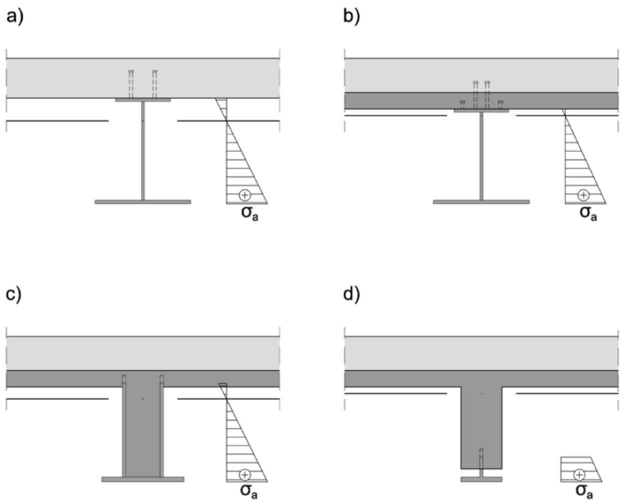

Fig. 3: Stress distribution on: a) common composite steel and concrete beam, b) pcb girder, c) + d) pcb-W girder [5]

Pcb-W girders can be used in industrial buildings and bridges due to their high strength, high stiffness and large slenderness at the same time. Mainly for railway bridges the high strength and convenient slenderness providing small deformation is desirable. The composite dowels provide a high fatigue bearing capacity.

II. Failure modes of composite dowels

The bearing capacity of a composite dowel is limited by steel or concrete failure. In a good design both failures of a steel and concrete dowel are balanced up to the maximum load.

Steel failure is limited in the ultimate limit state by the shear resistance, yielding due to bending of the dowel and in the fatigue limit state by fatigue cracks due to dynamic loading.

Concrete failure is characterized by several failure modes. Which mode finally occurs depends on the boundary conditions like geometry, concrete grade, reinforcement design, adding of fibers etc. [9].

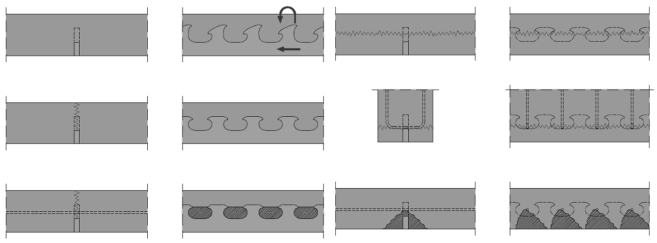

Fig. 4: Failure modes of composite dowels – yielding of steel dowel by bending and shearing, vertical crack in the non-reinforced concrete deck, shearing of concrete dowel, horizontal crack in concrete deck, spalling of concrete cover, pry-out cone in the concrete cover [7]

The standard push-out tests according to [1] have been performed at the University of Federal Army in Munich to investigate new geometry of cut-line developed by SSF. It has been concluded, that the ULS resistance of the steel is almost independent from the shape of the dowel. However fatigue cracks have been observed. So far, the MCL shape dowels seem to have the best fatigue load bearing capacity.

III. Verification of composite dowels´ behavior

The main aim of my recent work is to verify the behavior of the composite dowels in particular to determine the bearing capacity of both steel and concrete dowels, decide which failure mode finally occurs, what is the influence of using high strength steel or high performance concrete and to specify the necessary reinforcement area in the concrete dowels.

The results of this work are required for further development of pcb-W technology.

I have divided the amount of work into three major steps. The first step includes the choice of material strength grades, geometry of composite dowels and calculation of the bearing capacity of steel and concrete dowels. Such parameters are based on the results of a parametric study. The second step is to verify the results of the first step using FEM modeling. For determining the bearing capacity of shear connectors

ISBN: 978-1-61804-325-2

according to [1] it is common practice to perform standard push out test. Therefore the FEM numerical models are arranged in order to meet the requirements of standard push out test. The third step, which is for the large volume of information not included in this papers, is the standard push out test itself.

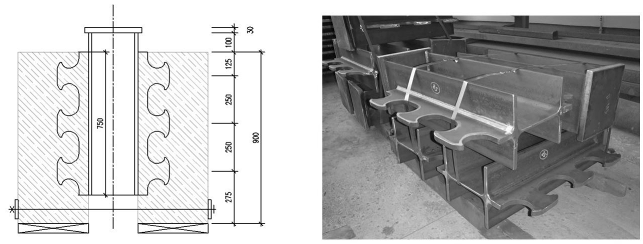

Fig. 5: The geometry of the numerical model meets the requirements of standard push out test

A. The material properties

The choice of strength grades of steel and concrete dowels is based on the results of previous parametric study. The main aim of the study was to find the most effective combination of high strength steel and high performance concrete. It is very important to choose the strength grades properly, since there were several cases identified in the study, where the bearing capacity of a composite cross-section was lower with the use of steel of higher strength grade than with the use of lower strength grade.

Taking into account the results of parametric study and parameters of available molding machine, the strength grade of steel and concrete were chosen according to Table 1 and 2.

Table 1: The properties of steel cross-section

Strength grade of steel	**Yield strength**	**Ultimate strength**	**Axial distance between dowels**	**Thickness of the steel plate**
-	f_y [MPa]	f_u [MPa]	a [mm]	t [mm]
S 355	355	490	250	20

Table 2: The properties of concrete deck

Strength grade of concrete	**Char. comp. strength**	**Reinforcement of concrete dowel**	**Reinforcement above concrete dowel**	**Thickness of concrete deck**
-	[MPa]	A_b	A_t	h_c [mm]
C 30/37	30	2ϕ12	2ϕ12	230

With the given parameters, the bearing capacity of the concrete dowel was calculated according to [7]. The values of the bearing capacities for all the possible failure modes related to the bearing capacity of the steel dowel are given in Table 3.

Table 3: The bearing capacities of concrete dowel related to the bearing capacity of steel dowel

Design of steel dowel	**Shearing of concrete dowel**	**Pry-out cone in the concrete cover**	**Spalling of the concrete cover**
$P_{pl,k}$	$P_{sh,k}$	$P_{po,k}$	$P_{cov,k}$
$\mathbf{P_{pl,k}}$	**1,65·$P_{pl,k}$**	**0,63·$P_{pl,k}$**	**0,38·$P_{pl,k}$**

The results show, that with the chosen configuration of the composite cross-section, the critical failure modes for ULS are spalling of the concrete cover and pry-out cone in the concrete cover, which are mainly affected by the reinforcement area.

B. Numerical models

To verify the behavior of the composite dowels during standard push out test, the numerical model was created in FEM software RFEM of the Dlubal Software Ltd. Company. The geometric parameters of the model corresponds to those of the specimens for the standard push out test, see Fig. 6.

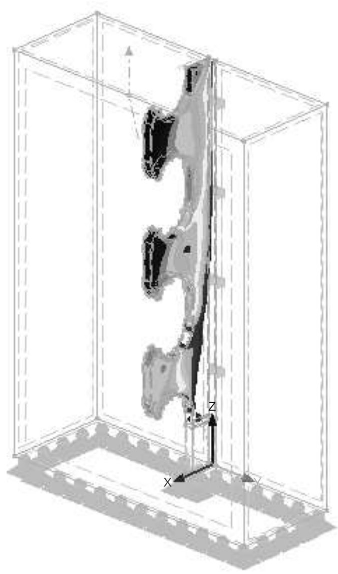

Fig. 6: The numerical model

The model was exposed to different load conditions, that correspond to the values of bearing capacity of composite dowels for all the failure modes, Fig. 7. The numerical model shows, that the first failure to appear is the concrete failure.

C. Determining of the location with the greatest value of stress - HOT SPOT

Another purpose of the numerical model is to specify the stress distribution which is important for comparison with results of an experiment.

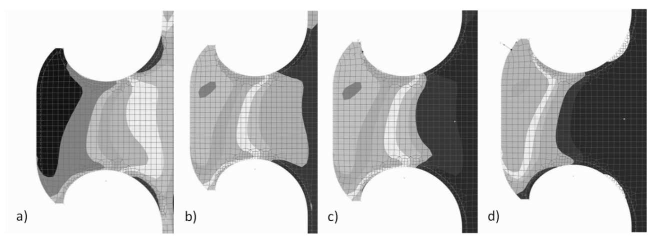

Fig. 7: FEM model, stress distribution in steel dowel under different load condition

Thanks to the numerical model, it is possible to identify the place with the highest value of the stress, so called HOT SPOT. This is the place where the strain gauges are located in

ISBN: 978-1-61804-325-2

the third step for comparing the results of the numerical model and an experiment, see Fig. 8.

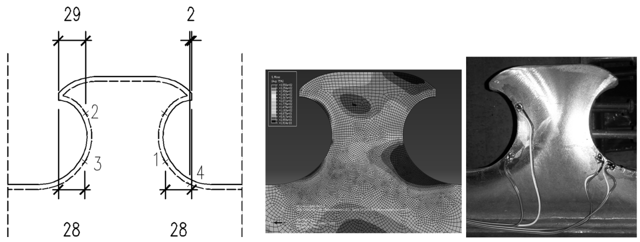

Fig. 8: Location of HOT SPOT

IV. Conclusion

The paper presents several important outcomes of my recent work on composite steel and concrete structures using pcb-W technology. One of the main aspects is the determination of the right material strength grades, which is very important since it influences the behavior of the composite cross-section and load bearing capacity of the composite dowel as well. The choice of the material strength grades was based on the parametric study.

The further step is the verification of the composite dowel which consists of numerical approach according to [7], numerical modeling and experimental verification which is not part of this paper. So far, the results shows, that the first failure to occur is the concrete failure.

The bearing capacity of the concrete dowel is mainly affected by the reinforcement area. The minimum or recommended area of the reinforcement is given in [7]. If greater bearing capacity of concrete dowel was required, it would be possible to employ more reinforcement bars or use reinforcement bars of larger diameters. However, we have to consider the armoring and mounting of the structure which is more complicated the more reinforcement we use, see Fig. 9.

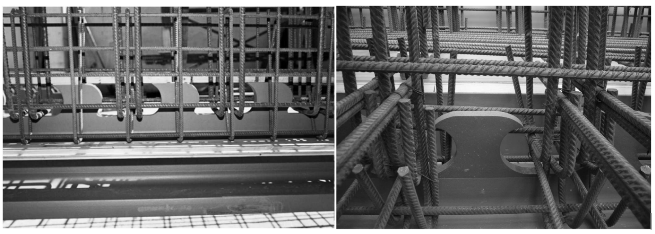

Fig. 9: Examples of reinforcement of composite dowels

For this reason, another specimens are prepared for the standard push-out test, some with common concrete and recommended area of reinforcement and some with fiber reinforced concrete and lower degree of reinforcement. The results of this upcoming experiment may be useful for further development of pcb-W technology since they may allow to use less reinforcement in the concrete dowel to make the technology even less laborious to manufacture.

The pcb-W technology is quite a newborn in composite steel and concrete structures given that the method has been developing since 2003. In Czech republic, this innovative system has been used since 2010 and several laboratory test have been made. So far, the technology uses only common concrete. However the ongoing laboratory tests show very promising results with fiber reinforced concrete. The combination of pcb-W technology and fiber reinforced concrete promises wide use in bridge construction for its economical, structural and low laborious advantages.

References

[1] ČSN EN 1994-1-1. *Eurokód 4: Navrhování spřažených ocelobetonových konstrukcí – Část 1-1: Obecná pravidla a pravidla pro pozemní stavby.* Praha: Český normalizační institute. 2006. 101 s.

[2] PŘIVŘELOVÁ, V. *Optimization of composite steel and concrete beams in terms of the influence of material strength on carrying capacity - parametric study.* Published in JUNIORSTAV 2014, Brno. 2014.

[3] PŘIVŘELOVÁ, V. *Optimization of composite steel and concrete beams with lightweight concrete deck in terms of the influence of material strength on carrying capacity – parametric study.* Published in 6th Ph.D. Student Conference of Civil Engineering and Architecture Young Scientist, Herlany. 2014. ISBN-978-80-553-11668-0.

[4] PŘIVŘELOVÁ, V. *Modelling of Composite Steel and Concrete Beam with the Lightweight Concrete Slab. International Journal of Civil, Architectural, Structural and Construction Engineering, Volume 8, Number 11.* World Academy of Science. 2014. ISSN-1307-6892. P 1070-1074.

[5] PŘIVŘELOVÁ, V. *The use of pcb-w technology and concrete with added value in composite steel and concrete structures.* In: 17. odborná konference doktorského studia Juniorstav 2015, Brno. 2015. ISBN 978-80-214-5091-2.

[6] BUBA, R. *Mosty v technologii VFT®. Příručka pro projektanty a výrobu.* München. 2010. 42 s.

[7] SEIDL, G. - HOYER, O. *WFT - WIB Technology. Design, Construction and Applications.* Berlin. 2012. 103 s.

[8] SCHMITT, V. - BUBA, R. *Innovative Building Methods for Bridges with Small and Medium Spans - VFT and VFT-WIB.* Sborník konference Steel Bridges. Praha. 2006. Str. 66 - 74.

[9] HECHLER, O., LORENC, W., SEIDL, G., VIEFHUES, E. *Continuous shear connectors in bridge construction.*

V. Přivřelová (M´15) was born in Olomouc, Czech republic in 1987. She graduated in 2013 at Brno University of Technology and got the degree Master of Civil Engineering (Ing.). Her major was Steel structures and Building construction. She also got Bachelor´s degree in Law at Masaryk University in Brno. Her major field of study was Land law and Real estate register. In 2009/2010 she had an internship at Vilniaus Gedimino technikos universitetas in Vilnius, Lithuania. So far, the author continues with her studies to get the Doctorś degree of Civil engineering. So far, she is in her third year of study.

She gained work experience in Statika Olomouc Ltd. during her studies (2011 - 2014). Her occupation was designer of steel, timber and concrete structures. Currently she works in Vladimír Fišer Company in Brno as a research worker in steel and concrete bridges which enables her to continue with her studies at the university. The author published some articles on conferences of PhD students in Czech and Slovak republic. Last year, she participated in the conference of Civil Engineering in London.

Ing. Přivřelová is a member of professional society WASET.

ISBN: 978-1-61804-325-2

Influence of the skin effect and the form of slot on the starting characteristics of induction motor squirrel cage

Zakari MADDI, Djamel AOUZELLAG, Toufik LADDI
Laboratory Control of Renewable Energies, Faculty of Technology, University of Bejaia 06000, Algeria, Email: zakari.maddi@gmail.com

***Abstract*—This article presents the influence of the form of rotor slot on the startup characteristics of the induction motor (IM). Three methods are presented allowing the taking into account of the real shape of the slot rotor and the highlighting of the skin effect, the first is an analytical method classic, the second is a numerical method based on the finite element (MFE) under software FEMM and the last is a method of analysis of circuits based on the use of the equivalent circuits of a rotor bar in the form of stairs.**

Keywords- Start, form of slot rotor, skin effect, IM.

I. INTRODUCTION

The asynchronous machine with a static frequency converter or directly to the network is the more repented in the industry. The modeling of the dynamic behavior can be performed simply by equivalent circuits has fixed elements. This method does not take into account the frequency behavior of the machine [1] .The eddy currents in the rotor bars indeed induce large changes so that the inductance of the rotor resistance [2]. This phenomenon called skin effect is a physical phenomenon in diffusive character, well use for different geometric shapes of rotor slots in order to see its influence on IM starting characteristics.

II. MODELING OF DEEP RECTANGULAR SLOT

There are several forms of rotor slots (rectangular, trapezoidal ...), in the case of engines with deep slots, at start, the current is on the upper part of the slots, it follows that the rotor behaves as if the section the conductors being wound was reduced, resulting in an increase of the ohmic resistance of the rotor. Late start speed, current moves downward slot and is distribute nearly uniformly over the entire section of the beam. From the AC gap exists only to a depth called penetration depth given as follows:

$$\delta = \sqrt{\frac{2\rho}{\mu g \omega}} = \sqrt{\frac{\rho}{\pi \mu g f}} \quad (1)$$

With δ : Depth of penetration of the alternating field; ρ: Resistivity of the material of the cage; μ: Permeability of the material of the cage; *f*: Frequency of the alternating field; *g*ω: Heartbeat of the current in the slots.

As the speed increases, the slip *g* decreases and the current extends over the entire section of the bar, the resistance is diminished, and after the expression (1), the depth of penetration increases up to embrace the entire surface of the bar, for the low slip of the nominal market. One thus gets, an engine with the resistance of the rotor varies by current movement [2]. We can therefore express the resistance r_2' and the leakage reactance x_2' in the following way:

$$r_2' = k_r r_{2e}' + r_{2f}' \quad (2), \qquad x_2' = k_n x_{2e}' + x_{2f}' \quad (3)$$

For the rectangular shape:

$$k_r = \frac{r}{r_0} = \frac{h}{\delta} \frac{\sinh\left(2h/\delta\right) + \sin\left(2h/\delta\right)}{\cosh\left(2h/\delta\right) - \cos\left(2h/\delta\right)} \quad (4)$$

$$k_n = \frac{n}{n_0} = \frac{3\delta}{2h} \frac{\sinh\left(2h/\delta\right) - \sin\left(2h/\delta\right)}{\cosh\left(2h/\delta\right) - \cos\left(2h/\delta\right)} \quad (5)$$

k_r and k_x : Coefficients that take into account respectively for the increase of the resistance r_2' and of the decrease of the reactance x_2''; h: Height of the bar [3].

III. NUMERICAL CALCULATION OF PARAMETERS OF ROTOR BARS

The calculation of *kr* and *kx* a rectangular bar by the analytical solution seems relatively easy and gives exact solutions, born less it has a major drawback it does not take into account the non-linearity and distortion of the geometry. Another solution is needed to address this problem, in this case a numerical calculation MEF is performed, it is to mesh the space (subdivide the area) element [3]. The mesh size can be formed of triangles or quadrilateral for areas axisymetrical or 2D and prisms or headers for areas 3D.

A. Simulation of a rectangular bar

The simulation conditions, similar to that which the rotor bars are subject requires to properly attaching the boundary conditions. n our case, Neumann conditions are applied to the left and right sides of the bar, and Dirichlet conditions on the high and low sides, distribution of the field lines and the variation of the current density are presented by following figure [4].

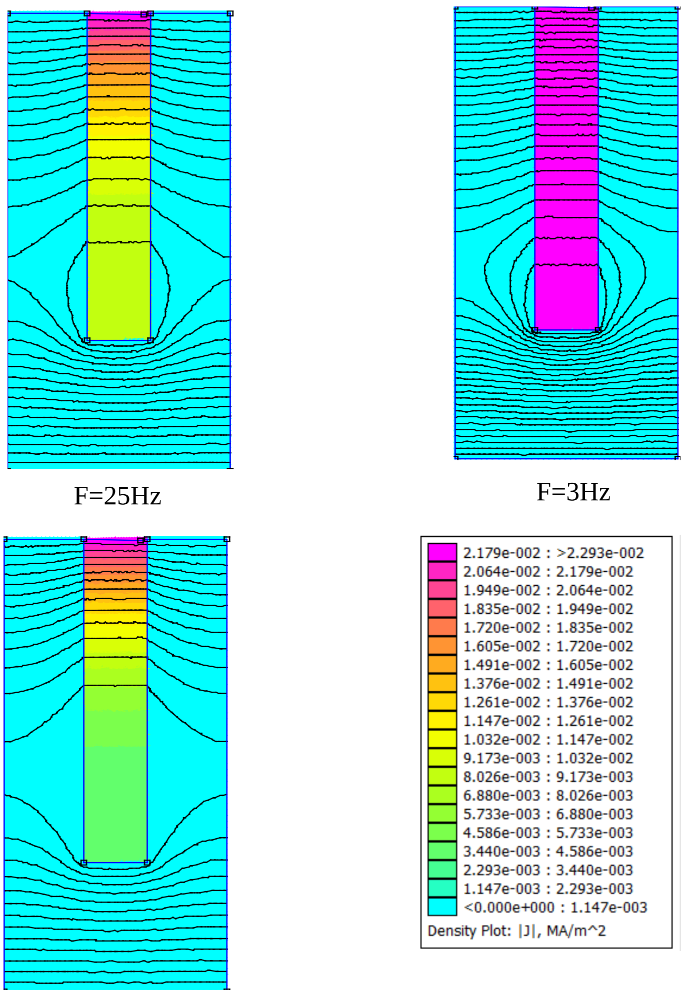

Fig.1. Current densities and field lines in a rectangular bar under different frequencies

III. MODELING OF SLOTS BY THE THEORY OF THE CIRCUITS

Now we present another method of calculation of coefficients k_r and k_x When the rotor bars are traversed by currents comers of the starting frequency to said vacuum operation. The skin effect occurs it could be analyzed using the circuit theory; this method is very suitable for bar cross−section of the rotor of arbitrary shape (double cage, trapezoidal ...). In this method, a solid conductor was divided into n layers imaginary or actual sub−conductors. The height of the driver is h_c the height of the sub-driver is h_k. The width of the slots varies of b_1 to b_n also width of driver can vary. This usually occurs when the skin effect of a bar mold under pressure to squirrel cage is evaluated. The length of the iron core is l [5].

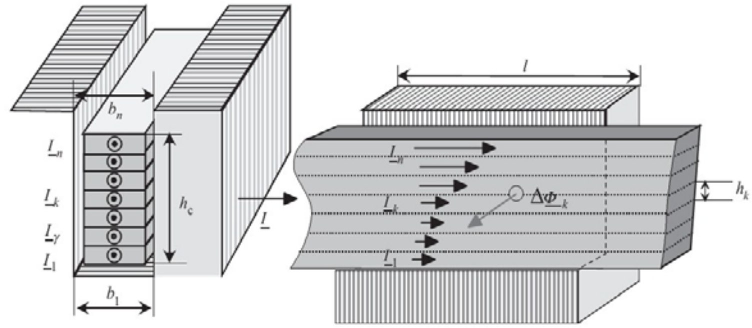

Fig.2. Slot rotor divided into sub-elementary conductors

The currents in the sub-conductors k and k+1 are I_k et I_{k+1}

In the steady state, the equation for the voltage is:

$$E_k = -j\omega\Delta\phi_k = R_k I_k - R_{k+1} I_{k+1} \quad (6)$$

Or ΔΦk is the leakage flow circulating between the k^{th} and $(k+1)^{th}$ sub-conductors.

The flux density of B_k in the sub-driver k depends on the F.M.M $\xi_k$of connection of current calculated from the lower part of the slot of the sub-driver k. $\xi_k = \int \frac{B_k}{\mu_0} dl$ (7)

$$B_k = \mu_0 \frac{\xi_k}{b_k} = \mu_0 \frac{1}{b_k} \sum_{\gamma=1}^{k} I_\gamma \quad (8)$$

Where b_k is the width of the slot to the position of the k^{th} sub-driver.

$$\Delta\phi_k = B_k l h_k = \mu_0 \frac{\xi_k}{b_k} l h_k = \mu_0 \frac{l h_k}{b_k} \sum_{\gamma=1}^{k} I_\gamma \quad (9)$$

By substituting (9) into (6), we get:

$$E_k = -j\omega\mu_0 \frac{l h_k}{b_k} \sum_{\gamma=1}^{k} I_k = R_k I_k - R_{k+1} I_{k+1} \quad (10)$$

Then, one obtains:

$$I_{k+1} = \frac{R_k}{R_{k+1}} I_k + \frac{j\omega\mu_0 l h_k}{R_{k+1} b_k} \sum_{\gamma=1}^{k} I_\gamma = \frac{R_k}{R_{k+1}} I_k + j \frac{\omega L_k}{R_{k+1}} \sum_{\gamma=1}^{k} I_\gamma \quad (11)$$

The resistance and inductance of the driver elementary k are:

$$R_k = \rho \frac{l}{h_k b_k} \quad (12) \qquad , \qquad L_k = \mu_0 \frac{l h_k}{b_k}$$

(13)

If the initial value of the current I_1 is not known, one can choose a value arbitrarily (for example 1A), and the rest of the currents will be resolved according to the system of equations (14).

$$\begin{cases} I_1 = 1 \\ I_2 = \frac{R_1}{R_2} I_1 + j \frac{\omega L_1}{R_2} I_1 \\ I_3 = \frac{R_2}{R_3} I_2 + j \frac{\omega L_2}{R_3} (I_1 + I_2) \\ \dots\dots\dots\dots\dots\dots\dots\dots\dots\dots \\ \dots\dots\dots\dots\dots\dots\dots\dots\dots\dots \\ I_{k+1} = \frac{R_k}{R_{k+1}} I_k + j \frac{\omega L_k}{R_{k+1}} (I_1 + I_2 + \dots + I_k) \\ I_n = \frac{R_{n-1}}{R_n} I_{n-1} + j \frac{\omega L_{n-1}}{R_n} \sum_{\gamma=1}^{n-1} I_\gamma \end{cases} \quad (14)$$

In this way, all the currents of sub-conductors of the bar are determined.

The total current of the bar is: $I_b = \sum_{\gamma=1}^{n} I_\gamma$ (15)

After you have obtained the currents from (14), the rest of calculation will be as follows:

The resistance of the $R_{b\varepsilon}$ bar taking into account the skin effect is given by: $R_{b\varepsilon} = \frac{\sum_{\gamma=1}^{n}(I_\gamma^2 R_\gamma)}{I_b^2}$ (16)

The coefficient, which takes into account the increase in resistance of the bar, is: $k_r = \frac{R_{b\varepsilon}}{r_0}$ (17)

With r_0: resistance of the bar without taking into account the skin effect.

The coefficient of the conductivity of dispersion of the slot : $\lambda_{b\varepsilon}$ taking into account the skin effect is given by the following expression: $\lambda_{b\varepsilon} = \frac{\sum_{\gamma=1}^{n}\left(\lambda_\gamma \left|\sum_{k=\gamma}^{n} I_k\right|^2\right)}{I_b^2}$ (18)

The coefficient of the conductivity of dispersion of the slot without taking into account the skin effect is given by the following expression: : $\lambda_{b2} = \frac{\sum_{\gamma=1}^{n}\left(\lambda_\gamma \left(\sum_{k=\gamma}^{n} q_k\right)^2\right)}{q_b^2}$ (19)

With $\sum_{k=\gamma}^{n} q_k$)Sum of sections of elementary conductors.

The coefficient which takes into account the decrease of the conductivity of dispersion of the slot is given by the following formula: $k_x = \frac{\lambda_{b\varepsilon}}{\lambda_{b2}}$ (20)

IV. RESULT OF SIMULATION OF THE THREE METHODS

The curves of developments of parameters k_r and k_x sont obtained from the simulation results, they are represented as follows:

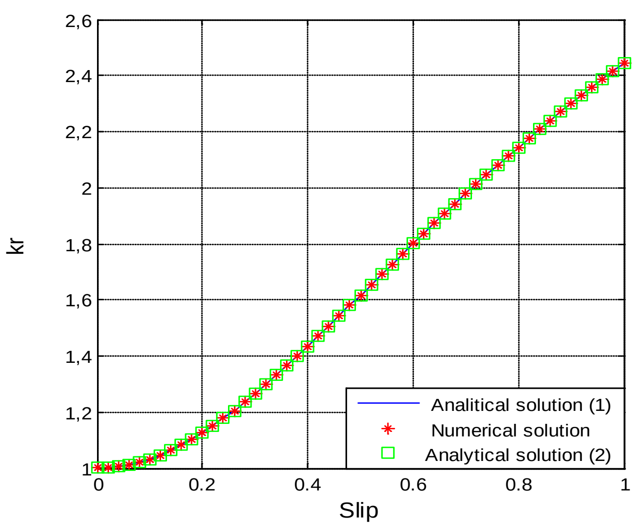

Fig.3. Evolution of k_r in function of the slip

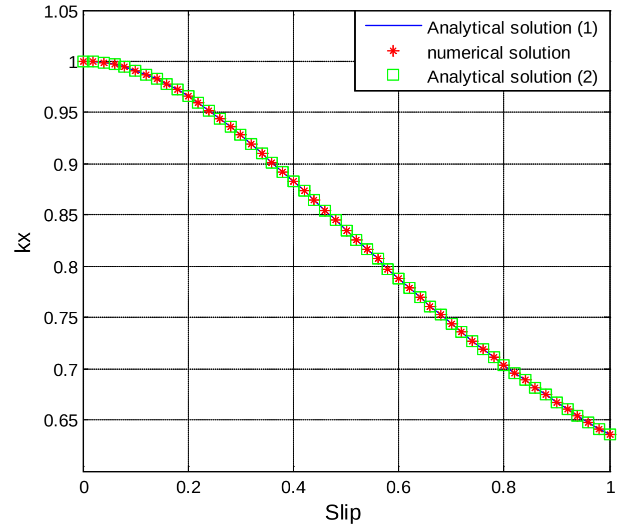

Fig.4. Evolution of k_x in function of the slip

The results obtained by the three analytical methods, digital and that of theory of the circuits are almost similar (the relative error maximum is estimated at 0,075 %) of or the validity of use of these last two methods for other forms of notches of geometry more complex.

IV.1. APPLICATION FOR THE DIFFERENT FORMS OF SLOTS

A. Slot trapezoidal in shape

The curves of developments of settings k_r and k_x for a slot trapezoidal in shape from two numerical method and theory of circuits (analytical) are as follows:

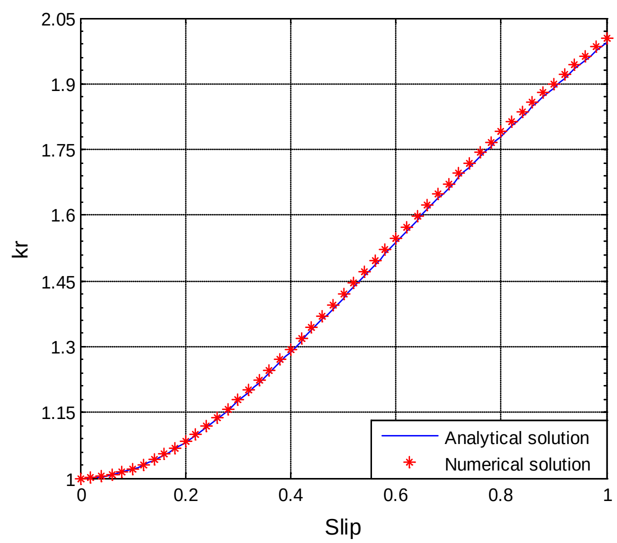

Fig.5. Evolution of k_r in function of the slip

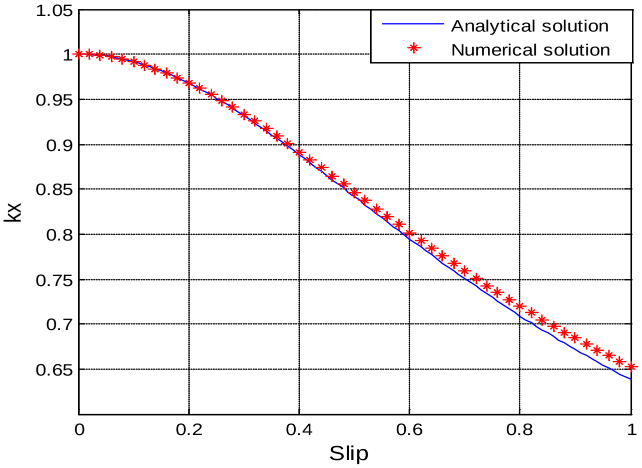

Fig.6. Evolution of k_x in function of the slip

B. Slot of trapezoidal shape reverse

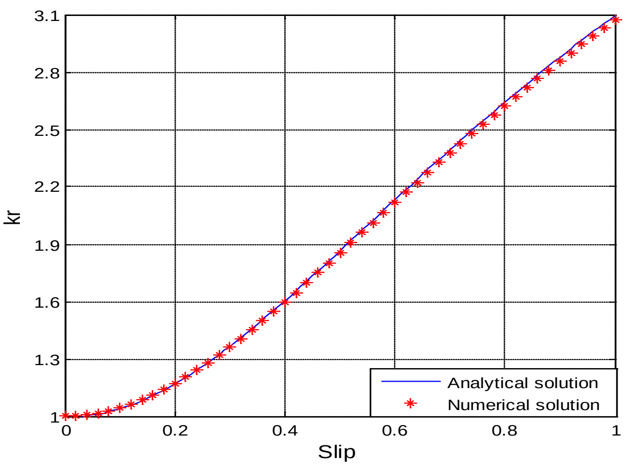

Fig.7. Evolution of k_r in function of the slip

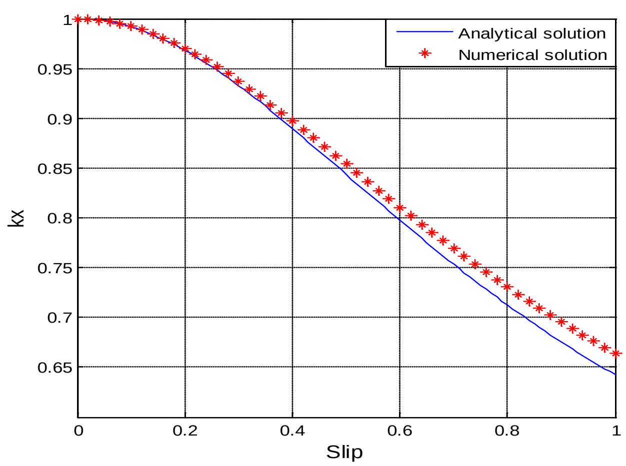

Fig.8. Evolution of k_x in function of the slip

The figures below represent, respectively, evolutions of the $k_r$and k_x for parameters a slot of inverted trapezoidal shape.

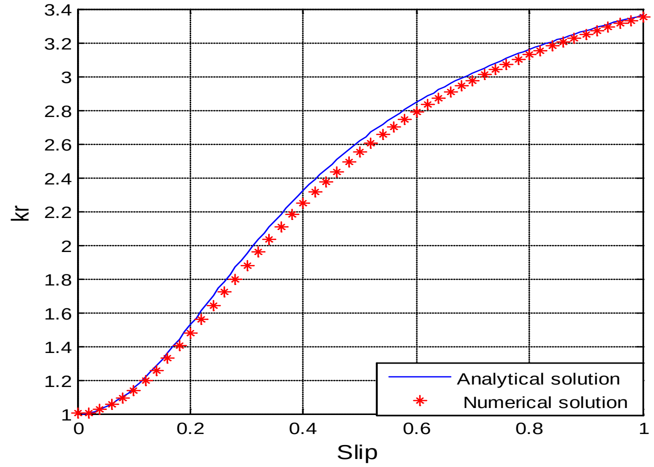

Fig.9. Evolution of k_r in function of the slip

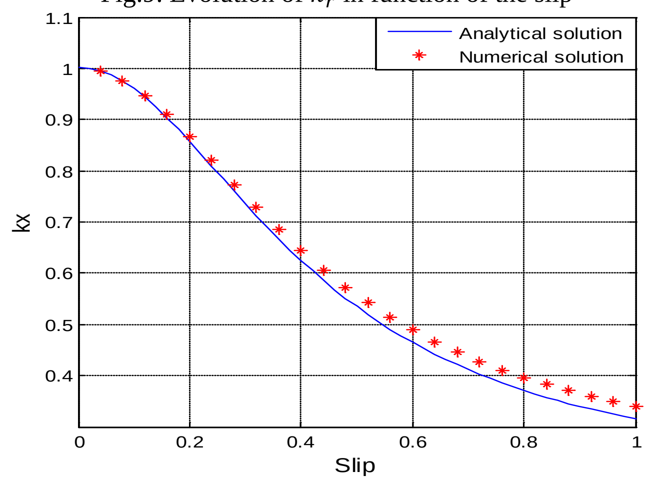

Fig.10. Evolution of k_x in function of the slip

C. Slot to form double cage

The results of the simulation for a double notch gage is as follows:

V. DYNAMIC MODELING OF THE IM

The above results have allowed us to observe the skin

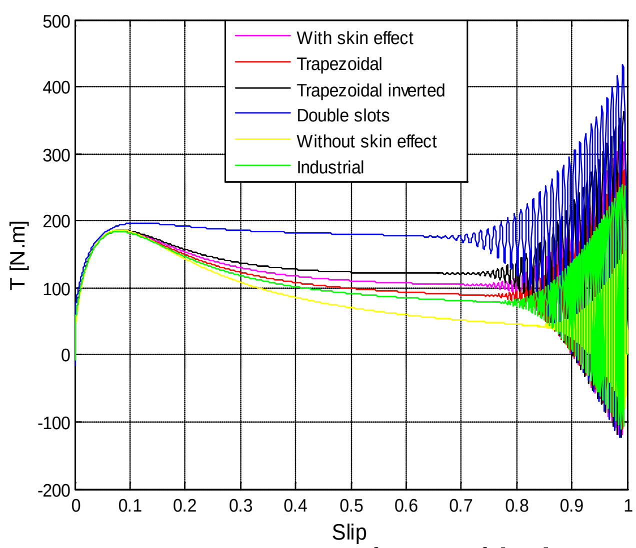

Fig.11. Various torque in function of the slip

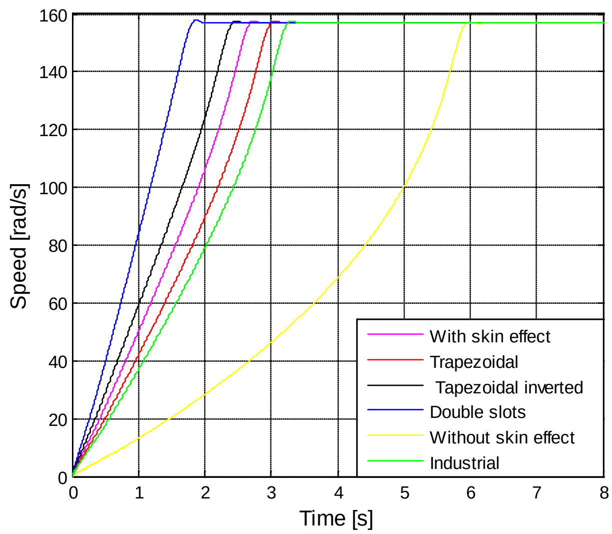

Fig.12. Evolution of speed in function of the slip effect for deferent forms of rotor slots and use it in a model of MI of average power (15kW) by means of resistance r_2 and the leakage reactance x_2 defined screen, has obtained the results shown in Figures below:

V.1. INTERPRETATION OF RESULTS

According to the results obtained for the different forms of slots rotor blade rows, it was found that the latter to a significant influence on the characteristics of starting the machine(very good improvement of the starting torque, as well as the startup time), the forms of slot which tend to reduce the width of the bar in the direction of the slot (reverse trapezoidal, double cage) have a better starting torque and a smaller time, since the current tends to flow on the upper part of the driver starting torque and a smaller time, since the current tends to flow on the upper part of the driver.

These forms of slots further increases the resistance of the rotor, unlike in the case of rectangular slot the width is constant, the increase of the resistance is due only to the effect of skin, the torque developed by the engine during start-up, is more important than the one developed if account is not taken of the latter, whereas for the case of the trapezoidal slot, the section is large where the current density is high, therefore it is in the direction of reducing the effect of skin.

VI. CONCLUTION

We studied the influence of slot shape on the startup characteristics of IM (15kW and 2p=2 pole), exploiting the phenomenon of skin effect using three methods discussed earlier to determine the coefficients that take into account the increase resistance r_2''and the decrease in the leakage reactance rotor x_2' to various forms of rotor slots. We found that the skin effect and more important in the cage and double-reverse trapezoid notch and offer improved torque and low startup time since the current tends circulated on the upper part of the driver**.**

REFERENCES

[1] G. D. GRENIER, F. LABRIQUE, H. BUYSE et E. MATAGNE, « *Electromechanical, energy converters and actuators"*, Editions Dunod, Paris, 2001.

[2] P. BARRET, "*Electrical Machines, theory and implementation*", Ellipses Editions Marketing S.A. , 2002.

[3] MR. KOSTENKO, L. Piotrovsky, "*Electrical Machines*", Tome II, Editions Mir, Moscow, 1979.

[4] S. CANAT, *"Contribution to the dynamic modeling of the asynchronous machine to cage*" ,Phd thesis of the Institut national polytechnique of Toulouse.2006.

[5] J.PYRHÖNEN, T.JOKINEN et V.HRABOVCOVÀ "*Design of rotating electrical Machines* ", Wiley, 2008.

Multi-objective optimization of layered composite plate for thermal stress control

A. Elsawaf, Yasser M. Shabana, and T. Vampola

***Abstract*—**Layered composite materials are increasingly used in many engineering applications. Recently, composites are used in aircraft structures, automobiles, sporting goods, and many consumer products. On the other hand, particle swarm optimization gains lots of attention in many research fields because of its simplicity, convergence and robustness. This article deals with a multi-objective optimization problem of a composite plate of three layers in order to control the thermal stresses induced by a prescribed thermal load. The plate contains nontraditional interfaces between the layers whose profiles follow a power law. The numerical model is solved using the finite element analysis while the optimization is done by applying the particle swarm optimization technique. Different parameters are optimized simultaneously so that the induced normal and shear thermal stress components are minimized simultaneously. It is found that the stresses can be minimized greatly by the proper choose of the optimum values of the different parameters.

***Keywords*—**finite element analysis, layer composites, Multi-objective optimization, layered composites.

I. Introduction

BECAUSE of their high performance, extensive attention has been paid to layer composite materials to be used in different engineering applications. Many research works dealt with the behaviors of layer composites under different loading conditions considering the interfaces as flat surfaces perpendicular to the lay-up direction of the layers [1-4]. It is found that high stresses may induce at the interface between any two successive layers due to the properties mismatches. Some studies were accomplished to investigate the effects of modifying the interferences on the induced stresses. Introducing a convex interface/joint design that inspired by the shape and mechanics of trees was among the considered modifications of the interfaces [5-6]. Nontraditional interface profiles, curved interfaces, were investigated concluding that the stresses can be reduced by the proper selection of the interference profile parameters [7]. However, Innumerable data were required for the best choice of the interface profiles to reduce the induced stresses sufficiently. Therefore, optimization methods should be applied for more successful and efficient control of the stresses that induce in such structures.

A. Elsawaf is with the Helwan University, in Egypt and Czech Technical University in Prague, Czech Republic.(elsawafahmed@gmail.com)

Yasser M. Shabana is with Egypt-Japan University of Science and Technology, *Egypt and* Helwan University, Egypt (*yasser.shabana@gmail.com*).

T. Vampola is with Czech Technical University in Prague, Czech Republic (Tomas.Vampola@fs.cvut.cz).

Optimization is an important issue faced every day in the manufacturing industry to meet special requirements and ensure the best performance of a structure. The population-based optimization algorithms are becoming increasingly more popular than the traditional search optimization techniques for solving complex optimization problems. The major difference between them is that the traditional search techniques start with initial population, while the population-based optimization algorithms start with a single initial guess value. Therefore, the population-based optimization is more efficient in finding global or near global optimum solutions, while the final result of the traditional optimization method depends on the initial guess. Moreover, the traditional optimization methods are time consuming in solving nonlinear and complex optimization problems. Therefore, the heuristic search techniques, such as genetic algorithm, simulated annealing, particle swarm optimization algorithm (PSO), immune algorithm, and harmony search algorithms, are more effective than the gradient techniques in finding the global optimum. The PSO is more advantageous over other techniques as it is algorithmically simpler, generally converges faster and more robust [8, 9]. Thus, PSO encouraged researchers from various backgrounds to use it in solving many optimization problems. Elsawaf et al. [10] and Elsawaf et al. [11] combined PSO with the simplex method for an optimum structure design of a composite disk with single and multiple piezoelectric layers to control the maximum thermal stress induced in the structural layer. For other application, Metered et al. [12] recently introduced an investigation into the use of a PSO algorithm to tune the PID controller for a semi-active vehicle suspension system incorporating magnetorheological damper improving the ride comfort and vehicle stability. Shabana et al. [13] applied PSO for a single-objective optimum design of a three layer composite plate with nontraditional interface. The objective was to minimize the maximum normal thermal stress induced in the structure while the design variables were including the interface profile parameter. It was found that the maximum normal stress can be minimized greatly using the optimum values of the different parameters, compared to those obtained without optimization [7]. However, only the normal stress was considered. For more successful design of such structures, it is required to minimize not only the normal stress but also the shear stress.

ISBN: 978-1-61804-325-2

A multi-objective optimization algorithm generally provides a set of optimal solutions called Pareto-optimal solutions. There may be no single solution from the Pareto-optimal set of solutions to be recognized as superior to whatever other Pareto solution for admiration to the specified and identified objective functions. The main goals of a multi-objective optimization algorithm are to guide the search towards the global Pareto-optimal front and also to maintain population diversity in the Pareto-optimal solutions. Once those set of Pareto solutions are obtained, trade-off investigations can be performed by the designer and from that the most suitable solution based on site or problem specific requirements is chosen. Jacob et al. [14] used a multi-objective genetic algorithm (GA) for optimization of laminated composite materials. Two model problems having multiple, conflicting, objectives of laminated composite materials were studied. In the first model, the objectives were to minimize the mass of the laminate while maximizing the load carrying capacity. For the second model, the objectives were to maximize the axial and hoop rigidities while minimizing the mass of the laminate. Lee et al. studied a stacking sequence design optimization for multilayered composite plate [15]. He illustrated that the design of the stacking sequence of fibres had a dramatic influence on the strength of multilayered composite plates and the optimized composite structures had lower weight, higher stiffness and reasonable cost. The study of a multi-objective optimization method for fibrous composite plates with curvilinear fibers to maximize the mechanical properties, including fundamental frequencies or in-plane strengths, and minimizing the average curvatures of fibers was presented in [16]. Omkar et al. [17] used another evolutionary algorithm called Artificial Bee Colony (ABC) for multi-objective design optimization of composite structures. Multiple objectives of minimizing weight and the total cost of the composite component to achieve a specified strength were studied. PSO used in [18] for the optimum design of a composite box beam of a helicopter rotor blade. It was observed that the PSO gives better solution quality with less computational cost compared to GA.

In this article, the maximum induced normal and shear stresses in a three layer plate with nontraditional interface are minimized by optimizing the different geometrical parameters. These optimized parameters include the interface profile parameter and the height of the nontraditional interface on the right surface relative to the mid-surface. The considered composite plate is an isotropic mixture of two components: Nickel (Ni) and Alumina (Al_2O_3). The finite element analysis is used to evaluate the thermal stresses in the plate and the particle swarm optimization technique is used for optimizing the interface geometrical parameters.

II. Problem Statement and Solution

The improvement of layered composite materials offers great prospective for use in advanced aerospace and vehicle applications, which may expose to unavoidable thermal environment. Modifying the composite behaviors, such as the thermal response, is one of the main objectives in order to be used for structures with severe loading conditions. The maximum weakness in a structure can be observed at the interfaces between the layers as they exhibit the maximum induced stress. Thus, the composites behaviors are depending mainly on the properties of the interfaces between the layers. The aim of the present study is to provide the designers of layer composites with better choices of the interface geometry so as to minimize the induced stresses and have safe designed components.

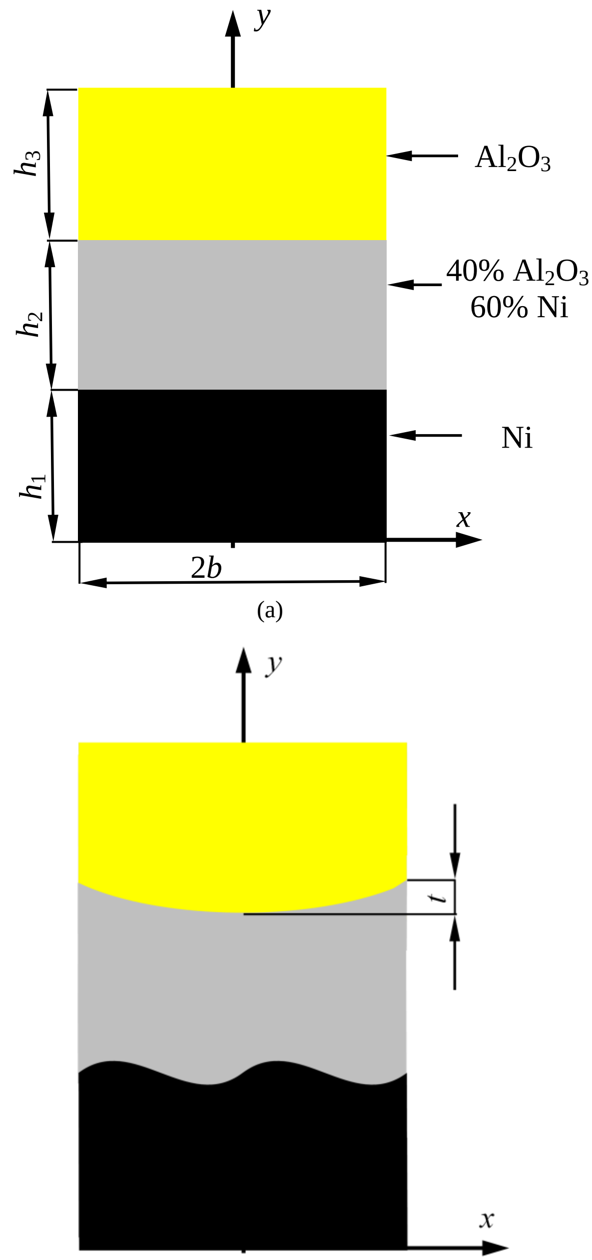

Fig. 1 Layered composite plate,
(a) Traditional interfaces (b) Non-traditional interfaces.

The two-dimensional plane-strain specimens with three layer plate in both traditional and non-traditional interfaces are shown in Fig. 1. The considered structure consists of three layers with thicknesses of h_1, h_2 and h_3 starting from the bottom layer and measured at the mid-surface of the plate. The plate width equals $2b$ whereas its thickness equals $h_1+h_2+h_3$. The upper nontraditional interface (Fig. 1-b) has a height t on the right surface relative to the mid-surface of the plate. The height is considered to have a negative value if the interface on the right surface is below its position on the mid-surface. The origin of the coordinate system xy is supposed to lie at the mid-point of the lower face as shown in the figure. The y axis is chosen to be orthogonal to the faces of the layers and along their lay-up direction while, the x axis is assumed to be orthogonal to the lay-up direction and parallel to the lamina faces.

The bottom and top layers are made of nickel (Ni) and, alumina (Al_2O_3) respectively, while the intermediate layer is a mixture of 60% Ni and 40% Al_2O_3. Therefore, the ceramic volume fraction satisfies the following relations

$$v_c = \begin{cases} 1 & \text{for} \quad y \ge h_1 + h_2 \\ 0.4 & \text{for} \quad h_1 \le y \le h_1 + h_2 \\ 0 & \text{for} \quad y \le h_1 \end{cases} \tag{1}$$

For such cases, the through-thickness variation of the different properties, such as Young's modulus, Poisson's ratio and coefficient of thermal expansion, in the three-layer composite system can be written as

$$P(y) = \begin{cases} P_c & \text{for} \quad y \ge h_1 + h_2 \\ P(P_c, P_m) & \text{for} \quad h_1 \le y \le h_1 + h_2 \\ P_m & \text{for} \quad y \le h_1 \end{cases} \tag{2}$$

where P_c and P_m are the properties of the homogeneous ceramic and metal materials, respectively. $P\ (P_c,\ P_m)$ is the interlayer properties following the rule of mixtures. Also, the temperature-dependent properties [19] of the constituent materials are considered and these properties are assumed to vary linearly with the temperature for reliable and accurate prediction of the structure response. Therefore, the material properties of the layered plate are both position and temperature dependent. Table 1 lists the considered materials properties at different temperatures [19].

Table I: Material properties used in the FEM simulations [19]

Temperature	300 (^oK)				800 (^oK)			
Material	E (GPa)	v	σ_Y (MPa)	α x10^{-6} ($1/^oK$)	E (GPa)	v	σ_Y (MPa)	α x10^{-6} ($1/^oK$)
Ni	208	0.31	148	13.4	166	0.31	124	16.7
Al_2O_3	380	0.25	-	5.4	380	0.25	-	8.4

In the present analyses, the interfaces between the different layers are assumed to be perfectly bonded at all times and the multilayer system behavior to be elastic-plastic originate from the elastoplasticity of the metal while the ceramic behaves elastically. The plane strain as a geometric approximation of structures is considered. For the finite element mesh, the element used is an 8-node isoparametric element and the numbers of elements along the horizontal and vertical directions are 80 and 70, respectively. Therefore, 2800 elements are used for one half of the model. The element size is refined near the interfaces between the layers and the free edges to accommodate the concentration of stress, and the smallest element size is 5×10^{-5} m. For the loading conditions, uniform cooling (no thermal gradient) is assumed while cooling from the fabricated temperature of 1100 K to the room temperature. Therefore, the temperature difference (T) in the current analysis is considered to be 800 K.

The upper interface exhibits higher stresses than the lower one [19] therefore, the geometry of the upper interface is the one of the considered optimized parameters for the sake of minimizing the critical induced stresses. On the other hand, the lower interface is assumed to be a traditional one. The considered profile of the upper interface is following a power

$$Y(X) = X^m \tag{3}$$

where $Y\{=[y-(h_1+h_2)]/t\}$ denotes the non-dimensional vertical coordinate of the interface relative to the mid-surface; $X\{=x/b\}$ denotes the non-dimensional horizontal coordinate normalized by the half width of the plate; t is the height by which the upper interface is moved on either the right surface (X=1) or the mid-surface (X=0) from its traditional level; and m is an exponent. When $t=0$, the interface is the traditional one that is perpendicular to the lay-up direction of the layers. When t is positive/negative, the ceramic content is decreased/increased relative to its traditional value. Figure 2 shows the interface profiles for various values of the parameter m when t is upward on the right surface of the plate.

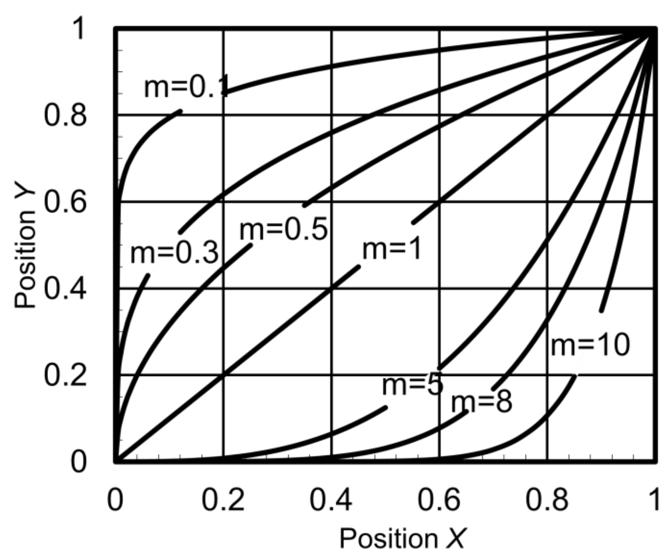

Fig. 2 Interface profiles following the power law.

When m=1, the interface is a flat surface inclined on the lay-up direction of the layers. For a lower value of the parameter m, the interface profile changes sharply at the mid-surface of the plate and changes smoothly at the right surface.

On the other hand, for higher values of the parameter *m*, the phenomena of the interface profile are vice versa of those of the lower values. However Eq. (3) is valid when *t* occurs on the right surface, the following relation is to be applied when *t* occurs on the mid-surface of the plate

$$\mathrm{Y(X)} = (1-\mathrm{X})^{\mathrm{m}} \tag{4}$$

III. Interface Geometry Optimization

A. Optimization Problem

The main aim of solving an optimization problem of a structure is to minimize the induced stresses and therefore decrease the damage probability. For the considered layer composite structure, it is required to independently evaluate the optimum values of the interface geometrical parameters (interface profile parameter *m* and the height *t* of the interface) to minimize the maximum induced thermal stresses. The nonlinear optimization problem which determines the interface parameters is defined as:

$$\begin{aligned} &\textit{Find} && K \\ &\textit{Minimize} && f(K) = f_1(K), f_2(K) \end{aligned} \tag{5}$$

Where K represents the required design variable either *m* or *t*, f_1 stands for the maximum induced normal stress (σ_y) and f_2 stands for the maximum induced shear stress (τ_{xy}). If the optimization problem Eq. (5) is solved to only minimize either f_1 or f_2, it is a single objective problem whereas if considering both f_1 and f_2, it is a multi-objective problem. Since there are many local optima in the solution space of the optimization problem (5), PSO technique is applied to get the global optimum.

B. Particle Swarm Optimization Algorithm

PSO algorithm is a computational technique originally contributed by Kennedy et al. [20] which was inspired from the social behavior of the movement of organisms in a bird flock or fish school. PSO algorithm optimizes a problem using a population called swarm of candidate solutions called particles. Particles are initially scattered in the solution space with random initial positions. The position of a particle $y_{\mathrm{p}}^{(\tau)}$ and its velocity $v_{\mathrm{p}}^{(\tau)}$ are iteratively enhanced in the solution space towards the optimum solution with the influence of its local best position $b_{\mathrm{p}}^{(\tau)}$ and the overall best position $g^{(\tau)}$ obtained from all the candidates. When the process is repeated for sufficient number, the best solutions eventually will be found. Updating the particles' positions for a single objective optimization is controlled by [21];

$$\mathrm{y}_{\mathrm{p}}^{(\tau+1)} = y_{\mathrm{p}}^{(\tau)} + v_{\mathrm{p}}^{(\tau+1)} \tag{6}$$

$$\begin{aligned} \mathrm{v}_{\mathrm{p}}^{(\tau+1)} = {} & W \times v_{\mathrm{p}}^{(\tau)} + c_1 \times rand_1 \times [b_{\mathrm{p}}^{(\tau)} - y_{\mathrm{p}}^{(\tau)}] + \\ & c_2 \times rand_2 \times [g^{(\tau)} - y_{\mathrm{p}}^{(\tau)}] \end{aligned} \tag{7}$$

where W is a nonnegative inertia weight, c_1 and c_2 are acceleration coefficients, and $rand_1$ and $rand_2$ are random numbers between 0 and 1. In most cases of multi-objective optimization problems, there is no exact solution but many alternative solutions. This family of potential solutions cannot improve all the objective functions simultaneously and it is called Pareto optimality [22]. PSO has been advocated to be suitable for multi-objective optimization [23]. The multi-objective particle swarm optimization (MOPSO) algorithm is used to find nondominated (Pareto) solutions. The main characteristic of this algorithm is the use of an external repository which stores nondominated solutions. The algorithm starts by generating an initial population. At each iteration, the repository is updated for the new non-dominated solutions. At the end of the process, the repository contents form the Pareto front. In MOPSO Eq. 7 is updated to the following;

$$\begin{aligned} \mathrm{v}_{\mathrm{p}}^{(\tau+1)} = {} & W \times v_{\mathrm{p}}^{(\tau)} + c_1 \times rand_1 \times [b_{\mathrm{p}}^{(\tau)} - y_{\mathrm{p}}^{(\tau)}] + \\ & c_2 \times rand_2 \times [R_h^{(\tau)} - y_{\mathrm{p}}^{(\tau)}] \end{aligned} \tag{8}$$

where R_h is a solution selected from the external repository in each iteration *t*. Further details for the algorithm implementation can be found [23]. The values used in this study for W, c_1 and c_2 are 0.729, 1.496 and 1.496 respectively.

IV. Results and Discussions

It is considered that all layers of the plate have the same thickness and a layer thickness equals 5 *mm*. Also, the plate width is related to the default layer thickness by $b/h_1 = 8$. Moreover, the default values of *m* and *t* are 1 and 1 *mm*, respectively when they are not considered among the optimized parameters. The considered optimization ranges of the interface parameter and the interface height on the right surface are $0 \leq m \leq 8$ and $-5 \leq t \leq 5$ mm, respectively. The effects of both the interface profile parameter *m* and the height on the right surface *t* of the interface are studied individually considering f_1 and f_2 for the multi-objective problem.

A. Optimizing the Interface Profile Parameter (m)

Considering only f_1 as a single-objective problem in Shabana et al. [13], it was found that the optimum value of the interface profile parameter $m = 8$ at which f_1=615 MPa. Figure 3 shows the numerical results obtained by solving the multi-objective problem given in Eq. (5). It can be seen that minimum f_1, which is consistent with the results of the single objective study [13], occurs while f_2, the shear stress component, is at its highest value of 67.4 MPa. It seems from the obtained results that generally by increasing the interference profile parameter *m* above 3.80, the shear stress component increases while the normal stress component decreases. The minimum normal stress component obtained when *m* is selected between 7.98 to 8.0 while, the minimum shear stress component acquired when *m* is equal to 3.83.

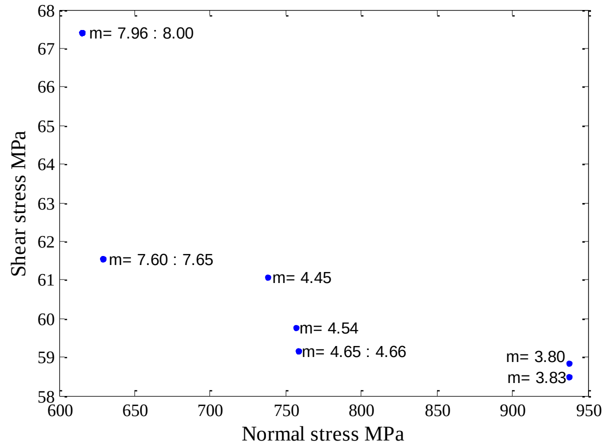

Fig. 3. Pareto fronts for the effect of *m* on stress components where *t*=1 (mm).

B. *Optimizing the Interface Height on the Right Surface (t)*

The solution of the single-objective problem for f_1, Shabana et al. [13], revealed that the optimum value of the interface height t = 5 at which f_1=472 *MPa*. The numerical results obtained by solving the multi-objective problem given by Eq. (5) when considering f_1 and f_2 are shown in Fig. 4. The figure again confirms same result obtained in [13] from the single objective study at which f_1 is at its lowest value whereas f_2 is at its highest value. It is clearly seen that lower values of shear stress component obtained when *t* is negative where the interface on the right surface is below its position on the mid-surface. However, lower values of normal stress component obtained when *t* is positive where the interface is above its position on the right surface as shown in Fig. 4. The minimum value of the normal stress component can be obtained by selecting *t*=5 *mm* whereas the minimum shear stress component can be obtained when *t*=-4.58 *mm* is selected.

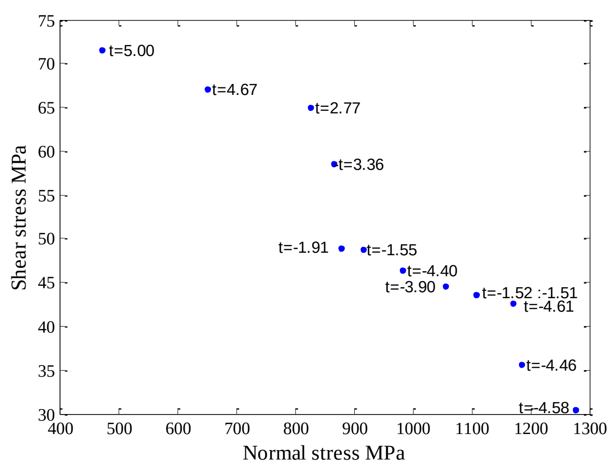

Fig. 4. Pareto fronts for the effect of *t* on stress components where *m*=1.

The stress variations along the vertical right surface *y* for both the traditional and the optimized nontraditional interfaces are shown in figures 5 and 6.

Figure 5 shows the normal stress variations for two cases compared with the traditional interface. The first case selected for the optimum value of *m* for minimizing the normal stress depicted in figure 3 while, the second case selected for the optimum value of *t* for minimizing the normal stress illustrated in figure 4. Those values are *m*=8 and *t*=5 mm with their default corresponding values of *t*=1 mm and m=1 respectively.

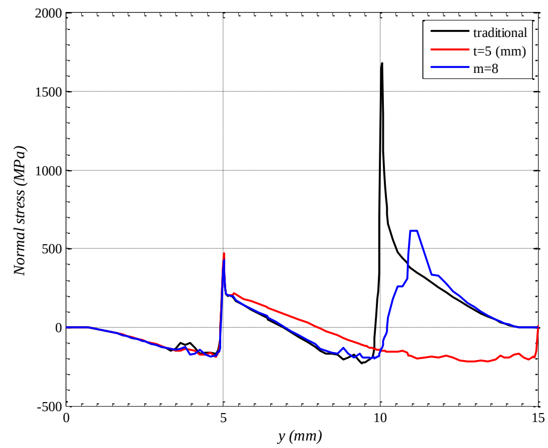

Fig. 5. Normal stress variations for the traditional and nontraditional interfaces.

It seems from figure 5 that, the maximum normal stress component has been reduced by 63.45% for the first case and 71.79% for the second case compared to the similar value with the traditional interface.

The shear stress variations compared with the traditional interface are shown in figure 6. Similar to figure 5, the best two values for minimizing the shear stress component, shown in figures 3 and 4, are selected for comparison. Those values are *m*=3.83 and *t*= -4.58 mm with their default corresponding values of *t*=1 mm and *m*=1 respectively.

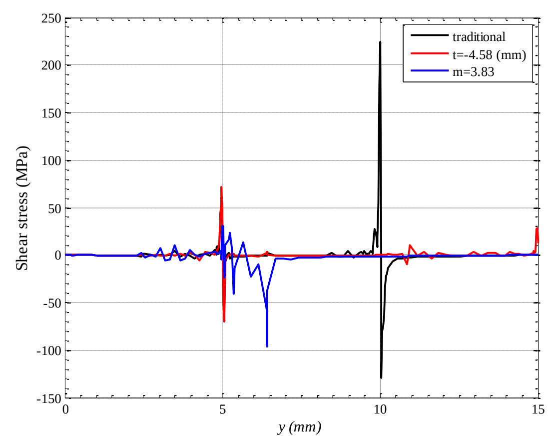

Fig. 6. Shear stress variations for the traditional and nontraditional interfaces.

The maximum shear stress component has been reduced by 86.34% for the first case and 73.38% for the second case compared with the traditional interface as seen in figure 6.

V. CONCLUSION

The multi-objective optimization problem of a composite plate of three layers, which made of Ni and Al_2O_3, in order to control the thermal stresses is investigated. The maximum induced normal and shear stresses in a three layer plate with nontraditional interface are minimized by optimizing the different geometrical parameters. These optimized parameters include the interface profile parameter and the height of the nontraditional interface on the right surface relative to the mid-surface. The numerical model is solved using the finite element analysis while the optimization is done by applying the particle swarm optimization technique. It is found that the stresses can be minimized greatly by the proper choose of the optimum values of the different parameters. For the future work, the multi-objective optimization will be used to optimize the different geometrical parameters simultaneously.

ACKNOWLEDGMENT

This publication was supported by the European social fund within the frame work of realizing the project "Support of inter-sectoral mobility and quality enhancement of research teams at Czech Technical University in Prague", CZ.1.07/2.3.00/30.0034. Period of the project's realization 1.12.2012 – 30.9.2015.

REFERENCES

[1] H. Bruck, and A. Gershon, "Three-Dimensional effects near the interface in a functionally graded Ni-Al2O3 plate specimen," *Int J. Solids Struct*, vol. 39, pp. 547, 2002.

[2] Y. Ootao, Y. Tanigawa, and A. Takano, "Transient thermoelastic analysis for a laminated composite strip with an interlayer of functionally graded material," *J. Thermal Stresses*, vol. 32, pp. 503-506, 2007.

[3] H. Koguhi, "Influence of interlayer thickness on the intensity of stress singularity for residual thermal stress in three-dimensional bonded joints," *Thermal Stresses 2007: Proc. The Seventh International Congress on Thermal Stresses, National Taiwan University of Science and Technology, Taipei, Taiwan*, pp. 623-626, 2007.

[4] Y. M. Shabana, M. Pines, H. Bruck, and J. Kruft, "Modeling the evolution of stress due to differential shrinkage in powder-processed functionally graded metal-ceramic composites during pressureless sintering," *Int J Solids Struct*, vol.43, pp. 7852-7868, 2006.

[5] L. Xu, H. Kuai, and S. Sengupta "Dissimilar material joints with and without free-edge stress singularities: Part I. A biologically inspired design," *Exp Mech*, vol. 44, pp. 608-615, 2004.

[6] L. Xu, and S. Sengupta "Dissimilar material joints with and without free-edge stress singularities: Part II. An integrated numerical analysis," *Exp Mech*, vol. 44, pp. 616-621, 2004.

[7] Y.M. Shabana, "Minimizing stresses of layer composites by controlling the interface geometry," *Mech Adv Mater Struc*, vol. 21, pp. 47-52, 2014.

[8] M. Sunwoo, K.C. Cheok, and N.J. Huang, "Model reference adaptive control for vehicle active suspension systems," *IEEE Trans Ind Electron*, vol. 38, pp. 217–222, 1991.

[9] M. Omran, "Particle swarm optimization methods for pattern recognition and image processing", PhD Thesis, University of Pretoria, South Africa, 2005.

[10] A. Elsawaf, F. Ashida, and S. Sakata, "Hybrid constrained optimization for design of a piezoelectric composite disk controlling thermal stress," *Journal of Theoretical and Applied Mechanics Japan*, vol. 60, pp. 145-154, 2012.

[11] A. Elsawaf, F. Ashida, and S. Sakata, "Optimum Structure Design of a Multilayer Piezo-Composite Disk for Control of Thermal Stress," *J. Thermal Stresses*, vol. 35, pp. 805–819, 2012.

[12] H. Metered, A. Elsawaf, T. Vampola, T. and Z. Šika, "Vibration control of MR-damped vehicle suspension system using PID controller tuned by particle swarm optimization," *SAE. Int. J. Passeng. Cars - Mech. Syst.*, vol. 8, 2015.

[13] Y.M Shabana, E.I. Morgan, and A. Elsawaf, "Optimization of layer composites with nontraditional interfaces for minimizing stresses," *2nd International Conference of Engineering and Technology (ICET)*, At Cairo, Egypt, Apr. 2014,2014.

[14] L.P. Jacob and S.V. Senthil, "Multi-objective optimization of fiber reinforced composite laminates for strength, stiffness and minimal mass," *Comput Struct*, vol. 84, pp. 2065-2080, 2006.

[15] DS. Lee, C. Morillo, G. Bugeda, S. Oller and E. Onate, "Multilayered composite structure design optimisation using distributed/parallel multi-objective evolutionary algorithms," *Comput Struct*, vol. 94, pp. 1087-1096, 2012.

[16] S. Honda, T. Igarashi and Y. Narita "Multi-objective optimization of curvilinear fiber shapes for laminated composite plates by using NSGA-II," *Compos Part B: Eng*, vol. 45(1), pp. 1071- 1078, 2013.

[17] S.N. Omkar, J. Senthilnath, R. Khandelwal, G.N. Naik and S. Gopalakrishnan, "Artificial bee colony (ABC) for multi-objective design optimization of composite structures," *Applied Soft Computing*, vol. 11 (1), pp. 489–499, 2011.

[18] S. Suresh, P. B. Sujit and A. K. Rao "Particle swarm optimization approach for multi-objective composite box-beam design," *Comput Struct*, vol. 81, pp. 589-605, 2007.

[19] H. Bruck, and A. Gershon, "Three-Dimensional effects near the interface in a functionally graded Ni-Al2O3 plate specimen," *Int J Solids Struct*,vol. 39, pp. 547, 2002.

[20] J. Kennedy, and R. Eberhart, "Particle Swarm Optimization," *Proceedings of IEEE International Conference on Neural Networks*, pp.1942–1948, 1995.

[21] M. Clerc, and J. Kennedy, "The particle swarm: Explosion, stability, and convergence in a multidimensional complex space," *IEEE Transactions on Evolutionary Computation*, vol. 6, pp. 58-73, 2002.

[22] V. Pareto, "Manuale di Economica Politica, Societa Editrice Libraria. Milan; In: Schwier AS , Page AN (eds) translated to English by Schwier AS as Manual of Political Economy,Kelley, New York, 1906.

[23] C. A. Coello Coello, G. T. Pulido, and M. S. Lechuga, "Handling multiple objectives with particle swarm optimization" *IEEE Trans. Evol. Comput*, vol. 8, pp. 256–79, 2004.

The geo-radar in the service of concrete durability

K.HADJA, F.KHARCHI, and J.P.BALAYSSAC

***Abstract*—** Concrete has become a universal building material. Its mechanical resistance is considered as a basic criterion. Currently we see that the concrete can be affected by its environment. Its performance decreases when it is exposed to moisture, pollution and other aggressive substances such as chlorides and sulfates. Aggressive substances are generally conveyed by the water. The water content is thus a good indicator of the durability of concrete.

Non-destructive methods were developed for diagnosing the state of a structure at a given time. This allows monitoring and preventive maintenance work. The technical Radar (Radio Detecting And Ranging) is one of the buildings auscultation techniques used. It is an application of electromagnetism and was mainly used for finding buried objects in concrete and recognition of discontinuities or geometries. Relatively recent research has shown that the radar can also be used as a tool for characterizing the state of the material. This enables new application fields.

The water content is an essential parameter in the durability of concrete. The radar signal is analyzed in terms of mitigation and speed, by the use of different reflected signals and also the direct wave signal between the transmitter and receiver. The measurements made in the laboratory or on site indicate the sensitivity of this signal to the desired settings. The propagation speed is directly related to the dielectric constant. This measure gives an idea about the actual concrete moisture condition.

***Keywords*—**concrete, durability, geo-radar, non-destructive methods.

I. INTRODUCTION

The mechanical strength of concrete was long considered a basic criterion for the concrete but experience shows that this material can be weakened by the environment. Thus, It appears pathologies such the steel reinforcement corrosion and spalling of the concrete. The presence of water is an essential parameter leading to these pathologies. For this, it has been developed several techniques for auscultation of used constructions, among them, the Radar technical Radar (Radio Detecting And Ranging). It is an application of electromagnetism as support of measures, it was mainly used for finding objects buried in the concrete as frames, or for the recognition of discontinuities or geometries. Research [1], [2] and [3] Recently enough showed that the radar may also be used as a characterization tool of the state of the material. This opens up new applications for the evaluation of some sustainability indicators, in particular the water content, by analysis of radar signals in terms of mitigation and speed.

II. PRINCIPLE OF MEASUREMENT

The radar technique is based on the use of electromagnetic pulse emitted by an antenna. The pulses spread by reducing materials. At each interface between two electromagnetically different materials, a part of the pulse energy is reflected back to the surface. Thus the successive echoes are recorded in a time signal by the receiving antenna. In general, the antennas are in a same box, this corresponds to a conventional configuration of acquisition.

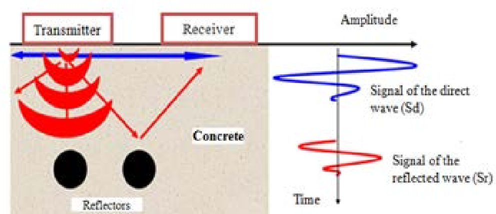

Fig. 1 Principle of measurement by Radar

III. RELATIONSHIP BETWEEN THE DIRECT WAVE AND MOISTURE OF MATERIAL

The direct wave is propagated directly from the transmitter to the receiver. The sensitivity of the direct wave in the moisture condition of the materials (eg soil, concrete) has been studied by many authors [4] and [5].

Increasing water content of concrete leads to a sharp variation of the radar signal parameters. This is usually due to the increase of permittivity and conductivity of concrete. Thus the presence of water and / or water-filled cracks can affect the behavior of the radar signal.

IV. ANALYSIS OF THE RELATIONSHIP BETWEEN EMW SPEED AND MATERIAL MOISTURE.

The analysis is made on samples of concrete. The sample is cut by a cylindrical sawing. These types of samples are commonly called "carrots concrete." The study of samples allows to characterize accurately the state of the material. This also has a necessary calibration operation for future on-site measurements. It was used a radar system (CRS 20 GSSI) with antennas frequency 1.5 GHZ.

Fig. 2 concrete core

Fig. 3 Measure system

Fig. 4 Antennas 1.5 GHz

A. *Measuring device*

The device is composed of two vertical square screens of 1m from the side. They are covered by a self-adhesive aluminum foil to have reflectors character. The screens are drilled in the middle to receive the concrete core which is also covered with aluminum in order to ensure a linear propagation of electromagnetic waves and avoid wave reflection to the contour. The transmitter and receiver are applied to each end of the core.

This measurement system requires certain conditions to the core: it must have a height of 150 mm and a diameter of 75 mm to fit the experimental device. Otherwise it was completed by polystyrene.

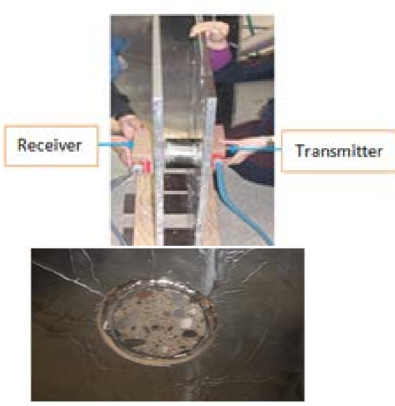

Fig. 5 Experimental device

The measure is affected on core of concrete and full air core to determine the initial time of propagation.

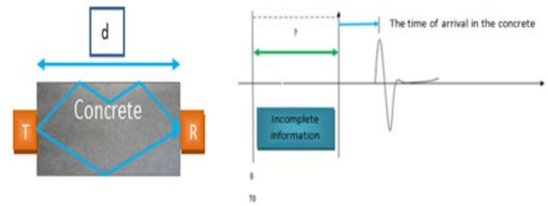

Fig. 6 Measure on the concrete core

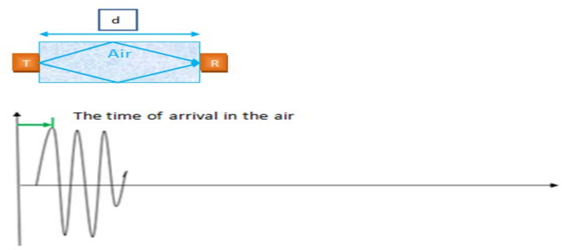

Fig. 7 Measure on the air

B. *Results on the concrete core*

From these graphs we determined: the arrival time of EMW in the concrete and the initial time t_0

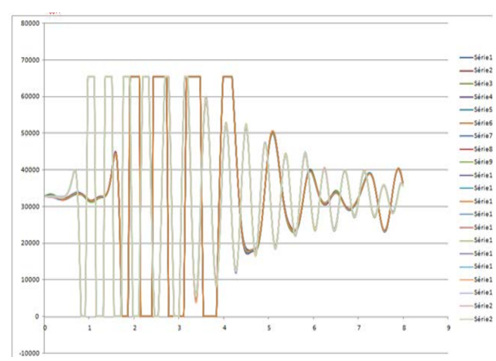

Fig. 8 Radar signals in the concrete and in the air

The velocity in concrete is calculated using the following equation:

$$v_{concrete} = \frac{d}{t_{concrte} - \left(t_{air} - \frac{d}{v_{air}}\right)} \qquad (1)$$

With :$t_{concrete}$ = 1.58 ns et t_{air} = 0.68 ns

$v_{concrete}$ = 10.58 cm/ns

From this speed value, we deduced the value of the dielectric constant e which is equal to 8.2, this corresponds to a concrete more or less wet.

The same operation was performed on the same core oven dried at 80 ° C to constant mass, The results are as follows:

$t_{concrete}$ = 1.02 ns, t_{air} = 0.39 ns and $v_{concrete}$ = 13.06 cm/ns

This speed value corresponds to a dielectric constant equal to 5.27.

ISBN: 978-1-61804-325-2

Therefore the EMW propagation speed is directly related to the moisture content of the material. More concrete is dry over the speed of propagation of electromagnetic waves, the higher the dielectric constant is low.

V. SENSITIVITY OF RADAR TECHNIQUE TO THE WATER CONTENT

In order to study the effects of water content on the radar signal, researchers used large specimens with a water content is controlled and evenly distributed [6], [7].

The specimens were used to measure the propagation speed using radar antennas in bi-static mode. [6] Two concrete compositions have been used with respective water / cement ratios of 0.66 and 0.48 and porosity accessible to water of 14.7% and 12.5%. Figure 2 shows the speed changes depending on the volume of water related to the volume of the sample (volumetric water content) for both tested concretes.

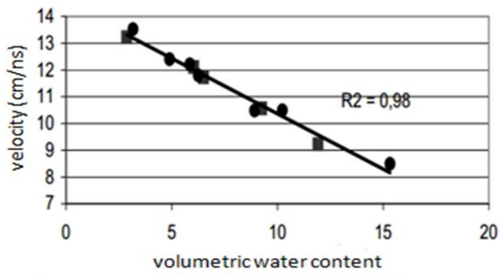

Fig. 9 Speed variation of direct wave with water content.

The test shows that the variation of speed of the direct wave depends only on the volume of water and not on the type of concrete or of its intrinsic porosity, Fig. 9.

The attenuation, it is function of the amplitude. The amplitude decreases (attenuation increases) with the increase of water content, Fig.10.

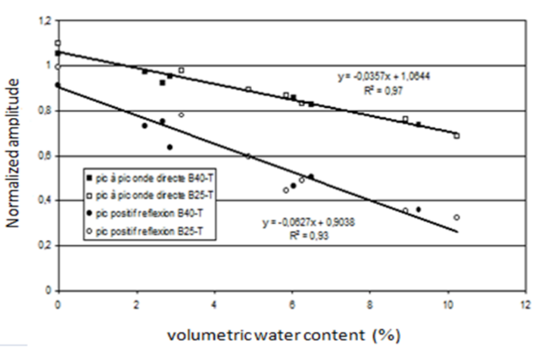

Fig. 10 Relationship between the amplitude of the direct wave and the reflection on steel bar and a water content in the concrete

The researches were conducted [8] at the same topic they have shown that the permittivity (dielectric constant) of the concrete is proportional to the volumetric water content. Fig.11

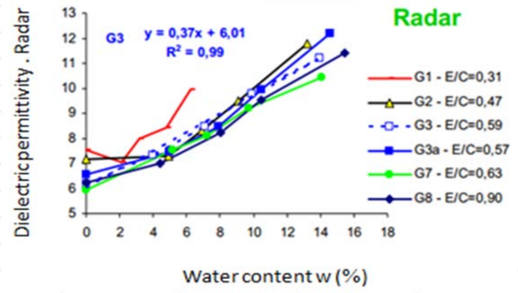

Fig. 11 Variation of the concrete permittivity with water content.

VI. SENSITIVITYOF RADAR TECHNIQUE TO CHLORIDES

Measurements were performed on specimens conditioned at different degrees of saturation with more or less loaded with NaCl solution (40 to 120 g / l). [9]

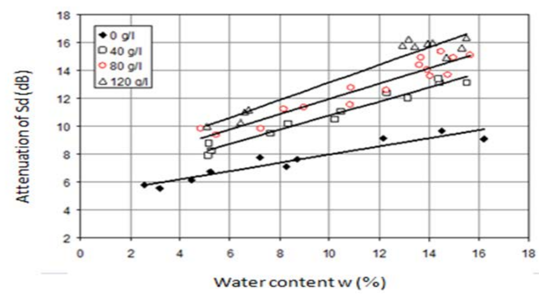

Fig. 12 Effect of Chlorides on the attenuation of the direct signal [9]

The results showed that the presence of chlorides attenuates significantly the amplitude of the radar but this does not have an effect on the speed.

VII. SENSITIVITY OF RADAR TECHNIQUE TO CHANGES IN ENVIRONMENTAL ELECTROMAGNETIC PROPERTIES

A. *Determination of concrete bedding*

As already shown in figure 1, there are two types of EM wave, the direct wave and a reflected wave, it is obtained where there's a change in the middle of the EM properties (permittivity and conductivity)

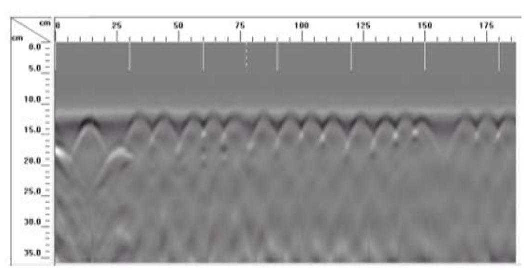

Fig. 13 Profile radar indicating the position of the reinforcements in a reinforced concrete wall (Radan 7)

Fig.13 shows the different phases and elements obtained as a result of changes in EM properties. Hyperbolic shapes shown the position of steel bars in the concrete.

The identification of reinforcement allows us to determine the depth of the coating; it is by the method of Kirchhoff migration, which converts the information X-T to XZ, from the knowledge of the speed radar waves in concrete.

This allows transforming hyperboles obtained in radar imaging to rounded shapes corresponding to reinforcement of concrete.

This method helps us to monitor the depth of the coating over time.

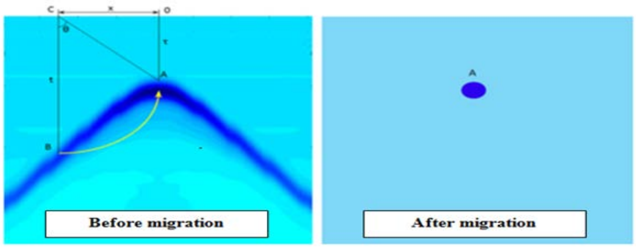

FIG. 14 KIRCHHOFF MIGRATION [10]

VIII. CONCLUSION

By relationship between the electromagnetic waves of radar and some physical and geometrical characteristics of the material, it is possible to determine parameters informing on concrete durability because:

-the Speed of the direct wave is a function of physical characteristics of the material (moisture and salinity).

-From The reflected electromagnetic waves, it is possible to determine some geometrical characteristics of the material (detection frames, determination of the coating and identification of anomalies).

By its sensitivity to changes in water content and chloride, technical radar would enable the prevention of reinforcement corrosion in reinforced concrete structures. The radar has a large capacity of acquisition, but interpreting the results need the use of software such as RADAN.

REFERENCES

[1] Laurens S., "Aptitude de la technique radar à la caractérisation du béton d'enrobage _ Aide au diagnostic de la corrosion des armatures", Thèse de Doctorat, INSA Toulouse (France), Université de Sherbrooke (Canada), 2001, p 211.

[2] Garciaz J.L., Perrin J.L., "Application du radar géophysique pour l'évaluation des antennes spécifique et traitement de données", Journées Scientifiques ENDGC 2, Bordeaux, Novembre 2001.

[3] Dérobert X., "Techniques radar appliquées au génie civil", LCPC, n°J1050343, ISSN 1167-4865, 2003.

[4] Lataste J.-F. (2002). Évaluation Non Destructive de l'état d'endommagement des ouvrages en béton armé par mesures de résistivités électriques, Thèse de doctorat, Université Bordeaux I, page 295 .

[5] Greaves, R.J, Lesmes, D.P, Lee, J.M, Toksöz. N. (1996). Velocity variations and water content estimated from multi-offset, ground-penetrating radar, Geophysics, 61 (3), p.683- 695.

[6] Klysz G. « Caractérisation du béton d'enrobage par technique radar : exploitation de l'onde directe émetteur-récepteur » Thèse de doctorat, Université Paul Sabatier – Toulouse III, 2004, 240 p

[7] Sbartaï M., «Caractérisation physico-chimique des bétons par radar –approche neuromimétrique de l'inversion », Thèse de Doctorat, Université Paul Sabatier Toulouse (France), Université de Sherbrooke (Canada), 2001, p244.

[8] Dérobert X et al .Complémentarité de techniques non destructives pour déterminer les propriétés de différents bétons hydrauliques, Laboratoire Central des Ponts et Chaussées (LCPC) - Centre de Nantes.2008.

[9] J.-P. Balayssac, V. Kringkaï, M. Sbartaï, G. Klysz, S. Laurens, G. Arliguie Contribution au développement du radar pour la caractérisation non destructive du béton Laboratoire Matériaux et Durabilité des Constructions (LMDC). 25e rencontres de l'AUGC, 23-25 mai 2007, Bordeaux.

[10] Rani HAMROUCHE "Reconnaissance géométrique des structures en maçonnerie ou en béton par imagerie radar multi récepteurs : approche numérique et expérimentale". Thèse Doctorat LMDC- Toulouse-France. Novembre 2011,p82 .

K.HADJA Doctor candidate **B**uilt **E**nvironment Research **L**aboratory LBE, civil engineering faculty, USTHB, Algiers, ALGERIA.

F.KHARCHI Professor Research Director, **B**uilt **E**nvironment Research **L**aboratory LBE, civil engineering faculty, USTHB, Algiers, ALGERIA.

J.P.BALAYSSAC, Professor Research Director LMDC, INSA, UPS, Toulouse, FRANCE

Comparison between techniques for generating 3D models of cultural heritage

V. Barrile, G. Bilotta, D. Lamari, G. M. Meduri

***Abstract*—** In recent years 3D digitizing and modeling of cultural heritage has become increasingly common. This is due mainly to advances in laser-scanning techniques, to modeling techniques based on images, to increasing the computing power and to virtual reality. In this work we compared consolidated operating mode of the laser scanner with the techniques of image capture and generation of 3D models based on photographs made with ordinary digital cameras. Through the help of special software exploiting appropriate photogrammetric techniques and algorithms defined in "Structure from Motion" (SfM) we can get reconstructions and high-resolution DEMs (Digital Elevation Model) of high quality. Object of study is a masonry tower dating back to the fifteenth and sixteenth century located in the south of Italy (Marina di Gioiosa Jonica, Reggio Calabria).

***Keywords*—**Geometrical survey, Masonry structures, Photogrammetric techniques, Structure from motion, Terrestrial laser scanner.

I. Introduction

THE world of cultural heritage is experiencing a phase of promotion and development of its assets thanks to the progress of survey techniques and multimedia communication.

The introduction of new measuring devices such as 3D laser scanners, spherical photogrammetry, structure-from-motion photogrammetry and the latest methods of image-based modeling produced a strong change in the mode of acquisition, treatment and restitution of metric information. These new techniques allow the construction of digital photo-realistic 3D models that can be used as an information system and as an aid to structural modeling.

The digital model becomes an operational tool that can be implemented in new information systems able to handle complex and typologically heterogeneous data for both single buildings and large geographical areas.

V. Barrile is with the DICEAM Department, Faculty of Engineering Mediterranean University of Reggio Calabria, Reggio Calabria 89100 IT (phone: +39-0965-169-2301; e-mail: vincenzo.barrile@unirc.it).

G. Bilotta was with the Department of Planning, IUAV University of Venice, Venice 30135 IT. She now collaborates with the DICEAM Department, Faculty of Engineering Mediterranean University of Reggio Calabria, Reggio Calabria 89100 IT (e-mail: giuliana.bilotta@iuav.it).

D. Lamari is with the DICEAM Department, Faculty of Engineering Mediterranean University of Reggio Calabria, Reggio Calabria 89100 IT (email: antonio.lamari@gmail.com).

G. M. Meduri is with the DICEAM Department, Faculty of Engineering Mediterranean University of Reggio Calabria, Reggio Calabria 89100 IT (email: ing.giuseppemariameduri@gmail.com).

In this paper, a promising photogrammetric technique is applied to a XV-XVI century masonry castle in southern Italy (Marina di Gioiosa Jonica, Reggio Calabria) called Torre Galea (Fig. 1) for the purpose of building surveying and structural modeling.

Fig. 1 Views of Torre Galea- Marina di Gioiosa Jonica (RC)

The flow chart of Fig. 2 shows the workflow, starting from the digital images, yields to the 3D structural model.

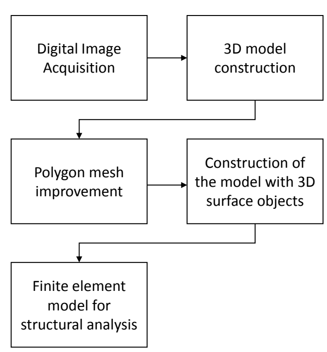

Fig. 2 Workflow for transition from photogrammetric 3D survey to a structural model

II. Construction of 3D Model

The procedure of photographs processing and 3D model construction comprises four main steps.

1. The first phase is the alignment of the camera. At this step, PhotoScan seeks common points on the photographs to merge with each other through the identification of a matching camera for every image and parameters of aging and calibration. As a result, they form a cloud of scattered points and a series of shots. The points of the cloud representing the alignment results between photos and will not be used directly in a further procedure of construction of the 3D model (except for the method of reconstruction cloud based Fig. 3). However, it can be exported for further use in external programs. For example, the cloud obtained can be used in a 3D editor as a reference to any evaluations. On the contrary, the set of positions taken by the camera are essential for the construction of the 3D model via PhotoScan.

2. The next phase is the construction of dense point cloud. (Fig. 4) Based on the positions of recovery estimated and extracted from the photos, PhotoScan generates a point cloud more dense and detailed. This point cloud can be modified and classified before proceeding with the export or the generation of three-dimensional mesh model.

3. Then we proceed with the construction of the mesh. (Fig. 5) PhotoScan reconstructs the surface of a 3D polygon mesh representing the object based on the dense point cloud obtained from the previous stage. In this case, Point Cloud based method can be used for the rapid generation of geometries based on point clouds scattered. Generally, there are two algorithmic methods available in PhotoScan that can be applied for the generation of 3D meshes: Field Height - for the type planar surfaces, or Arbitrary - for each object type.

4. After building the polygonal network, it may be necessary to adjust them. PhotoScan is able to make some corrections, such as decimation of the mesh, the removal of isolated components, the closing of holes, etc. When a more complex and detailed editing is pursued, a professional editing software has to be used. In this regard, PhotoScan allows exporting the mesh and to edit it with another software and then reopen it in PhotoScan through the most common interchange formats.

5. After the geometry (and hence the mesh) has been reconstructed, it can be structured and/or used for the production of orthophotos. There are several ways in texturing PhotoScan, described in detail in the manual supplied with the software.

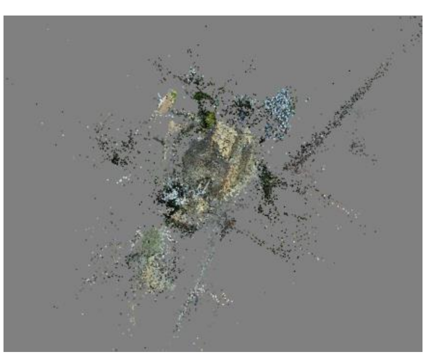

Fig. 3 Point Cloud Base

Fig. 4 Dense Point Cloud

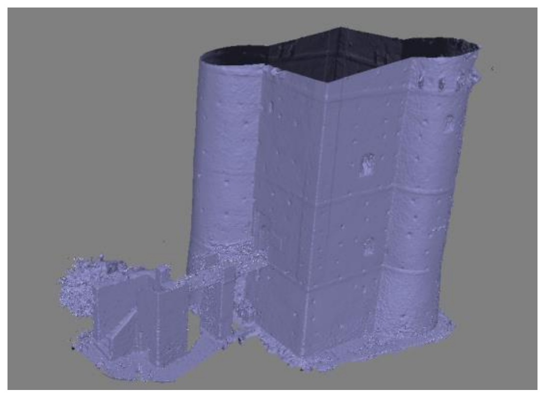

Fig. 5 Mesh

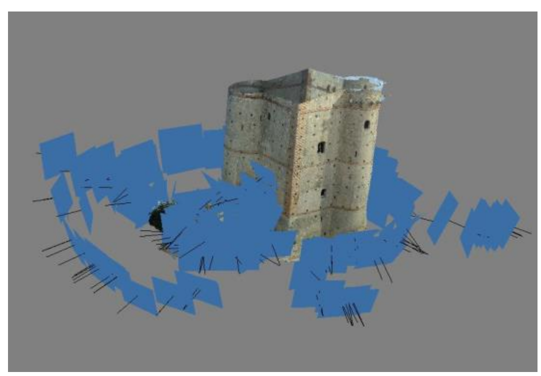

Fig. 6 Texture with the position of the camera (blue square)

It is possible to scale the 3D model starting from a known measurement, for example, we measured in a site the size of the door, which was found to be 0.90 meters.

In order to scale the model we define two markers (Fig. 8) that allow defining the distance between two known points, then we proceed to create a "scale bar" and to change the known distance.

Fig. 7 3D model with texture

Fig. 8 Markers with flags

III. POLYGON MESH IMPROVEMENT

For eliminating defects of mesh, we proceed exporting the 3D model from PhotoScan in STL format, and then we imported the model into Geomagic Studio software. This software provides editing point cloud, mesh and editing functions of advanced surfacing, in addition to its accurate functions of processing 3D data.

The Mesh Doctor is an automatic improvement of polygon mesh. It is generally preferable to use the Mesh Doctor after importing a polygonal model.

The steps to follow in order to improve the mesh are:

1. Import the model (STL) within Geomagic Studio to set the unit of measurement.

2. The software automatically recognizes the presence of mesh and then provide information to that effect and asks if you want to launch an analysis mesh doctor, once made the analysis shows us graphically (Fig. 9) identifying with red areas the parts of the mesh that need to be repaired.

3. If necessary, we can rescale the model using the specific tool available in Geomagic (Figg. 10, 11).

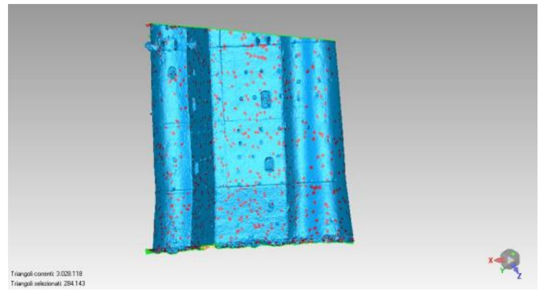

Fig. 9 Mesh with damaged areas identified in red

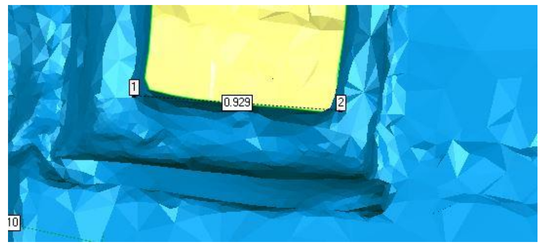

Fig. 10 Measurement of the door by two points

Fig. 11 The tool "Resize"

IV. INSTRUMENTS AND SOFTWARE USED

For the survey we used the laser scanner Leica HDS 3000 distributed with the software supplied by Leica (Cyclone™) that allows we to manage both scanning operations and those of computing and data processing.

The scans required the use of 16 targets arranged on the frame in such positions that, the various scans, had in common at least 4 targets, fundamental for the subsequent phase of recording and sewing of consecutive scans.

After the survey phase, in the laboratory, we generated the 3D model of the structure through the recording operations of the various scans (whose characteristics are shown in table III) and the subsequent thinning of the raw data by eliminating the highest number of points not belonging to the structure and surrounding vegetation. We thus obtained a single cloud of points representative of the investigated object. Since, also, the tool equipped with an inner camera to the CCD for the simultaneous acquisition of images of the raised portion, it was obtained a model highly realistic (Fig. 12) resulting from the association, with each point laser detected, of information of the color of its digital image.

3D laser scanning of the tower was carried out by two operators. There have been 4 scans around the outer perimeter of the object in a time of ca. 1.4 hours. To merge the scans have been used 16 target. For the next RGB color scans have been used 52 photographs. The entire point cloud thus obtained ca. 26 million, was sampled up to a distance of 1 cm with Geomagic Studio software. It was subsequently generated a 3D mesh with 1.3 million vertices ca. and 2.5 million faces ca. The work activities related to TLS can be so summarized: 1,4 hours for the acquisition of the 4 scans, 1.5 hours for the RGB coloring of all scans, 2.5 hours to the meshing in Geomagic Studio for a total 5.4 hours for the entire workflow

The generation of 3D point clouds from photogrammetric data with related models was carried out with the open-source software bundler / PMVS2 and VisualSFM and with low-cost software PhotoScan produced by Agisoft. A feature common to both VisualSFM that PhotoScan is the use of algorithms that make wide use of the GPU in order to significantly accelerate the processing of data. The images were captured with a Samsung model PL20 with CCD sensor 1/2:33" and shutter aperture f/3.5-5.9. The images obtained have dimensions of 4320 x 33240 pixels.

The images were taken at eye. A total of 219 photographs were taken for the entire outdoor area. The generation of point clouds was conducted with a Workstation DELL T7610 processor XEON 2680 v2 10 core with 32 GB of RAM equipped with an NVIDIA Quadro FX 4800 with 1.5 GB of RAM and running Windows 7 Professional 64-bit. Table I summarizes the results obtained from the use of the three software.

Table I Statistics on the production of clouds of points with the use of the three software

	Visual SFM	Bundler/PMVS2	PhotoScan
No. images	219	219	219
No. points	8741118	13527920	28431222
Time	2,10 h	3,25 h	4,75 h
Standard deviation σ	8 cm	4,5 cm	2 cm

You may notice the important differences in the results obtained. All the clouds generated by the three software have been scaled using different reference distances measured in the field. The accuracy of the distances of the reference appears significantly influenced by the density of the points constituting the cloud. It is to highlight how the software PhotoScan offers the possibility to locate and fix the control points in the shots made at high resolution, to use a sophisticated model of camera calibration including the determination of the focal length and the distortion of the radial lens.

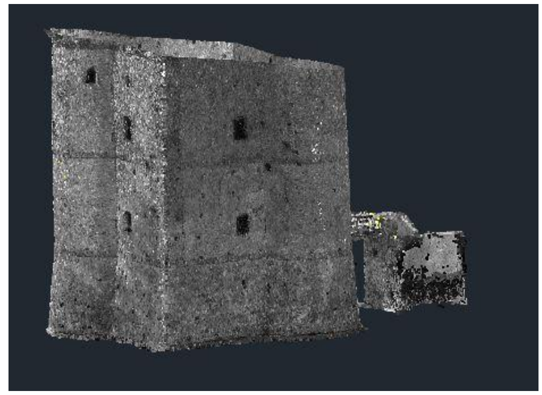

Fig. 12 Grayscale point cloud obtained by laser scanner survey

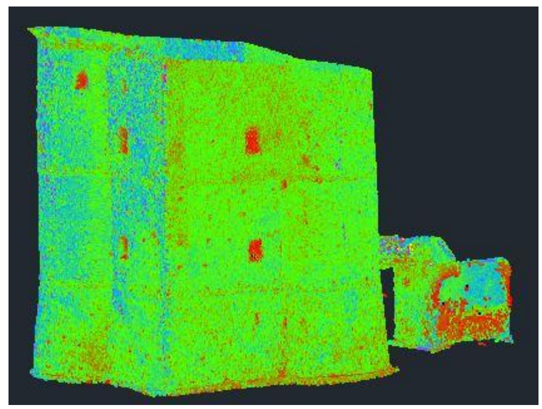

Fig. 13 Point cloud (spectrum) obtained by laser scanner survey

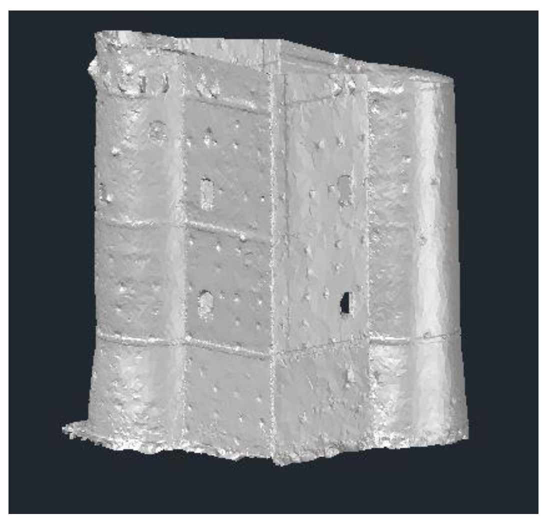

Fig. 14 Texture obtained by laser scanner survey

V. 3D MODELS IN COMPARISON

We compared the 3D models of the Tower, made with VisualSFM, Bundler/PMVS2 and Agisoft Photoscan, with reference data obtained from laser scanning to assess the geometric quality of the 3D models. The quality of the 3D data obtained from VisualSFM and Bundler/PMVS2 does not match the high quality geometric obtained by TLS. In particular, in the generation of the 3D model, there was a deviation of 20 cm with VisualSFM and 16 with Bundler/PMVS2. The deviation detected with PhotoScan was 4 cm. The tables summarize the results obtained from the survey and Photoscan TLS.

Table II Summary results from PhotoScan

Photo No.	Acquisition time	Processing time	Dense cloud	Vertices No.	Sides No.	Standard deviation σ
219	*0,4 h*	*4,75 h*	*28431222*	*1516899*	*3028118*	*4 cm*

Table III Summary results from TLS method

Setting up No.	Acquisition time	Processing time	Dense cloud	Vertices No.	Sides No.	Standard deviation σ
4	*1,4 h*	*4 h*	*25822457*	*1314597*	*2518047*	*0,5 cm*

VI. CONCLUSIONS

This work shows that, next to the surveys carried out with laser scanner systems, even low cost systems based on photographic shots are able to produce 3D of large objects such as the Tower under study. Data acquisition with cameras is fast, flexible and economical than laser scanning. The results obtained with the software PhotoScan show mean deviations of two centimeters resulting geometrically very close to the data obtained by laser scanning.

The software VisualSFM and Bundler/PMVS2 well suited to the acquisition and generation of 3D models of small objects, for the return of large objects show all their limits. As regards the quality and the reliability, the limiting factors of SFM are, in general, and especially for large objects, the light conditions, the number of images, and the resolution of the photographs taken. They are also to be particularly important measurement procedures and the identification of control points for resizing the 3D model obtained. To this purpose, the use of a camera with high resolution and with the objectives of superior quality could improve the results obtained. In the present case, we could obtain results significantly more optimized and precise if the acquisition of the images was made using UAV systems.

It is evident as the performance capabilities of the computers are critical to the minimization of the processing time of the data, especially for larger objects, characterized by a large number of photographs necessary for a complete reconstruction of the object acquired. At present, experimentations continue in order to optimize the generation of 3D models with particular reference to the findings of archaeological. To do this, we make extensive use of UAV systems with substantial results.

REFERENCES

[1] A. Bandiera, J. A. Beraldin, M. Gaiani, “Nascita ed utilizzo delle tecniche digitali di 3D imaging, modellazione e visualizzazione per l’architettura e i beni culturali”, *Ikhnos*, 2011, pp. 81-134.

[2] L. Guidi, *Acquisizione 3D e modellazione poligonale*. Edizione Mondadori, Milano, 2010.

[3] L. Barazzetti, G. Forlani, F. Remondino, R. Roncella, M. Scaioni, “Experience and achievements in automated image sequence orientation for close-range photogrammetric projects” in *Proceedings of SPIE Optics+Photonics*, vol. 8085, 23-26 May, Munich, Germany, 2011.

[4] M.T. Como, “Il restauro di monumenti a torre in muratura”, *Restauro*, 2000, pp.152- 153.

[5] V. Barrile, G.M. Meduri, G. Bilotta, “Comparison between Two Methods for Monitoring Deformation with Laser Scanner”, *WSEAS Transactions on Signal Processing*, vol.10, 2014, pp. 497-503.

[6] V. Barrile, G.M. Meduri, G. Bilotta, “Laser scanner technology for complex surveying structures”, *WSEAS Transactions on Signal Processing*, no.3, vol.7, 2011, pp. 65-74.

[7] V. Barrile, G.M. Meduri, G. Bilotta, “Laser scanner surveying techniques aiming to the study and the spreading of recent architectural structures” in *Proceedings of the 9th WSEAS International Conference on Signal, Speech and Image Processing (SSIP '09): Recent Advances in Signal and Systems*, 2009, pp. 92-95.

[8] Agisoft PhotoScan v.1.1 (http://www.agisoft.com/).

[9] Geomagic Studio 2013 (http://www.geomagic.com/).

[10] Autodesk Autocad 2016 (http://www.autodesk.it/).

[11] V. Barrile, G. M. Meduri, R. Pucinotti, “Il rilievo di strutture esistenti mediante l’impiego della scansione laser finalizzato alla modellizzazione strutturale: un caso di studio” in *Atti del Convegno Nazionale "Sperimentazione su Materiali e Strutture"*, Venice, december 2006, pp. 831-838.

[12] R. Pucinotti, G. M. Meduri, V. Barrile, "L’applicazione della scansione laser e della tecnologia radar ad un ponte in cemento armato" in *Atti del 12° Congresso Nazionale dell’AIPND – Conferenza Nazionale sulle Prove non Distruttive Monitoraggio Diagnostica*, Milan, 11-13 October 2007, pp. 1-8.

[13] V. Barrile, G. M. Meduri, G. Bilotta, "Laser scanner surveying techniques aiming to the study and the spreading of recent architectural structures" in *Proceedings of the 2nd WSEAS International Conference on Engineering Mechanics, Structures and Engineering Geology, EMESEG '09: "Recent Advances in Engineering Mechanics, Structures and Engineering Geology"*, Rodos, Greece, July 22-24, 2009, pp. 25-28.

[14] V. Barrile, G. Bilotta, G. M. Meduri, “Archaeological Investigations with TLS and GPR Surveys and Geomatics Techniques”, in *Towards Horizon 2020 - Proceedings of 33rd EARSeL Symposium 2013* 3-6 June 2013, Matera, Italy, pp. 857-864.

[15] F. Remondino, F. Menna, “Image-based surface measurement for close-range heritage documentation”, *International Archives of Photogrammetry, Remote Sensing and Spatial Information Sciences*, vol. 37(B5-1), 2008, pp. 199-206.

[16] F. Remondino, S. F. El-Hakim, A., Gruen, L. Zhang, “Turning images into 3-D models”, *IEEE Signal Processing Magazine*, vol. 25 no. 4, 2008, pp. 55-65.

[17] D. Scharstein, R. Szeliski, *Middlebury Stereo Vision Page*, 2009, http://vision.middlebury.edu/stereo/, visited at 7.1.2012.

[18] N. Snavely, S. M. Seitz, R. Szeliski, “Modeling the World from Internet Photo Collections”, *International Journal of Computer Vision*, vol. 80 no. 2, 2008, pp. 189-210.

[19] D. Abate, G. Furini, S. Migliori, S. Pierattini, “Project Photofly: New 3D Modelling Online WEB Service”, *International Archives of*

Photogrammetry, Remote Sensing and Spatial Information Sciences vol. 38 (5/W16), 2011, pp.391-396.

[20] M. A. Fonstad, J. F. Dietrich, B. C. Courville, J. L. Jensen, P. E. Carbonneau, "Topographic structure from motion: a new development in Photogrammetric measurement", *Eart. Surf. Process. Landforms*, no. 38, 2013, pp. 421-430.

[21] M. Bolognesi, A. Furini, V. Russo, A. Pellegrinelli, P. Russo, "Accuracy of cultural heritage 3D models by RPAS and terrestrial photogrammetry", *The International Archives of the Photogrammetry, Remote Sensing and Spatial Information Sciences*, no. XL-5, 2014, pp. 113-119.

A Novel Modeling Approach for the Drying of Leafy Materials

A. Orphanides, V. Goulas and V. C. Gekas.

Abstract— Although during the drying unit operation a severe shrinkage of leafy material occurs no explicit account of this fact is taken in herb plant drying modelling. Even more rare , not to say un-existed, are applications of the true driving force, that is the thermodynamic driving force , according to the opinion of the authors. In this work both aspects have been considered and explicitely applied in the modeling of drying of a common herb plant, mentha viridis, used as a model aromatic herb plant material. Application of the two before mentioned aspects leads to interesting findings which are thoroughly discussed in the present paper.

Keywords—Drying, modeling, shrinkage, water activity

I. Introduction

THIS paper carries some new ideas concerning the modeling of the unit operation of drying. Conventional modeling of convective air drying implies the use of the so-called apparent or effective diffusion coefficient, D_{eff}, although the dehydration occurring during the drying process does not follow a strict diffusion mechanism. Application of the above mentioned coefficient as predictive tool presents serious difficulties since reported values of that coefficient in the literature show differences of several orders of magnitude even for the drying of the same species [1],[2].

Main factors affecting mass transfer during the drying are the shrinkage which alters the geometry of the examined specimen and also the driving force, which should not be based on the water content but rather on the water activity in the leafy material and in the air, i.e. the water potential, given that water activity is closely connected to the chemical potential which is also closely connected to energy, according to Thermodynamics [3]-[5]. Concerning shrinkage, dehydration studies have shown that there is a linear relationship between the volume change ratio and the water content change ratio.

Thus, these two factors are taken explicitly in to consideration upon modeling of the drying of leafy materials. To or knowledge , no such study has ever been done before. The conventional approach includes in the Deff parameter all factors influencing. The alternative approach , on the contrary, applied in the present paper takes in to account both important factors , namely , the shrinkage effect and the true driving force and leads in interesting observations.

A. Orphanides was with the Department of Agriculture, Biotechnology and Food science at the Cyprus University of Technology, Limassol, CY-3036, Cyprus, antia.orphanides@cut.ac.cy

V. Goulas is with is with the Department of Agriculture, Biotechnology and Food science at the Cyprus University of Technology, Limassol, CY-3036, Cyprus , vlasios.goulas@cut.ac.cy

V. C. Gekas, the corresponding author is the Dean of the School of Geotechnical Sciences and Environmantal Management, Cyprus University of Technology, Anexartissias 33, CY-3036, Limassol, Cyprus, Vassilis.gekas@cut.ac.cy, tel. 0035725002301

II. Materials and Methods

A. *Mentha viridis herb*

Fresh Mentha viridis leafy material was provided by AGROPLANT LTD in Limassol, Cyprus, and was used the same day in all experiments carried out in the drying equipment which was the pilot plant air dryer , described below.

A. *Experimental Design*

A complete factorial design was performed, where the independent variables were air temperature (40, 50, 60 and 70°C) and air velocity (1.5, 2, 2.5, 3 m s-1) leading to 16 total of combinations. For each treatment, approximately 100g of fresh, healthy leaves were separated from the stems and subsequently placed in thin layers onto the five trays of the dryer chamber. The weight loss was recorded every 10 sec; the end of drying was defined when the weight remained stable for more than 10 min and the moisture content was lower than 12%. Each experiment was repeated twice and samples were kept at -22°C for further analysis.

B. *The pilot plant air dryer*

The pilot scale air dryer An air-dryer was designed and developed based on previous work[6]. An automatic scale (accuracy ±0.1g) was mounted on top of a flow chamber with controlled temperature and horizontal air flow. A metallic structure comprising of 5 perforated stainless steel trays (allowing the air movement in-between leaves and trays) was hanged by the scale (Fig.1).

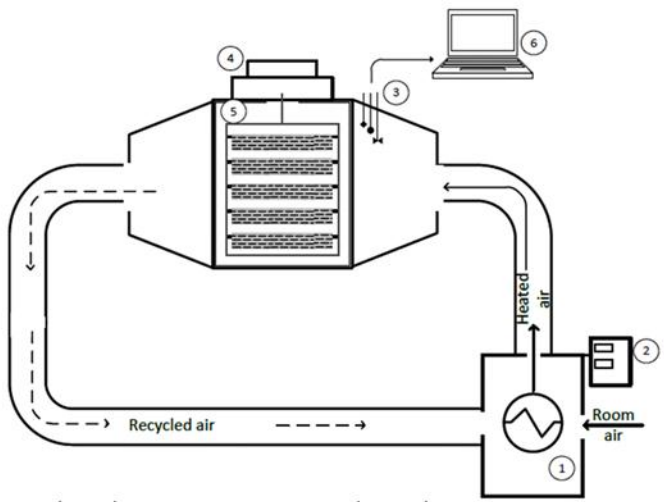

Fig.1 Schematic representation of lab scale air dryer with major parts: 1. Heating Unit; 2. Control Unit; 3. Thermometer, Hygrometer, Anemometer; 4. Electronic Scale; 5. Perforated Stainless Steel Trays; 6. Computer for data recording and processing

D Shrinkage and water activity measurements

The shrinkage ratio was obtained by measuring the dimensions of the leafy material before and after each experiment. The water activity was obtained through the sorption isotherm of the leafy material. The sorption isotherm for 50 oC is shown below (Fig.2).

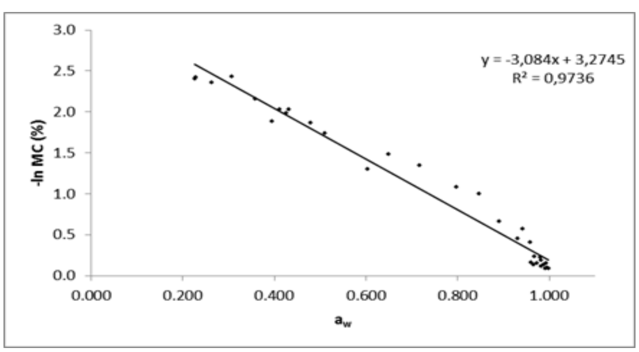

Fig. 2. Sorption Isotherm of *Mentha viridis* at 50 ^{o}C

III. THEORY

Here the principles of the development of the model are given.

- The leaves are assumed covering uniformly the area through which the water transport takes place..
- The medium in which the transport takes place includes the convective boundary layer attached to the leafy material, thus the leaf layer and the boundary layer are taken as a unit.
- The temperature remains constant during drying thus we refer to isothermal drying.
- The shrinkage is assumed to occur isotropically. I
- The driving force for drying is given by the active concentrations 9activities) rather than simply concentrations. Thus the model belongs to the Thermodynamic models

In the following the utterly important aspects of shrinkage , the flux and the driving force are considered. Assuming isotropic shrinkage [7], the relationship between water content and volume of the leafy material is as follows:

$$A_t=A_0\,(M_t/M_0)^{\wedge}(2/3) \qquad (1)$$

Mo and Mt being the moisture content the initial one and at time t respectively and Ao and At the surface area, the initial one and at time t respectively. The area as a function of the moisture content is introduced in the expression of the mass transfer flux, J

$$J_t= \Delta M_t/(\Delta t.\ A_t) \qquad (2)$$

being Jt the flux at time t, during a time interval Δt, ΔMt is the moisture loss during the interval time Δt, and At the surface area of the leafy material to be dehydrated. Thus the effect of shrinkage is explicitly taken into account.

The driving force is modeled as the difference between the water activity in the air (that is the relative humidity of the air) and the water activity in the leafy material of *Mentha viridis*. The relative humidity of the air, ψ, was obtained from registered data in the pilot dryer and the water activity, aw, of the leafy material obtained through the sorption isotherm as mentioned above in the Materials and Methods section.

Finally the constitutive equation connecting the flux with the driving force

$$J_t=\text{Leff}\,(\alpha w_{,t}-\psi) \qquad (3)$$

L_{eff} is the thermodynamic mass transfer coefficient, known also as mass conductivity a term coined by G. Crapiste (the Bahia Blanca model) [8].

IV. RESULTS

The results in terms of reduced moisture content versus time for different temperatures at constant air velocity 1.5 m/s, are given in Fig. 3

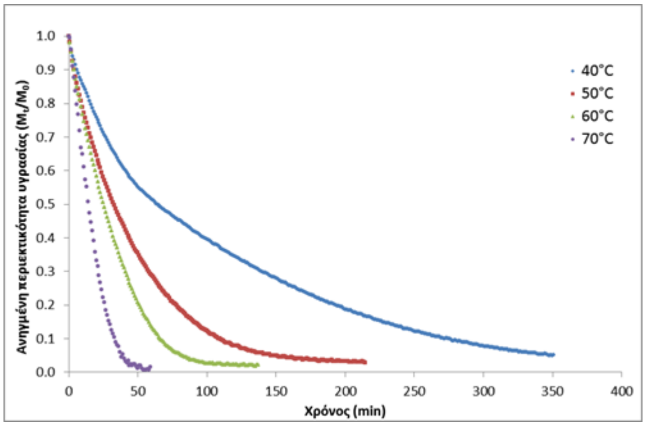

Fig.3. Reduced moisture content vs time at different temperatures for air speed of 1.5 m/s.

Choosing the temperature of 50 ^oC, for herb product quality reasons, the effect of the air velocity on the reduced moisture content is given in Fig.4.

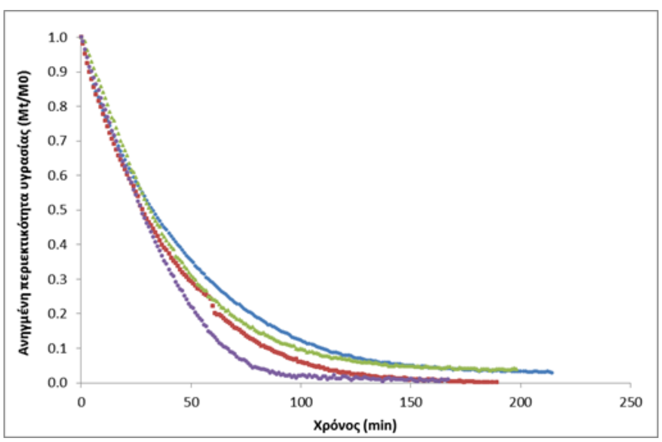

Fig.4. Reduced moisture content vs time at different air velocities for a drying temperature of 50 ^oC.

Furthermore, plotting the flux vs the driving force as defined above in the section of Theory, straight lines are obtained. An example of such a diagram is shown in Fig.5. This result provides a first strong evidence for the validity of the model developed in this paper.

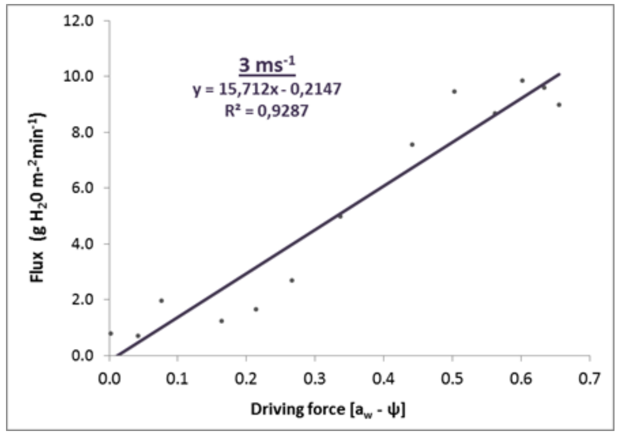

Fig.5 Flux versus driving force for the drying at 50 oC

V. DISCUSSION

Figures 3 and 4 predict a severe shrinkage ration between initial and final values (up to 90% decrease in volume) and this has been verified by the experiment. In the present approach the shrinkage has been taken in to account in the water flux. The decrease in the surface leads to an increase of the flux, other thinks equal, since the surface area A is in the denominator of the expression for the flux.

Furthermore, eq. 5 shows a clear tendency of a phase of increased drying rate for leafy materials, in terms of dehydration flux, opposite to the common establishment of constant and falling rate periods. Of course more experiments are needed to support this interesting finding.

Also eq. 5 provides a strong evidence that the driving force should be based on the water activity than on the moisture content. Thirdly the Leff (mass conductivity) behaves as a real constant, for the same temperature, compared to the traditionally used Deff.

As ideas for a future research, more experimentation is required to draw final con clusions on the first findings of the present study. In addition to the *Mentha viridis* , other leafy materials should be examined.

Acknowledgment

The authors acknowledge Dimitris Panayiotou, Director of the AGROPLANT LTD company located in Limassol Cyprus for his support to the project and never theless for the supply of raw material, the *Mentha viridis* herb.

References

[1] D.M. Kadam, R.K. Goyal, K.K. Singh , & M.K. Gupta . Thin layer convective drying of mint leaves. *Journal of Medicinal Plants Research*, 5(2), 164-170, 2011.

[2] I. Doymaz, Thin-layer drying behaviour of mint leaves. *Journal of Food Engineering*, 74(3), 370-375, 2006

[3] J.A. Wesselingh, R. Krishna (2006). *Mass transfer in multicomponent mixtures.* Delft Academic Press, Delft, 2006

[4] V. Gekas, Mass Transfer Modeling *Journal of Food Engineering*, Vol 49, 2-3, pp 97-102, 2001

[5] A. Orphanides, V. Goulas ,, & V. Gekas.. Introducing the concept of sono-chemical potential: A phenomenological model for ultrasound assisted extraction. *Journal of Food Engineering*, 120(1), 191-196, 2014.

[6] J.V. García-Pérez, J.A. Cárcel, S. de la Fuente-Blanco, &E. Riera-Franco de Sarabia . Ultrasonic drying of foodstuff in a fluidized bed: Parametric study. *Ultrasonics*, 44(SUPPL.), e539-e543, 2006.

[7] N. P. Zogzas, Z. B. Maroulis & D. Marinos-Kouris (1994) Densities, shrinkage and porosity of some vegetables during air drying, *Drying Technology*, Vol. 12, Issue 7, pp 1653-1666, 1994.

[8] V. Gekas, *Transport Phenomena of Foods and Biological Materials*, CRC Press, Boca Raton (FL), 1992.

ISBN: 978-1-61804-325-2

An Investigation of Sloped Surface Roughness of Direct Poly-Jet 3D Printing

John D. Kechagias[1*], and Stergios Maropoulos[2]

***Abstract*—**This paper presents an experimental investigation of sloped surface roughness of the direct Poly Jet 3D printing process (DPJ-3DP). The parameter tested is the angle θ of the slopped surfaces in X and Y directions. The surface roughness parameter measured were the average mean surface roughness (Ra, μm), and the total height of the roughness profile (Rt, μm). The investigation shows that both Ra and Rt increased when the angle θ increased, in both X and Y directions. Additionally, the best value of surface parameters was achieved at angle θ equal to zero and the worst at θ equal to 90 degrees.

***Keywords*—**Surface roughness, direct poly-jet 3d printing, Sloped Surfaces

I. Introduction

The transition from the Rapid Prototyping (RP) and Rapid Tooling (RT) to the 3D Printing era has been taking place over the last years. The potentials brought about from such a technology aim to affect the way products are produced in a similar way that RP and RT transformed the traditional approaches for the design and development of a product. RP is an advanced manufacturing technology commercialized in the mid '80s. Currently, RP technology is widely utilized in manufacturing for conceptual and functional models. The application of RP has been shown to greatly shorten the design-manufacturing cycle, hence reducing the cost of product and increasing competitiveness. Further development of this technology is focusing on short and long term tooling which again has been proved in some cases to reduce costs and cycle times. Evolution of RP is the so called 3D printing processes. Recently developed technologies, such as Selective Laser Sintering (SLS), three-dimensional printing (3DP) and PolyJet enable to produce customized and complex parts in a short amount of time [1], compared to traditional RP technologies such as Stereolithography (SL). The Polyjet Direct 3D Printing (PJD-3DP) system builds detailed models with smooth surfaces by a process of addition photopolymer resin layers. This is enabled by a technology utilizing simultaneous jetting of modeling materials to create physical free form prototypes [2]. It is capable of creating parts of complex geometry with materials such as photo-curable resins that can be used in the areas of automotive, electronics, consumer goods, medical development, etc. In 3D printing, layers of a photopolymer resin are selectively jetted onto a build-tray via inkjet printing [3]. The printing head, composed by a number of micro jetting heads, injects a 16 μm thick layer of resin onto the built tray, corresponding to the built cross-sectional profile. The jetted photopolymer droplets are immediately cured with ultraviolet lamps that are mounted onto the print carriage. The repeated addition and solidification of resin layers produces an acrylic 3D model with a dimensional resolution of 16 microns. The PJD-3DP process has the ability to simultaneously jet multiple materials with different mechanical and optical properties. 3D printing could be considered a fully controllable process, since the majority of the process parameters can be altered on user's demand. Consequently the quality of the part does depend on a number of factors. Two basic quality indicators can be considered as major i.e. the model's surface roughness and model's dimensional accuracy. Both depend on the machine and the process variables [4]. Several attempts have been made to make a systematic analysis of errors and the quality of the prototypes.

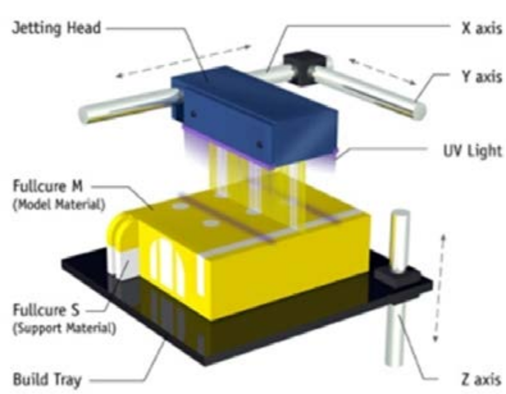

Fig. 1: The PolyJet Direct 3DP Process [2]

Experimental analysis of dimensions, surface roughness, and mechanical properties between PJD-3DP and ZCORP-3DP processes has been investigated in study [5]. Determination of surface texture parameters Ra and Rz for

This research is implemented through the Operational Program "Education and Lifelong Learning" and is co-financed by the European Union (European Social Fund) and Greek national funds.

*[1]J. Kechagias is with the Department of Mechanical Engineering, Technological Educational Institute of Thessaly, Larissa 41110, Greece (corresponding author: phone: 0030 2410684322, fax: 0030 2410684305, email: jkechag@teilar.gr)

[2]S. Maropoulos is with the Department of Mechanical Engineering and Industrial Design, Technological Education Institution of Western Macedonia, Kozani 50100, Greece (email: maropou@teikoz.gr)

horizontal surfaces of parts produced by PJD-3DP have been performed in [6]. The results indicate that for mate surfaces Ra equals approximately 1.04μm while Rz about 5.6μm. For glossy surfaces Ra is approximately 0.84μm and Rz 3.8μm. Mechanical properties of parts produced by PJD-3DP, have been investigated in [7]. The study concluded that the part orientation has an effect on mechanical properties due to the heterogeneity of light energy by the photopolymer material during jetting process. The variability in the mechanical properties of parts manufactured via PJD-3DP has also been examined in [3]. It has been concluded that part orientation affects tensile strength and tensile modules with highest tensile modulus occurring in the XZ orientation. An investigation of the process parameters effects, concerning the dimensional accuracy of parts produced by the Polyjet Direct 3D Printing Process, was presented in [8]. The results indicate that the dimensional accuracy of external dimensions are affected in principle by the blade movement and the Layer Thickness, while the internal, primary by the Layer Thickness and the Scale factor. Additionally, an investigation of the process parameters effects, concerning the vertical and planar surface roughness of parts produced by Polyjet Direct 3D Printing Process was presented in [9]. The results indicate that the 16 microns layer thickness, and glossy style provide the optimum surface roughness results while scale factor could not be considered as a dominant factor.

In the current work, the slopped surface roughness is investigated in direction X and in direction Y as indicated in Figures 5 and 6. The results were compared with the analytical model (eq. 1) which is extracted in the [10]

$$\mathrm{Ra} = \frac{L_t \sin(\theta)}{4\tan(\theta)} \tag{1}$$

where Lt is the layer thickness-height and θ is the sloped surface angle.

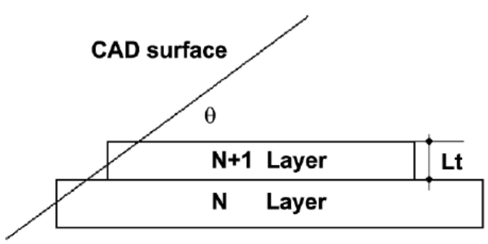

Fig. 2. Platform setup-Side view (Y-Z plane)

II. EXPERIMENTAL SETUP

A part has been designed with two details on the top surface (see Fig. 3) and then is placed seven times, on the same platform, as shown in Figures 4-6. Slopped surfaces on both X and Y directions are 0, 15, 30, 45, 60, 75 and 90 degrees from build platform. The selected part geometry has been prepared in STL format.

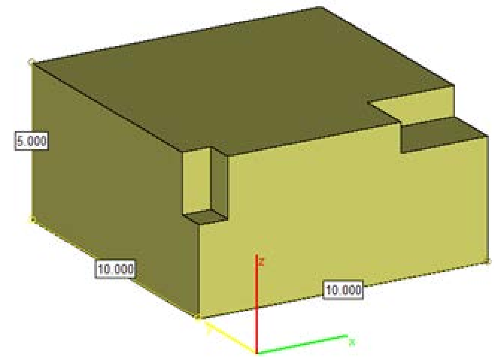

Fig. 3: CAD file of the test part

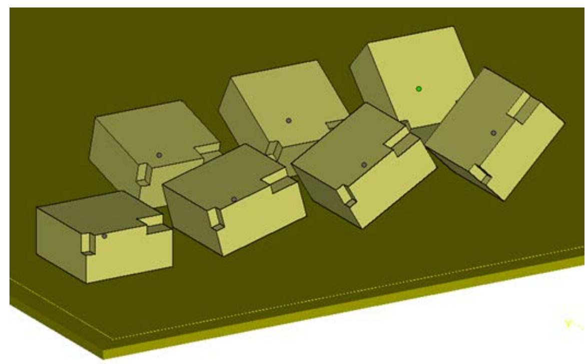

Fig. 4. Platform setup-ISO view

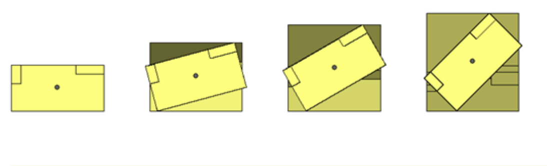

Fig. 5. Platform setup-Side view (X-Z plane)

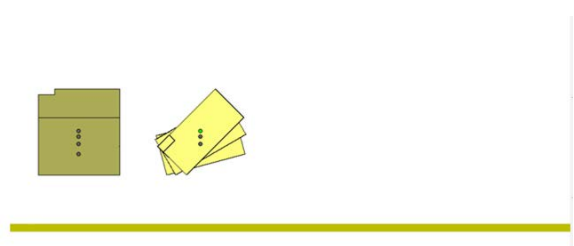

Fig. 6. Platform setup-Side view (Y-Z plane)

The surface texture parameters measured during this study were the following (Fig.7):

- Ra (μm): the arithmetic mean surface roughness (arithmetical mean of the sums of all profile values). Ra is by far the most commonly used parameter in surface finish measurement and for general quality control. Despite its inherent limitations, it is easy to measure and offers a good overall description of the height characteristics of a surface profile [3].

and

- Rt or Rmax (μm): total height of the roughness profile, i.e., the vertical distance between the highest peal and the lowest valley along the assessment length of the profile. From Fig.1, Rt= Zp + Zv. This parameter is very sensitive to the high peaks or deep scratches.

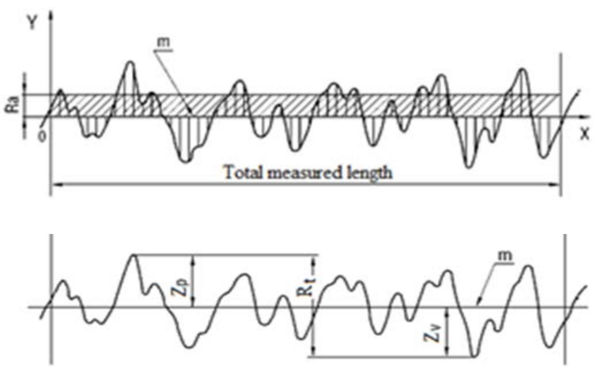

Fig. 7: Surface texture parameters

The seven prototypes have been built on an Objet Eden 250 using the Objet Fullcure 720 RGD material (Fig.8). The layer height was 16 microns, and the parts were built in mate mode.

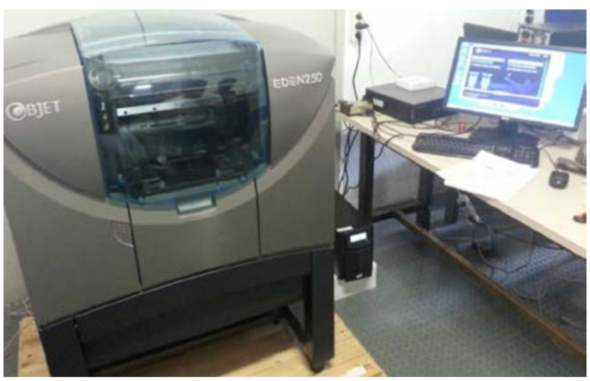

Fig. 8. Eden250™ 3D Printing System

III. I. EXPERIMENTAL RESULTS AND CONCLUTIONS

The seven parts were oriented and set on platform as shown in Figures 4-6. The layer thickness was set at 16 microns and the build style was set on mate mode. After the manufacturing the seven parts were cleaned using a waterjet machine and then sloped surfaces were measured using the Mitutoyo Surftest RJ-210 tester. The measurements of the sloped surfaces surface roughness were shown at Tables 1 and 2 in both X and Y directions. At Figures 9 and 10 the comparison between experimental and analytical (eq. 1) measurements are presented. The results shows that analytical model is not appropriate for surface roughness (Ra) prediction. Additionally, experimental results shows that the surface roughness increased when the angle degrees increased.

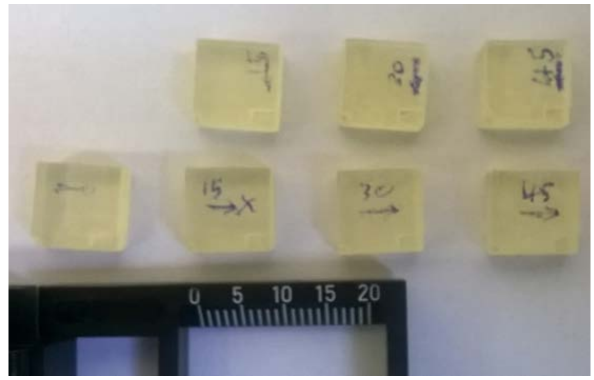

Fig. 9. Parts with sloped surfaces in X and Y directions

degrees	Ra (μm)	Rt (μm)
0	0.537	4.294
15	4.188	29.311
30	6.259	44.345
45	8.377	61.807
60	12.425	102.28
75	15.211	140.93
90	18.722	137.54

Table 1: X-Direction measurements (Y Rotation)

degrees	Ra (μm)	Rt (μm)
0	1.985	13.393
15	3.584	25.167
30	5.367	43.641
45	8.729	76.513
60	12.035	80.545
75	14.142	97.445
90	14.496	105.62

Table 2: Y-Direction measurements (X Rotation)

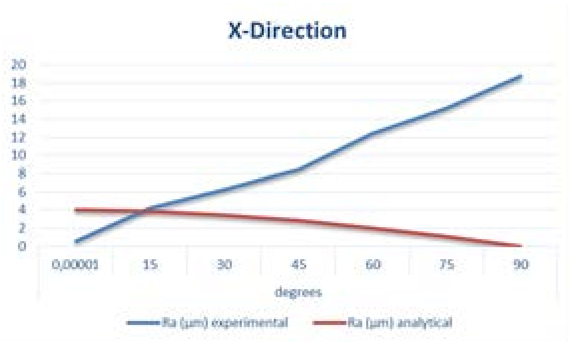

Fig. 9. Experimental and analytical measurements in X-Direction

Fig. 10. Experimental and analytical measurements in Y-Direction

REFERENCES

[1] M.F. Zaeh, 2006, “Wirtschaftliche Fertigung mit Rapid-Technologien. Anwender-Leitfaden zur Auswahl geeigneter Verfahren, iwb Application Centre Augsburg”, Technische Universitaet Muenchen. Munich, Germany, Hanser, ISBN:9783446228542.

[2] "Objet Polyjet Process." Objet Geometries Ltd. www.Objet.com, n.d. Web. <http://www.objet.com/products/polyjet_technology/>.

[3] M.W. Barclift, C.B. Williams, 2012, “Examining variability in the mechanical properties of parts manufactured via polyjet direct 3D printing”, International Solid Freeform Fabrication Symposium, August 6-8, Austin, TX.

[4] W. Konig, I. Celi, St. Noken, 1992, “Stereolithography process technology”, Proceedings of the 3rd European Conference on RP&M

[5] A. Pilipovic, P. Raos, M. Sercer, 2009, “Experimental analysis of properties of materials for rapid prototyping”, Int J Adv Manuf Technol., 40, 105–115.

[6] R. Udroiu, L.A. Mihail, 2009, “Experimental determination of surface roughness of parts obtained by rapid prototyping, CSECS'09 Proceedings of the 8th WSEAS International Conference on Circuits, systems, electronics, control & signal processing, 283-286.

[7] A. Kesy, J. Kotlinski, 2010, “Mechanical properties of parts produced by using polymer jetting technology”, Archives of civil and mechanical engineering, Vol. X, No.3, pp. 37-50.

[8] J. Kechagias, V. Iakovakis, E. Giorgo, P. Stavropoulos, A. Koutsomichalis and N. Vaxevanidis, 2014, “Surface roughness optimization of prototypes produced by Polyjet Drirect 3D printing Technology”, Proceedings of the OPT-i, International Conference on Engineering and Applied Sciences Optimization, Kos Island, Greece, 4-6 June.

[9] J. Kechagias, P. Stavropoulos, A. Koutsomichalis, I. Ntintakis, N. Vaxevanidis, Dimensional Accuracy Optimization of Prototypes produced by PolyJet Direct 3D Printing Technology, 2014 International Conference on Industrial Engineering (INDE '14), Santorini Island, Greece, July 17-21, 2014.

[10] P.E. Reeves, and R.C. Cobb, Surface deviation modelling of LMT processes: a comparative analysis, Proceedings of the 5th European Conference on Rapid Prototyping & Manufacturing, Helsinki, Finland, pp. 59-76, 1996.

[11] D.A. Schaub, K. Chu, D.C. Montgomery, 1997, “Optimizing stereolithography throughput”, Journal of Manufacturing Systems, Vol. 16, No. 4, pp. 290 – 303.

[12] P.T. Lan, S.Y. Chou, L.L. Chen, D. Gemmill, 1997, “Determining fabrication orientations for rapid prototyping with Stereolithography apparatus”, Journal of Computer-Aided Design, Vo. 29, No. 1,pp. 53 – 62.

[13] S. Throup, 1996, “A comparison of build accuracy for a Stereolithography Build Using two different resins”, European Stereolithography User Association.

[14] M. N. Islam, Brian Boswell and A. Pramanik, 2013, “An Investigation of Dimensional Accuracy of Parts Produced by Three-Dimensional Printing”, Proceedings of the World Congress on Engineering Vol I, WCE 2013, July 3 - 5, London, U.K.,

[15] G. Hirpa, K. Lemu and K. Safet, 2012, “3D Printing for Rapid Manufacturing: Study of Dimensional and Geometrical Accuracy, J. Frick and B. Laugen (Eds.), APMS 2011, IFIP AICT 384, pp. 470–479.

[16] J.G. Zhou, D. Herscovici, C.C. Chen, 2000, “Parametric process optimization to improve the accuracy of rapid prototyped stereolithography parts”, Journal of Machine Tools and Manufacture, Vol. 40, 363-379.

[17] S.O. Onuh, K.K.B. Hon, 1998, “Optimizing build parameters for improved surface finish in stereolithography”, Journal of Machine Tools and Manufacture, Vol. 38, No. 4, pp. 329-392.

[18] A. Carosi, D. Pocci, L. Luluiano, L. Settimeri, 1996, “Investigation on Stereolithography accuracy on both solid and QuickCast parts”, Proceedings of the 5th European Conference on Rapid Prototyping and Manufacturing,

[19] M.S., Phadke, 1989, “Quality Engineering Using Robust Design, Prentice-Hall, Englewood Cliffs, NJ.

[20] J. Kechagias J, 2007, “Investigation of LOM process quality using design of experiments approach”, Rapid Prototyping Journal, Vol. 13, No. 5, pp. 316-323.

Nonlinear Dynamic Response of a Steel Frame with Bolted Apex Connection to a Strong Seismic Shock

Dorota Jasinska[1], Joanna M. Dulinska[2], Pawel Boron[3]
Faculty of Civil Engineering
Cracow University of Technology
Krakow, Poland
e-mail: jasinska@limba.wil.pk.edu.pl [1], jdulinsk@pk.edu.pl [2], pboron@pk.edu.pl [3]

***Abstract*—In the paper the global nonlinear dynamic response of a steel frame, constituting the basic module of the primary structural system of the steel hall, to a strong seismic shock was analyzed. Additionally, the nonlinear behavior of the roof ridge of the frame designed as a bolted apex connection was studied in detail. A strong earthquake of Northridge (1994) was applied as the kinematic excitation of the structure. To guarantee the real nonlinear behavior of the steel material the material parameters of the structural steel were determined experimentally on the basis of the tensile test of the steel specimen. The dynamic analysis revealed that the seismic response of the frame to the shock was strongly nonlinear. It occurred, that the frame lost global stability during the phase of strong ground motion of the shock. The frame also experienced the out-of-plane motion and the roof ridge was rotated by circa 60°. The disintegration of the bolted apex connection appeared: the end plates went plastic and they partially lost contact. The complete yielding of some of pre-tensioned bolts was caused by additional tension resulting from the split of the end plates. The bending of the bolts occurred due to the split of the connection and the deformation of the end plates.**

Keywords-steel frame; bolted apex connection; nonlinear dynamic response; plastic behavior; earthquake

I. INTRODUCTION

Engineering structures, especially made of steel, indicate strong nonlinearities, both material and geometrical, while exposed to heavy earthquakes. The problem of nonlinear seismic behavior, which concerns industrial steel halls have been extensively studied in last decades [1, 2, 3, 4].

Strong geometrical nonlinearity of a primary structural system of steel structures, which occurs in large displacements, may lead to global loss of dynamic stability, or even total collapse of buildings [3]. Then, material nonlinearity results in local plastic behavior of the steel material, like yielding with associated plastic flow or plastic hinges [4].

For these reasons nonlinear behavior of a whole primary structural system of a steel structure is the key issue of the dynamic analysis. Additionally, the performance of connections linking particular members of a primary structural system, like column-to-rafter or rafter-to-rafter roof connections, seems to be of crucial importance in the dynamic analysis [5, 6, 7]. These connections, usually designed as frictional links, are exposed to degradation or even disintegration during strong seismic shocks. Partial loss of contact resulting in the decrease of contact surface between connection's members or even total separation of connection's elements may happen due to seismic action.

In the paper the global nonlinear dynamic response of a steel frame, which is the basic module of the primary system of the steel hall, to a strong seismic shock is analyzed. Additionally, the nonlinear behavior of the roof ridge of the frame, designed as a bolted apex connection, is identified and explained in details.

II. BASIC DESCRIPTION OF THE ANALYZED STEEL FRAME

The calculations of the dynamic response to a strong earthquake were performed for a part of industrial steel hall. The main geometry and dimensions of the hall were based on the existing design. The industrial hall had a rectangular shape of the following dimensions: the width 21.0 m and the length 66.0 m.

The primary structural system of the hall consisted of 12 single-storey steel frames arranged regularly at spacings of 6 m in the longitudinal direction. Each frame had straight vertical columns and tapered rafter sections. No interior column was mounted; the frame was created as a clear span.

The height of the frame measured from the base level (concrete underlayment) varied from 6.5 m at the eave struts to 7.5 m at the ridgeline of the roof. The frames were fixed at the base.

Both columns and rafters were made of straight, rolled H section profiles: HEB 300. The main frame of the primary structural system of the hall is presented in Fig. 1.

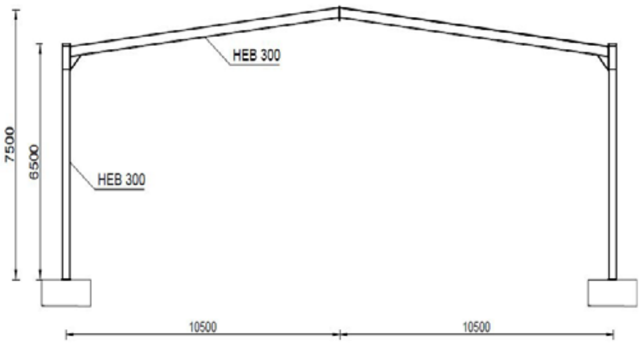

Figure 1. The primary structural frame of the hall.

The exterior columns of the frame were fixed in the base. The connections between columns and rafters were created as end-plate joints. The end plates were welded to the rafters and fastened to the columns by eight 24-mm diameter bolts arranged in four rows. The bolts were pre-tensioned with the force of 200 kN. Additionally, the connection was strengthened by a haunch. The details of the column-rafter connection are presented in Fig. 2.

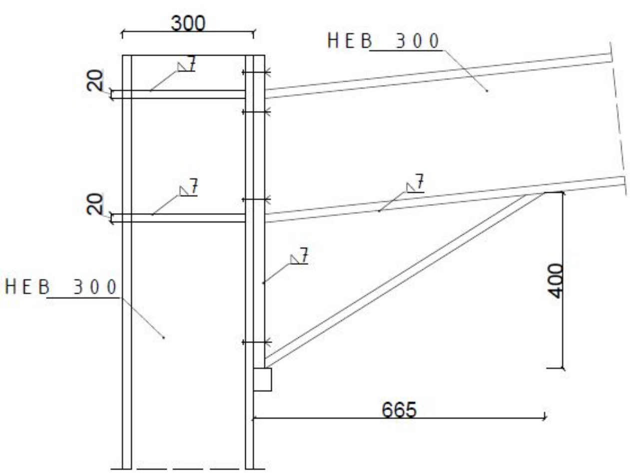

Figure 2. The end-plate joint connection between the column and the rafter.

The roof ridge constructed as bolted apex connection (accordingly to Eurocode 3-8 [8]) is shown in Fig. 3. The connection consists of two end plates and three rows of 24-mm diameter bolts (two bolts in a row). The end plates were made of 25 mm thick steel sheets of dimensions 30 x 41.5 cm. The end plates were welded to the rafters and joined together by the bolts. The bolts were pre-tensioned with the force of 200 kN.

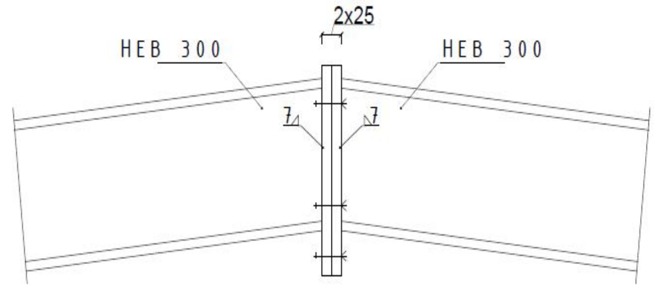

Figure 3. The bolted apex connection between rafters in the roof ridge.

The geometry of the end-plate metal sheet along with the location of the bolts is shown in Fig. 4. The typical behavior of such connection under the dead and live load from snow results in tension of the bottom side and compression of the upper side of the connection. For this reason two rows of bolt were placed in the bottom part and one in the upper part of the end plate.

Both the end-plate column to rafter and the rafter to rafter connections were designed as frictional connections. According to Eurocode 3-8 a friction coefficient was assumed 0.2. This value is usually expected in case of surfaces with no pretreatment.

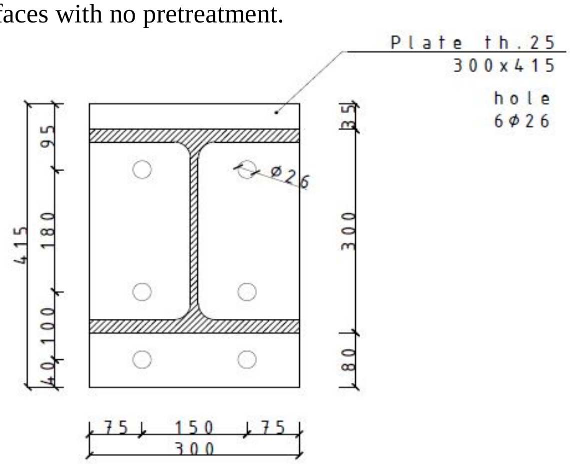

Figure 4. The end-plate metal sheet of ridge connection.

The secondary structural system of the main hall consisted of roof purlins, girts, eave struts and bracings. The roof area was equipped with purlins: horizontal beams spanning between frames. The purlins were the principal members of the roof secondary support system supporting roof panels, transferring loading to the frames and helping stabilize the roof. The girts constituted the principal members of the wall secondary support system. They, like the purlins, transferred the loads imposed on the covering system of the wall panels onto the frames. Both the purlins and the girts were design as simply supported beams, connected to the main steel frames by bolts (Fig. 5a). They do not constitute continuous beams (Fig. 5b).

ISBN: 978-1-61804-325-2

(a)

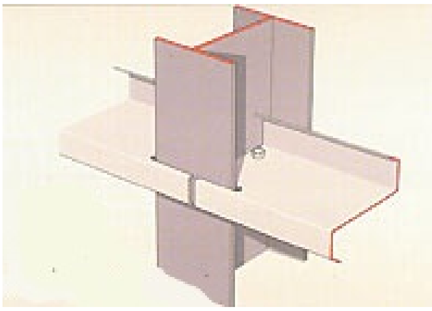

(b)

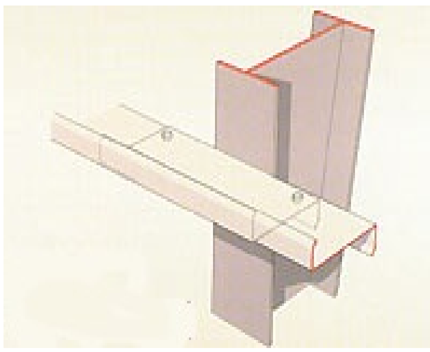

Figure 5. Details of : a) simply supported girts; b) continuous girts [9].

The fact that the purlins and girts are constructed as simply supported beams (see Fig. 5a) is of a crucial importance for the dynamic analysis. Since the whole structure is relatively soft in the direction perpendicular to the planes of the main frames, the dynamic analysis can be carried out for one steel frame only instead of analyzing the whole structure. Such simplification is possible due to the fact that the elements of the secondary structural system, i.e. purlins and girts, constructed as simply supported beams do not stiffen the whole structure as much as continuous beams. The torsion of the rafters is almost free in this case. The displacements of frames in the out-of-plane direction are also less limited.

III. EXPERIMENTALLY DETERMINED CONSTITUTIVE PARAMETERS FOR STEEL MATERIAL

The elements of the analyzed frame were made of structural steel of a commercial symbol S235JR. It was decided that in dynamic analysis the elasto-plastic model of the steel material will be used. The real nonlinear behavior of the structural steel during the dynamic analysis was guaranteed by experimentally determined material parameters. The stress-strain curve for the structural steel was obtained on the basis of the tensile test of the rectangular steel specimen, which was performed using the Zwick-Roell universal testing machine. For comparison, a numerical simulation of above mention test was also carried out. The numerical process was conducted with the ABAQUS software [10]. The specimen was discretized by the SHELL S4R finite elements. In the numerical calculations the parameters of the non-linear elasto-plastic steel material were taken from the experiment.

The theoretical strain-stress curve was determined as a result of the experiment. Hence, it could be stated that the parameters of the elasto-plastic model of steel were verified experimentally.

Figures 6a and 6b show the experimental tensile test and its numerical simulation, respectively, for a specimen made of the structural steel material.

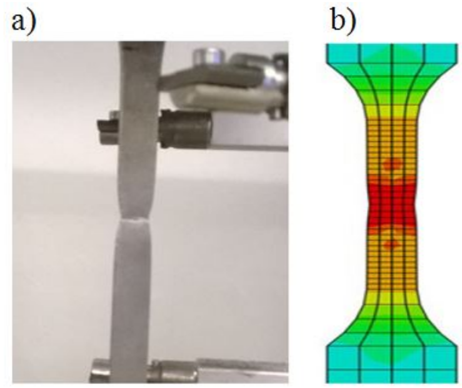

Figure 6. Tensile test of the steel material: a) experiment, b) numerical simulations.

Fig. 7 presents the comparison of the curves obtained from the numerical simulation and from the experimental tensile test. On the basis of Fig. 7 it could be noticed that good agreement of both curves was obtained.

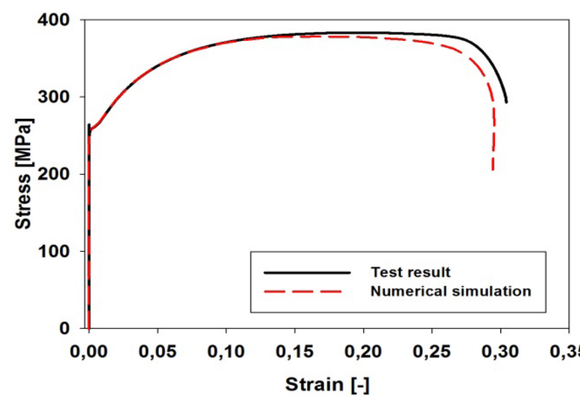

Figure 7. The comparison of the stress-strain curves obtained from the experimental tensile test and from the numerical simulation.

The experimentally obtained yield curve data of the structural steel are summarized in Table 1.

TABLE I. CONSTITUTIVE PARAMETERS OF THE ELASTO-PLASTIC STEEL MATERIAL

Yield stress [MPa]	*Plastic strain [-]*
245	0.00000
250	0.00020
251	0.00026
252	0.00032
255	0.00055
257	0.00100
259	0.00168
260	0.00250

265	0.00631
270	0.00870
280	0.01270
290	0.01680
300	0.02150
320	0.03300
330	0.04050
340	0.04900
350	0.06000
360	0.07500
370	0.09600
375	0.11200
378	0.12600
380	0.13750
383	0.17300
383	0.22000

The elasticity modulus of 195 GPa was also obtained from the experimental test. The Poisson's ratio of 0.3 and the mass density 7850 kg/m^3 were assumed.

The material of the bolts was also described as an elasto-plastic. Due to the lack of experimental data, the material parameters were assumed on the basis of the literature data [11]. The elasticity modulus of 210 GPa was used. The adopted strain-stress elasto-plastic curve is shown in Fig. 8. The yield stress of 900 MPa and the limit stress of 1003 MPa were assumed for the steel material of bolts.

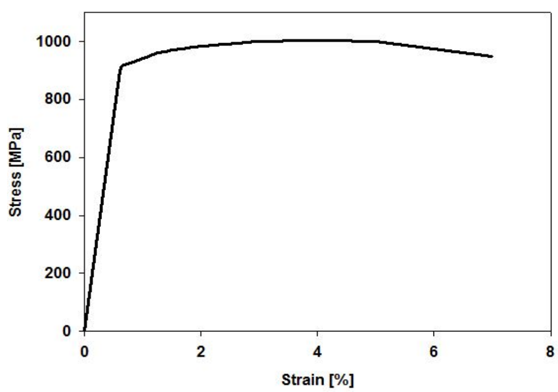

Figure 8. The adopted stress-strain curve for the bolt steel material [11].

IV. SEISMIC INPUT DATA

A strong seismic shock of Northridge (1994) [12] was applied as the kinematic excitation (accelerations) for the dynamic analysis of the structure. The magnitude of the shock equaled 6.7. Two components of the Rayleigh shock wave, horizontal and vertical, were taken into consideration during the dynamic analysis. The time history of accelerations acting in the horizontal, in-plane direction is shown in Fig. 9a, whereas the time history of accelerations in the vertical direction is presented in Fig. 9b. The maximal values of accelerations in horizontal and vertical direction equaled 17.45 and 10.28 m/s^2, respectively.

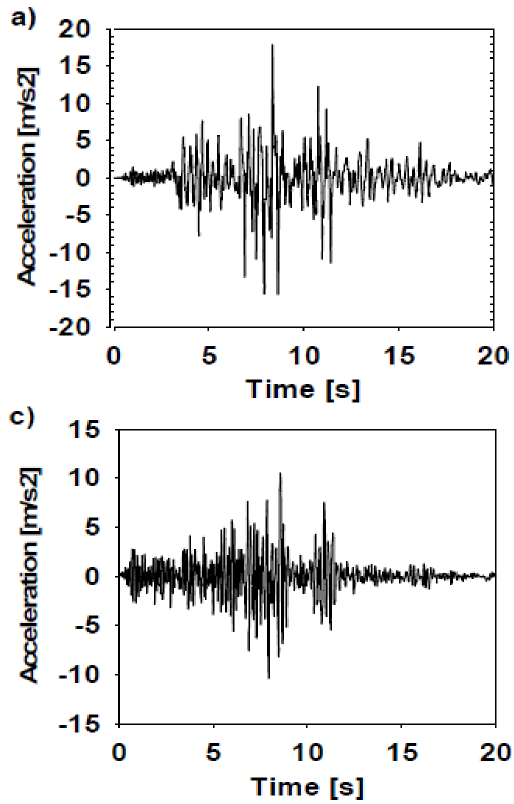

Figure 9. Time history of accelerations in: a) horizontal in-plane direction; b) vertical direction.

V. THE NUMERICAL MODEL OF THE FRAME WITH BOLTED APEX CONNECTION

A. Comments on the numerical model of the entire frame

A three dimensional FEM model of the steel frame was created using the ABAQUS software. The whole structure except the analyzed bolted apex connection and the column-rafter connection was discretized with about 5000 8-node continuous shell finite elements SC8R, provided by the ABAQUS element library.

The elements of the secondary structural system were not included in the numerical model. They were replaced by concentrated forces which represent the dead load of the roof and the walls and the live load.

Neither springs representing soil-structure interaction nor dashpots characterizing ground damping were taken into consideration in the numerical model. Such boundary conditions reflected the very stiff ground that the frame is founded on. Hence, it was possible to apply the seismic motion of the ground directly to the column footings.

B. Details of the numerical model of the bolted apex connection

In order to obtain accurate results the mesh of the analyzed connection was densified. The apex and the end-plate joints (end plates, bolts, and fragments of rafters and columns close to the end plates) were modelled with about 30000 brick, linear C3D8R finite elements provided by the

ABAQUS library. The numerical model of the bolted apex connection with a FE mesh is presented in Fig. 10 whereas the single bolt with a washer is demonstrated in Fig. 11.

.

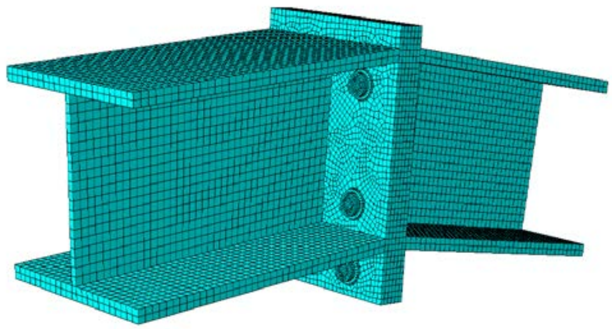

Figure 10. The bolted apex connection model with a FE mesh.

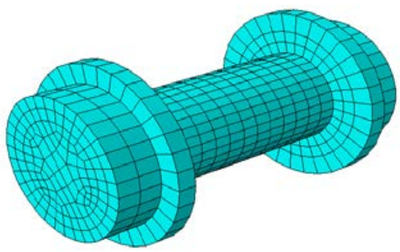

Figure 11. The model of the single bolt with a FE mesh.

The unilateral frictional contact between end-plates and bolts (both shanks and washers) as well as between two end plates, was modeled by surface-to-surface contact elements. To allow for misplaced bolts, holes in end plates were 2 mm oversized.

The pretension of the bolts was realized by generating initial thermal strains by assuming thermal expansion coefficient of the bolt material $1.08 \cdot 10^{-5}\ {}^{1}\!/_{{}^{0}C}$, and cooling the bolts by $530^{0}C$. The bolts' pretension caused initial compression of the end-plates resulting in concentration of plastic zones (about 0.8% equivalent plastic strain) around the bolt holes even before the dynamic shock had been imposed on the structure (see Fig. 12).

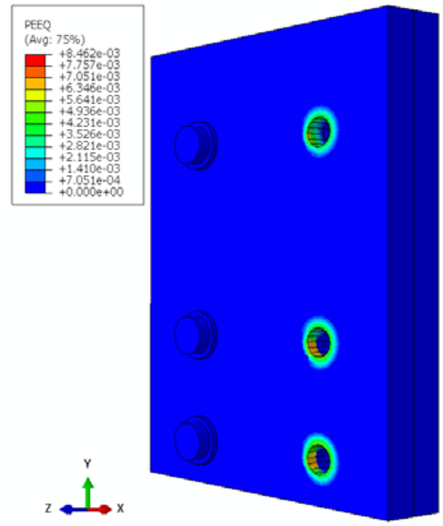

Figure 12. Distribution of equivalent plastic strains concentrated around the bolts due to the application of compression forces

VI. Dynamic Response of the Frame to the Seismic Shock

A. Global dynamic loss of stability of the frame

The dynamic response of the frame to the strong seismic shock was evaluated by the time history analysis using the Hilber-Hughes-Taylor direct integration method for the solution of equations of motion. A minimal time step increment of 10^{-5} s was necessary for this highly nonlinear analysis to obtain convergence.

The Rayleigh model of damping, proportional to the stiffness and the mass of the structure, was applied with coefficients determined for damping ratios 2.5 % referring to the first and the second circular frequencies.

The global frame behavior during the phase of strong motion of the ground is presented in Figs 13-15.

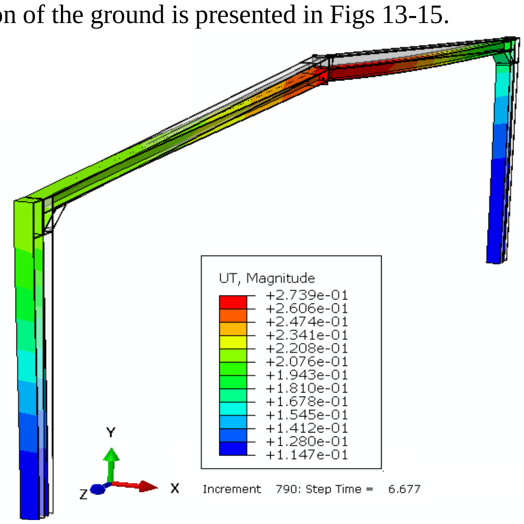

Figure 13. The in-plane motion of the frame performed up to about 7 s

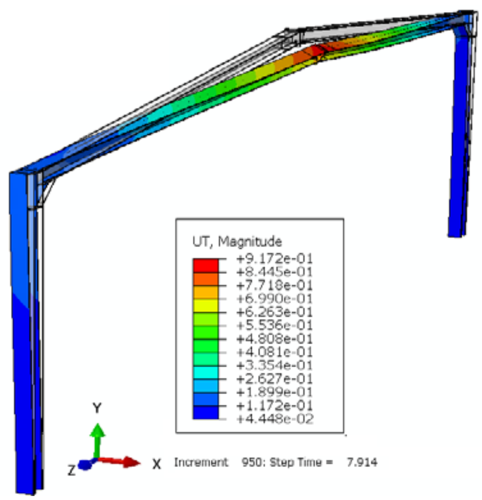

Figure 14. The out-of-plane configuration of the frame resulting from the global loss of dynamic stability during the phase of strong ground motion

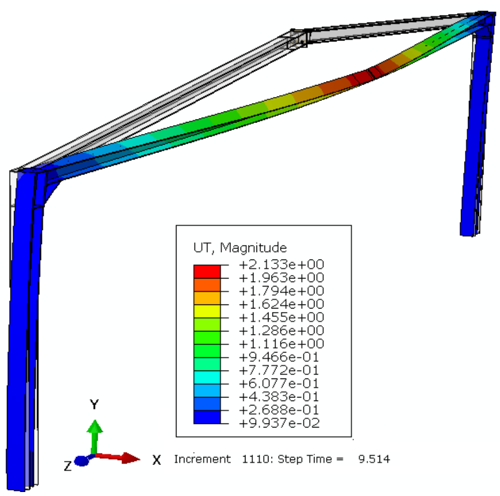

Figure 15. The final equilibrium configuration of the frame (at the end of the phase of strong ground motion) with the bolted apex connection displaced approximately by 2 m and rotated by 60°

From the very beginning of the shock the frame, excited in longitudinal direction Z and vertical direction Y, performed the in-plane motion up to about 5.6 s (Fig. 13). Then, the phase of strong movements of the ground started and the frame was reported to have the out-of-plane motion (Fig. 14). Once the amplitudes of ground motion had grown substantially, the frame lost its global dynamic stability. This phenomenon appeared due to some material imperfections, like non-uniform mass distribution resulting from irregularities of the mesh. The global configuration of the frame at the end of the phase of strong ground motion (9.5 s) is presented in Fig. 15. The roof ridge of the frame is displaced by approximately 2 m. The rotation of the roof ridge, reaching about 60°, is also clearly visible (Fig. 15). Despite the large displacements and rotations caused by the phase of strong ground motion, the frame did not collapse. It stabilized in a new state of equilibrium configuration and from now on (9.5 s) to the end of the shock (16 s) oscillated around this new configuration.

B. Local non-linear behaviour and degradation of the bolted apex connection

The final configuration of the bolted apex connection along with the distribution of equivalent plastic strains are presented in Fig. 16. One raw of bolts is removed from the view to reveal the plastic strain concentration in the end plates in the vicinity of the bolts holes. The rotated connection is shown along with the global coordinate system to present the rotation of the roof ridge, which was initially placed vertically (parallel to the vertical axis Y), having two upper bolts located at the top.

The zones of equivalent plastic strains in the end plates were enlarged significantly in comparison with the small areas affected by yielding caused by the bolts pre-tension (see Fig. 12). The maximal value of this plastic measure reached 5.7% in the end plates.

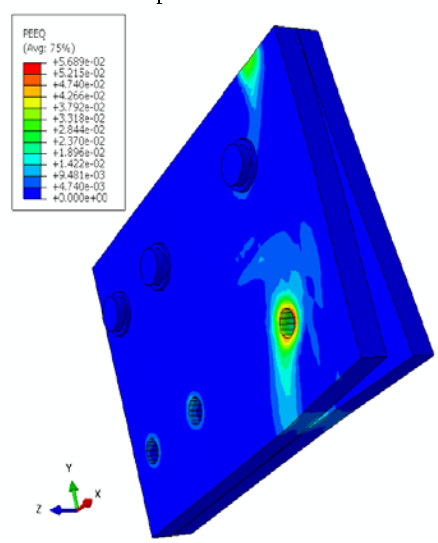

Figure 16. The final position of the bolted apex connection rotated by approximately 60° along with equivalent plastic strains distribution

It is clearly visible that significant displacement and rotation of the bolted apex connection is accompanied by the partial separation of the end plates. The contact surface between the end plates considerably decreased as shown in Fig. 17.

ISBN: 978-1-61804-325-2

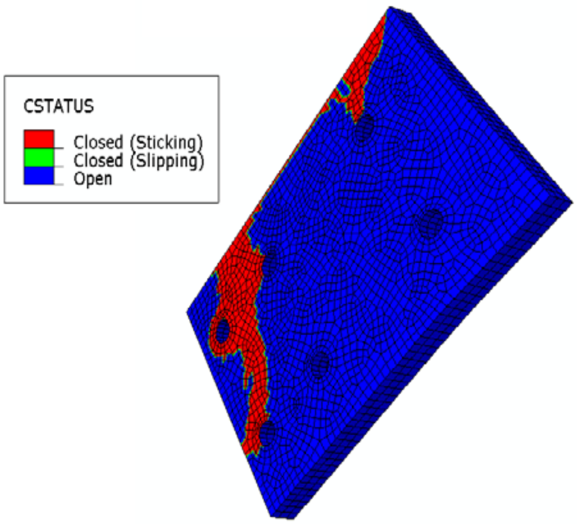

Figure 17. The final contact surface between the end plates (red area) reduced by the seismic shock

The loss of contact between the end plates is also evident in Fig. 18. The split of the end plates resulted in further indicators of degradation of the connection: the parts of the rafters adjacent to the end plates as well as the bolts affected by additional tension resulting from the split underwent significant yielding.

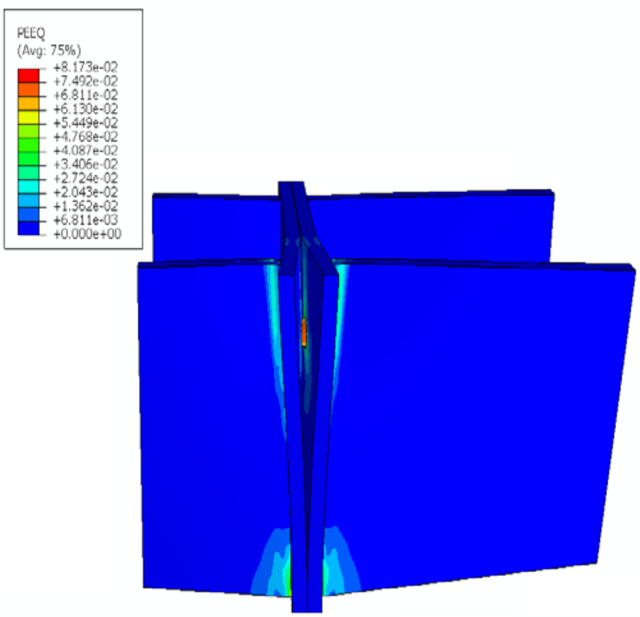

Figure 18. The deterioration of the bolted apex connection: the lost of contact between the end plates, the yielding of the rafters in zones adjacent to the end plates, the yielding of the bolt resulting from additional tension

However, it must be emphasized that the mechanisms of the additional plastic zones evolution are not the same for the rafters as for the bolt. In case of the rafters, the parts adjacent to the end plates yielded in compression, whereas the bolt experienced strong tension.

Fig. 19 shows the time history of equivalent plastic strain (black line) and the logarithmic minimal principal strain (red line) at a point located in the rafter's plasticized zone, whereas Fig. 20 presents the development of plastic measures at a point situated in the bolt shank.

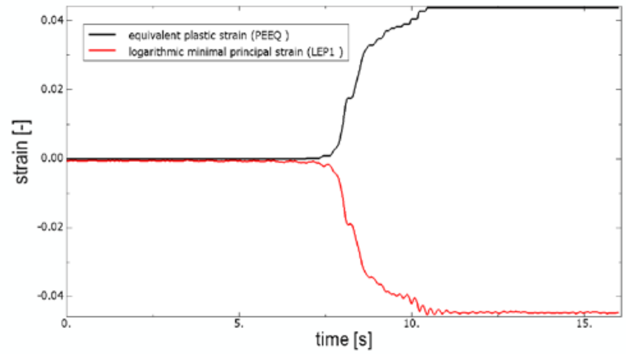

Figure 19. Time history of of equivalent plastic strains (black line) and the minimal principal strains (red line) at a point located in the rafter's plastic zone

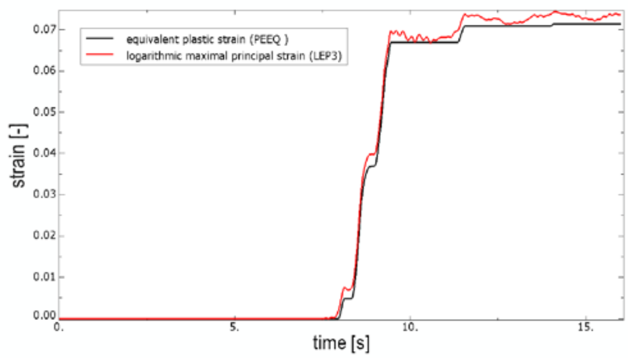

Figure 20. Time history of of equivalent plastic strains (black line) and the maximal principal strains (red line) at a point located in the bolt's plastic zone

First of all, it could be noticed that the time histories of both, minimal and maximal, logarithmic principal strains presented in Figs 19 and 20 respectively, show that the oscillations of strains resulting from ground vibration were negligibly small in comparison with the rapid increase in strains that occurred due to the loss of dynamic stability at about 7 s.

It is also clearly visible that the rafter dominant strain is compressive - the maximal equivalent plastic strain (around 4 %) and the minimal principal strain were almost the same (see Fig. 19).

The opposite situation can be detected in case of the plastic behavior of the bolt shank. The maximal equivalent plastic strain was almost identical with the maximal principal strain developed in the bolt strongly pulled after the connection disintegration (see Fig. 20).

The chart in Fig. 21 illustrates the stress-strain curve for the pre-tensioned bolt shank. After the global loss of stability of the frame, the bolt underwent plastic yielding and the substantial jumps of principal strain were observed twice, reaching a level of approximately 4 and 7.5 %, respectively.

ISBN: 978-1-61804-325-2

Also several stages of elastic loading-unloading cycles can be recognized, with the final elastic stress-strains oscillations around the new state of equilibrium configuration (see Fig. 15), that started after the phase of the strong ground motion had been finished.

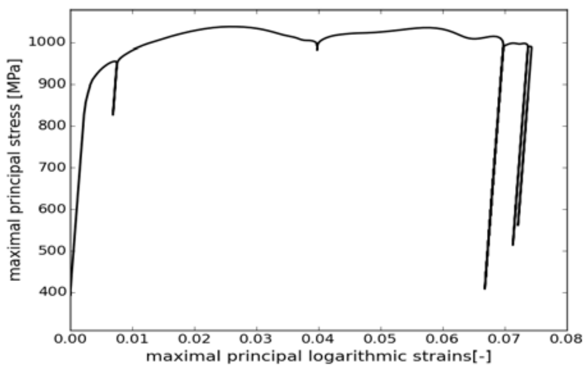

Figure 21. The stress-strain curve for the pre-tensioned steel bolt under the earthquake

The equivalent plastic strains in the bolt with the maximal value of approximately 7.3 % were distributed as shown in Fig. 22. This distribution of plastic strains as well the bolt deformation indicate the effect of bending of the bolt. It occurred due to the partial split and the deformation of the end plates.

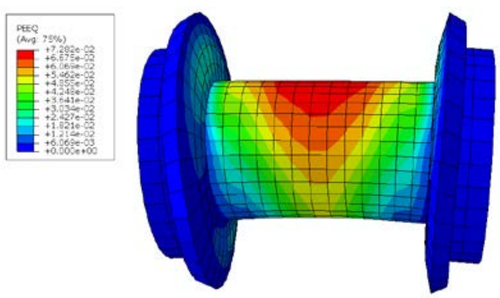

Figure 22. The distribution of the equivalent plastic strains in the pre-tensioned steel bolt bent due to the end plates deterioration

VII. CONCLUSIONS

In the paper the global nonlinear dynamic response of a steel frame, which is the basic module of the primary structural system of the steel hall, to a strong seismic shock was analyzed. Additionally, the nonlinear behavior of the roof ridge of the frame designed as a bolted apex connection was studied in detail. The following conclusion can be formulated on the basis of the analysis:

1. Global nonlinear behavior of the frame occurred – it lost dynamic stability during the phase of strong ground motion. The time histories of plastic measures showed rapid grow when the strong ground motion initiated.
2. Local non-linear behavior and disintegration of the bolted apex connection took place - the contact surface between the end plates of the connection considerably decreased. The pre-tensioned bolt underwent bending due to the partial split and the deformation of the end plates.

It should be strongly emphasized that only a 3D modelling of the structure enables to identify both global and local nonlinearities of dynamic behavior.

REFERENCES

[1] E. M.Lui, A. Lopes, “Dynamic analysis and response of semirigid frames”, Engineering Structures, vol. 19 , no. 8, pp. 644-654, 1997.

[2] J. McCormic, R. DesRoches, D. Fugazza, F. Auricchio, “Seismic assessment of concentrically braced steel frames with shape memory alloy braces”, Journal of Structural Engineering, vol.133(6), pp. 862-870, 2007.

[3] S. H. Chao, S. C. Goel, “A seismic design methodfor steel concentric braced frames for enhanced performance”, 4th International Conference on Earthquake Engineering Taipei, Taiwan 2006, papier no. 227.

[4] D. Jasinska, J. M .Dulinska, P. Boron, “Influence of spatial variability of seismic shock on steel hall with experimentally determined elasto-plastic parameters of steel material”, Applied Mechanics and Materials, vols. 744-746, pp. 884-889, 2015.

[5] M. Ghassemieh, M. Jalalpour, A. A. Gholampour, “Numerical evaluation of the extended endplate moment connection subject to cyclic loading”, Current Advances in Civil Engineering, vol. 2, pp. 35-43, 2014.

[6] M. R. Bahaari, A. N. Sherbourne, “3D simulation of bolted connections to unstiffened columns-II.Extended endplate connections”, Journal of Constructional Steel Research, vol. 40, no. 3, pp. 189-223, 1996.

[7] H. M. Mahmoud, “Seismic behavior of semi-rigid steel frames”, PhD Thesis, University of Illinois at Urbana-Champaign, 2011.

[8] PN-EN 1993-1-8, ”Design of steel structures: Design of joints”

[9] http://www.hale-multiprojekt.pl/?page=19 [access 30.05.2015]

[10] ABAQUS, Users Manual V. 6.13, Dassault Systemes Simulia Corp., Providence, RI (2013)

[11] https://pisarzdz.sd.prz.edu.pl/file/MjMsNjcsMzYxMixsMy5wZGY [access 30.05.2015]

[12] https://ngawest2.berkley.edu [acces 30.05.2015]

The influence of energy-efficient floor construction technology on vibration perception by humans in buildings

A. Kowalska-Koczwara, P. Kiszka

Abstract**—**Residents of buildings are increasingly calling on designers to take comfort conditions of living spaces into account in their analysis in addition to the safety of use or functionality. This is particularly important in the case of low-energy and passive buildings, buildings for which only we elaborate rules of good design. Ensuring comfort of living spaces includes taking account different aspects of it. One of the aspect is vibrational comfort which is difficult to ensure. In this article the possibility of using one of the energy-saving technology to reduce the influence of vibration on humans is presented. Two variants of FEM models of the same building were made to compare traditional technology of construction slabs with the technology with using insulation materials. Both variants have been subjected to kinematic excitation coming from a passing tram. Then influence of vibrations on humans using the RMS value in both variants was analyzed. The results of the analysis and conclusions are also presented in this paper.

Keywords**—**FEM model, Insulating materials, RMS value, Vibrational comfort.

I. Introduction

IN recent years the importance of environmental influences gradually increasing. This is because we live in an increasingly polluted environment. The pollution should be understood as not only air or water pollution, but in accordance with Polish Law on Environmental Protection [1] this is also a noise and vibrational pollution. The first recommendations for ensuring acoustic comfort and vibration may be found in [2]. The Regulation [2] sets 6 basic requirements for the performance of buildings. They concern:

• mechanical resistance and stability,
• fire safety
• health and environmental hygiene,
• safety in use, protection against noise,
• energy savings and thermal insulation.

The Act [3] introduces a set of functional requirements to be met by buildings - including protection against acoustic noise, complementing acoustic requirements for the protection against vibrations that are received passively by man located in a building. And in [4] the issue of protection against noise and vibration is dedicated section IX, which defines the scope and the way to protect the building and its surroundings, with an indication of the acoustic requirements included in the technical standards. The essence of the requirements of anti-noise and anti-vibration protection is very well captured in § 325 (included as the first in section IX).

To give technical sense of this requirement in the Regulation [4] are listed a number of issues that must be considered during designing a building:

• suitable for reasons of acoustic locations of residential buildings, housing and public buildings: the recommendation of locating in the least exposed to the occurrence of noise and vibration,

• reduce the risk to the building caused by noise and vibration - by maintaining the distance between sources of noise and vibration and buildings in which there are rooms that require protection against external noise and vibration, as well as the use of appropriate protection against noise and vibration in the form of suitably shaped building,

• suitable acoustic properties of interior and exterior partitions in the building,

• the acoustic quality used in building technical devices representing the equipment of the building,

• anti-noise and anti-vibration protection installations - limiting the generation of noises and vibrations, and spread them in the building and penetration into the building environment.

The Annex to Regulation [4] "List of Polish Standards mentioned in the Regulation" gives the following standards relating to Section IX "Protection against noise and vibration":

• PN-87 / B-02151.02, "Limit values sound levels in rooms" [5], defines acceptable levels of noise penetrating into spaces subject to acoustic protection,

• PN-B-02151-3: 1999, "Acoustic partitions in buildings and acoustic insulation of building elements. Requirements " [6], lays down minimum acoustic properties of the interior and exterior partitions in the building,

• PN-88/B-02171, "Evaluation of vibration influence on humans in buildings" [7], defines acceptable levels of vibrations transmitted to the building and received passively by humans staying in the building,

• PN-85/B-02170, "Evaluation of the harmfulness of building vibrations due to ground motion" [8] gives methods to assess the influence of vibration on buildings giving a

A. Kowalska-Koczwara is with the Cracow University of Technology, Cracow, Warszawska 24 St., 31-155, Poland (corresponding author phone: +48126282121; fax: +48126282340; e-mail: akowalska@pk.edu.pl).

P. Kiszka is with the Cracow University of Technology, Cracow, Warszawska 24 St., 31-155, Poland (corresponding author e-mail: pawel.kiszka08@gmail.com).

detailed assessment methodology, and the approximate assessment of the scale SWD, which are subject to compact masonry buildings up to 5 storeys.

A set of the issues listed in the Regulation [4], which should be taken into account by the designer of the building is a list of issues relating to the anti-vibration and anti-noise protection of the building together with a general indication of the ways to resolve them. According to this arrangement every building design should be analyzed and the acoustic effects of chosen designing solution should be evaluated.

II. Procedure for evaluation the vibration influence on people residing in the buildings

The primary level of reference in assessing the influence of vibrations on humans is called perception threshold of vibration. The results of research in this area are basis for formulating criteria for assessing the influence of vibrations on humans. If the vibrations at the point of their perception by human are characterized below the perception threshold then vibrations can be considered as undetectable by humans. Fig. 1 shows two lines which represents perception threshold of vibrations in horizontal and transverse directions.

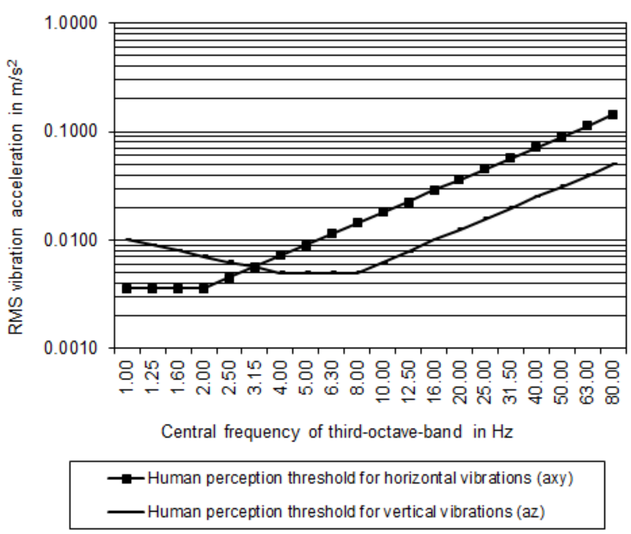

Fig. 1 Perception threshold of vibration for humans in buildings.

One of the factor that influences on the sensibility of vibration by the people is the position of the vibration perception by human. In standards approaches in order to ensure comparability of measurements results are adopted in the same receiving positions of vibration by human. Standing and sitting positions are treated as one because of the axis "z", which extends along the spine in these positions is the vertical axis, while the axes "x" and "y" are horizontal axes. In the supine position while the axis "z" becomes the horizontal axis, the axis "x" is the axis on the back-chest, while the axis "y" assumes a direction side by side (see Fig. 2 acc. [9]).

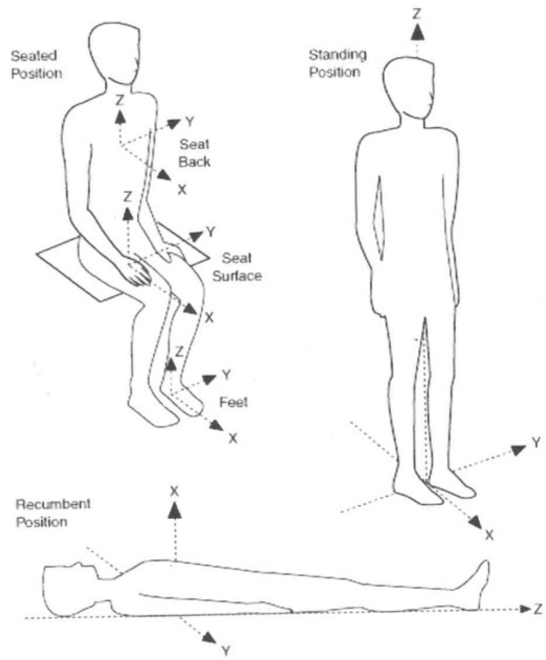

Fig. 2 Directions of receiving vibration by human.

To receive from the perception threshold of vibration, lines that are representing the vibration comfort they should be multiplied by the appropriate factor (see Table 1 acc. [7]). As shown in the following table, the value of the correction factor depends on the time of a day, a room destination and the frequency of vibration.

Table 1

Values of correction factor

Room destination	The time of day	Value of correction factor depending on repeatability of vibration	
		Continuous vibrations or vibrations occurring more than 10 times per day	Vibrations occurring less than 10 times per day
operating theaters, precision laboratories, etc.	day night	1	1
hospitals, patients rooms etc.	day	2	8
	night	1	4
apartments, residence rooms, dormitories, etc.	day	4	32 [1)]
	night	1,4	4
offices, schools, etc.	day night	4	64 [2)]
workshops, factories, etc.	day night	8	128 [3)]

[1)] factor refers to the time in which the operations take place or in which laboratories are precise actions
[2)] factor may be doubled if there are applicable occasional vibrations previously announced
[3)] factor may be doubled for work in heavy industry workshops

ISBN: 978-1-61804-325-2

To evaluate the influence of vibrations on humans according to [7,9] so-called effective value RMS of vibration acceleration determined from the formula (1) is needed:

$$a_{RMS} = \sqrt{\frac{1}{T}\int_0^T a^2(t)dt} \quad (1)$$

where: T- averaging period [s].

In vibration perception points by humans based on the recorded signal of vibration acceleration for analyzed vibration direction, the RMS value is calculated in 1/3 octave bands. Than calculated RMS is compared with the limit values resulting from multiplying the perception threshold of vibrations by a correction factor. An example of such an analysis is shown in Fig. 3 (acc. [10]):

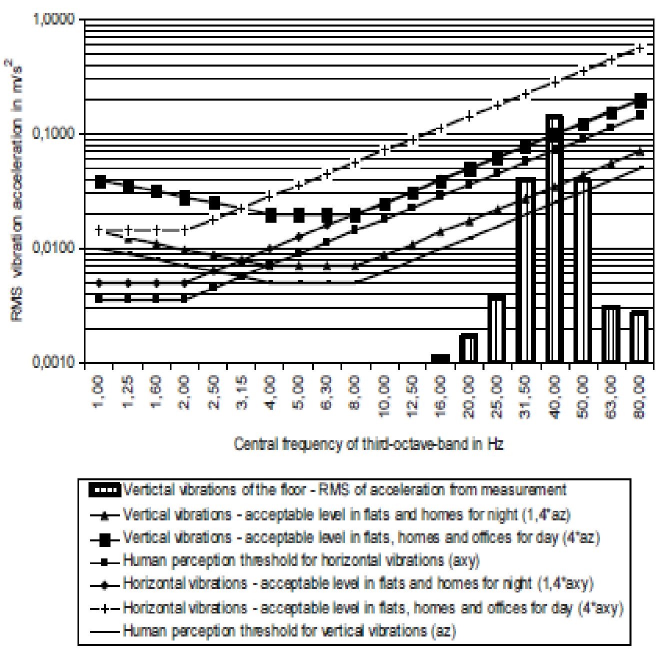

Fig. 3 The result of RMS analysis of floor vertical vibrations caused by train passing (acc. [10])

As it can be seen from the above figure for frequency equal 31,5 and 50 Hz the perception threshold of vibration in vertical direction has been exceeded and for frequency 31,5 Hz even comfort level at night has been exceeded. However for these both frequencies the perception threshold of vibrations in horizontal direction has not been exceeded. The highest value of exceedance occurs at the frequency equal 40 Hz, in which comfort level for vertical vibrations has been exceeded even during a day and for horizontal vibrations this level has been exceeded during a night. Similar analysis were made in several papers, for example in [11], [12], [13].

III. Description of Analyzed Building

Building selected for analysis is located in Cracow near two kinematic excitation sources:

- road with heavy traffic located 3,6m from the building,
- tramway located 13,8m from the building (distance measured from the railhead)

It is two-storey building built in traditional brick technology, typical in Poland (see Fig.4).

Fig. 4. View of the building from the side of the tramway.

Horizontal floor plans and vertical cross-section of the building are given in Fig. 4 -7 (acc. [14]).

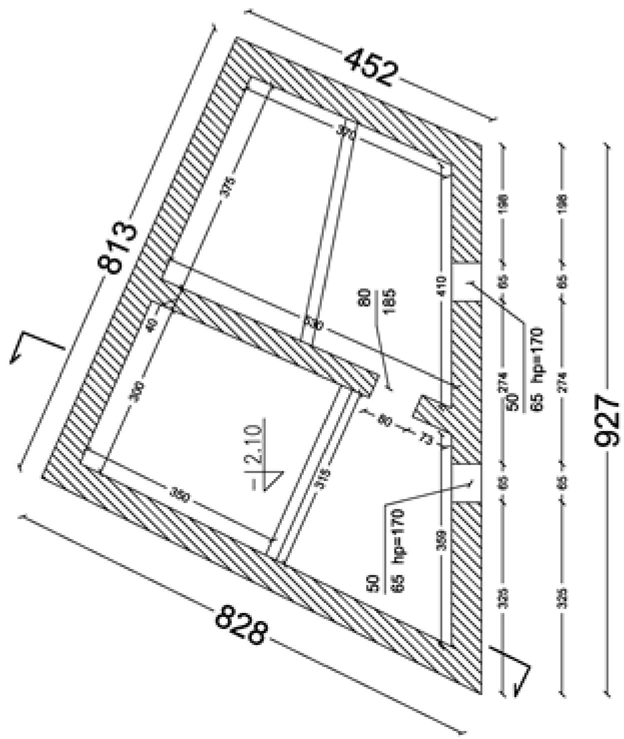

Fig. 4 Horizontal plan of building basement.

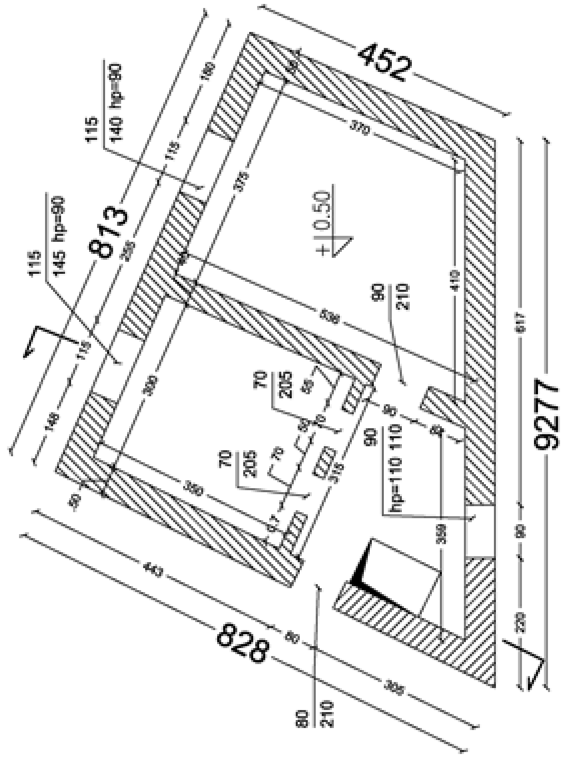

Fig. 5 Horizontal plan of the first floor.

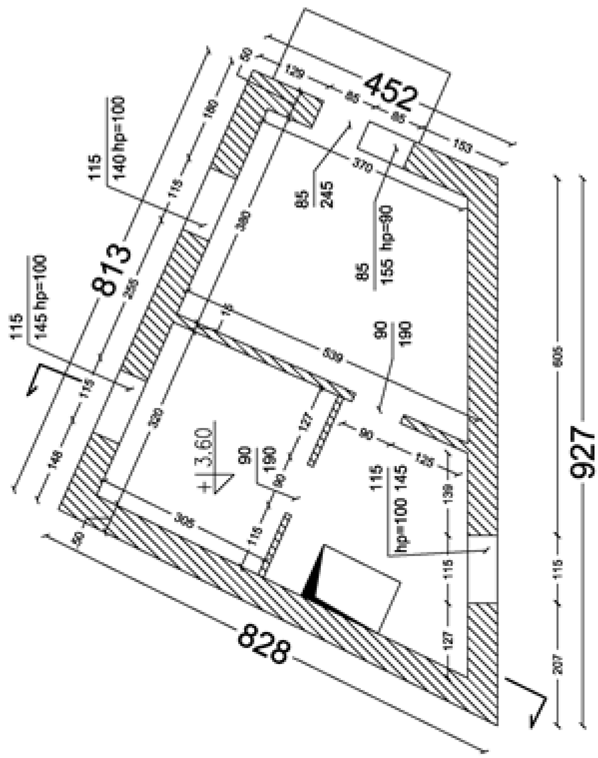

Fig. 6 Horizontal plan of the second floor.

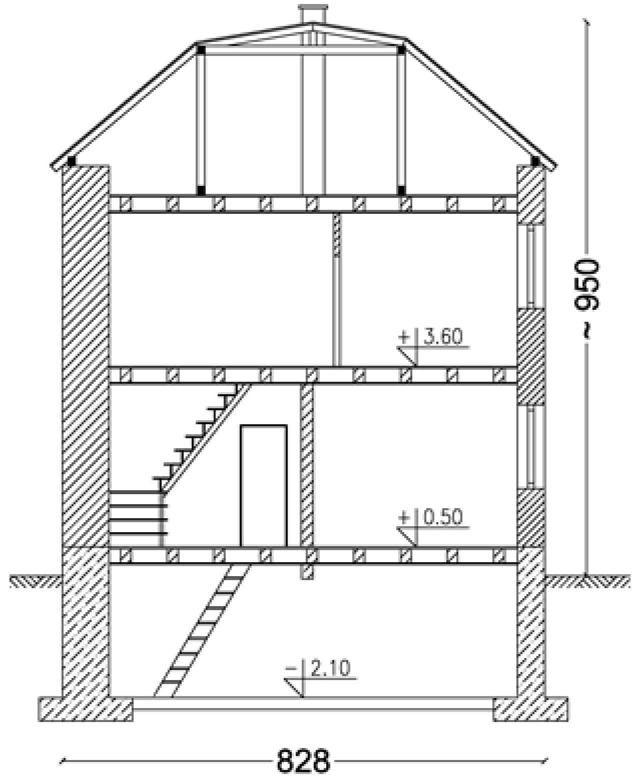

Fig. 7 Cross-section of the building.

IV. Description of the Building Model

FEM model was made using ABAQUS program in two variants: model of the construction (variant 1) and model of construction with floor with insulating materials (variant 2). Material properties adopted in these two variants of the model are summarized in Table 2.

Table 2

Values of material properties.

Parameter / Material	Young's modulus E [GPa]	Poisson's ratio ν [-]	Mass density ρ [kg/m^3]
Reinforced-concrete	25	0,17	2400
Masonry walls	1,5	0,25	1800
Mineral wool	0,04	0,20	150
Fermacell floor element	1,15	0,33	1125

The geometry of the building was introduced into the ABAQUS program on the basis of inventory based on which Fig. 4-7 were formed. Critical damping of the entire structure is equal to 5%. Then boundary conditions of the model were adopted – it was rigid support. After the introduction of boundary conditions finite element mesh was assumed, using the triangular spatial elements (see Fig. 8).

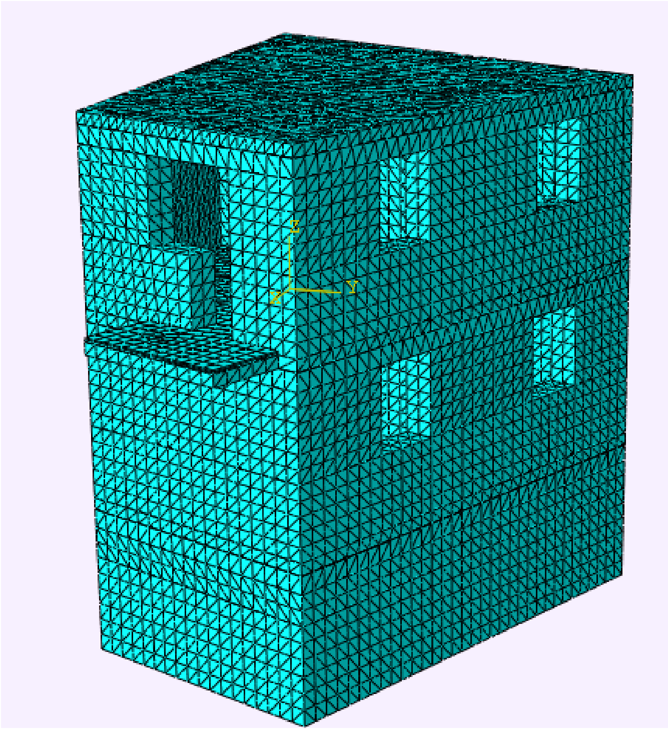

Fig. 8. View of the building model.

Correctness of the construction model has been tested by performing modal analysis, resulting in the first few natural frequencies. Results of modal analysis for first five natural frequencies are listed in Table 3.

Table 3

Results of modal analysis

Mode number	Natural frequency [Hz]	Description of mode shape (orientation)
1	7,95	1st in East-West direction
2	10,11	1st in North-South direction
3	13,24	Torsional
4	21,81	2nd in in East-West direction
5	26,07	2nd in North-South direction

In an east-west direction the building has a smaller stiffness hence the lower values of frequency in this direction. The natural frequencies obtained from the model were compared with the frequency values measured on building of similar design and height (see [15]). FEM building model seems to be correct because the values obtained from the model are close to those obtained from the measurements carried out on a similar building.

After verification of the structural model, numerical simulation of passing the tram was performed and RMS values were calculated in points of vibration perception by humans (in the middle of the floors). RMS values were calculated and compared with lines corresponding to perception threshold of vibration and to comfort level for both analyzed variants of building model.

V. RESULTS OF ANALYSIS

To obtain the RMS values in the middle of floors on the ground floor and upstairs (see Fig. 9) it was necessary to load the building foundation with excitation registered at ground level.

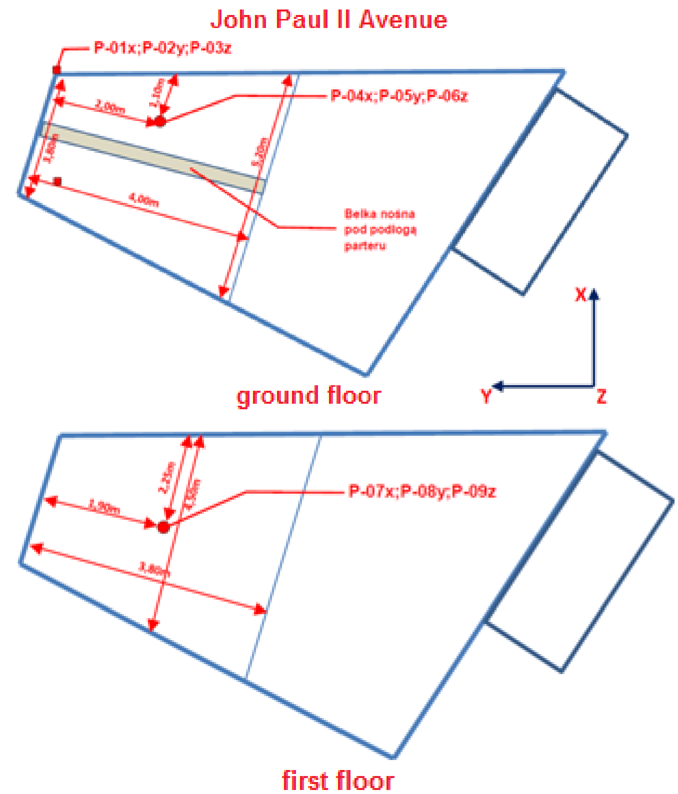

Fig. 9. Localization of measurement point.

The registered excitation signal was obtained due to measurements which were made on this building [14]. After loading the foundations of the model of the building with registered excitation it was possible to obtain vibrograms at selected points. The example of such vibrogram obtained on the construction in the middle of the first floor is shown on Fig. 10.

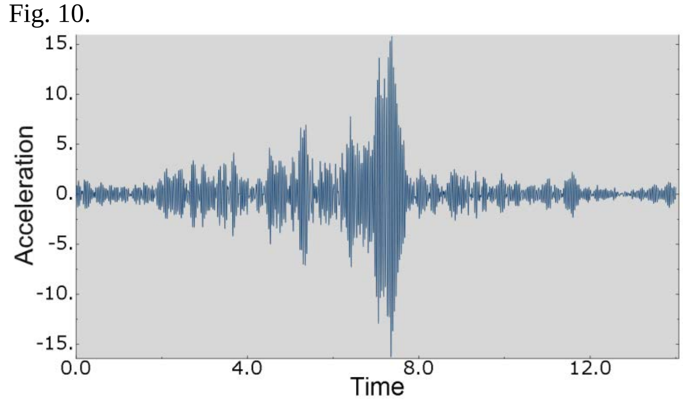

Fig. 10. Vibrogram registered on the first floor.

From such a vibrogram it is possible to make RMS analysis according to formula (1). Results of RMS analysis of construction model are shown on Fig. 11-12. As can be seen from figures below the perception threshold of vibration by humans is exceeded on the first floor of the building. On the ground floor vibrations are on the edge of the human perception threshold of vibration. On the first floor not only the perception threshold of vibration is exceeded, but also the comfort level has been exceeded in the daytime, which represents the line marked on the graph as 1.4 az.

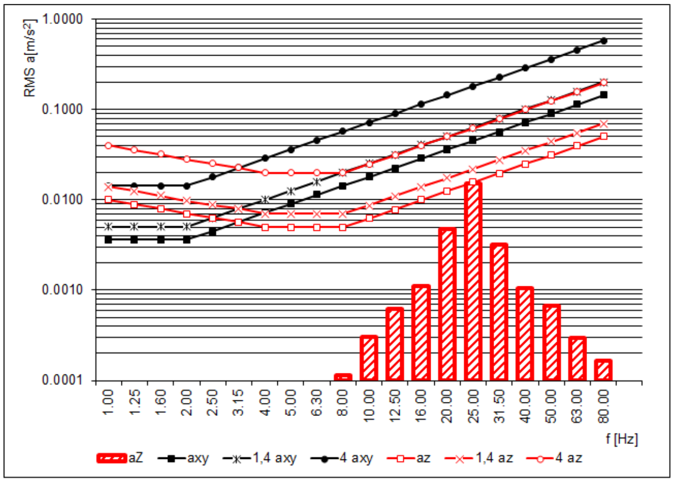

Fig. 11. The results of RMS analysis obtained on the ground floor of the construction.

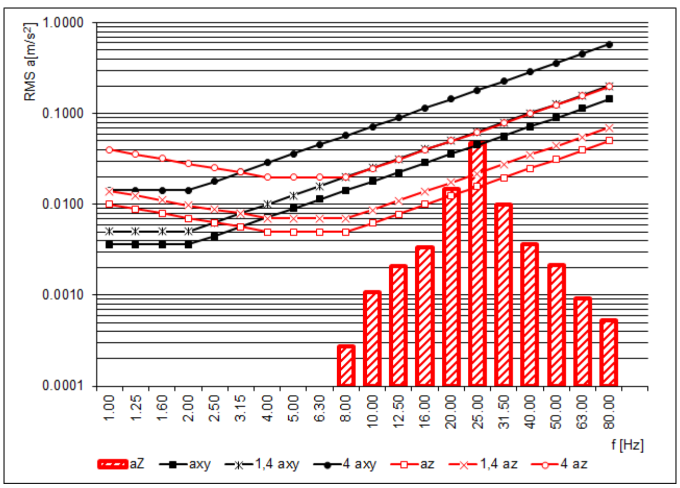

Fig. 12. The results of RMS analysis obtained on the first floor of the construction.

After the RMS analysis made for building construction, the floor slab has been modified by adding layers of the floor. Layers of the floor selected to analysis are made of energy-efficient materials that meet a high acoustic requirements and in particular with the high impact sound insulation factor. Material properties of insulation layers of the floor are listed in Table 2 and due to their high damping characteristics the critical damping value is equal to 7% according to [16]. The cross-section of the chosen floor is shown on Fig. 12.

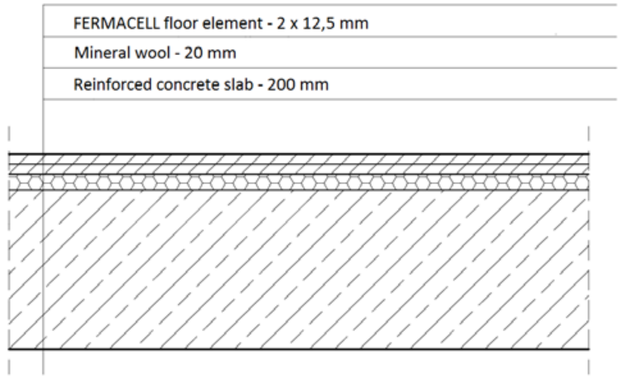

Fig. 13. Cross-section of the floor.

After adding layers of flooring on the ground floor and first floor, the building's foundations were loaded again with the same dynamic forcing caused by tram passing. Once again vibrograms were received and on their basis the RMS analysis was made in the same points as for the model of construction itself. Fig. 14-15 shows the results of RMS analysis obtained from building model with acoustic floor.

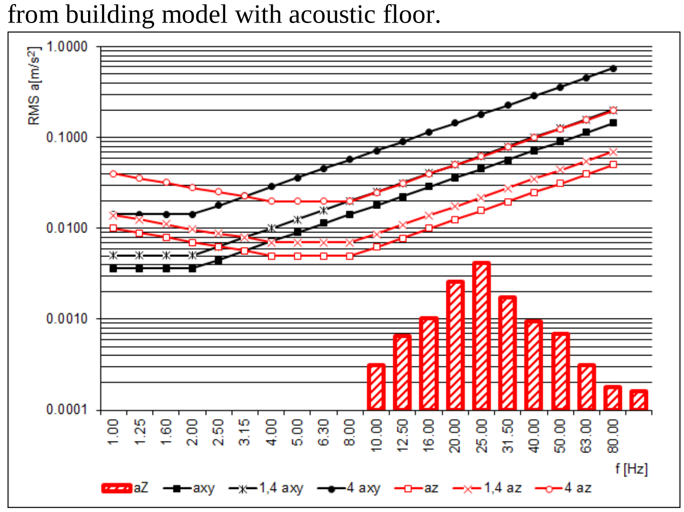

Fig. 14. The results of RMS analysis obtained on the ground floor of the construction with acoustic floor.

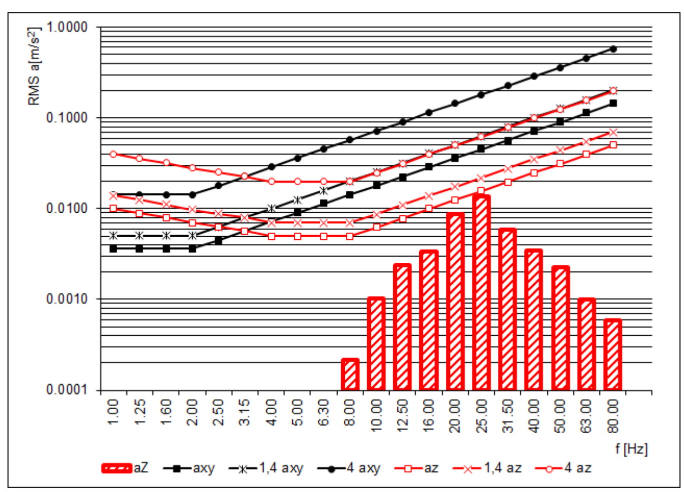

Fig. 15. The results of RMS analysis obtained on the first floor of the construction with acoustic floor.

ISBN: 978-1-61804-325-2

As can be seen from above figures the perception threshold of vibration by humans is not exceeded on both the ground and the first floor of the building. To be sure that on the first floor the perception threshold of vibration is not exceeded vibration perceptibility ratio WODL [17] was calculated. Maximum values of human vibration perceptibility ratio WODL and the corresponding frequency f with respect to both variants of the building model are presented in Table 4.

Table 4

Maximum values of human vibration perceptibility ratio WODL

Floor		Ground floor	First floor
Construction	WODL	0,98	3,07
	f [Hz]	25	25
Construction with acoustic floor	WODL	0,89	0,27
	f [Hz]	25	25

WODL values above 1,0 are indicating exceed of the human perceptibility threshold of vibration. On the first floor of construction of the building this ratio is three times exceeded. But after addition acoustic floor, WODL value decreased below the human perceptibility threshold of vibration.

It is also worth noting that the maximum WODL values are at frequency of 25 Hz, which is a dominant frequency of tram passing.

VI. Conclusion

The above example demonstrates that by using insulating materials on the floor it is possible to reduce vibrational influence on people in buildings which are localized near tramway. Floor layers were chosen due to their acoustic and energy-efficient properties. This kind of materials are not being measured for their dynamic properties. This is a major difficulty in numerical modeling to enter the relevant data for these materials. The dynamic material properties were assumed according to similar materials which were examined in available literature.

The article presents situation that may occur when assessing the influence of vibration on people in buildings. This paper also presents the procedure that can be useful in the design situation when it’s not possible to introduce changes in the structure of the building but it’s possible to make some changes in the floor’s layers.

The correctness of the presented method has been proven by comparing the building model with measurements of a similar object. During the RMS analysis the vibration character has not been lost, the maximum value of WODL ratio occurred for the dominant frequency of vibrations caused by tram passing.

Using a simple linear analysis the method of estimating the influence t of vibrations on people in buildings is shown. The next step of analysis will be to conduct nonlinear analysis for this purpose and compare both linear and nonlinear analysis with each other. If the differences will be not significant the linear analysis will be better because of computing time.

A good direction for future research activities will be also comparing the numerical models with measurements on the real structure and to analyze other solutions of the inter floors.

References

[1] Act of 27th April 2001 Environment Protection Law (Polish Law)
[2] REGULATION (EU) No 305/2011 OF THE EUROPEAN PARLIAMENT AND OF THE COUNCIL of 9 March 2011
[3] Act No 414 of 7 July 1994 Construction Law.. OJ 1994 No. 89 item. (in Polish)
[4] Minister of Infrastructure Ordinance of 12.04.2002on the technical requirements to be met by buildings and their location.(in Polish)
[5] PN-87 / B-02151.02, "Limit values sound levels in rooms".(in Polish)
[6] PN-B-02151-3: 1999, "Acoustic partitions in buildings and acoustic insulation of building elements. Requirements ".(in Polish)
[7] PN-88/B-02171, "Evaluation of vibration influence on humans in buildings"(in Polish)
[8] PN-85/B-02170, "Evaluation of the harmfulness of building vibrations due to ground motion"(in Polish)
[9] ISO 2631-2, 2003: *Guide to the evaluation of human exposure to whole body vibration. Part 2- vibration in buildings*. International Organization for Standardization.
[10] J. Kawecki andK. Stypuła, “Designing Roads Near the Buildings Providing the Necessary Vibrational Comfort for the Residents.”Procedia Engineering 57 (2013), pp. 549-556.
[11] M. Nader and E. Purta “The effect of traffic generated vibrations on people staying in office buildings” in Proc. 12th Int. Cong. On Sound and Vibration, Lisbon, 2005.
[12] K. Gnyp “Influence of passing trains in the neighborhood of the designed building on this object and on people staying in it and technical equipment”, Building and Architecture 13(1) (2014), pp. 29-40. (in Polish).
[13] A. Cappellini, A. Cataneo, S. Manzoni, M. Scaccabarozzi and M. Vanali “Effects of People Occupancy on the Modal Properties of Stadium Grandstand” in Proc. 33rdIMAC,A Conference and Exposition on Structural Dynamics, 2015, pp. 289-298.
[14] Expertise "Analysis of dynamic influence on the buildings in the neighborhood in connection with tram line modernization from the Mogilski Roundabout to Nowa Huta in Krakow - Stage I " under the direction of prof. K. Stypula, Krakow 2014
[15] A. Kowalska “Analysis of influence of non-structural elements on the dynamic characteristics of buildings” Ph.D. dissertation, Dept. of Civil Engimeering, Cracow University of Technology, Poland, 2007.
[16] A. Ossa and M. P. Romo “Dynamic characterization of EPS geofoam”. Geotextiles and Geomembranes 29 (2011), pp. 40-50.
[17] J. Kawecki and K. Stypuła, “Ensuring the vibration comfort to people residing in buildings exposed to the impact of communication.” Cracow University of Technology Publishing House (2013), ISBN 978-83-7242-710-6.

Dr Alicja Kowalska-Koczwara(born March 10, 1977 in Bedzin) - Doctor of Technical Sciences, specializing in building structures, structural mechanics, an employee of teaching Cracow University of Technology, received her Ph.D. in 2007.

V-ce Director of Instittute of Structural Mechanics at the Faculty of Civil Engimeering, Cracow University of Technology.

She is currently conducting research on influence of vibrations on human body and on humans residing in buildings.

Expert working actively in the work to implement Polish standard “Evaluation of vibrations influence on people in buildings”. She takes part in many expert opinions on the dynamic effects on buildings and on people in buildings. The main directions of interest are dynamic influences of paraseismic origin.

Eng. Paweł Kiszka (born March 23, 1992 in Myślenice) - Engineer of Technical Sciences, student on Cracow University of Technology, specialization Building and Engineering Constructions.

He joined to dr A. Kowalska-Koczwara's research on influence of vibration on human body and on humans residing in building. The mail directions of interest is combining real dynamic influence with computer model equivalent.

Using body gestures and voice commands for assistive interaction

Răzvan Gabriel Boboc, Mihai Duguleană and Gheorghe Leonte Mogan

***Abstract*—**This paper discusses a human-machine interaction paradigm based on an operator's body gestures and voice commands for assistive applications. In the context of the humanoid robots already present on the market for the large public use, assistive robotics became a wide usage area to exploit the potential synergy of human-robot cooperation in order to extend and enable human activities that would otherwise be difficult or even not possible for the human alone. To enable these applications, simple and natural communication and interaction means are needed. The algorithms presented in this paper can be used for solving various assistive tasks and are based on Dynamic Time Warping (DTW) and Isolated Word Recognition (IWR). The system is tested successfully on the particular case of NAO humanoid robot, within an experimental scenario.

***Keywords*—**gesture recognition, voice commands, DTW, assistant robot, HRI.

I. Introduction

THE recent research in human-robot interaction is focused on creating domestic applications, with an increasing number of personal service robots that invade our homes or offices. Intelligent robots provide their support in many unpleasant, tedious human activities. These robots need to be capable of acquiring sufficient understanding of the environment, being aware of different situations, detecting and tracking people, as well as establishing a successful communication with humans in order to be able to cooperate with them [1].

An assistant robot should be able to interpret the verbally or non-verbally given instructions of the human [2]. In such context, researchers strive to find new simpler, more intuitive and human-like ways of interaction, that at the same time require less computational power and less sophisticated sensor devices. Along with other more recent approaches, the use of body gestures still remains a natural and thus an attractive alternative to cumbersome interface devices for human-computer interaction (HCI). Among various actions, the pointing gesture is natural, and perhaps, the most intuitive interaction paradigm, effective even in noisy environments and useful for commanding or simply messaging a robot [3].

In this paper we focus on the development of natural human-robot communication by means of human speech and gesture commands. In particular, we focus on using Dynamic Time Warping (DTW) for gesture recognition. The resulting module is used in combination with voice recognition to create human-like capabilities and behavior of the assistant robot. Thanks to this approach the robot gathers a very powerful ability: that of moving in an indicated direction and perform a required task - a High Level Interaction (HLI) paradigm [4] that we refer hereinafter as "point-and-command". Basically, this interaction metaphor is about indicating the robot a spatial location and a task to be performed there.

II. Background

Robots have been used as research tools in a variety of applications [1], [5], [6]. Some of them focus on how robots are accepted in the current society [7], suggesting an increasing presence of intelligent robots in our daily life, provided natural interaction is enabled. Latest research points the use of gestures as a way of interacting with computers and robots, as a natural and intuitive way of communication or option selection [1], [8].

There are many techniques used for gesture recognition [9], [10]. Commonly, these techniques are divided in two main categories: sensor-based and vision-based. While for the first category, the user is forced to bear different sensing devices attached to his body (gloves, magnetic trackers), in the vision-based approach the user does not require to wear any contact devices. The technique uses a set of visual sensors and algorithms to recognize gestures [8]. At the same time, gestures can be static or dynamic. For detecting dynamic gesture recognition in real time, there are issues in determining the start and the end points of a meaningful gesture pattern from a continuous stream [11]. While static gesture (pose) recognition can typically be accomplished by template matching and pattern recognition techniques, the dynamic gesture recognition problem involves the use of more advanced techniques [12].

Given these observations, researchers have proposed various solutions to optimize recognition of gestures [3], [11]. In this paper we will refer only to those based on vision,

This paper was sopported in part by the NAVIEYES research project (project code PN-II-PT-PCCA-2013-4-2023), financed by UEFISCDI.This work was supported in part by the Sectoral Operational Programme Human Resources Development (SOP HRD), ID134378, financed by the European Social Fund and the Romanian Government.

R. G. Boboc is with the Automotive and Transport Engineering, Transilvania Universtity of Brașov, 500024 Romania (phone: +40 268 236537; e-mail: razvan.boboc@ unitbv.ro).

M. Duguleană is with the Automotive and Transport Engineering, Transilvania Universtity of Brașov, 500024 Romania (e-mail: mihai.duguelan@ unitbv.ro).

G. L. Mogan is with the Automotive and Transport Engineering, Transilvania Universtity of Brașov, 500024 Romania (e-mail: mogan@ unitbv.ro).

generally body gestures. As shown in [13], the most widely used techniques for recognizing body movements are Hidden Markov Model (HMM), Dynamic Time Warping (DTW), Finite State Machine (FSM) and Neural Networks (NN). HMM was used in [3] for recognizing pointing gestures in order to control a mobile robot. They used 3D particle filters and a cascade of two HMM to estimate the pointing direction, dealing both with large and small pointing gestures. In [14] a probabilistic model, dynamic Bayesian network (DBN) was used for hand gesture recognition, which includes HMMs and Kalman filters. Also, NN in combination with HMM was used in [15] for hand gesture recognition, but the algorithm involves high computational costs.

Dynamic Time Warping was first used for speech recognition [16], but was extended also to other areas, including gesture recognition [17]. As we have seen above, there are several techniques used for detection and recognition of human gestures, but the most popular are HMM and DTW. Some papers have demonstrated that better results can be obtained with DTW instead of HMM both in voice recognition (animal vocalization) [18] and gesture recognition [12].

A. Gesture recognition with DTW

In order to detect gestures with a video camera, pattern matching technique or other similar algorithms can be used. Pattern matching involves the use of recorded drawings of gestures that serve as templates against which detected gestures can be compared. An example of such a technique is DTW, a template matching algorithm. The patterns are in this case a time sequence of measurements. DTW computes the cumulative distance between each pair of values of both time sequences, giving a measure of similarity between the two time sequences.

Various improvements have been made to the DTW algorithm, to make it more efficient, according to various authors. The methods used to make DTW faster fall into three categories [19]: constraints, data abstraction, indexing. In [20] a parallelisation of the original DTW algorithm is presented, in order to monitor multiple data streams using graphic processor units (GPUs). Lately, a probabilistic approach was proposed in [21]. Our technique combines data abstraction with lower bounding technique to improve performance.

B. Voice commands recognition

There are many studies on speech recognition with specific interest in commanding robots. The main goal of almost any work in this area is to achieve a natural-language communication with the robot assistant.

Various algorithms are used to achieve speech recognition. One of them is the Dynamic Time Warping (DTW), which is based on pattern comparison, fairly similar to the one used in video processing [22]. Other studies use Hidden Markov Models (HMMs) [23], empowering statistics to handle a specific vocabulary. Artificial Neural Networks (ANNs) is another technique used one its own or combined i.e. with HMM for achieving speech recognition [24].

For this study, we use a vocabulary approach based on Microsoft Kinect speech recognition library. The algorithm behind the library is as follows: an audio stream taken from Kinect sensor is parsed and then vocal utterances are interpreted. If the engine recognizes some elements, they are sent to the processing unit. If the command is not recognized, it removes that part from audio stream.

III. Overview of the Proposed System

To identify the human gestures we used a Kinect camera mounted in front of the user. This corresponds to a human sitting at his desk situation (Fig. 1). The Kinect camera records the movements and listens for voice signals recognizing the words spoken by the user. As a result, it sends a 'wake up' command to the robot.

The assistive robot is physically able to autonomously walk to a specified location, recognize an object and grab it. In order to be able to command the robot for performing these tasks, a vocabulary of words and gestures was designed. It consists of several arm movements and speech commands which may be combined in several ways. Since the environment can be noisy or with poor lighting conditions, some commands have been chosen for use in both modes of interaction (by gesture and voice). Thus, for starting the interaction with the robot, the users can perform an initialization gesture or can speak the robot name.

The robot has a fixed initial position, which is marked with a NAOmark, as in Fig. 2. Objects are placed in different positions in the room. After the connection with the robot is established, the user can ask the robot to bring him an object indicated by pointing gesture (Fig. 8). The robot will move in the indicated direction, will identify the object and will grab it, then will move back to the user. If the robot encounters certain

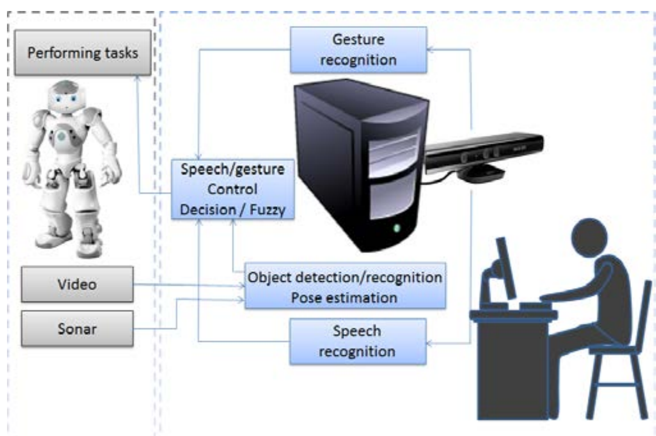

Fig. 1. Overall view of the system architecture

difficulties such as obstacles or can't identify an object, it asks by voice or by a predefined gesture. In [4] this paradigm (name here "point-and-command") was defined as a high-level command, which do not explicitly specify the target location, but help robots in autonomous target selection.

A. Hardware and software prerequisites for theoretical and experimental studies

Microsoft Kinect sensor was used in this work for both gesture and speech recognition. This sensor is a low cost capture device originally developed for the Xbox 360 video game console. It contains a RGB-D camera for image acquisition and an array of four microphones for capturing

ISBN: 978-1-61804-325-2

sound and locating its source. Due to its benefits, Kinect was used for research purposes, enabling touch-less interactions through voice and gesture. Users can move freely, without being constrained to wear other sensors or devices on their body.

Kinect for Windows SDK was used, which is a toolkit that provides an interface to interact with the device. It provides API libraries for .NET and C/C++ applications that run on Windows platforms.

Kinect SDK tracks 3D coordinates of 20 body joints in real time (30 frames per second) and the obtained joint positions are used to recognize the gesture or posture which will command the robot.

A desktop PC is the main processing unit. As is illustrated

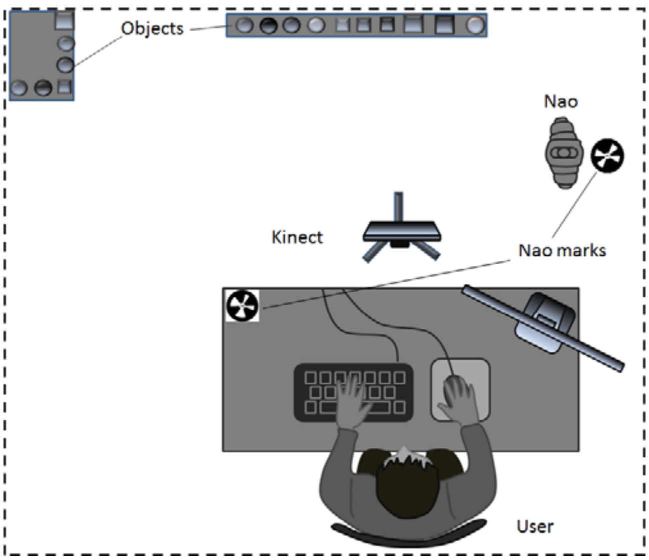

Fig. 2. Layout of the testing room

in Fig. 1, on this computer runs the application that allows gesture recognition, voice recognition, a speech/gesture integrator system and the communication with the robot. The computer is equipped with an Intel core i7 X 990 CPU 3.47 GHz, 12 GBs RAM.

IV. Metods

A. Human's gestures recognition

In gesture recognition, a comparison between two sequences is essential. Dynamic gesture recognition typically contains two components: segmentation and recognition [25]. Segmentation is the process of locating a gesture from a frame sequence. We use DTW technique to assess the similarity between two video sequences obtained from Kinect sensor. The input data is compared with a predefined sequence; the two sequences are aligned in order to determine the minimum cost path. This minimum cost represents the optimal alignment between the two sequences, which means that the corresponding gesture is considered to be recognized.

A problem that occurs is to know when to start the gesture recognition procedure, because if a gesture differs only in starting position from the predefined sequence, the result of the alignment with DTW technique will be very different. For this, we choose to use an initialization phase, which consists of a simple word spoken by the user, by which the robot is warned that the user wants to start a gesture interaction. When that predefined word is pronounced, the program automatically starts the gesture recognition process. The end of the gesture is considered when the hands stops moving.

B. Structure of the proposed algorithm

The flow diagram of the proposed algorithm is shown in Fig. 3. As it can be seen, the first stage is to detect the human. After that, features are extracted. The DTW algorithm is applied to the extracted vectors and if the gesture is recognized, then the robot will perform the requested action. Otherwise, it will initiate a speech interaction in order to ask for further details.

The proposed gesture recognition algorithm involves 4 steps: 1) automatic human detection, 2) feature extraction, 3) a gesture pattern stage, where gestures are compared with reference gestures, 4) gesture recognition (Fig. 3).

The first stage of the algorithm is to detect the human body. This is facilitated by the Kinect sensor that can find the skeleton using a very fast and accurate recognition system that requires no setup, because a learning machine has already been instructed to recognize the skeleton. Joint positions are obtained like in Fig. 4. For this study, just the arm joints are relevant, especially hand, wrist and elbow joints. The coordinates of that joints form a feature vector.

For simplicity, two assumptions were made: first, it was assumed that a single person is presented at a time in front of the sensor and second, that person has a sitting posture. The initiative of initiating an interaction with the robot belongs to operator. After the initialization stage, the system is 'prepared' to recognize the gesture performed by the user. The gesture should be performed quickly because is represented on 33 frames. After the 33th frame, the feature vector is compared with sample gestures. Once a gesture is recognized, depending on its significance, the system will decide what task the robot should be performed.

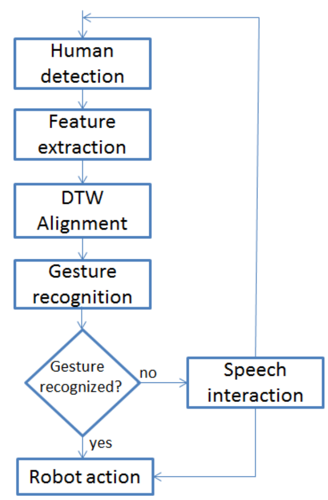

Fig. 3. Gesture recognition flow diagram

Feature extraction. The most important information about a body gesture is the motion of limbs. In this case, upper limbs are relevant because the system was designed for humans sitting on chair. The motion of an arm is described by its trajectory in space. This trajectory represents a time sequence of positions of the arm.

The feature vector captured from Kinect contains the x, y positions of each arm joint. This vector is then preprocessed in order to prepare it for DTW computation. Preprocessing stage includes eliminating missing or redundant data and other variations and set vector length. The feature vectors that are

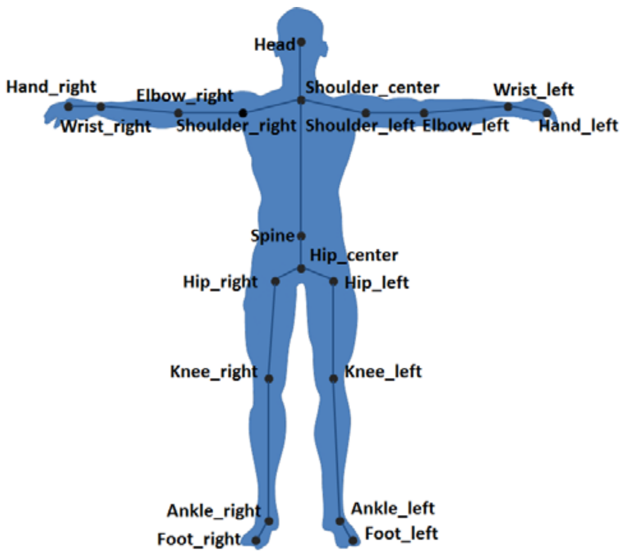

Fig. 4. Kinect joints

characteristic for a command gesture are extracted and then stored into a database.

The minimum distance from the Kinect device for an accurate detection is 60 cm. The sensor is placed on a tripod, in front of the user's desk (see Fig. 8).

C. DTW Method

Dynamic time warping (DTW) is a powerful technique in the time-series similarity search [26]. An overview of this method is given below.

Given two time series sequences: $x = x_1, x_2, \dots, x_i, \dots, x_n$ of length n and $y = y_1, y_2, \dots, y_j, \dots, y_m$ of length m, a n-by-m matrix can be obtained, where each element of the matrix represents the distance between two elements of the time series, named *cost matrix*. The optimal alignment between x and y needs to be found, such that the overall cost is minimal. A *warping path* $w = w_1, w_2, \dots, w_k, \dots, w_p$ defines such mapping between the elements of the two time series (Fig. 5).

$$DTW(x, y) = \min \sum_{k=1}^{p} d(w_k)$$

The DTW warping path is constrained to follow some restrictions, like monotonicity, continuity, warping window, slope constraint and boundary conditions [27].

The cost for the optimal alignment is recursively obtained by:

$$\gamma(i,j) = d\left(x_i, y_j\right) + \min[\gamma(i-1, j-1), \gamma(i-1, j), \gamma(i, j-1)]$$

As we said above, new versions of DTW algorithm were developed for improving speed, while others were developed for improving accuracy. The lower bound technique for DTW was first proposed in [28]. A lower-bound function for DTW is a function that always returns a value smaller than or equal to the actual DTW distance. The most cited lower bound is LB_Keogh, which uses the warping path to compute an envelope on the warping cost. Improved versions of the envelope technique were proposed in [29].

The warping envelope of time series x is represented by the pair U(x) and L(x), where:

$U(x)_i = \max_k \{x_k \mid |k-i| \le \gamma\}$

$L(x)_i = \min_k \{x_k \mid |k-i| \le \gamma \}$, i = 1, .., n, where γ is a local constraint

The lower bounding function LB_Keogh is defined as:

$$LB\_Keogh(x,y) = \sqrt{\sum_{i=1}^{n} \begin{cases} (y_i - U_i)^2, & y_i > U_i \\ (y_i - L_i)^2, & y_i < L_i \\ 0, & otherwise \end{cases}}$$

In order to satisfy the requirements of a robust gesture recognition system for interaction with a mobile robot, we propose an improved version of DTW, that combines several techniques, as will be shown below.

The time complexity of DTW algorithm is O (n*m) for two sequences like those presented above, which makes the method not practice for longer time series. Although our sequences, represented by feature vector are small, we decide to use the algorithm presented in [19], which is O(n) both in time and space. The presented method, named FastDTW, uses a multilevel approach with three steps: coarsening, projection and refinement. First, the size of time series is reduced by averaging adjacent pairs of points, and then a warp path is calculated for this lower resolution, which will be used to find the warping path for higher resolutions. Finally, the warping path is refined, searching for the optimal path on each side of the projected path, according to a *radius* parameter, that indicates the number of cells to be evaluated.

FastDTW was slightly modified. After the coarsening step, the minimum distance warping path was obtained using another technique, a lower bound function introduced in [29], that that offers a plausible speedup [30]. Given the time series presented in section 2.1, LB_Improved is defined as:

LB_Improved (x,y) = LB_Keogh(x,y) + LB_Keogh(y, H(x,y)) , where H(x,y) is the projection of x on y:

$$H(x,y)_i = \begin{cases} U(y)_i, & x_i \ge U(y)_i \\ L(y)_i, & x_i \le L(y)_i \\ x_i, & otherwise \end{cases}, \ i = 1, 2, \dots, n$$

DTW compares the sequence obtained for an unknown gesture to one or more reference templates. Having more reference templates, the recognition rate will be higher, but the computing time also increases. For this reason, an approach implemented in [31] for speech recognition is used. This algorithm, named Quantized DTW, stores one reference model for each gesture. This algorithm was adapted for gesture recognition.

The Quantized DTW together with FastDTW and LB_Improved were combined in order to obtain a fast and accurate gesture recognition algorithm.

V. Human-Robot Interaction

HRI inputs are diverse, but we focus in this paper on vision and speech. Computer vision was used to process human gestures and to detect objects, while speech was used to exchange information between human and robot. User can give instruction to the robot using both gesture and voice, in the same way as people communicate with each other.

A. Gesture interaction

A gesture is a bodily movement made intentionally by a human in conversation, in order to aid in better understanding

ISBN: 978-1-61804-325-2

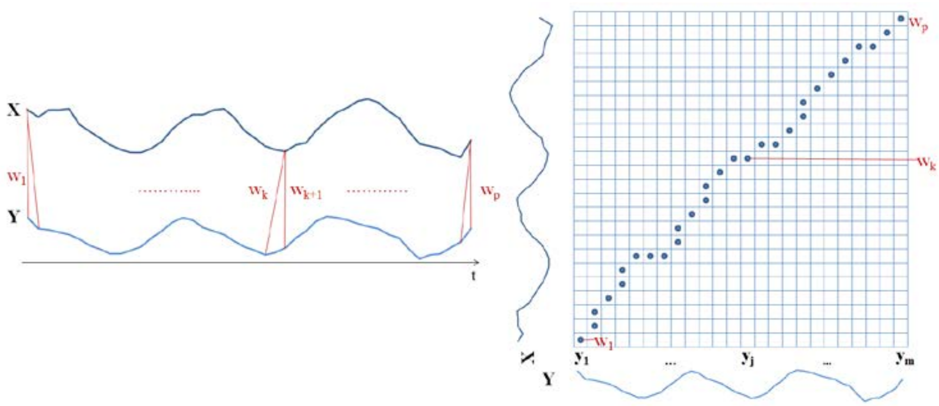

Fig. 5. a) The alignment of two time series (x, y) by DTW; b) and the mapping between them – the warping path (with blue dots)

of what he said. In human communication, hand, head and arm gestures play an important role.

In HRI domain, since assistive robots interact with non-expert users, natural interfaces are essential and therefore robots should be able to understand the modalities used by humans during interaction. The same as in human-human interaction, a gesture can provide information or to communicate intention to robot. A set of gestures was created, which represents the 'command vocabulary' for HRI. In Table 1 are shown the defined gestures. Most of the gesture were inspired from [32].

Special attention was given to pointing gesture because is an easier way to draw robot's attention indicating an object or a location in space and is useful for non-expert users. Once the gesture was been detected, the next step is to estimate the pointing direction. For this work, we need to calculate the angle between user's arm and shoulder center. Three joints from the skeleton describe this gesture: shoulder center, shoulder and hand (Fig. 6). The estimated angle was calculated using the following formula:

$\alpha = acos \frac{v1.x * v2.x + v1.y * v2.y}{\sqrt{v1.x^2 + v1.y^2} * \sqrt{v2.x^2 + v2.y^2}} * \frac{180}{\pi}$, where v1, v2 are two vectors:

v1 = Shoulder – Hand

v2 = Shoulder_Center - Shoulder

The pointing gesture is used only when the robot is in the home position, knowing its orientation and the distance from Kinect. Otherwise, it does not know in which direction to go.

All gestures are made with arms, excepting two: head nod and head shake. We choose to use these gestures because are the most commonly used in interpersonal communication when they accept or reject something. As simple head tracking algorithm was used, taking into account the head rotation on the sagittal or transverse plane.

Table I. Gesture vocabulary

Gesture name	Abb	Description	Meaning
Attention	A	One hand pointing up	'Hey!'
Big	B	Both hands are held at head level with large distance between them	'A bigger object'
Break	Br	One hand placed perpendicular to the other hand	'Time out!'
Calm	Ca	Both hands pressing down repetitively	'Go slowly'
Circle	O	Draw a circle in space	'An object like this'
Come	C	Hand moves repeatedly from outward toward the body	'Come here!'
Despair	D	Both hands are raised at head level	'What have you done?'
Doubt Shrug	Do	Hands are opened in an outward arc	'I don't know'
Head nod	HN	Head is tilt vertically once or several times	Acceptance
Head shake	HS	Head is turned left and right repeatedly	Rejection
Left	L	Left arm raised at shoulder level in the left side of the body	'Go left!'
Object	Ob	Hand points towards an object	'That object!'
Rectangle	R	Draw a rectangle in space	'An object like this'
Refuse	Re	One hand is moved outward in a wiping motion	Negation
Right	R	Right arm raised at shoulder level in the right side of the body	'Go right!'
Small	S	Both hands are held at head level with small distance between them	'A smaller object'
Space	Sp	Hand points into the space	'Go there!'
Sway	Sw	Both hands alternate in an up-down movement	'Keep going!'
To-Fro	TF	Both hands move from one side to the other	'Move there'
Triangle	T	Draw a triangle in space	'An object like this'
Turn left	TL	Both hands imitating the rotation of an object in counterclockwise direction	'Rotate left 15°!'
Turn right	TR	Both hands imitating the rotation of an object in clockwise direction	'Rotate right 15°!'
Wave	W	The at hand is outstretched, upward, with small sideways movements	Calls robot attention
Wipe	Wi	Both hands start near each other and move apart in a straight motion	Termination, finish
X	X	Hand crossed	Exit application

Some gestures have different meanings depending on the context. For example, when the user says 'Rotate left' and robot is moving, it will change direction of walking to left with 15°. If the robot is not moving, the same command will refer to robot' camera, and then it will rotate the head 15° to left.

To make the interaction more realistic some basic behavior for humanoid robot were developed (like shrugging, confused - *robot scratches its head*.

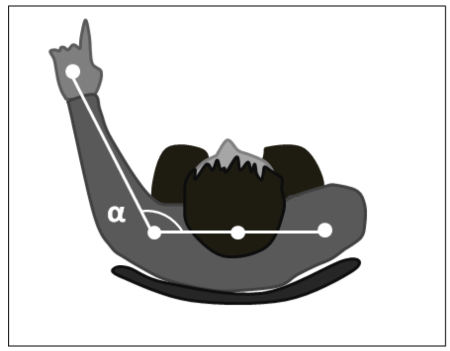

Fig. 6. Pointing angle

B. Speech interaction

As for gesture interaction, a set of speech commands was created. In Table 2 are shown the basic verbal phrases used in interaction, but is not a complete table because some of them can be combined to form predefined utterances, as it will be shown in below.

For starting the interaction with the robot, the user is required to say the robot's name ("NAO") in order to know that user is speaking with it.

The voice command system was created using Kinect for

Table II. Speech vocabulary

Command	Abb	Meaning
Nao!	N	Start interaction
Stand up!	SU	Robot stand up from rest position
Sit down!	SD	Robot sits in the rest position
Go there!	GT	Robot goes in the indicated direction
Go left!	GL	Go in the left direction, rotating with 90°
Go right!	GR	Go in the right direction, rotating with 90°
Turn left!	TL	Turn left 15°
Turn right!	TR	Turn right 15°
Grab the object!	GO	Robot will autonomously catch an object, calculating the distance to it
Drop object!	DO	Robot release object from his hand
Leave object!	LO	Robot raise its arm and open the hand
Let me control you!	C	Teleoperation mode
Learn this!	LT	Learn a new task
Bring it to me!	B	Bring object to user
Open hand!	OH	Robot open its hand
Close hand!	CH	Robot close it hand
Thank you!	TK	Robot wait for another command
Yes!	Y	Acceptance
No!	N	Rejection
Stop!	S	Robot stops the action it perform
Exit!	E	Close the application

Windows SDK, combined with Microsoft Speech Recognition (MSR) API. Kinect SDK provides various audio capabilities and Microsoft Speech platform provides classes to work with speech recognition captured by Kinect sensor, converting spoken words to written text. The sensor can detect audio that is within ± 50 degrees in front of sensor and also supports up to 20 dB of ambient noise cancellation.

Microsoft Speech Recognition has advanced grammar and vocabulary and it doesn't require any training for the models. The user should create his grammar with the desired keywords. A Kinect handler will initialize audio stream and will start the audio capturing. Once the speech recognition engine starts, user will load the grammar and from now the system is ready to listen from Kinect. Then, each recognized word has a confidence level, showing the reliability of the detection.

C. *Gesture/speech fusion*

Speech and gesture recognition modules are run simultaneously. After the command "Attention" (by gesture) or "NAO" (by voice), the system waits for another command that can be by gesture or by voice. There are four possibilities resulting from combination of interaction modalities: only gesture (G), gesture+voice (GV), voice+gesture (VG), only voice (V). Each command is sent to the decision system, which is based on different rules and, according to these rules, the task that have to be performed is identified. If the commands are GV or VG, the system decide if gesture command is congruent or not with voice command. The tasks or actions implemented are the following: navigation (N), fetching (F), grabbing (G), pushing (P), and teleoperation (T).

The following rules constitute part of the knowledge base and express how the system has to react:

If <gesture command> is C and <voice command> is GL then task is N

If <gesture command> is Sp and <voice command> is B then task is F

If <gesture command> is Ob and <voice command> is GO then task is G

If <gesture command> is A and <voice command> is C then task is T

If a gesture command is incongruent with the voice command, the robot will respond by predefined behaviors or by speech. Otherwise, the system decides the action given by one command only or both congruent commands.

D. *Robot tasks*

Programming of the robot consists of path planning according to the target. So a *task* in our work is defined as movement to a location plus a simple manipulation (two sub-programs). Each task has so need 2 essential inputs: location and handling. These two information are obtained by the robot through dialogue: the robot asks by voice and human answer by one of the mentioned metaphors. We choose to use some simple tasks that are commonly found in home environments: push, fetch.

We choose also to use only the basic capabilities of the robot and not to enhance them. The system uses an external computer to perform all the computations concerning gesture/speech interaction, video processing, and so on.

For grabbing an object task, an algorithm inspired from [33] was used for measuring the distance to the object with video camera and sonar sensors.

For simplicity, we choose objects with known shapes: balls, cubes, and cones (Fig. 7). Each object has some particular properties or attributes that are shown in Table 3.

Shape attribute refers to volumetric property of the object (2D form). The software associates the object name with a simplified representation of the object, corresponding to shape, color, and size properties.

An image taken by the robot's camera is first segmented using a color detection algorithm using OpenCV. In this operation, the robot tries to separate the object in the scene from the background. The shape of the objects is detected using edge detection algorithm [34].

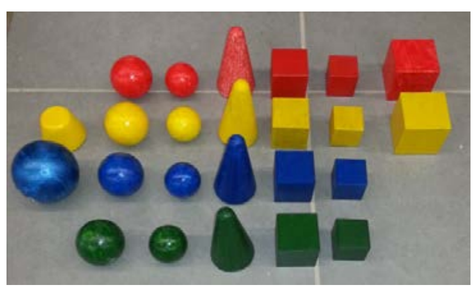

Fig. 7. The objects used for experiment

VI. Results

In this section will be presented the experiment conducted with the aim to test the performance of the system and to evaluate operation and precision dialogue in global application. The experiments were conducted in our institute environment. The user asked NAO to follow his instructions given by means of multimodal requests. NAO is asked to go in a desired direction indicated with pointing gesture. The robot will navigate in that direction and will bring to the user an

ISBN: 978-1-61804-325-2

object whose name and properties are sent to robot by voice command.

A simple dialogue between user (U) and NAO humanoid robot (N) is proposed. The experiment was conducted by 4 persons for 3 times. The user asks NAO to bring him a red ball located in a certain position in the environment. Below is shown the whole dialogue.

U: 'NAO!'
N: 'Yes, I hear you"
U: 'Please, give me the red ball from there!'
N: 'Can you show me how the red color looks like?'
(*user show it a sample painted in red*)
N: 'What about the shape of the object?'
U: 'The ball has this shape'(user show it a circle drawn on a paper or by gesture – draw a circle in the air with his hand)
(*the robot walk in that direction – when it identify the red color, it will goes toward to identify the shape*)
N: 'Is that the object?'
U: 'No, I need a bigger one'
(*the robot will continue looking until it find a bigger ball*)
U: 'Grab the object!'
(*the robot decide if it can grab the object with one hand or with both hands*)
U: 'Bring it to me!'
(*NAO is looking for NAO mark and go in that direction*)
U: 'Leave it'
(*NAO leave the object*)
U: 'Thank you!'
N: 'Do you want another thing?'
U 'No'
(*NAO will go to home position*)

During the experiment more gestures have been used in order to test the performance of recognition algorithm, especially for navigation task. The confusion matrix among gesture commands for 4 users is shown in Table 4.

VII. Discussion

In this work we describe a framework for a natural and easy human-robot communication and interaction. While most of the multimodal HRI systems proposed in literature focus on a single modality, our system allows the users to express their instructions as combinations of gestures and speech inputs. The main strengths of our system are: the improved method of gesture detection, easy and natural interaction through gestures and voice commands, and the gestures and voice feedback provided by the robot.

Table III. Objects and their attributes

Object name	Attribute name	Values
Ball	Shape	Circle Triangle Square
Cube	Colour	Red Yellow Blue White
Cone	Size	Smaller Larger

The purpose of the interface is to allow expert and non-expert users to cooperate and interact with an assistant robot operating in a domestic environment. A gesture and a speech vocabulary were implemented and the commands can be sent by one or both modalities. So, a first objective of our research was to provide the robot with social interaction capabilities, which are essential for assistive robots applications.

Most of the work was focused on gesture interaction, specifically gesture recognition. An improved DTW method was implemented and tested, with good results both in accuracy and efficiency. The method increases the robot reactivity at the human requests enhancing the naturalness of the interaction. Combined with the speech/gesture capability resulted in a versatile interface that facilitates powerful interaction paradigms like the "point-and-commands" one.

However, there are some problems or limitations that were encountered during the experiments and that still need to be addressed. The recognition accuracy is dramatically affected when there are poor lightning conditions or noise in the operation environment. On the other hand, when multiple humans appear in the visual range of sensor, the system has difficulties in identifying the right user. In some situations the robot was unable to identify markers and lose orientation. Also, some smaller obstacles were not detected and sometimes the robot falls.

The above problems and others show that several further developments are needed to be addressed in our future research, as follows:

- Expanding the gesture vocabulary by adding also hand gestures, that are more intuitive and which can express more of the user wishes.
- Implementing a more advanced method to detect object with different shapes and colors and for object manipulation.
- Considering the possibility that more users wish to interact with the robot in the same time. In this case, the system must be intelligent enough to select the user that will interact with the robot.
- Developing more complex scenarios with a variety of tasks that have to be performed by the robot.

Table IV. Confusion matrix for navigation task

		Recognized gesture										
		B	Ca	C	L	R	Sp	Sw	TF	TL	TR	W
Performed gesture	B	90%	0	0	0	0	0	0	0	0	0	0
	Ca	0	100%	0	0	0	0	0	0	0	0	0
	C	0	0	90%	0	0	0	0	0	0	0	0
	L	0	0	0	95%	0	0	0	0	0	0	0
	R	0	0	0	0	90%	5%	0	0	0	0	0
	Sp	0	0	0	0	0	95%	0	0	0	0	0
	Sw	0	0	0	0	0	0	85%	0	0	0	0
	TF	0	0	0	0	0	0	0	90%	0	0	0
	TL	0	0	0	0	0	0	0	0	95%	0	0
	TR	0	0	0	0	0	0	0	0	0	95%	0
	W	0	0	0	0	0	0	0	0	0	0	90%

ISBN: 978-1-61804-325-2

Fig. 8. The testing room. The user indicates the location by pointing and verbally the task to be executed

ACKNOWLEDGMENT

This paper was supported by the Project no. 240/2014, code PN-II-PT-PCCA-2013-4-2023, entitled "Intelligent car navigation assistant for mobile devices based on eye gaze tracking and head pose - NAVIEYES" financed by UEFISCDI and by the Sectoral Operational Programme Human Resources Development (SOP HRD), ID134378, financed by the European Social Fund and the Romanian Government.

REFERENCES

[1] V. Alvarez-Santos, R. Iglesias, X. M. Pardo, C. V. Regueiro, and A. Canedo-Rodriguez, "Gesture-based interaction with voice feedback for a tour-guide robot," *Journal of Visual Communication and Image Representation,* 2013.

[2] J. Richarz, A. Scheidig, C. Martin, and S. Mueler, "A Monocular Pointing Pose Estimator for Gestural Instruction of a Mobile Robot," *International Journal of Advanced Robotic Systems,* vol. 4, pp. 139-150, 2007.

[3] C.-B. Park and S.-W. Lee, "Real-time 3D pointing gesture recognition for mobile robots with cascade HMM and particle filter," *Image and Vision Computing,* vol. 29, pp. 51-63, 2011.

[4] A. Caltieri and F. Amigoni, "High-Level Commands in Human-Robot Interaction for Search and Rescue," in *The 17th annual RoboCup International Symposium,* Eindhoven, Netherlands, 2013.

[5] T. Breuer, G. Giorgana Macedo, R. Hartanto, N. Hochgeschwender, D. Holz, F. Hegger, *et al.*, "Johnny: An Autonomous Service Robot for Domestic Environments," *Journal of Intelligent & Robotic Systems,* vol. 66, pp. 245-272, 2012.

[6] M. Duguleana, F. G. Barbuceanu, A. Teirelbar, and G. Mogan, "Obstacle avoidance of redundant manipulators using neural networks based reinforcement learning," *Robotics and Computer-Integrated Manufacturing,* vol. 28, pp. 132-146, 2012.

[7] M. M. A. de Graaf and S. Ben Allouch, "Exploring influencing variables for the acceptance of social robots," *Robotics and Autonomous Systems,* 2013.

[8] A. Sanna, F. Lamberti, G. Paravati, and F. Manuri, "A Kinect-based natural interface for quadrotor control," *Entertainment Computing,* vol. 4, pp. 179-186, 2013.

[9] S. Mitra and T. Acharya, "Gesture Recognition: A Survey," *Systems, Man, and Cybernetics, Part C: Applications and Reviews, IEEE Transactions on,* vol. 37, pp. 311-324, 2007.

[10] V. I. Pavlovic, R. Sharma, and T. S. Huang, "Visual Interpretation of Hand Gestures for Human-Computer Interaction: A Review," *IEEE Trans. Pattern Anal. Mach. Intell.,* vol. 19, pp. 677-695, 1997.

[11] J. Kang, K. Zhong, S. Qin, H. Wang, and D. Wright, "Instant 3D design concept generation and visualization by real-time hand gesture recognition," *Computers in Industry,* vol. 64, pp. 785-797, 2013.

[12] J. Carmona and J. Climent, "A Performance Evaluation of HMM and DTW for Gesture Recognition," in *Progress in Pattern Recognition, Image Analysis, Computer Vision, and Applications*. vol. 7441, L. Alvarez, et al., Eds., ed: Springer Berlin Heidelberg, pp. 236-243, 2012.

[13] S. Rautaray and A. Agrawal, "Vision based hand gesture recognition for human computer interaction: a survey," *Artificial Intelligence Review,* pp. 1-54, 2012.

[14] H.-I. Suk, B.-K. Sin, and S.-W. Lee, "Hand gesture recognition based on dynamic Bayesian network framework," *Pattern Recognition,* vol. 43, pp. 3059-3072, 2010.

[15] C. Zhu and W. Sheng, "Online Hand Gesture Recognition Using Neural Network Based Segmentation," in *The 2009 IEEE/RSJ International Conference on Intelligent Robots and Systems*, St. Louis, USA, 2009.

[16] H. Sakoe and S. Chiba, "A dynamic programming approach to continuous speech recognition," in *the 7th International Congress on Acoustics*, Budapest, Hungary, 1971.

[17] H. Li and M. Greenspan, "Model-based segmentation and recognition of dynamic gestures in continuous video streams," *Pattern Recognition,* vol. 44, pp. 1614-1628, 2011.

[18] J. A. Kogan and D. Margoliash, "Automated recognition of bird song elements from continuous recordings using dynamic time warping and hidden Markov models: a comparative study," *Journal of the Acoustical Society of America,* vol. 103, pp. 2185-2196, 1998.

[19] S. Salvador and P. Chan, "Toward accurate dynamic time warping in linear time and space," *Intell. Data Anal.,* vol. 11, pp. 561-580, 2007.

[20] Jason Chang and M.-Y. Yeh, "Monitoring Multiple Streams with Dynamic Time Warping using Graphic Processors," in *Parallel Data Mining Workshop (IPDM),* Mesa, Arizona, USA, pp. 11-20, 2011.

[21] Miguel Ángel Bautista, Antonio Hernández-Vela, Victor Ponce, Xavier Perez-Sala, Xavier Baró, Oriol Pujol, *et al.*, "Probability-Based Dynamic Time Warping for Gesture Recognition on RGB-D Data," *Advances in Depth Image Analysis and Applications,* vol. 7854, pp. 126-135, 2013.

[22] L. Hong and X. Li, "A selection method of speech vocabulary for human-robot speech interaction," in *IEEE International Conference on Systems Man and Cybernetics (SMC),* pp. 2243-2248, 2010.

[23] S. O. Caballero Morales, G. B. Enríquez, and F. T. Romero, "Speech-Based Human and Service Robot Interaction: An Application for Mexican Dysarthric People," *International Journal of Advanced Robotic Systems,* vol. 10, pp. 1-14, 2013.

[24] P. Varchavskaia, P. Fitzpatrick, and C. Breazeal, "Characterizing and processing robot-directed speech," in *IEEE/RAS international conference on humanoid robots*, ed. Tokyo, Japan, 2001.

[25] J. Cheng, W. Bian, and D. Tao, "Locally regularized sliced inverse regression based 3D hand gesture recognition on a dance robot," *Information Sciences,* vol. 221, pp. 274-283, 2013.

[26] M. Zhou and M. H. Wong, "Boundary-based lower-bound functions for dynamic time warping and their indexing," *Inf. Sci.,* vol. 181, pp. 4175-4196, 2011.

[27] D. J. Berndt and J. Clifford, "Using Dynamic Time Warping to Find Patterns in Time Series," in *KDD Workshop*, Seattle, Washington, USA, pp. 359-370, 1994.

[28] B. K. Yi, H. V. Jagadish, and C. Faloutsos, "Efficient retrieval of similar time sequences under time warping," in *Proceedingsof 14th International Conference on Data Engineering,* pp. 201-208, 1998.

[29] D. Lemire, "Faster retrieval with a two-pass dynamic-time-warping lower bound," *Pattern Recogn.,* vol. 42, pp. 2169-2180, 2009.

[30] X. Wang, A. Mueen, H. Ding, G. Trajcevski, P. Scheuermann, and E. Keogh, "Experimental comparison of representation methods and distance measures for time series data," *Data Mining and Knowledge Discovery,* vol. 26, pp. 275-309, 2013.

[31] T. Zaharia, S. Segarceanu, M. Cotescu, and A. Spataru, "Quantized Dynamic Time Warping (DTW) algorithm," in *the 8th International Conference on Communications (COMM),* pp. 91-94, 2010.

[32] M. Kipp, "Gesture generation by imitation: From human behavior to computer character animation," Ph. D, Saarland University, 2004.

[33] G. Jingwei and M. Q. H. Meng, "Study on distance measurement for NAO humanoid robot," in *IEEE International Conference on Robotics and Biomimetics (ROBIO),* pp. 283-286, 2012.

[34] J. Canny, "A Computational Approach to Edge Detection," *Pattern Analysis and Machine Intelligence,* vol. PAMI-8, pp. 679-698, 1986.

Urban risk assessment: fragility functions for masonry buildings

D. Ottonelli, S. Cattari and S. Lagomarsino

***Abstract*—**The seismic risk analysis of buildings at urban scale requires the effective classification of the exposure and the definition of the vulnerability through reliable fragility curves. Fragility curves give the probability of attainment of certain damage measures (limit states) as a function of a proper intensity measure of the earthquake. A suitable taxonomy for ordinary masonry buildings and its use in the assets classification is proposed. With regards to vulnerability models a procedure for estimating the fragility curves, from both expert elicitation and analytical models, is described. In particular, the latter considers a rigorous evaluation of uncertainties.

***Keywords*—**Seismic vulnerability, Risk assessment, Fragility curves, Masonry, Taxonomy.

I. Introduction

THE definition of fragility functions for masonry buildings is a hard task because we refer to a wide variety of constructions, which are characterized by very different types of masonry and structural systems, moving through historical periods and geographical areas.

As regards the first point, masonry is a composite material and the mechanical properties are related not only to those of the constituents, blocks (stone, solid clay bricks, adobe, etc.) and mortar (mud, lime, hydraulic lime, cement), but also to the dimensions and shape of the blocks, the interlocking in the external leaves and the transversal connection through thickness.

With reference to the structural systems, ancient constructions, but also recent vernacular ones, are very different from engineered masonry buildings, such as confined or reinforced masonry. The former were built by an empirical approach and are usually vulnerable, first of all to local mechanisms (out-of plane behavior); however, in high seismic areas specific details were adopted to prevent from damage (metallic tie rods, timber belts, buttresses, connections of horizontal diaphragms to masonry walls, etc.). The latter have been specifically conceived to withstand the earthquake, after a detailed damage observation, as in the case of confined masonry (widely adopted in South American countries), or on the base of modeling and capacity design criteria, as in the case of unreinforced masonry building (with RC, reinforced concrete, ring beams at floor level) or reinforced masonry.

Among the masonry building may also be considered the mixed structures, such as the traditional mixed masonry-timber buildings or the rather modern mixed masonry-RC buildings. The formers may have different configurations: a) timber reinforced masonry buildings, with horizontal timber ties at various levels and connected through thickness (e.g. in the Balkan, Greek and Turkish area); b) timber-framed masonry buildings (e.g. frontal walls of Pombaline buildings in Portugal, or smaller building with main bearing walls confined and braced with timber elements, all over the world); c) buildings with masonry walls at the lower stories and timber frames at the upper ones. Besides confined masonry, the spread of RC technology in the first half of 20th century has caused the birth of different types of mixed masonry-RC buildings, results of functional choices and often quite vulnerable: a) masonry perimeter walls and RC interior frames; b) raising of masonry buildings with RC framed structures.

Another important distinction is between ordinary and monumental masonry buildings. The latter category collects special type of assets, from the morphological point of view, such as: churches, mosques, towers, minarets, fortresses, etc.; they have a specific seismic behavior and, usually, a higher vulnerability, as testified by the last seismic events. Models and fragility functions defined for ordinary masonry buildings can be also used for monumental palaces, but in addition it is required an additional vulnerability assessment of some specific elements, if present (loggias, cloisters, colonnades, wide halls with double height, etc.).

This paper is focused on ordinary masonry buildings. In particular mechanical models and fragility functions are proposed for ordinary unreinforced masonry buildings. However, the general framework of the procedure outlined in the §III, in terms of key assumptions, uncertainties treatment and modeling issues, can be adopted also for the derivation of fragility functions of other masonry buildings typologies.

In Table 1 the main features that are useful for the taxonomy of masonry buildings are listed. Each building is described by a string of codes, separated by slashes and hyphens. Slashes mark the main categories of the taxonomy: FRM – Force Resisting Mechanism; FRMM – Force Resisting Mechanism Material; P – Plan; E – Elevation; CO – Cladding & Openings; DM – Detailing & Maintenance; FS – Floor

This work was funded by the project ReLUIS 2014-2018 (www.reluis.it), supported by the Italian Civil Protection Agency.

S. Lagomarsino, Professor. Dept. of Civil, Chemical and Environmental Engineering, University of Genoa, Italy (phone: +39-010-3532521; fax: +39-010-3532546; e-mail: sergio.lagomarsino@unige.it).

D. Ottonelli, PhD Student. Dept. of Civil, Chemical and Environmental Engineering, University of Genoa, Italy (e-mail: daria.ottonelli@unige.it).

S. Cattari, Assistant Professor. Dept. of Civil, Chemical and Environmental Engineering, University of Genoa, Italy (e-mail: serena.cattari@unige.it).

System; RS – Roof System; HL – Height Level; CL – Code Level. Within each category, the list of possible options is defined by proper acronyms; a more detailed classification and sub-classification (in square brackets, Table 1) is related to some of the category options and can be indicated in the taxonomy by separating codes by hyphens.

Table 1 proposal of taxonomy for Masonry Buildings

	CATEGORY	CLASSIFICATION
FRM	Bearing Walls (BW)	Out of plane (OP); In plane (IP) [Equivalent Frame (EF), Weak Spandrels Strong Piers (WSSP), Strong Spandrels Weak Piers (SSWP)]
FRMM	Unreinforced Masonry (URM) Reinforced Masonry (RM) Confined Masonry (CM) Timber-framed Masonry (TM)	*Blocks*: Adobe (A); Fired brick (FB); Soft Stone (SS); Hard Stone (HS) [Regular Cut (RC), Uncut (UC), Rubble (RU)]; Hollow clay tile (HC) [High % of voids (H%), Low % of voids (L%), Concrete Masonry Unit (CMU), Autoclaved Aerated Concrete (AAC)] *Mortar*: Lime mortar (LM); Cement mortar (CM); Mud mortar (MM); Hydraulic mortar (HM) *Strengthening*: Strengthened masonry (Sm) *Timber*: Confined and braced masonry panels (TC); Horizontal timber tie (TT) *Concrete and reinforcement*: [Average Strength (20-50 MPa)(ASC), Low Strength (<20 MPa)(LSC)]; [Vertical Reinforcement Bars (RBV), Vertical and Horizontal Reinforcement Bars (RBVH)]
P	Regular (R) Irregular (IR)	[Isolated (I), Aggregate (A)]
E	Regular geometry (R) Irregular geometry (IR)	
CO	Regular openings (RO) Irregular openings (IRO)	[High % voids (H%), Low % voids (L%)]
DM	*Details*: High quality details (HQD), Low quality details (LQD) *Maintenance*: Good Maintenance (HM), Low Maintenance (LM)	*Tie rods*: Without tie rods (WoT); With tie rods (WT)] *Ring beams*: Without ring beams (WoRB); With ring beams (WRB)
FS	Rigid (R) Flexible (F)	Reinforced concrete (RC); Steel (S); Timber (T); Vault (V)
RS	Peaked (P) Flat (F) Gable End Walls (G)	*Material*: Timber (Ti); Corrugated Metal Sheet (CMS); Reinforced Concrete (RC); Thatch (Th) Thrusting roof (Tr); Unthrusting roof (UTr)
HL	Low-rise (1-2) (L) Mid-rise (3-5) (M) High-rise (6-7) (H) Tall (8+) (Ta)	Number of stories (indicate the number)
CL	Pre-Code (PC) None (NC) Low (<0.1g) (LC) Moderate (0.1-0.3g) (MC) High (>0.3g) (HC)	*Pre-code Aseismic Construction*: Low Level (LAC); Moderate Level (MAC); High Level (HAC)

FRM – Force Resisting Mechanism; FRMM – Force Resisting Mechanism Material; P – Plan; E – Elevation; CO – Cladding & Openings; DM – Detailing & Maintenance; FS – Floor System; RS – Roof System; HL – Height Level; CL – Code Level

In the case of masonry buildings the FRM is always the Bearing Walls system (BW), which can present very different seismic behavior depending on geometry and constructive details. Usually reference is made to Out-of-Plane (OP) and In-Plane (IP) mechanism, depending on the connections and distance between masonry walls, as well as on the stiffness of horizontal diaphragms. If a global seismic (box-type) behavior can be assumed, a sub-classification is possible: each single wall may be analyzed by an equivalent frame model (EF) or by simplified models that assume the hypotheses of strong (SSWP) or weak (WSSP) spandrels. The choice of the most reliable model depends on available as-built information.

The category FRMM considers different structural material: Unreinforced Masonry (URM); Reinforced Masonry (RM); Confined Masonry (CM); Timber-framed Masonry (TM); mixed Masonry-RC (MRC). In particular, in the URM case, a detailed classification is important, with reference to blocks and mortar characteristics, because the mechanical properties vary in a wide range.

The configuration of the building Plan (P) is very important for the seismic vulnerability, both with reference to the regularity (R, IR) and to the possible interaction with other buildings (Isolated – I – or Aggregated in urban blocks – A). This information is useful to address the most probable collapse mechanisms (BW classification).

Information on the regularity in Elevation (E) may help in the definition of the behavior factor and the ductility, due to the possible different localization of the weak story.

The role of non-structural elements is almost negligible in masonry buildings, but it is important to know the regular distribution and percentage of openings (CO). A regular distribution (RO) may promote the WSSP behavior, which is characterized by a higher displacement capacity but a lower strength than the SSWP case. Moreover, a High percentage of openings (H%) at the base story, typical in the case of shops, may produce a weak story mechanism, which has a low displacement capacity.

Another important category, in particular in the case of URM buildings, is the quality of constructive details and the state of maintenance, which is an essential prerequisite in order to exploit the former aspect (DM). The attribution of High Quality Details (HQD) must consider the adherence to the rules of the art, which altogether define a local code of practice referred to different scales of the construction: the masonry (way to assure interlocking and transversal connection), the wall (distribution of openings, lintels, etc.) and the global construction (wall-wall and wall-horizontal diaphragms connections). The systematic presence of effective tie rods (WT) or ring beams (WRB) may prevent from out-of-plane mechanisms and increase the strength and ductility of spandrels, for the in-plane behavior; it is worth noting that RC ring beams drive the seismic response to weak story mechanism (SSWP behavior), while tie rods increase the ductility of uniform mechanisms (WSSP behavior).

The Floor System (FS) influences the seismic behavior, with reference both to its mass (which increases the horizontal seismic actions) and its stiffness (which allows a certain degree of redistribution of the horizontal seismic actions between the vertical walls). A rough categorization is obtained by distinguishing between Rigid (R) and Flexible (F); the attribution has to consider not only the stiffness but also the effectiveness of the connection with vertical walls. A more detailed classification can consider also the material and configuration (i.e. the presence of masonry vaults can also induce horizontal thrusts).

Similar information are required on the Roof System (RS), which is an important parameter for the vulnerability assessment, because of its mass (dynamically amplified due to its position at the top of the building) and the possible presence of a horizontal thrust (Tr), which can induce local collapse mechanisms.

The Height Level (HL) is very important because it influences very much the seismic vulnerability and is always available or very easily detectable. The possible categories (L, M, H and Ta) must be redefined, in terms of number of stories, for masonry buildings, because they are on average lower than RC or steel buildings.

Finally, the Code Level (CL) category is very important and must be properly defined in the case of masonry buildings, which are usually old and not seismically designed (PC); in this case, it is useful to estimate the local seismic culture, which is high (HAC) in areas frequently affected by earthquakes. For modern buildings, designed by considering a seismic code (LC, MC and HC), the categories should mainly consider the seismic hazard used for the design, taking also into account the accuracy of the code provisions.

The vulnerability assessment at territorial scale requires to group the buildings that have a similar seismic behavior in order to evaluate the damage and losses of the built environment due to a given hazard assessment. To this aim, the proposed taxonomy cannot be directly used, because available information is always incomplete and, anyway, a too very detailed subdivision of the building stock considered in the risk analysis might be useless and difficult to be managed.

Depending on the available data and after a preliminary study of the characteristics of the built environment in the urban area under investigation, the first step of the vulnerability assessment is to proceed to a proper classification of buildings. To this aim, among the available information, the parameters that mostly affect the seismic behavior must be singled out. Each vulnerability class, which can be synthetically named by a number or a short acronym, is clearly identified by a precise taxonomy, that is a list of category and related classification information. Missing information in the taxonomy means that no data are available to better describe the buildings, so fragility functions must represent the average vulnerability of a large set of configurations. On the contrary, if some parameter is excluded, all other options should be listed in the taxonomy.

Fragility functions must be defined, according to suggestion of section §IV, for each building class. It is worth noting that the dispersion is higher when few building classes are used, each one including constructions characterized by quite different behavior; on the contrary, a too much detailed classification may lead to the definition of classes with quite similar fragility functions, but with a lower dispersion.

As an example, in the case of a risk analysis at regional scale, when little information is available, the following tags of the taxonomy could describe a possible classification:

- Class 1: /BW/URM-FB-HM/R/R/RO/HM/R/P/M/PC-MAC/
- …….

If the analysis is focused on a urban district, with a small number of buildings, it is possible to limit the possible options, after a quick sample check survey, and split the classes proposed above, on the base of: quality of seismic design and construction details, materials of floor and roof system, etc.

II. Review of Existing Fragility Functions

Many fragility functions have been developed and can be taken from the literature for the risk analysis of masonry buildings [1]-[10]. They have been derived according to different approaches, which can be traced back to the classification of §III.B: 1) empirical (e.g. [11]-[13]); 2) expert elicitation based (e.g. [14]); 3) analytical, based on nonlinear static approaches through simplified (e.g. [2], [15]-[24]) and detailed models (e.g. [25]) or based on linear dynamic approaches (e.g. [26], [27]); 4) hybrid methods (e.g. [28]).

Many fragility functions have been obtained from observed damage after the occurrence of an earthquake; these data are valuable, because they are directly correlated to the actual seismic behavior of buildings and can be very useful for validation of analytical methods and calibration of hybrid fragility functions. However, empirical fragility functions are strongly influenced by the reliability of the damage assessment, which is often made by a quick survey aimed to other scopes, as the building tagging for use and occupancy.

Once in the study area masonry building typologies have been analyzed and building classes defined, it is necessary to derive the appropriate fragility functions. To this end, for each class, fragility functions taken from different authors may be used and properly combined, but attention must be paid because these functions could be biased due to some parameters or aspects.

First of all, a crucial factor is the choice of the seismic intensity measure. Empirical data are usually referred to macroseismic intensity, which is not an instrumental measure but is based on a subjective evaluation. This approach is suitable when the aim of the risk analysis is to draw a comparative scenario, probably useful to plan mitigation strategies; for an accurate loss estimation, however, it is necessary to convert macroseismic intensity into an instrumental intensity measure, and this step introduces important approximation and normally huge uncertainties. On the contrary, if empirical fragility functions are given in terms of Peak Ground Acceleration (PGA), it is worth noting that this parameter is directly related to the spectral characteristics of the input motion of the specific seismic event. In these cases, the correlation between intensity and damage should present a low dispersion, which has to be increased before using those functions.

Another difficult task is the definition of consequences that are evaluated by the fragility functions. Usually Damage States (DS) are considered, which are referred to physical damage to structural and non-structural elements, but fragility functions can be also drawn in terms of a Damage Index (DI), related the cost of repair, or of some Performance Indicators (PIs), which are related to the conditions of use (operational, occupancy, life safety). All the above-mentioned effects (except DI) are discrete states and are defined by a qualitative judgment (in case of observational functions) or by a correlation with some structural parameter, as the interstory drift (in case of analytical based functions).

Finally, it is worth noting that the characteristics of masonry buildings are dependent from the local seismic culture and the available materials in the area; as an example, the apparently detailed description “irregular stone masonry with lime mortar” may correspond to very different seismic capacities, if it is assigned to buildings in different countries. Thus, the extrapolation of empirical fragility functions for traditional masonry buildings to other geographic areas is questionable.

In conclusion, the use of existing fragility functions has to be made carefully. In order to increase the reliability of the results, it is suggested to combine a significant number of fragility functions, obtained from different authors and with different methods, assigning to each one a proper subjective probability, related to the reliability of the source and the fitting with the characteristics of the building class under investigation, in order to obtain a weighted fragility function. Depending on the availability and reliability of fragility functions, the building classification should be more or less detailed. An excessive splitting of the built environment into detailed classes, with associated low dispersed fragility functions, turns out to be specious if their reliability is not robust; in these cases it is better to reduce the number of buildings classes and ascribe to each one a more reliable fragility function, even if defined by a bigger dispersion.

In the context of analytical based on nonlinear static approaches, this chapter proposes a procedure to derive fragility functions for masonry buildings, once a building class is defined by tagging the various categories of the taxonomy (Table 1). The general framework of the method, the probabilistic key assumptions and the modeling bases are treated in §III, while some operative recommendations for the different possible approaches are given in §IV. The development of tailored fragility functions is the suggested way to improve the reliability of the vulnerability and risk analysis.

III. Uncertainties and Modeling Issues

The fragility function gives the probability that a generic Limit State (LS) is reached given a value *im* of the Intensity Measure IM:

$$p_{LS}(im) = P(d > D_{LS}|im) = P(im_{LS} < im) = \Phi\left(\frac{log\left(\frac{im}{IM_{LS}}\right)}{\beta_{LS}}\right)$$

where: d is a displacement representative of the building seismic behavior, D_{LS} is its Limit State threshold, IM_{LS} is the median value of the lognormal distribution of the intensity measure im_{LS} that produces the LS threshold of the and β_{LS} is the dispersion.

A fragility function is thus defined by two parameters: IMLS and β_{LS}. The median intensity IMLS can be obtained from the statistical analysis of data from damage observation after earthquakes (empirical methods) or by a mechanical model (analytical methods), that is representative of the average seismic behavior of buildings of that particular class.

The dispersion β_{LS} depends on different contributions, related to: a) the uncertainties in the seismic demand (epistemic β_H, for the derivation of the hazard curve, and intrinsic β_D, in the variability of the seismic input described only by the value of IM); b) the uncertain definition of the Limit State threshold (β_T); c) the variability of the capacity (β_C) of buildings that belong to the considered vulnerability class (which collects buildings of different behavior, even if characterized by the same taxonomy tags). As all the above contributions can be assumed statistically independent, the dispersion is given by:

$$\beta_{LS} = \sqrt{\beta_H^2 + \beta_D^2 + \beta_T^2 + \beta_C^2} \quad (2)$$

In case of analytical methods each contribution can be computed, while for empirical methods □LS is directly evaluated from the damage distribution of observed data, which includes all of them; however, in this case, it is necessary to verify if the dispersion has to be increased, because empirical data are not fully representative, in terms of masonry typology (β_C) or characteristics of the input motion (β_D).

The following sub-sections describe the main aspects related to the derivation of fragility functions for masonry buildings from analytical methods, based on nonlinear static approaches.

A. Capacity and demand by nonlinear static analysis

The seismic vulnerability of building is described by its capacity curve that gives the acceleration A of an equivalent nonlinear single-degree-of-freedom system, as a function of its displacement D. The capacity curve can be obtained by a proper conversion of the pushover curve, obtained by a nonlinear static analysis of a multi-degrees-of-freedom model of the structure, or through simplified analytical models. In the latter case the capacity is usually described by a bilinear curve, without hardening for masonry buildings.

The seismic demand is expressed by an Acceleration-Displacement Response Spectrum (ADRS), which gives the spectral acceleration S_a as a function of the spectral displacement S_d, for a damping coefficient ξ_0=5%, considered valid in the initial elastic range. Usually in hazard analysis the spectral shape is assumed constant with the annual rate of exceeding, which is given by the hazard curve as a function of a proper IM of the ground motions.

The evaluation of the displacement demand for a given value *im* of the IM can be obtained through various methods, like the N2-Method originally proposed by Fajfar [29], the Capacity Spectrum Method [30], the Displacement-Based Method [16], Coefficient Method [31], [32], the MADRS Method [33]. They all consider, under different approaches, the reduction of the seismic demand in the nonlinear phase of the building response. These methods look for the intersection of the capacity with the properly reduced demand, by using either acceleration/displacement or displacement/period as coordinates (S_d=$S_aT^2/4\pi^2$).

For the evaluation of fragility functions it is necessary to get the value IM_{LS} of the IM that produces any LS threshold. To this end the use of over-damped spectra [30] is very effective, once these thresholds D_{LS} have been fixed on the capacity curve (§III.C) and the corresponding equivalent viscous damping ξ_{LS} is evaluated, which also takes into account the hysteretic contribution. It results:

$$IM_{LS} = \frac{D_{LS}}{S_{d1}(T_{LS})\eta(\xi_{LS})} \quad (3)$$

where: S_{d1} is the displacement response spectrum, normalized to IM, T_{LS} is the linear equivalent period corresponding to LS:

$$T_{LS} = 2\pi\sqrt{\frac{D_{LS}}{A(D_{LS})}} \tag{4}$$

and $\eta(\xi_{LS})$ is the damping correction factor [34]:

$$\eta(\xi_{LS}) = \sqrt{\frac{10}{5+\xi_{LS}}} \tag{5}$$

It is worth noting that overdamped spectrum is obtained simply multiplying by $\eta(\xi_{LS})$ in the range of typical periods for buildings, while for very low and high periods the effect of damping tends to vanish. Figure 1 shows the procedure, considering LS on the capacity curve and the identification of IM_{LS}, using PGA as IM and a typical response spectrum shape.

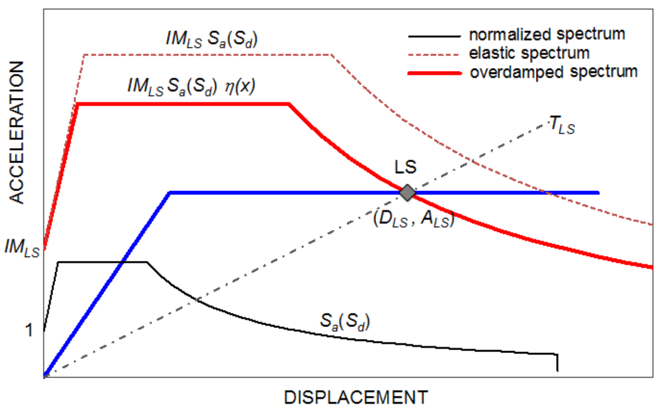

Fig. 1. Application of overdamped spectra for the evaluation of IM_{LS}.

B. *Identification of proper Intensity Measures*

The vulnerability assessment, embodied by the application of fragility functions, is one of the steps of the seismic risk analysis. The identification of the proper Intensity Measure (IM) comes out from different constraints, which are first of all related to the adopted hazard model, to the typology of the exposed asset but also to the availability of data and fragility functions for all different exposed assets.

Empirical fragility functions are usually expressed in terms of the macroseismic intensity *I* (defined according to the different Macroseismic Scales: EMS, MCS, MM), which can be regarded as an empirical IM. The macroseismic intensity already contains implicitly the vulnerability, because it is defined on the basis of the damage observation; in order to overcome this gap, modern macroseismic scales, such as EMS, assign the intensity taking into account a detailed building types classification. The accuracy of the risk analysis results is then linked to the reliability of the hazard assessment, if an empirical IM is used.

Analytical based or hybrid fragility functions are, on the contrary, related to instrumental IMs, which are related to parameters of the ground motion (PGA, PGV, PGD) or of the structural response of an elastic SDOF system (spectral acceleration S_a or spectral displacement S_d, for a given value of the period of vibration *T*). Sometimes, integral IMs can be useful, which consider a specific integration of a motion parameter (Arias Intensity I_A) or of a spectral value (Housner Intensity I_H) [35].

Correlation is necessary when hazard and vulnerability assessments are made by using different IMs or one wants to calibrate analytical fragility functions (related to a detailed building classification) by available empirical fragility functions (referred to wider classes of buildings). Anyhow, the use of correlation always increases the uncertainties of the results (dispersion β_{LS} of the fragility function).

Similarly to what was said on different types of fragility functions (empirical, expert elicitation, analytical based and hybrid), for the identification of proper IMs it is worth noting that empirical ones give results coarse but correct on average, while instrumental IMs allow to better take into account a detailed taxonomy, in the definition of building classes, and the local site effects, but, when these fragility functions are used, it is necessary to pay attention to the characteristics of the input motion that was considered for their derivation.

The seismic performance of a masonry building cannot be described by only one IM but, at least, the response spectra shape should be known. If a vector-valued hazard assessment is available [36], more than one IM could be used and vector-valued fragility functions derived (e.g. [27]). If already available fragility functions are used, it is better to refer to the spectral value for the period compatible with the specific Limit State threshold (acceleration $S_a(T)$ and displacement $S_d(T)$ response spectra are linked by the period of vibration *T*, so the two IMs are equivalent). In this case the dispersion β_{LS} of the fragility function is mainly due to the variability of the capacity of buildings in the class.

Most of available fragility functions are in terms of PGA; in this case, if the difference between the spectral shapes of the input motion obtained by the hazard assessment and that used for deriving the fragility function is known, it is possible to properly tune the last one. Otherwise, the use of PGA as IM implies a wider dispersion β_{LS} of the fragility function, due to the uncertainty in the spectral shape.

As masonry buildings are usually not flexible, PGD or spectral values for long periods (T>1 s) are not significant, except for some types of monumental structures (churches, slender towers) or for the verification of local mechanisms.

With reference to local site amplification, spectral values are better correlated with vulnerability, because they take into account the modification of the seismic input for the significant periods. If PGA is used, fragility functions should be tuned by considering a mean ratio between the spectral values on local site and stiff soil conditions, for the relevant periods of the buildings, or a greater value of the dispersion should be used, in order to consider the increased uncertainty due to the spectral demand ($\beta_{\square}$).

In case of using empirical IM (macroseismic intensity), it is not correct to include local site amplification in the hazard curve, because this phenomena affects buildings depending on their dynamic properties; a possible solution is to modify the empirical fragility function, so considering it as representative of the vulnerability of a particular class of buildings on a specific soil type [14].

C. Definition of Damage States and Performance Levels

In seismic risk analysis the scenario of the built environment is expressed in terms of Damage States (DS), which are a discrete qualitative description of the overall damage in structural and non-structural elements of the building. Usually five damage states are considered: DS1 slight, DS2 moderate, DS3 extensive, DS4 near collapse and DS5 collapse.

Empirical methods describe the DS through a qualitative damage observation, on the basis of distribution and severity of cracks, according to specific forms and sketches; to this end, modern macroseismic scales can be a good reference (e.g. EMS98 [37]).

In the case of analytical methods, if a detailed numerical model of the building is available, the damage in each structural element is obtained through static or dynamic nonlinear analysis and a sort of virtual damage state attribution could be made. However, it is worth noting that numerical models give continuum damage variables and identification of discrete DS is not an easy task. As an example, [38] have proposed a multi-scale approach for masonry buildings that defines Limit States (LS) on the capacity curve by checking (i) the spread of damage in masonry elements (piers and spandrels), (ii) the interstory drift in masonry walls and (iii) the global behavior of the building (described by its capacity curve). LSs are the thresholds that separate various DSs (Figure 2).

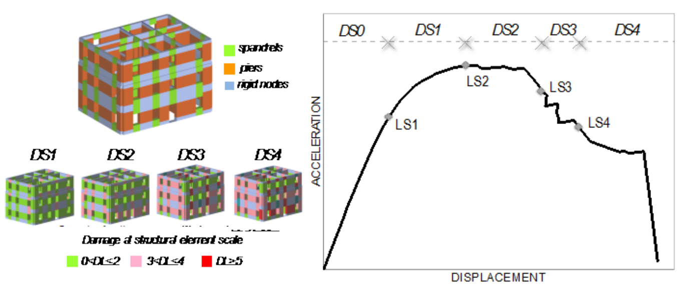

Fig. 2. Example of capacity curve of a masonry building, obtained by pushover analysis on a detailed model, with the definition of LS thresholds and DS ranges.

Damage States can be related to specific performances of the building: the use and occupancy, the safety of people and the reparability (in terms of economic convenience). Usually Performance Limit States (PLS) are defined as coincident to related Damage Limit States (LS); this means the fulfillment of a performance is guaranteed if the seismic displacement demand is not beyond the corresponding LS threshold.

The above mentioned detailed mechanical based methods are used in hybrid approaches, while analytical methods adopt simplified models, which give directly the capacity curve without a detailed description of damage in the building. In these cases, LSs may be defined: a) by considering limit values of macro-parameters of the building response, on which the simplified model is based (as, for example, the interstory drift); b) by a heuristic approach, which considers that the transition from a DS to the following one usually occurs in certain positions of the capacity curve. In the latter, a possible positioning of LSs is obtained as follows (Figure 3a): LS1: $D_1=0.7D_y$; LS2: $D_2=c_2D_y$; LS3: $D_3=c_3D_2+(1-c_3)D_4$; LS4: $D_4=D_u$. The position of LS2 depends on the complexity and irregularity of the building; the coefficient c_2 may vary between 1.2 and 2, being lower for simple and regular buildings. LS3 is usually closer to LS4, in particular for simple and regular buildings ($0.3<c_3<0.5$).

Equivalent viscous damping may be defined for each LS as a function of the displacement (Figure 3b), by a simple relation [16], [39], [40]:

$$\xi_{LS} = \xi_0 + \xi_H\left[1-\left(\frac{D_y}{D_{LS}}\right)^{\zeta}\right] \tag{6}$$

where: ξ_0 is the initial damping (usually assumed equal to 5%), ξ_H is the maximum hysteretic damping and ζ is a free parameter (ranging between 0.5 and 1).

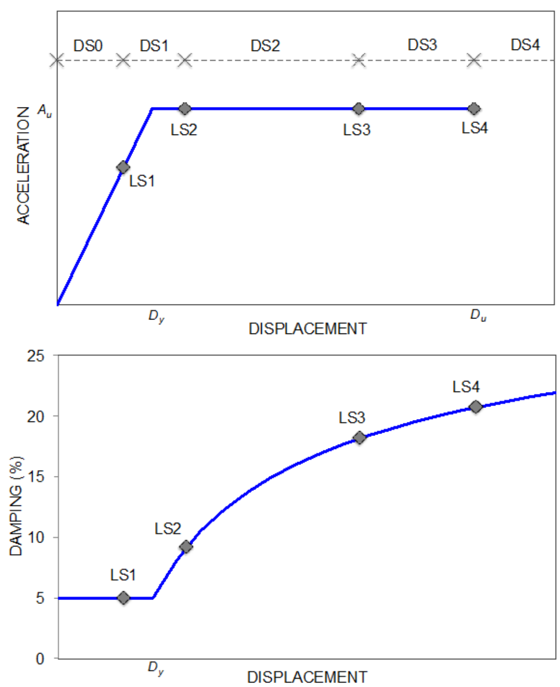

Fig. 3. a) Example of capacity curve of a class of masonry buildings, with heuristic definition of LS thresholds (c_2=1.35, c_3=0.4) and b) typical equivalent viscous damping relation.

Once the seismic demand is defined (§III.B), by the spectral shape and the selection of a proper Intensity Measure to scale it, the values IM_{LSk} and the dispersions β_{LSk} (k=1,..4) can be evaluated by (3) and by the procedure described in §III.D. Fragility curves are then given by (1) and shown in Figure 4a.

The DS probability distribution, for a given value of the IM, can be thus obtained from fragility functions; for k=1, 2 and 3, the discrete probabilities are given by:

$$p_{DSk}(im) = p_{LSk}(im) - p_{LSk+1}(im) = \Phi\left(\frac{\log\left(\frac{im}{IM_{LSk}}\right)}{\beta_{LSk}}\right) -$$

$$\Phi\left(\frac{\log\left(\frac{im}{IM_{LSk+1}}\right)}{\beta_{LSk+1}}\right) \quad (7)$$

With regards to DS4, it is worth noting that analytical methods usually are not able to define LS5, and thus p_{LS5}; this LS occurs after important local collapse mechanisms that make the mechanical model meaningless. If it is considered that DS4 is generically named "complete" damage, including both "near collapse" and "collapse" DSs, it results that $p_{DS4}=p_{LS4}$. However, by assuming that the probability distribution of DSs is well represented by the binomial distribution, it is possible to share p_{LS4} according to the following formulas ($\mu_{DS} = \sum_1^4 p_{LSk}$):

$$p_{DS5}(im) = 0.8[1-(1-0.14\mu_{DS}^{1.4})^{0.35}]p_{LS4}(im) \quad (8)$$

$$p_{DS4}(im) = p_{LS4}(im) - p_{DS5}(im) \quad (9)$$

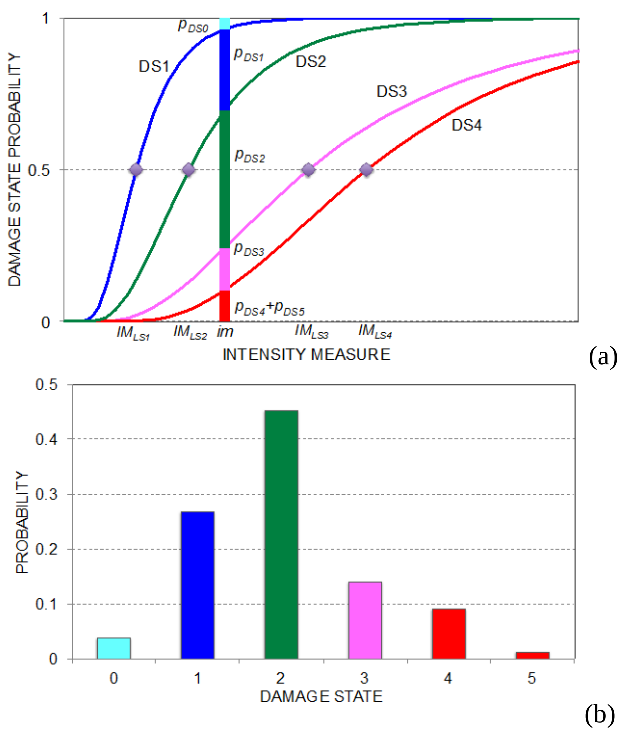

Fig. 4. a) Fragility curves, b) Damage States probability distribution.

In order to complete the DS distribution it is necessary to evaluate the probability that the building has "no damage" (DS0):

$$p_{DS0}(im) = 1 - p_{LS1}(im) = 1 - \Phi\left(\frac{\log\left(\frac{im}{IM_{LS1}}\right)}{\beta_{LS1}}\right) \quad (10)$$

Figure 4b shows a typical discrete damage distribution of damage states, directly obtained from fragility functions of Figure 4a for a given value IM=*im*.

D. Sources of uncertainties and propagation

In a probabilistic seismic risk analysis many uncertainties have to be taken into account; Pinto gives a general overview in chapter §II. Their propagation is considered in fragility functions through the dispersion β_{LS}, which can be evaluated by Eq. (2). The estimation of different contributions is discussed in the following.

β_D – Uncertainty on the spectral shape of the seismic demand

The Probabilistic Seismic Hazard Analysis (PSHA) gives the occurrence of earthquakes with a proper IM through the hazard curve $\lambda(im)$. Usually a fixed shape of Acceleration-Displacement Response Spectrum is associated, except the case of a complex Vector-Valued PSHA [36]. The normalized response spectrum $S_{a1}(S_d)$, scaled to the value *im*=1, can be defined as a stepwise function or through some analytical formulas in fixed ranges of the period *T* (as it is made in seismic codes).

In order to take into account the uncertainty on the spectral shape, which plays a significant role due to the large variability of possible records, it is necessary to define the response spectra $S_{a1,16}(S_d)$ and $S_{a1,84}(S_d)$, for the confidence levels 16% and 84%. They can be obtained by the selection of a large number of real digital records, compatible with the characteristics of earthquakes that give the maximum contribution to the hazard and of soil conditions; in particular, from the disaggregation of the PSHA, it is important to consider: magnitude, epicentral distance, focal depth, source mechanism. Figure 5a shows a typical example of a median response spectrum and the corresponding confidence intervals, if the Peak Ground Acceleration *PGA* is used ad IM; Figure 5b shows the same response spectra in the case where the maximum spectral acceleration $S_{a,max}$ is assumed as IM.

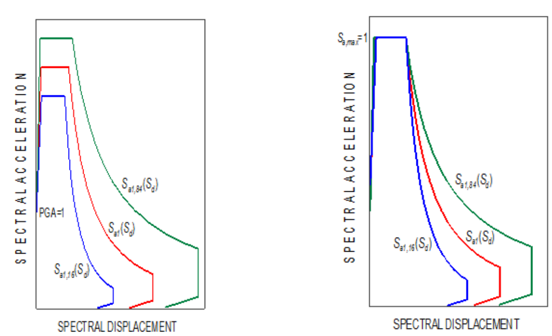

Fig. 5. Influence of the selection of the IM on the propagation due to the uncertainty on the spectral shape of the seismic demand: a) IM=PGA; b) IM=$S_{a,max}$.

For each LS, the estimation of $\beta_{\square}$requires the evaluation of the intensity measures $IM_{D,16}$ and $IM_{D,84}$ that correspond to a displacement demand equal to D_{LS}, on the median capacity curve of the considered class of buildings, by using the confidence levels response spectra $S_{a1,16}(S_d)$ and $S_{a1,84}(S_d)$ respectively. It results:

$$\beta_D = 0.5|\log(IM_{D,84}) - \log(IM_{D,16})| \quad (11)$$

This contribution to the dispersion is lower if a good IM is used. It is quite evident from Figure 5 that, at least for LS1 and LS2, $S_{a,max}$ is better than *PGA*.

β_H – Epistemic uncertainty on the hazard curve

Epistemic uncertainties in the seismic sources and the attenuation laws give rise to confidence intervals, which can be summarized by the hazard curves $\lambda_{16}(im)$ and $\lambda_{84}(im)$, representative of the confidence levels 16% and 84%.

For each LS, it is necessary to valuate IM_{LS} that corresponds to the displacement demand D_{LS} on the median capacity curve of the considered building class, by using the median response spectrum $S_{a1}(S_d)$. The dispersion β_H is given by:

$$\beta_H = ½\left[log\left(IM_{H,84}[\lambda(IM_{LS})]\right) - log\left(IM_{H,16}[\lambda(IM_{LS})]\right)\right] \qquad (12)$$

where $IM_{H,16}$ and $IM_{H,84}$ are the inverse functions of $\lambda_{16}(im)$ and $\lambda_{84}(im)$, respectively, and $\lambda(im)$ is the median hazard curve.

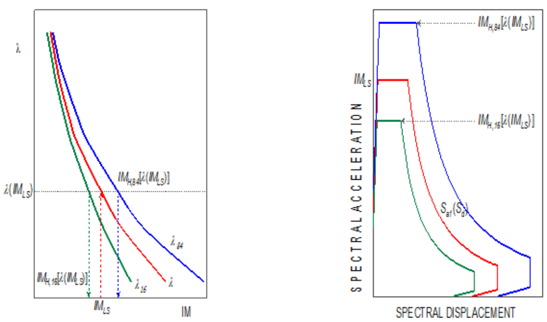

Fig. 6. Influence on the spectral demand of the epistemic uncertainty on the hazard curve.

Figure 6 shows an example of hazard curves, median and confidence intervals, and the corresponding response spectra; in this case for the evaluation of β_H only the median response spectrum is used.

β_C – Uncertainty on the capacity curve

The dispersion on the capacity curve of a masonry building is related to random variables, such as the material parameters (strength and stiffness on masonry), the geometry (effective thickness of masonry walls and vaults), the drift capacity of masonry panels or the in-plane stiffness of horizontal diaphragms, but also to epistemic model uncertainties, related for example to the assumptions in the definition of the equivalent frame or in modeling the connection between walls. Usually, if accurate as-built information is available, these uncertainties can be reduced.

This is not the case in seismic vulnerability analysis at territorial scale, when an "equivalent capacity curve" must be evaluated representative of a wide class of buildings, defined by the taxonomy through a proper list of tags. Then the above parameters have to be considered as random variables, with a dispersion compatible with the variability of the characteristics of buildings in the class.

The uncertainty propagation can be evaluated by Monte Carlo simulations or by using the response surface method [23], [41]. The latter approach is very effective and is based on the approximation of the surface of $log(IM_{LS})$, in the hyperspace of the significant random variables, by a hyper-plane, whose coefficients are determined by a least square regression on a set of numerical experiments. If N is the number of random variables, $M=2^N$ models are defined by a complete factorial combination at two levels, in which each variable assumes values correspondent to the confidence levels of 16% or 84%. The matrix $\mathbf{Z}$ (M rows × N columns) collects in each row the combination of values assumed by each standard normalized random variable (-1 for confidence level 16%, +1 for confidence level 84%).

For the i-th model, the capacity curve $A_i(D)$ is obtained and the Limit States are fixed ($D_{LSk,i}$, k=1,..4). By considering a generic LS, the value $IM_{LS,i}$ is evaluated by the median seismic demand $S_{a1}(S_d)$, using (3). The vector $\mathbf{Y}$ (M rows) collects the values $log(IM_{LS,i})$, i=1,..M. The angular coefficients of the hyper-plane are obtained as:

$$\boldsymbol{\alpha} = (\mathbf{Z}^T\mathbf{Z})^{-1}\mathbf{Z}^T\mathbf{Y} \qquad (13)$$

The dispersion β_C is given by:

$$\beta_C = \sqrt{\boldsymbol{\alpha}^T\boldsymbol{\alpha}} \qquad (14)$$

β_T – Uncertainty on the Limit State thresholds

The definition of the LS thresholds is also subjected to dispersion, because models adopted for the evaluation of the capacity curve are simplified and the displacements D_{LS} usually derives from a heuristic approach.

Considering the median capacity curve, obtained by using the mean values of the N random variables, D_{LSk} (k=1,..4), usually distributed as in Figure 3a, can be assumed as median values. Proper distributions should be defined for these random variables, which take into account that in a single building the k-th DS could be reached a little bit before or after the median value D_{LSk}. It is reasonable to assume the four distributions do not intersect. LS1 is always in the "elastic" branch of the capacity curve. LS2 is in the first part of the "plastic" branch and it is not reasonable to assume it moves too much further the median value D_{LS2}. The position of LS3 is very variable and sometimes it occurs even for a low value of the displacement, but the possible intervals of LS2 and LS3 can be separated.

The use of a Beta distribution seems to be the best option, but for the sake of simplicity, due to the large number of uncertainties involved in a seismic risk analysis, very simple uniform distributions are suggested, which probably lead to a slight overestimation of β_T. Figure 7 shows a proposal, with the indication, for a generic LS, of the 16% and 84% confidence levels of D_{LS}, named $D_{LS,16}$ and $D_{LS,84}$; they are simply obtained by moving from the median value, on the left and right side, of 2/3 of the semi-wide of the uniform distribution.

For each LS, it is then necessary to evaluate $IM_{T,16}$ and $IM_{T,84}$ that corresponds to a displacement demand equal to $D_{LS,16}$ and $D_{LS,84}$ on the median capacity curve of the considered class of buildings, by using the median response spectrum $S_{a1}(S_d)$. The dispersion β_T is given by:

$$\beta_T = 0.5\left[log\left(IM_{T,84}\right) - log\left(IM_{T,16}\right)\right] \qquad (15)$$

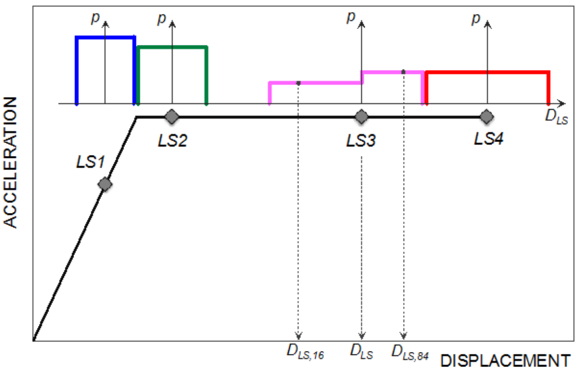

Fig. 7. Uncertain definition of the LS thresholds.

IV. Derivation of Fragility Functions

After a proper building classification, tailored to data already available or that can be acquired through the survey, fragility functions can be defined by using existing ones or developing new customized curves.

In the first case, for each building class, the available functions have to be collected and examined. After the assignment of a subjective probability to each one (logic tree approach), related to its reliability and coherence with the considered building class, the fragility function can be obtained by a simple weighted summation. The use of existing fragility functions must consider several critical aspects. When a fragility function refers to a broader class of buildings, the dispersion β_{LS} should be reduced and it is worth considering if the mean value IM_{LS} has to be modified (if the behavior of the subclass is better or worse than the average). When a fragility function refers to a subclass of buildings, within the class of interest, it would be necessary to have fragility functions for the other subclasses (in the other branches of the logic tree), otherwise the obtained final fragility function would result biased; as an alternative, the dispersion β_{LS} should be increased and the mean value IM_{LS} properly modified, on the base of expert judgment.

Next sections give some hints for the development of new fragility functions. This can be done either by empirical data, if a robust database of damage observations is available in the area or in other regions where built environment has similar characteristics, or by analytical data, by the definition of mechanical models representative of each building class and able to assess the dispersion due to the variability of seismic behavior in the class.

A. *From empirical/macroseismic data*

In this ambit, Lagomarsino and Giovinazzi [14] have proposed a macroseismic vulnerability model, which can be considered an expert elicitation method. It is directly derived from the European Macroseismic Scale [37], which defines six vulnerability classes (named from A to F) and various building types (seven of them related to masonry buildings).

It is worth noting that macroseismic scales are not instrumental based and they implicitly contain a vulnerability model. If a building class is considered, the linguistic definitions of EMS98 may be translated in quantitative terms, by the fuzzy set theory, and an incomplete Damage states Probability Matrix (DPM) is obtained. The completion is made by using the binomial probability distribution. The vulnerability is synthetically expressed by a vulnerability curve [42], which gives the mean damage μ_D (=$\sum k p_{DSk}$) as a function of the macroseismic intensity I:

$$\mu_D = 2.5 + 3\, tanh\left(\frac{I + 6.25V - 12.7}{Q}\right) \quad (0 \le \mu_D \le 5) \qquad (16)$$

where: the vulnerability index V and the ductility index Q are parameters representative of the seismic behavior of a group of homogeneous buildings.

The vulnerability index has been defined to vary between 0 and 1 for the six vulnerability classes of EMS98. To each building class a plausible range of values of V is associated, defined by a proper membership function, according to the fuzzy set theory [43]; Table 2 shows intervals for each class of maximum plausibility. The ductility index is equal to 3, in order to obtain the best fit.

Table 2. Ranges of maximum plausibility for vulnerability index of the six EMS98 classes

Class	A	B	C	D	E	F
V	0.84÷0.92	0.68÷0.76	0.52÷0.60	0.36÷0.44	0.20÷0.28	0.04÷0.12

Fragility functions, in terms of macroseismic intensity I, can be evaluated by the binomial distribution:

$$p_{LSk} = \sum_{i=k}^{5} p_{DSi} \quad (k = 1,..5) \qquad (17)$$

$$p_{DSk} = \frac{5!}{k!(5-k)!}\left(\frac{\mu_D(I)}{5}\right)^k \left(1 - \frac{\mu_D(I)}{5}\right)^{5-k} \quad (k = 0,..5) \qquad (18)$$

Limit States can be identified on the vulnerability curve as points for which p_{LSk}=0.5 (k=1,..5). The vulnerability curve is, for the macroseismic method, analogous of the capacity curve for the analytical ones. Figure 8a shows vulnerability curves, with LS thresholds, for the central (white expected) values for the six EMS98 vulnerability classes. Figure 8b shows the correspondent fragility functions of DSs for Class B (V=0.72).

If a proper correlation law between intensity and PGA is assumed, the fragility functions in terms of PGA are obtained; it is worth noting that, given the high number of uncertainties involved in the process, all macroseismic intensity scales may be assumed equivalent to this end. Many correlations may be found in literature, which have been calibrated in different areas and are usually in the form:

$$I = a_1 + a_2 Log(PGA) \qquad (19)$$

Figure 8c shows the fragility functions in terms of PGA, having assumed two different correlation laws: a) Faccioli and Cauzzi [44], described by (16) with a_1=6.54, a_2=4.51 (PGA in m/s^2); b) Murphy and O'Brien [45] for Europe (a_1=7, a_2=4), which gives higher values of PGA for I>8, if compared to the former one. It is worth noting that fragility functions looks very similar to a lognormal cumulative distribution; the dashed lines represent the best fit, which is obtained for all LSs by the following values of the dispersion: a) β_{LS}=0.54; b)

ISBN: 978-1-61804-325-2

β_{LS}=0.61.

It is worth noting that fragility functions in Figure 8 refer to the central value of V for Class B and can be considered representative of a subset of buildings in the class. In order to consider the whole class, the range of plausible values of the vulnerability index V must be considered. As an example, Figure 9a shows fragility functions of LS4 in terms of macroseismic intensity, for the extreme plausible values of the vulnerability index V and for the two values that define the interval of maximum plausibility (Table 2). Figure 9b shows the fragility functions in terms of PGA (considering Murphy and O'Brien correlation law). The fragility function of the whole vulnerability class is obtained by a convolution of all plausible fragility functions; the result is the dashed line in Figure 9b, which is well fitted by a lognormal cumulative distribution with dispersion β_{LS4}=0.64 (0.57 in case of Faccioli and Cauzzi correlation law). The dispersion is increased a little because in this case the fragility function represents the behavior of all different building of the class, instead of a small sub-set of these.

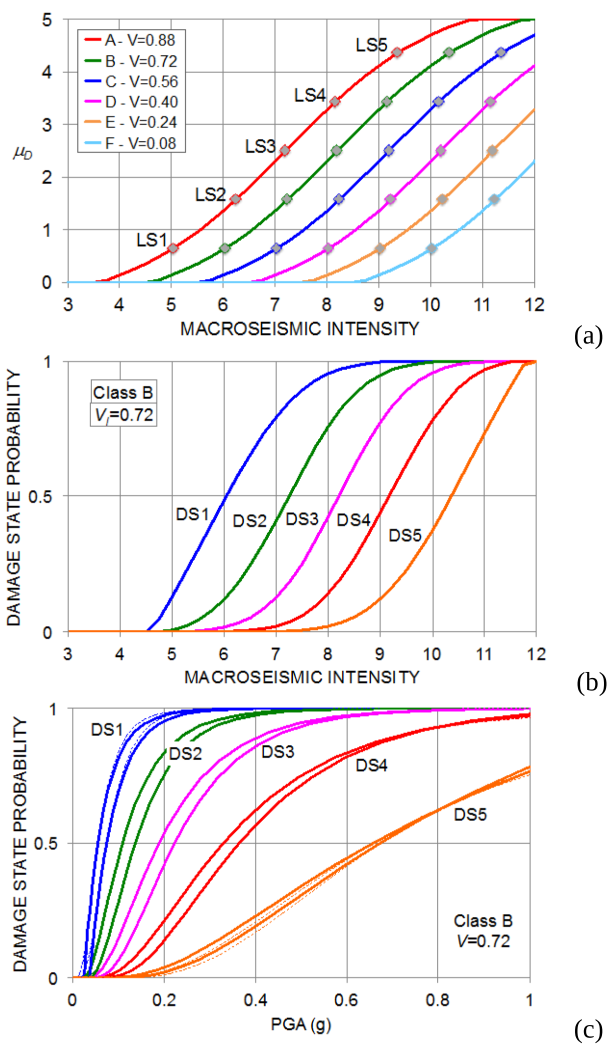

Fig. 8. Central values of V: a) vulnerability curves for the EMS98 vulnerability classes, with indication of LS; fragility functions of Class B in intensity (b) and PGA (c).

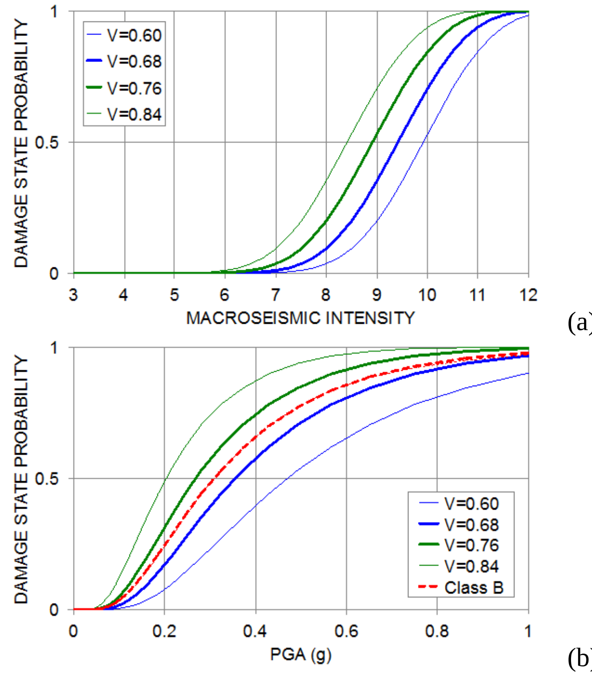

Fig. 9. a) Fragility curves of DS4 for Class B, by macroseismic intensity, considering all plausible values of V; b) corresponding fragility curves in terms of PGA, with derivation of the overall behavior of Class B (dashed lines).

EMS98 proposes a classification of buildings into various types, according to masonry and horizontal diaphragms characteristics. The seismic behavior of these macro-typologies can include two or even more vulnerability classes, each one with a different subjective probability (see Fig. 5 in [14]). The corresponding vulnerability functions for each DS can be obtained with the procedure described above and showed in Figure 9b. As an example, if the building class involves two EMS98 vulnerability classes, the value of β_{LS}, for the two considered correlation laws, increases to: a) 0.62; b) 0.7.

Once the building classes have been defined by a proper list of tags from the taxonomy, fragility functions may be derived through the macroseismic method by defining a proper membership function for the vulnerability index (range of plausible values). The range can be very wide, if the building class is generic, while can be very narrow, smaller than that of a single EMS98 vulnerability class, if much information is available.

The general format of the macroseismic vulnerability method can also be used when empirical data are available. In this case, for a specific building class (defined by data acquired and by the constructive characteristic of the built environment in the area where damage survey was made), the DSs distribution (and thus the mean damage μ_D) is supposed to be known for one or more values of the macroseismic intensity. If only one point of the vulnerability curve is available, the vulnerability index V can be fitted and, for each LS, the corresponding IM_{LS} can be evaluated and a proper value of β_{LS} can be assumed, by considering the variability of behavior in the class. If damage data are available for more values of the intensity, both V and Q can be fitted. After the conversion into fragility functions, the values of β_{LS} may be directly fitted.

B. *From analytical methods*

The use of simplified mechanical models presents the following main advantages: a) fully employ all results of PSHA (instrumental IMs, seismic input in the spectral form); b) keep explicitly into account the various parameters that determine the structural response (and evaluate accurately the uncertainty propagation). However, the reliability of the vulnerability assessment is affected by the capability of the model to simulate the actual seismic response of the examined class; to this end simplified models must be validated and calibrated with observed damage or results from more sophisticated models.

As far as global response of existing masonry buildings is concerned, in-plane behavior of masonry walls can be modeled by an Equivalent Frame (EF), made by vertical piers (the columns) and horizontal spandrels (the beams), connected by rigid nodes of non-zero size. The generalized actions in masonry elements, all along the pushover analysis, depend on the relative stiffness and strength of piers and spandrels. The solution can be obtained only numerically, while analytical simplified models can make reference to two limit conditions: 1) Strong Spandrels Weak Piers (SSWP), which corresponds to the shear-type frame model and is associated to the occurrence of a soft-story failure; 2) Weak Spandrels Strong Piers (WSSP), in which full height piers (from the base to the top) work like fixed-end cantilevers and fail at the base due to axial and bending failure (rocking with crushing at the toe). Figure 10 summarizes the effects of the coupling effectiveness of masonry piers, both in terms of deformed shape at collapse and distribution of the generalized forces (shear V and bending moment M), in a masonry building subjected to seismic loads, passing from the case of very weak spandrels (WSSP) to the shear-type idealization (SSWP). The effects on the capacity curve, in terms of overall strength, stiffness and displacement capacities, are also shown.

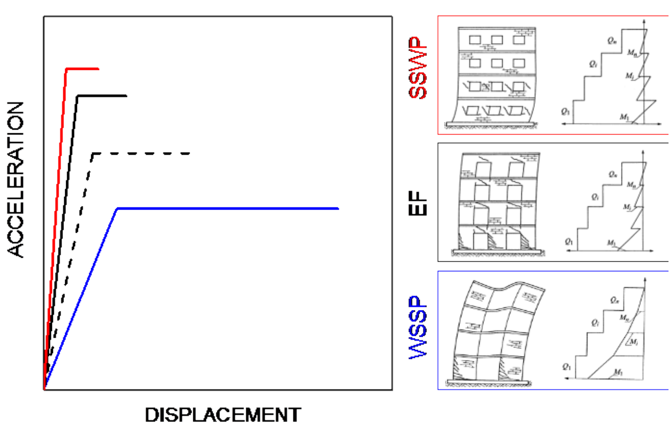

Fig. 10. Influence of stiffness and strength of piers and spandrels on the capacity curve: generalized internal forces (V, M) in masonry piers and damage patterns according to the EF model and the two limit conditions of SSWP and WSSP (adapted from Tomaževič [46])

It is evident, in particular for medium and high-rise buildings, the range of variation of the seismic response is significant; thus, it is necessary to be able to catch these different behaviors for a reliable assessment. Usually, the presence of specific constructive details plays a crucial role in addressing the choice of the correct intermediate behavior between the two limit idealizations (WSSP and SSWP*)*. In general, the SSWP hypothesis is consistent with new masonry buildings, in which masonry spandrels are always connected to lintels, tie beams and floor slabs, made of steel or reinforced concrete. On the contrary, in ancient buildings spandrels are in many cases quite weak elements, as lintels are in timber or made by masonry arches, tie beams are very rare and horizontal diaphragms are flexible (e.g. due to the presence of vaults or wooden floors). In these cases the behavior is closer to WSSP.

Among the different mechanical models proposed in literature (as mentioned in §II), in this section the DBV-*masonry* (Displacement Based Vulnerability) method is suggested. It was originally proposed in [47] with some further modifications [23], [24]. The analytical formulation makes reference to the SSWP model, under the simplified hypothesis, in the evaluation of the total base shear, that all masonry piers fail at the same time, which is true if they are more or less of the same size and the building is regular in plan. The vulnerability of actual buildings, which do not meet these hypotheses, is estimated applying proper corrective factors. Similarly it is possible to evaluate the capacity curve of buildings characterized by EF or WSSP behavior.

An alternative to the use of simplified analytical models is to assume, for each building class, one or more then one completely defined prototype buildings, and to perform static pushover or incremental dynamic analyses with detailed MDOF nonlinear models. The variability of seismic response can be evaluated by analyzing the uncertainties propagation of model parameters and/or by considering a proper number of different prototypes, representative of the class.

This approach can be more detailed because specific constructive details of buildings in the region under investigation may be taken into account explicitly. However, it is strongly dependent from the choice of prototypes and it is necessary to be sure they are really representative of all the building stock.

C. *From hybrid approaches*

Hybrid approaches are based on a combination of the methods described in §IV.A and §IV.B.

In particular, empirical data in terms of macroseismic intensity can be interpreted by means of the macroseismic vulnerability method [14], [42], by fitting, for each defined building class, the two free parameters: the vulnerability index V and the ductility index Q. Then, fragility functions can be obtained through a proper I-PGA correlation. Simplified or detailed mechanical models provide fragility functions by a complementary approach.

The comparison provides a cross-validation of the two methods and helps in the definition of more reliable function for the seismic risk analysis. Depending on the specific case, a different degree of reliability can be ascribed to the two approaches.

V. Conclusion

The paper presents two procedures to derive fragility curves for masonry buildings. For the first, it is important to note that each component of the dispersion coefficient can be evaluated analytically, differently from other studies that numerically estimate just one component (due to the demand) of the overall uncertainty. In the paper also the definition of a suitable taxonomy and the criteria to be adopted for a consequent classification of the built environment are discussed. Moreover, it is worth noting that the combined use of the two approaches may give interesting results:

- the analytical model, that has the advantage to keep explicitly into account the various parameters that determine the structural response of each vulnerability class, allows a more detailed classification of the assets present in hazard zones that are thereby subjected to potential losses;
- the expert elicitation based models are obtained from observed damage and directly correlated to the actual seismic behavior of buildings.

Therefore, the latter becomes the fundamental support to make reliable the results from the analytical method.

Acknowledgment

This work was funded by the project ReLUIS 2014-2018 (www.reluis.it), supported by Italian Civil Protection Agency.

References

[1] Benedetti D, Benzoni G, Parisi MA (1988) Seismic vulnerability and risk evaluation for old urban nuclei. Earthq Eng Struct Dyn 16: 183–201. doi: 10.1002/eqe.4290160203

[2] Bernardini A, Gori R, Modena C (1990) An application of coupled analytical models and experiential knowledge for seismic vulnerability analyses of masonry buildings, In: A. Koridze (ed) Engineering Aspects of Earthquake Phenomena, Vol. 3: 161-180. Oxon: Omega Scientific, 1990

[3] HAZUS (1999) Earthquake loss estimation methodology. Technical and user manuals. Vol. 1–3. Federal Emergency Management Agency (FEMA), National Institute of Building Sciences, Washington D.C.

[4] Kappos AJ, Panagopoulos G, Penelis GG (2008) Development of a seismic damage and loss scenario for contemporary and historical buildings in Thessaloniki, Greece. Soil Dynamics and Earthquake Engineering, Vol. 28(10-11): 836-850

[5] D'Ayala D, Ansal A (2009) Non Linear Push Over Assessment of Historic Buildings in Istanbul to Define Vulnerability Functions. In: Proc. of Earthquake and Tsunami, International Conference. Istanbul, Turkey

[6] Barbat AH, Carreño ML, Pujades LG, Lantada N, Cardona OD, Murulanda MC (2010) Seismic vulnerability and risk evaluation methods for urban areas. A review with application to a pilot area. Struct Infrastruct Eng 6(1–2): 17–38

[7] Cattari S, Lagomarsino S, Pagnini C, Parodi S (2010) Probabilistic seismic damage scenario by mechanical models: the case study of Sulmona (Italy). In: Proc. of 14th ECEE, Ohrid, Macedonia, CD-Rom

[8] Cattari S, Lagomarsino S, Pagnini LC, Parodi S (2013) Validazione di scenari di danno ottenuti con modelli meccanici: il caso studio di Pettino (L'Aquila, 2009). In: Proc. of 15th Italian Conference on Earthquake Engineering. Padua, Italy (in Italian)

[9] D'Ayala D, Paganoni S (2010) Assessment and analysis of damage in L'Aquila historic city centre after 6th April 2009. Bull Earthq Eng 9: 479-509

[10] Ferreira TM, Vicente R, Mendes da Silva JAR, Varum H, Costa A (2013) Seismic vulnerability assessment of historical urban centres: case study of the old city centre in Seixal, Portugal. Bull Earthq Eng. doi:10.1007/s10518-013-9447-2

[11] Nuti C, Santini S, Vanzi I (1998) Seismic risks of the Italian hospitals. In: Proc. of 11th European Conference on Earthquake Engineering. Paris, France

[12] Colombi M, Borzi B, Crowley H, Onida M, Meroni F, Pinho R (2008) Deriving vulnerability curves using Italian earthquake damage data. Bull Earthq Eng 6(3): 485–504

[13] Rota M, Penna A, Strobbia CL (2008) Processing Italian damage data to derive typological fragility curves. Soil Dynamics and Earthquake Engineering, Vol. 28(10-11): 933-947

[14] Lagomarsino S, Giovinazzi S (2006) Macroseismic and mechanical models for the vulnerability assessment of current buildings. Bull Earthq Eng 4(4): 445– 463

[15] D'Ayala D, Spence R, Oliveira C, Pomonis A (1997) Earthquake loss estimation for Europe's historic town centres. Earthq Spectra, 13(4): 773–793

[16] Calvi GM (1999) A displacement-based approach for vulnerability evaluation of classes of buildings. Journal of Earthquake Engineering, vol. 3(3): 411–438

[17] Glaister S, Pinho R (2003) Development of a simplified deformation-based method for seismic vulnerability assessment. Journal of Earthquake Engineering 7(SI 1): 107-140

[18] D'Ayala D (2005) Force and Displacement Based Vulnerability Assessment for Traditional Buildings. Bulletin of Earthquake Engineering, Vol. 3: 235-265

[19] Restrepo-Vélez LF, Magenes G (2004) Simplified Procedure for the Seismic Risk Assessment of Unreinforced Masonry Buildings. In: Proc of 13th World conference on earthquake engineering. Vancouver, Canada

[20] Borzi B, Crowley H, Pinho R (2008) Simplified pushover-based earthquake loss assessment (SP-BELA) method for masonry buildings. International Journal of Architectural Heritage 2(4): 353–376

[21] Molina S, Lang DH, Lindholm D (2009) SELENA: An open-source tool for seismic risk and loss assessment using a logic tree computation procedure. Computers & Geosciences

[22] Oropeza M, Michel C, Lestuzzi P (2010) A simplified analytical methodology for fragility curves estimation in existing buildings. In: Proc. 14th European Conference on Earthquake Engineering. Ohrid, Macedonia

[23] Pagnini LC, Vicente RS, Lagomarsino S, Varum H (2011) A mechanical model for the seismic vulnerability assessment of old masonry buildings. Earthq Struct 2(1): 25–42.

[24] Lagomarsino S, Cattari S (2013) Seismic vulnerability of existing buildings: Observational and mechanical approaches for application in urban areas - Chapter 1. In: Seismic Vulnerability of Structures. P. Gueguen (ed), pp. 1-62. ISTE Ltd and John Wiley and Sons, ISBN 978-1-84821-524-5

[25] Rota M, Penna A, Magenes G (2010) A methodology for deriving analytical fragility curves for masonry buildings based on stochastic nonlinear analyses. Engineering Structures 32: 1312–1323

[26] Erberik MA (2008) Generation of fragility curves for Turkish masonry buildings considering in-plane failure modes. Earthq Eng Struct Dyn 37: 387–405

[27] Gehl P, Seyedi D, Douglas J (2013) Vector-valued fragility functions for seismic risk evaluation. Bull Earthquake Eng 11: 365–384. DOI 10.1007/s10518 012-9402-7

[28] Jaiswal K, Wald D, D'Ayala D (2011) Developing empirical collapse fragility functions for global building types. Earthq Spectra, 27(3): 775-795

[29] Fajfar P (1999) Capacity spectrum method based on inelastic spectra. Earthquake Engineering and Structural Dynamics, 28(9): 979-993

[30] Freeman SA (1998) The capacity spectrum method as a tool for seismic design. In: Proc. of 11th European Conference of Earthquake Engineering, Paris, France
[31] FEMA 356 (2000) Pre-standard and commentary for the seismic rehabilitation of buildings, Applied Technology Council (ATC), Washington D.C.
[32] ASCE/SEI 41/06 (2007) Seismic Rehabilitation of Existing Buildings. American Society of Civil Engineers, Reston, VA.
[33] FEMA 440 (2005) Improvement of nonlinear static seismic analysis procedures, Applied Technology Council (ATC), Washington D.C.
[34] CEN (2004) Eurocode 8: Design of Structures for Earthquake Resistance - Part 1: General Rules, Seismic Actions and Rules for Buildings. EN1998-1:2004. Comité Européen de Normalisation, Brussels
[35] Douglas J, Seyedi D, Ulrich T., Modaressi H, Foerster E, Pitilakis K, Pitilakis D, Karatzetzou A, Gazetas G, Garini G and Loli M (2015) Evaluation of seismic hazard for the assessment of historical elements at risk: description of input and selection of intensity measures, Bulletin of Earthquake Engineering, 13(1): 49-65
[36] Bazzurro P, Cornell CA (2002) Vector-valued Probabilistic Seismic Hazard Analysis (VPSHA), In: Proc. of 7th U.S. National Conference on Earthquake Engineering, Boston, MA, July 21-25, Paper No. 61
[37] Grunthal G (1998) European Macroseismic Scale. Chaiers du Centre Européen de Géodynamique et de Séismologie, Vol. 15, Luxembourg
[38] Cattari S, Lagomarsino S (2012) Perfomance-based approach to earthquake protection of masonry cultural heritage. In: Proc. of Structural Analysis of Historical Constructions – Jerzy Jasieńko (ed) © 2012 DWE, Wrocław, Poland, ISSN 0860-2395, ISBN 978-83-7125-216-7, pp. 2914-2922
[39] Priestley MJN, Calvi GM, Kowalsky MJ (2007) Displacement-based Seismic Design of Structures. IUSS Press, Pavia, Italy, 721 pp.
[40] Blandon CA, Priestley MJN (2005) Equivalent viscous damping equations for direct displacement based design. Journal of Earthquake Engineering, Vol. 9, SI 2: 257-278
[41] Liel AB, Haselton CB, Deierlein GG, Baker JW (2009) Incorporating modeling uncertainties in the assessment of seismic collapse risk of buildings. Structural Safety, 31: 197-211
[42] Bernardini A, Lagomarsino S, Mannella A, Martinelli A, Milano L, Parodi S (2011) Forecasting seismic damage scenarios of residential buildings from rough inventories: a case-study in the Abruzzo Region (Italy). Proc. of IMech E, Part O - J. Risk and Reliability, 224: 279-296
[43] Klir GJ, Yuan B (1995) Fuzzy sets and fuzzy logic. Theory and applications. Prentice Hall, New Jersey
[44] Faccioli E, Cauzzi C (2006) Macroseismic intensities for seismic scenarios estimated from instrumentally based correlations. In: Proc. of the First European Conference on Earthquake Engineering and Seismology, Ginevra, September 3-8, 2006, CD-ROM
[45] Murphy JR, O'Brien LJ (1977) The correlation of peak ground acceleration amplitude with seismic intensity and other physical parameters. Bulletin of the Seismological Society of America, 67: 877-915
[46] Tomaževič M (1999) Earthquake Resistant Design of Masonry Buildings. Imperial College Press, Series on Innovation in Structures and Construction, Vol. 1, ISBN 1-86094-006-8
[47] Cattari S, Curti E, Giovinazzi S, Lagomarsino S, Parodi S, Penna A (2005) Un modello meccanico per l'analisi di vulnerabilità del costruito in muratura a scala urbana. In: Proc. of 11th Italian Conference on Earthquake Engineering. Genoa, Italy (in Italian)

ZnO Nanostructure Alignment on Alumina Surface by Carbon Seeding

A. Marcu, L. Trupina , T. Yanagida, C. P. Lungu and T. Kawai

***Abstract**:** ZnO nanostructures were grown on alumina substrate by Pulsed Laser Deposition (PLD) and Vapor-Liquid-Solid (VLS) technique using Au catalyst. While the catalyst disposal on the substrate surface had a random distribution, we were trying to align the grown nanostructures by controlling nucleation process by additional seedings. While pressing substrate surface with a carbon contaminated aluminum foil, a weak tendency of nanowire alignment on paralel lines could be observed on some substrate areas. More evident results were obtained for ZnO nanobels growing case. We interpret nanostructure lining as preferential interaction of the vicinal plane edges with the contaminated foil and respectively ZnO preferential nucleation on the vicinal planes edges, after interaction with the foil surface.

***Keywords*:** ZnO nanowires, Nanostructure alignment, Carbon seeding

I. INTRODUCTION

Zinc Oxide (ZnO) is a direct band-gap (Eg = 3.37 eV) semiconductor with a large excitation binding energy (60 meV), exhibiting near UV emission, transparent conductivity and piezoelectricity [1]. Thus, ZnO nanomaterials are promising candidates for nanoelectronic and photonics. Compared with other semiconductor materials, ZnO has higher exciton binding engery, is more resistant to radiation, and is multifunctional with uses in the areas as a piezoelectric, ferroelectric and ferromagnetic. ZnO-based semiconductor and nanowire devices are also promising for the integration on a single chip. So far, the various applications of ZnO nano materials such as UV detectors [2-5], chemical sensors [6-8] and FED [9-11] are under way. Moreover, ZnO is biocompatible and can be used for biomedical applications without coating so biosesors are also a promising opportunity for the ZnO nanostructures.

Nano-devices fabrication involve a precise control of nanostructure morphology, properties and spatial positioning. In applications as microfluidics or surface acustic senzors (SAW), the structures alignment is crucial for the device performances. Even if the nanostructures fabrication is more and more effective using so called Bottom-UP techniques as vapor-liquid-solid (VLS) for structure growing, the precise positioning of the catalyst on the substrate surface is still a challenge. The best performance in catalyst positioning still belongs to the Top-Down techniques by using beam lithography which is in many cases not an affordable option. There are also non-lithographic techniques for structure alignment involving growing the structures using templates [12-15] or various self assamblig monolayers [16-18] to pattern the catalyst before growing the structures while still using VLS method. However, the available non-lithographic options are still rather sophisticated and limited as performances.

Previous studies have shown that oxide nanowires growing by VLS technique might be in some particular experimental conditions significantly enhanced by the presence of carbon seeds [19]. Thus, for these cases, the nanowire growth process is conditioned not only by the disposal of the gold liquid catalyst but also by the carbon seed presence. In these circumstances, we can virtually control the nanostructure growth process by controlling booth catalyst and seed disposal over the surface. By using a random gold catalyst distribution on the substrate surface we report here some results on the ZnO nanostructures alignment on the alumina substrate using the substrate mechanical interaction with a carbon contaminated aluminum foil surface.

II. EXPERIMENTAL SYSTEM

Our experimental system consist of a Pulsed Laser Deposition (PLD) using an Lambda Physics ArF excimer laser. We have gown ZnO nanostructures based on the Vapor-Liquid-Solid (VLS) technique using Au catalyst on (11-20) Al_2O_3 substrate. Some special plume filtering techniques are necessary for growing ZnO nanowires using our experimental system [20-21]. By considering plume interaction with obstacles [22,23], we opted in this experiment for the axe-off system geometry (Fig. 1) filter technique, and a variable offset 'h' of the substrate surface ax from the plume central horisontal propagation plane. The 'h' value control would help as controlling the plume filtering efficiency and respectively the plume particle fluency. We used a sintered ZnO target for the ablation process and a single crystal alumina substrate. Ambient oxygen pressure was 1 Pa and substrate temperature about 800^0 C.

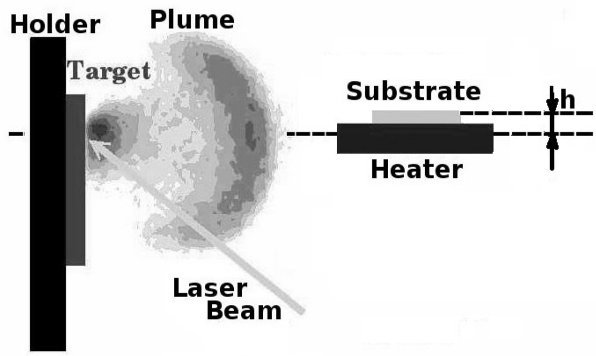

Fig. 1 Experimental PLD system in a axe-off configuration

For the disposal of the seeds over the substrate surface, we were using an aluminum (flat) foil heaving a carbon contaminated surface. Such a foil was placed on the alumina substrate and pressed against the deposition surface (Fig. 2). in order to transfer the carbon contaminant on the substrate surface.

*This work was supported in part by a grant of the Romanian National Authority for Scientific Research,CNCS – UEFISCDI, project number PN-II-IDPCE- 2011-3-0522 and PN-II-ID-JRP-RO-FR-2012-0160

A.Marcu** and C.P. Lungu are from National Institute for Laser Plasma and Radiation Physics, Bucharest-Magurele, 077125, Romania, Tel/Fax: +40 21 457 4027, e-mail**: aurelian.marcu@inflpr.ro

L.Trupina is from National Institute for Material Physics, Atomistilor 405 bis, P.O.Box MG7, Magurele, Romania

T.Yanagiga and T.Kawai are from Institute of Scientific and Industrial Research, Osaka University, 8-1 Mihogaoka, Ibaraki, Osaka567-0047, Japan

III. RESULTS

For the case of the optimal system parameters, and respectively for appropriate plume filtering and particle fluency, corresponding in our system to a 5 cm target-substrate distance and about 5 mm 'h' off-ax distance, vertical ZnO nanowires (Fig. 3 a) could be obtained on the several square millimeters (11-20) alumina substrate as could be seen in a scanning electron microscopy (SEM) image in Fig. 3a. However, while reducing the plume filtering efficiency and increasing the fluency, (in our case by decreasing 'h' with few millimeters) the grown morphology would change from nanowire to nanobelts with no preferential orientation and a top view image of the substrate surface is presented in Fig. 3 b. For such experimental conditions, previous investigations proved that by sputtering carbon seeds on the substrate surface we could still grow nice and vertical nanowire [19] but with no preferential alignment of the grown structures over the substrate surface. In this experiment, by pressing the substrate surface instead of sputtering the carbon seeds the nanowire growing enhancement was also obtained. However, unlike for the carbon sputtering case, a weak tendency of linear alignment of the grown structures could be noticed. In figure 4 are presented a top view SEM image of ZnO nanowires on alumina substrate surface and respectively a 45^0 angle view image.

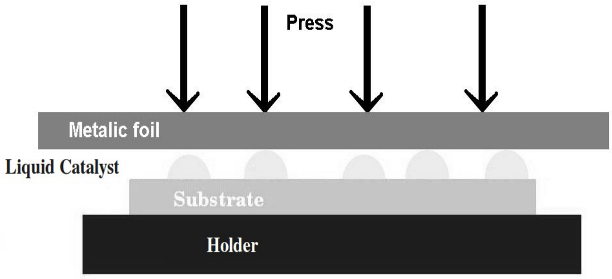

Fig. 2 Substrate contamination using a carbon contaminated aluminum foil

By further decreasing the 'h' offset value, the plume filtering get worse and the particle fluency increase. Even by using carbon seeds, in this case, ZnO grown morphology would be a mix of nanowire and nanobelts. Interesing fact is that the grown structures where heaving a more evident alignment tendency and SEM images of such a substrate surface are presented in Fig. 5. The ZnO structures are still grown vertical on the substrate surface but tend to form parallel lines. The distance between the alignment lines is of the order of tens of nanometers. The alignment tendency is visible on areas of square micrometers order or more, but without covering uniform the hole substrate area.

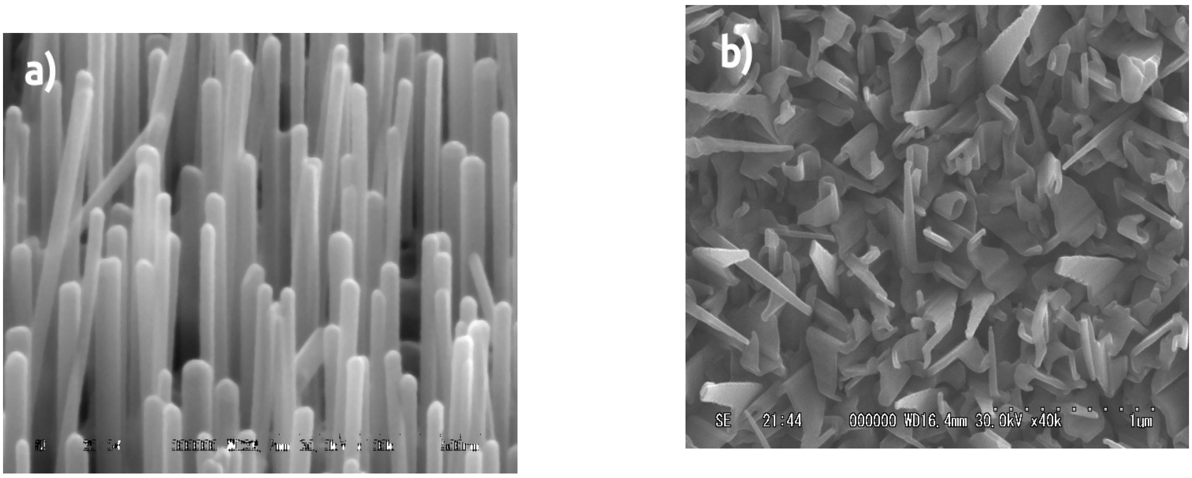

Fig. 3 ZnO nanostructures growing in a) optimal conditions and b) non optimal conditions

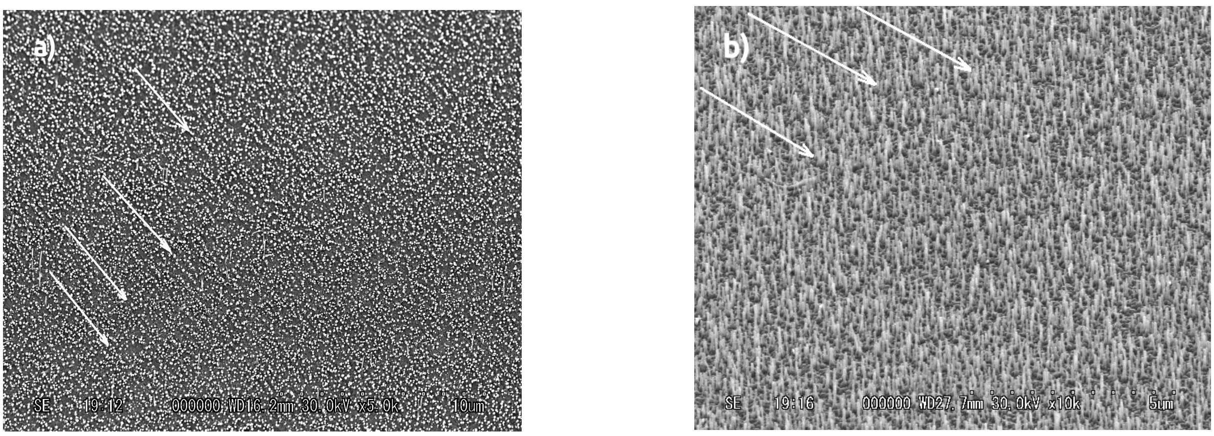

Fig. 4 ZnO nanowire alignment tendencies on alumina substrate a) top view and b) 45^0 view

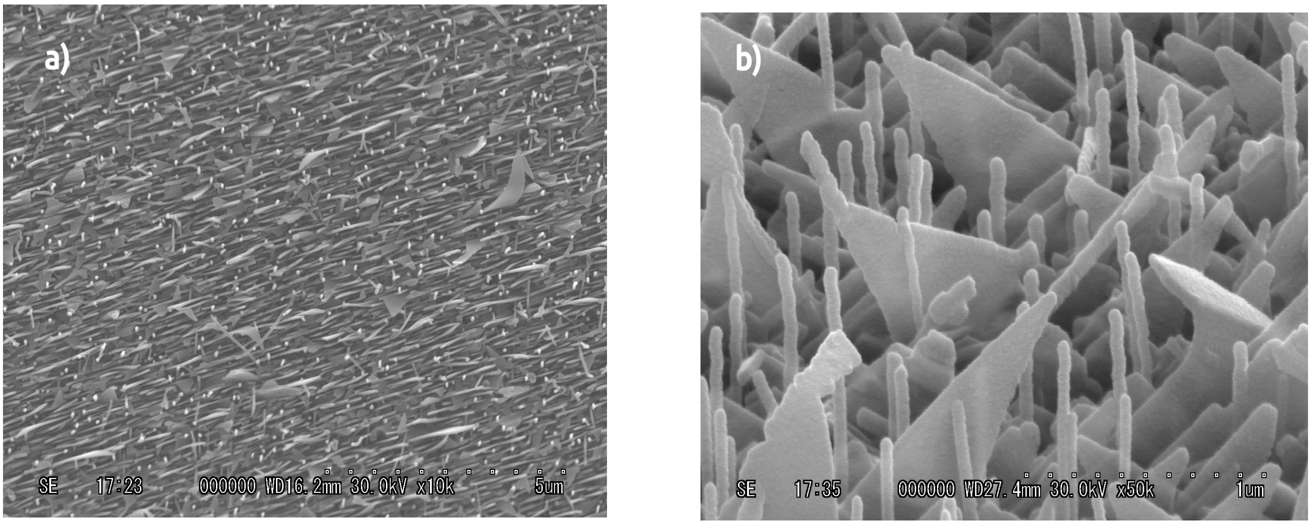

Fig. 5 ZnO nanobelts alignment tendencies on alumina substrate a) top view and b) 45^0 view

IV. RESULTS INTERPRETATION AND DISCUSSIONS

An atomic force microscopy (AFM) investigation was used to compare the substrate surface in different stages of the sample preparation. We started with a clean 11-20 alumina surface. In order to see the vicinal plane edges, the alumina substrate was initially thermally treated [24] and an AFM image of the 11-20 alumina surface is presented in Fig. 6a. The substrate vicinal plane edges could be clearly seen and it is interesting to notice that the distances between the plane ages is of the order with the ZnO aligned nanoblets inter-space. After the gold catalyst deposition, the substrate was heated up to the deposition temperature (800^0 C) end kept for several minutes in order to form the catalyst droplets, but no alignment of gold catalyst could be observed Fig. 6b. After pressing the surface with the contaminated aluminum foil surface no differences from the initial surface could be traced by AFM. EDX techniques could not detect traces of carbon presence either. However, the carbon seeds disposed by sputtering, even if they were also experimentally confirmed as enhancing the growing process they were also no traceable. By transferring more carbon the changes could become traceable by booth AFM and EDX investigations (Fig. 6c) but this case is far from the optimal seeding condition. Thus, we could only conclude that that we do transfer traces of carbon using this technique, but the amount of transferred material could not be detected with our methods.

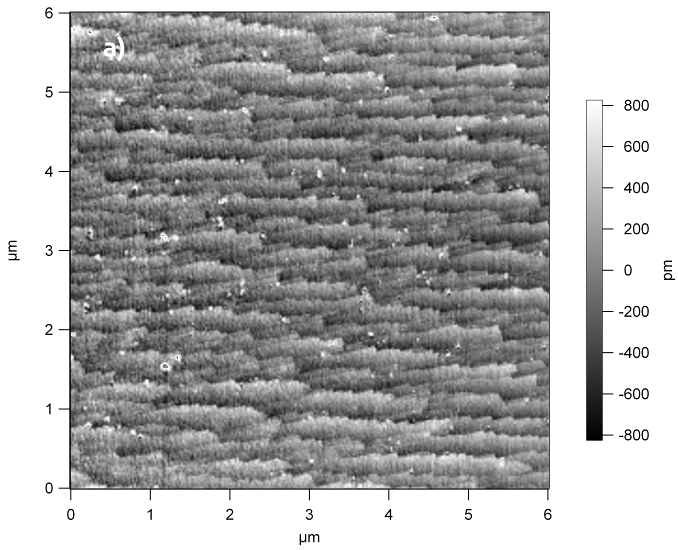

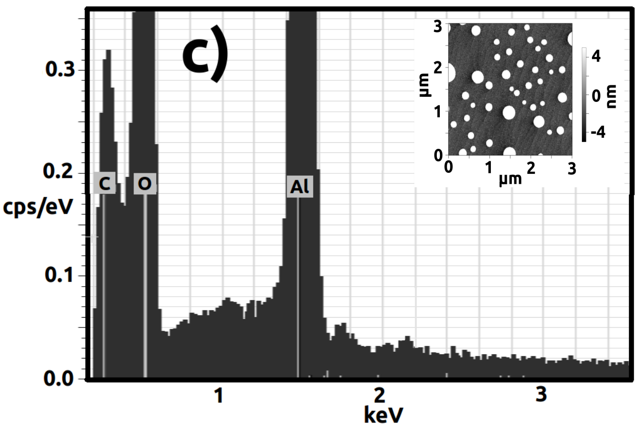

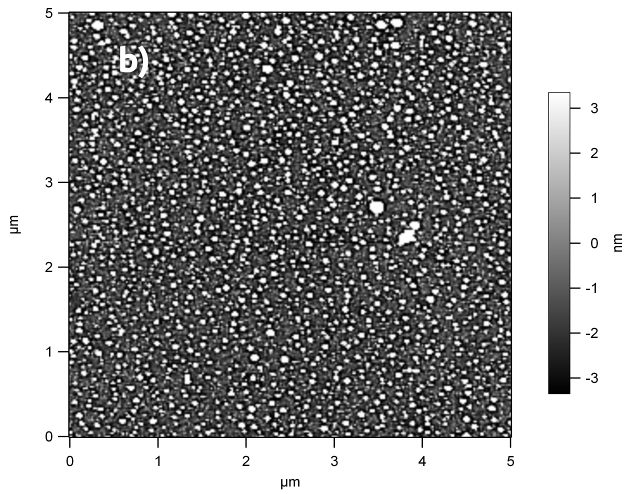

Fig. 6 AFM images of the : a) 11-20 alumina surface, b) gold catalyst after being heated at the working temperature (800^0 C) and c) EDX pattern of over-contaminated surface with AFM surface image inlet (inset SEM image of the scanne area)

A transmission electron microscopy (TEM) image of a ZnO structure is presented in Fig. 7a. Since the gold droplet is still on the top of the structure it means that the VLS mechanism is still the leading process of the nanostructure growing. This is sustained by the previous observation that, generally, no nanostructure growing could be observed in the absence of gold catalyst. However the triangular membrane growing process, between the nanowire and the substrate, does not seem to be related with the VLS process. Thus, in Fig. 7b, we can see SEM images of a ZnO nanowires heaving a triangular membrane which are not up the nanowire tip. Furthermore, in Fig. 7c we can see not only nanowires growing together with nanobelts, but nanowire grown through a membrane of a different wire suggesting that the nanowire and the nanobelt growing processes are independent processes which do not actually affect each other. However, the ZnO membrane alignment has to be related with the carbon contamination technique since no aligment could be observed while using carbon sputtering. Taking also into consideration that the distance between aligned structures is comparable with the distance between substrate vicinal plane edges and that the surface 'steps' and defects are also known to work as seedings [25-27], we can came to the conclusion that, in our experiment, the membrane growing is related with the ZnO preferential nucleation on the vicinal surface edge. If the assumption is true, the vicinal surfaces edge has to be particularly affected by the interaction with the carbon contaminated aluminum foil, in spite of the fact that these modifications were untraceable within our investigations. Thus, a preferential seeding on the vicinal plane edges seems effective for booth nanowire and nanobelts samples. The assumption is a reasonable one since for a 'plane-plane' interaction, the contact between surfaces would take preferentially place between the peak zones, which in our case correspond to the edges of the vicinal planes. However, the interaction between substrate surface and the foil seems to have rather critic parameters for observing this phenomenas, since the alignment of the grown structures could be observed only on some of our investigated samples and only over square millimeter order areas at most.

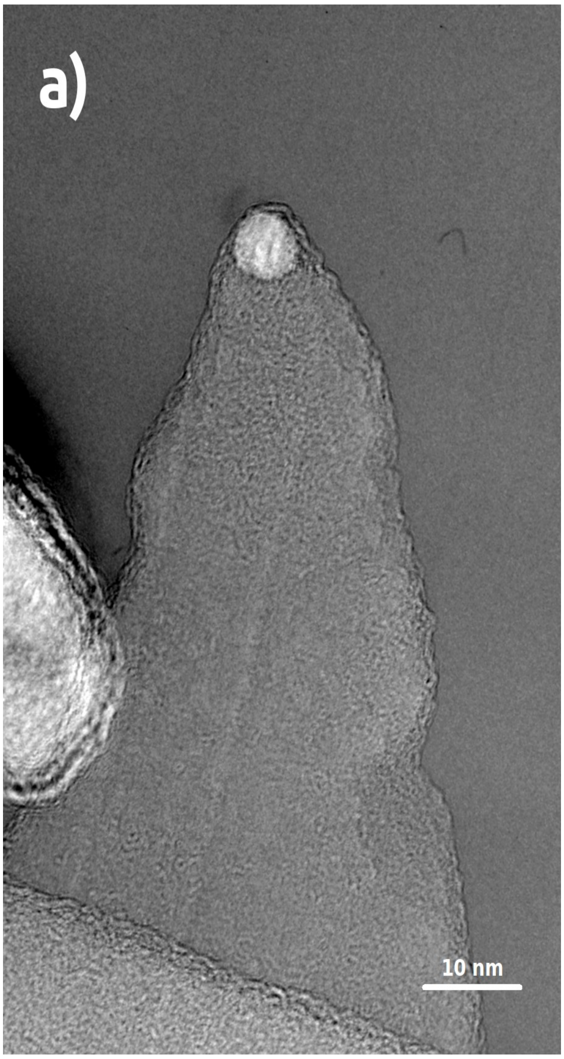

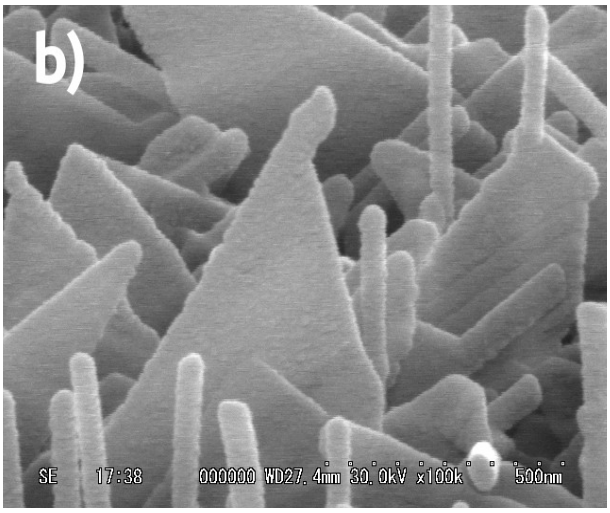

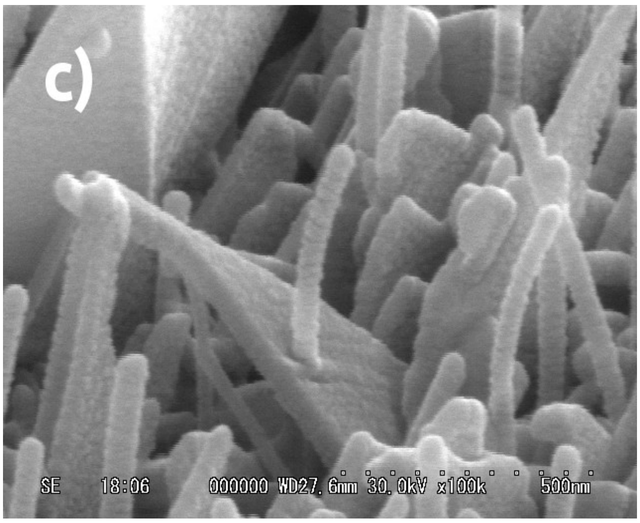

Fig. 7 Microscopy images of ZnO nanobelts: a)TEM image of a ZnO nanostructure, b) SEM image of an incomplete ZnO membrane and c) SEM image of a nanowire grown through a membrane

ISBN: 978-1-61804-325-2

V. CONCLUSIONS

ZnO nanostructures were grown on alumina substrate by PLD/VLS technique using gold catalyst. We placed carbon seeds on the substrate surface by pressing the it over a carbon contaminated aluminum foil. Even if the catalyst droplets were having a random distribution over the surface, in some areas, the grown nanostructures tend to align on on parallel lines at distances of the order of vicinal surfaces edges distances. We interpret this alignment results as being related with the vicinal surfaces edges preferential interaction with the contaminated foil surface and and contamination leading to a preferential nanostructure nucleation on these edge regions.

VI. REFERENCES

[1] Ü. Özgür, Ya. I. Alivov, C. Liu, A. Teke, M. A. Reshchikov, S. Doğan, V. Avrutin, S.-J. Cho, and H. Morkoç, "A comprehensive review of ZnO materials and devices", J. Appl. Phys. Vol. 98, pp. 041301-041301-103, 2005

[2] J. Goldberger, D. J. Sirbuly, M. Law, and P. Yang, "UV detecting properties of hydrothermal synthesized ZnO nanorods", Phys. E, Vol 1, pp.1141–1145, 201

[3] M. Misra, P. Kapur, M. Singla, "Optoelectronics behaviour of ZnO nanorods for UV detection", J. Mat. Sci. Vol. 24 pp. 3940-3945 , 2013

[4] J. Kim, Ju-H. Yun, C. H. Kim, Y. C. Park, J. Y, Woo, J. Park, J.-H. Lee, J. Yi and C.-S. Han, "ZnO nanowire-embedded Schottky diode for effective UV detection by the barrier reduction effect", *Nanotechnology* Vol. 21, pp. 115205, 2010

[5] L. Guo, H. Zhang, D. Zhao , B. Li, Z. Zhang, M. Jiang and D. Shen, "High responsivity ZnO nanowires based UV detector fabricated by the dielectrophoresis method" Sens. Ac B: Chem., Vol 20, pp.12-16, 2012

[6] C.Viespe, "Surface Acoustic Wave Sensors Based on Nanoporous Films for Hydrogen Detection", Key Eng. Mat., Vol 605, pp. 331-335, 2014

[7] K Mirabbaszadeh and M Mehrabian, "Synthesis and properties of ZnO nanorods as ethanol gas sensors", *Phys. Scr.* Vol. 85, pp. 035701, 2012

[8] A.Marcu, C. Viespe, "Laser-grown ZnO nanowires for room-temperature SAW-sensor applications", Sen. Act B-Chem, Vol. 208, pp. 1-6, 2015

[9] R. Kumar, O. Al-Dossary, G. Kumar and A. Umar, "Zinc Oxide Nanostructures for NO_2 Gas Sensors Application: A Review", Nano-Micro Lett., Vol. 7, pp 97-120, 2015

[10] K Mirabbaszadeh and M Mehrabian, K Mirabbaszadeh and M Mehrabian, "Synthesis and properties of ZnO nanorods as ethanol gas sensors", *Phys. Scr.*, Vol 85, *pp.* 035701, *2012*

[11] Hsu, Cheng-Liang, and Tsung-Ying Tsai. "Fabrication of Fully Transparent Indium-Doped ZnO Nanowire Field-Effect Transistors on ITO/Glass Substrates", *J. Elect-Chem Soc. Vol.* 158, pp. K20-K23, *2011*

[12] J. Goldberger, D. J. Sirbuly, M. Law, and P. Yang, "ZnO Nanowire Transistors", J. Phys. Chem B Lett Vol. 109, pp. 9-14, 2015

[13] W. Chen Xiaoming Tao, Yuyang Liu, Xiaohong Sun, Zhigang Hu, Bin Fei, "Facile route to high-density, ordered ZnO nanowire arrays and their photoluminescence properties", Appl. Surf. Sci. Vol. **252,** 2006, pp. 8683–8687

[14] M. Sima, I. Enculescu, E. Vasile, "Growth of ZnO micro and nanowires using the template method Journal of Optoelectronics and Advanced Materials ", J. of Opt. Adv. Mat. Vol. 2, pp. 825 – 828**,** 2006

[15] Ching-Jung Yang, Shun-Min Wang, Shih-Wei Liang, Yung-Huang Chang, and Chih Chen and Jia-Min Shieh, Appl. Phys. Lett. Vol. 90,, pp. 033104 2007

[16] H. Chik, J. Liang, S. G. Cloutier, N. Kouklin, and J. M. Xu, "Periodic array of uniform ZnO nanorods by second-order self-assembly", Appl. Phys. Lett. Vol. 84, pp. 3376-3379, 2006

[17] Xudong Wang,Xudong Wang, Christopher J. Summers, and Zhong Lin Wang, "Large-Scale Hexagonal-Patterned Growth of Aligned ZnO Nanorods for Nano-optoelectronics and Nanosensor Arrays", *Nano Letters*, Vol. 4, pp 423–426, 2004

[18] Dongmok Whang, Song Jin and Charles M. Liebe, "Nanolithography Using Hierarchically Assembled Nanowire Masks", *Nano Letters*, Vol. 3, pp 951–954, 2003

[19] T. Yanagida, A.Marcu, H.Matsui, K.Nagashima, K.Oka, K.Yokota, M.Taniguchi and T.Kawai, "Enhancement of Oxide VLS Grow by Carbon on Substrate Surface", J. Phys. Chem C Vol. 112, pp.18923 – 18926 , 2008

[20] A.Marcu, C.Grigoriu, W.Jiang and K.Yatsui, "*Pulsed Laser Deposition of YBCO Thin Films in a Shadow Mask Configuration*", Thin Solid Films, Vol. 360, pp.166-172, 2000

[21] A.Marcu, C.Grigoriu and K.Yatsui, "Particles Interaction with Obstacles in Pulsed Laser Deposition ", Applied Surface Science, Vol. 248, pp. 466-469, 2005

[22] A.Marcu, C.Grigoriu and K.Yatsui, "*Simplified Model for RMS Variation in Pulsed Laser Deposition*", SPIE, Vol. 4430, pp. 241-246, 2001

[23] A.Marcu, C.Grigoriu and K.Yatsui, "Particles Movement and Surface Quality in PLD/PR systems", Applied Surface Science, Vol. 252, pp. 4733, 2006

[24] A.Marcu, C. Grigoriu, C.P.Lungu, T.Yanagida and T.Kawai, "Ablation Particles Parameters Influences on VLS Oxide Nanowire Growing", Physica E Vol. 44, pp. 1071-1073, 2012

[25] E. Thune, A. Boulle, D. Babonneau, F. Pailloux, W. Hamd, R. Guinebretiere, "Nanostructured sapphire vicinal surfaces as templates for the growth of self-organized oxide nanostructures", Appl. Surf. Sci. Vol. 256, pp. 924–928, 2009

[26] L. Xu, C. T. Campbell, H. Jonsson, G. Henkelman, "Kinetic Monte Carlo simulations of Pd deposition and island growth on MgO(100)", Surface Science Vol. 601, pp.3133–3142, 2007

[27] J.B.K. Lawa,b, C.B. Boothroydb, J.T.L. Thong, "Site-specific growth of ZnO nanowires from patterned Zn via compatible semiconductor processing", Journal of Crystal Growth Vol. 310, pp. 2485–2492, 2008

Expansive Clay Soil-Structure Interaction: A Case Study

Omer Mughieda
Abu Dhabi University/Department of Civil Engineering, Abu Dhabi, UAE
Email: omer.mughieda@adu.ac.ae

Kenan Hazirbaba
Khalifa University/Department of Civil Infrastructure and Environmental Engineering, Abu Dhabi, UAE
Email: kenan.hazirbaba@kustar.ac.ae

Abstract—**Expansive soils are problematic due to the extensive damages they may cause to structures and infrastructure. This paper presents results from a case study conducted in an area (Irbid, Jordan) that is characterized by a surficial formation of highly expansive soil. A school building suffering from damages that are attributed to the shrinkage of the soil layer under the foundation was investigated. The interaction between the expansive clay soil layer and the structure was studied through diagnostic investigation of the existing cracks, the properties of the foundation ground, and the climatic and other relevant stratigraphical factors. The results of this study indicated that the structural damages in building members (columns, beams and footings) were mainly due to the swelling gradient. Remedial measures were proposed to rehabilitate and strengthen the structure and prevent further damages.**

Index Terms—**expansive clay, soil-structure interaction, shrink-swell of clay**

I. INTRODUCTION

Expansive soils pose a severe threat to civil engineering infrastructure worldwide. Excessive cost of damages to infrastructure mainly due to expansive soils is reported each year. Expansive soil is typically characterized by its potential for significant volume change with varying water content. Expansive soils are especially abundant in arid zones [1]. The primary factors governing the behavior of expansive soil are grouped under three categories: i) geology, ii) soil index properties, and iii) environmental factors. Geology is important in determining the formation and presence of expansive clay minerals as well as the amount of aging. Soil index properties indicate the type and amount of clay particles, dry density and water content of the soil. The most relevant environmental factors are the presence of vegetation, as it affects the moisture content of the soil, and amount of precipitation and wetting-drying cycles as they can cause great variation in the moisture content. In addition to all these factors, when it comes to design of foundations on expansive soil, the surcharge pressure plays a significant role on the expansion potential and the interaction between the soil and structure. In general, light structures (i.e., low rise buildings) are very prone to damages resulting from expansive soil. This paper presents a case study from an area (Irbid, Jordan) characterized by a surficial formation of highly expansive soil. A low-rise school building with symptoms of distress and visible cracks was investigated to address the source and extent of damages and propose rehabilitation measures.

II. SITE DESCRIPTION

A. Location, Climate and Stratigraphy

The site is located in Irbid, Jordan Fig. 1, which is a semi-arid area with a long rainy season (November through April), followed by a hot dry summer (May through September). The annual precipitation in the study area varies from 200 mm to 800 mm. The site is covered by a surfacial layer of expansive clay soil. The typical soil profile in the area consists of 2 - 3 m of dark grayish brown clay layer underlain by reddish brown clay layer down to a depth of 10 m. Then, weathered materials of large rounded boulders of basalt exist just above the clay/basalt interface [2].

Figure 1. Location map of the study site.

B. Current State of Structure

The structure of study is a reinforced concrete (RC) structure consisting of a “library building” and “main building” as shown in Figs. 2 and 3, respectively. The main building consists of ground, first, and second floors

ISBN: 978-1-61804-325-2

while library buildings are ground floor only. The visual inspection of the structure revealed evidence of cracking of external and internal walls of the western portion of the buildings. The structure had been subjected to cosmetic repair for cracks, however cracks have redeveloped and reappeared. Some photographs showing the current state of cracks/damages are presented in Fig. 4

III. Field Exploration and Laboratory Testing

A. Field Exploration

For field exploration purposes four test pits were excavated. The approximate locations of these test pits are marked in Figs. 2 and 3. The test pits reached to depths of 210 cm to 265 cm below ground surface. Disturbed soil samples were collected at various depths for laboratory testing. All sides and the bottom of each test pit, including foundations, were thoroughly examined. Soil strata and material recovered were described.

Existing cracks were spotted and monitored for a period of about 3 months by using thin glass till tales that were fixed across existing cracks at different locations at the interior face of the building walls.

B. Laboratory Testing

Laboratory tests were performed on selected samples from each test pit. The percentage of sand, silt, and clay for the studied soil were determined in accordance with ASTM procedure [3] and found to be (8-11) %, (52-54) % and (35-40) %, respectively. Atterberg limits were determined according to ASTM procedure [4]. The results showed that the soil samples have Liquid Limit (LL) of (58-63) %, Plastic Limit (PL) of (30-31) %, and Plasticity Index (PI) of (28-32) %. Based on Unified Soil Classification System (USCS), the soil was classified as high plasticity clay (CH). The degree of potential expansiveness was determined as *high expansiveness* according to the chart given by [5].

IV. Foundation Inspection

A. Test Pit 1(Library Building)

The RC foundation has dimensions of 100 x 130 x 30 cm and depth of 250 cm from the adjacent external sidewalk level. The foundation is underlain by a plain concrete layer with thickness of 15 cm and protrudes a distance of 15 cm from the external face of the footing. The foundation materials are composed of dark brown, very stiff to hard silty clay material with occasional gravels of chert and limestone.

B. Test Pit 2 (Library Building)

The RC foundation has dimensions of 120 x 150 x 35 cm and depth of 265 cm from the adjacent internal ground level. Similar to the formation of Test Pit 1, the soil beneath the foundation is dark brown, very stiff to hard silty clay with occasional gravel of chert and limestone.

C. Test Pit 3(Main Building)

The RC strip foundation has width of 180 cm and thickness of 30 cm. The foundation is placed 215 cm below the adjacent external sidewalk level. The soil formation underlain the foundation is consistent with that of previous test pits (i.e., Test Pits 1 and 2), revealing dark brown, very stiff to hard silty clay with occasional gravels of chert and limestone.

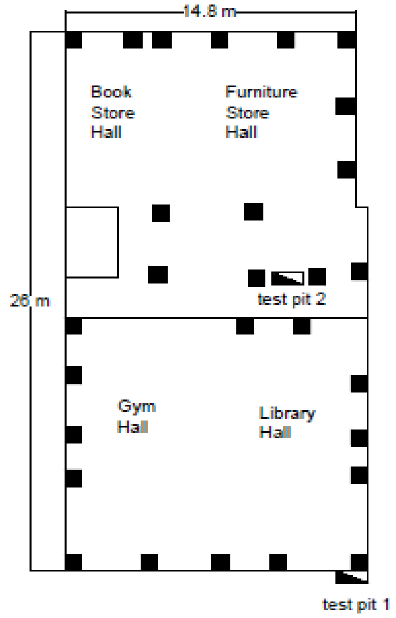

Figure 2. General layout of library building and test pits

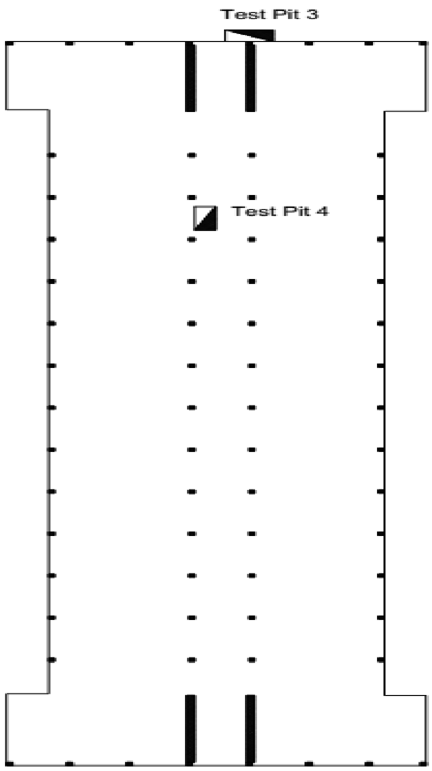

Figure 3. General layout of main building and location of test pits.

D. Test Pit 4 (Main Building)

The RC strip foundation has width of 190 cm and thickness of 30 cm. Depth of foundation is 210 cm from the adjacent internal ground level. The soil beneath the foundation was found to be the same as that discovered in the other test pits; dark brown, very stiff to hard silty clay material with occasional gravels of chert and limestone. Location of test pits in the library and main buildings are shown in Figs. 2 and 3, respectively. Fig. 5 shows cross section of the foundation in the main building Test Pit 4.

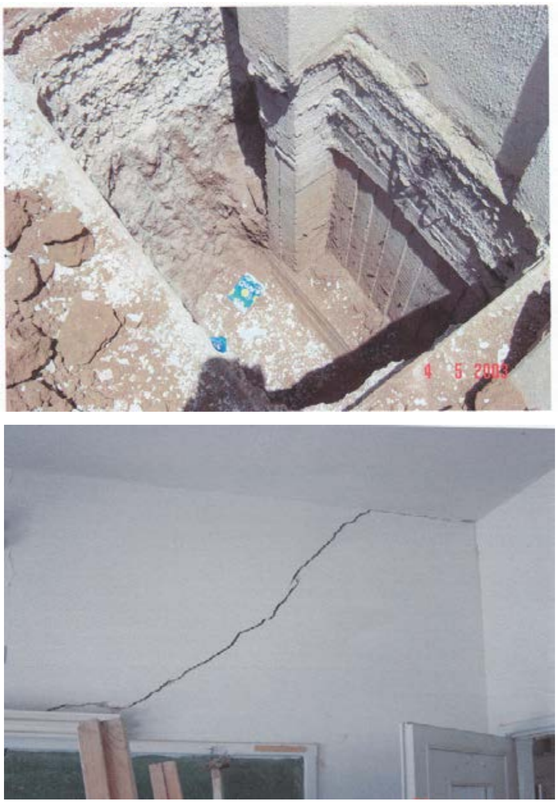

Figure 4. Test pit 3 and state of cracks in main building

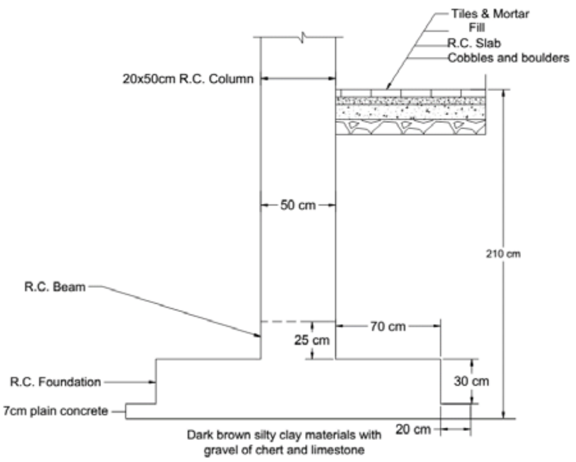

Figure 5. Elevation view of foundation at test pit 4 in the main building

V. Analysis of the Laboratory And Field test Results

The expansive clay layer is the focus of this study. To understand the interaction between the soil and the structure, it is important to quantify the swell/shrink potential and bearing capacity of this founding clay layer. The average value of the measured corrected standard penetration test blows/ft, N_{60} at the depth of foundation was 17. The undrained compressive strength may be found through empirical correlations employing N_{60} value and PI [6]. Using such correlation, the unconfined compressive strength of the stiff clay was estimated as 200 kN/m^2. The allowable bearing capacity of the foundation was calculated based on [7]: $q_{ult} = S_u N_c/ FS = 100 \times 5.14/3 = 171$ kN/m^2. The dead load and live load on the slab were computed as 7 kN/m^2 and 4 kN/m^2 respectively. The calculated bearing pressure was 156 kN/m^2 which is less than the allowable bearing capacity of the soil.

VI. Description and Classification of Cracks

A. Cracks in the Library Building

Most of the cracks took place at the western portion of the building, and particularly at the southern west and northern west corners of the building. Diagonal, vertical and horizontal cracks were observed at internal and external walls, particularly at the library room and in the furniture store room.

B. Cracks in the Main Building

Most of the cracks in the Main Building were found to be at the external and internal walls of the western staircase of the building, at the ground and first floors. Two diagonal cracks were observed at internal partitions, and columns located in the ground and first floors.

Based on the cracks classification given by [8] the observed cracks classification ranged from *negligible* to *moderate*.

VII. Swelling Pressur and Swell Potential

The relationship between the swell potential and plasticity index can be expressed as follows [9]

$$S_p = Be^{A(I_p)} \qquad (1)$$

Where, $A = 0.0838$, $B = 0.2558$ and I_p = plasticity index. Using Eq. (1) the swell potential of the clay can be calculated as 3.7 %. In the present study the depth of the expansive clay layer was found to be 8 m below the ground surface. The depth of foundation was found to be on average about 2.0 m in the main building as shown in Fig.6, and 2.5 m in the library building. The depth of the active zone extends down to 3.5 m. Thus, the thickness of clay layer beneath foundation that is susceptible to heave due to moisture content variation is 1.5 m in the main building and 1.0 m in the library building.

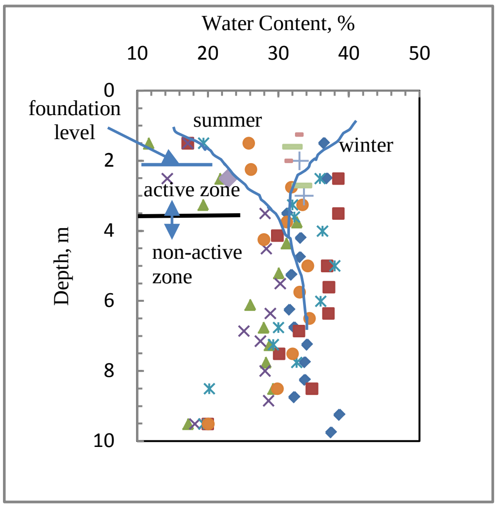

Figure 6. Seasonal variation of water content with depth for Irbid soil. [12].

Based on the calculated percent heave, the total surface heave is estimated to be 5.6 cm under the main building and 3.7 cm under the library building. These values of heaving result in significant angular distortion; 1/135 and 1/90 for the library building and main building, respectively. Such large values of angular distortion are immediate cause for cracking in the structure, as they exceed the allowable limit of 1/500 for single and multistory structures [10]. The variation of swelling pressure in the area with natural moisture content may be calculated from Eq (2) [11]. The results of this equation coincides well with measured values of Irbid clay [12].

$$log p_s = -2.0 + 0.02LL + 0.001\rho_d - 0.04w_n \quad (2)$$

Where p_s = swelling pressure in kg/cm^2
LL = liquid limit (%)
w_n = natural moisture content (%)
ρ_d = dry density of soil in kg/m^3

The variation of swelling pressure with the moisture content variation is plotted in Fig. 7 as predicted by Eq. (2).

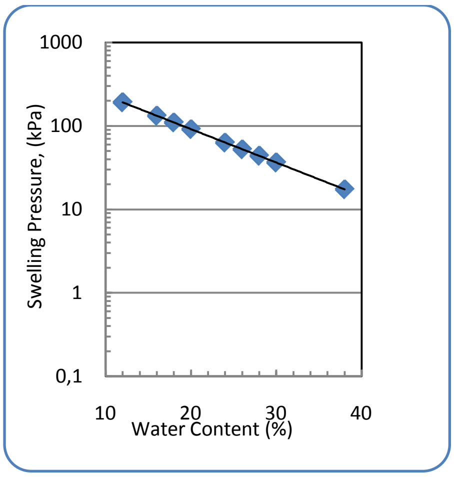

Figure 7. Variation of swelling pressure with the moisture content for the studied soil.

VIII. Causes Of Cracks

Based on the field observation and Laboratory tests conducted in this study the following factors were found to contribute to foundation movement observed cracks.

A. *Depth of Foundation*

The foundation is located within the active zone i.e. the zone of the seasonal moisture variation. Depth of foundation ranges from 215 to 265 cm below the adjacent external sidewalk level while the depth of the active zone is 300 cm.

B. *Foundation soil*

The foundation soil was found to bee highly plastic with high swelling potential. Thus, the soil is susceptible to movement by swelling and shrinkage as a result of moisture content variation.

C. *Moisture Content Variation*

The main cause of foundation movement either upward or downward is the change in soil moisture content. This change is resulted from changes in the field environment from natural conditions. For the library building, the moisture content at the time of the investigation (April) was found to be 25.1 % at the base of the foundation outside the building (Test Pit 1) while it was found to be 12.9 % under the footprint of the building (Test Pit 2). Such discrepancy between the values of moisture content inside and outside the building may be explained by the presence of plants and tress surrounding the perimeter of the building. Further, the footprint area of the building is covered by the structure itself that limits the exposure, thus is likely to experience less variation in the moisture content when compared to the outer perimeter which is open with direct exposure. The difference in moisture content between inner and outer perimeters leads to dish-shape heaving as shown in Fig. 8. This may explain the cracks in the exterior walls of the library building.

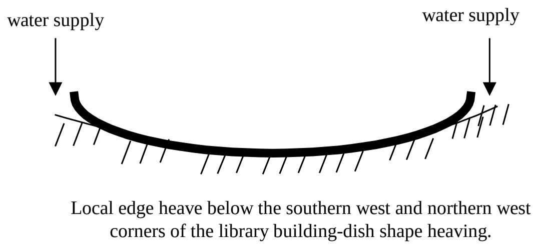

Figure 8. Local edge heave below the southern west and northern west corners of the library building-dish shape heaving

The moisture content for the main building at the time of the investigation was found to be 17.3 % in the soil of uncovered area and 19.2 % in the soil of covered area at the base of the foundation. The high value of moisture content in the covered area is due to the migration of water vapor from higher temperature uncovered area to the cooler inside covered area to equalize the thermal energy of the two areas. The construction of the main building was started in the summer where the moisture content was low. However, the moisture content has

ISBN: 978-1-61804-325-2

increased with time.. It is important to pint out that the moisture content in the uncovered area starts a decreasing trend towards the summer, and especially because of the plants and tress nearby. Such decrease in the uncovered will result in what is called doming heave as shown in Fig. 9.

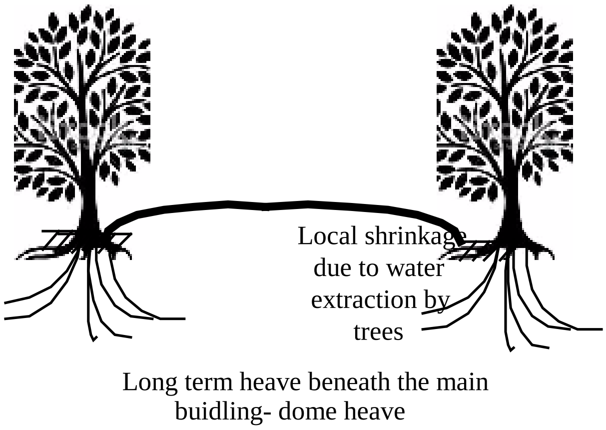

Figure 9. Long term heave beneath the main building- dome heave

D. Surrounding pavement

It was observed that the library building is surrounded by a pavement of width of 1 m from the south and north sides of the building. The pavement showed sagging, settlement and cracks and separation from the adjacent walls. Thus water from rainfall and surface water is allowed to drain towards the foundation causing moisture content variation.

E. Effect of Trees

At the site, trees and various plants of dense population were found to surround the building. The extraction of water from soil due to the existence of trees and plants is expected to be substantial.

Building damage can be noticed as trees height becomes approximately equal to their distance away from the building. In nearly every such case damage has subsequently increased in severity as the trees have grown higher heights. In most cases the crack patterns have indicated relative downward movement of the part of the building nearest to trees. This fact can be taken as circumstantial evidence that the building damage has been caused by moisture extraction from the ground associated with tree growth and root spread. The main cause of water removal and replenishment is the weather; shrinkage of the ground occurs due to evaporation in the hot dry season, and swelling occurs due to rainfall infiltration in the cool wet winter season. The ability of the climate to remove water from ground is greatly increased by the pumping action of plants which transpire moisture through their leaves into the atmosphere; the moisture is taken from the ground by fine roots.

IX. BUILDING REPAIR AND REMEDIAL MEASURES

The type of building repair and any remedial measures undertaken on a damaged building will depend on three factors: the extent and scale of the damage, the nature of the movement causing the damage and the cost of the repairs and remedy in relation to the value of building. In the current study the following remedial measures and building repair types were recommended:

A. Environmental Control

1. Sloping the ground down and away from the buildings so that any water run-off flows away from it.
2. Ensuring that water supply pipes and sewer pipes are all not damaged and not leaking and sufficiently flexible, or are flexible connected, to accommodate movements.

3. Ducting all rainwater falling onto roofs well away from the foundations to the adjacent streets or areas.

4. Cutting all trees around the buildings particularly, the tress located at the northern side of the library building, and the western side of the main building.

5. For library building. It is recommended to reconstruct the pavement (approximately 2 m wide) at the northern and southern sides of the building. The pavement in general shall be slopping outwards at 2.5 % in order to protect the soil near the building from surface water. The pavement should not be connected to the building though dwells instead it should be separated from the building by sealed vertical slip joint. Suggested typical details for the pavement are shown in Fig. 10.

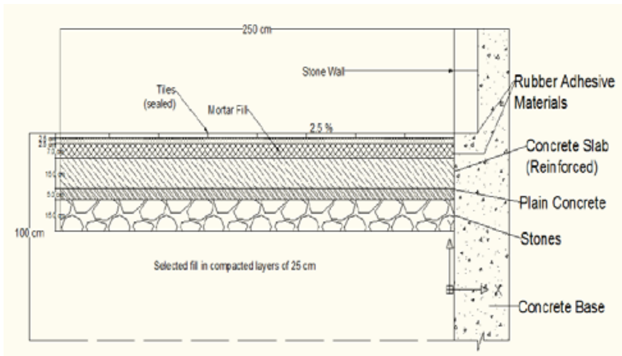

Figure 10. Pavement Details

B. Building Repair

It is expected that the implementation of the remedial technical and environmental measures specified in (A) will restrict the problem and swelling and shrinkage of the foundation soil appreciably. Continuous monitoring of crack progression is recommended and in case there is any underpinning to the foundation in away to increase the depth of the foundation below the active zone region (3 m depth) below the ground surface. If no further movement is detected at least six months after the implementing of the remedial measures, crack repair may proceed.

X. CONCLUSION

A damaged RC building due to an expansive soil was investigated in the form of a case study. Diagnostic analyses of the damage were conducted through reconnaissance measurements. The investigation showed that the foundation soil is highly plastic and has high expansiveness potential. The field and laboratory measurements showed that the main reason for building cracking was the swell/shrink movement of the foundation soil and consequently the building foundation. Calculated angular distortion was found to exceed by far the allowable limit for typical residential buildings. This finding was significant in identifying the causes of differential movement of foundation and eventual cracking of the walls of the building. Remedial measures were prescribed in the current study. The proposed remedial measures focused on isolating the foundation of the building from the water so, there will be no change in moisture content over the year which will substantially reduce the swell/shrink movement of the foundation and ceasing the building movement.

References

[1] A. Seco, F. Ramirez, L. Miqueleiz, B. Garacia, "Stabilization of expansive soils for use in construction", Applied Clay Science, vol 51, 2011.

[2] R. Sharif and R. Stevens, "Building on clay soil in Jordan," Seminar held at the Royal Scientific Society, Amman, Jordan, 1983

[3] ASTM D422-63 Standard test methods for particle size analysis of soils. Annual Book of ASTM Standards, Section 4, Vol. 04.08, Soil and Rock; Building Stones, ASTM, Philadelphia.

[4] ASTM D4318-00 Standard test methods for liquid limit, plasticity limit, and plasticity index of soils. Annual Book of ASTM Standards, Section 4, Vol. 04.08, Soil and Rock; Building Stones, ASTM, Philadelphia.

[5] A. B. Williams, and G. W. Donaldson, ‘‘Building on expansive soils in South Africa: 1973–1980.’’ *Proc., 4th Int. Conf. on Expansive Soils,* Vol. 2, ASCE, New York, 834–844. 1980.

[6] K. Terzaghi, R. Peck and G. Mesri, *Soil Mechanics in Engineering Practice,* 3rd ed. John Wiley, 1996.

[7] A. W. Skempton, "The bearing capacity of clays," *Proc. Building Research Congress*, vol. 1, pp. 180-189, 1951.

[8] BRE Digest 242, Low-rise building on shrinkable clay soils: part 3. Building Research Establishment, HMSO, London, 1980.

[9] F. H. Chen, *Foundations on Expansive Soils.* Elsevier Science Publishing Company Inc., New York, 1988

[10] US Army technical manual, TM 5-818-7, *Foundations in expansive soils,* 1983.

[11] G. Wiseman, A. Komornik and J. Greenstein, "Experience with Roads and Buildings on Expansive Clays," *Transportation Research Record*, TRB, 1023. 1985.

[12] O. Mughieda and K. Bani-Hani, "Cracking of RC school building due to soil expansion," International Jordan Journal of Civil Engineering. Vol.1, No4, 2007

ISBN: 978-1-61804-325-2

The development of energy-efficient construction in the Malopolska region by the projects SPIN. Malopolska Certified Energy-Efficient Building.

M. Fedorczak-Cisak, M.Furtak

Abstract — Within the framework of Cracow University of Technology through innovative project by University of Technology and Malopolska autonomy ‘Spin – transfer model of innovations in Malopolska’ was created Malopolska’s Energy Efficient Construction Center **(MCBE).**

MCBE groups together Cracow University Of Technology researchers working in energy efficient construction field. It is a place which disseminate information of the energy efficient construction area and also entity involved in implementing innovations in construction. MCBE promotes energy efficient construction. As part of the laboratories which are promoted by MCBE most innovative is newly created technologies Malopolska Laboratory Of Energy Efficient Constructions **(MLBE).**

One example of MCBE activities is development of first in Poland energy efficient buildings certificate. The first certified building is Malopolska Laboratory Of Energy Efficient Constructions (MLBE).

Keywords—energy-efficient buildings, MCBE Certificate, Near Zero Energy Buildings.

I. Introduction - Energy efficient building - Certification of buildings

Bilding sector in Poland is undergoing significant transformation which in the end will be filling the obligations of Poland as a Member State in the EU in this area.

MCBE - MALOPOLSKA’S CENTER OF ENERGY EFFICIENT CONSTRUCTIONS – 2012

This investment is an innovative unit of Cracow University of Technology, whose aim is to establish a partnership network of cooperation between science and business. Such cooperation enables scientists and entrepreneurs to develop and implement new technologies in the field of energy efficient construction.

Malopolska’s Centre of Energy-Efficient Construction unit of Cracow University of Technology - Project "SPIN - Model transfer of innovation in Malopolska" realized by the Human Capital Operational Programme, Priority VIII: Regional human resources, Measure 8.2. Transfer of knowledge, Sub 8.2.1. Support for cooperation zone of science and Enterprises. The aim of the project is to increase the intensity of knowledge transfer and exploit the potential of universities by companies in Malopolska. In this study Design Builder software was used (that has been purchased under this project).

M. Fedorczak-Cisak is working in Malopolska Laboratory of Energy Efficient Constructions Civil Engeneering on Cracov Uniwersity of Technology, Poland (corresponding author to provide phone: 0048-696 04 60 50; fax: 0048-12-628-30-61; e-mail: mfedorczak-cisak@pk.edu.pl).

M.Furtak – Director of Malopolska Laboratory of Energy Efficient Constructions Civil Engeneering on Cracov Uniwersity of Technology, Poland, (corresponding author to provide phone: 0048-608 177 419; e-mail: mfurtak@pk.edu.pl).

Implementation of the Directive 2002/91/EC and its detailed version Directive 2010/31UE [10] about buildings energy performance. Requires us to necessity of buildings design with a much reduced demand for energy – buildings ‘almost zero energy’. The process of designing buildings with so low compared with traditional energy consumption objects affects the choice of construction materials and insulations system solutions to ensure, on the one hand, the structural safety as well as fulfillment of the sharp heat protection requirements. Objects with almost zero energy demand require a specific approach to both, the design process and the implementation and use of the objects. This type of buildings have very tight external enclose and restrictive parameters of thermal insulation. These buildings are equipped with specialized systems of technical installations, rising in a maximum possible, active or passive, of renewable energy for example, by opening the object on the southern side and the extraction of energy from solar radiation. As a result, these objects have minimized demand for energy both, primary (indicating the non-renewable sources of energy consumption) and the final determining actual energy needs of the building. The low energy buildings design is a challenging job for architects, particularly in the aspect of providing appropriate thermal protection but also ensure the comfort of using the building (Fig 1) [1], [3]. All aspects of comfort experienced by the use shall be taken into consideration and very thoroughly analyzed during the process of designing energy efficient buildings [5-8].

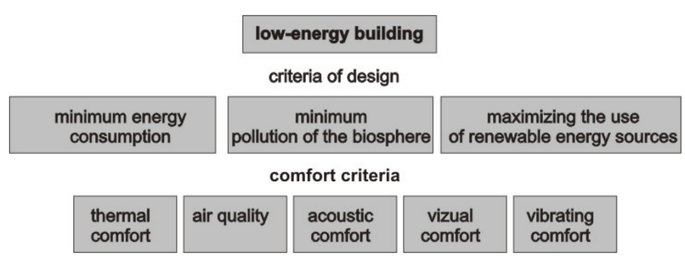

Fig.1. The criteria considered in designing nearly zero energy buildings.

Necessary element to the design and implementation of energy efficient buildings is to check its parameters for appropriate thermal insulation, energy demand, comply with the comfort requirements or uses eco-friendly materials. A guarantee of good design and object’s execution is certification, which will indicate assessment of the selected parameters, standard in which the building was constructed.

The certification process may include both the process of the concept and the design and construction process, and the use of the object.

Around the world there are certificates – environmental assessment of buildings. One of the most important is the LCA method (life cycle assessment). This method assumes the building assessment throughout the life cycle. The processes of acquiring row materials, productions of building materials and use of the buildings are significant consumer of natural resources and one of the main emitters of harmful substances. Although it is not possible to completely eliminate the negative impact of the building on the environment, such tools as LCA allow to minimize this impact. Rational use of resources and raw materials is possible through a detailed analysis of the impact of proposed building on the man, the climate and the environment.
The analysis is carried out both for the entire building's life cycle as well as distinguishing between the different stages of its life: the production of construction materials, building erection phase, operation of building and its demolition, which makes it one of the most methodically advanced tools for environmental assessment. The analysis takes into account the most important environmental indicators, the green house effect, soil and water acidification, photochemical ozone synthesis ability, capacity to consumption of fresh water.

Other certification methods developed in different countries are considerably simplified to the LCA [2]. All are listed in table 1. Presented evaluation systems as the main criterion shall assess the building impact on the environment, partly include social and economic aspects. Table 2 shows the main evaluation criteria which are taken into account in the various certification system.

Table1. Developed for different countries environmental assessment [1].

System	**Environment**	**Social aspects**	**Economic aspects**	**under development**
EU Flower	YES	NO	NO	under development
BREEAM	YES	Partly	NO	for environmental assessment
LEED	YES	Partly	NO	the US is not adapted to the conditions of the EU
DGNB	YES	YES	Partly	Only Germany
SBTool	YES	YES	YES	research
CASBEE	YES	YES	YES	Only Japan

Table2. Developed for different countries environmental assessment.

System	**Country**	**Rated issue**
BREEAM	U.K.	management comfort energy transport water consumption materials land use ecology waste
LEED	U.S.A.	sustainability the effectiveness of water management energy and atmospheric pollution materials and resources indoor environmental quality innovation and design process
GBTool	iiSBE	consumption of resources environmental burden Indoor environmental quality quality of service economy management transport and communication
CASBEE	Japan	quality of the building internal environment quality of service external Environment environmental burden energy raw materials and consumables external Environment

All of the presented environmental assessment systems require a long period of time to prepare the final version of the certificate, because are involved in each of the stages: design, erection and use of the buildings.
Each of the systems has been developed for the climatic conditions of the concerned country (United Kingdom, United States, Germany, Japan), including not only the local climate, but also the database available for the given country of construction materials, whether specific requirements for buildings.

II. Malopolska Certificate Energy efficient Buildings (MCBE)

Experts of the Malopolska's Energy Efficient Construction Center (MCBE) with cooperation with Malopolska's Energy Efficient Construction Laboratory (MLBE) recognizing the need for certification of buildings developed MCBE Certificate. This document confirms the high power characteristics of a building, its reliable performance and minimal impact of building on the environment, and residents comfort and health.
The certification process begins right from the design stage, where the MCBE team helps to determine the design parameters of the future investment. During erection experts

of the Cracow University of Technology verify that the building is made correctly, in accordance with construction and design assumptions and while building is used will be examined for correctness of proper execution and the quality of the internal environment. Additionally there will be specified carbon footprint of the building, which will determine how much the building impacts on the environment. The building that meets the criteria of the MCBE Certificate only positives for the user – from health, through better housing comfort, protection of the environment up to the specific savings for the owner. Such a building is characterized by a much less demand on the energy required for heating and ventilation as compared with traditional technology, largely uses the heat produced from a variety of renewable energy sources, uses natural light (Fig 2).

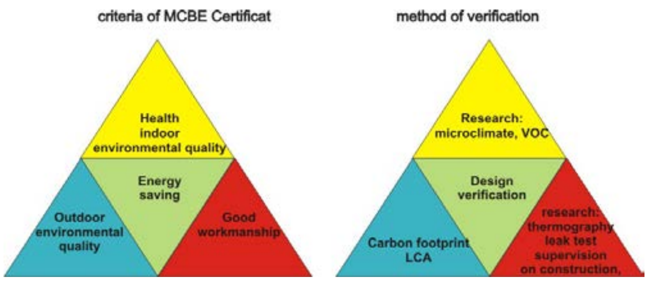

Fig.2 MCBE Certificate Criteria.

III. Design assumptions of MCBE Certificate

To adopt a correct assumption about establishing the level of the energy parameters and parameter limits for heat protection of buildings for the purpose of the MCBE certificate, there was a series of energy simulation carried out. Simulations included calculating the energy demand for heating, the preparation of domestic hot water, cooling (if there is cooling installation in the building) and lighting (in the case of public buildings) for various types of buildings. As a basis of calculation for the buildings certification in Malopolska province, we used a method adopted in the Regulation of the Minister Of Infrastructure And Development dated June 3rd 2014, a methodology for the calculation of the energy performance of the building and dwelling.

The requirement calculation for energy demand, primary and final was made on the basis of the monthly balance sheet method in accordance with the methodology for calculating the energy performance of the building. [9-23].

Weather data

Malopolska province is diverse in terms of climatic conditions. There are three different climate zones in accordance with the standard PN-80/B-02403. MCBE experts assumed, that the MCBE certificate will take into account different climatic conditions of Malopolska. The figure below shows the breakdown of the climate zones (fig 3).

Fig 3. Climate zones in Malopolska.

Malopolska province is diverse in terms of climatic conditions. There are three different climate zones in accordance with the standard PN-80/B-02403. MCBE experts assumed, that the MCBE certificate will take into account different climatic conditions of Malopolska. The figure below shows the breakdown of the climate zones.

The calculation uses the weather data posted on the website of the Ministry Of Infrastructure And Development for meteorological stations representing the areas of Malopolska province: Krakow III climate zone, Nowy Sacz climate zone IV and Zakopane climate zone V (Fig 3). Meteorological data include the average multi-annual values of the external temperature, and solar radiation for each month of the year.

Calculations were made for the following types of buildings:
-single family (in addition to phase 1-calculation according to current regulations, checking classes)
− three single-family houses of different A/V shape factor, one store building, building with occupied attic, two store building with unoccupied attic,
-multi-family – four multifamily buildings with different A/V shape factor,
-residential with services – one multi-family building with services on the ground floor,
-public building – two office buildings of different A/V ratio, two school buildings of different A/V ratio and one building with more floor height for example. Sports Hall
-commercial – two commercial buildings with different A/V ratio.

Table 3. Geometric data of analyzed buildings.

Model of building	**Usable area**	**The cubic capacity with controlled temp.**	**A/V**	**The degree of glazing in exterior walls**
	m2	m3	1/m	-

Single-family 1	150	367,5	0,66	0,09
Single-family 1 with garage	178,9	448,6	0,63	0,07
Single-family 2	122,1	310,9	0,73	0,09
Single-family 3	149,2	356,3	0,8	0,08
Multi-family 1	5286,7	13713,7	0,32	0,23
Multi-family 2	2627,3	6581,7	0,35	0,20
Multi-family 3	1956,1	4996,9	0,44	0,18
Multi-family 4	966,53	2404,8	0,47	0,16
services part	1956,1	5175,9	0,44	0,18
Living part	1480,3	3749,2		
Services part	475,8	1426,7		
Office 1	4952,8	17209,2	0,10	0,60
Office 2	11031,4	38873,4	0,12	0,59
Sports hall 1	633,4	2620,4	0,41	0,06
Merchant 1	10062,1	83313,9	0,16	0,00
Merchant 2	2261,2	13197,4	0,26	0,06
School 1	2651	10668,7	0,18	0,07
School 2	2663,7	11156,4	0,31	0,07

In the analysis adopted in all buildings following values of the coefficients heat transfer through external walls , which is set in the table below (Tabl. 4).

Table 4 summary of coefficients heat transfer through external walls

The type of partition	**Coefficient heat transfer U**
	[W/m2K]
Externall wall	0,15
ground floor	0,20
The ceiling above unheated space	0,15
The roof above unheated space	0,25
Windows	0,9
Eksternal walls	1,3

Heating system

The calculation of the final and primary energy demand is performed for two commonly used solutions. The first of these is the installation of central heating systems supplied with gas furnace while the second installation is supplied with the district heating. The tables below show the partial efficiency used in calculations.

Ventilation system

The analysis includes two types of ventilation: natural and mechanical ventilation intake-exhaust, with heat recovery efficiency up to a maximum of 80%. The tightness of the building in the case of natural ventilation is n50 = 3,00 1/h in the case of mechanical ventilation n50 = 1.5 1/h. In the technical conditions is written that in the building of up to 9 stories gravitational or mechanical ventilation may be used. In case of higher buildings shall be used mechanical exhaust ventilation or intake-exhaust ventilation. Therefore, in the multi-family buildings 1 and 2 was used instead of natural ventilation mechanical exhaust ventilation. The tightness of the building in case of exhaust ventilation is n50 = 1.5 1/h.

Hot water preparation system.

The calculation of the final and primary energy demand was made for two commonly used installation solutions. The first of these is the installation prepares the hot water out of gas furnace and the second is the municipal district heating network. Tables below show the partial efficiency applied in the calculations.

Non-renewable primary energy factors

Non-renewable primary energy factors are in accordance with the regulation on the production of the energy performance of the building and data given on the pages by the district heating companies and are as follows:
– network gas = 1,1;
– energy eclectic w = 3.0;
- MPEC-Krakow 2013w = 0.62;
- New Sacz w MPEC = 1,3;
- Geotermia Podhalańska w = 0.39.
As a result of the carried out analysis assumes the following values for buildings that meet the assumptions of the energy-saving Buildings Certificate

Table 5 Parameter values for Malopolska energy-efficient Building certificate, and verification method.

Parameters		**Method of verification**
Coefficient U [W/m2K]		
External walls: a) $t_i \geq 16^oC$ b) $8^oC \leq t_i < 16^oC$ c) $t_i < 8^oC$	0,15 0,45 0,90	architectural and building documentations
External Roofs a) $t_i \geq 16^oC$ b) $8^oC \leq t_i < 16^oC$ c) $t_i < 8^oC$	0,15 0,30 0,70	architectural and building documentations

Parameters		**Method of verification**
Ground floors a) $t_i \geq 16^oC$ b) $8^oC \leq t_i < 16^oC$ c) $t_i < 8^oC$	 0,20 1,20 1,50	architectural and building documentations
External windows a) $t_i \geq 16^oC$ b) $t_i < 16^oC$	 0,9 1,4	architectural and building documentations
External doors	1,3	architectural and building documentations
Energy consumption [kWh/m^{2}a]		
Coefficient EP (Primary Energy)	70	energy performance
Coefficient EU (Use Energy) single family building	60	energy performance
Coefficient EU (Use Energy) multi family building	40	energy performance
Research „in situ"		
Loak test	Yes	In situ
Air quality	Yes	In situ
Thermovision	Optional	In situ
Thermal comfort	Optional	In situ

The value of the indicator of Energy Use of a building which satisfies the assumptions of the MCBE Certificate, taking into account the climate zones in Malopolska

Table 6 Reference indicator of energy demand for heating and cooling EU'ref taking into account of the correction value factor related to the location of the building ΔE

Type of building	**Reference indicator of primary energy demand $EU'_{ref} = EU_{ref}\Delta E$ [kWh/(m^{2}rok)]**			
	Kraków	Nowy Sącz	Tarnów	Zakopane
Single-family building	60,0	58,8	56,4	74,3
Multifamily buildings	40,0	39,2	37,6	49,5
single-family houses with a system of cooling	62,5	61,3	58,8	77,4
multi-family buildings with the installation of cooling	42,5	41,7	40,0	52,6
public buildings	60,0	58,8	56,4	74,3
public buildings with the installation of cooling	65,0	63,7	61,1	80,5

The value of primary energy ratio of the building which satisfies the assumptions of the MCBE Certificate, taking into account the climate zones in Malopolska

Table 7. Primary energy demand reference indicator to heating and cooling EP'ref taking into account of the correction value factor related to the location of the building ΔE

Type of building	**Reference indicator of primary energy demand $EP'_{ref} = EP_{ref}\Delta E$ [kWh/(m^{2}rok)]**			
	Kraków	Nowy Sącz	Tarnów	Zakopane
Single-family	70,0	68,6	65,8	86,6
Multi family	70,0	68,6	65,8	86,6
single-family houses with a system of cooling	75,0	73,5	70,5	92,8
multi-family buildings with the installation of cooling	75,0	73,5	70,5	92,8
public buildings	120,0	117,6	112,8	148,5
public buildings with the installation of cooling	145,0	142,1	136,3	179,5

IV. Malopolska Laboratory of Energy Efficient Constructions

The first certified Certificate object is a super innovative building - Malopolska Laboratory of Energy Efficient Constructions.

It is a building erected in the center of Cracow, adapted to existing buildings.

The building is realized in pole-plate technology.

Geometric parameters:

-The usable area of the building: 1,039.39 m^2

-The cube of the building: 5 050,41m^3

-Number of floors of the building: 5

-Building-height: 19.24 m

-The geometry of roof - flat roof

ISBN: 978-1-61804-325-2

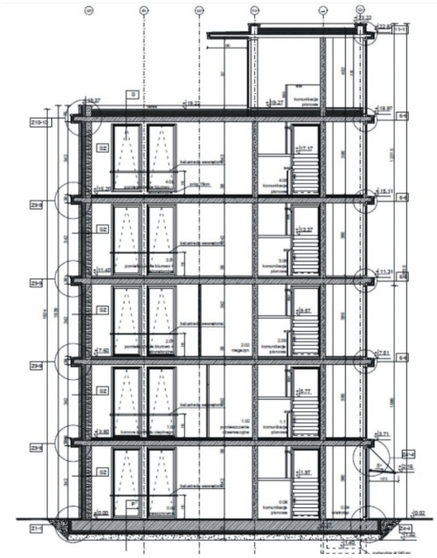

Fig.4. Cross-section of the MLBE building

MLBE building is fully automated and it is a laboratory to test energy-saving technologies "in situ".

MLBE is equipped with the research systems:
- 6 independent heating sources
- 14 independent climate zones
- 3 thermal wells (125 m)
- 2 ground heat exchangers
- 3000 sensors

Table 8,9. Thermal parameters MLBE:

The type of partition	**Coefficient heat transfer U**[W/m2K]
Externall wall	0,12
Ground floor	0,10
Roof	0,13
Windows	0,70
External door	0,80

Energy consumption coefficient	**[kWh/m^{2}a]**
EP	119,6
EU_{H+W}	13,6

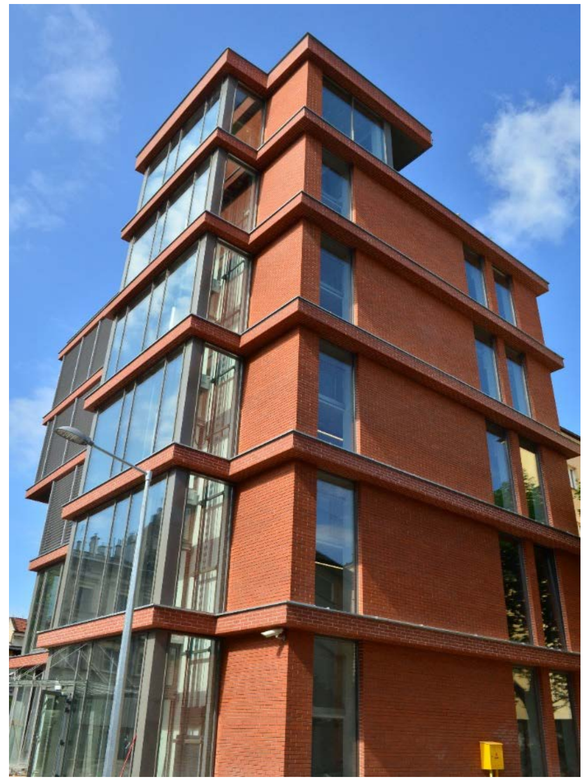

Fig.5. View of the building MLBE. Laboratory "in situ" energy efficient technology.

V. Summary

Whether the building is energy-efficient is decided by many factors. First, the design of the building must be made in accordance with the principles of integrated design. Appropriate design assumptions must be taken on the heat transfer coefficients and energy consumption. Just as important is the quality of the materials used for its construction and execution stage care. A comprehensive review of the whole process, both the executive and the design is a difficult task for the investor, because it requires knowledge of many engineering disciplines. Certification of energy-efficient buildings is a necessary part of the verification of the buildings for adequate heat protection and comfort of the rooms.

References

[1] LEED Certyficate http://www.usgbc.org/leed
[2] LCA http://www.gdrc.org/uem/lca/lca-define.html
[3] Fergus N, Humphreys M."Adaptive Thermal Comfort"
[4] Dylla A "Fizyka cieplna budowli w praktyce"PWN.
[5] "Standards for Thermal Comfort, F.Nicol", M. Humphreys, O. Sykes, S. Roaf, ISBN 0 419020420 2
[6] "The Future of Thermal Comfort in an Energy-Constrained World", Tim Law, ISBN 978-3-319-00148-7
[7] "Human Thermal Environments", Ken Parsons, ISBN 978-1-4665-9599-6
[8] "Progress in Exergy, Energy, and the Environment", Ibrahim Dincer, Adnan Midilli., Haydar Kucuk, Volume 1, Volume 2, ISBN 978-3-319-04680-8

European and Polish standards and design guidelines, in particular:

[9] Regulation of the Minister of Transport, Construction and Maritime Economy amending the regulation on technical conditions to be met by buildings and their location (Journal of Laws of 2013., Pos. 926)
[10] European Parliament and Council 2010/31 / EU of 19 May 2010. On the energy performance of buildings (recast) (Journal of Laws EU L 153, 18.06.2010, p. 13)PN-EN 13829:2002
[11] "Regulation of the Minister of Infrastructure ', Journal of Laws Of 2002 No. 75, item. 690, on the technical requirements to be met by buildings and their location
[12] Regulation of the Minister of Infrastructure of 12 April 2002. On the technical requirements to be met by buildings and their location (Dz. U. No. 75, item. 690, as amended. D.),
[13] Regulation of the Minister of Infrastructure and Development of 3 June 2014. On the methodology for calculating the energy performance of the building and dwelling or part of the building constituting an independent whole technical-utilitarian and the preparation and design of energy performance certificates,
[14] Regulation of the Minister of Transport, Construction and Maritime Economy of 25 April 2012. On the detailed scope and form of construction (OJ 2012, pos. 462)
[15] Regulation of the Minister of Economy of 10 August 2012. On the detailed scope and method of preparation of energy efficiency audit, the audit card template energy efficiency and energy savings calculation methods (OJ 58 2012, pos. 962)
[16] Regulation of the Minister of Infrastructure of July 5, 2013. (Dz. U. 926, item 2013) amending the regulations on technical conditions to be met by buildings and their location,
[17] Standard PN-EN ISO 6946 “Building components and building elements. Thermal resistance and thermal heat transfer. The method of calculation”
[18] PN-B-03421:1978 – „Ventilation and air conditioning - Calculation parameters of indoor air in rooms intended for permanent human habitation "
[19] PN-EN ISO 13789:2008 – "Thermal performance of buildings - heat transfer coefficients by transmission and ventilation - The method of calculating"
[20] PN-EN ISO 14683: 2008 - "Thermal bridges - Linear heat transfer coefficient - Simplified methods and default values"
[21] software supporting the design and analysis of energy in the building industry,
[22] Requirements for programs NF15 NF40 the National Fund for Environmental Protection file:///C:/Users/mcbe/Downloads/wytyczne_do_pp%20(2).pdf
[23] priority program content, technical guidelines and the definitions and concepts used in the provisions of the program NFOŚiGW LEMUR.

PhD Malgorzata Fedorczak-Cisak

Director of the Malopolska’s Center of Energy-Efficient Construction. A graduate of the Cracow University of Technology. Represents the scientific field of building physics and energy efficient construction. Expert actively participating in the meetings of the advisory and opinion of the representatives of the Malopolska Regional Government, the effect of which is to develop the provisions of the Malopolska Region strategy and long-term development of the Malopolska take into account the development of measures to improve energy efficiency especially in the area of construction. Expert working actively in the work to implement EU Directives, inter alia, for the development and implementation of the definition of near zero energy buildings in Poland. She is a member of the Polish Committee for Standardization, the Association of Energy Auditors and expert appointed to evaluate international projects related to the area of energy saving measures.

PhD arch. Marcin Furtak

Director of the Malopolska’s Laboratory of Energy-Efficient Construction. A graduate of the Cracow University of Technology. Represents the scientific field of architectura and energy efficient construction. Expert actively participating in the meetings of the advisory and opinion of the representatives of the Malopolska Regional Government, the effect of which is to develop the provisions of the Malopolska Region strategy and long-term development of the Malopolska take into account the development of measures to improve energy efficiency especially in the area of construction. Expert working actively in the work to implement EU Directives, inter alia, for the development and implementation of the definition of near zero energy buildings in Poland. She is a member of the Polish Committee for Standardization, the Association of Energy Auditors and expert appointed to evaluate international projects related to the area of energy saving measures.

ISBN: 978-1-61804-325-2

Multi-level integrated process control and energy management on the example of the Malopolska Laboratory of Energy Efficient Building

A. Romańska-Zapała

Abstract — Presented in this paper Malopolska Energy-Efficient Building Laboratory (MLBE) of Cracow University of Technology provides the ability to perform research in the field of improving energy efficiency in the building industry while taking into account to ensure comfortable conditions. The basic installations and technical equipment to ensure proper functionality of the building MLBE will be discussed. Examples of the type of "in situ" measurements that can be done using building technology and integrated process control system equipped with a BMS in the context of the research for energy-efficient installation solutions.

***Keywords*—**energy-efficient building, integrated control systems, Building Management System (BMS), optimal process control, "in situ" measurement of LonWorks technology**.**.

I. Introduction

Under Polish membership in the European Union there were possibilities of financing a number of construction projects from EU funds. Thanks to financial support, a number of modern buildings with diverse functionality were built. Innovative technologies help to reduce the operating costs of these objects. After the first phase optimistic use of modern technical solutions, installation and material came reflection that often this type of approach is not the best.. Investors began to prudently choose the solutions. There were reports supported research that the use of certain technologies are not optimal.

Poland is obliged to introduce regulations for building with low energy consumption [1].

Currently, the implementation of Directive 2010/31 / EU [2] on the energy performance of buildings causes that special attention is given to issues related to the energy consumption of buildings. User requirements for thermal comfort newly constructed buildings grows. It all makes energy saving solutions are being sought to enable a high comfort while providing the lowest possible investment costs.

It is therefore necessary to conduct scientific research "in situ" in the real scale in order to guarantee optimum configuration of devices and systems used in the selected building.

Nowadays it is the rapid development of integrated process control systems in buildings. In Poland issue of standardization in the field of building automation has been ordered.

Less and less problems arise in the case of the need to integrate automation systems, using various communication standards.

In accordance with current legislation, the use of building automation for buildings with low energy consumption is not obligatory.

In special cases it is not possible to achieve some heat protection requirements of the building without the use of a properly configured process control system.

II. Functionality of Integrated Automation System

Computer simulations on the building structure or functioning of its individual installations, performed in computer programs DesignBuilder type, in the context of limiting its energy consumption are very useful tool.

MLBE –LESSER ENERGY-EFFCIENT CONSTRUCTION LABOARATORY

Construction and equipment of the Malopolska Laboratory of Building Energy-Efficient (MLBE) were financed by the Project MRPO.05.01.00-12-089 / 12-00 - funded under the Malopolska Regional Operational Programme for the years 2007-2013; Priority Axis 5 - Krakow Metropolitan Area; Action 5.1 - Krakow Metropolitan Area as an important junction of the European Research Area, value of the Project is approx. 20 million - for 2014 year.

The Laboratory is the first place in Poland to do such large-scale research on energy efficient technologies and the comfort of the occupants of low - energy buildings. This interesting project gives the University the leading position in the sector of energy efficient building.

A. Romańska-Zapała pracuje w Małopolskim Laboratorium Budownictwa Energooszczędnego Wydziału Inżynierii Lądowej na Politechnice Krakowskiej, Polska, (corresponding author to provide phone: 0048-12-628-30-62;fax: 0048-12-628-30-61; e-mail: a.romanska@pk.edu.pl).

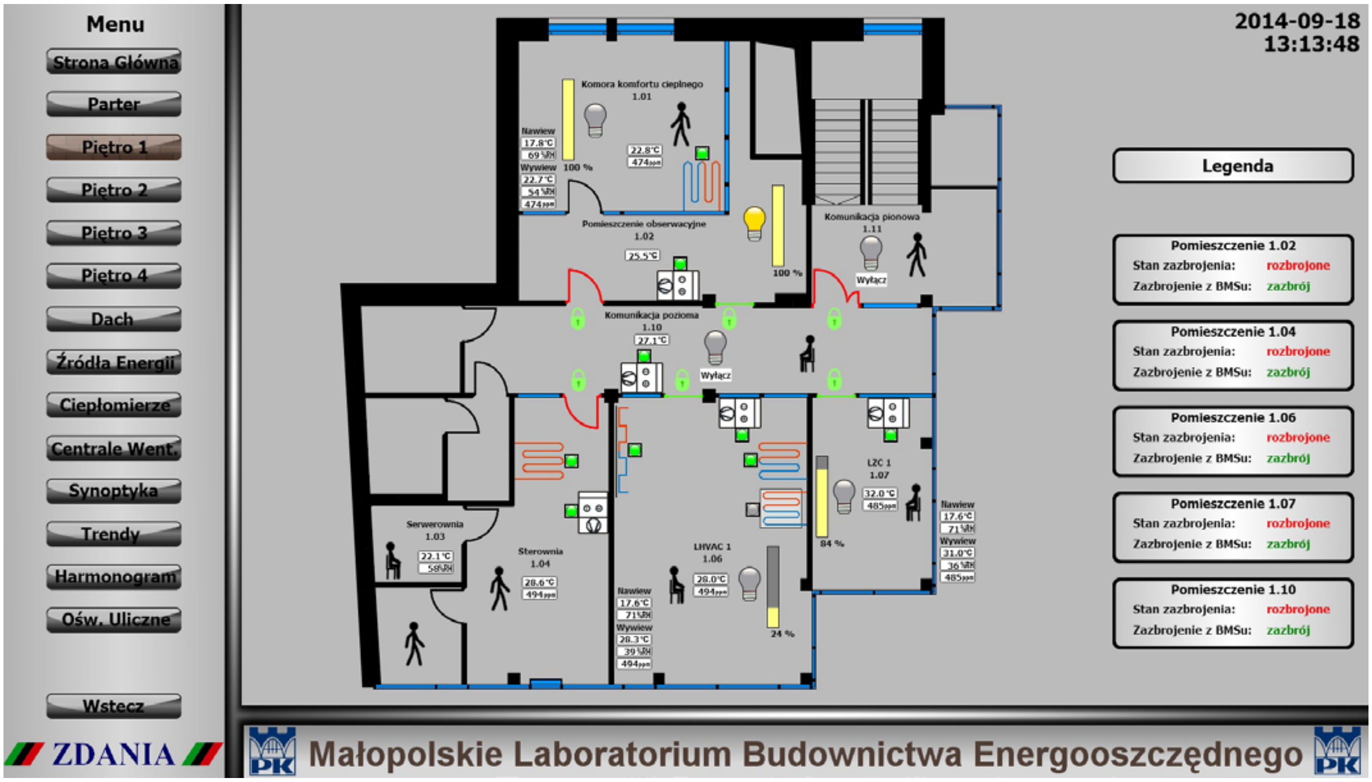

Fig.1. A plan of the first floor of MLBE building

However, in the case of multivariate analysis processes with respect to energy consumption and optimal work of individual systems such as ventilation, heating, lighting, and air conditioning, this type of computer calculations are not sufficient.

If comfort is also taken into account in this process, to perform correct analysis and assessment of parameters characterizing the building the "in situ" measurements are also needed. It was also the justification for the idea of creating the Malopolska Energy Efficient Building Laboratory of Krakow University of Technology. The construction was completed in September 2014.

The Laboratory is the first place in Poland to do such large-scale research on energy efficient technologies and the comfort of the occupants of low-energy buildings. This interesting project gives the University the leading position in the sector of energy efficient building.

The innovative building is situated on the University campus in Warszawska street. It has 5 floors (built area is 258,41m2, utility space is 1039 m2, the front elevation is 17,02 m wide and 19,24 m high). It is a slab and column construction with self-supporting external walls and glass elevations.

Owing to this, materials and construction can be changed to meet research needs.

Inside there is 14 climate and energy zones where researchers study properties of materials and technologies in relation to climate conditions.

The object has an intelligent control system and relies on varied systems of heating and ventilation. Energy supply also comes from different sources including renewables.

All installations such as heating, cooling and ventilation have meters so as to allow current monitoring. The object comprises of 14 thermal zones working independently of one another so as to make their comparative analyses possible.

The laboratory is supplied with specialist research equipment for testing and implementing new technologies, material and construction solutions and installations.

Thermal comfort of the occupants is studied and analyses of air quality are made for the tested technologies.

The integrated automation system used in this building is based on the technology Lon Works. The combination of all installations (see Fig. 1) allows remote monitoring and control of all devices including heating and cooling. The integrated process control system includes both automation systems, control and data acquisition (including lighting, heating, air conditioning, ventilation, and monitoring of measurement systems) and safety systems (including systems intruder alarm and access control system) . The integration of automation systems with security systems can increase building energy efficiency through the implementation of process control strategies in different rooms depending on the current degree of utilization of these rooms by users.

Network infrastructure system was developed on the basis of several data transmission standards such as IP, BACnet, LON, MBus, Modbus, Dali, OPC, combining logical systems automation equipment rooms, access control, intruder alarm, media monitoring, and technical devices and drivers for central ventilation and air conditioning. Ability to work using the most popular standards allows to research facilities and technology with almost no restrictions.

ISBN: 978-1-61804-325-2

The main goal of the integrated control system is to use the signals from all available sensors and corresponding control depending on the data obtained from these sensors. To facilitate the the work of users monitoring data are presented using visualization system. Systems created in addition to the present values of the parameters that are important for the process control gives full control over installations. The visualization of the flow of control is built in such a way that each person after a brief training could use this system. Of course, for security reasons workstations, visualization systems are located in places inaccessible to random people, and access is further protected by passwords and access levels. The workstation is not the control unit, but the device through which you can reprogram, view job status, control the system. To ensure the functionality of individual installations systems are connected with BMS (Building Management System). The building management system (installations) along with sensors arranged on the object, detectors (including specialist measurement devices) creates a so-called intelligent building. Such a structure collecting data element of the system can adjust system parameters to the environmental conditions which currently occured inside and outside of the controlled object. The solution is adjusted primarily to maximize comfort and functionality, in addition to minimizing costs associated with maintenance of the building.

The system includes three levels - the master level (its task is to support operator, collection, processing and data collection), the controllers level (implementation of control algorithms of individual subsystems such as lighting heating, air conditioning, ventilation, etc.) and object level, including sensors and implementing components related with tested technology.

Devices of master level and of the drivers level are connected by separate computer network-based on structured cabling (Ethernet IP). Object devices are connected with controllers or via direct connections with individual inputs and outputs drivers, or by local fieldbuses data, specific to the industry for example heat meters are connected to M-bus, the ventilation control / air conditioning fieldbus BACnet MS / TP, lighting elements system are connected by DALI fieldbus , and automation components and, among others, parameters from weather stations or heat pump control was carried out using LON bus. Sequentially Modbus protocol was used in the process control unit AWS and heat pump air-glycol.

Master management level (BMS) realizes operator station, which acts as a server system automation, control and data acquisition (USAD). The system automation, control, data collection and management of the building Malopolska Laboratory of Building Energy-Efficient is a distributed control system (DCS), which in addition to the standard functions performed by the modern BMS enables research in the range energy efficiency of different technologies used in building installations.

The BMS MLBE thanks to a number of international data transmission standards found in building automation systems, it is possible to turn on the system and examine the work of external devices. Standard base system is PN-EN ISO 14908 (LON) [4].

The system integrates control of all building technological installations (air ventilation / air conditioning, heat pumps, cooling unit, fan coil units Room &, wall heating, underfloor heating, ceiling heating, chilled beams, variable air flow regulators). This functionality can be expanded by adding additional devices planned.

The automation system integrated object-level building security systems such as the system intruder alarm and access control system. This solution will allow to carry out research on the impact of integration on the energy efficiency of the building in accordance with DIN EN 15232 [3].

The control system uses modern, programmable automation servers LINX-121 / LINX-151, Lioba-180 modules, modules IBAS drivers L-DALI and touch panels L-VIS.

The room automation and monitoring system was carried out on the basis of automation servers which are enable to communicate with object level devices. Equipments that are used belong to the group of freely programmable in accordance with IEC 61131-3, which allows object-oriented data integration from various sectoral fieldbuses.

The software L-WEB allows direct access to the data and functions of automation servers from the operator station and the external terminals. Part of the system responsible for the implementation of safety functions (burglary and access control system) communicates directly with the master server level via a router control network.

In the laboratory rooms freely programmable controllers are applied in order to implement any control strategy within a given space. In selected areas of laboratory touch panels that allow to preview of the current parameters of the room (eg temperature, humidity, air velocity on supply and exhaust, the state apparatus), to control of individual local systems: lighting (internal and external - street lighting), for heating / cooling and to ask the required parameters, were installed.

On the roof of the building and on three sides of the world weather stations with control module are located. In some rooms it is possible to carry out control in relation to the supply air temperature, extract air or room temperature. All the measured parameters and modulation are made available and archived in the system USADA.

In selected places heat / refrigeration installation system is used to measure the consumption of heat/cold. Heat meters with M-Bus interface were used for measurements. They provide the ability to read parameters such as flow rate, temperature control and return temperature.

Integrated master level control system was implemented using three computer stations. Each of them has a specific function. The first is the system operator station USADA, which includes the following software - MSDE SQL Server, Software Lon Maker (for example system configuration is shown in Fig. 2), NL-OPC Server, L-LOGICAD (see fig. 3) and L-WEB. At the second station were installed LabView software, which is used to manage research experiments. The third computer includes specialist software dedicated to specific research.

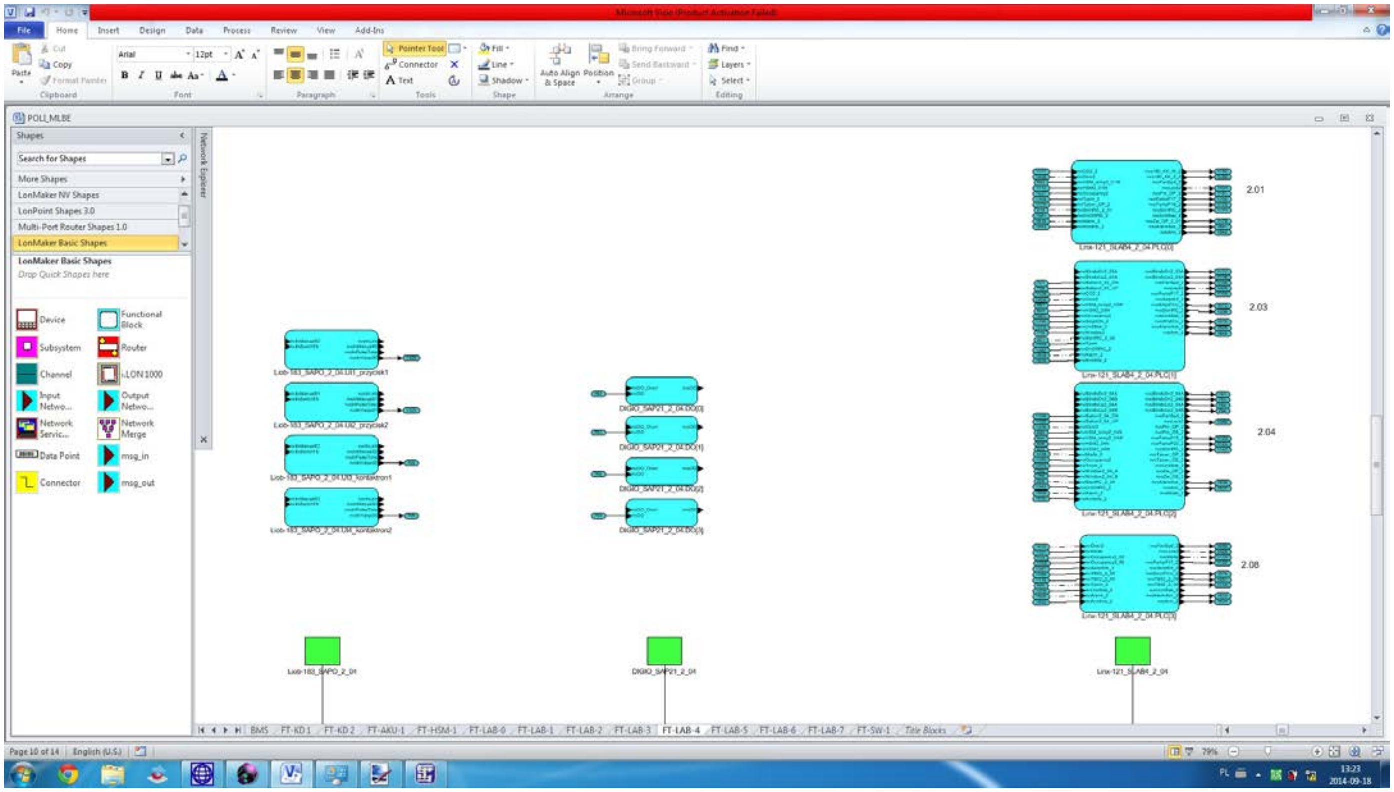

Fig. 2. Example of system configuration using the software Lon Marker

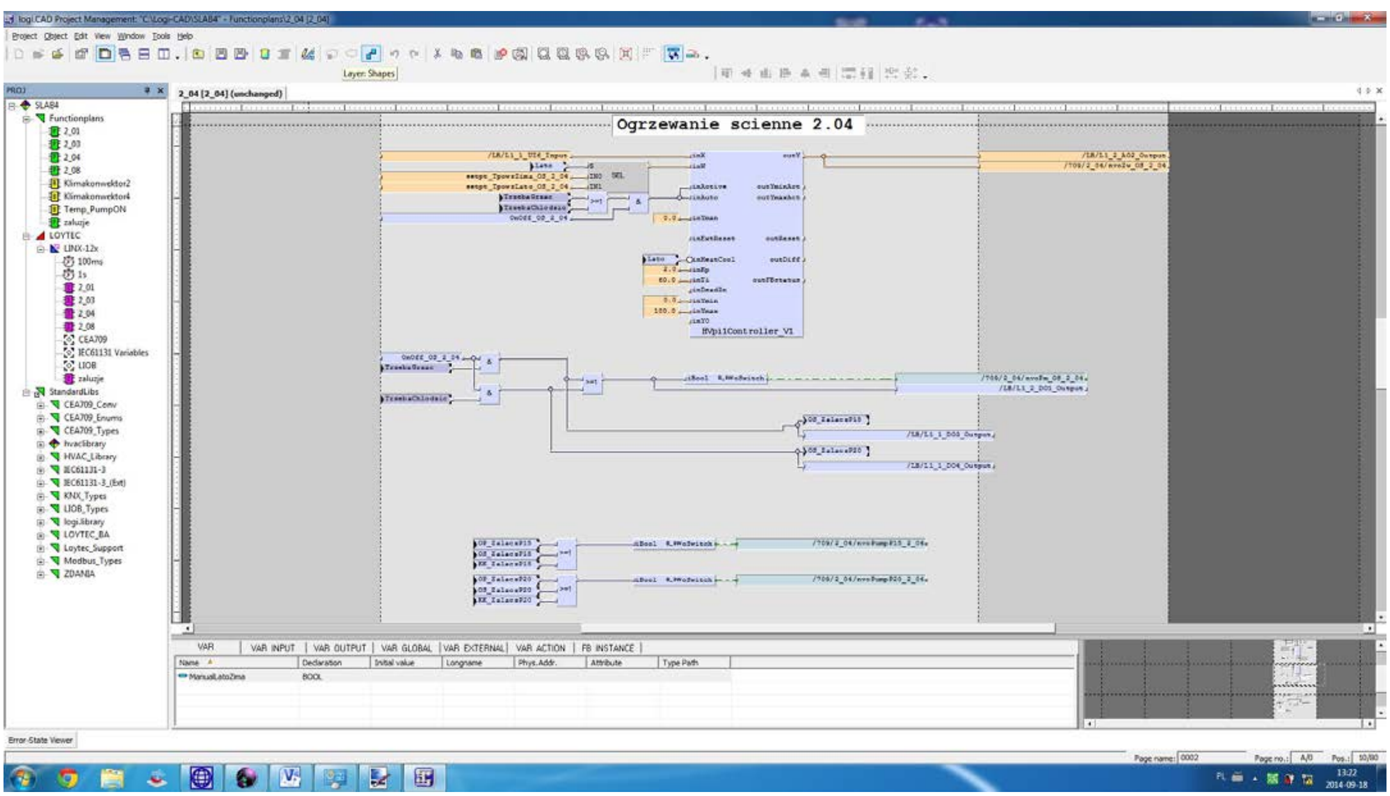

Fig. 3. Example of system configuration using the software LogiCAD

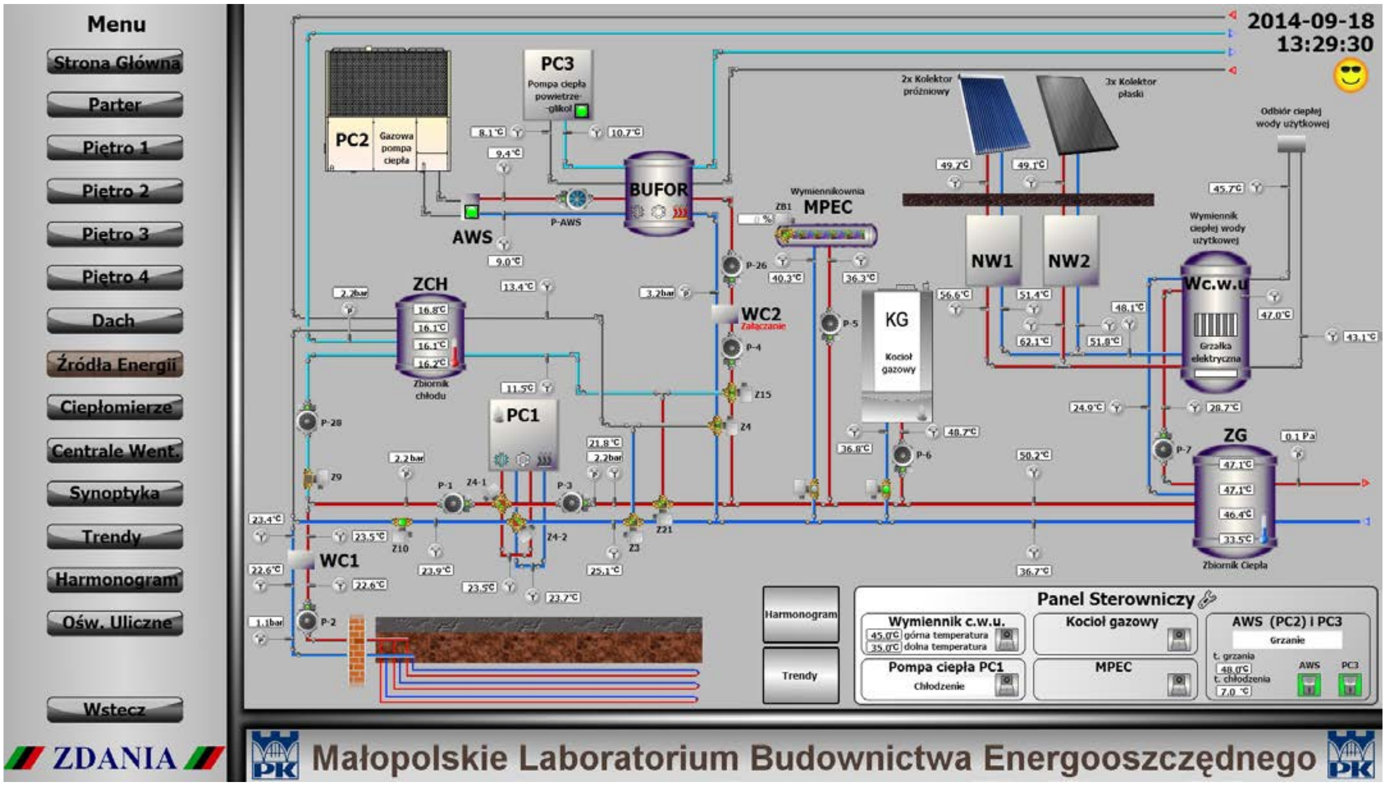

Fig. 4. The control panel work sources of heat and cold

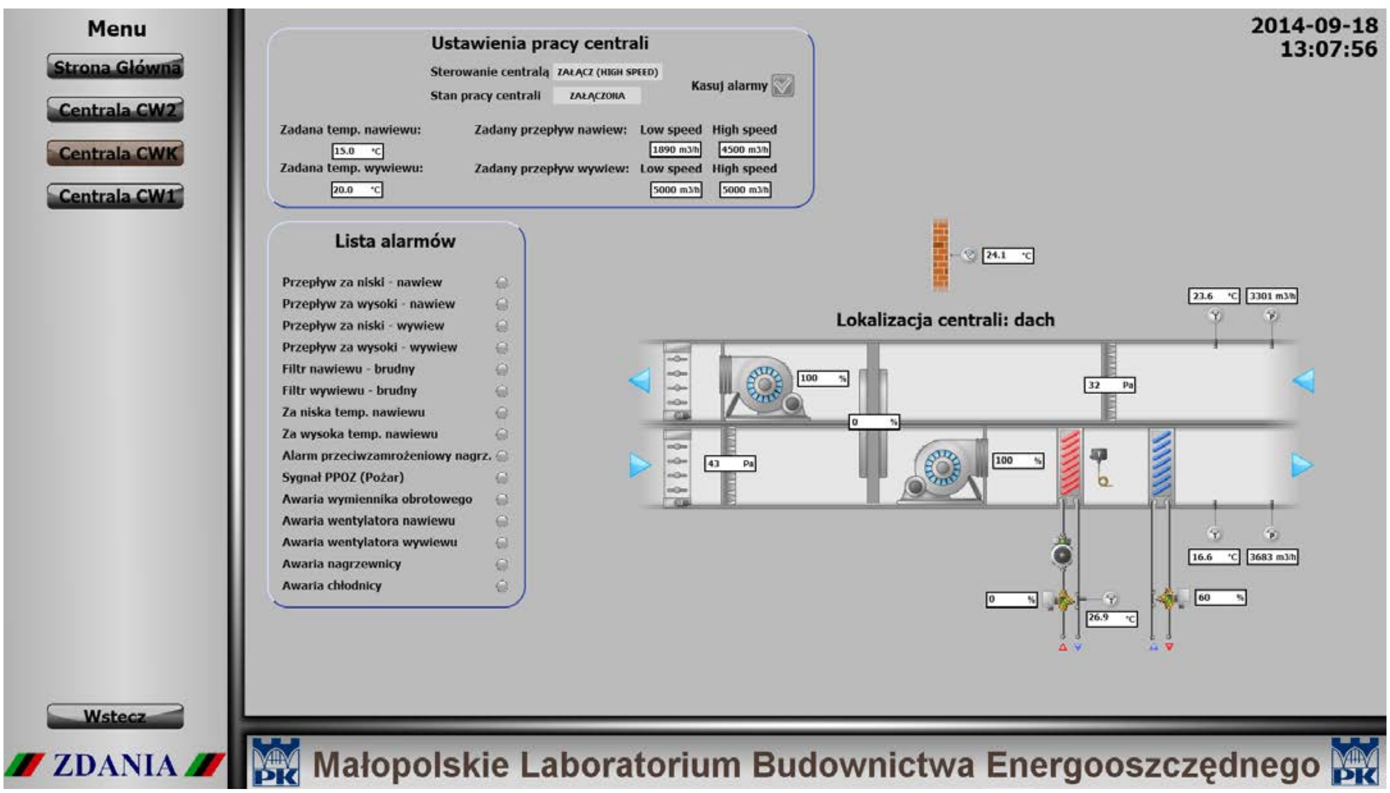

Fig. 5. Control panel operation of the ventilation system

programs such as ANSYS, DesignBuilder and software, presented in the previous section.

Then, after evaluation of obtained results, parameters of examined system are selected and the schedule of "in situ" research shall be established.

In Figure 4 shows a control panel work of individual sources of heat and cold, installed in the building MLBE. It is possible to free programming in a wide range and selection of a parallel mode of operation of the equipment. As another example, Figure 5 presents the control panel ventilation.

It is possible to configure any operation of the ventilation unit according to the criterion of control.

In order to make an objective assessment of the analyzed parameters, measurements are carried out in two identical rooms. One of them acts as a room with assumed control parameters.

Application during the research an integrated process control in LonWorks technology enables repeatablness of experimental conditions and automatic data collection in SQL database.

In addition, in some rooms it is possible to connect additional devices which are not elements of the existing building infrastructure, such as fan coil units, or various types of heating or cooling devices. Additionally, in two rooms used for research on the integration of building automation systems, made in a variety of corresponding standards, KNX bus system is installed. Using these hardware capabilities, the real becomes conducting research in all basic standards on the effectiveness of building automation devices in a very wide range.

After carrying out cycle of measurement, the obtained data are processed using programs such as STATISTICA in which numerical methods are used to search relationship between the measured parameters. The results and statistically significant dependencies are the basis for the correction of process control algorithms.

The final effect of such actions is to develop optimized process control algorithms, and subsequently to carry out an atempt to implement self-learning algorithms.

IV. FUNCTIONAL PROGRAM OF „IN-SITU” RESEARCH

Performed experimental studies are carried out in natural conditions typical for using the building in urban areas monthly, quarterly and annual.

Used in MLBE building integrated control system allows, among others, the following examples of controls of selected process:

- Control of VAV systems as a function of CO2 - in selected rooms of air flow control is based on measurement of carbon dioxide concentration. The measurement is carried out by sensors mounted on the CO2 exhaust channel from the room. Increase of the concentration of CO2 in the air above the 700 ppm increases the flow of air in the room through the activation of VAV air supply and exhaust with taking into account existing legislation [5, 6, 7].
- lighting control system administration and DALI system – communication lighting is controlled with buttons or dependent on the presence of motion detectors. You can choose one of several available operating modes of lighting: "attached", "disabled", "the motion detectors". For laboratory, teaching and office rooms lighting fixtures with adjustable light intensity were used. In the conference rooms luminaires with DALI system which gives the possibility to change the intensity of light were used. Intensity control takes place in these rooms from the touch panel. Selection of control is also possible from the BMS operator station.
- blind control - the building is equipped with external blinds controlled by local switches in the rooms, the touch panel or BMS station. External blinds are from 2 to 4 floor.
- ceiling, wall and floor heating / cooling - temperature stabilization of medium in relation to the set room temperature.

These are only examples. The scale of the research is much wider.

V. CONCLUSION

At present integrated process control systems are used in buildings more often. Both in new buildings and in the case of modernized building are introduced building automation components. The rapid development of information technology and changes in the legislation obliging investors to the use of energy-saving materials and technologies, meant that building automation is an important element of energy-efficient construction

In addition, to ensure adequate comfort of use of buildings and maintenance of energy consumption at a certain predetermined level may be easier in the case of application of advanced building automation solutions.

There is a need for scientific research into innovative technical solutions in an independent and objective research by specialized units. This is also the role of the newly created Malopolska’s Laboratory of Energy Efficient Building.

REFERENCES

[1] Regulation of the Minister of Transport, Construction and Maritime Economy amending the regulation on technical conditions to be met by buildings and their location (Journal of Laws of 2013., Pos. 926)
[2] European Parliament and Council 2010/31 / EU of 19 May 2010. On the energy performance of buildings (recast) (Journal of Laws EU L 153, 18.06.2010, p. 13)
[3] PN EN 15232 Energy performance of buildings - Impact of automation, control and technical management of buildings
[4] PN-EN ISO 14908 (LON)
[5] European Standard BS EN 13790: 2008 - "Energy performance of buildings - Calculation of energy consumption for heating and cooling”.
[6] Polish PN-B-03421: 1978 - "Ventilation and Air Conditioning - Calculation parameters of indoor air in rooms intended for permanent human habitation".
[7] Polish PN-B-03430: 1983 / Az3: 2000 - "Ventilation in residential and public buildings - Requirements".

Dr Anna Romanska-Zapala

Anna Romanska-Zapala dealing with the issues of intelligent building. Participated in creating Laboratory of Integrated Control Systems at the Department of Electrical and Computer Engineering and the Malopolska Laboratory of Energy Efficient Building at the Faculty of Civil Engineering, Cracow University of Technology. She is currently conducting research on the influence of integrated systems for comfort and energy efficiency issues related to various types of buildings. Anna Romanska-Zapala also conducts interdisciplinary team research on the impact of noise and vibration stimuli on human psycho-physiological parameters. In particular, looking for opportunities to use these stimuli in the rehabilitation of osteoporosis, cardiovascular diseases and respiratory diseases.

Energy saving building development in Małopolska thanks to SPIN project. Examples of solutions for energy saving buildings·

M. Fedorczak-Cisak, M.Furtak, K.Rainholc

Abstract — Malopolska Centre for Energy-saving Building (MCBE) came into being thanks to an innovative project "SPIN – a transfer model of innovation in Malopolska" of Cracow University of Technology and Malopolska Government. MCBE gathers around itself research workers of Cracow University of Technology, active in the field of energy-saving building. It is a place of popularizing information on energy-saving building, as well as a unit participating in realization of building innovations. MCBE helps to solve problems connected with designing and realizing buildings of low energy consumption. One of the examples of MCBE scholarly activity is analysing the problem of overheating the rooms in energy-saving buildings and the influence of all types of solar screens on the users' comfort improvement.

Keywords—energy-efficient buildings, comfort, Solar gains.

I. INTRODUCTION – NEAR ZERO ENERGY BUILDINGS IN POLAND. LAW, DEMANDS.

One of the main aims of the European policy are activities aiming at protection of the environment resources, including limiting energy usage in building. Such a policy started to be shaped in the 70's of the previous century, when **during** XXIV General Session of the United Nations Organization on the present state of the environment in the world, a report **alerting to progressing environment degradation** was resented**.** In the report the UN Secretary postulated the necessity of **the environment protection and rational usage of its resources**

In 1987 another report was presented **„Our common future", i**n which the basis of the sustainable world development idea was defined as " **development that meets the needs of the present without compromising the ability of future generations to meet their own needs".**

The effect of those postulates was that the European Union initiated meetings during which the situation of the Earth natural resources depletion was analysed and activities aiming at limiting this process were postulated. The meetings of the representatives of the whole world countries called the Earth Summits or Climatic Summits took place already in: **1992** UN "Earth Summit", in Rio de Janeiro Agenda 21, in **1997** Climatic Summit in Kyoto, in **2002** Earth Summit in Johannesburg, in **2014** Climatic Summit in New York.

During the meetings, in result of long negotiations and agreements, many documents were accepted and introduced, such as: a declaration on environment and development; Global Activities Programme – Agenda; Convention on Biological Diversity; Convention on Climate protection; or one of the most important: **20 20 Energy Package.According to the Package, the member countries declare to: reduce CO_2 emission by 20% in 2020 in comparison to 1990, increase usage of energy from renewable sources in the EU from 8.5% at present to 20% in 2020 (for Poland an increase from 7% to 15% was established), increase energy effectiveness in 2020 by 20%.**

In 2010 Directive 31/2010/UE [8]was developed and accepted. It is a document of significant influence on the future of the building sector in all EU member countries. The document points at the development policy direction as far as designing and realisation standards in building are concerned. The primary aim is to reduce usage of energy from non-renewable sources and to increase energy effectiveness of the buildings. The Directive presents generalized definition of the near zero energy consumption of the buildings and the terms by which such buildings have to be elaborated as a building standard in EU member countries.

Signing the 31/2010/UE Directive is connected with its implementation in the state legislation by creating the mechanisms of the Directive regulations implementation in the Polish legal acts and orders. The Ministry responsible for legal changes in this respect, in Poland the Ministry of Infrastructure and Development developed and introduced the following documents:

- **Novelized** Technological Conditions (Minister of Transport, Construction and Marine Economy's order from 5July 2013

MCBE - MALOPOLSKA'S CENTER OF ENERGY EFFICIENT CONSTRUCTIONS – 2012

This investment is an innovative unit of Cracow University of Technology, whose aim is to establish a partnership network of cooperation between science and business. Such cooperation enables scientists and entrepreneurs to develop and implement new technologies in the field of energy efficient construction.

Malopolska's Centre of Energy-Efficient Construction unit of Cracow University of Technology - Project "SPIN - Model transfer of innovation in Malopolska" realized by the Human Capital Operational Programme, Priority VIII: Regional human resources, Measure 8.2. Transfer of knowledge, Sub 8.2.1. Support for cooperation zone of science and Enterprises. The aim of the project is to increase the intensity of knowledge transfer and exploit the potential of universities by companies in Malopolska. In this study Design Builder software was used (that has been purchased under this project).

M. Fedorczak-Cisak is working in Malopolska Laboratory of Energy Efficient Constructions Civil Engeneering on Cracov Uniwersity of Technology, Poland (corresponding author to provide phone: 0048-696 04 60 50; fax: 0048-12-628-30-61; e-mail: mfedorczak-cisak@pk.edu.pl).

M.Furtak – Director of Malopolska Laboratory of Energy Efficient Constructions Civil Engeneering on Cracov Uniwersity of Technology, Poland, (corresponding author to provide phone: 0048-608 177 419; e-mail: mfurtak@pk.edu.pl).

K. Rainholc - graduate of Cracow University of Technology, phone 0048-500-310-678; e-mail: karolina.rain@gmail.com

changing the order concerning technological conditions the buildings and their localization should fulfil (Journal of Laws of the Republic of Poland, abbreviated Dz.U. nr75,pos.690 with later amendments) (in effect since 1 January 2014). [9] [10].

- **Novelized scope and form of construction project (**Minister of Transport, Construction and Marine Economy's order from 25 April 2012 concerning the detailed scope and form of construction project (Dz.U. 2012, pos. 462), **(in effect since od 3 October 2014)** [11]**.**
- **Novelized methodology of certificate compiling** (Minister of Infrastructure and Development's order from 3 June 2014 concerning methodology of calculating energy characteristics of a building and dwelling being an independent techno-usable whole and the way in which certificate specimens of energy characteristics are compiled **(in effect since 3 October 2014)** [12].
- **Act on energy characteristics of buildings** (Dz.U. from 2014, pos. 1200) **(came into effect on 9 March 2015)** [13].
- Minister of Infrastructure and Development's order from 17 Feb. 2015 **on the specimens of protocols from heating system or air-condition inspection** –9 March 2015 [14].
- Minister of Infrastructure and Development's order from 27 Feb. 2015 **on the method of the detailed scope of carrying out verification of energy characteristics certificates** and protocols from heating or air-condition systems inspection –9 March 2015 [15].
- Minister of Infrastructure and Development's order from 27 Feb. 2015 **on methodology of determining energy characteristics** of a building or its part and energy characteristics certificates - 19 April 2015 [16].

EU Parliament and Council 2010/31/UE Directive from 19 May 2010 on energy characteristics of buildings (OJ of EU UE L 153 from 18 June 2010, p. 13) in Article 9 imposes on the EU countries the necessity of developing and introducing into the state legal order the state plan aiming at increasing the number of building with near zero energy consumption [8].

According to art. 39 sect.2 of the act on energy characteristics of buildings the state plan has to include:

1. **Definition of buildings of low energy consumption characteristic of each member country specificity**
2. **Government administration activities** undertaken in order to **promote** buildings of low energy consumption, including designing, constructing and reconstructing of the buildings in such a way as to ensure their energy-saving and to increase obtaining energy from renewable sources in new and already existing buildings:
3. time table of achieving the goals discussed in point 2.

EU DEFINITION of „near zero energy consumption"

General definition included in art.2 of **2012/31/EU directive defines** *"a building of near zero energy consumption"* as a building of very high energy characteristics. Near zero or very low amount of required energy should come in a very high degree from renewable sources, among them from renewable sources of energy produced on the spot or in the vicinity.

Polish DEFINITION of „a building of near zero energy consumption"

Developed by the Ministry of Infrastructure and Development *the state plan aiming at increasing of the number of buildings with near zero energy consumption* determines the level of energy characteristics that a building is to fulfill for Polish climatic conditions. By "*a building of low energy consumption"* is to be understood a building which **fulfills the requirements connected with saving of energy and heat insulating power included in the technological and building regulations** presented in art.7 sect.1 point 1 of the act from 7 July 1994,to be **in effect since 1 January 2021 and for buildings occupied by public authorities and being their property – since 1 January 2019.**

Parameters determining a Polish definition of near zero energy consuming building are thus included in Technological Conditions elaborated for the year 2021.

Heat parameters determine minimum requirements for heat penetration coefficient $\mathbf{U_C}$ [W/m^{2}K] and for non-renewable primar energy indicator **EP**[kWh/m^{2}year]. Below, in table 1 and 2 heating requirements for buildings are quoted, included in Technological Conditions novelized in 2014.

Table 1. Basic requirements of heat protection referring to UC heat penetration coefficient in buildings, in effect since 2013, 2017 and 2021

Lp.	**Type of partition**	**Coefficient $U_{C(max)}$ [W/(m^2·K)]**		
		1.01.2014	1.01.2017	1.01.2021
1	External walls			
	a) $t_i \geq 16°C$	0,25	0,23	0,20
	b) $8°C \leq t_i < 16°C$	0,45		
	c) $t_i < 8$ °C	0,90		
2	Roofs			
	a) $t_i \geq 16°C$	0,20	0,18	0,15
	b) $8°C \leq t_i < 16°C$	0,30		
	c) $t_i < 8$ °C	0,70		
3	Ground floors			
	a) $t_i \geq 16°C$	0,30		
	b) $8°C \leq t_i < 16°C$	1,20		
	c) $t_i < 8$ °C	1,50		
4	Windows			
	a) $t_i \geq 16°C$	1,3	1,1	0,9
	b) $t_i < 16°C$	1,8	1,6	1,4
5	Skylights			
	a) $t_i \geq 16°C$	1,5	1,3	1,1
	b) $t_i < 16°C$	1,8	1,6	1,4
6	External doors	1,7	1,5	1,3

Table 2. Heat protection requirements referring to Primar Energy for buildings, in effect since 2013, 2017 and 2021

lp	Type of building	Partial maximum index value EP_{H+W} for heating, ventilation and DHW [kWh/(m^{2}rok)]		
		2014	2017	2021
1	Building:			
	One-family	120	95	70
	Multi-family	105	85	65
2	Collective residential	95	85	75
3	Public			
	Health care	390	290	190
	Other	65	60	45
4	Budynek gospodarczy, magazynowy i produkcyjny	110	90	70

II. NEAR ZERO ENERGY BUILDING IN POLAND. STATE EXPERIENCE

Building in Poland has been shaped according to the changing regulations on heat protection, particularly in external lining of the buildings, which serve to protect the building from heat loss through penetration. Till the 50s of the previous century heat protection of the buildings was not taken into consideration in the standards. The first demands were presented in 1953 in PN-B-02405:1953 and were to prevent outdropping of water vapour on the inner surface of partitions rather than protect the buildings against heat losses.

Growing care about heat protection of the buildings can be traced in the Polish regulations in the 90s. The subsequent standards were more and more restrictive in demanding heat protection of the buildings. In 2008 the requirements referring to the coefficient of heat penetration U were accompanied by an alternative notation on the indicator of non-renewable primar energy EP (PN-EN-ISO 6946: 2008) [3]. In spite of gradually growing restrictions in the state regulations, Poland does not have considerable experience in designing and realizing low energy objects. Buildings of near zero energy demand mean a great jump in the building standards. There are a few examples of passive buildings realized in Poland, which may be accepted as extreme standard of energy saving buildings. The first passive building in Poland built near Wrocław (Fig. 1) is an example, another one is a passive sports hall in Słomniki near Cracow (Fig.2).

Fig. 1 The first passive building in Poland in Smolec near Wrocław

Fig. 2 The first passive sports hall in Słomniki near Cracow

Because low energy buildings are at the same time very tight and have external partitions of very good heat parameters (heat penetration coefficients) excess of energy from solar radiation, especially in summer, may result in overheating of the rooms. Overheating is a process which negatively influences the user's comfort and the work of the whole construction.

Rooms overheating is an important problem especially in the case of energy saving buildings with large glazing from the southern side. Wrongly designed glass façade may cause excess of solar energy stored in well insulated rooms.

In Technological Conditions the problem of rooms overheating is expressed through demands referring to the restrictions in solar radiation permeability [1] [2].

The condition concerning protection against overheating is defined as a coefficient of total energy permeability of the solar radiation of the windows and glass as well as transparent partitions **g** [1].

$$g = f_C \cdot g_n \qquad [1]$$

where:

g_n – coefficient of total permeability of energy of solar radiation for the type of glazing,

f_C – coefficient of radiation reduction due to the applied anti-solar facilities,

ISBN: 978-1-61804-325-2

The values of radiation reduction coefficient due to the applied f_C anti-solar facilities are determined in Technological Conditions depending on the applied anti-solar protection.

Table 3. Values of the coefficient of total energy permeability of the solar radiation for different types of glazing [17].

Lp	The type of glazing	Coefficient g [-]
1	Single glazing	0,85
2	Double glazing	0,75
3	Double glazing with selective coating	0,67
4	Triple glazing	0,70
5	Triple glazing with selective coating	0,50
6	Double windows	0,75

Elements reducing solar radiation permeability may be different breakers of solar radiation, internal and external shutters, roller blinds, awnings or elektro-chromic glass, window panes changing properties depending on the electric impulse applied. Screens limit the amount of solar radiation stream coming through the window pane, what influences the user's comfort [4] [5].

III. ANALYSIS OF ANTI-SOLAR SCREENS INFLUENCE ON THE USER'S COMFORT

In order to test the effect of solar shutters comfort analysis was performed for the model building energy simulation program Design Builder [18].

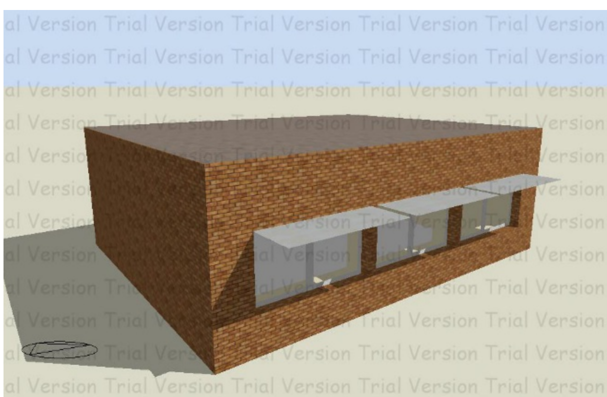

Fig. 3 Analyzed building model

The examination aim

The aim of the simulation carried out on the Model is to check the influence of different anti- solar screens on the conditions inside the room exposed to the direct solar radian

Description of the task

All calculations were carried out for the hottest summer week of the year. Analysis was carried out for the following variants:

a) No screen
b) Shield over the windows of 0.5 [m] in length
c) Shield over the windows of 1.0 [m] in length
d) Shield over the windows of 1.5 [m] in length
e) Shield over the windows of 2.0 [m] in length
f) external shutters
g) electro-chromatic widows

The first case is used to evaluate efficiency of the remaining analyzed shields and does not take into consideration any protection against solar radiation. The following cases are the shields in the form of non-transparent canopies localized above the windows (Fg.3) differing in length. Variant 5 are external shutters of average reflectance. In the case when temperature inside the room exceeds 24[°C] the shutters protect against exceeding radiation. The final variant are the electro=chromatic windows. They are steered by means of data coming from the sensor of light intensity whose boundary value was accepted as 200 [Lx].

The analysis was carried out for four sizes of the southern wall glazing being subsequently 30%,50%, 70% and 90% of the glazed southern wall. In order to free the model from many variables having influence on rooms overheating the remaining walls are full walls.

Results

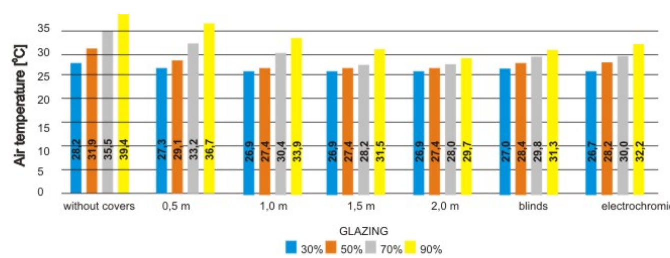

Fig.4 Graph of maximum dependence of inner air temperature on the kind of shield for chosen sizes of glazing.

The graph presented in Fig.4 shows in what way the kind of anti-solar protection, working on the windows in a southern wall, influence the maximum temperature noted in the examined room. For 30% of glazing the lowest temperature value was obtained for electro-chromatic windows, however, the difference between them and the variant with no shields is only1.5 [^{o} C].

Together with the growth of the size of glazing the effectiveness of the shields grows. In the case of glazing equal to 90% the most effective proved installing a canopy of 2 [m] in length what made it possible to reduce inner temperature by 9.7 [^{o} C]

Smaller effects observed for30% glazing were caused mainly by a smaller amount of solar radiation coming to the room, what causes that temperature inside the room is closer to that outside. For larger glazing the larger amount of radiation energy reaches the inside of the building and is accumulated ,thus in the calculations the inside temperature was unusually high, equal to 39.4[^{o} C]

From the above data it becomes obvious that using shield for small glazing does not significantly influence the conditions inside the room, while in the case of large surface of the windows it is an essential element deciding about the resulting inner temperature.

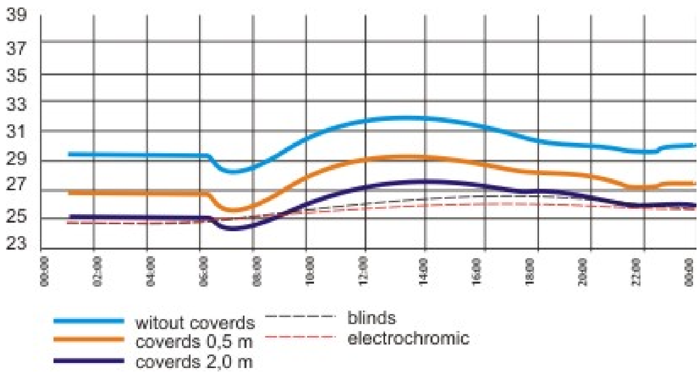

Fig.5 Graph of temperature course during 24 hours for glazing equal to 50% for different anti-solar shields

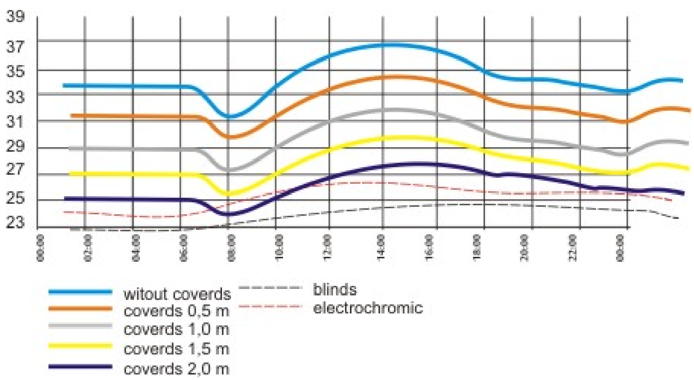

Fig.6 Graph of temperature course during 24 hours for glazing equal to 90% for different anti-solar shields

In figures 5 and 6 shown above there are graphs of inner air temperature course on the day on which the highest external temperatures were noted. In the case of glazing equal to 50% favourable lowering of inner temperature could be observed for shields of 0,5 [m] and 1 [m] in length, also for the external shutters and electro chromatic windows. Bigger lengths of the shields do not significantly influence the conditions in the room. The situation is different for glazing equal to 90% of the southern wall surface. Together with the length of the shield temperature inside the building lowers significantly. Even between a 1.5 [m] and 2[m] shield temperature is lowered by about 2[^{o} C]. In the case of large glazing the most effective solution is to apply external shutters which allow to maintain considerably stable inner temperature within the range of 25÷27 [°C].

In the case of all kinds of anti-solar protection temperature is lowered both during direct activity of solar rays in the day time and during the night. In the model it was assumed that there is gravitational ventilation in the building, which acts only in the presence of people and the amount of the exchanged air is about 35 [m^3/h] per person. Assuming such a low ventilation level there is no possibility to lower temperature inside the room considerably during the night, therefore in all the cases the difference between day and night is not big.

IV. CONCLUSIONS

Designing, realisation and usage of the buildings of low energy consumption is a very complicate process. To make optimum use of all possible energy sources, such as solar radiation in energy balance, the design of the building should be analysed in respect of both profits and losses caused by excessive overheating of the rooms, especially in summer time.

From the analyses carried out in this article it is clear that using shading systems favourably reduces temperature inside the rooms and thus effectively improves the user's comfort.

REFERENCES

[1] Chwieduk D. "Solar power"
[2] Fergus N, Humphreys M."Adaptive Thermal Comfort"
[3] Dylla A "Building physics in the practice"PWN.
[4] "Standards for Thermal Comfort, F.Nicol", M. Humphreys, O. Sykes, S. Roaf, ISBN 0 419020420 2
[5] "The Future of Thermal Comfort in an Energy-Constrained World", Tim Law, ISBN 978-3-319-00148-7
[6] "Human Thermal Environments", Ken Parsons, ISBN 978-1-4665-9599-6
[7] "Progress in Exergy, Energy, and the Environment", Ibrahim Dincer, Adnan Midilli., Haydar Kucuk, Volume 1, Volume 2, ISBN 978-3-319-04680-8

European and Poilsh standards and design guidelines, in particular:

[8] European Parliament and Council 2010/31 / EU of 19 May 2010. On the energy performance of buildings (recast) (Journal of Laws EU L 153, 18.06.2010, p. 13)PN-EN 13829:2002
[9] Regulation of the Minister of Transport, Construction and Maritime Economy amending the regulation on technical conditions to be met by buildings and their location (Journal of Laws of 2013., Pos. 926)
[10] Regulation of the Minister of Infrastructure ', Journal of Laws Of 2002 No. 75, item. 690, on the technical requirements to be met by buildings and their location
[11] Novelized scope and form of construction project (Minister of Transport, Construction and Marine Economy's order from 25 April 2012 concerning the detailed scope and form of construction project (Dz.U. 2012, pos. 462)
[12] Novelized methodology of certificate compiling (Minister of Infrastructure and Development's order from 3 June 2014 concerning methodology of calculating energy characteristics of a building and dwelling being an independent techno-usable whole and the way in which certificate specimens of energy characteristics are compiled
[13] Act on energy characteristics of buildings (Dz.U. from 2014, pos. 1200)
[14] Minister of Infrastructure and Development's order from 17 Feb. 2015 on the specimens of protocols from heating system or air-condition inspection.
[15] Minister of Infrastructure and Development's order from 27 Feb. 2015 on the method of the detailed scope of carrying out verification of energy characteristics certificates and protocols from heating or air-condition systems inspection
[16] Minister of Infrastructure and Development's order from 27 Feb. 2015 on methodology of determining energy characteristics of a building or its part and energy characteristics certificates
[17] Standard PN-EN ISO 6946 "Building components and building elements. Thermal resistance and thermal heat transfer. The method of calculation"
[18] software supporting the design and analysis of energy in the building industry

**PhD Malgorzata Fedorczak-Cisak**
Director of the Malopolska's Center of Energy-Efficient Construction. A graduate of the Cracow University of Technology. Represents the scientific field of building physics and energy efficient construction. Expert actively participating in the meetings of the advisory and opinion of the representatives of the Malopolska Regional Government, the effect of which is to develop the provisions of the Malopolska Region strategy and long-term development of the Malopolska take into account the development of measures to improve energy efficiency especially in the area of construction. Expert working actively in the work to implement EU Directives, inter alia, for the development and implementation of the definition of near zero energy buildings in Poland. She is a member of the Polish Committee for Standardization, the Association of Energy Auditors and expert appointed to evaluate international projects related to the area of energy saving measures.

**PhD arch. Marcin Furtak**
Director of the Malopolska's Laboratory of Energy-Efficient Construction. A graduate of the Cracow University of Technology. Represents the scientific field of architectura and energy efficient construction. Expert actively participating in the meetings of the advisory and opinion of the representatives of the Malopolska Regional Government, the effect of which is to develop the provisions of the Malopolska Region strategy and long-term development of the Malopolska take into account the development of measures to improve energy efficiency especially in the area of construction. Expert working actively in the work to implement EU Directives, inter alia, for the development and implementation of the definition of near zero energy buildings in Poland. She is a member of the Polish Committee for Standardization, the Association of Energy Auditors and expert appointed to evaluate international projects related to the area of energy saving measures.

Karolina Rainholc is a student of the Cracow University of Technology specialties Intelligent Civil Engineering Structures. She writes a diploma in MLBE. She is interested in technologies related to low-energy buildings and thermal comfort of rooms. At present she is writing a thesis about the influence of traditional and modern technologies on energy consumption and thermal comfort of buildings. In her spare time she likes to walk in the mountains and learn about new cultures in Europe.

ISBN: 978-1-61804-325-2

Energy simulations of residential building using a dynamic energy-balanced software

M. Fedorczak-Cisak, A. Kowalska-Koczwara, A. Romańska-Zapała

Abstract — The aim of this study is to investigate whether, by using commonly available insulation materials it is possible to achieve building parameters as:

- low energy demand,
- for passive building.

The article presents the results of analyzes of selected building designed in accordance with the Technical Conditions in relation to the Standard NF15 and NF40 which are Polish passive building design guidelines. The study analyzed opportunities to reduce energy requirements of the building and this study also attempts to optimal selection of design elements of the building due to the energy requirements using computational simulation tool which is the program Design Builder. External partitions due to the number of layers, the thickness of layers and air tightness of enclosure were adopted as the decision variables. The scope of work includes energy analysis of existing residential house, built in the 80s.

***Keywords*—**energy-efficient buildings, dynamic energy models, tightness of buildings, parametric optimization.

MCBE - MALOPOLSKA'S CENTER OF ENERGY EFFICIENT CONSTRUCTIONS – 2012

This investment is an innovative unit of Cracow University of Technology, whose aim is to establish a partnership network of cooperation between science and business. Such cooperation enables scientists and entrepreneurs to develop and implement new technologies in the field of energy efficient construction.

Malopolska's Centre of Energy-Efficient Construction unit of Cracow University of Technology - Project "SPIN - Model transfer of innovation in Malopolska" realized by the Human Capital Operational Programme, Priority VIII: Regional human resources, Measure 8.2. Transfer of knowledge, Sub 8.2.1. Support for cooperation zone of science and Enterprises. The aim of the project is to increase the intensity of knowledge transfer and exploit the potential of universities by companies in Malopolska. In this study Design Builder software was used (that has been purchased under this project).

M. Fedorczak-Cisak is with the Małopolskim Laboratorium Budownictwa Energooszczędnego Wydziału Inżynierii Lądowej na Politechnice Krakowskiej, Polska, (corresponding author to provide phone: 0048-12-628-30-62; fax: 0048-12-628-30-61; e-mail: mfedorczak-cisak@pk.edu.pl).

A. Kowalska-Koczwara is with the Cracow University of Technology, Cracow, Warszawska 24 St., 31-155, Poland (corresponding author phone: +48126282121; fax: +48126282340; e-mail: akowalska@pk.edu.pl).

A. Romańska-Zapała pracuje w Małopolskim Laboratorium Budownictwa Energooszczędnego Wydziału Inżynierii Lądowej na Politechnice Krakowskiej, Polska, (corresponding author to provide phone: 0048-12-628-30-62;fax: 0048-12-628-30-61; e-mail: a.romanska@pk.edu.pl).

I. Introduction

NOWADYS the function that buildings perform is not only shelter, security and convenience, but equally important is how they influence on our environment (see for example [1], [2], [3]). In response to the growing awareness and concern about the environment in Poland and in Europe gaining popularity energy-efficient and passive constructions. This is not caused only by lower energy consumption or non-renewable resources consumption such as coal, oil and gas, but also the construction shall be equal to reduced CO_2 emissions compared with traditional construction whilst ensuring better indoor environment quality for humans. Energy efficient building, despite higher investment costs, minimizes expenses related to the use of the building, so the overall balance of costs from the point of view of users, it is more advantageous financially.

Along with the growing demands for energy savings in the building, the energy for exploitation of buildings is minimizing and has become one of the main topics of analysis and research.

Important parameters for evaluation of energy efficiency of the building is an indicator of seasonal heating demand for heating and air-tightness of the building. As a result of careful selection of these parameters for example by computer simulations the energy consumption and indirectly reduction of CO_2 emissions of the selected building could be improved.

The indicator seasonal heating demand is a very important element for evaluating the energy consumption of the building.

Estimated data for the average multi-family buildings in Poland, seasonal heat demand depending on the year, are as follows:

- in buildings built before the entry into force of PN-82 / B-02020 (ie. before approx. 1985). - approx. 250-280 kWh / (m2a)w budynkach wzniesionych zgodnie z wymaganiami PN-82/B-02020 (tj. po ok. 1985r.) – ok. 220 kWh/(m2a)
- in buildings built in accordance with the requirements of PN-91 / B-02020 (ie. after approx. 1995). - Approx. 160 kWh / (m2a)
- in buildings built in accordance with the requirements of 1997 (ie. after approx. 1999). - approx. 120-140 kWh / (m2a).

The Regulation of the Minister of Transport, Construction and Maritime Economy was signed on 5th July 2013. This regulation changes the ordinance on technical conditions to be met by buildings and their location (Journal of Laws of 2013., Pos. 926) [4]. The regulation came into force on January 1st

2014. It contains a new "technical conditions to be met by buildings and their location". The regulation changes the existing requirements of thermal insulation of the building envelope, and exacerbating value of the indicator for primary energy demand of the building. These parameters will be much stricter until 2021.

Published regulation is a consequence of the implementation of art. 4 to 8 of the Directive of the European Parliament and the EU Council of 19 May 2010 on the energy performance of buildings (recast) (Dz. U. EU L 153, 18.06.2010, p. 13) [5].

The role of the member states is to establish rules that will define the energy standards of the building and its components whereas the three fundamental aspects: technical, economic and financial, that is, the cost-effectiveness of the solutions.

The purpose of Directive 2010/31/EU is the use of economically reasonable improvement energy performance of buildings as a result of lower heat demand for heating, cooling, domestic hot water and lighting, through the use of appropriate materials (with good thermal insulation parameters λ [W/mK]), the technology performance of heating system and tap water and mounting techniques with a responsible and thoughtful use of selected power sources.

II. Building design using dynamic energy simulations

Computer simulations of the building allow to make a decision that will be able to optimize the architectural design and installation, which leads to a reduction in energy demand and allows for ensuring adequate internal environmental conditions. Building energy simulations, also called the energy modeling of the building, it is the use of software to predict energy consumption of the building. Building Energy Modeling is the practice of assessing energy consumption of the building through simulations using a lot of of energy-related elements. Programs for simulation energy performance are powerful tools for studying energy efficiency and thermal comfort throughout the life cycle of the building. Most programs for thermal simulations consist of calculation tool based on simple input and output text file.

There are many programs for dynamic energy simulation based on specific, simplifying assumptions. It is important to be aware of these assumptions and be able to decide whether they are justified and which may influence on the results of the simulation. For example, the weather data are adopted on the basis of measurements from previous seasons and based on them future external thermal loads are assumed. Another assumption is that the temperature in the room is spatially uniform. This is a good foundation for not so high spaces, but not so good for larger rooms where the temperature varies depending on the height of the storey.

There are two main elements in energy design programs: calculations tool and graphical interface. Calculation tool uses input files of a particular form taken from the geometry model. Compared to other graphical interface design architecture, the energy modeling programs are very weak. This tool defines simple architecture and reads only the simple geometry. This is one of the main reasons for difficulties in communication between architecture design and designing using energy programs.

Computer simulations presented in this article are based on DesingBuilder software.

A method of modeling of buildings is the formation of blocks which are the basic elements used to create the model in DesingBuilder program. There are three types of elements that could be added to the building model:

- Building Blocks - constitute the outer shell of model or part of model, they can be divided inwardly to form a series of zones. The finished house consists of a set of construction elements, which may include external walls, roofs and floor tiles.
- Outline Blocks - are used to help to create a more complex geometry. They are created and edited in exactly the same way as main element, but is only created a 3D shape without related building components such as walls, floors, roofs, etc.
- Component Blocks - are used to create visual elements, an external area and shading of structures that zones do not contain.

In DesignBuilder program there are three types of HVAC systems:

- Simple - suitable for use in the initial design phase, heating / cooling system is modeled by a calculation algorithms of basic load.
- Compact - can be useful when modeling in EnergyPlus. They allow for modeling of HVAC systems in some detail, without necessarily been drawn air flow network and coping with complexity of control systems and connection nodes. The compact HVAC is an intermediate between simple and detailed model HVAC options.
- Detailed - DesignBuilder system models are connected by a placing several predefined installation schematic diagrams, which are then combined to form a complete system.

In this study was used DesignBuilder software capabilities to perform residential building model and simulate the four selected variants of external partitions. The influence of external partition structures and tightness of the building on its energy consumption was also investigated.

III. Description of analyzed building

The object subjected to analysis is an existing residential building located in Tarnow. Single-family home design dates from the year 1979. The building was built in the years 80s-90s using economic method. Over the years, changes were made in the body of the building, and used expanded polystyrene insulation with a thickness of 10cm (with λ = 0.035 [W / mK]).

<u>General design data</u>

Usable area: 107,57 m^2

Building area: 88,63 m^2

Cubature: 718 m^3

<u>General characteristics of the building:</u>

Residential detached house – one-storey building with a garage in the basement. Designed in traditional construction.

Construction-material data:

- Concrete continous footings
- Basement walls - concrete, faced with brick inside / thickness equal 12cm
- Ground floor and upper floors walls made of brick and cinderblock MAX on cement and lime mortar
- Internal dividing walls made of full and hollow bricks
- Slabs over the basement and floors are ceramics FERT type.
- Envelope Roof - covering: galvanized sheet steel
  wooden structure
  warming of the floor – Suprema
- lintels, balconies, stairs, cornice - reinforced concrete
- Waterproofing - a double roofing felt on glue situated on continuous footings and under ground floor slab.
- Ridge height: 8,3 m
- Roof angle: 40 °

Finishing works

- Floors - residential rooms - wooden floor, cork; in the hall, kitchen, bathrooms - terracotta.
- Plasters - cement and lime.

The figures below summarizes the plans of individual storeys with taking into account the surface area and the cross-section of the building chosen for analysis.

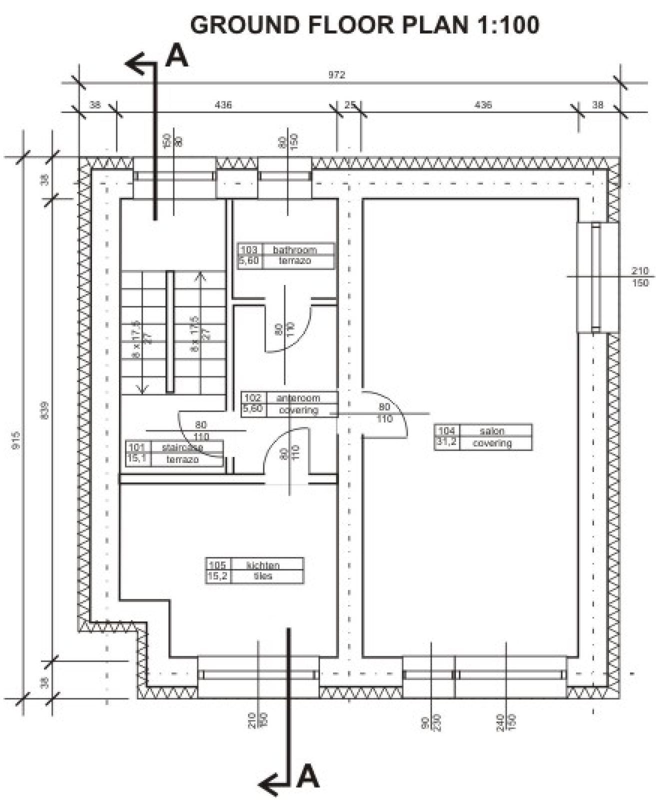

Fig. 1. Ground floor plan

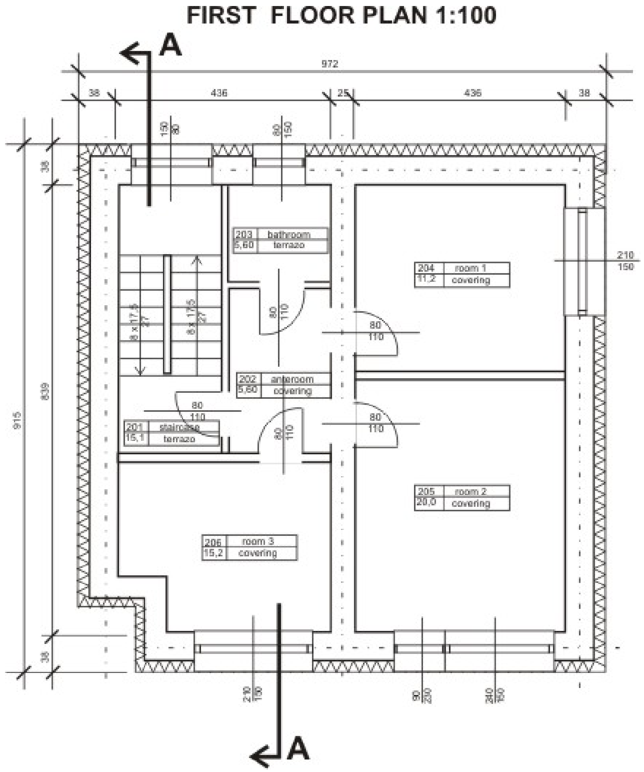

Fig. 2. First floor plan

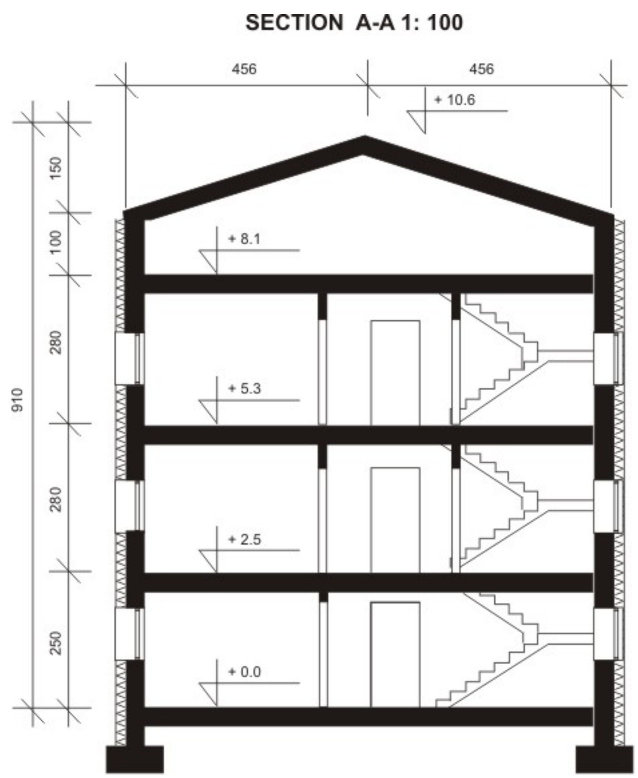

Fig. 3. Cross-section of the building

IV. Modelling and Energy Simulations of Buildings on Chosen Building Example

Basic data are given before creating a model. These data concern on:

- Location - determines the geographic location and weather data for all buildings on this site,
- Standards, legislation and building regulations in the given region.

The figures below illustrate the boundary conditions introduced to the program DesignBuilder.

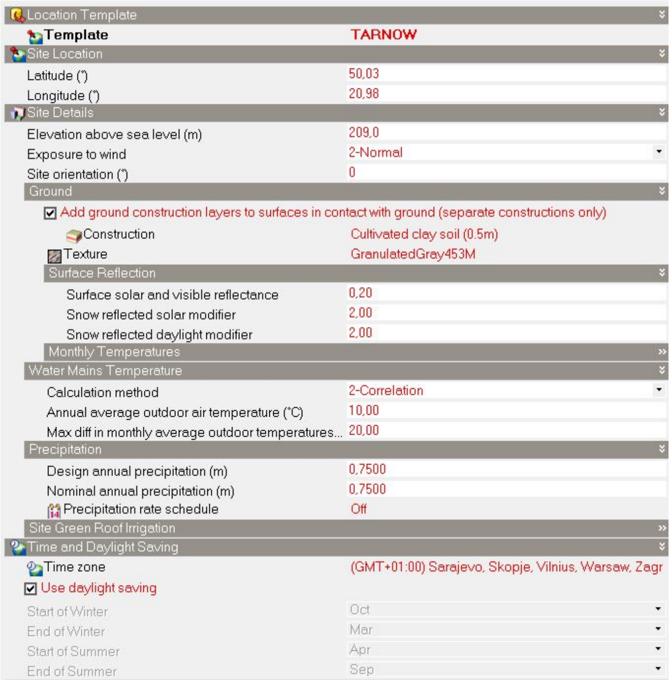

Fig.4. Boundary conditions of the model

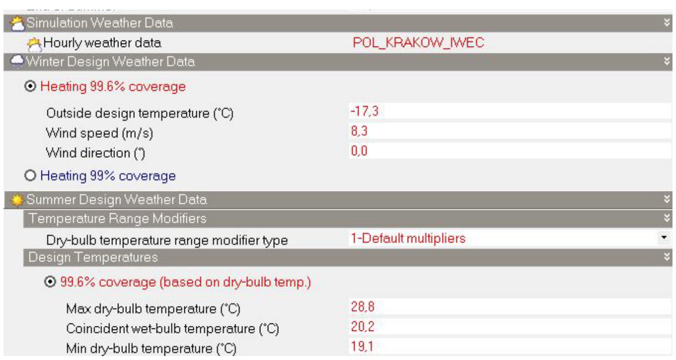

Fig. 5. Designed weather data

Data taken for analysis:
Heat transfer coefficient:
U_g= 1,0 W/m2K, - coefficient U for glass window
U_f = 1,8 W/m2K - coefficient U for window frame (see [6]).
Light transmission Lt = 80%,
The total transmission coefficient of solar energy g = 62%.

HVAC simple modeling system was selected for designing, due to the lack of complex systems such as heat pump systems, air conditioning or ventilation with heat recovery.

The HVAC system selected in the design is based on a template "Hot water radiator heating, nat vent." which means :

- heating system using coal boiler of the central heating (efficiency ratio equal 0.85%).
- natural ventilation; 3 ac / h - the amount of ventilation air (fresh air),
- DHW system - gas heater 100l volume; (efficiency ratio equal 0.85%).

The figures below illustrate the visualization of modeled building.

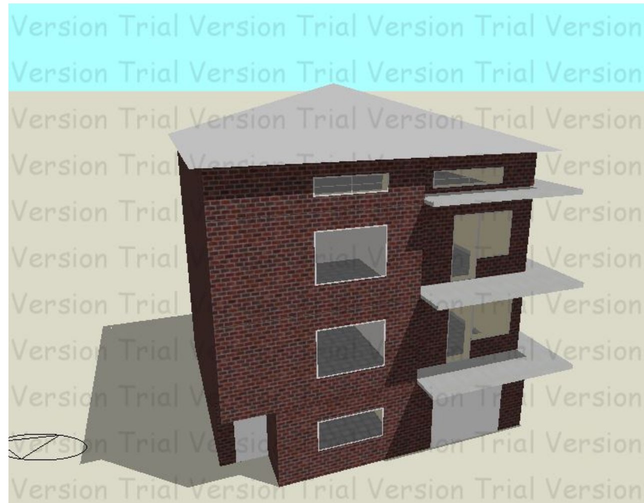

Fig. 6. Visualization of building model

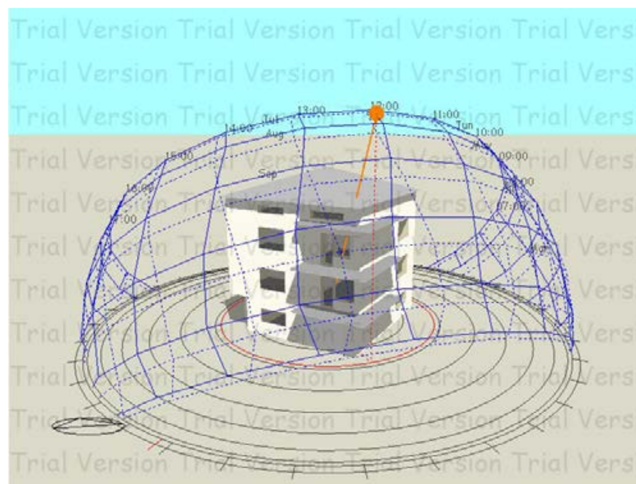

Fig. 7. Visualization of the building withstaging path of the sun

The path of the sun in relation to the location of the building has an impact on the analysis and was included in the model (Fig. 7).

Four variants of the model have been analyzed:

- Option I - variant design - a wall with air gap (see fig. 8)

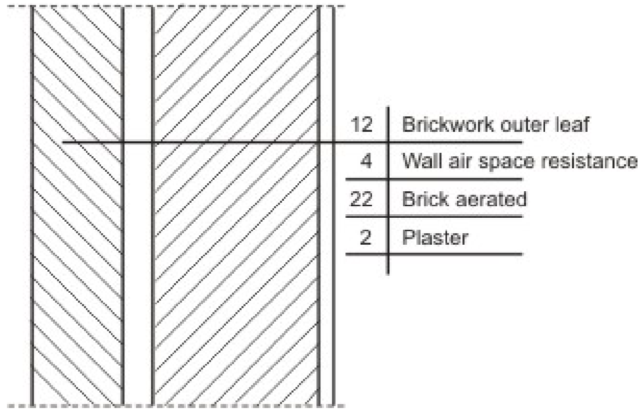

Fig. 8. Cavity wall without insulation

- Option 2 – the existing situation - cavity wall with air gap + 10cm Styrofoam insulation (see. Fig. 9)

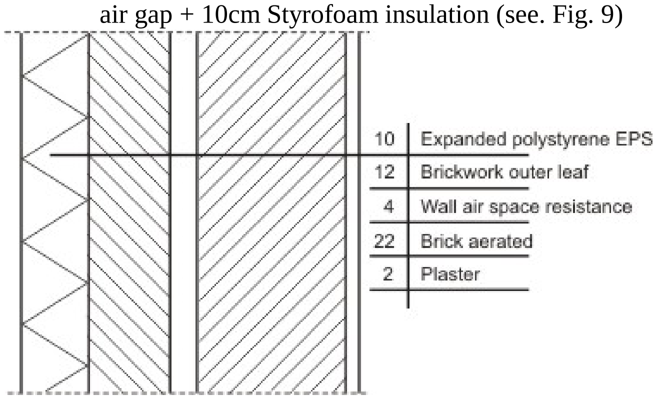

Fig. 9. Cavity wall with 10cm thermal insulation

- Option 3 - cavity wall with air gap + 20cm Styrofoam insulation (see. Fig. 10)

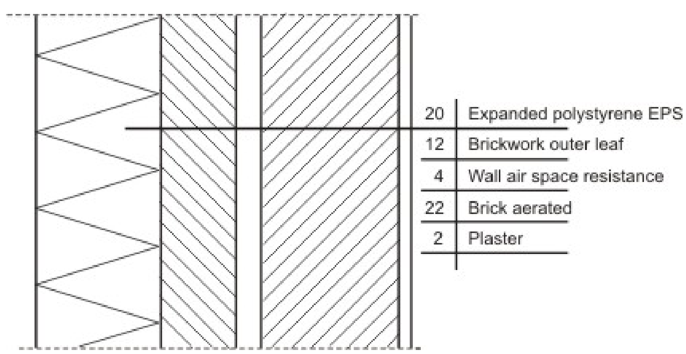

Fig. 10. cavity wall with air gap + 20cm Styrofoam insulation

- Option 4 - cavity wall with air gap + 30cm of insulation (see. Fig. 11)

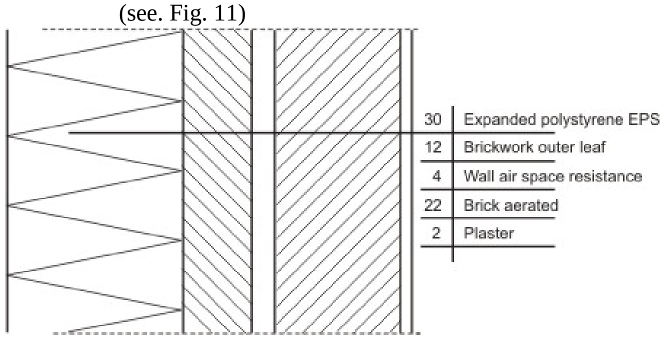

Fig. 11. Cavity wall with 30cm thermal insulation

V. Analysis results

The calculation of designed heating are conducted in order to determine the size of heating equipment to meet the required conditions for internal temperatures to the weather - the coldest winter, which can occur in a given location. In the statement profits from solar heating and internal gains such as: lighting, electrical equipment, heat exhausted from users are not considered. Wind speed and direction were adopted by design data. The calculations include heat conduction and convection between the zones of different temperatures.

The simulation calculates the heating capacity required to maintain the set temperature in each zone, and displays the total loss of heat divided into:

- Glazing
- Walls
- Floors
- roof
- Departed outer
- The internal natural ventilation (ie heat losses to other colder adjacent rooms and the vents, windows, doors, openings).

The total loss of heat in each zone are multiplied by a safety factor of 1,2. It provides additional heat required in the building to bring the required temperature in a relatively short period of preheating and allows you to be sure that comfortable conditions are maintained in all, including the most extreme winter conditions. In the test case, the coefficient is smaller than in the case of public buildings where buildings are not used by the weekend. Then we must be sure that the installation is large enough to heat the building shortly after a cold start in the winter on Monday morning when the building cooled during the weekend. In the case of a residential building such situations doesn’t take place, because during the week there are not large differences in energy demand.

Tightness is a leak, air permeability, related to the infiltration of cold / hot air into the building and / or loss of the heated / cooled air from the inside by means of splits, cracks, pinholes, etc.. In the building material.

The loss of cooled / heated air through the "uncontrolled ventilation" influence on the energy consumption of the building. This loss will cause the need for additional energy to re-heating or re-cooling of the air. It also influence on the comfort level of residents of the building. Therefore it is important to carefully and conscientiously make connections and transitions.

Assessment of tightness of the building is carried out at 50 Pa pressure difference between the internal pressure of the building and the external atmospheric pressure. PN-EN 13829: 2002 [7] provides for the examination method of measuring the pressure with ventilator.

Requirements for tightness - n50 value - are defined in the "Regulation of the Minister of Infrastructure ', Acts Of 2002 No. 75, item. 690, on the technical requirements to be met by buildings and their location [8]. However, Polish legislation does not impose the obligation to perform leak testing of buildings - they are only recommended.

The maximum values of air changes are as follows:

- buildings with gravitational ventilation: n50 ≤ 3.0 [1 / h]
- buildings with mechanical ventilation: n50 ≤ 1.5 [1 / h]
- passive buildings, energy-saving: n50 ≤ 0.6 [1 / h].

Passive and energy-efficient buildings must meet the condition of air change n50 ≤ 0.6. The air ventilation in passive houses should be provided through heat recovery units.

Because the tightness of the building has a significant impact on energy demand, examined building will be analyzed with taking into account this parameter. Depending on the variants of the outer layer air change at a pressure of 50 Pa will be also varied.

The first value is five air exchanges. It was chosen on the basis of similar buildings constructed in the 80s. The tightness and accuracy in these years was not particularly important aspect, which values N50 can range from 4 [1 / h] to 10 [1 / h]. The value of n50 ≤ 5.0 [1 / h] is the maximum value that can be assumed in DesignBuilder program. In the simulations were also analyzed three air exchanges, this is the number of air exchanges that should satisfy buildings with gravitational ventilation and the requirements for passive buildings - 0.6 [1 / h].

Table 1. Matrix simulation variants [9]

	U [W/m2K]	n50 [1/h]		
V1- without insulation	0,84	5.0	3.0	0.6
V2 - 10 cm of insulation	0,24	5.0	3.0	0.6
V3 - 20 cm of insulation	0,14	5.0	3.0	0.6
V4 - 30 cm of insulation	0,10	5.0	3.0	0.6

Thanks to simulations in an easy way, it is possible to compare different solutions. On the basis of statements it can be concluded that the problem of leakage, which is usually overlooked is extremely important. Only improving the U-value in order to obtain better performance of the building, without proper tightness, we will not achieve the planned savings in the use of building. Leaks translate directly into increased demand for heating energy.

In the case under examination system of mechanical ventilation and infiltration dominates the greatest heat loss as shown in Fig. 12.

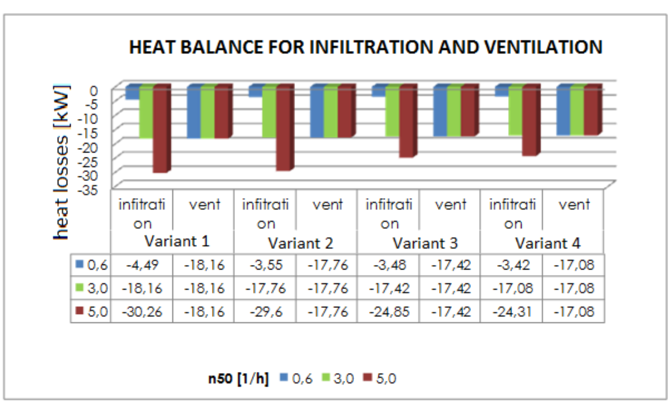

Fig. 12. Summary of energy losses through infiltration for all variants

Ensure better tightness of the building has a direct impact on its final energy demand. This relationship is shown in Figure 13, which were included to compare the results of simulation variants.

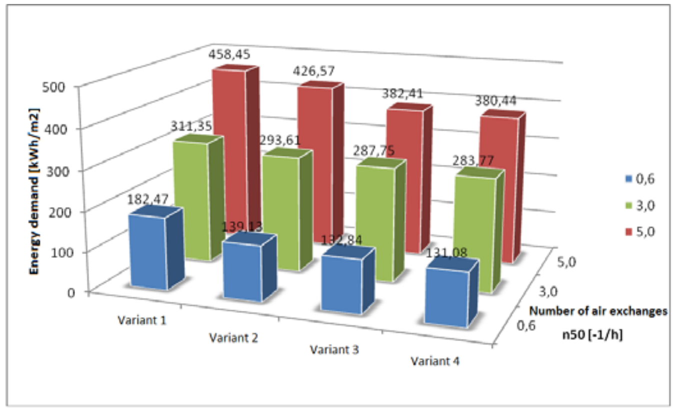

Fig. 13. Final energy demand - comparative summary results of simulation variants

The characteristics of energy-efficient construction is low power consumption while ensuring better indoor environment for humans. As a result, for considered four different variants with an increase airtightness of the building envelopes, there was also observed a reduction of CO_2 production. Suitable variants are shown in Fig. 14.

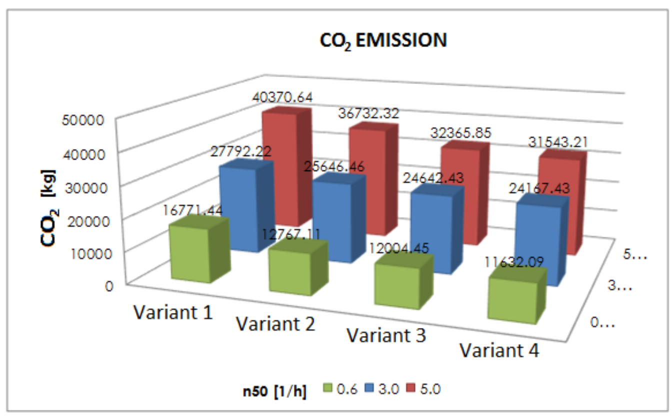

Fig. 14. CO_2 emissions, summary of simulation variants

When calculating annual energy consumption for heating for all examined variants of the outer shell of the building there was observed a decrease of energy consumption with an increase in air tightness of the building envelope. In shown in Fig. 15 graph can be observed large differences in energy consumption for air exchange n50 = 0.6 [1 / h], and N50 = 5 [1 / h]. For variants W2 and W4 biggest differences were observed.

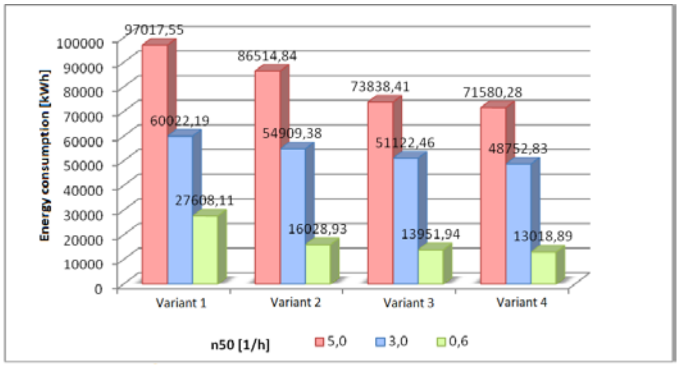

Fig. 15. Annual energy consumption for heating - comparative summary

VI. Conclusion

The tool, which are energy simulations, meets our expectations and growing needs for rapid analysis. However, this is still a new field, complicated and may cause difficulties in use. You have to understand the limitations of the software, their complexity, as well as a wealth of knowledge about the processes of energy in buildings. The main value of the simulation is to compare different solutions rather than absolute energy consumption prediction.

Based on the analysis of simulation it can be concluded that only by meeting requirements for building envelope, without heat recovery and renewable energy sources, it is not possible to satisfy the NF40 and NF15 [10] conditions.

The heat losses caused by lack of tightness of the partitions (see Fig. 12) have a significant impact on energy demand of buildings, they may even increase it to 50%, what can be seen on Fig. 15. Improving the U-values for the building envelope without improving the tightness will not bring significant results in energy savings for heating (see Fig. 12). In addition, uncontrolled air infiltration can reduce indoor environmental quality, causing unpleasant for residents, local drafts. The penetration of the hot moist air may lead to an interlayer condensation that may cause decreased of durability of the envelope.

Increasing the air tightness of the building, while improving the value of factor U of external partitions, as shown in Figure 14, results in a reduction in CO_2 production.

Computer simulations are very helpful in the design of energy efficient buildings and the selection of the parameters of external partitions used in the design. An important factor directly influencing on energy consumption and CO2 emissions is tightness, and so in energy efficient building design process, special attention must be paid to the elimination of the so-called "uncontrolled ventilation" [11].

References

[1] T. Law: "The Future of Thermal Comfort in an Energy-Constrained World", ISBN 978-3-319-00148-7

[2] K. Parsons: "Human Thermal Environments", ISBN 978-1-4665-9599-6

[3] I. Dincer, A. Midilli., H. Kucuk-"Progress in Exergy, Energy, and the Environment", ISBN 978-3-319-04680-8

[4] Regulation of the Minister of Transport, Construction and Maritime Economy amending the regulation on technical conditions to be met by buildings and their location (Journal of Laws of 2013., Pos. 926)

[5] European Parliament and Council 2010/31 / EU of 19 May 2010. On the energy performance of buildings (recast)

[6] A. Dylla " Thermal physics of buildings in practice" PWN.

[7] PN-EN 13829:2002 provides for the examination method of measuring the pressure with a fan.

[8] "Regulation of the Minister of Infrastructure ', Journal of Laws Of 2002 No. 75, item. 690, on the technical requirements to be met by buildings and their location

[9] Standard PN-EN ISO 6946 "Building components and building elements. Thermal resistance and thermal heat transfer. The method of calculation"

[10] Requirements for programs NF15 NF40 the National Fund for Environmental Protection file:///C:/Users/mcbe/Downloads/wytyczne_do_pp%20(2).pdf

[11] Fergus N, Humphreys M. "Adaptive Thermal Comfort"

Dr Malgorzata Fedorczak-Cisak
Director of the Malopolska's Center of Energy-Efficient Construction. A graduate of the Cracow University of Technology. Represents the scientific field of building physics and energy efficient construction. Expert actively participating in the meetings of the advisory and opinion of the representatives of the Malopolska Regional Government, the effect of which is to develop the provisions of the Malopolska Region strategy and long-term development of the Malopolska take into account the development of measures to improve energy efficiency especially in the area of construction. Expert working actively in the work to implement EU Directives, inter alia, for the development and implementation of the definition of near zero energy buildings in Poland. She is a member of the Polish Committee for Standardization, the Association of Energy Auditors and expert appointed to evaluate international projects related to the area of energy saving measures.

Dr Alicja Kowalska-Koczwara
V-ce Director of Instittute of Structural Mechanics at the Faculty of Civil Engimeering, Cracow University of Technology. She is currently conducting research on influence of vibrations on human body and on humans residing in buildings. Expert working actively in the work to implement Polish standard "Evaluation of vibrations influence on people in buildings". She takes part in many expert opinions on the dynamic effects on buildings and on people in buildings. The main directions of interest are dynamic influences of paraseismic origin.

Dr Anna Romanska-Zapala
Anna Romanska-Zapala dealing with the issues of intelligent building. Participated in creating Laboratory of Integrated Control Systems at the Department of Electrical and Computer Engineering and the Malopolska Laboratory of Energy Efficient Building at the Faculty of Civil Engineering, , Cracow University of Technology. She is currently conducting research on the influence of integrated systems for comfort and energy efficiency issues related to various types of buildings. Anna Romanska-Zapala also conducts interdisciplinary team research on the impact of noise and vibration stimuli on human psycho-physiological parameters. In particular, looking for opportunities to use these stimuli in the rehabilitation of osteoporosis, cardiovascular diseases and respiratory diseases.

On modeling the chemical apparatuses for reactions with insoluble products

Laura Suleimen, Alia Bekaulova, Lyazzat Ramatullaeva, Zaurekul Kerimbekova

***Abstract*—**The paper deals with methods for modeling and optimizing chemical reactors in which chemical transformation are accompanied with formation of insoluble dispersed phase. Work is devoted to the analysis of the mechanism of formation and evolution of solid particles in chemical apparatuses with formation of an insoluble phase in a reaction zone. In the paper the system analysis of processes is carried out and their basic stages are proved.

***Keywords*—**Chemical reactor, insoluble products, aggregation and sedimentation, reactor modeling

I. INTRODUCTION

IN many cases processes in chemical technologies are accompanied by formation of the new solid disperse phase. It can be phase transition, as in cases of crystallization or desublimation, or it can be formation of low soluble substances during chemical reactions [1]-[5].

As a whole it is possible to allocate a lot of directions of a modern science dealing with processes and apparatuses of chemical technologies in which the problems of calculating the kinetic and dynamical characteristics of reactors with formation of a polydispersed solid phase in a working zone are relevant [6]-[8].

1. Production of nano-dispersed powders of oxides of precious metals for constructional and functional bioceramics.

2. Creation of sorbents, catalysts and molecular grids with given structure.

3. Creation of methods for calculating and optimal engineering of technological processes dealing with a method of chemical sedimentation.

Methods for calculating apparatuses in which there are phase transitions of types “liquid-solid” or “vapour-solid” are developed more or less in detail [1], [3]. However engineering methods of calculation and designing of processes in chemical reactors with formation low soluble products of chemical reaction in working zones of the apparatuses are developed to a lesser degree [9]-[14].

The area of researches in this work is limited to working out methods of calculation and designing of processes and chemical apparatuses in which there exist formation and aggregation of suspensions of low soluble products of chemical reactions [14], [15].

Therefore, the goal is to create theoretical foundation and engineering procedures for calculating the chemical apparatuses in the conditions of joint course of chemical reactions and processes of aggregation and sedimentation of an insoluble dispersed phase formed in working zones of the reactor.

L. Suleimen is with the Department of Informational Technology, State University of South Kazakhstan, Shimkent, 160012, Kazakhstan (phone: +7-725-242-1513; e-mail: olimp_mktushi@mail.ru).

All other co-authors are with the Department of Ecology and life Safety, State University of South Kazakhstan, Shimkent, 160012, Kazakhstan (e-mail: ramatullaeva_l@mail.ru).

II. SYSTEM ANALYSIS

The first stage is the primary nucleation. According to modern representations during this process microscopic roentgen – amorphous particles appear in a solution. These primary particles are exposed further to aggregation and crystallization. These primary particles are exposed further to aggregation and crystallization. These processes occur simultaneously and are kinetic competing. Crystallization occurs by way of reorganization of structure of particles with using substance of the given particle, i.e. without mass transfer with environment [14], [16]- [20].

Aggregation is induced by interaction between primary particles with simultaneous re-crystallization. As a result larger secondary crystals are forming. These processes occur in kinetic area.

Under the theory of block growth [1], [21], [22] the transfer of substance from a liquid phase into a solid phase of a deposit is a result of formation of primary particles. Then the substance stream into a deposit phase is equal to speed of occurrence of crystallizing substance in a solution. According to last data [2], [22]-[24] during crystallizing low soluble substances the particles of a dispersed phase are distributed not only by the size, but also by the degree of completion of crystallizing.

For the description of the second zone of the reactor as a zone of diffusion limited aggregation (DLA), the mathematical apparatus of fractal theory can be involved. According to fractal model the deposit of low soluble substances in this zone is the single cluster. Growth of this cluster occurs by joining to it the primary particles and the secondary crystals arriving to a cluster surface by diffusion mechanism [22], [25], [26].

Thus deposit growth is described as movement of an active zone, i.e. area where new particles have been joined to the cluster. Trajectories of particles begin out of the area occupied

ISBN: 978-1-61804-325-2

by the cluster, and come to an end at the moment of contact of a particle with cluster surface. This process also can be described as random walk by means of the Smoluhowski equation [25]:

$$\frac{dn_k(t)}{dt} = \frac{1}{2}\sum_{i+i+j=k} K_{ij} n_i(t) n_j(t) - n_k(t)\sum_{j=1}^{\infty} K_{jk} n_j(t) \quad (1)$$

Here $n_k(t)$ is the density of n_k - particle clusters.

The kernel of system of the Eq. (1) considers dependence of section of collisions on the sizes and mobility of clusters. Such approach can be successfully applied to problems where there are sources and drains which correspond to presence of an external field in a vicinity of a point of equilibrium phase transition. The probability of joining of a particle is highest to ledges of clusters: Probability of joining of the particle which has reached the cluster in an active zone can be estimated as $1 - p_{\max}$. As a result it is received a following kinetic equation of growth of the cluster at a big quantity of particles:

$$\frac{d\bar{r}_N}{dN} = p_{\max}(N)a\,, \quad (2)$$

where a – is the characteristic size of an attached particle.

As a whole the formed cluster is characterized by two parameters: the average radius of sedimentation $\bar{r}_N$ and the width of an active zone ψ. At great numbers of particles N we can obtain:

$$\bar{r}_N \sim N^{\gamma} - N^{1/D_F}\,, \quad (3)$$

where D_f is fractal dimension of cluster structure, γ - is an indicator depending on characteristic length. Corresponding expression for width of an active zone also is given by fractal theory as average distance between branches of the cluster:

$$\psi \sim \bar{r}_N^{(3-D_F+\chi)/2}\,, \quad (4)$$

where χ – is an indicator of anisotropy of a deposit. As characteristic length in the zone of DLA the diameter of the reactor can be used. From this it follows that at the methodical organization of experimental researches Eqs (3) and (4) can be used as the base form of empirical dependences.

The described mathematical model reflects the basic features of process of sedimentation and can be offered for the regular organization of experimental researches and optimization of the reactor. However, use of known mathematical models of formation and aggregation of insoluble phases for engineering calculation leads to variety of mathematical difficulties and, is connected with definition of a great quantity of parameters, and acceptance of adequate engineering decisions is very difficult.

In that work we submitted the generalized mathematical model on the basis of the scheme of the cascade of three reactors connected consistently with different working volumes and rates of mixing. The re-circle between reactors I and II is caused by the fact that the deposit layer in the second area is friable

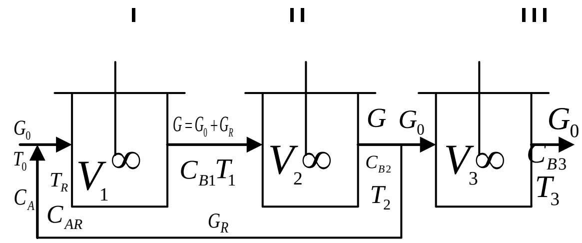

Fig. 1. The structural schemes of the reactor in the form of the cascade of three reactors with intermediate re-circle

The submitted model allows calculating time stays of reagents in each of cascades of the scheme of the reactor. The characteristics of the re-circle can be calculated with the help of the fractal model of the deposit in the second zone. This approach gives the closed description of heat and mass transfer processes in the reactor with deposit formation in working volume. The model takes into account the structure of the basic zones of the reactor. However, definitions of the managing criteria in given model, taking into account real dynamics of structure of streams, are not perfected. Therefore model use in engineering calculations demands additional researches, and the estimation of efficiency of the model cannot be given with full definiteness.

III. Aggregation Model

The primary nucleation is the first stage of aggregation process. During this process microscopic amorphous particles or partially crystalline particles-monomers have been generated in a solution.

Let us consider the first order reaction occurring in a solution under the conventional scheme $A \to B$. The analysis of known data allows asserting that as a result of primary nucleation there are mainly monomers of an insoluble phase. Then Smoluchowski equation expanded by the chemical source looks as follows

$$\frac{dC_i}{dt} = \frac{1}{2}\sum_{j=1}^{i-1} N_{j,i-j} C_j(t) C_{i-j}(t) - \sum_{j=1}^{\infty} N_{i,j} C_i(t) C_j(t)\,, \quad (5)$$

$$\frac{dC_1}{dt} = -\sum_{j=1}^{\infty} N_{1,j} C_1(t) C_j(t) + \chi \frac{A_0}{\tau_c} \exp\left(-\frac{t-\tau_n}{\tau_c}\right), \quad (6)$$

where factor χ considers the monomer mass, and C_i is the concentration of i-mer.

Figures 2, 3 depict some results of the numerical experiments [27] and theoretical researches. Here E_0 is the specific control parameter:

$$E_0 = \frac{A_0 \exp(\tau_n/\tau_c)}{\tau_c}. \tag{7}$$

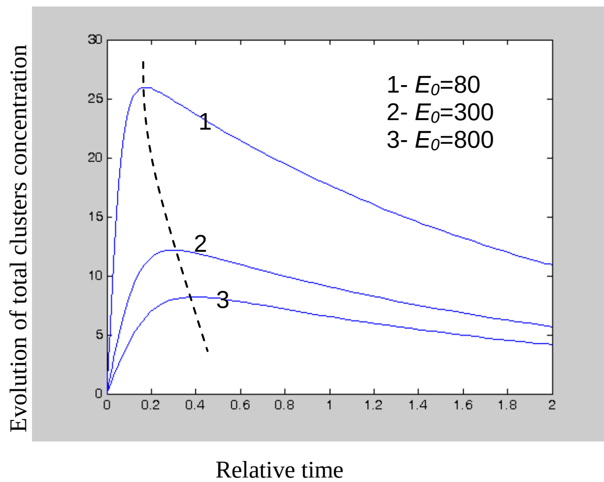

Fig.2 Total concentration of clusters in the system with first-order reaction

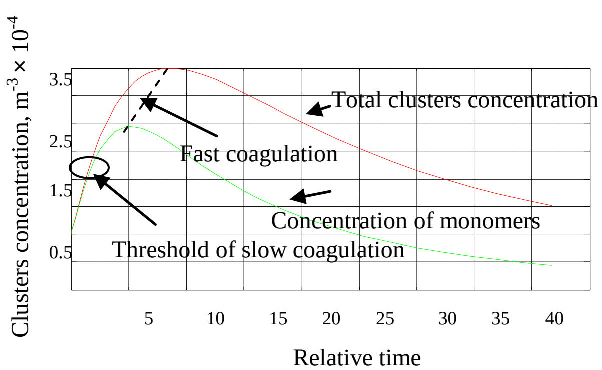

Fig.3. Stages of aggregation

IV. Reactor Model

This section deals with the methods for modeling chemical reactors in the case when an insoluble dispersed phase is being formed in a working zone. Following problems are thus solved:

1. Distribution of concentration of a dispersed solid phase over height of the periodic reactor with mixing has been described.
2. The procedure for calculating the time of reagents stay in the reactor taking into account the formation and sedimentation of solid phase has been developed.

The general model reads [5]

$$D_{ef}\frac{\partial^2 C}{\partial z^2} - (W_{oc} - V)\frac{\partial C}{\partial z} + I_{chem} = \frac{\partial C}{\partial t}, \tag{8}$$

where I_{chem} - intensity of a chemical source depending on a reaction order.

The rate of sedimentation taking into account the evolution of average size of solid particles in consequence of aggregation is:

$$W_{oc} = \zeta a^2 \left(1 - \exp\left(-\frac{t}{\tau}\right)\right)^2. \tag{9}$$

Formation of suspension in the periodic reactor with a mixer is considered in approach of isotropic turbulence. The decision of the equation of diffusion for the reactor of periodic type in case of reaction of the first order looks as follows

$$C_{sol} = -\frac{D_{ef} C_l^0 \exp(-kt)}{W_{sol}} + C_{sol}(0)\exp\left(\frac{W_{sol} z}{D_{ef}}\right). \tag{10}$$

The concentration of solid phase averaged over height of the reactor reads

$$\overline{C}_{sol} = \frac{D_{ef C_{sol}(0)}}{W_{sol} H}(\exp(W_{sol} H / D_{ef}) - 1) - \frac{D_{ef} C_l^0}{W_{sol}}\exp(-kt). \tag{11}$$

The stage of the end of chemical transformations and achievement of demanded conversion in the reactor with mixing is characterized by an exit on a stable curve of distribution of density of suspension over height of the apparatus (Figure 4).

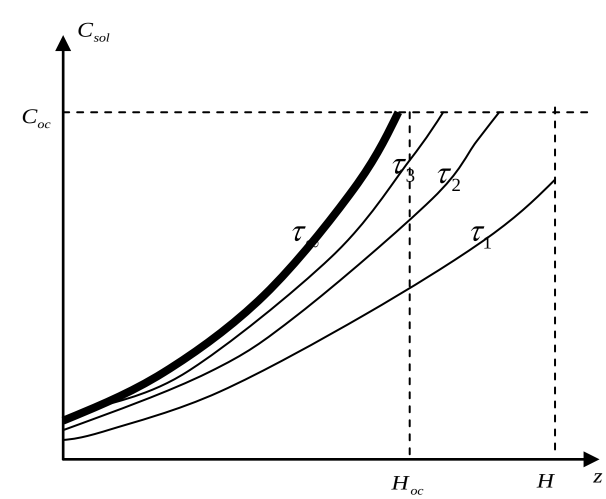

Fig. 4. Plots of exit to stable curve of the density of suspension:

$\tau_1 < \tau_2 < \tau_3 < \tau_\infty$

Further the example of calculation of a stage of sedimentation of solid phase and formation of dregs is considered in case of model representation of suspensions in the form of two initial different fractions and fraction of theirs aggregate.

After the end of the first period of sedimentation in the reactor still there are dregs of the first fraction in a zone of height

$$H_1 = (W_2 - W_1)T_2 \ , \tag{12}$$

where W_1, W_2 are the sedimentation velocities of small (index 1) and big (index 2) fractions; T_2 is the time of complete sedimentation of the big fraction.

In this zone the gradient of density of the first fraction will be observed. This gradient can be calculated from following reasons.

Inasmuch as $\rho_1(t) = \rho_{10} - \rho_3(t)$, for the time delay of sedimentation between fronts of different fractions it is possible to write.

$$t = \frac{z}{W_2 - W_1} , \tag{13}$$

where z is the current vertical coordinate.

Then we obtain the expression for calculating the density of small fraction in a zone between sedimentation fronts:

$$\rho_1(z) = \rho_{10} - \rho_3\left(z/(W_2 - W_1)\right) , \tag{14}$$

where ρ_3 is the density of the aggregate fraction.

Thus, the presented model allows counting almost all basic characteristics of process of sedimentation.

V. Conclusions

The model of aggregation of a disperse phase in systems with chemical reactions which is based on the Smoluchowski's equation for binary coagulation is submitted. Regularities of process of aggregation in systems with a chemical source of monomers of an insoluble phase are studied, and presence of two critical concentrations in the course of coagulation of an insoluble phase in the reacting systems caused by achievement of a threshold of coagulation for primary monomers and end of an active stage of chemical reaction in the periodic reactor is confirmed. The mathematical model of periodic chemical reactors with mixing devices for calculating and optimizing processes with formation of an insoluble phase in a working zone has been carried out.

References

[1] Sontag, H., Strenge, K. (1970) Koagulation und Stabilitat Disperser Systeme. *Veb Deutsher Verlag der Wissenschaften*, Berlin. .

[2] Stechemesser, H., Dobias, B. (eds.) (2005). Coagulation and Flocculation Gooding, *Taylor & Francis, Boca Raton*, London..

[3] Wattis, J. A. D. (2006). An introduction to mathematical models of coagulation-fragmentation processes: a discrete deterministic mean-field approach. *Physica D 222*, 1.

[4] Brener, A.M., Balabekov, B. Ch., and Kaugaeva, A. M. (2009) Non-local model of aggregation in uniform polydispersed systems. *Chem. Eng. Transactions 17*, 783.

[5] Fadda, S., Cincotti, A., Cao, G. (2009). Modelling breakage and reagglomeration during

[6] Bodmeier R., Paeratakul O., 1989, Spherical agglomerates of water‐insoluble drugs, Journal of pharmaceutical sciences, 78(11), 964-967.

[7] Bittanti S., Laub A. J., Willems J. C., 1991, The Riccati Equation, Springer-Verlag, New York.

[8] Blackman J.A., Marshall A., 1994, Coagulation and Fragmentation in cluster-monomer reaction models, J. Phys. A.: Math. Gen. 27, 725-740.

[9] Boehm A.B., Poor C., Grant S.B., 1998, Particle coagulation and the memory of initial conditions, J. Phys. A 31, 9241.

[10] Brener A.M., 2006, Nonlocal Equations of the Heat and Mass Transfer in Technological Processes, Theor. Found. Chem. Eng, Vol. 40, 564-573.

[11] Brener A.M., Nonlocal Model of Aggregation in Polydispersed Systems, 2011, Theor. Found. Chem. Eng, Vol. 45, 349-353.

[12] Brener A.M., Balabekov B.Ch., Kaugaeva A.M., 2009, Non-local model of aggregation in uniform polydispersed systems, Chem. Eng. Trans. (CET), Vol 17, 783-789.

[13] Davies S.C., King J.R., Wattis J.A.D., 1999, The Smoluchowski coagulation equations with continuous injection, J. Phys. A 32, 7745.

[14] Ernst M.H., 1986, Kinetics of clustering in irreversible aggregation, Fractal in Physics, Pietronero L., Tosatti E., Eds., North-Holland, Amsterdam.

[15] Friedlander S.K., 2000, Smoke, Dust and Haze, Oxford University Press, Oxford.

[16] Leyvraz F., 2003, Scaling theory and exactly solved models in the kinetics of irreversible aggregation, Phys. Reports, 383, 95-212.

[17] Liu R. (ed.), 2008, Water-insoluble drug formulation, CRC Press.

[18] Logan B.E., 2012, Environmental Transport Processes, Wiley, Hoboken, New Jersey, 479.

[19] Menon G., Pego R.L., 2004, Kinetics of a precipitation from supersaturated solid solutions, Comm. on Pure and Appl. Math, vol. LVII, 1197-1232.

[20] Slemrod M., 1990, Coagulation-diffusion systems: derivation and existence: derivation and existence of solutions for the diffuse interface structure equations, Physica D, 46, 351-366.

[21] Spicer P.T. and Pratsinis S.E., 1996, Coagulation and Fragmentation: Universal Steady-State Particle-size Distribution, AIChE J., vol. 42, No6, 1612-1620.

[22] Voloshcuk V.M. and Sedunov Y.S., 1975, Coagulation in disperse systems, Leningrad (in Russian).

[23] Yu Jiang, Hu Gang, 1989a, Generalized Smoluchowski equation with gelation, Phys. Rev. B 39, 4659.

[24] Yu Jiang, Hu Gang, 1989b, Long-time behaviour of the cluster size distribution in joint coagulation processes, Phys. Rev. B 40, 661.

[25] Wattis J.A.D., 2006, An introduction to mathematical models of coagulation-fragmentation processes: A discrete deterministic mean-field approach, Physica D 222, 1-20.

[26] Wong B. A., Nash D. G., Moss O. R., 2009, Generation of nanoparticle agglomerates and their dispersion in lung serum simulant or water, Journal of Physics: Conference Series, IOP Publishing, 151(1), 012036.

[27] Jin J. M. and Jjie Z. S., 1996, Computation of special functions, Wiley.

Shear panel for seismic protection of structure

Dora Foti

***Abstract*—**The paper describes a new dissipation device that can be used to preserve the structural integrity of civil engineering structures under seismic loads. The proposed device is made in aluminum and dissipates energy through the hysteretic behavior and the local plasticization. It is a very simple device with a low cost of production. The proposed dissipator has been tested using a monotonic type of experiment in order to define its main characteristics, then its dynamic characteristic behavior has been obtained through some tests on a 3D shaking table. The frame has been subjected to a series of accelerograms allowing to determine the dynamic behavior of the shear panels under severe work conditions, and to assess the efficiency of the device.

***Keywords*—**Seismic protection, Steel and Aluminum devices, Hysteretic dissipaters, Shaking-table tests.

I. INTRODUCTION

VIBRATION control is a subject that has received large attention in the field of earthquake engineering, and, accordingly, a variety of new techniques and devices have been developed for controlling structural vibrations induced by earthquake ground motions. Among passive control devices, tuned mass dampers (TMDs), tuned liquid dampers (TLDs), viscous dampers, and hysteretic dampers are particularly popular. TMDs, TLDs and viscous dampers are very efficient in controlling vibrations produced by small ground motions, but they do not sufficiently dissipate energy during large ground motions. Moreover, some problems related to their weight (TMDs,TLDs) or to their accommodation (viscous dampers) into the structure limit their use.

Hysteretic dampers develop their damping from the energy dissipation due to the hysteretic behavior of their material (like steel) that are strained beyond the yield limit. They can provide relatively large dissipation for their size, and thus can be cost-effective.

Studies have been developed from numerical and experimental points of view on hysteretic dampers subjected to near-field motions [1] to understand their efficacy during this kind of seismic events. Comparisons have also been developed between frames equipped with hysteretic dissipaters or friction dissipaters [2, 3], and equipped with dissipators or isolators [4].

A critical drawback of such hysteretic dampers is that they cannot function as dampers unless their materials receive inelastic excursions, since the materials' post-yielding hysteresis is the source of energy dissipation. Because of this drawback, they are effective only for larger earthquake excitations but fail in providing the required damping for smaller vibrations.

Moreover, most of the seismic codes are oriented to the concept of damage control: the structure should resist to minor or moderate ground motions with minimum structural damage, and may be damaged during large earthquake without collapse and loss of lives. For these reasons structural steel has been used for the seismic control of structures in recent years. To overcome the problem that steel devices cannot be used for smaller vibrations since in this case they have not inelastic deformation, dampers made of low yield steels [5], having a yield stresses as small as 100Mpa, have been designed [6-8].

The application of low-yield steel plates acting in shear allows a large amount of earthquake energy to be dissipated by complementary elements, which, therefore, serve as hysteretic dampers.

Actually, there are several types of dampers that could be profitably used for the seismic control of structures, but the combination of low-yield steel and shear panels is particularly effective.

First, the use of low-yield material insures the damper to undergo large inelastic deformations at the first stages of the loading process, thus enhancing the energy dissipation capability of the whole system in a wide range of deformation demand. Secondly, the use of a plate subjected to uniform in-plane shear force allows the yielding of the material to be spread over the entire damper, ensuring a very large global energy dissipation capability. Thirdly, low-yield strength shear panels are characterized by a very stable hysteretic response up to large deformations, with a conspicuous strain-hardening under load-reversals and with limited strength and stiffness degradation arising from buckling.

The difficulty to produce low-yield steel have pushed to use the aluminum alloy that could offer a similar behavior.

Shear devices have been designed either as large panels rigidly and continuously connected along the confining frame elements, either as elements installed in the frameworks of a building connected by bracing or pillar type system [5-14].

The difficulty to find low-yield steel on the market has pushed to use aluminum, which could offer a behavior similar to low-yield steel.

In this paper the behavior of new dissipation devices made in aluminum and steel is discussed. To maximize the energy dissipation, it is necessary that the panels start to deform

This work was supported This work was supported by RELUIS 2015 project, research line 6 on "Isolation and Dissipation", UR POLIBA.

Dora Foti, Department of Civil Engineering and Architecture, Technical University of Bari, Bari, Italy.

plastically at relatively low forces, and they could still guarantee an adequate resistance before the final rupture. The aluminum is characterized by a low-yield behavior. To avoid the easy out-of-plane deformation of the aluminum plates, high-resistance steel stiffeners have been added. Therefore the aluminum panel presents some area with facilitated plasticization, due to the lower yield point of the aluminum and the geometric configuration adopted.

Starting from the initial idea and on the basis of theoretical considerations and numerical simulation, the optimal geometry of the panel has been defined. A detailed report on this first phase of design of the devices is summarized in previous works [15,16].

The optimized device has been tested for dynamic characterization, the shear force-deformation hysteresis has been obtained to evaluate the plasticization under loading. Quasi-static tests have been performed in the testing laboratory of the Technical University of Bari to verify the design; then shaking-table tests have been performed at LNEC laboratory (Lisbon, Portugal) to simulate the real in situ behavior of these devices [16,17].

II. Description of the Dissipative Device

The two types of shear panels that have been tested on the shaking table are principally made of a 2mm-thick aluminum plate (AW-8006 EN573-3) which is symmetrically coupled to two 6.5mm-thick steel plates. The steel plates present some wide openings, its function in order to give a lateral stiffness to the device. In this way, the out-of-plane instability phenomena of the aluminum plate is avoided, or at least delayed. The geometrical configuration and the dimensions of the panels are shown in Fig. 1.

The two different kinds of panel differ only in the means of connection of the plates. In the first solution, the three plates have been fixed with epoxy resin and uniformly bolted to the steel plates. In the second one, brazing has connected the plates. In the last junction modality, the initial geometry has been varied and two lateral 500x100x100mm wings have been welded in place, to limit the lateral out-of-plane deformations of the panels. The sole use of epoxy resin to join the plates has been rejected, because this solution has not been effective during the preliminary tests.

In fact, these tests proved that the load transmission among the plates is critical for the device, since the plasticization of the aluminum plates could be obtained if the same deformation of all the plates is achieved.

The bolted specimen had the most efficient response, while in the brazed connection the existence of imperfectly adherent areas led to delamination. This result is not due to bad junction execution, but to a manufacturing difficulty.

III. Testing

A. Preliminary quasi-static tests

Some preliminary tests have been performed at the Laboratory of the Technical University of Bari to evaluate the mechanical characteristics of the shear panels, both in terms of global and local behaviors. The tested panels were made: a) one made with an aluminum plate and two steel reinforcements (referred as “aluminum shear panel”), b) another with an inner steel plate and two steel reinforcements (referred as “steel shear panel”).

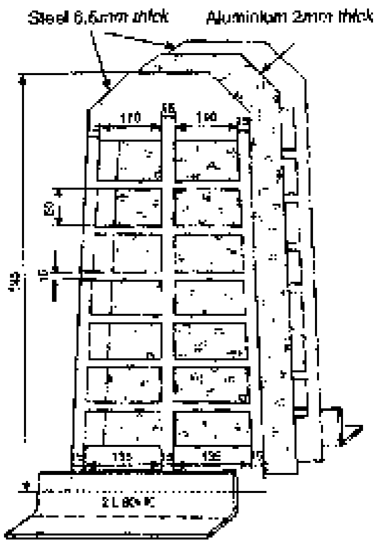

Fig. 1 Geometric description of the panel.

On the basis of the quasi-static results [17] the design of the panel was improved:

1. A first type of panel has been designed tightening the three plates by epoxy glue and a series of 108 M6(8.8) bolts.
2. A second type of panel has been designed welding the three plates by brazing; in addition, the two steel plates were welded laterally, once at each side of the dissipator, to cope with the out of the plane forces.

B. Shaking-table tests

The shaking table tests were performed at the laboratory of the “Laboratorio National de Engenharia Civil” (LNEC) in Lisbon. The two types of aluminum devices were mounted on a frame connected to a shaking table (Fig. 2).

The shaking table measures 5.6x4.6m in plane and has three degree of freedom, two horizontal and one vertical. The characteristics of the shaking table are illustrated in detail in a report published by LNEC [16].

The measuring system is composed of: LVDT displacement transducers, optical absolute displacement sensors located at the nodes of the frame and at the top and base of the panels, tridimensional piezoelectric accelerometers. The nodes of the framed structure and the top and base of the panels have been instrumented. Each side of the frame is identified by the four cardinal points; the earthquake direction is the East-West (Fig. 3), and the panels (Figs. 4 and 5) are installed on the North and South sides of the frame to work in their plans for the East-West direction of the signal.

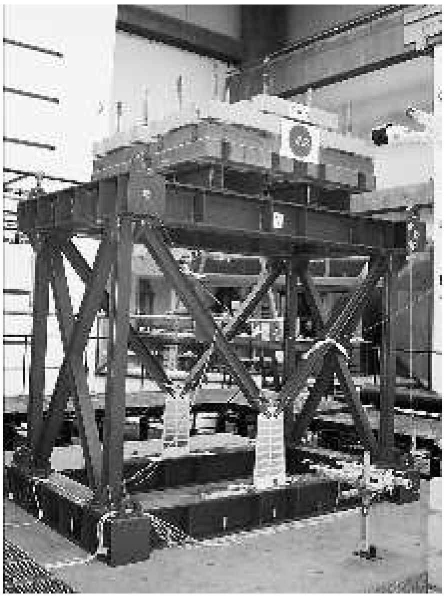

Fig. 2 Frame on shaking table.

The transducers measured:

- the accelerations in the three directions (vertical, transverse and longitudinal) of the shaking table;
- the (vertical, transverse and longitudinal) accelerations of the top of the panel on the North and South sides of the frame;
- the (vertical, transverse and longitudinal) accelerations of the top and base of the frame's columns on the North-West side;
- the displacements (in vertical and transverse directions) of the shaking table;
- the displacements (in vertical and transverse directions) of the top and base of the frame column on the South-East side;
- the displacements (in vertical and transverse directions) of the top and base of both panels.

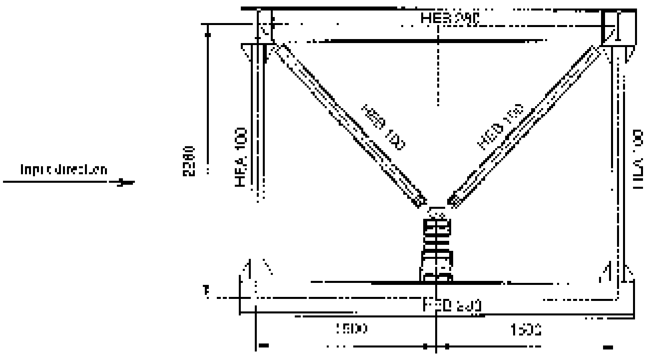

Fig. 3 Geometric characteristics of the frame.

Moreover, to catch the possible out-of-plane instability of the panel the longitudinal displacements in the middle of the external wings of the panels have been measured (Fig. 5).

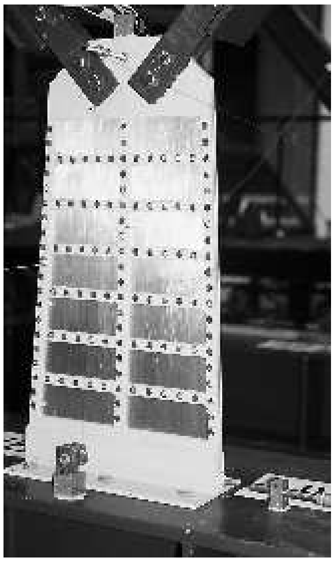

Fig. 4 The bolted panel on the frame for shaking-table tests.

Characteristics of the test frame

The frame utilized for the tests is made of four HEA100 columns and HEB280 beams, the V bracing system consists of HEB100 diagonals connected to the upper nodes of the frame and the top of the panel through M10 bolts. The frame is stiffened with two diagonals to avoid torsional vibrations of the frame (see Fig. 5).

A mass of 8500 kg is added on the top of the frame to simulate the masses that usually act on a real structure.

The structure without panels and bracing (bare frame) has been also tested to obtain some comparisons with the results of the frame with panels for a low level of seismicity.

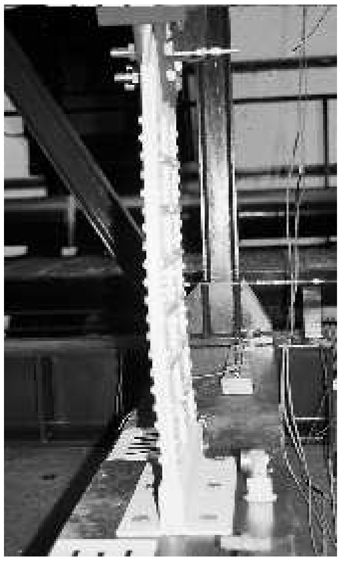

Fig. 5 The bolted panel after the test.

Characteristics of the earthquake

The earthquake used in the test is the Aigio (EW component) earthquake (Fig. 6) scaled by a factor of two. It is

ISBN: 978-1-61804-325-2

characterized by a maximum peak ground acceleration of PGA=0.54g and a duration of 6s. This choice of an impulsive earthquake like Aigio is motivated on the necessity of catching the dissipative capacity of the panels. The tests were performed at increasing levels of peak ground acceleration. A "pink noise" has been applied to the structure after a sequence of tests using the Aigio input, to evaluate the natural frequencies of the frame, and to identify possible changes of its dynamic characteristics.

Tests on the frame with bolted and with brazed panels have been performed. In addition and for comparison aims, tests on the structure without any dissipating device have been also performed.

IV. Tests results

The tests performed with increasing PGA have demonstrated that a large dissipation capacity has been offered by both types of aluminum shear panels (bolted and brazed).

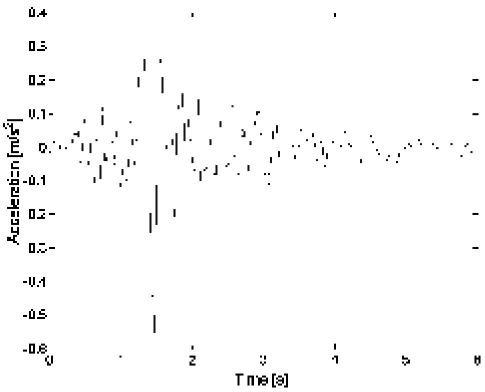

Fig. 6 Aigio earthquake, component E-W (1995).

During the first tests at a low seismic intensity no damage on the panels appeared, but the cycle is already quite large, showing a dissipative capacity at these levels. Figs.7 and 8 show the hysteresis cycles of both panels (bolted and brazed) at low seismic intensity levels. When the PGA increases, the hysteresis cycles become wider and the energy dissipated is higher. Moreover, it can be seen that the panel does not lose its initial stiffness. From the comparison of the hysteresis cycles of the bolted and brazed panels it can be noticed that the cycles are similar in shape and in size at low PGA.

At higher seismic level, the bolted panels showed some buckling phenomena. In particular, the out-of-plane inflection started at PGA=0.5g.

The brazed panels have been subjected to the same deformation only at high levels of PGA because of the presence of the lateral stiffeners on the wings. Two transducers located to measure the displacement orthogonal to the input direction of the panel corresponding to the out-of-plane deformation. Figs. 9 and 10 show the out-of-plane displacement of the panels due to six repetitions of the Aigio earthquake record. Each repetition produce an increment into the permanent deformation in both panels.

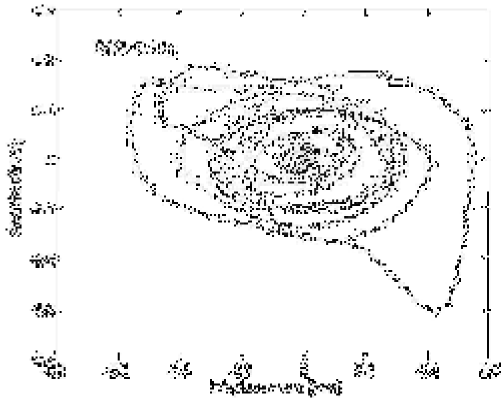

Fig. 7 Bolted panel: hysteresis at low level of seismicity.

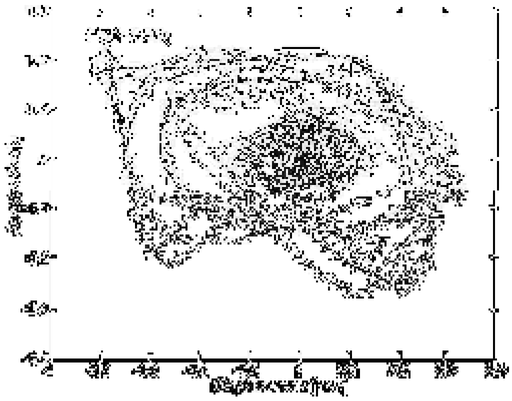

Fig. 8 Brazed panel: hysteresis at low level of seismicity.

It can be noticed that the permanent deformation and the consequent loss of planarity of the panels, verified at medium-high earthquake intensities, do not seem to affect their dissipative capacity.

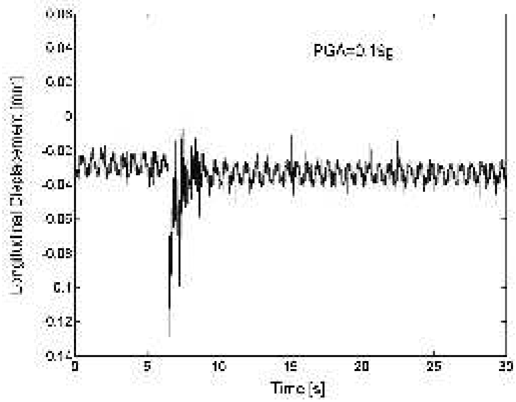

Fig. 9 Out-of-plane displacement of the bolted panel at low level of seismicity.

Moreover, the wings added to the brazed panels reduced the out-of-plane deformation and assured a better cohesion between the plates. However, it reduced the plasticization, and consequently the dissipative capacity of the brazed panels that is effective at high levels of the seismic intensity. Fig. 5 shows the final deformed configuration of the bolted panel at the end of the test, where a clear out-of-plane deformation is registered.

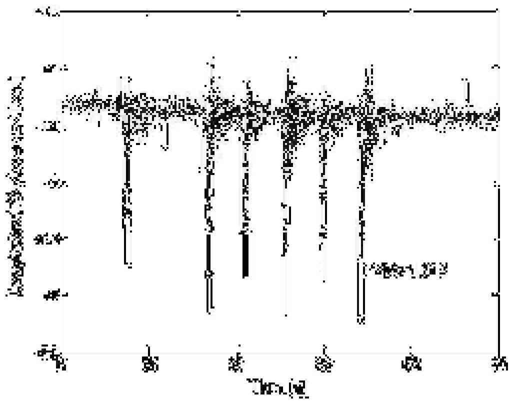

Fig. 10 Out-of-plane displacement of the brazed panel at low level of seismicity.

In Fig. 11 the maximum displacement at the top of the frame column is reported versus to the PGA of the input. At low level of the seismic intensity, the frame with both the types of devices, as expected, had smaller displacements compared to the ones of the bare frame. For medium levels of the input intensity the bolted panels gave a better response with a reduced displacement at the top of the column, while at high levels of the input intensity the brazed panels gave smaller displacements, probably due to the presence of the wings that initially (at low PGA) reduced the inelastic deformation but did not limit the plasticization for large earthquakes. This result proves how critical can be the design of this type of shear panels, since an added stiffness could reduce the efficiency in dissipation. In the meanwhile the problem of buckling should be taken into account to avoid instability problems.

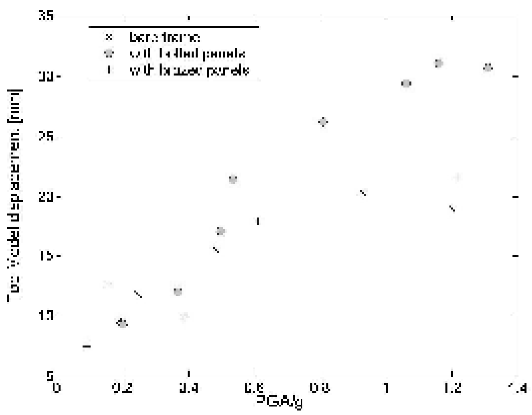

Fig. 11 Maximum transverse displacements of the top of the frame at increasing PGA.

V. Conclusions

The new aluminum-steel panels proposed have been shown to be able to dissipate a large amount of seismic energy, limiting and concentrating the seismic damage. The simple device has the advantage of an easy replacement that allows to restore rapidly the functionality of a building

The performed tests on a frame protected with the proposed shear panels have shown their capability to dissipate a large amount of seismic energy, limiting and concentrating the damage. In fact, the tested frame was found to withstand even catastrophic events without damage. The localized damage was exclusively concentrated in the panels.

Two types of dampers have been tested on the shaking table. The comparison of the experimental results has shown that the total behavior of the brazed panels was not completely satisfactory for the lower plasticization capacity and the delamination danger that showed up in the most severe test conditions. The first problem was due to the presence of the wings in the brazed panels, that had been added with the aim of guaranteeing better cohesion of the plates. However, they negatively influenced the plasticization capacity, since this inelastic phenomenon appeared at high levels of the seismic intensity.

Both bolted and brazed panels suffered of the out-of-plane deformations, the buckling phenomenon of the aluminum plate and permanent deformations.

The test results have proved the importance of an optimum design of the device to avoid buckling phenomena, to transfer properly the shear force among the plates, and to make possible the plasticization at low levels of the input seismic intensity. To solve these problems in the damper design the choice of the stiffeners, the type of connections among the plates and the plates thickness are crucial points to be accurately considered.

Acknowledgment

This work was supported by RELUIS 2015 project, research line 6 on “Isolation and Dissipation”, UR POLIBA.

References

[1] L. D. Tirca, D. Foti, M. Diaferio, “Response of middle-rise steel frames with and without passive dampers to near-field ground motions”, *Eng Struct*, vol. 25, no. 2, pp. 169-179, 2003. ISSN: 0141-0296.

[2] D. Foti, L. M. Bozzo, F. Lopez-Almansa, “Numerical Efficiency Assessment of Energy Dissipators for Seismic Protection of Buildings”, *Earthq Eng and Struct Dyn*, vol. 27, pp. 543-556, 1998, ISSN: 0098-8847.

[3] D. Foti, “Local ground effects in near-field and far-field areas on seismically protected buildings”, *Soil Dyn and Earthq Eng*, vol. 74, pp. 14-24, 2015. DOI: http://dx.doi.org/10.1016/j.soildyn.2015.03.005

[4] D. Foti, “Response of frames seismically protected with passive systems in near-field areas”, *Int J of Struct Eng*, vol. 5, no.4, 2014, pp. 326-345.

[5] E. Saeki, M. Sugisawa, T. Yamaguchi, A. Wada, “Mechanical properties of low-yield point steels”, *J of Mat in Civil Eng*, vol. 10, no.3, paper n. 12127, 1996.

[6] M. Nakashima M., S. Iwai, M. Iwata, T. Takeuchi, S. Konomi, T. Akazawa, K. Saburi, “Energy dissipation behaviour of shear panels made of low-yield steel”, *Earthq Eng and Struct Dyn*, vol. 23, pp.1299-1313, 1994.

[7] M. Nakashima, “Strain-hardening behaviour of shear panels made of low-yield steel I: Test”, *J of Struct Eng*, vol. 121, no.12, paper n.9718, 1995.

[8] A. Formisano, G. De Matteis, F.M. Mazzolani, “Numerical and experimental behaviour of a full-scale RC structure upgraded with steel and aluminium shear panels”, *Comp & Struct*, vol. 88, pp.1348-1360, 2010.

[9] L.M. Bozzo, X. Chais, L.I. Torres, “A shear type of energy dissipator for the protection of masonry infill walls”, *Proc of the 6th US National Conference on Earthquake Engineering*, Seattle, 1998.

[10] G. De Matteis, A. Formisano, F.M. Mazzolani, “An innovative methodology for seismic retrofitting of existing RC buildings by metal shear panels ”, *Earthq Eng and Struct Dyn*, vol. 38, no.1, pp. 61-78, 2009.

[11] M. Yamada, T. Yamakaji, “Steel panel shear wall. Behaviour of steel structures in seismic area”, in: *Proc. of Stessa ’97*, pp.477-480, 1997.

[12] M. Yamada, T. Yamakaji, “Steel panel shear wall – Analysis on the center core steel panel shear wall”, in: *Proc. of Stessa 2000*, pp.541-548, 2000.

[13] L.A. Fulop, D. Dubita, “Performance of wall-stud cold-formed shear panels under monotonic and cyclic loading. Part II: Numerical modelling and performance analysis”, *Thin –walled Struct*, vol.42, pp.339-349, 2004.

[14] D. Foti, M. Diaferio, R. Nobile, “Dynamic Behavior of New Aluminum-Steel Energy Dissipating Devices”, *Struct Control and Health Monitoring*, vol. 20, no. 7, pp. 1106-1119, 2013, DOI: 10.1002/stc.1557.

[15] D. Foti, M. Diaferio, R. Nobile, “Optimal Design of a New Seismic Passive Protection Device Made in Aluminium and Steel”, *An Int J of Struct Eng and Mech*, vol. 35 no. 1, pp.119-122, 2010, ISSN: 1225-4568.

[16] *Shaking Table Tests on shear panels for the seismic protection of buildings*, Report 304/00 –C3ES, Laboratorio Nacional de Engenharia Civil, 2000.

[17] D. Foti, R. Nobile, “Optimum Design of a New Hysteretic Dissipater”, Chapter 12 in: *Design Optimization of Active and Passive Structural Control Systems*, by N.D. Lagaros, V. Plevris, C.C. Mitropoulou, pp. 274-299; Ed. IGC Global USA, Hershey PA 17033 USA, DOI: 10.4018/978-1-4666-2029-2, ISBN 978-1-4666-2029-2 (hardcover) -- ISBN 978-1-4666-2030-8 (ebook) -- ISBN 978-1-4666-2031-5 (print & perpetual access), 2012.

ISBN: 978-1-61804-325-2

Gamma Radiation Induced Preparation of Poly(vinylpyrilidone -Maleic acid-Amidoxime) Resin for Sorption of Some Metal Ions.

Emad H. Borai[1] and Mahmoud G. Hamed[2]

1) Analytical chemistry Department, Hot Laboratories Center, Atomic Energy Authority, 13759, Egypt
2) Waste Management Department, Hot Laboratories Center, Atomic Energy Authority, 13759, Egypt

Abstract-This work was undertaken to prepare new modified polymeric adsorbent containing amidoxime functional group. Poly(vinylpyrilidone-maleic acid-acrylonitrile) P(PVP-MA-AN) was prepared, modified and functionalized with amidoxime, P(PVP-MA-AO). The P(PVP-MA-AO) resin was prepared by gamma irradiation grafting polymerization of P(PVP-MA-AN) in the presence of ammonium ferrous sulfate. Conversion of nitrile groups into the amidoxime was carried out by hydroxylamine in alkaline solution. The identification of amidoxime group was qualitatively performed. The structure of the prepared modified polymeric resin was characterized and confirmed by FTIR, TGA, SEM and surface area analyzer. Results showed that the monomers were successfully grafted and converted into amidoxime. The ion exchange behavior of P(PVP-MA-AO) resin was investigated for sorption of La^{3+}, Ce^{3+}, Nd^{3+}, Eu^{3+},and U^{+4}. Batch experiments were carried out to investigate the effect of pH, contact time and metal ion concentration on the sorption capacity of P(PVP-MA-AO) resin. The obtained results demonstrated that the new prepared sorbent has higher sorption uptake for U^{4+} than that for La^{3+}, Ce^{3+}, Nd^{3+}, Eu^{3+}. The results also revealed that the new P(PVP-MA-AO) resin has relatively high selectivity and high capacity for U^{4+} reached to 152 mg/gm.

Keywords- Grafting copolymer, Irradiation, Lanthanides, Uranium, Sorption.

1. INTRODUCTION

The preparations of newly functionalized grafting polymer by gamma irradiation technique are reported in the present study. Modified polymeric ion exchange polymers are moderately crosslinked hydrophilic polymer networks. The modification of polymers has been of considerable importance in various polymer applications for a long time. Introduction of new functionalities on to existing polymer surfaces has been useful in several applications [1]. In metal uptake applications, can absorb large quantities of water or other aqueous fluids [2], they are mostly used for recovery of rare metal ions from sea water [3] and removal of traces of radioactive metals from wastes [4]. Thus, modified polymers found widespread applicability due to their high capacity [5]. Ion exchange polymers can be prepared by different methods [6], including polymerization processes for functional monomers to obtain homopolymers or copolymers, which can be used in our desired application. Also, they can be prepared by chemical modification of existing polymers. In this method, the modification can be carried out through many ways. One of them is the modification by grafting of functional monomers onto suitable polymeric substrates [7-8]. Polymers modified by radiation are frequently used as synthetic materials for metal adsorption. Their main advantages are high chemical and mechanical stability, high ion exchange and high exchange rate.

This paper focused on the development of polymer formulations to produce modified polymeric resin containing selective function groups. The use of gamma radiation technology is expected to improve the functional properties, therefore, the present study has been conducted to synthesize free radical vinylpyrilidone polymer by grafting copolymerization of VP, MA and AN by means of simultaneous gamma irradiation.

This project was supported financially by the Science and Technology Development Fund (STDF), Egypt, Grant No 5021.

Emad H. Borai, Analytical chemistry Department, Hot Laboratories Center, Atomic Energy Authority, 13759, Egypt, e-mail: emadborai@yahoo.com
Mahmoud G. Hamed, Waste management Department, Hot Laboratories Center, Atomic Energy Authority, 13759, Egypt, e-mail: mahmoud_g_hamed@yahoo.com

2. Experimental.

2.1. Chemicals and Reagents.

All chemicals and reagents were of analar grade and were used without further purification. All salts of lanthanium, Cerium, Neodymium and Eurobium were obtained from Merck. De-oxygenated water was prepared by boiling bi-distilled water for about 15 minutes followed by cooling under a stream of pure dry nitrogen gas at room temperature [9-11].

2.2. Equipment and Instruments.

A cobalt-60 gamma cell of type MC-20 (Russia), was used as an irradiation source for polymerization at the Cyclotron Project, Inshas, Egypt. It has two chambers of 5 liters for sample irradiation. The samples were irradiated in glass bottles at room temperature in the presence of air compressor. A digital analytical balance of model WH 205-4, Wiggen Hauser manufacturing (Germany), with a sensitivity of 1×10^{-4}g, was used for weighting the samples and the standards. The balance was calibrated periodically for quality control of the analysis. A laboratory oven, OF-02G, JEIO TECH manufacturing (Korea), was used for drying the polymeric samples. A programmable shaker thermostat, BS-21, Lab. Companion, JEIO TECH manufacturing (Korea), was used for shaking samples during the preparation and experimental processes. Bi-distilled water system GFL Bi-Dest 2104, KARL KOLB manufacturing (Germany), was used for obtaining the double distilled water. pH meter of model 420A+, thermo Orion manufacturing (USA), was used for adjusting the pH of solutions.

The prepared resins were dried and grinned to a fine powder, then mixed with KBr and pressed to a disk for IR analysis. The FTIR (Fourier transformed infrared) spectra were performed on a computerized spectrophotometer in the range of 4000-400 cm^{-1}, Bomem, Hartmann & Braun, Michelson, MB-Series 157 (Canada).

A computerized UV/Vis double beam spectrophotometer of model T80, PG Instruments Ltd. (England), was used for spectrophotometric determination of metal ions.

Thermal analysis was undertaken using a Shimadzu thermogravimetric analyzer model TGA-50 (Tokyo, Japan). The prepared polymeric materials were washed several times with bi-distilled water, Dried under vacuum and powdered. In order to remove water completely, the samples were dried for 30 min before being characterized by TGA. The thermal stability was investigated at a heating rate of 10°C/min, under nitrogen atmosphere (20 ml/min) from room temperature up to 600°C. The morphology of the prepared resins was Determined JEOL-JSM 6510 LA (Japan). Scanning electron microscope at accelerating voltage of 15 kV was used for investigating the pore structure of different prepared resins at high magnification and resolution by means of an electron beam.

2.3. Preparation of Modified polymeric Resin.

2.3. 1. Preparation of Hydroxylamine Solution.

42.1 g of Hydroxylamine hydrochloride ($NH_2OH.HCl$) was dissolved in 300 ml methanolic solution (methanol to bi-distilled water ratio of 5:1). The HCl of $NH_2OH.HCl$ was neutralized by NaOH solution and the precipitate of NaCl was removed by filtration. The pH of the reaction solution was adjusted to 10.0 by adding NaOH solution. The reaction medium was maintained at methanol to bi-distilled water ratio of 5:1.

2.3.2. Preparation of Poly (Vinylpyrilidone - Maleic Acid – Amidoxime) P(VP-MA-AO) Resin.

Poly(vinylpyrilidone– Maleic acid-Amidoxime) P(VP-MA-AO) was prepared in two steps, the first step prepare P(VP-MA-AN) by grafting polymerization technique of monomers and polymer in de-oxygenated water using γ-rays and the second step modification of acrylonitrile group to amidoxime group by treatment with hydroxylamine solution[12].

The first step was carried out as following, 48 g of MA was dissolved in 100 ml bi-distilled water, mixed with 32 ml of AN and 3 g ammonium ferrous sulphate as inhibitors and

ISBN: 978-1-61804-325-2

complete the mixture to 200 ml bi-distilled water, the solution was mixed with 4 g DAM as crosslinker dissolved in 50 ml bi-distilled water, the total solution mixed with 12 g of PVP which dissolved in 50 ml bi-distilled water.

The mixture was transferred into glass ampoules and nitrogen gas was purged into the ampoules to remove air from the solutions. The glass ampoules were sealed and then subjected to gamma-rays at irradiation dose 15 kGy in air at ambient temperature. The obtained resins were cut into small pieces with a stainless steel scissors, soaked in acetone for removal of unreacted monomers, washed with bi-distilled water dried and stored.

The second step is the amidoximation of acrylonitrile present in P(VP-MA-AN) resin to P(VP-MA-AO) resin. Resin is based on the treatment of acrylonitrile with hydroxylamine [12]. About 20 g of the prepared P(VP–MA–AN) resin was placed into the two-neck flask, which was equipped with a mechanical stirrer, condenser and thermostat water bath. Then 40 ml of hydroxylamine solution was added to the flask with 300 ml methanolic solution (methanol/bi-distilled water 5:1) and the reaction was carried out at 70°C for 2 h duration. The resin was separated from the solution by filtration and washed several times with methanolic solution (methanol/bi-distilled water 5:1). Then, the resin was treated with 200 ml of acidic solution (0.1 N HCl) for at least 5 min. Finally, the resin was filtered, washed several times with methanolic solution (methanol/bi-distilled water 5:1) and then dried at 50°C to a constant weight.

2.3.4. Qualitative Test of Amidoxime Functional Groups.

There are several methods have been employed for confirmation of amidoxime groups in the resin [13]. Many metal ions bind with amidoxime to produce visual color in the resin bead. Therefore, the presence of amidoxime groups in the resin was confirmed by vanadium ion test in the formation of a purple complex. About 0.2 g of wet resin was shaken with solution of vanadium(V) ions in dilute hydrochloric acid where, a purple coloured complex on the resin beads was observed[14].

2.4. Adsorption Studies.

The interaction of the prepared polymeric resins with La^{3+} , Ce^{3+}, Nd^{3+}, $Eu^{3+}$and U^{4+} metal ions aqueous solution was carried out by contacting under mechanical stirring 0.05 g of the prepared resins with 10 ml 100 mg/l of aqueous solution of each element individually at room temperature for 3 hrs. The polymeric resins were separated from solution by centrifugation and then filtration using 0.45µm whatman membrane filter to ensure for the removed of suspended material in solution. Metal ions concentrations were measured by using a computerized UV/Vis double beam spectrophotometer using 4–(Pyridyl–2–azo) resorcinol (PAR) as sensitive coloring reagent. Based on the initial and final metal concentrations, after measurement the remaining metal ions in the filtrate percent uptake and the capacity were determined respectivly by:-

$$q(mg/g) = \frac{(C_i - C_e)V}{m} \quad \ldots\ldots (1)$$

$$\%\ uptake = \frac{(C_i - C_e)}{C_i}100 \quad \ldots. (2)$$

Where (q)is the maximum capacity(mg/g) C_i and C_e are the initial and equilibrium concentrations (mg/l) of metal ions solution, respectively, V is the volume of solution in liter and m is the weight of the resin in gram.

The effects of shaking time, pH and initial metal concentrations, were tested using batch conditions by magnetic stirrer at 180 rpm. The effect of shaking time was performed at pH = 4, concentration 100 mg/l and various shaking time from 5 min to 24 hrs. For these investigations 0.05 g of the studied resin was immersed into 10 ml of solutions, after that the mixture was centrifugation and then filtrated and measured. The effect of pH on the adsorption of La^{3+} ,Ce^{3+}, Nd^{3+}, Eu^{3+} and U^{4+} metal ions onto P(VP-MA-AO) resin was studied by equilibrating the mixture containing a 50 mg of dried resin and 10 ml of 100 mg/l stock metal ions solution at different pH values between 1.0 and 5.0, depending on the precipitation curve studied. The effect of initial metal ion concentration on the adsorption process onto resin was studied by varying initial metal concentration from (25 to 2000) mg/l for uranium metal ion. For these investigations, 0.05 g of each resin was contacted with 10 ml of metal solution then shaked at room temperature for 3hrs. The mixture was centrifuged, filtrated and measured.

3. RESULTS AND DISCUSSION

3.1. Preparation of P(VP-MA-AO) Resin.

The grafting by the mutual irradiation includes irradiation of polymer and monomers simultaneously, to form free radicals for polymerization process [15]. P(VP-MA-AN) resin was prepared by grafting copolymerization of MA and AN monomers onto P(VP) as a grafting polymer in the presence of DAM as acrosslinker and ammonium ferrous sulphate as inhibitor, by using gamma-radiation technique. The conversion of nitrile group to amidoxime one was carried out by treatment of the prepared resin P(VP-MA-AN) with hydroxylamine hydrochloride in an alkaline medium, carried out at optimum experimental conditions of copolymer-hydroxylamine ratio 1:1, reaction period 2 h, temperature 70°C, reaction medium methanol to water ratio of 5:1 and pH 10.0. The reaction mechanism for synthesis of P(VP-MA-AO) resin is shown on Sch. (1).

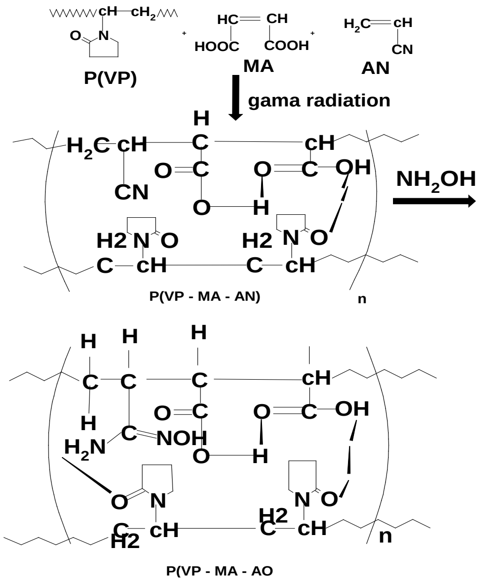

Sch. (1): Synthesis of P(VP-MA-AO) resin.

3.2. Characterization of the Prepared Polymeric Resins.

3.2.1. FTIR Analysis of Poly(vinylpyrrilidone - Maleic Acid - Amidoxime) P(VP-MA-AO).

According to chemical structure of the polymers, hydrogen bonding must be between the carboxylic group and the amide group. Fourier transform infrared spectroscopy was used for the identification of hydrogen bonds in P(VP-MA-AN) as shown in FTIR spectrum Fig.1. From the literature the carbonyl group of PVP exhibits a peak between 1640 and 1680 cm^{-1}[16]. When the carbonyl group forms intermolecular bonding there is anegative shift exhibited in the IR spectrum. The absorption peaks appeared at 1640, 2147 and 1709 cm^{-1} are attributed to contributions of carbonyl (–C =O) ,cyano (–≡N) and carboxylic (–COOH) groups of PVP, AN and MA respectively, the presence of these peaks verifies the polymerization of PVP, MA and AN by gamma-radiation technique. The bands appearing at 3058 corresponding to the adsorbed water molecule [17,18]. The absorption peak around 3500 cm^{-1} can be ascribed to the C–N group and Shows the absorption peaks at 1729 cm^{-1} for C=O of carboxylate group. After amidoximation, the CN band (2147 cm^{-1}) disappeared, a new band of amidoxime groups >C=N stretching vibration formed at 1648 cm^{-1} and the amide II band of NH formed at 1570 cm^{-1}. This proved the conversion of cyano groups to amidoxime.

3.2.2. Scaning electron microscope

The morphology of P(VP-MA-AN), P(VP-MA-AO) resins is observed by SEM in Fig. 2. It can clearly observe that the thin-layer P(VP-MA-AN) that the spontaneous stacking curls form petal-shaped aggregates. This flocculent aggregate in the absence of external forces will remain stable and it is difficult to separate from each other. Fig. 2b shows that P(VP-MA-AO) has flake structure and the size is also larger than the previous. This is mainly due to that the AO makes the surface layer peeling off more obvious and the layers become thinner, thus increasing the adsorption capacity.

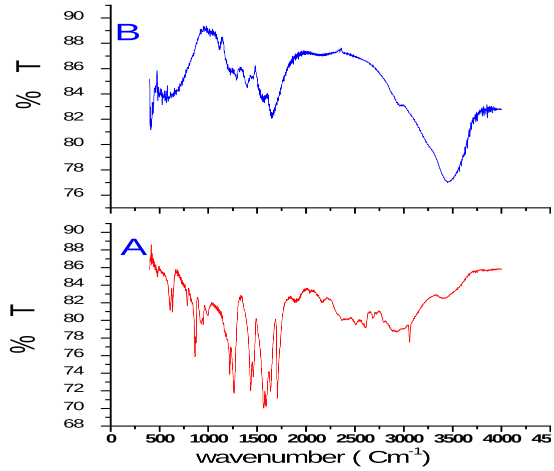

Fig.1. FTIR spectrum of of (a) P(VP-MA-AN) *and* (b) P(VP-MA-AO)

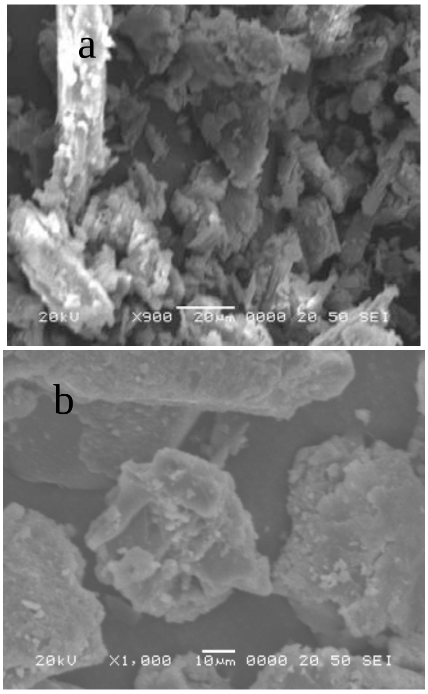

Fig. 2. The scanning electron micrograph of (a) P(VP-MA-AN) resin and (b) P(VP-MA-AO) resin.

3.2.3. Thermogravimetric Analysis (TGA).

The TGA and DTA curves for P(VP-MA-AO) resin are shown on Fig. 3, in which the thermogram of P(VP-AA-AO) resin is divided into three stages based on TGA and DTA. It can be seen that, the first stage from 63 to 190°C with a maximum at 118°C exhibits a weight loss of 21.44% due to the removal of absorbed or coordinated water molecules. The second stage from 190 to 420°C with a maximum at 343°C exhibits a weight loss of 23.2% due to release of water as a result of anhydride decarboxylation. This decomposition may be occurred through a cyclization process with the removal of water molecules from two carboxylic groups Sch. 2. The third stage from 420 to 800°C with a maximum at 453-665°C, decomposition of P(VP-MA-AO) resin is characterized by a weight loss of 27.74% due to a short chain fragments created by chain scission. This stage is the main one, its weight loss being almost higher than that occurring in the other two stages.

The thermal stability was evaluated by TGA/DTA analysis within the temperature range 25°~1000°C. The result of TGA and DTA for P(VP -MA-AN) resin indicates two different weight loss ranges 20-220°C, 220-700°C. The first weight loss is due to the desorption of water from the resin, the second weight loss may be related to chain scission, anhydride decarboxylation Sch 3. These findings suggest that the P(VP-MA-AN) resin is thermally stable up to 200°C.

The TGA and DTA curves for P(VP-MA-AN) resin are shown on Fig. 3, in which the thermogram of P(VP-MA -AN) resin is divided into two stages based on TGA and DTA. It can be seen that, the first stage from 20 to 220°C with a maximum at 158°C exhibits a weight loss of 57.9% due to the removal of absorbed or coordinated water molecules. This stage is the main one, its weight loss being almost higher than that the other stage. The second stage from 220 to 700°C with a maximum at 456°C exhibits a weight loss of 41% due to release of water as a result anhydride decarboxylation Sch.3. This decomposition may be due to a short chain fragments created by chain scission [19, 20].

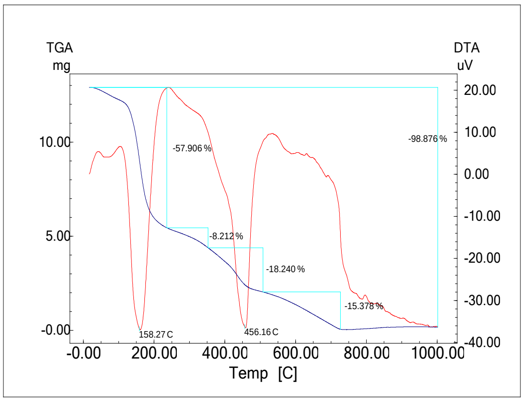

P(VP-MA-AN) resin

ISBN: 978-1-61804-325-2

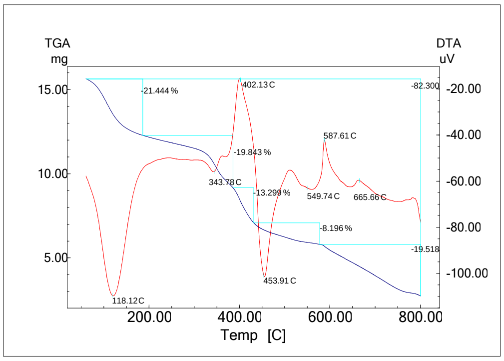

P(VP-MA-AO)

Fig. 3. DTA and TGA curves for P(VP-MA-AN) and P(VP-MA-AO) resins.

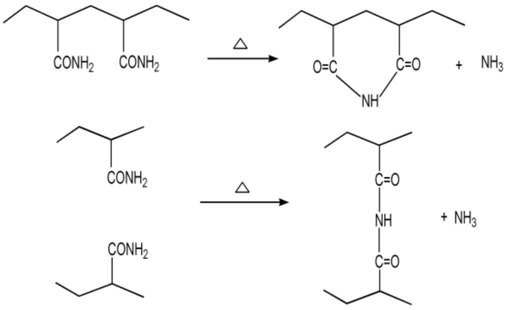

Sch. 2. Effect of heat on MA (dehydration).

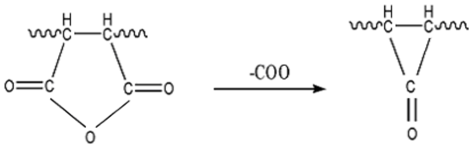

Sch. 3. Decarboxylation of MA anhydride.

3.2.4. Surface Morphology of the Prepared Polymeric Resins.

The BET-surface area depends on particle size distribution, partical shape and number distribution of sracks and pores in the material [21]. The surface area and pore volume of P(VP-MA-AN) and P(VP-MA-AO) resins, illustrated in Table 1, showed small specific surface area and pore volume which, indicated that the porosity is very low.

Table 1. Show porous properties of amidoxime resin.

Resin	Surface area (m^2/g)	Pore volume (Cm^3/g)
P(VP-MA-AN)	13.2	0.045
P(VP-MA-AO)	12.8	0.027

3.3. Sorption of Metal ions.

3.3.1. Metal Hydrolysis.

The main sorption processes of La^{3+}, Ce^{3+}, Nd^{3+}, Eu^{3+} and U^{4+} metal ions are mainly affected by the side reaction that may be occurred due to the precipitation which mainly depends on solution pH. In this respects, series of experiments have been tested separately to evaluate the degree of contribution of each of the two reaction mechanisms (sorption and precipitation). The results are not demonstrated for brevity. Based on the obtained data, it could be observed that all the investigated ions are partially precipitated at pH 6. Therefore, the sorption experiments for all the metal ions were tested in the pH range from 1 to 5 to avoid the metal hydrolysis.

3.3.2. Adsorption of La^{3+}, Ce^{3+}, Nd^{3+}, Eu^{3+} and U^{4+} metal ions by P(VP-MA-AO) and P(AM-MA-AO) Resins.

3.3.2.1. Effect of Contact Time.

The influence of contact time on the rate of the adsorption of La^{3+}, Ce^{3+}, Nd^{3+}, Eu^{3+} and U^{4+} metal ions is shown in Fig. 4. The adsorption results of P(VP-MA-AO), P(AAm-MA-AO) resin show an initial rapid adsorption rate. It can be attributed to the fact that, at the initial stage, the adsorption sites are more available and the metal ions can interact easily with the sites. Therefore, high adsorption rate is takes place. Besides, the driving force for adsorption is the concentration gradient between the bulk solution and the solid-liquid interface and the concentration gradient is high in the initial period, which results in a high adsorption rate. The sorption uptake percentage was attained to equilibrium after 3 hrs for all the investigated metal ions.

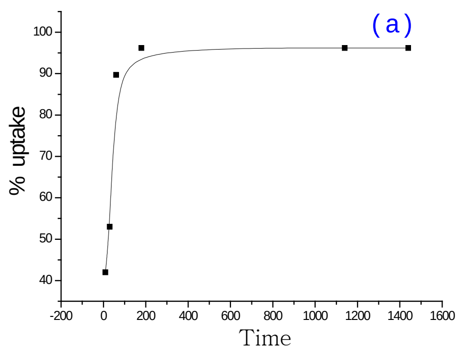

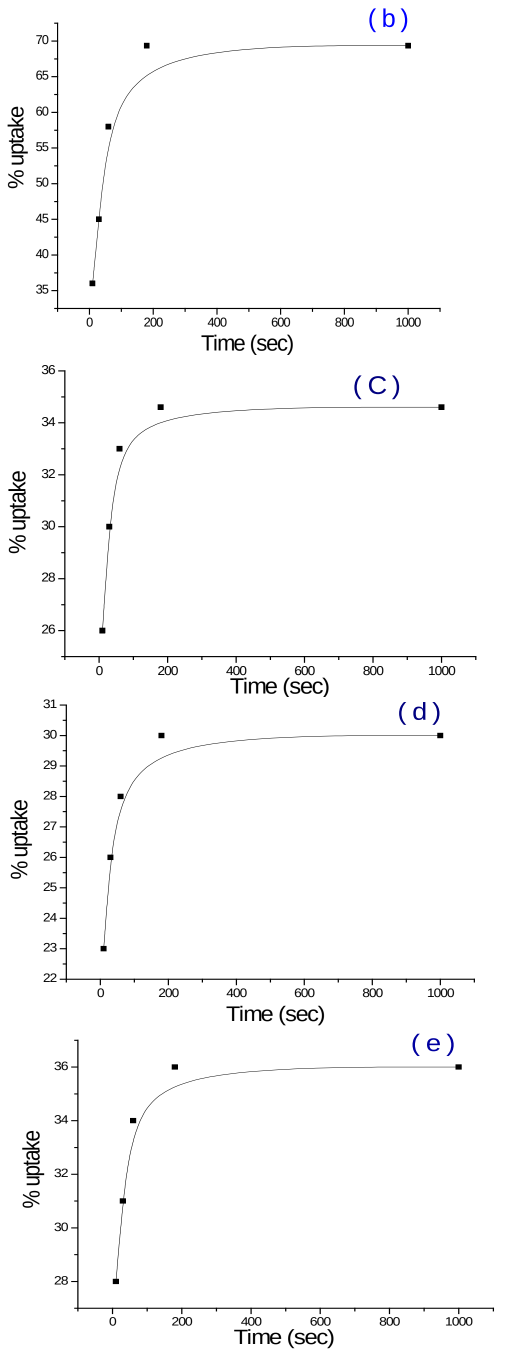

Fig. 4. Effect of contact time on the adsorption of (a)U^{4+}, (b)La^{3+}, (C)Ce^{3+}, (d)Nd^{3+}, (e)Eu^{3+} metal ions onto P(VP-MA-AO) resin.

3.3.2.2. Effect of pH.

pH plays an important role for the adsorption of La^{3+}, Ce^{3+}, Nd^{3+}, Eu^{3+} and U^{4+} metal ions on the prepared resins. The results are shown in Fig. 5 revealed that the percentage of sorption steeply increases with increasing pH up to 5. The low degree of sorption of elements at low pH values 1-2, can be explained by the fact that at low pH values the H^{+} ion concentration is high and therefore protons can compete with the cations on the surface sites. In addition, as pH increases, surface positive charge decreases, this would result in lower columbic repulsion of the adsorbed metal ions. In aqueous solution, the hydrolysis of trivalent lanthanides begins at pH 6 and various species can be formed, such as metal hydroxide. Thus, as pH increases, (over pH 5.0) hydrolysis precipitation most probably would start due to the formation of various hydrocomplexes in aqueous solution. It is also found that, the adsorption of (U^{4+}) metal ions is higher than the adsorption of La^{3+}, Ce^{3+}, Nd^{3+} and Eu^{3+} metal ions.

The maximum uptake percent onto P(VP-MA-AO) resin at pH 5.0 reached to 87, 48.24, 39.84, 32, 24 % for U^{3+}, La^{3+}, Ce^{3+}, Nd^{3+} and Eu^{3+} respectively. It is clear that, P(VP-MA-AO) is more effective for the quantitative removal of (U^{4+}) than La^{3+} , Ce^{3+}, Nd^{3+} and Eu^{3+}. This can be explained in terms, the dissociation of amide, carboxylic and amidoxime groups increase with the increase of pH providing additional binding sites for the adsorption of metal ions. At higher acidic conditions, i.e.low pH value of 1.0-3.0, low adsorption of metal ions was occurred. This is attributed to the competition between H^{+} ions and metal ions for the active sites (amide, carboxylic and amidoxime groups) on the adsorbent surface. Hydrogen bonds may be formed between the active sites of the adsorbent surface causing the surface layer to shrink. This surface layer acts as a barrier slowing down the adsorption of metal ions. With the increase of the pH of the solution, the amount of adsorbed metal ions increases and maximum adsorption was obtained at pH of 5.0.

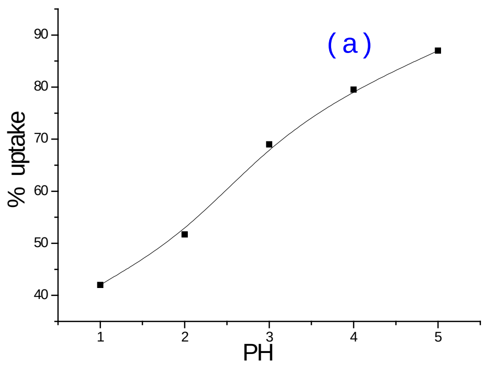

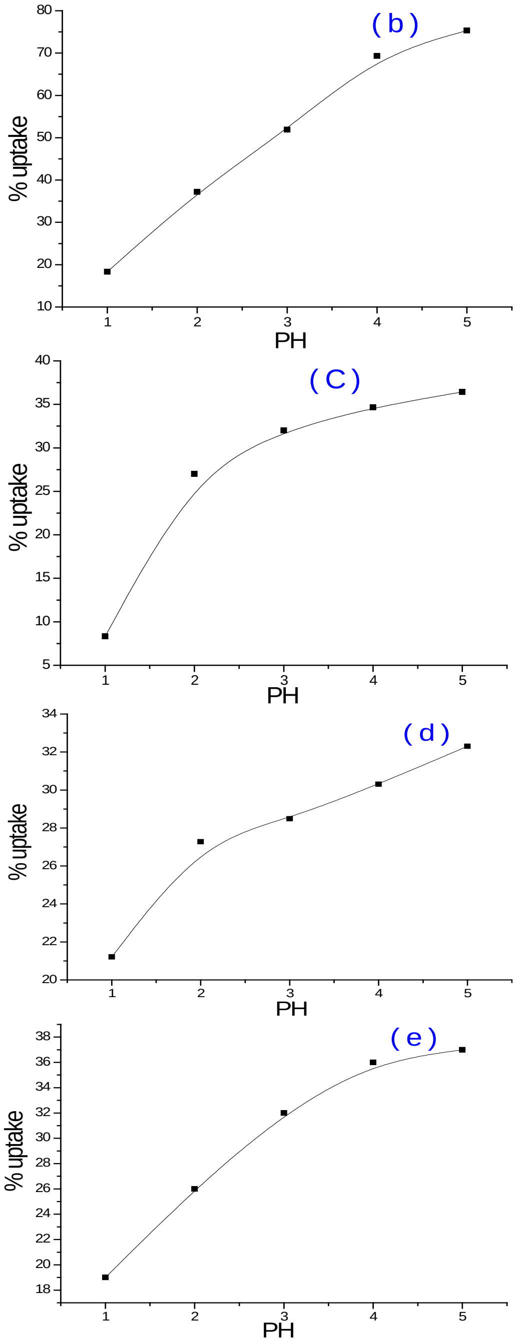

Fig. 5. Effect of pH on the adsorption of (a) U^{4+}, (b) La^{3+}, (c)Ce^{3+}, (d)Nd^{3+}, (e)Eu^{3+} metal ions onto P(VP-MA-AO) resin.

According to the previous metal ions uptake, the effect of initial metal ion concentration on the adsorption process for P(VP-MA-AO) resin will be investigated in details for U^{+4} to evaluate it maximum capacity.

3.3.2.3. Effect of initial U^{4+}concentration on the adsorption process of P(VP-MA-AO) resin.

Batch experiments was performed to study the effect of the initial U^{4+} concentration on the metal uptake onto P(VP-MA-AO) resin. The results are illustrated in Fig. 6. The adsorption results show an initial rapid adsorption rate. The maximum capacity was reached to 152 mg/gm for U^{+4} onto P(VP-MA-AO) resin.

The functional groups of P(VP-MA-AO) resin as weak acids are dissociated at pH 5 and consequently, the adsorption of U^{+4} ion from the solution takes place. The surface of the adsorbent is expected to be negatively charged, which facilitate the adsorption of the positively charged uranium ions, consequently, the adsorption capacity of U^{4+} metal ions increases. The amidoxime groups on the adsorbent surface, also, increase the adsorption of (U^{4+}) metal ions [20].

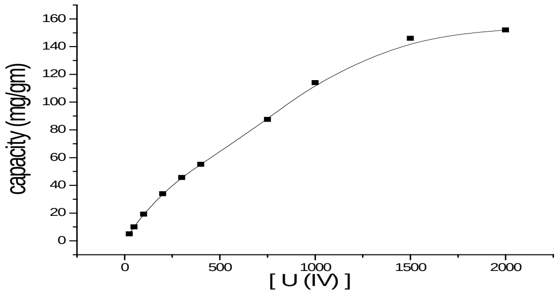

Fig. 6. Effect of initial U^{4+} metal ion concentration on the adsorption capacity onto P(VP-MA-AO) resin.

4. CONCLUSION

In this study, P(VP-MA-AN) resin was prepared by gamma irradiation induced grafting polymerization technique. The surface of polyacrylonitrile resin was modified through a simple functionalization process using 3% hydroxylamine solution in alkaline condition. The poly(amidoxime) resin possessed, -H2NC=NOH- function groups on the surface, which is responsible for the increase in the exchange capacity of the poly(amidoxime) resin. This structure was confirmed by the FTIR, TGA, surface area and pore volume analyzer and SEM micrographs. The characteristic data confirmed the grafting of poly(VP) remarkably alters the structure of the resin and indicate that conversion of acrylonitrile to amidoxime. The thermal stability of P(VP-MA-AO) is higher than that of P(VP-MA-AN). This may be due to the presence of AO function group. The application of P(VP-MA-AO) for sorption of La^{3+}, Ce^{3+}, Nd^{3+}, Eu^{3+} and U^{4+} metal ions was tested at different shaking time and pH. The results showed that P(VP-MA-AO) is highly selective for U^{4+} rather that lanthanide metal ions. The maximum adsorption capacity P(VP-

ISBN: 978-1-61804-325-2

MA-AO) toward U^{4+} reached to 152 mg/g at pH 4.

ACKNOWLEDGMENTS

This project was supported financially by the Science and Technology Development Fund (STDF), Egypt, Grant No 5021.

REFERENCES

[1] K , Uyama.Y,Kato and Y. Ikada ; Sakyo-Ku, Kyoto 606 , Japan ; Yoshito . Ikada , 2014.

[2] F.L. Buchholz, Graham, A.T. Modern Superabsorbent Polymer Technology, Wiley, New York, 1997.

[3] F.Vernon, Hydrometallurgy; Wiley: New York, 1979.

[4] B.L.Rives,; Maturana, H.A.; Campo, X.O.; Peric, I.N. Absorption behavior of Cu(II) and UO2 (II) ions on crosslinked poly[2,2-bis(acrylamido)acetic acid]. J. Appl. Polym. Sci. 1995, 58, 2201.

[5] E.A. Hegazy, El-Nagar, A.M.; Senna, M.M.; Zahran, A.H. Removal of Industrial Pollutants from Wastewater's by Graft Copolymers.International Conference on Hazardous Waste, Sources, Effects and Managements, Cairo, Egypt, December 12–16, 1998; 1347–1361.

[6] S. Cobianco, Lezzi, L.; Scotti, R. A spectroscopic study of Cu(II) complexes of chelating resins containing nitrogen and sulfur atoms in the chelating groups. React. Funct. Polym. 2000, 43, 7–16. Table 4. DSC parameters for copper loaded and unloaded resins. 199.6 221 218.6 235 1202 Senna, Siyam, and Mahdy Downloaded by [Universiteit Twente] at 08:15 14 November 2012

[7] A. Akelah, Functional Polymers and Their Applications; Akelah, A., Moet, A., Eds.; Chapman and Hall: U.K., 1990.

[8] T. Siyam, Ashour, A.H.; Youssef, H.A. Thermal and radiation chemical stabilities of some polymers after Cu (II) build-up. Polym. Int. 1999, 48, 799.

[9] A. K. Klimchuk, Martain .B .Hocking > and Stephen .L .; John wiley sons, inc , Doi . 10 . 1002 . 2001.

[10] T. Siyam, El-Naggar, I.M.; Aly, H.F. Nuclear and Hazardous Waste Management. Int. Topical Meeting (Spect. 96), Washington, USA, 1996; 66.

[11] T. Siyam, Gamma radiation induced preparation of some polyelectrolytes and its use for treatment of waste water. In Handbook of Engineering Polymeric Materials; Cherenisin off, N.P., Ed.; Marcel Dekker: New York, 1997; Vol. 9, 11. 8. Vernon, F. and Shah, T., Reactive Polymers, 1, 301, 1983.

[12] M. R. Lutfor, S. Silong,; W.M. Zin, M.Z. Ab Rahman, M.M. Ahmad, M. J. Haron, Eur Polym J 2000, 36, 2105.

[13] F. Vernon, and T. Shah, Reactive Polymers, 1, 301. 1983.

[14] A. Faraj Ab, A. Muataz At, B.A. Mansor, A. Nor Ib, Z. Mohamad Ab. Rahman and Wan. Z. W.Yunus; United Kingdom. Preparation and Characterization of Polyamidoxime Chelating Resin from Rubberwood Fibre-g-Polyacrylonitrile , 2009 Volume 27 Number 7 Multi-Science Publishing Co. Ltd. 5 Wates Way, Brentwood.

[15] Surface modification by graft polymerization Advanced Topics in Science and Technology in China 2009, pp 80-149

[16] S. F. Abo-Zahra, PhD. Thesis, Faculty of science, Ain shams university, Cairo, Egypt. 2012.

[17] S. Lowell, J. E. Shields, M.A. Thomas, Characterization of Porous Solids and Powders: Surface Area, Pore Size, and Density, Kluwer Academic Publishers, Dordrecht, The Netherlands, 2004.

[18] G. Socrates. Infrared and Raman Characteristic Group frequencies: Tables and Charts, 3rd ed., John Wiley & Sons, 2001.

[19] S.T. Dubinsky, G.I.S. Grader, G.E. Shter, M.S. Silverstein, Haifa 32000, Doi: 10.1016LJ. degradstab. 2004, 04, 009.

[20] S. Kyoichi, U. Kazuya, H. Takahiro, F. Shintaro, S. Takanobu and O. Jiro, American Institute of Chemical Engineers, DOI: 10.1002/aic.690340308. 17 JUN 2004.

[21] K. Joseph, B.Viswanathan, effect of surface area, pore volume and portical size. Indian journal of chemistry, 48A, 10,1378-1382, 2009.

Preparation of functionally graded mullite-zirconia composite using electrophoretic deposition (EPD)

HENK S. C. METSELAAR | AHMED S. MAHDI | ZAID A. SABRE
University of Malaya
Center of Research Advanced Materials
University of Malaya
Lembah Pantai, 50603 Kuala Lumpur
MALAYSIA
h.metselaar@um.edu.my | ahmedalanni80@yahoo.com | zaid_esaam@yahoo.co.uk

Abstract: The mechanical properties such as hardness and especially fracture toughness of present structural ceramics are not enough to permit design of high performance products. It is generally believed that further improvement of fracture toughness and hardness is only possible by making composites of ceramics with ceramic fiber. The wide-spread use of mullite–zirconia (MZ) composites is due to the fact that the zirconia dispersion in the mullite matrix improves the thermo-mechanical properties. The preparation process to produce the composite sample using electrophoretic deposition (EPD) which deals with three types of powder: α-alumina, silica and zirconia, mixed with the suspension based on 2-butanone, n-butylamine and polyvinyl butyral (PVB). Hardness and fracture toughness were measured using indentation methods on cross sections of the sample with applying two loads: 5 kg and 10 kg. Electron microscopy analysis (SEM) and X-ray diffraction (XRD) tests were used to examine the microstructure, composition and crystallization behavior of the deposits. The results were compared with mullite matrix properties to detect the enhancement in mechanical properties.

Key–Words: Electrophoretic deposition, ceramic matrix comppsites, mullite, zirconia, functionally graded material, mechanical properties

1 Introduction

During the last 25 years, tremendous progress has been made in the development and advancement of CMCs (ceramic matrix composites) under various research programs. CMCs find applications in advanced aerojet engines, stationary gas turbines for electrical power generation, heat exchangers, hot gas filters, radiant burners, heat treatment and materials growth furnaces, nuclear fusion reactors, automobiles, biological implants [1]. Mullite is one of the basic ceramic materials traditionally used for refractories and is considered an attractive selection for many industrial applications because of its high temperature mechanical properties. For the development of the structural materials, mullite has been delayed since it has a low fracture toughness and relatively low strength at room temperature compared with other engineering ceramics.

The extensive use of mullite/zirconia composites is due to the fact that the zirconia dispersion in the mullite matrix improves the thermo-mechanical properties, leading to toughness by transformation and microcracking[2].

Mullite/zirconia composites can be prepared using various methods: (1) Sintering of mullite powder and zirconia powder (2) Reaction sintering of alumina and zircon powders (3) Reaction sintering of alumina, silica and zirconia powders [2–3].

It has been reported that the optimum content of zirconia is ≈ 15 wt%[4].

In this research the third method was used and the fracture toughness and hardness are improved when zirconia reinforced mullite matrix using EPD technique to fabricate the composite sample.

2 Experimental

2.1 Materials

Commercially available (SiO_2 , 99.9% purity, Aldrich Chemical Company Inc., USA) and α-Al_2O_3 (99.95% purity, Alfa Aesar Chemical Company Inc, USA) powders were used as the starting materials representing the composition of mullite ($3Al_2O_3.2SiO_2$) and ZrO_2 (99.5% purity, Aldrich chemical company Inc, USA). 2-butanone (96% purity-Ajax), n-butylamine and PVB form the suspension medium.

2.2 Suspension preparation

A total of 50 g of mullite (α-Al_2O_3/SiO_2) with 60 wt% for α-Al_2O_3, 40 wt% for SiO_2 and 10 g ZrO_2 were prepared for the sample. These three powders were separately milled for 24 h in a planetary ball mill at 200 rpm using zirconia balls with 10 mm diameter as milling media with a ball to powder ratio of 5:1. Subsequently, the powders were milled horizontally in ethanol for 24 h using the same balls to break up hard agglomerates. The ethanol was evaporated in an oven at 90 °C for 48 h, then the powders were placed in a drying cabinet at 25 °C.

The present study used non-aqueous EPD which uses organic solvents which normally are less polar than water. A basic requirement for EPD is that suspended particles must have a high electrophoretic mobility that can be increased by adding dispersants, so n-butylamine was used as dispersant in this suspension, and polyvinylbutyral (PVB) as a binder. The suspension system used technical grade 2-butanone, n-butylamine and PVB as suspension medium. n-butylamine was used to disperse the metal oxide powders in 2-butanone and PVB.

The mixing proportion is 10 g of powder per 100 mL in the ratio of 60 wt% for α-Al_2O_3 and 40 wt% for SiO_2. All weight percentages of additives are taken from total powder weight. 2 wt% of PVB was added as well as 10 vol% of n-butylamine. PVB was first dissolved in 40 mL of 2-butanone and then added to the main suspension.

Three suspensions were prepared and mixed with the powders that were prepared previously in a glass container by a magnetic stirrer for 24 hour, and then the pH value was measured by a pH meter for each suspension. The suspensions were then put in glass containers and placed in an ultrasonic cleaning bath with a frequency of about 15 kHz to 45 kHz for 30 min. Table 1 indicates the suspension compositions.

2.3 Electrophoretic deposition and sintering

EPD is one of the colloidal processes that is used in ceramic production with many advantages: short formation time, simple equipment and the process can be applied to any shape depending on the electrode shape such as cylinder, spherical and flat plates.

The parameters affecting EPD, can be classified in two types, firstly those related to the suspension properties such as electrical conductivity, pH, particle size and size distribution, binder and dispersant concentration and ζ-potential, and secondly the parameters that relate to the EPD process, such as deposition time, the applied voltage, size and shape of the electrode and the distance between the electrodes.

The EPD cell in this study was described in [5] and consisted of two stainless steel electrodes with a surface area of 10 cm^2 (5.25 cm $\times$ 1.923 cm) and a thickness of 0.5 cm. The surfaces of the deposition electrodes were polished to facilitate the removal of the deposit and to avoid cracking of the deposit during drying. Furthermore, the edges of the deposition electrode were enclosed by tape in order to avoid deposition around the edges of the electrode. The electrodes were cleaned with acetone then vertically placed in a polytetrafluoroethylene (PTFE) vessel. PTFE was used in order to avoid deposition between suspension and vessel as PTFE is a non-conductive polymer. The PTFE container had a volume of 100 mL. The distance between the electrodes was fixed at 3 cm.

A DC voltage source, Apparatus Corporation, was used to apply the electric field. The source was capable of performing either as a constant current or as a constant voltage source. A voltage of 275 V was applied for 30 min. The suspensions were pumped through the deposition cell by peristaltic pumps. Peristaltic tubing with a diameter of 4 mm was used for the circulation system. The maximum and minimum feed rates were 4.25 $mL\,s^{-1}$ and 0.12 $mL\,s^{-1}$, respectively.

The total deposition time for composite material was 30 min. A magnetic stirrer was used to mix the suspension during all EPD steps. Initially suspension I, loaded with 100 $g\,L^{-1}$ mullite (silica and alumina), was poured in the deposition cell and circulating process continued between the deposition cell and the circulating beaker using pump 1 for 600 s, and then suspension II with 50 $g\,L^{-1}$ mullite and 50 $g\,L^{-1}$ ZrO_2 was added into the beaker of circulating suspension using pump 2 and was pumped through the deposition cell by means of pump 1 at a rate of 2.5 $mL\,s^{-1}$. The pump rate between deposition cell and circulating suspension was fixed throughout the deposition process.

Table 1: Compositions for 200 mL suspension

suspension	Mullite (g)		ZrO_2	2-butanone (mL)	n-butylamine (mL)	PVB (g)	pH at 25 °C
	α-Al_2O_3	SiO_2					
I	12	8	0	180	20	0.4	12.6
II	6	4	10	180	20	0.4	12.36
III	12	8	0	180	20	0.4	12.29

ISBN: 978-1-61804-325-2

After 1200 s of deposition, suspension III, with $100\,\mathrm{g\,L^{-1}}$ mullite was added to the circulating suspension by pump 2 at a rate of $0.4\,\mathrm{mL\,s^{-1}}$. After 300 s of deposition, the addition of the suspension was completed. During the subsequent step, the suspension was circulated for 300 s without any future additions, and during all the described steps, EPD was continued in the deposition cell. The powder deposits took place on the anode electrode due to the negative charge of the particles.

After EPD, the green bodies were dried in air for 48 h. Afterwards, the powder deposits were removed from the electrode. The green bodies were dried in an oven at 100 °C for 12 h in order to avoid cracking and preparation for sintering. The two main factors affecting sintering are sintering temperature and time. Pure oxide ceramics require relatively long time and high temperature because the diffusion proceeds in solid state. The green bodies obtained by the EPD were sintered in a chamber furnace, after the sample had dried; the sintering process took place at 1500 °C for 2 h. Fig. 1 shows the sample after EPD.

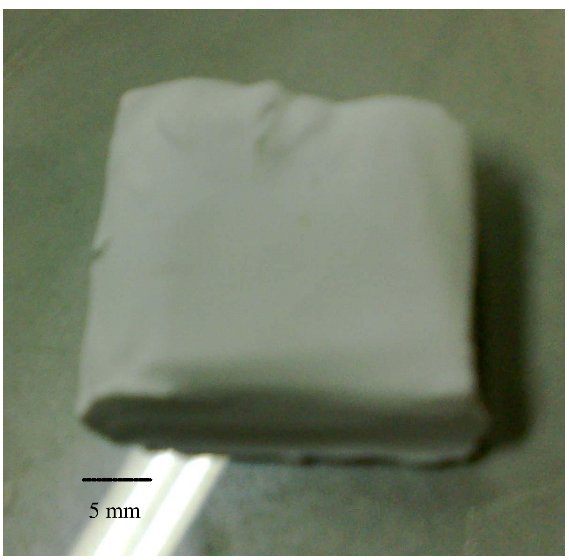

Figure 1: The sample after EPD

To provide time for the binder to burn out, the sample was heated at $3\,^{\circ}\mathrm{C\,min^{-1}}$ to 500 °C, held at 500 °C for 30 min and then heated to the final sintering temperature at a rate of $5\,^{\circ}\mathrm{C\,min^{-1}}$ and held at 1500 °C for 2 h and furnace cooled. To avoid and minimize the damage to the samples during sintering, the samples were placed on an alumina crucible. Length and width of sample were measured before and after sintering to determine linear shrinkage.

2.4 Preparation of samples

The sintered samples were cross-sectioned on a diamond cutter using sufficient flow of non-oily coolant. The surfaces of the sintered samples were ground with emery paper of 400, 600, 800, 1200 and 1500 grit and polished to a near mirror finish. The ground samples were polished with cotton to reduce scratches on the surface, and to make a mirror surface finish with minimum scratches. After grinding and polishing, the samples were thermally etched at 1350 °C for 30 min.

Finally, the samples were moulded in epoxy to allow easier handling during the hardness tests.

2.5 hardness and toughness test

The Vickers hardness was determined on a Mitutoyo, AVK-C2. The test force is maintained for 15 s and 5 kg and 10 kg loads were applied by the indenter to the sample's cross-sectioned surface to obtain a hardness profile.

The indentation fracture toughness, K_{Ic} was calculated from the length of the cracks induced by the same indent using the Anstis formula, as shown in eq. 1[6].

$$K_{Ic} = \eta\sqrt{\frac{E}{H}}\frac{F}{C^{\frac{3}{2}}} \tag{1}$$

Where η is a geometric factor, estimated at 0.016, E the Young's modulus, H is the hardness, F is the indentation load, and C is the indentation radial crack half length of the cracks parallel to the layers at the surface. Since the E value for the composite is not known $\eta\sqrt{\frac{E}{H}}$ is estimated to be 0.062 which is a suitable value for mullite ceramics.

3 Results and Discussion

3.1 Density and porosity

The sample deposit was smooth and an approximately flat surface was obtained. Exactly how roughness is affected by the suspension stability is unclear but one can assume that the convective motion, powder amounts and applied voltage play important roles. The dimension of the green deposit and shrinkage of the deposit with dimensions after sintering are shown in Table 2.

It is observed that the shrinkage perpendicular to the deposition surface is significantly higher than parallel to the deposition surface.

Density measurements were taken according to the Archimedes method. The result is shown in Table 3. The porosity may be caused by exaggerated grain growth.

ISBN: 978-1-61804-325-2

Table 2: Dimensions and shrinkage of the deposits before and after sintering

	length (mm)	width (mm)	thickness (mm)
Green	32.25	30.62	8.18
Sintered	30.45	29.28	7.15
Shrinkage (%)	5.6	4.4	12.6

Table 3: Theoretical and sintered density and open porosity of the sample.

Theoretical density ($g\,cm^{-3}$)	Sintered density ($g\,cm^{-3}$)	Open porosity (%)
3.50	3.067	12.4

The level of porosity would decrease with increasing sintering temperature, but this might also lead to cracking due to the mismatch in coefficients of thermal expansion between the constituents of the composite. The porosity and the grain size affect hardness and fracture toughness of the product.

3.2 Microstructure

The microstructures of the sample were analysed on SEM. Mullite phase commences to appear in temperature range 1400 °C to 1500 °C during sintering process[7] when alumina (Al_2O_3) and silica (SiO_2) powders combine in solid state reaction to form mullite phase. The microstructure was observed after thermal etching.

A highly porous microstructure with small pores homogeneously distributed was observed after sintering at 1500 °C, due to the diffusion processes in zirconia, silica, and alumina grains. Sintering at 1500 °C produced important changes in the microstructure. A dense matrix composed of grey and black areas (mullite and alumina, respectively) in zone (A), white grains (tetragonal zirconia) were observed in zone (B), mullite grains were well developed in the dense matrix and some of grains showed a change from rounded to slightly elongated shape and it was difficult to detect zirconia grain boundaries in zone (C). The SEM images show that some microcracks appear clearly due to the difference in average particles size, 0.3 μm, 0.5 μm and 0.5 μm for alumina, silica and zirconia respectively and the mismatch of the coefficient of thermal expansion. The porosity is observed while two types of grains were noticeable dispersed grains (white) of zirconia, and a mullite matrix (gray) in zone (D) as indicated in Fig. 2.

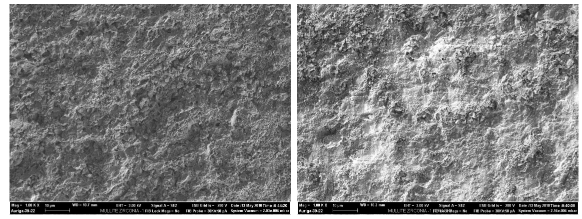

(a) Mullite (gray) from the edge of the sample surface.

(b) Mullite (gray) and zirconia (white) in center zone of the sample from the edge.

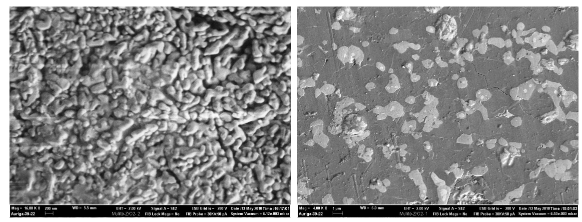

(c) Dense micrograph for central region in the middle of the sample

(d) Microcracks appear in central zone of the sample

Figure 2: SEM images of the microstructure

3.3 XRD

XRD analysis showed that the formation of mullite was essentially complete with omly traces of residual alumina or silica detected. Furthermore, due to the presence of yttria as well as the containing effect of the matrix on the submicrometer grains, the zirconia was present in the tetragonal phase, which is beneficial for transformation toughening. The addition of zirconia caused rapid mullite formation in the presence of the Y_2O_3 that is used to stabilise the zirconia [8].

3.4 Hardness and toughness

The hardness and toughness were measured across the cross section at regular intervals. The results are depicted in Figs. 3 and 4 for hardness and toughness, respecively.

As expected the material close to the surfaces was harder than the core material due traces of alumina due to incomplete reaction between alumina with silica to form mullite phase. The alumina traces affect hardness and other mechanical properties of composite, as alumina is harder than zirconia , ($H_{Al_2O_3} = 18\,GPa > H_{mullite} \approx H_{ZrO_2} = 10\,GPa$ to $15\,GPa$) [9]. Besides this, the coefficient of thermal expansion for zirconia is larger than that of mullite (10.3×10^{-6} *vs* 5.3×10^{-6}), causing the zirconia-rich inner layer to be under tension and the surface layer to be under compression[5]. Therefore in this case the outer layers are more enduring than the inner layer against

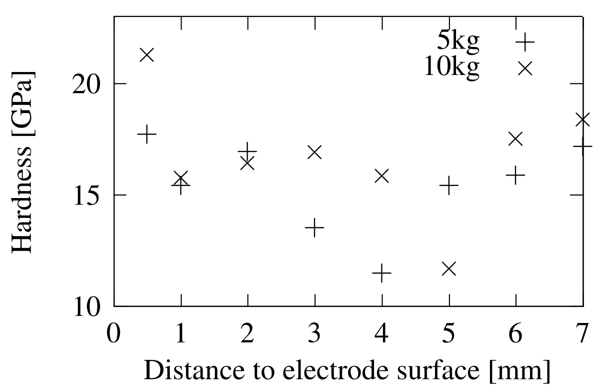

Figure 3: Vickers hardness measured on the cross-section at two different indentation loads

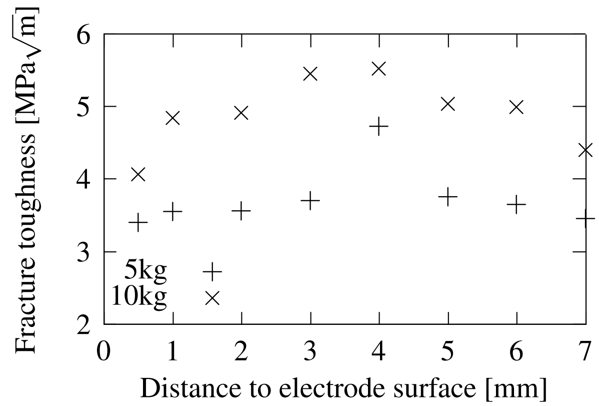

Figure 4: Fracture toughness measured on the cross-section at two different indentation loads

wear and stress.

The lowest hardness was found in the core of the sample and was around 11 GPa for both indentation loads. This is slightly lower than the literature value for mullite, perhaps due to porosity or microcracking. The highest measured hardness was 21.3 GPa.

The indentation load is critical in the measure of hardness and fracture toughness using the indentation method. The amount of load could affect the indentation size and the crack length, being dependent of the sample dimension and the microstructure of the material.

The presence of zirconia promoted the densification through a marked reduction in porosity by filling of interparticle voids which was considered to be the important contributor for the increase in strength and K_{Ic}. The major improvement in K_{Ic} in the mullite/zirconia composite is also due to the presence of microcracking and crack-closure compressive strains as a result of transformation toughening. This is because of thermal contraction mismatch between the phases and volume expansion associated with zirconia transformation and mullite formation.

The fracture toughness for the pure components is $K_{\mathrm{Ic,\,Al_2O_3}} = 1.5\,\mathrm{MPa}$ to $4.5\,\mathrm{MPa}\sqrt{\mathrm{m}}$, $K_{\mathrm{Ic,mullite}} = 2.6\,\mathrm{MPa}\sqrt{\mathrm{m}}$ and $K_{\mathrm{Ic,ZrO_2}} = 14\,\mathrm{MPa}\sqrt{\mathrm{m}}$. The highest measured fracture toughness was $5.5\,\mathrm{MPa}\sqrt{\mathrm{m}}$, while the lowest value was $3.4\,\mathrm{MPa}\sqrt{\mathrm{m}}$. Both are significantly higher than the toughness of pure mullite.

4 Conclusions

A functionally graded zirconia/mullite composite was prepared from alumina, silica and partially stabilised zirconia by EPD with single phase mullite near the surface and composite containing $\approx 15\%$ zirconia in the core.

The formation of mullite from alumina and zirconia was essentially complete, with traces of unreacted alumina increasing the surface hardness to 21.3 GPa whereas the zirconia in the core increased the fracture toughness to $5.5\,\mathrm{MPa}\sqrt{\mathrm{m}}$. However, the hardness in the core layer was lower, perhaps due to the occurrence of micro-cracking.

It was found that the measurement of hardness and toughness depends critically on the applied load during testing.

Acknowledgements: Financial support from the University of Malaya in the form of P0067/2010A and P0068/2010A is gratefully acknowledged.

References:

[1] N. P. Bansal, *Handbook of Ceramic Composites,* Kluwer Academic Publishers, USA 2005

[2] N. Rendtorff, L. Garrido and E. Aglietti, Mullite-zirconia-zircon composites: Properties and thermal shock resistance, *Ceram. Int.* 35, 2009, pp. 779–786.

[3] T. Koyama, S. Hayashi, A. Yasumori, K. Okada, M. Schmucker and H. Schneider, Microstructure and Mechanical Properties of Mullite/Zirconia Composites Prepared from Alumina and Zircon under Various Firing Conditions, *J. Eur. Ceram. Soc.* 16, 1996, pp. 231–237.

[4] Liang Shu-quan, Zhong Jie, Tan Xiao-ping and Tang Yan, Mechanical properties and structure of zirconia-mullite ceramics prepared by in-situ controlled crystallization of Si-Al-Zr-O amorphous bulk, *Trans. Nonferrous Met.* 18, 2008, pp. 799–803.

[5] M. Mehrali, H. Wakily and I. H. S. C. Metselaar, Residual stress and mechanical properties

of Al_2O_3/ZrO_2 functionally graded material prepared by EPD from 2-butanone based suspension, *Adv. Appl. Ceram.* in press.

[6] G. R. Anstis, P. Chantikul, B. R. Lawn and D. B. Marshall, A critical evaluation of indentation techniques for measuring fracture toughness, Part I:direct crack measurements, *J. Am. Ceram. Soc.* 64, 1981, pp. 533–538.

[7] C. Aksel, The influence of zircon on the mechanical properties and thermal shock behaviour of slip-cast alumina–mullite refractories, *Mater. Lett.* 57, 2002, pp. 992–997.

[8] M. K. Haldar, T. K. Pal and G. Banerjee, Preparation and properties of Y_2O_3 containing zirconia–mullite composites derived from sillimanite beach sand, *Ceram. Int.* 28, 2002, pp. 311–318.

[9] E. F. Aglietti, L. Martorello, M. A. Camerucci and A. L. Cavalieri, Hardness and fracture toughness of mullite–zirconia composites obtained by slip casting, *Mater. Sci. Eng. A-Struct.* 419, 2006, pp. 290–296.

The Effect Of The Modern Structure Systems Upon The Space Perception

Rabia KÖSE DOĞAN[1]

[1] Faculty of Fine Arts, Department of Interior Architecture and Environmental Design, Selcuk University, Konya, Turkey.

ABSTRACT

In the 20th Century the technological developments also caused the change in the building systems as in every area of life. The plate systems, the shell systems, the space-cage systems, structure systems, the pneumatic systems and the cabled systems defined as the modern structure systems were also included into the concentration system known as the traditional structure system and the system developed following it. The place's perception also changes together with the changed structure systems. In this study the effect of the modern structure systems upon the interior place and its perception upon human shall be evaluated via the survey study with the determined bicuspid adjective couples. As a result, the study shall direct the pragmatists by analyzing the effects left as the place perception by the modern structure systems upon the human.

Key Words: Structure Systems, Engineering, Space, Perception.

INTRODUCTION

The development of the developing structure system solutions and the development of the construction materials in the engineering progress in parallel to this case while a formal anxiety is being searched in the aesthetic concept, in the architecture comprehension changed at the beginnings of 20th Century. The modern structure systems develop in addition to teh concentration and skeleton systems. These systems are separated into 6 groups as the folded plate system, the shell systems, the space-cage systems, membrane systems, the pneumatic systems and the cabled systems. Every carrying system has the different solutions and the different perceptions for the place in it.

It is seen by examining the building's development that the new structure designs' building weight decreased and minimized the building material in the architectural history [1].

Innovation in architecture represents developments in specifications of materials and functionality that is provided to the architect. Function of material and to discover innovative methods in its application require creative approach [2]. As for the architectural design process, it is the mass established by deforming and fictionalizing, sites, surfaces, and an attempt becoming objective with structural elements. As a result, once looked at theproduct, we could see the architectural design as fictionalization, building of structure, and an action of formation [3].

As how important designing is, the application of a designed project, sturdy construction, and a structure that remains tall are as important as it is [4]. Differences exist between physical structure and perceptual structure in modern-day buildings [5]. While the physical structure provides carrier system to stand tall, as for the perceptual structure, the real carrier that varies from the system leads to an optical illusion.

The changes in the engineering field affects the architectural design process directly, affect the place's main elements such as ceiling, wall, flooring and also the design decisions depending on it directly besides standing besides sustenance of the building.

1. Space Components:

It is important to examine the place by separating it into its components limiting it in order to understand the three dimensional concept better. The units defining the architectural place are examined as the horizontal and vertical units in general in the scope of Euclid's geometry. The horizontal units can be classified such as the flooring, the ceiling, the beam; the vertical units can be classified such as the walls, the columns, the joinery dividers. The columns, the beams and the floorings defining the place are also the structural units forming the structure system [6].

He emphasised in ''Ten Books Upon Architecture'' named famous work by Vitruvius that it is necessary to think of the security (durability) , function (convenience) and aesthetic (beauty) scales together [7]. The human started to develop the structure systems and units even from the first times when he had the skill to design the events in his mind. For example it is one of the greatest building problems that the interval between the walls of a place or between the carrying units is passed/exceeded. In the first times the new solutions were produced with the building units such as the lintel, the arch, the vault, the dome by covering of the wooden materials onto the upper parts of the place and particularly by using the stone-brick materials. The new construction methods were developed with the power of the design, the architecture and the engineering [8].

It shall be possible with a good work and a compatible team work among the experts related to the subject to be able to perform the complex processes such as building together [9]. The building has the usage aim and function firstly. It is important to design the building in conformity with this aim in that regard. Also another condition of that the building is useable is that it is built with the materials appropriate for the aim [4].

2. Classifying of the Structure Systems

2.1. Concentration Systems: The most specific characteristics of the concentration systems are that they are formed by superimposing the carrying units by the result of agglomeration and by integrating them with a connective substance. The stone is a material durable against pressure tension used since the old ages until now. In the accumulation system the carrying components and the components dividing the place or covering the structure clashes with each other. As it is a building system enabling to pass through the wide spaces by gathering the small dimensional building materials such as the arch, stone-brick thought as a curve beam, it might also have an aesthetic image characteristic in terms of the place perception [10].

2.2. Skeleton Systems: It is called the skeleton (carcase) systems to the systems where the components supporting the carrying system with the components classifying the structure. We can exemplify the reinforced concrete, wooden and steel systems as the most common examples for the skeleton system. The spaces that cannot be passed with the accumulation system could be passed with the skeleton system. The components formed the structure in the skeleton system are separated into two parts as the carrier one and the carried one. These are the columns and the beams.

2.3. Modern Systems (Superficial Structure Systems): The folded plates, shells, the space cage systems, membranes, the pneumatic and cabled systems are included in this group. They generally have the geometers formed by the curve and folded surfaces. The wall, flooring, roof are not discriminated in the whole of the main structure system. These components are united structurally and functionally by the integration of the structure system [8].

1. Folded Plate Systems: The load carrying way of the folded plates formed by the superfacial continuously carrier components is likened to the plate and screen works in terms of the static principles. The plates are the planar carrier components carrying the loads that are big in comparison to its two dimensions' thickness and affecting its surfaces perpendicularly to the vertical structure components by bending.

2. Shell Systems: Another modern structure system where the structural advantages ensured by the surface's shape are benefitted from is the thin shells that are made of the curve superficial components. The shell system is the single or double curvature volumetric structure systems resisting with the axial powers tangential to the middle line of the shell against the external powers, that process the carrying and covering at the same time, its two dimensions are much bigger than its thickness.

3. Space Cage Systems: The space cage systems are the three dimensional structure systems consisting of the smooth bars and the jointed knot points. As all of its components that were made in order to cover the very wide spaces are connected to each other, it is in the three dimensional cage shapes working in a whole in every direction. These systems are more effective and economic in comparison to the structure systems dominated by the beding case by being affected by only the pressure and pulling powers [10].

4. Membrane Systems: Thee tents are the best examples for membranes. Its material is used as a superficial carrier factor only trying to pull and does not have any important stable bending, that is flexible/bendable [8].

5. Pneumatic Systems: As the membrane is a surface uniting both the covering and also carrying duties in the group also defined as the closed membranes, it forms a completely closed volume. The system's carry is allowed by giving pre stress to the membrane cover with the pressure difference created within a closed volume.

6. Cabled Systems: The cable bunches and the steel ropes shortly defined as cable are the components formed by collecting and uniting many of the units as thin, long and lineal as the fibre or the wire according to the construction characteristics. They are this system's advantages that the cable systems are light, the cables are high resistant, the components trying to pull do not have any flexion problem and therefore the material can be made as thin as possible [10].

MATERIAL and METHOD:

The impression left on them was measured by the survey method by giving double-edged 5 different adjective couples, on the trial group of 30 persons, by selecting the photographs of the fronts and the interior places of the structures took important places in the literature, belonging to each one of the systems collected in 6 groups in order to measure the modern structure systems' affect in place and perception upon the human. The trial group was not informed about the places, only the structure system's kind was determined. The visuals were showed in company with the slide. The adjective couples were determined as Extraordinary-Ordinary, Warm-Cold, Dynamic-Static, Emotional-Rational, Persistent-Disappearing. The proportional approach was determined upon the adjective couples given according to the surveys' results. As the values closed to the top and bottom end, of the adjective couples were determined according to the rating system of 100%, the comparison was made.

Definitions of the Adjective Couples:

1.Extraordinary: Marvelous, that is different than its similar ones, the accustomed one. **Ordinary:** Any, coarse, common, accustomed.

2.Warm: That its first affects stir the liveability and the belonging. **Cold:**That stirring up the negative disquieting thoughts.

3.Dynamic: Alive, effective, movable, changeable any moment. **Stagnant:** Not alive, dull, immovable.

4.Emotional: That the emotion dominates, the emotion affects extremely. **Rationalist:** That agrees with rationalism prone to logic, mentalist, rational.

5.Persistent: Sign, clue, indication remained in back from/after any event or any case. **Disappearing:** That is recessive, not left any specific effect.

Selections of Building: Yokohama International Terminal-Japan as the sample of the folded plate systems, Sydney Opera Building-Australia as the sample of the shell systems, Metropolis Umbrella-Spain as the sample of the space cage systems, Denver International Air Terminal-USA as the sample of the membrane systems, Soap Bubble Swimming Pool-China as the sample of the pneumatic systems and Millennium Dom-England as the sample of the cabled systems were selected/elected. The sample of the structure that is mostly common in literature, of the elected samples was taken in the scope of the structure system.

1. Plate Systems

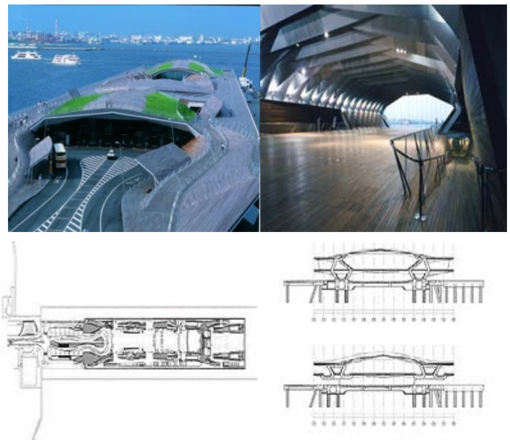

Figure 1.2.3.4. Yokohama International Terminal-Japan View, Plan, Section [11-12]

Adjective	Ratios (%)	Adjective	Ratios (%)
Extraordinary	90	Ordinary	10
Warm	10	Cold	90
Dynamic	76.66	Stagnant	13.33
Emotional	---	Rationalist	100
Persistent	93.33	Disappearing	6.66

2. Shell Systems

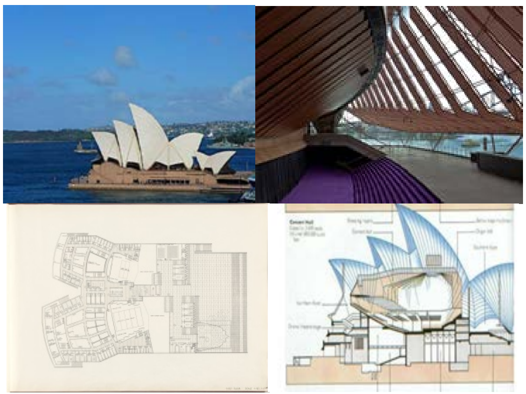

Figure 5.6.7.8. Sydney Opera Building-Australia View, Plan, Section [13-14-15-16]

Adjective	Ratios (%)	Adjective	Ratios (%)
Extraordinary	96.66	Ordinary	3.33
Warm	90	Cold	10
Dynamic	90	Stagnant	10
Emotional	40	Rationalist	60
Persistent	100	Disappearing	----

3. Space Cage Systems

Figure 9.10.11.12. Metropolis Umbrella-Spain View, Plan, Section [17-18-19]

Adjective	Ratios (%)	Adjective	Ratios (%)
Extraordinary	100	Ordinary	---
Warm	70	Cold	30
Dynamic	93.33	Stagnant	6.66
Emotional	13.33	Rationalist	86.66
Persistent	100	Disappearing	----

4. Membrane Systems

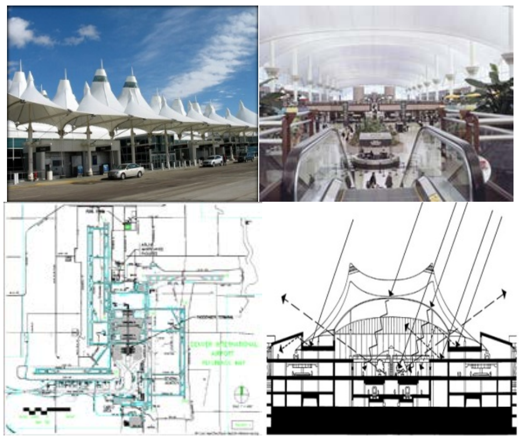

Figure 13.14.15.16. Denver International Air Terminal-USA View, Plan, Section [20-21-22]

Adjective	Ratios (%)	Adjective	Ratios (%)
Extraordinary	---	Ordinary	100
Warm	10	Cold	90
Dynamic	23.33	Stagnant	76.66

ISBN: 978-1-61804-325-2

Emotional	----	Rationalist	100
Persistent	----	Disappearing	100

5. Pneumatic Systems

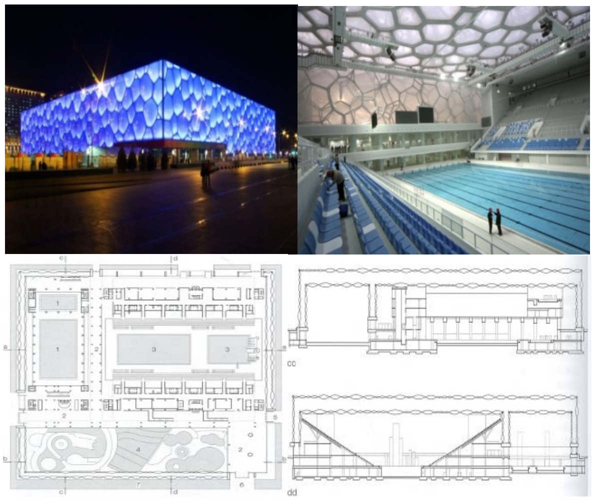

Figure 17.18.19.20. Soap Bubble Swimming Pool-China
View, Plan, Section [23]

Adjective	Ratios (%)	Adjective	Ratios (%)
Extraordinary	93.33	Ordinary	**6.66**
Warm	93.33	Cold	**6.66**
Dynamic	96.66	Stagnant	**3.33**
Emotional	10	Rationalist	**90**
Persistent	100	Disappearing	**---**

6. Cabled Systems

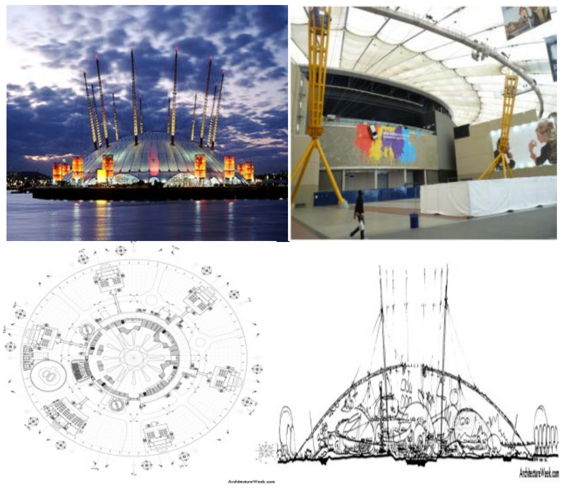

Figure 21.22.23.24. Millennium Dom-England
View, Plan, Section [24-25-26]

Adjective	Ratios (%)	Adjective	Ratios (%)
Extraordinary	93.33	Ordinary	**6.66**
Warm	86.66	Cold	**13.33**
Dynamic	93.33	Stagnant	**6.66**
Emotional	16.66	Rationalist	**83.33**
Persistent	90	Disappearing	**10**

EVALUATION:

The impressions left on the human by the modern structure systems by the result of the survey work performed were rated according to the slices of 100%. It was concluded that the folded plate systems were extraordinary, cold, dynamic, rationalist and persistent. It was seen that the shell systems were extraordinary, warm, dynamic, rationalist and persistent. The space cage system is extraordinary, warm, dynamic, rationalist and persistent. It came up that the membrane systems had the ordinary, cold, rational, disappearing feelings. It was determined that the pneumatic systems were extraordinary, warm, dynamic, rationalist and persistent. The cabled systems are in the extraordinary, warm, dynamic, rational and persistent case.

It came up that the membrane systems were ordinary, the folded, shell, space cage, pneumatic and cabled systems were extraordinary; the folded plate and membrane systems left a cold impression but however the shell, space cage, pneumatic and cabled systems left a warm impression, the folded plate, shell, space cage, pneumatic and cabled systems were dynamic despite the membrane system was static, all modern structure systems were rational and the membrane systems were disappearing, the folded, shell, space cage, pneumatic and cabled systems were persistent when we compared the modern structure systems to each other.

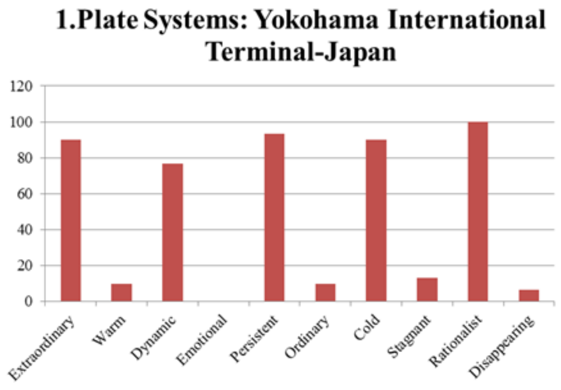

Figure 25. Plate Systems Graph

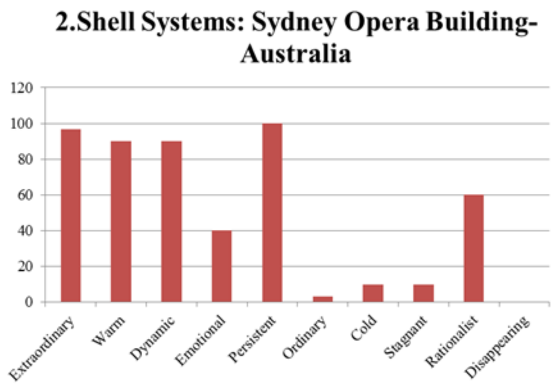

Figure 26. Shell Systems Graph

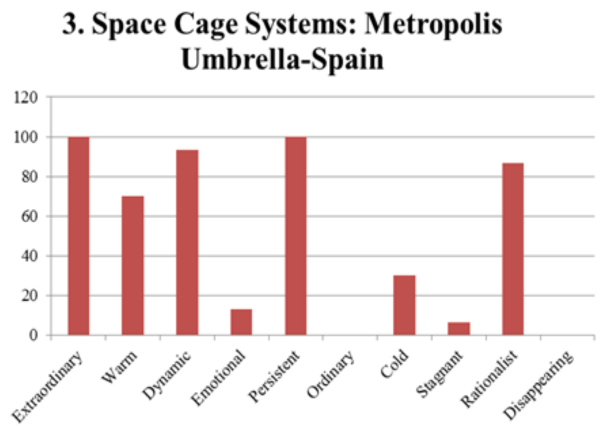

Figure 27. Space Cage Systems Graph

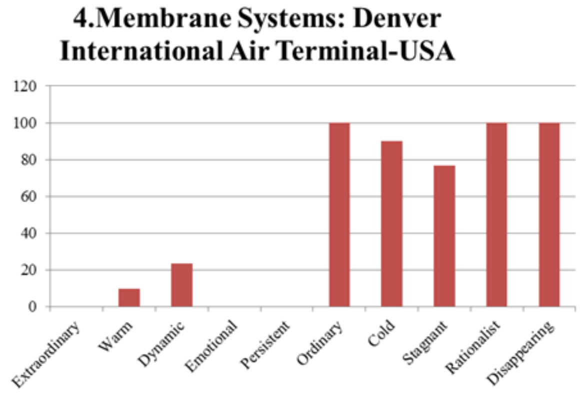

Figure 28. Membrane Systems Graph

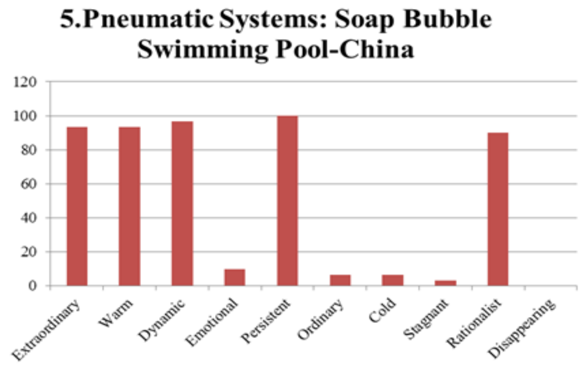

Figure 29. Pneumatic Systems Graph

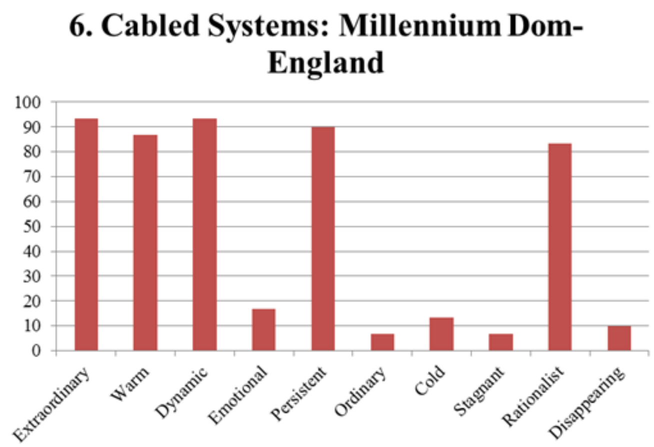

Figure 30. Cabled Systems Graph

ISBN: 978-1-61804-325-2

RESULTS:

It came up that the modern structure systems had an extraordinary set up in the slice of 83.34%, left a warm impression on the human in the slice of 66,66%, was dynamic in the slice of 83.34, 100% was rational, the slice of 83.34% was persistent in the meaning of the engineering, architecture and place arrangement.

This study gave the user's evaluation depending on his/her place perception of the system to be selected in conformity with the structure's function in the selection of the structure system that will be used in the wide spacious areas. The user measured the affect of the modern structure systems on the user. This research's result shall direct to the implementers/practitioners. It is the sample that the engineer, the architecture and the interior architect should be in interaction. The study shall also guide the young researchers.

REFERENCES:

[1]. Çamlıbel, N., Çağdaş Gelişmelerin Mimari Strüktüre Etkisi, Journal of İstanbul Kültür University, İstanbul, 2003/3.

[2]. Farrelly, L., Yapım+Malzeme, Literatür Yayıncılık, İstanbul, 2012.

[3]. Onat, E., Mimarlığa Yolculuk, Yem Yayıncılık, İstanbul, 2006.

[4]. Küçük, B., Strüktür Bilgisine Giriş, Aybil Yayınları, Konya, 2012.

[5]. Roth, L., Mimarlığın Öyküsü, Kabalcı Yayınları, İstanbul, 2000.

[6]. Soydeğiş S., Mimarlık, Düşünmek, Düşlemek, Yem Yayıncılık, İstanbul, 2006.

[7]. Vanlı, Ş., (Vitruvius), Mimarlık Üzerine On Kitap, Yem Yayıncılık, İstanbul, 1993.

[8]. Türkçü, Ç., Yapım İlkeler-Malzemeler-Yöntemler-Çözümler, Birsen Yayınları, İstanbul, 2004.

[9]. Çoşkun, Kıymaz, Yapı Dergisi, Sayı:208, Yem Yayıncılık, İstanbul, 2007.

[10]. Gündoğ, G., Çağdaş Strüktür Sistemlerin Mekana Etkileri, Yüksek Lisans Tezi, 2007

[11].http://www.archdaily.com/554132/ad-classics-yokohama-international-passenger-terminal-foreign-office-architects-foa/

[12].http://www.arcspace.com/features/foreign-office-architects/yokohama-international-port-terminal/

[13].http://www.sydneycloseup.com/sydney-opera-house-history.html

[14].http://modernistarchitecture.blogspot.com.tr/2013/08/sydney-opera-house.html

[15].http://biddecor.blogspot.com.tr/2015/03/sydney-opera-house-floor-plans.html

[16].http://5osa.tistory.com/entry/J%C3%B8rn-Utzon-Sydney-Opera-House

[17].http://www.mimarlikbankasi.com/mimar/mimarlik/medya/haber/metropol-parasol-2

[18].http://www.yapi.com.tr/haberler/strongmetropol-parasol-metropol-semsiyesi-strong_96171.html

[19].http://www.arcspace.com/features/j-mayer-h-architects/metropol-parasol

[20].http://www.aeropuertos.net/aeropuerto-internacional-de-denver/

[21].http://www.architonic.com/aisht/denver-international-airport-fentress-architects/5100647

[22].http://www.directionsmag.com/images/articles/121_facilities_big.gif

[23].https://moreaedesign.wordpress.com/2010/09/13/more-about-watercube-%E2%80%93-beijing-china/

[24].http://www.rshp.com/work/all_projects/millennium_experience

[25].http://news-in-olympics 2012.blogspot.com.tr/2011/08/londons-dome.html

[26].http://www.architectureweek.com/cgi-bin/awimage?dir=2007/0404&article=news_1-2.html&image=13426_image_9.jpg

Authors Index